CRANFIELD UNIVERSITY

Dhinesh Thanganadar

Performance Analysis of Indirect sCO_2 Cycle Integrated with Different Heat Sources and Thermal Energy Storage

SCHOOL OF WATER, ENERGY, AND ENVIRONMENT
Ph.D. in Energy and Power

Ph.D.
Academic Year: 2019 - 2020

Supervisor: Dr Kumar Patchigolla
Associate Supervisor: Dr Faisal Asfand
September 2020

CRANFIELD UNIVERSITY

SCHOOL OF WATER, ENERGY, AND ENVIRONMENT
Ph.D. in Energy and Power

Ph.D.

Academic Year 2019 - 2020

Dhinesh Thanganadar

Performance Analysis of Indirect sCO_2 Cycle Integrated with Different Heat Sources and Thermal Energy Storage

Supervisor: Dr Kumar Patchigolla
Associate Supervisor: Dr Faisal Asfand
September 2020

This thesis is submitted in partial fulfilment of the requirements for the degree of Ph.D.

ABSTRACT

Increasing the efficiency of the power conversion cycles are crucial in order to reducing global carbon emission. Supercritical carbon dioxide (sCO_2) cycles can achieve higher efficiency than steam Rankine cycle at higher turbine inlet temperatures (>550 °C) with a compact plant footprint (up to tenfold).

This PhD study focused on investigating the thermodynamic performance of sCO_2 cycle configurations for three different heat sources: coal-fired, natural gas and concentrated solar power (CSP) plants. The proposed configurations have not only increased the efficiency compared with the state-of-the-art power cycle but also shows cost reduction potential for some heat sources.

- For natural gas based combined cycle power plant, the efficiency of the novel sCO_2 cascade cycle has increased by 1.4%pts compared to a triple-pressure steam Rankine cycle (base case efficiency is 58.4% LHV) for a commercial SGT5-4000F gas turbine. The CO_2 emission is reduced by 26,774 tons/year (2.3%).
- The proposed novel sCO_2 cycle configuration increases the efficiency of coal-fired power plant has increased by 3-4%pts compared to the state-of-the-art NETL baseline steam Rankine cycle (B12A efficiency is 40.7% HHV). This corresponds to a reduction of 6-8% in the cost of electricity, however, this falls within the uncertainty range of the equipment cost functions. The increased efficiency reduces the CO_2 emission by 204,031 tons/year (6.4% reduction).
- For a concentrated solar power plant, the sCO_2 cycle efficiency is increased by 3.8-7%pts compared to steam Rankine cycles and the novel proposed cycle can reduce the capital cost up to 10.8% compared to the state-of-the-art sCO_2 recompression cycle, which is equivalent to a reduction of about 12-26% compared with the steam Rankine cycle.

The performance of sCO_2 cycle is more sensitive to the variations in ambient temperature. In a CSP plant, operating the plant at high ambient temperatures, not only penalises the performance of the sCO_2 cycle (i.e., net power output and efficiency), but also the sensible heat storage capacity. For instance, the storage capacity reduces by 25% for a 13 °C increase of the ambient temperature from

its design value (i.e., 42°C) when maximising the power cycle efficiency. Therefore, these effect on the levelised cost of electricity is investigated in detail, which guides the effect of different plant operating modes.

The transient heat exchanger model informs that the first-order characteristic time of the recuperators is faster (20-90 secs) when using compact heat exchangers, indicating the potential of fast load ramping.

Keywords:

sCO_2 cycle, combined cycle, coal-fired plant, CSP, thermal energy storage, multi-objective optimisation, techno-economic

DECLARATION

I declare that no portion of the work referred to in the thesis has been submitted in support of an application for another degree or qualification of this or any other university or another institute of learning.

The 3 published journal papers, and the 1 submitted draft journal papers contained in this thesis were and will be published by the Elsevier which allows reproducing the entire published material in the PhD Thesis.

Elsevier[1]: "*Theses and dissertations which contain embedded PJAs as part of the formal submission can be posted publicly by the awarding institution with DOI links back to the formal publications on ScienceDirect.*"

[1]Elsevier (2020), Article sharing, Elsevier B.V., available online: https://www.elsevier.com/about/policies/sharing (last accessed: 21/10/2020)

ACKNOWLEDGEMENTS

First of all, I wish to acknowledge the Biomass and Fossil Fuel Research Alliance (BF2RA), UK for the financial support under grant 26 – "sCO_2 for efficient power generation". I also wish to extend the acknowledgement to Cranfield Industrial partnership PhD program for financial support. Likewise, I would like to acknowledge the Erasmus+ mobility grant 2018/19 and UKCCSRC ECR Collaboration Fund 2019 as they helped in establishing the collaboration link with Prof Sergio Camporeale, and Dr Francesco Fornarelli, Politecnico di Bari, Italy and Prof François Maréchal, Industrial Process and Energy Systems Engineering (IPESE), École polytechnique fédérale de Lausanne (EPFL), Switzerland as part of this PhD programme.

I would like to express my gratitude to Dr Kumar Patchigolla for giving me the opportunity to carry out this research project. To Dr Faisal Asfand, thank you for your valuable support. I also express my gratitude to Prof Sergio Camporeale and Dr Francesco Fornarelli, Politecnico di Bari, Italy for your counsel and for the opportunity to work with you. I also express my thanks to Prof François Maréchal for inspiring me and for the guidance you offered during my visit. My gratitude to Doosan Babcock for the technical support given during the PhD.

Of course, this work would have not been possible without the patience and sacrifice of my beloved wife, Jyoti and my cherished family, therefore, I would like to dedicate this PhD thesis them. My gratitude to all my good-hearted friends and former colleagues, who supported and motivated throughout my PhD journey.

Last, but not least, I would like to recognise the support from all the friends in B40, Cranfield I have had a chance to interact with. Your company has made my PhD journey in Cranfield more pleasant. In particular, I would like to thank Jon Gillard, Hisham, and Kalu for their critical support and proofreading my papers. I also would like to extend my thanks to Mr David Dewis, Principal Consultant at Peregrine Turbine Technologies® for providing constructive feedback relevant to this project.

TABLE OF CONTENTS

LIST OF FIGURES

LIST OF TABLES

LIST OF ABBREVIATIONS

CCPP	Combined Cycle Power Plant
CIT	Compressor Inlet Temperature
COE	Cost of Electricity
CSP	Concentrated Solar Power
GA	Genetic Algorithm
GT	Gas Turbine
HRSG	Heat Recovery Steam Generator
HT	High Temperature
HTR	High Temperature Recuperator
IC	Intercooler
LCOE	Levelised Cost of Electricity
LMTD	Log Mean Temperature Difference
LT	Low Temperature
LTR	Low Temperature Recuperator
MC	Main Compressor
MH	Main Heater
MS	Molten Salt
MSIT	Molten Salt Inlet Temperature
MSOT	Molten Salt Outlet Temperature
MT	Medium Temperature
NSGA	Non-dominated Sorting Genetic Algorithm
ORC	Organic Rankine Cycle
P	Perimeter
PC	Precooler
PCC	Partial Cooling Cycle
PHEX	Primary Heat Exchanger
PR	Pressure ratio
PreC	Pre-compressor
RC	Recompressor
RCBC	Recompression Brayton Cycle
RH	Reheater
sCO_2	supercritical Carbon Dioxide
SF	Split Fraction
SRBC	Simple Recuperative Brayton Cycle
TASC	Total as Spent Capital
TES	Thermal Energy Storage
TET	Turbine Exhaust Temperature
TIT	Turbine Inlet Temperature
TPC	Total Plant Cost
WHR	Waste Heat Recovery
L	Length

HTC	Heat transfer coefficient
t	time
CFL	Courant-Friedrichs-Levy
SS	Stainless Steel

LIST OF SYMBOLS

ρ	Density
$\dot{m}$	Mass flow rate (kg/s)
C_f	Fluid thermal capacity rate (mass flow rate × specific heat)
C_w	Wall thermal capacity (metal mass × specific heat)
T_c	Cold fluid temperature
T_w	Wall temperature
T_h	Hot fluid temperature
T	Temperature
V	Volume
R	Heat transfer resistance
P	Pressure
H	Enthalpy
U	Internal Energy
S	Flow cross-section area

Chapter 1

1 Introduction

1.1 Background and Motivation

1.1.1 Growing power plant fleet capacity

Global energy demand increased by 2.1% in 2017 which is more than twice the rate of previous years, with oil, gas and coal meeting most of this increase (~70%) while renewables accounted for the rest [1]. In particular, electricity generation increases by 3.1%, which is higher than the increased rate of overall energy demand [1]. Table 1-1 shows the projected growth of electricity demand based on new policies scenario (NPS) and future is electric scenario (FIES) and an expected growth rate is 2.1-2.8%. This indicates that the electricity generation sector fleet capacity has to increase to cope-up with this growing demand.

Table 1-1 Global electricity demand growth rate by sector [1]

Indicator	Sector	2017	2025		2040		CAAGR: 2017-40	
			NPS	FiES	NPS	FiES	NPS	FiES
Electricity demand (TWh)	Total	22 209	26 417	27 676	35 526	42 133	2.1%	2.8%
	Buildings	11 416	13 440	14 220	18 634	21 329	2.2%	2.8%
	Industry	8 945	10 630	11 087	13 074	14 757	1.7%	2.2%
	Transport	378	660	695	1 861	4 174	7.2%	11.0%
	Other	1 470	1 687	1 673	1 957	1 872	1.2%	1.1%
Share of electricity in sector consumption	Buildings	32%	35%	41%	43%	58%	1.2%	2.6%
	Industry	21%	21%	23%	23%	28%	0.4%	1.4%
	Transport	1%	2%	2%	4%	10%	6.0%	10.0%

Notes: CAAGR = Compound average annual growth rate; NPS = New Policies Scenario; FiES = Future is Electric Scenario; TWh = terawatt-hours. Other includes electricity demand from agriculture and energy transformation sectors.

1.1.2 Need for increasing efficiency

In order for the power sector to comply with the 2 °C Paris agreement, 1) the energy penetration from renewables have to be increased, 2) carbon capture and sequestration technologies have to be employed in the conventional generation units and 3) the energy efficiency of the power cycle technologies have to be

increased. Energy efficiency is critical for mitigating the CO_2 emission; for instance, if the efficiency has not been improved since 2000, the emission would have been increased by 12% in 2017, requiring 20% more fuel imports [2,3]. Figure 1-1 shows the significance of energy efficiency in greenhouse gas (GHG) emission. International Energy Agency (IEA) guidelines indicate that increasing energy efficiency combined with renewables is inevitable to achieving global climate targets, and they predicted that an investment in the efficiency world scenario payback by a factor of three [3]. This emphasises that the future electricity generation technology has to prioritise in maximising the power conversion efficiency. Increasing the efficiency of the power cycle requires to increase the maximum operating temperature and pressure so the mean Carnot heat addition temperature is improved, thus increasing the cycle efficiency. The conventional superheated and supercritical steam Rankine cycles operate at a pressure and temperature levels of around 250 bar and 600-650 °C respectively. Further increasing temperature is limited by material degradation owing to steam oxidation and corrosion issues. Therefore, thermally and chemically stable alternative fluids need to be investigated.

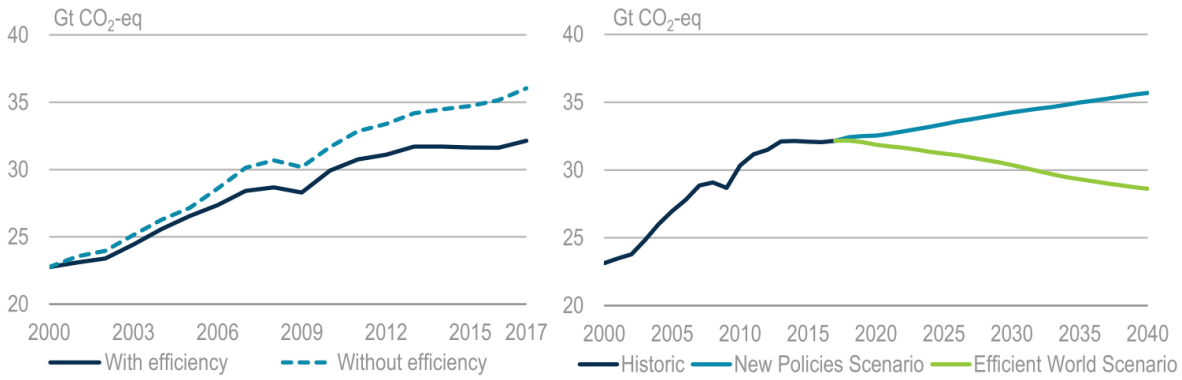

Figure 1-1 Energy related GHG emissions with and without efficiency [3]

1.1.3 Role of thermal energy storage

Higher energy penetration of variable renewable energy sources (>50%) can trade-off the grid reliable power supply, which forces the curtailment of renewable power sources leading to lower utilisation of the renewable assets [4,5]. In order to minimise the curtailment of renewable assets, the flexibility of the coexisting

conventional operating units has to be enhanced to cope-up with the variable renewable energy (VRE) generation. This changes the load profile of a plant (i.e., cyclic load profile), which penalties the efficiency and life of the plant owing to the longer part-load operation and high thermal stress, respectively. The flexibility can be increased by supply and demand side management such as load shifting, new operating procedures and new technologies including energy storage [4,5]. Thermal energy storage systems are more economical for mid and long-term storage (a few hours to days) compared to the battery storage and they can be readily integrated with the thermal power plants [6]. Therefore, the higher efficient new power conversion cycles have to be integrated with the energy storage systems to enhance flexibility. Thermal energy storage plays a critical in Concentrated Solar Power (CSP) power plants to increase the capacity factor, and increasing plant reliability [7].

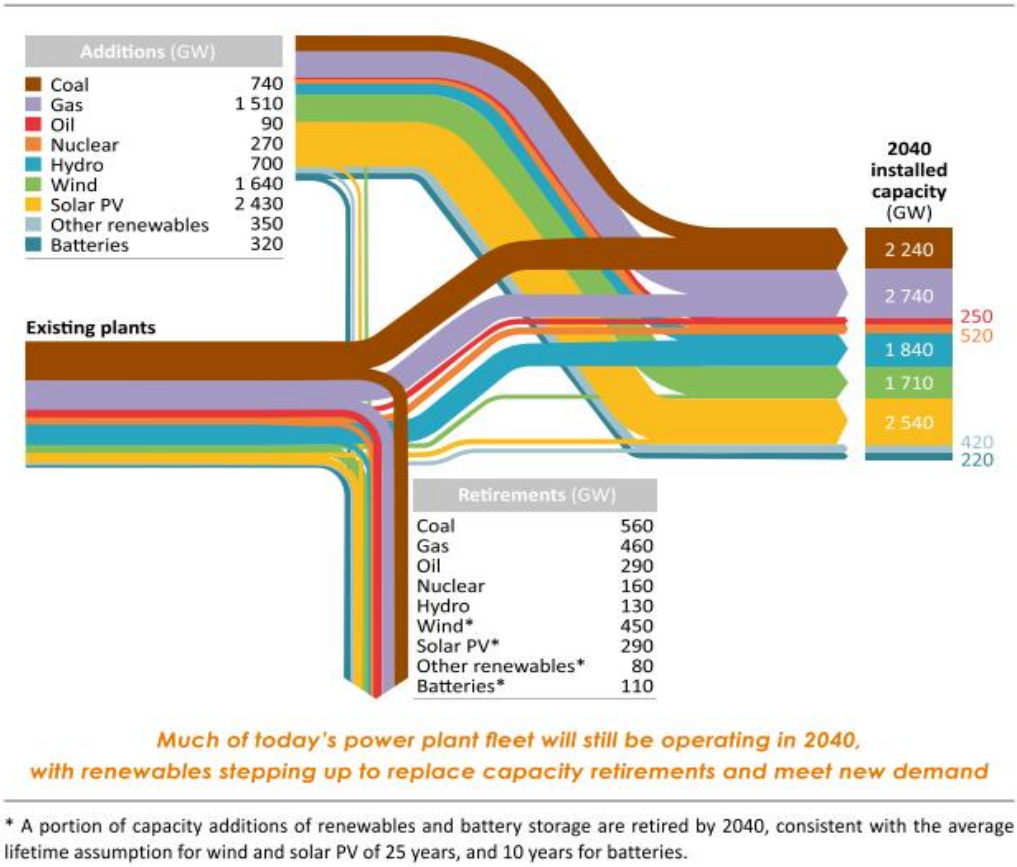

Figure 1-2 Global power generation capacity addition and retirement scenario, 2018 - 2040 [1]

The former is achieved as the solar field is optimally oversized to store the energy to keep the power block running during the night hours, whilst the latter is due to the fact that the power block can continue operation from the storage even though the solar field is tripped. Generally, higher annual energy generation, owing to higher capacity factor, indicating that the investment of the storage makes economic sense [8,9], and for a given size of solar field and power block capacity there will be an economic optimum storage size which reduces the Levelized Cost of Energy (LCOE).

1.1.4 Role of conventional technologies in the future grid

A small fraction of flexible conventional fossil-fired power generating units are therefore required to enhance the gird stability, black-start, spinning reserve capabilities, and IEA projected the required future installation capacity of fossil-fired units as shown in Figure 1-2 [1]. Therefore, a higher efficient power cycle that can support plant flexibility with a lower cost can be an attractive option to mitigate the global emission targets. The flexibility of the power plants are described by three critical parameters, 1) ramp rate (MW/min or % load/min), plant start-up time (hours), minimum stable load (%load) [10]. The ramp rate of a boiler is limited by the thermal stress limitations of the thick-wall tubes and reducing the thermal mass (metal mass × specific heat of the metal) of the boiler can notably increase the thermal response time of the plant. In order to increase the plant flexibility at a lower cost, a small-scale (50-350 MW) modular plants are attractive and the department of energy, USA is promoting research to develop efficient modular coal-fired power plants [11]. This implies that a compact power cycle with smaller thermal mass is preferred.

1.1.5 Economics of scale

The power plant economics of scaling ($Cost = Cost_{ref}\left(\frac{Capacity_{ref}}{Capacity}\right)^{n-1}$), which describes the changes in the power block unit cost ($Cost$ in \$/kW) as a function of the plant size using a scaling exponent (n) from a reference plant (subscript ref) [12]. Many authors investigated this for a coal-fired plant and nuclear plants and Phung [12] summarised most of the studies, concluding that the scaling

exponent of coal-fired plant cost can vary between 0.55-0.76, whist other researches proposed in the rage of 0.52-1. In other words, the unit cost ($/kW) of a 100MW plant is 2.2 times higher compared to a 600MW plant for a scaling exponent of 0.55. Kehlhofer et al. [13] presented the scalability of different technology (1998 price level) as shown in Figure 1-3, which clearly indicates that the conventional coal-fired steam Rankine cycles are economically not scalable to a smaller size as the cost monotonically increases (approximately by a factor of two from 600 MW to 100MW). This indicates that a huge reduction of specific cost is required for a smaller scale unit. The plant specific cost scaling exponent ($n = \sum_j M_j n_j$) is aggregated from the scaling exponent of the plant components (n_j) and fraction of component plant cost with respect to overall plant cost (M_j) [12].

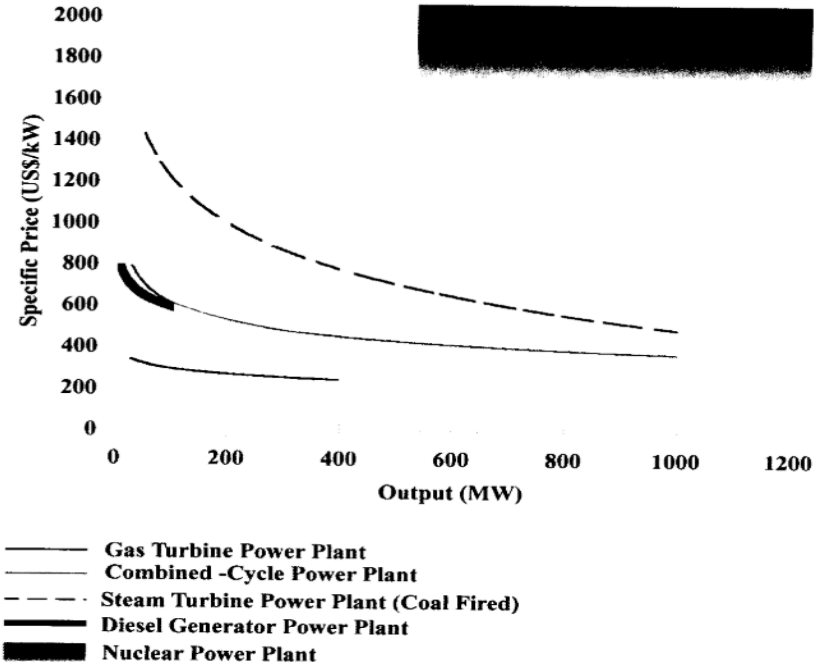

Figure 1-3 Economy of scaling for different turnkey power plant technology (1998 price) *[13]*

1.1.6 Need for sCO_2

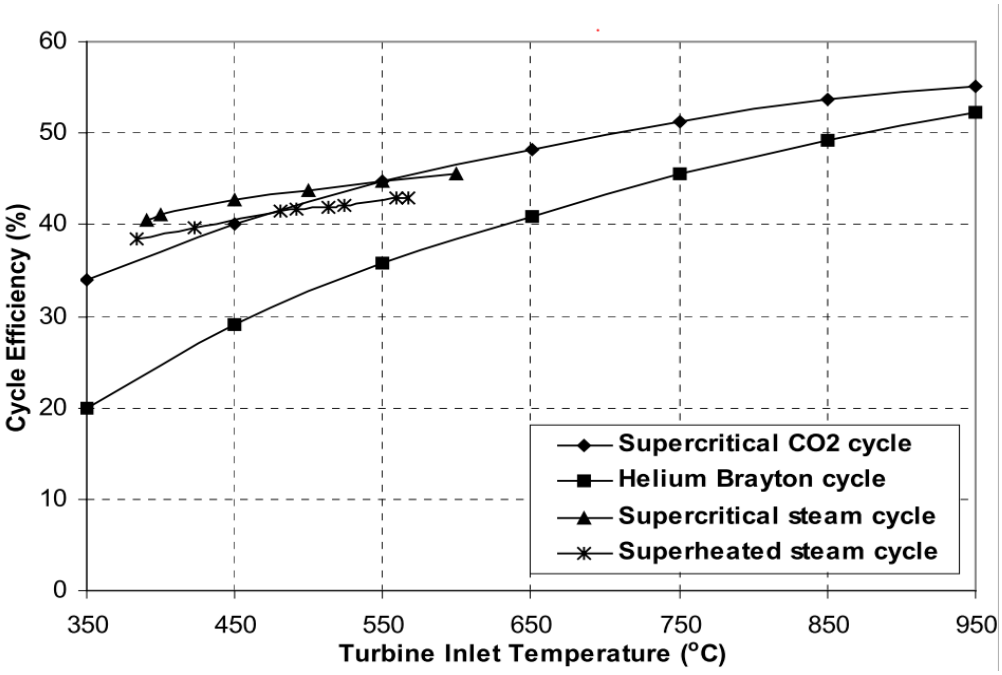

Figure 1-4 Cycle efficiency comparison of advanced power cycles *[14]*

An ideal power cycle has to achieve higher efficiency at a lower cost with simple cycle configurations, economically scalable across different size, compact (lesser thermal mass), and flexible to allow high penetration of VRE. Since the conventional steam Rankine cycles have constraints in increasing the operating temperature and poses a poor economy of scale, different high temperature working fluids are investigated to meet the requirements including supercritical carbon dioxide (sCO_2), helium, and argon, to name a few. In order to achieve higher efficiency, many advanced power generation cycles have been investigated including combined cycle [15], closed-loop Brayton cycle with alternative working fluids such as helium [16], argon [16] and sCO_2. Dunham et al. [17] investigated six power cycle configurations namely regenerated He-Brayton, regenerated CO_2-Brayton, CO_2 recompression Brayton, Steam Rankine and CO_2-organic Rankine Combined cycle, concluding that sCO_2 recompression cycle offers higher efficiency above 600 °C. Dostal [14] compared the performance of sCO_2 cycles against helium cycle and benchmarked their performance against steam Rankine cycles, concluding that sCO_2 cycle can achieve higher efficiency when the turbine inlet temperature is above 550 °C

(Figure 1-4) with a compact plant footprint owing to a high density of sCO_2. Klemencic et. al [18] compared steam Rankine cycle, ORC (Cyclopentane) and sCO_2 cycle for waste heat recovery application concluding that transcritical CO_2 Rankine cycle achieved highest efficiency (26.3%) and net power. Astolfi et. al [19] compared the performance of four sCO_2 cycles against four ORC cycles (working fluid selected from 47 candidates) for low-medium temperature waste heat recovery applications, concluding that ORC is attractive for temperatures below 300 °C, whilst sCO_2 cycles are attractive at higher temperatures. This project considers sCO_2 as a working fluid due to its compelling benefits such as higher efficiency, simple cycle configuration compared to steam Rankine and compact footprint, which aids in reducing the cost and increasing the flexibility.

The critical temperature and pressure of CO_2 are 30.98 °C and 73.8 bar respectively [20]. sCO_2 that has potential to provide most of the aforementioned features of the power cycle, therefore, it gained a lot of research interest in the last decade. The basic sCO_2 cycle is a closed-loop recuperative Brayton cycle, where the compressive power is reduced dramatically owing to the attractive properties of sCO_2, which helps to increase efficiency. Further efficiency improvement is achieved by high recuperation, and increasing the mean Carnot heat addition temperature to the cycle. The density of sCO_2 is higher throughout the cycle which helps in reducing the size of the volumetric components including turbomachinery by an order of magnitude (tenfold), reducing the capital cost [21]. Due to the attractive features of sCO_2 cycles, the US Department of Energy (DOE) SunShot program considered sCO_2 cycles to reduce the LCOE for all the three CSP receiver technologies including falling particle, molten salt and gas phase [7]. sCO_2 cycles appear similar to the Rankine cycle in terms of the cycle configurations whilst it performs similar to gas turbines (GT) from the component design and operational standpoint [21].

sCO_2 cycle has been introduced by Angelino [22,23] and Feher [24], later studied by Dostal [14] for nuclear applications. Subsequently, numerous cycle configurations have been proposed aiming to cover a range of applications including coal-fired plant [25] , CSP applications [26], nuclear [14], combined

cycle power plant [27], waste heat recovery [28], geothermal [29]. Crespi et al. [30,31] reviewed forty-two of them and presented the plots of efficiency and specific power, to aid cycle selection. However, the influence of heat source temperature and type (sensible heat or constant flux/temperature) on cycle selection is not thoroughly investigated. In addition, the design performance of sCO_2 cycle is investigated whilst the off-design performance of many cycles is seldom studied. Investigation of the cycle off-design performance is crucial to understand the optimal control strategies and to identify the operational challenges.

1.2 Aim and Objectives

Improving the performance of conventional thermodynamic power generation cycles using sCO_2 for fossil-fired plants and investigate the challenges of integrating sCO_2 cycle and TES for CSP application to enhance the thermal efficiency and reduce the cost of electricity. The following objectives and the research questions were formulated to accomplish the aim of this project,

Objective 1:

To identify and integrate the sCO_2 cycle configurations for bottoming cycle applications in a combined cycle power plant, answering the following research questions,

a. *What is the potential techno-economic performance? (Chapter 3)*
b. *Which component cost in the cycle is critical from exergo-economic perspective? (Chapter 4)*

Objective 2:

To identify and integrate the sCO_2 cycle configurations for coal-fired power plants, answering the following research question,

a. *What is the improvement in the thermal and economic performance of sCO_2 cycle compared with National Energy Technology Laboratory (NETL) baseline steam Rankine cycles? (Chapter 5)*

Objective 3:

To identify and integrate the sCO_2 cycle configurations for CSP applications with thermal energy storage, addressing the following questions,

a. *What is the optimal sCO_2 cycle configuration and what is the potential improvements in techno-economic performance? (Chapter 6)*
b. *How different sCO_2 cycle configurations compare based on off-design performance? (Chapter 7)*
c. *What are the operational challenges of sCO_2 cycle and their influence on sensible heat storage system? (Chapter 8)*
d. *Can the recuperator transient response be improved using compact heat exchangers? (Chapter 9)*

1.3 Dissemination from the PhD

The aforementioned objectives and the research questions were summarised in six number of papers, including four journal papers and two conference proceedings (*Chapter 6*, *Chapter 9*). Among these four journal papers, three of them have been published (*Chapter 3, Chapter 5, Chapter 9)*, and the remaining one journal paper is currently under review (*Chapter 6*).

The list of papers is given as follows:

[1] **Thanganadar** D, Asfand F, Patchigolla K. Thermal performance and economic analysis of supercritical Carbon Dioxide cycles in combined cycle power plant. Appl Energy 2019; 255. https://doi.org/10.1016/j.apenergy.2019.113836.

[2] **Thanganadar** D, Fornarelli F, Camporeale S, Asfand F, Patchigolla K. Off-Design and Annual Performance Analysis of Supercritical Carbon Dioxide Cycle with Thermal Storage for CSP application. Appl Energy 2020; 282: 116200. https://doi.org/10.1016/j.apenergy.2020.116200.

[3] **Thanganadar** D, Asfand F, Patchigolla K, Turner P. Techno-economic Analysis of Supercritical Carbon Dioxide Cycle Integrated with Coal-Fired

Power Plant. Energy Convers Manag 2021;242:114294. https://doi.org/10.1016/j.enconman.2021.114294.

[4] **Thanganadar** D, Fornarelli F, Camporeale S, Asfand F, Gillard J, Patchigolla K. Thermo-economic Analysis, Optimisation and Systematic Integration of Supercritical Carbon Dioxide Cycle with Sensible Heat Thermal Energy Storage for CSP Application (*under review*). Energy 2021.

[5] **Thanganadar** D, Fornarelli F, Camporeale S, Asfand F, Patchigolla K. Analysis of Design, Off-Design and Annual Performance of Supercritical CO_2 Cycles for CSP Application. Proc. ASME Turbo Expo 2020, 10.1115/GT2020-14790, 2020.

[6] **Thanganadar** D, Fornarelli F, Camporeale S, Asfand F, Patchigolla K. Recuperator Transient Simulation for Supercritical Carbon Dioxide Cycle in CSP Applications. Proc. ASME Turbo Expo 2020, 10.1115/GT2020-14785, 2020.

In addition to all the above written work, **Thanganadar** D. also co-authored one journal and one conference papers, which enriches the process modelling knowledge.

[1] Asfand F, **Thanganadar** D, Patchigolla K. Thermodynamic performance of a supercritical CO2 cycle integrated with a recuperative absorption cooling system. ECOS 2019 - Proc. 32nd Int. Conf. Effic. Cost, Optim. Simul. Environ. Impact Energy Syst., vol. 2019- June, WROCLAW, POLAND: 2019, p. 3895–903.

Contributions of Thanganadar D: Conceptualized the idea behind the novelty, methodology, software, validation, investigation, and writing-review & editing.

[2] Yan Y, **Thanganadar** D, Clough PT, Mukherjee S, Patchigolla K, Manovic V, et al. Process simulations of blue hydrogen production by upgraded sorption enhanced steam methane reforming (SE-SMR) processes.

Energy Convers Manag 2020; 222: 113144. doi.org/10.1016/j.enconman.2020.113144

Contributions of Thanganadar D: Conceptualized the idea behind the novelty, methodology, software, validation, investigation, formal analysis, data curation, visualization, writing-original draft.

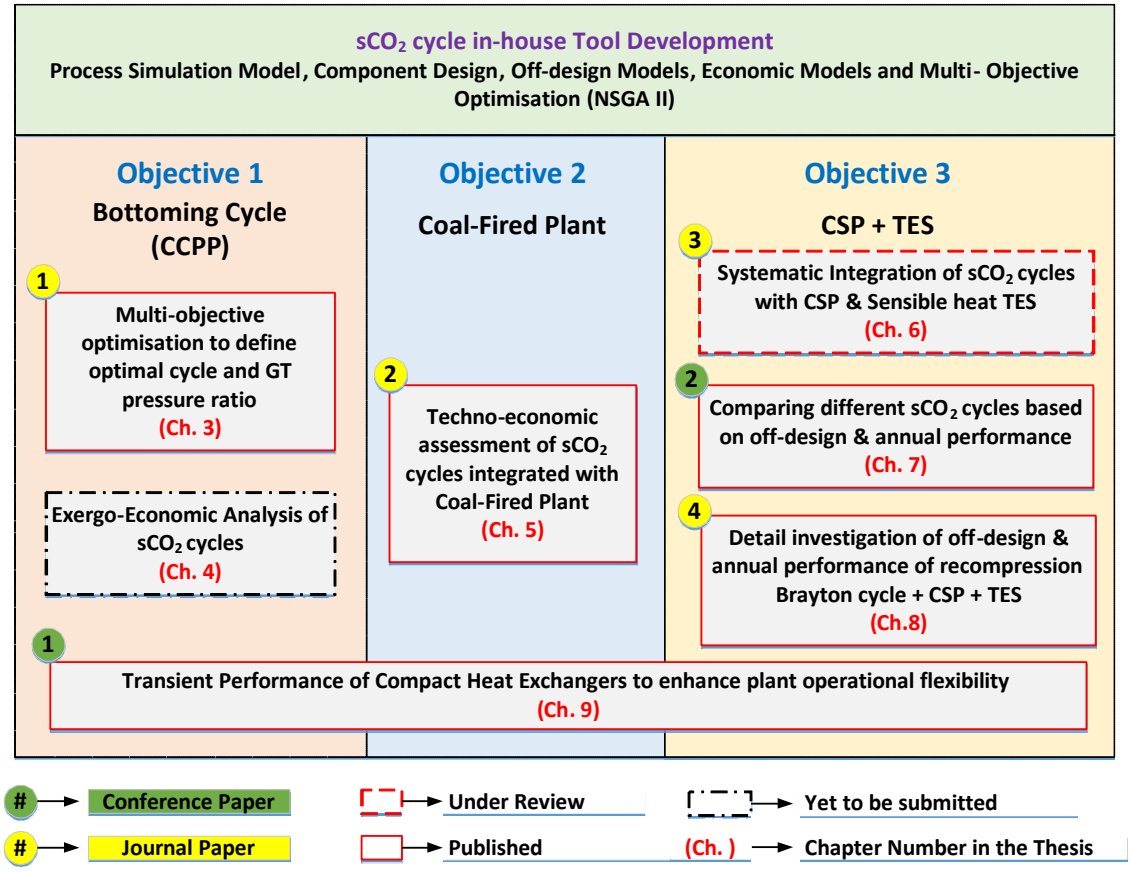

Figure 1-5 A map connecting the objectives with the papers

Figure 1-5 links all the papers to the corresponding research questions listed in section 1.2. Developing a sCO_2 cycle component model for design and off-design, which is flexible to simulate any cycle configuration is the prerequisites to answer the research question. Therefore, flexible in-house code is developed in MATLAB® as part of this project and verified with the data available in the literature. The model also includes the economic module for different technologies considered (coal-fired, combined cycle and CSP+TES) and multi-objective optimisation routine. Non-dominated sorting algorithm (NSGA II) is

applied for multi-objective optimisation to explore the complete Pareto front in order to explore the optimal solution. One journal article was published as part of objective 1 and one journal article is under review as part of objective 2. Two journal papers and two conference papers were submitted/published as part of objective 3.

The GT data of the combined cycle power plants were obtained from Thermoflex and simulated. Since the optimisation requires solving the process model few thousand times, the computational time is a big concern. Therefore, a flexible in-house tool which can simulate any sCO2 cycle configuration was developed and the code can utilise multiple-cores to save the computational burden. More details about the different modelling platform can be found in Chapter 10.

1.4 Outline of the PhD Thesis

The thesis structure is given as follows,

Chapter 1. The background and the motivation of this PhD project are presented, which includes the project aims and objectives. An overview of PhD outputs/dissemination is also described.

Chapter 2. The state-of-the-art review of sCO_2 cycles relevant to this PhD project that leads to establishing the project methodology and novelty is illustrated.

Chapter 3. This chapter describes the techno-economic results of five sCO_2 cascade cycles, including one novel cycle configuration, integrated with bottoming cycle application. This chapter contains the detailed literate review relevant to this study, methodology, model development, verification and optimisation results. Finally, a set of cycle performance maps are produced, which guides in estimating the expected performance of sCO_2 cycles integrated with any GTs.

Chapter 4. This chapter explains about the exergo-economic analysis applied to sCO_2 cycle integrated as bottoming cycle with two commercially available GTs, namely SGT5-4000F and 7HA.02. The details include the methodology, model development and the results which identify the component that requires critical

attention from exergo-economic perspective in order to reduce the exergy destruction cost.

Chapter 5. Four novel sCO_2 cycles are derived and integrated with a NETL baseline coal-fired boiler (B12A), and metaheuristic optimisation algorithm is applied to maximise the plant efficiency. This chapter describes the detailed literature review, methodology, model development and verification, optimisation, Monte-Carlo uncertainty quantification, and sensitivity study.

Chapter 6. A systematic cycle development and design point selection procedure to minimise the whole plant cost (power block, CSP solar field and sensible heat TES) is proposed. Nine sCO_2 cycles including two novel cycle configurations are integrated with CSP and TES system and the systematic integration procedure is verified. The impact of turbine inlet temperature and compressor inlet temperature on the selection of cycle configuration/design point are investigated in detail and Monte-Carlo uncertainty quantification is presented.

Chapter 7. This chapter discusses the off-design performance of sCO_2 cycle integrated with CSP and sensible heat TES system. Three sCO_2 cycle performances are compared based on their off-design and annual performance. Multi-objective Pareto fronts represent the optimal operational space and they are compared for different boundary conditions for three different cycles to realise the impact of changes in off-design performance between these cycles.

Chapter 8: A thorough investigation of the off-design performance of the standard sCO_2 recompression cycle integrated with CSP and sensible heat TES system. The effect of cycle performance for the variation of the boundary conditions including ambient temperature, molten salt inlet temperature and molten salt flow rate are investigated using a multi-objective optimisation approach. The critical control parameter trends are discussed, which aids in developing the plant controls. An annual simulation is performed to quantify the benefit of operating the power block in maximum efficiency mode or maximum power model is presented.

Chapter 9. A transient heat exchanger model based on conventional temperature based and enthalpy-based approaches are developed and the recuperator transient characteristics are quantified. A logarithmic indexed look-up table is generated in order to speed up the computational time of the transient code.

Chapter 10. Overall methodology, discussion connecting all the chapters and critical review of the assumptions are presented.

Chapter 11. Conclusions and recommendations for future work are provided.

1.5 References

[1] IEA. World Energy Outlook 2018. vol. 1. 2018. doi:10.1787/weo-2018-2-en.

[2] IEA. Multiple Benefits of Energy Efficiency 2019. https://www.iea.org/reports/multiple-benefits-of-energy-efficiency/emissions-savings (accessed 9 September 2020).

[3] International Energy Agency. Energy efficiency 2018 analysis and outlooks to 2040. 2018.

[4] NREL. Renewable Electricity Futures Study: Executive Summary. vol. 1. 2012. doi:NREL/TP-6A20-52409-1.

[5] Kroposki B, Johnson B, Zhang Y, Gevorgian V, Denholm P, Hodge B-M, et al. Achieving a 100% Renewable Grid. IEEE Power Energy Mag 2017:61–73. doi:10.1109/MPE.2016.2637122.

[6] EASE, EERA. European Energy Storage Technology Development Roadmap 2017. 2017.

[7] Mehos M, Turchi C, Vidal J, Wagner M, Ma Z, Ho C, et al. Concentrating Solar Power Gen3 Demonstration Roadmap. 2017.

[8] Musi R, Grange B, Sgouridis S, Guedez R, Armstrong P, Slocum A, et al. Techno-economic analysis of concentrated solar power plants in terms of levelized cost of electricity. AIP Conf Proc 2017;1850.

doi:10.1063/1.4984552.

[9] Kuravi S, Goswami Y, Stefanakos EK, Ram M, Jotshi C, Pendyala S, et al. Thermal Energy Storage for Concentrating Solar Power Plants. Technol Innov 2012;14:81–91. doi:10.3727/194982412X13462021397570.

[10] Agora Eergiewende. Flexibility in thermal power plants with a focus on existing coal-fired power plants. 2017.

[11] Office of Fossil Energy UD. Small-Scale Modular Coal-Fired Plants of the Future n.d. https://www.energy.gov/fe/articles/small-scale-modular-coal-fired-plants-future (accessed 9 September 2020).

[12] Phung DL. Theory and evidence of using the economy of cale law in power plant economics. 1987.

[13] Rolf Bachmann, Henrik Nielsen, Judy Warner, Rolf Kehlhofer RK-. Combined-cycle gas & steam turbine power plants. Choice Rev Online 1991;29:29-2125-29–2125. doi:10.5860/choice.29-2125.

[14] Dostal V, Driscoll MJ, Hejzlar P. A Supercritical Carbon Dioxide Cycle for Next Generation Nuclear Reactors. 2004. doi:MIT-ANP-TR-100.

[15] Spelling J, Laumert B, Fransson T. Advanced hybrid solar tower combined-cycle power plants. Energy Procedia 2014;49:1207–17. doi:10.1016/j.egypro.2014.03.130.

[16] Kusterer K, Braun R, Moritz N, Sugimoto T, Tanimura K, Bohn D. Comparative study of solar thermal brayton cycles operated with helium or argon. Proc ASME Turbo Expo 2013;4:1–9. doi:10.1115/GT2013-94990.

[17] Dunham MT, Iverson BD. High-efficiency thermodynamic power cycles for concentrated solar power systems. Renew Sustain Energy Rev 2014;30:758–70. doi:10.1016/j.rser.2013.11.010.

[18] Klemencic G, Flegkas S, Werner A, Haider M, Leibinger H. Comparison of conventional and CO2 power generation cycles for waste heat recovery. 5th Int Symp - Supercrit CO2 Power Cycles 2016:1–15.

[19] Astolfi M, Alfani D, Lasala S, Macchi E. Comparison between ORC and CO2 power systems for the exploitation of low-medium temperature heat sources. Energy 2018;161:1250–61. doi:10.1016/j.energy.2018.07.099.

[20] Lemmon EW, Huber ML, McLinden MO. NIST Standard Reference Database 23. Natl Inst Stand Technol 2013;V 9.1.

[21] Ahn Y, Bae SJ, Kim M, Cho SK, Baik S, Lee JI, et al. Review of supercritical CO_2 power cycle technology and current status of research and development. Nucl Eng Technol 2015;47:647–61. doi:10.1016/j.net.2015.06.009.

[22] Angelino G. Real Gas Effects in Carbon Dioxide Cycles. ASME- Pap 69-Gt-102 1969:1–12. doi:10.1115/69-GT-102.

[23] Angelino G. Carbon dioxide condensation cycles for power production. J Eng Gas Turbines Power 1968;90:287–95. doi:10.1115/1.3609190.

[24] Feher EG. The Supercritical Thermodynamic Power Cycle. Energy Convers 1968;8:85–90. doi:10.1016/0013-7480(68)90105-8.

[25] Le Moullec Y. Conceptual study of a high efficiency coal-fired power plant with CO_2 capture using a supercritical CO_2 Brayton cycle. Energy 2013;49:32–46. doi:10.1016/j.energy.2012.10.022.

[26] Turchi CS, Ma Z, Neises T, Michael W. Thermodynamic Study of Advanced Supercritical Carbon Dioxide Power Cycles for High Performance Concentrating Solar Power Systems. Proc. ASME 2012 6th Int. Conf. Energy Sustain., 2012, p. 375–83. doi:10.1115/ES2012-91179.

[27] Kimzey G. Development of a Brayton Bottoming Cycle using Supercritical Carbon Dioxide as the Working Fluid. 2012.

[28] Poerner M, Rimpel A. Waste heat recovery. Elsevier Ltd; 2017. doi:10.1016/B978-0-08-100804-1.00010-4.

[29] Li H, Yang Y, Cheng Z, Sang Y, Dai Y. Study on off-design performance of transcritical CO_2 power cycle for the utilization of geothermal energy.

Geothermics 2018;71:369–79. doi:10.1016/j.geothermics.2017.09.002.

[30] Crespi F, Gavagnin G, Sánchez D, Martínez GS. Supercritical carbon dioxide cycles for power generation: A review. Appl Energy 2017;195:152–83. doi:10.1016/j.apenergy.2017.02.048.

[31] Crespi F, Sánchez D, Sánchez T, Martínez GS. Capital Cost Assessment of Concentrated Solar Power Plants Based on Supercritical Carbon Dioxide Power Cycles. J Eng Gas Turbines Power 2019;141:1–9. doi:10.1115/1.4042304.

Chapter 2

2 Literature Survey- State of the art review

The literature review covered in this chapter is aimed to emphasize the state of the art and the research gaps of sCO_2 cycles relevant to this PhD project, and the detailed literature survey highlighting the research questions can be found in each of the chapters.

2.1 Equation of State

The equation of state provides the relation between pressure, temperature, and volume. The conventional cubical equation of state (EoS), such as Peng-Robinson can be applied to liquids, and gases, whereas it introduces a significant error for CO_2, particularly around the critical point [1]. Zhao et al. [1] concluded that only Lee-Kesler-Plöcker (LKP) and Span-Wagner (SW) equations show acceptable deviation from experimental data and the SW EoS is currently the most accurate equation of state available. Baltadjiev [2] also compared the SW and LKP around the critical point, concluding that LKP introduces a relative error of up to 0.05% in isobaric specific heat and density and considered LKP for their study owing to the faster computational speed of LKP compared to SW. NIST REFPROP [3] uses SW EoS, an iterative procedure that minimises the Helmholtz free energy, therefore, it is computationally heavy, particularly close to the critical point where the number of iterations can be higher owing to the higher nonlinearity.

2.2 Nonlinear variation of Fluid properties

The thermal physical properties of sCO_2 changes abruptly close to (pseudo) critical points. The variation of the density is shown in Figure 2-1 (a) and the typical compressor inlet and outlet conditions are also overlaid. It is clear that the compressor inlet density can vary about 2-4 times [4] for a variation of ±5 °C or ±10% of the compressor inlet temperature and inlet pressure respectively, which can be expected during the off-design operation of the plant. This variation is very

small compared to water/steam for example, where the variation can be up to 1000 times. This also implies that the problem of cavitation or erosion due to droplet formation can be less severe for sCO_2. In fact, the main compressor was operated in the two-phase region at the Sandia national lab (SNL) testing facility and found no evidence of erosion [5–7]. On the other hand, small changes in the cycle pressure/temperature at the inlet of the compressor significantly changes the inlet volumetric flow of the compressor for a given mass flow rate. This complicates the compressor design process to achieve a larger operational range, avoiding compressor surge. Variable Inlet guide vanes (VIGV) can be more justified to increase the surge margin because that reduces the larger variation of the volumetric flow at the compressor inlet stage [8,9].

The variation of the speed of sound is shown in Figure 2-1 (b). Although the variations are smooth at higher pressures, it varies drastically (steep gradient) close to the critical point. The fluid flow Mach number ($M = \frac{fluid\ velocity}{speed\ of\ sound}$) also varies around this region, which can chock the compressor when the Mach number is 1, or induce shock waves, resulting in a higher compressor loss. This further complicates the design of the compressor with a larger range and Anderson [10] indicated that sCO_2 critical mass flux is achieved at the nozzle throat for a Mach number of 0.3 as opposed to the Mach number of 1 for an ideal gas owing to atypical fluid properties close to the critical region (near the left saturation line). This can result in a premature choking in the compressor.

Close to the critical point the isobaric specific heat changes dramatically (Figure 2-1 (c)), which implies that a large heat transfer (enthalpy change) is required to notice a small change in the temperature. This poses additional challenges in measuring the temperature at the precooler outlet for compressor control, and in Sandia test loop the density was measured instead [5]. Hacks et al.[11] proposed to use the cooling power as the control variable to control the compressor instead of using the compressor inlet conditions. The isobaric specific heat and the expansion coefficient becomes infinity at the critical point [12].

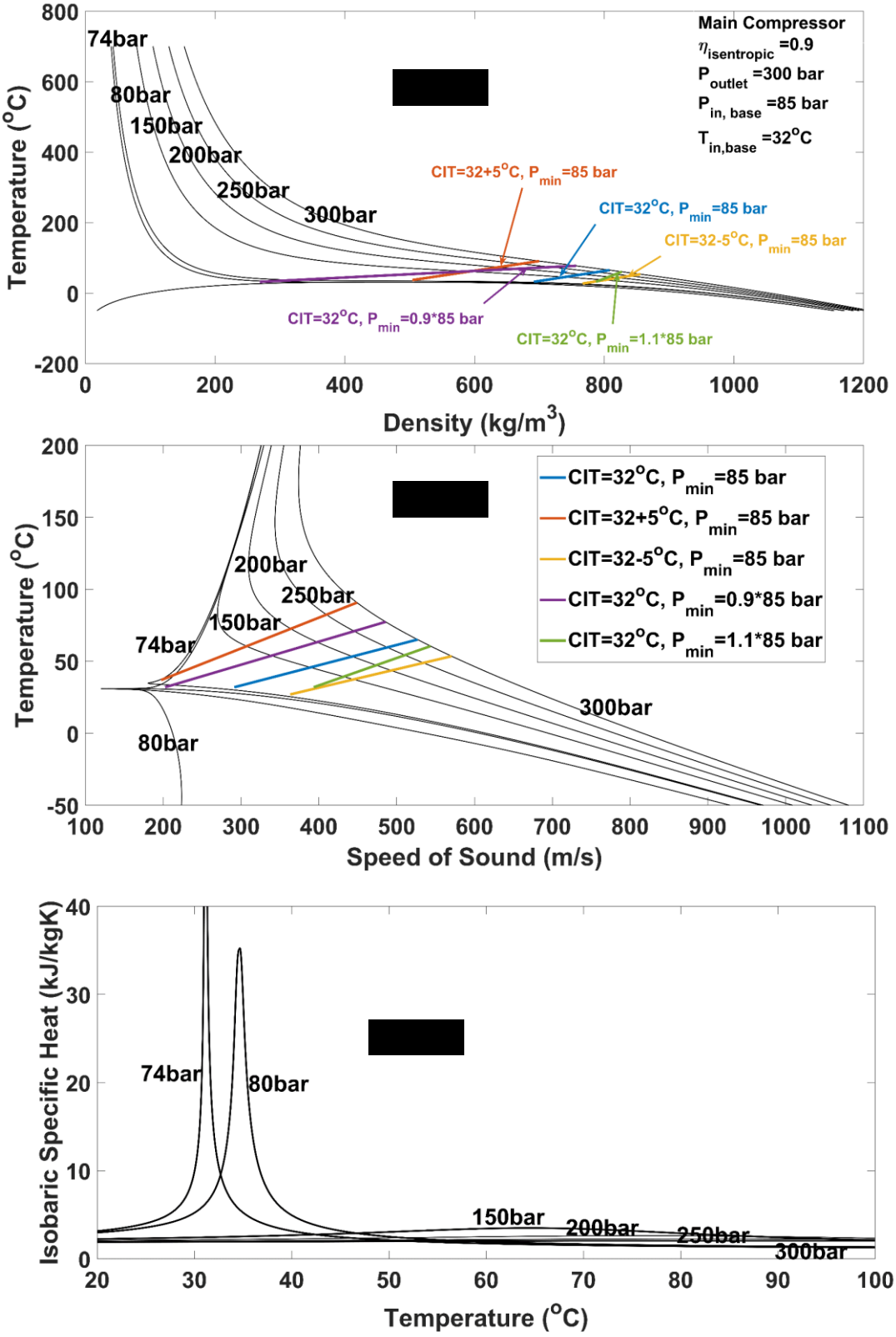

Figure 2-1 sCO_2 fluid properties produced using REFPROP a) Density, b) Speed of sound, c) Isobaric specific heat

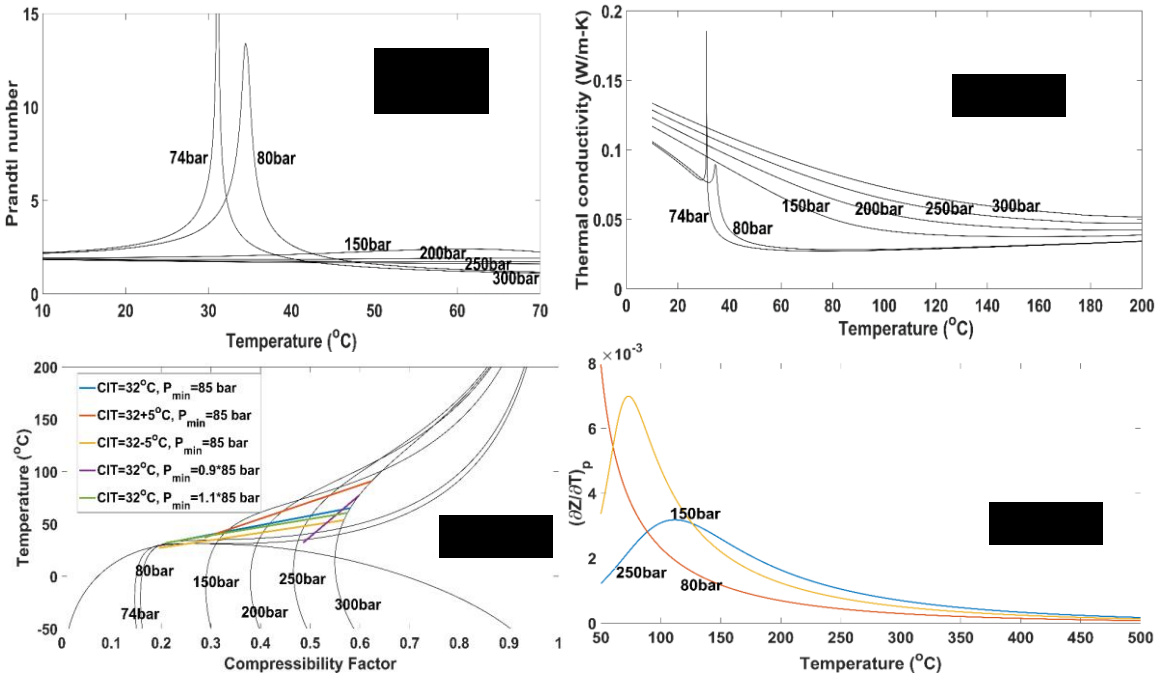

Figure 2-2 sCO_2 fluid properties produced using REFPROP a) Prandtl number, b) Thermal conductivity, c) compressibility factor, d) Isobaric gradient of compressibility factor

The pseudo critical point, which is where the gradient of isobaric specific heat is zero (c_p reaches a maximum) for any pressures above the critical pressure ($P>P_{crit}$), can be calculated using Eq. 2-1.

$$\left(\frac{\partial c_p}{\partial T}\right)_P = \left(\frac{\partial^2 h}{\partial T^2}\right)_P = 0 \qquad (2\text{-}1)$$

For temperature above the pseudo-critical temperature, the fluid density resembles gas (gas-like), and when the temperature is below the pseudo-critical temperature the fluid is called “liquid-like” [13]. Compressing CO_2 in the liquid-like region can increase the pressure ratio by 14% than compressing in the gas-like region for the same compressor geometry [14].

The Prandtl number ($Pr = \frac{c_p \mu}{k}$) and the thermal conductivity (k) also changes sharply close to the (pseudo) critical point (Figure 2-2 (a), (b)), which impacts the heat transfer coefficient ($h = \frac{CRe^a Pr^b k}{L}$), where the Reynolds number $Re = \frac{\rho v d}{\mu}$. The kinematic viscosity for the expected compressor inlet conditions is about 10

times lower than water (pressure =80 bar, temperature = 32 °C), which can reduce the friction losses. Furthermore, the reduction in the viscosity can also increase the Reynolds number through the compressor and this requires a relatively larger number of computational nodes (compared to water) close to the boundary in order to maintain the required y+ when performing computational fluid dynamics simulation (CFD), which is inversely proportional to kinematic viscosity [15]. The compressibility factor (z) is the measure of fluids deviation from the ideal gas law ($z = \frac{PV}{RT}$) and Figure 2-2 (c) show the changes of z close to the critical region and the isobaric compressibility factor gradients are shown in Figure 2-2 (d), which shows that the variation of $\left(\frac{\partial Z}{\partial T}\right)_p$ does not notably change after about >300 °C, which implies that applying ideal gas assumptions can be valid after this temperature. The enthalpy is not only a function of temperature but also the function of pressure close to the (pseudo) critical pressure and this can be calculated according to Eq. 2-2 [2].

$$dh = c_p dT + v\left(1 - \beta_p T\right)dp \tag{2-2}$$

where the isobaric compressibility (β_p) can be calculated using Eq. 2-3 [2].

$$\beta_p = \frac{1}{T} + \frac{1}{z}\left(\frac{\partial z}{\partial T}\right)_p \tag{2-3}$$

This clearly shows that, when $\left(\frac{\partial z}{\partial T}\right)_p$ approaches zero the isobaric compressibility reduces to $\beta_p = \frac{1}{T}$, which eliminates the contribution of the pressure dependence term in the enthalpy equation (Eq. 2-2).

2.3 sCO_2 cycle design Performance

Angelino [16–18] and Feher [19] first introduced the sCO_2 power cycles and it was later studied by Dostal [20] for nuclear applications. sCO_2 cycles are highly efficient with a compact plant footprint, by a factor of 10 than steam Rankine cycles [21], potential of reducing the capital cost up to 15% [22]. sCO_2 cycles can be broadly classified into two types 1) direct fired 2) indirectly heated.

Allam cycle [23,24] patented by Net Power® is an example of the direct fired cycle (shown in Figure 2-3), where the gaseous fuel (stream 14) is burned with a pure oxygen stream (stream 13) from the air separation unit and a dilution recirculation stream of CO_2 (stream 9) at a higher-pressure then expanding the high pressure hot gas mixture through the turbine (stream 1), passes via the recuperator (stream 2) followed by partial cooling and water separation (stream 3), then two-stage intercooled compression (stream 4), and the main heat rejection (stream 7), followed by a pump that aids in reaching the maximum cycle pressure using a multi-stage compressor. To balance the mismatch in the thermal capacitance between hot and cold streams in the recuperator owing to the higher isobaric specific heat of cold fluid, the heat from adiabatic compression of air separation unit (ASU) is transferred to stream 9. Since burning solid fuel produces ash, it is not possible to burn them in gas turbine. Consequently, Allam cycle requires a gasification unit when burning solid fuels [23].

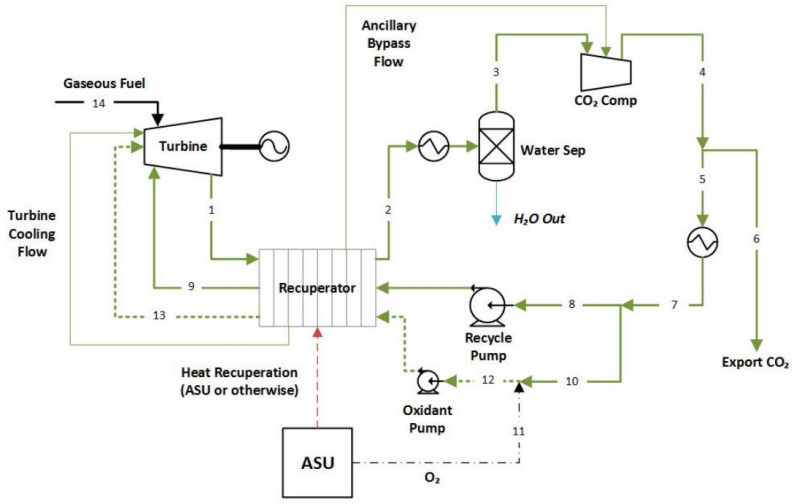

Figure 2-3 Direct fired Allam cycle configuration [23,24]

Indirect cycles connected with a heat source through a heat exchanger, enabling the integration of a wide range of heat sources. The critical pressure and temperature of CO_2 are 30.98 °C and 73.8 bar respectively [3]. The maximum cycle pressure is limited to 250-300 bar for economical reason, hence the sCO_2 cycle pressure ratio is around 3.4-4, limiting the temperature drop across the turbine. Therefore, a recuperator is essential to increase the cycle efficiency by utilising the exhaust heat from the turbine. The basic sCO_2 cycle configuration

i.e., simple recuperative Brayton cycle (Figure 2-4, C1) is a closed-loop recuperated Brayton cycle.

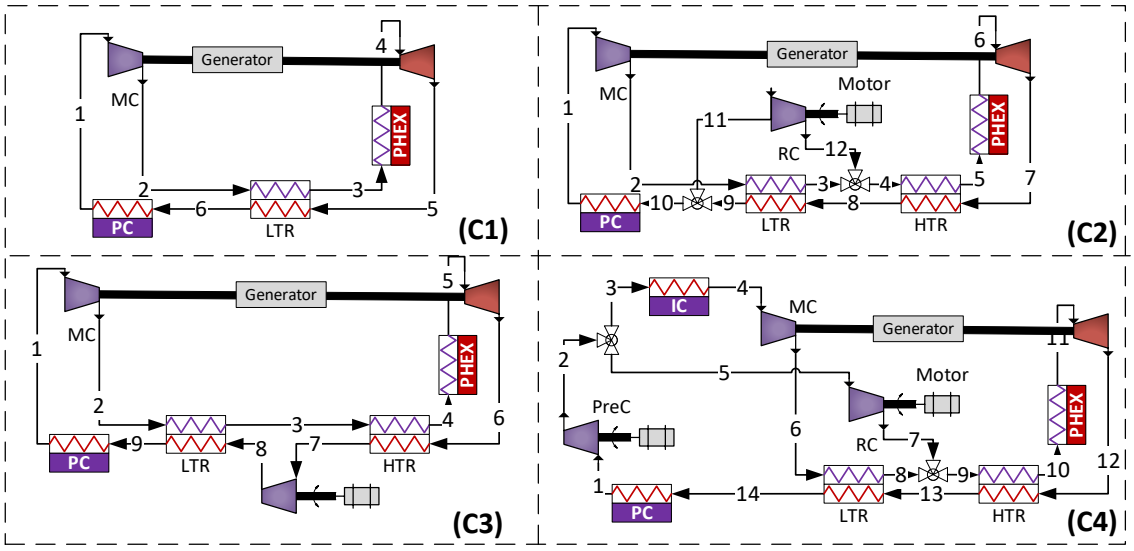

Figure 2-4 sCO_2 cycle configurations, C1) simple recuperative Brayton cycle, C2) Recompression cycle, C3) Pre-compression cycle, C4) Partial cooling cycle

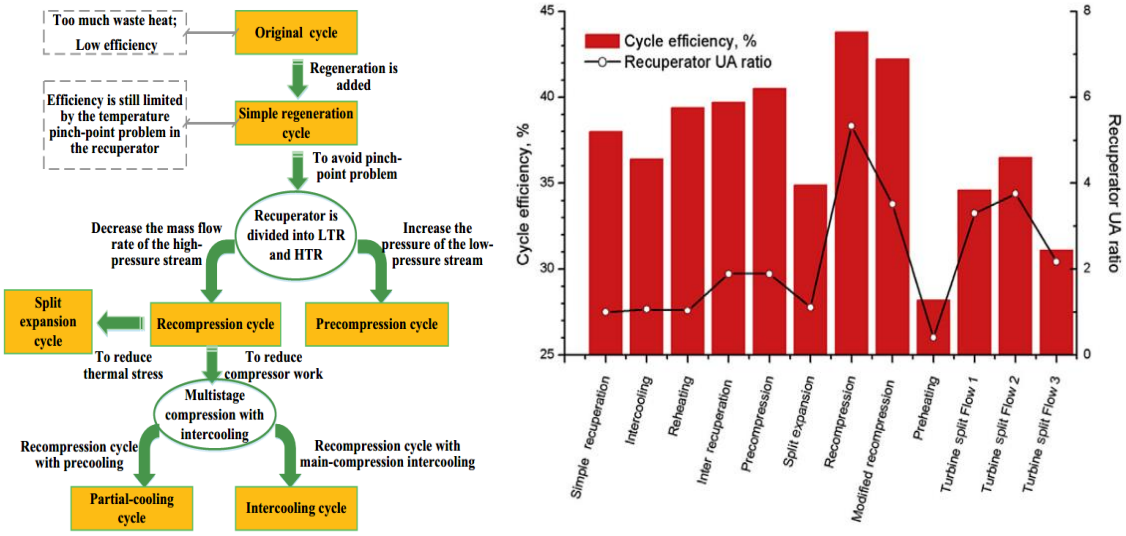

Figure 2-5 Different sCO_2 cycles, left) Derivative relationships between different cycles, right) Comparison of efficiency and recuperator conductance (UA) [21,25]

Since the isobaric specific heat (c_p) of CO_2 is higher close to the critical point, the thermal capacitance (mc_p) of the recuperator cold stream is typically higher than the hot stream, where the mass flow in both the sides are the same for a simple recuperative cycle, limiting the amount of recuperation owing to the occurrence

of the pinch. To further increase the amount of recuperation, the mass flow on the cold stream must be reduced (recompression cycle, Figure 2-4 (C2)) or additional heating source with the required range of temperature (Allam cycle) has to be added. The recompression cycle is mostly acknowledged as the highest efficient cycle [21]. All the state points in both C1 and C2 stays above the critical region. In the precompression cycle ((Figure 2-4, C3), however, the turbine exhaust is expanded to the superheated vapour region, then the hot stream outlet of the high-temperature recuperator (HTR) is compressed above the critical pressure prior to entering the low-temperature recuperator (LTR) which increases the enthalpy of this stream, minimising the heat capacitance imbalance between the cold and hot streams of LTR. Precompression cycle at higher turbine inlet temperatures are inefficient (compressing at a higher temperature is energy-intensive), reducing the cycle efficiency [26,27].

In the partial cooling cycle (Figure 2-4, C4), the turbine exhaust is expanded to a superheated vapour region, then partially cooled after the recuperation (LTR and HTR), then compressed above the critical pressure, then part of the flow is split and connected to the cold stream of the HTR. Partial cooling cycle outperforms recompression cycle above 600 °C turbine inlet temperature [26]. In precompression and partial cooling cycles, the turbine exhaust pressure can be varied independently from the main compressor inlet pressure, therefore, they can better handle the deviation in pressure ratio during part-load operation. Angelino [17] also introduced split expansion cycle, which modifies the recompression cycle by expanding the HTR hot outlet in a low temperature turbine prior to entering the main heater, therefore, the pressure of the high temperature components including primary heater and high temperature turbine can be lower, minimising the thermal stress. The thermal performance of these cycles can be further enhanced by adding intercoolers and reheater (isothermal heat addition). The summary of the derivative relationships of these cycles are shown in Figure 2-5 (left) [25]. The recuperator conductance (UA) varies significantly for different cycle configurations as compared by Ahn et al. [21], concluding that the conductance of the highest efficient recompression cycle is the highest among the other cycles studied (Figure 2-4, right). There are many

demonstration plants available in both laboratory/pilot scale and Lecompte et al. [28] and Cho et al. [29] reviewed the experimental facilities available currently (Table 2-1), and a 10MW scale-up plant construction is underway [28,30]. This PhD project focused only on indirect sCO_2 cycles.

Table 2-1 sCO_2 cycle experimental facilities [29]

	KIER (2013–2014) [11]	KIER (2014–)	KIER (2015–)	SNL (USA)	BMPC (USA)
Capacity/kWe	10	Sub-kWe	100	250 (125 + 125)	100
Cycle	Simple un-recuperated closed Brayton	Transcritical & Simple recuperated	Dual Brayton	Recompression closed Brayton	Simple recuperated closed Brayton
Turbomachinery	1 TAC	1 Turbo-generator	1 TAC (designed) + 1 Turbo-generator* (built)	2 TACs	1 turbo-compressor + 1 turbo-generator
Compressor	Centrifugal, shrouded	Positive displacement pump	Centrifugal	Centrifugal	Centrifugal
Turbine	Radial, shrouded	Radial w/Partial admission nozzle	Axial impulse w/ Partial admission nozzle*	Radial	Radial
Bearing	Gas foil journal/thrust	Angular contact ball (Oil lubrication)	Tilting-pad* (Oil lubrication)	Gas foil journal/thrust	Gas foil journal/thrust
Design speed/(RPM)	70000	200000	45000*	75000	75000
Heater	Thermal oil boiler (LNG fired)	Immersion electric heater	LNG fired flue gas heater	Immersion type electric heater	Heat transfer fluid electric heater
Recuperator	–	1 PCHE	2 PCHE	2 PCHE	1 wavy-fin, wire mesh
Electric power generation (kWe/ MPa/°C/kRPM/yr)	0.0/8.5/85/30/2014	0.4 (turbine) /2.95/110/90/ 2016 (operated with R134a as a working fluid)	0.0/0/0/0/2016 (preliminary testing)	15/10.5/477 /50/2012	40/14.1/282 /55/2014

2.3.1 Bottoming Cycle Application

Numerous cycle configurations are proposed for different heat sources and Crespi et al. [31,32] reviewed forty-two of them. Figure 2-6 compares the occurrence of the pinch in steam and sCO_2 cycle and it is clear that the sCO_2 better follows the flue gas temperature profile as no phase change is involved, minimising the exergy destruction [33]. It is also worth commenting that the mean temperature driving force can reduce when approaching close to ideal temperature glide, maximising the conductance. For a bottoming cycle, the net power or the overall efficiency, the product of $\eta_{boiler} \times \eta_{cycle}$, has to be maximised. Maximising the boiler efficiency requires (η_{boiler}) to cool the flue gas down to the minimum stack temperature, whereas maximising the cycle efficiency (η_{cycle}), maximises the turbine inlet temperature (higher Carnot efficiency). The temperature drop across the turbine is relatively smaller than steam Rankine cycle owing to the lower cycle pressure ratio, impacting the temperature rise

across the primary heat exchanger (ΔT). For instance, the ΔT of the recompression cycle is lower (220 °C), whereas it is as high as 285 °C for the simple recuperative cycle and partial cooling cycle when the turbine inlet temperature and pressure are 750 °C and 300 bar respectively [32]. This limits the ability to integrate the cycle with certain heat sources including waste heat recovery and bottoming cycle applications, where a large ΔT is necessary to maximise the boiler efficiency. Cascade cycles are proposed in order to increase the ΔT [34], maximising the heat recovery. Cho et al. [35] analysed the combination of recompression and partial heating cycles, and a combined precompression and partial heating cycle to overcome this problem, however, they concluded that the performance of cascade cycles remained superior to these cycles. Held et al. [36] proposed a dual rail cycle which is an extension of the cycle described as cascade 3 in this paper which offers an ideal temperature glide between the two streams of the exhaust heat exchanger because of the additional degrees of freedom. The installation cost of integrating simple recuperative Brayton cycle with LM - 2500PE gas turbine exhaust is about 1700$/kW [37]. The cycle selection is sensitive to the quality of the gas turbine (GT) exhaust [38], and the commercial GT exhaust temperature varies significantly. For instance, the heavy-duty industrial machine has a higher exhaust temperature (lower pressure ratio) compared to aero-derivative machines. Therefore, a set of performance maps for potential sCO_2 cycles that aids in estimating the performance when integrated with different GT exhaust conditions can solve this problem, which is solved as part of this PhD project (Obj. 1a) and elucidated in Chapter 3.

Exergo-economic analysis is a growing field in thermodynamics, which calculates the exergy related costs for thermal processes that aid in identifying critical components in the process on the basis of capital and exergy destruction cost [39,40][41]. Wang et al. [42,43] applied this method to recompression cycle and Luo et al. [44] compared the standard recuperative, recompression and partial cooling cycle. However, this technique has not been applied to the bottoming cycle with the objective of minimising the whole plant cost, which is performed as part of this PhD project (Obj. 1b) and explained in Chapter 4

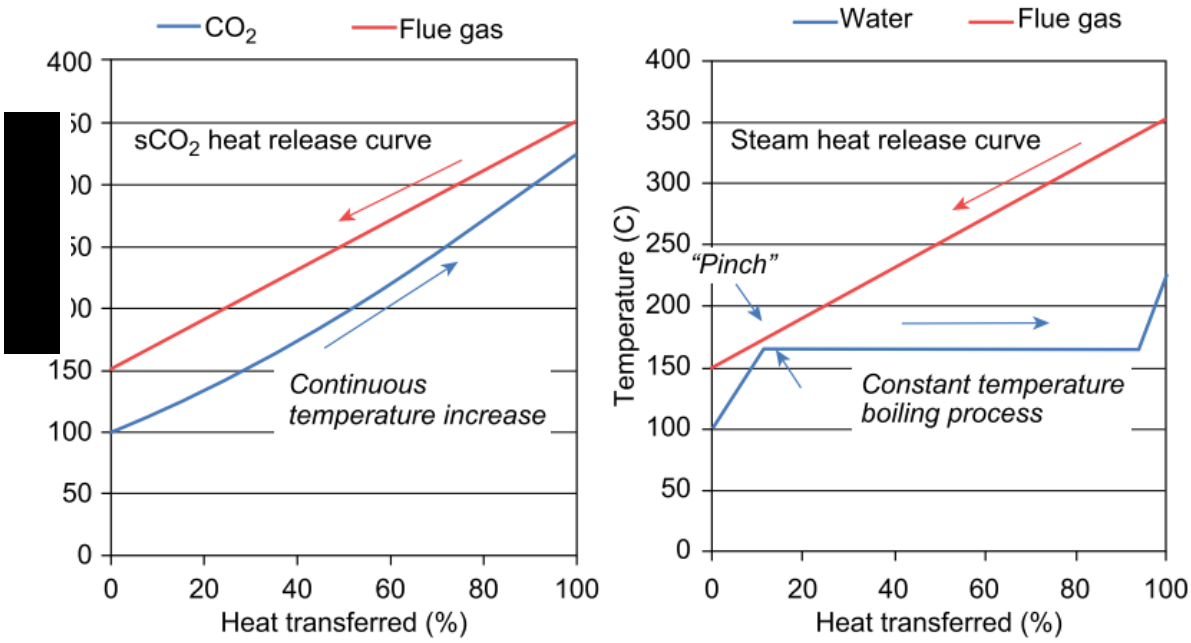

Figure 2-6 Pinch point of steam cycle (left) and sCO_2 cycle (right) [33]

2.3.2 Coal-Fired Power Plant

For a given power output, the sCO_2 mass flow rate through the turbine is about 8-12 times higher than steam Rankine cycles, not only because of the lower specific power (low pressure ratio) but also the isobaric specific heat of CO_2 is lower than steam (about 2.5 times) [27]. Being a low-pressure ratio cycle, sCO_2 cycles are sensitive to cycle pressure drop than the equivalent steam Rankine cycle. For instance, neglecting the boiler pressure drop can overestimate the efficiency by up to 1.6% [27]. The challenge is to minimise the pressure drop with a higher mass flow rate without notably increasing the tube diameter as bigger diameter tubes increase the capital cost, particularly when high temperature nickel-based alloys are required. Designing the boiler radiant section is also critical as the inlet sCO_2 temperature from a recompression cycle to the boiler is too high (~530 °C) to cool the membrane tubes, demanding the use of refractory lined heater walls behind the membrane wall [27].

Partial cooling cycle has a higher ΔT with a small penalty in efficiency, therefore this cycle could offer a lower CAPEX configuration [27]. Cascade cycles can accept the heat over a large temperature range; however, the efficiency of this

cycle is lower where internal recycling of hot sources is possible such as nuclear and CSP [36]. For a coal-fired plant, the flue gas must be cooled to the maximum air preheater (APH) temperature limitations to maximise the boiler efficiency, therefore, the Cascade cycles and their variants can be attractive depending on the ΔT requirement. Miller et al. [45] suggested a maximum APH temperature is 371 °C which is unlikely to be achieved with the standard proposed cycles, therefore, alternative cycle configurations are investigated. Miller et.al. [45] showed that the theoretical maximum efficiency of cascade cycles is 27% and 32% whilst the maximum efficiency of RCBC is 34% and 34.5% when the TIT is 593 °C and 730 °C respectively. Zhao et al. [46,47] performed a superstructure based optimisation to explore the optimal cycle configuration by fixing the boiler efficiency and concluded that the selection of compressor inlet temperature does not influence the optimal layout selection based on cycle efficiency, whilst the TIT impact the efficiency without notable changes in component size, within the investigated search space. Mercheri et.al. [48] integrated RCBC and their variants with coal-fired plant concluding that single reheater offers 1.5%pt increase in efficiency whilst double rehear and double recompression increases the efficiency by 0.3 and 0.5%pts respectively. Yann Le Moullec [49] has integrated a sCO_2 cycle with and without post combustion carbon capture (mono-ethanolamine as solvent) and showed that a net efficiency of 41.3% (LHV basis) is achievable when the CO_2 is compressed to 110 bar. There is no systematic optimisation of comparing sCO_2 cycles derived from recompression, partial cooling and cascade cycle with the realistic constraints including boiler pressure drop, state of the art APH temperature limits, which is performed as part of this PhD project (Obj. 2a) and elaborated in Chapter 5.

2.3.3 Concentrated Solar Power with Thermal Energy Storage

Although maximum internal recirculation of the heat (recuperation) within the cycle is desirable for a CSP application that increases the cycle efficiency ($\eta_{cycle} = f \times (1 - \frac{\overline{T_C}}{\overline{T_h}})$), where f is the Carnot factor and $\overline{T_c}$ is the mean sink temperature, owing to increasing mean heat addition temperature ($\overline{T_h}$), integration of sensible heat storage system requires to have higher ΔT to reduce

the storage cost. A partial cooling cycle results in a lower LCOE for a CSP plant integrated with sensible heat thermal energy storage (TES) than recompression cycle [50]. The partial cooling cycle also reduces the cost of sensible storage system due to the higher ΔT compared to recompression cycle, therefore, Neises and Turchi [51] recommended further research on this cycle as recompression cycle is mostly investigated for CSP application. However, maximising the power cycle ΔT reduces the efficiency as the mean Carnot heat addition temperature reduces, which penalties the cost of the solar field. Therefore, for a given set of solar field and TES cost functions, there should be an optimal ΔT at which the total cost of TES and solar field is minimised. An ideal power cycle has to have maximum efficiency at this ΔT in order to minimise the total plant cost. This has been studied as part of this PhD project (Obj. 3a) using nine sCO_2 cycle configurations (discussed in Chapter 6).

2.3.4 Off-design performance of sCO_2 cycle integrated with CSP and TES

Clementoni et al. provided the steady-state [52], off-design [53] and transient [54] operational results of a 100kWe experimental facility at the Naval Nuclear Laboratory, USA. Clementoni et al. [55] also reported the operational results of the test facility for different compressor inlet temperatures (CIT). Although the design point performance of sCO_2 cycles is extensively studied, the off-design performance is seldom investigated, except recompression cycle [56–58]. CSP plant encounters a significant variation in the heat input and ambient temperature, therefore, cycle off-design performance is crucial. Dyreby et al. [56] have developed a FORTRAN® based design and off-design code that can simulate the recompression cycle. Tse et al. [57] integrated a primary heat exchanger (PHEX) code with Dyreby's code through an external iterative procedure, concluding that the off-design performance not only affects the cycle performance, but also can influence the capacity of the TES and the solar receiver performance. The off-design cycle pressure ratio of sCO_2 cycle reduces at higher ambient temperatures [58]. This indicates that the turbine expansion ratio reduces which increases, the turbine exhaust temperature (TET) for a given TIT and since sCO_2 cycles are recuperative Brayton cycles, this higher TET increases the

recuperation. Consequently, the cold stream inlet temperature to the primary heat exchanger increases, which causes the molten salt outlet temperature (MSOT) to increase at higher ambient temperatures. This negatively affects solar field performance in two ways: 1) the energy absorption window of the solar receiver reduces when the molten salt mass flow reaches its maximum flow limit, and 2) the cold storage tank temperature gradually increases, reducing the capacity of thermal energy storage as the differential temperature reduces.

Clementoni et al. [59] analysed the effect of compressor inlet pressure on the performance of the sCO_2 cycle and compared with the operational results, concluding that the cycle power output and efficiency are directly affected by the compressor inlet density. Anselmi et al. [60] explained the test facility operations along with the preliminary modelling works of compressor design and control strategy. Duniam et al. [61] analysed the off-design performance of a sCO_2 cycle integrated with a natural draft dry cooling tower, concluding that the cycle net power reduces by 10% for each 10 °C increase in ambient temperature above the design temperature when cycle inventory and turbine inlet temperature (TIT) is maintained at the design values. Wright et al. [62] investigated four different sCO_2 cycle control strategies for a waste heat recovery application, including; cooling air fan speed control, boost compressor speed control, split fraction control and compressor inlet pressure control. They concluded that the combination of all four controls provides an efficient way to mitigate the effects of heat rejection at a higher ambient temperature. Wang et al. [63] analysed the performance of a direct air-cooled sCO_2 cycle under off-design conditions, observing that the cooling-tower approach temperature varies nonlinearly with the ambient temperature. the aforementioned studies investigated the performance of RCBC for different control techniques, however, there has been no systematic study that explores the optimal operational space (multi-dimensional Pareto front) for different boundary conditions, and investigate the trends of critical control variables including minimum/ maximum pressure, shaft speed and split fraction that aids in developing the optimal control strategy, which is investigated as part of this PhD project (Obj. 3b,3c) and discussed in Chapter 7.

2.3.5 sCO_2 cycle transient Performance

Several research groups have performed transient simulations of the standard recompression cycle [54,64], concluding that inventory control provides higher efficiency at part load compared to other control techniques such as turbine bypass, turbine inlet temperature and throttling control. Inventory control turndown is limited by the size of the CO_2 storage tank and the pressure pinch between that storage tank pressure and the system pressure. Although a bigger inventory storage tank can push the sCO_2 cycle turndown ratio further, the optimal size is an economical trade-off between the CAPEX and improvement in annual energy generation [55]. Researchers have proposed that turbine bypass control or throttle control is required to extend the plant turndown further [65–67] and to have a faster response during load throw-off as inventory control is slower. Since the turbomachinery is compact their volumes are negligible [68,69], therefore, the plant dynamics are mainly dictated by the response of the heat exchangers. Availability of the experimental data in the literate is uncommon, challenging the validity of the transient models. The nonlinear fluid properties variation not only increases the discretisation, consequently the computational time, but also complicates the numerical schemes. A faster, numerically stable numerical scheme for the heat exchanger is essential to aid in developing the plant controls and the heat exchanger numerical scheme is developed as part of this project (Obj. 3d) and explained in Chapter 8.

2.4 Component development review

The main cycle components include heat exchangers and turbomachinery including compressor and turbines.

2.4.1 Compact Heat Exchanger

sCO_2 cycles are highly recuperative cycles, recovering the heat from the turbine exhaust. The heat exchangers must withstand high temperatures and pressures as showing in Figure 2-7 (left). The design of HTR and the primary heater may require high nickel alloy due to its high design temperature and material maximum allowable stress (Figure 2-7, right). Moreover, the material requires to have high

corrosion, creep and oxidation resistance and with CO_2 and other impurities expected during the lifetime of the cycle [70–72].

Different types of compact heat exchanger configurations (>700 m^2/m^3 heat transfer surface area density [73,74]) are examined (Figure 2-8, left) and microtube and stacked-sheet type heat exchangers are recommended [75], whereas the cost of other types of heat exchanger such as corrugated heat exchanger including manifold cost, helical, spiral-wound and plate-fin are higher [75].

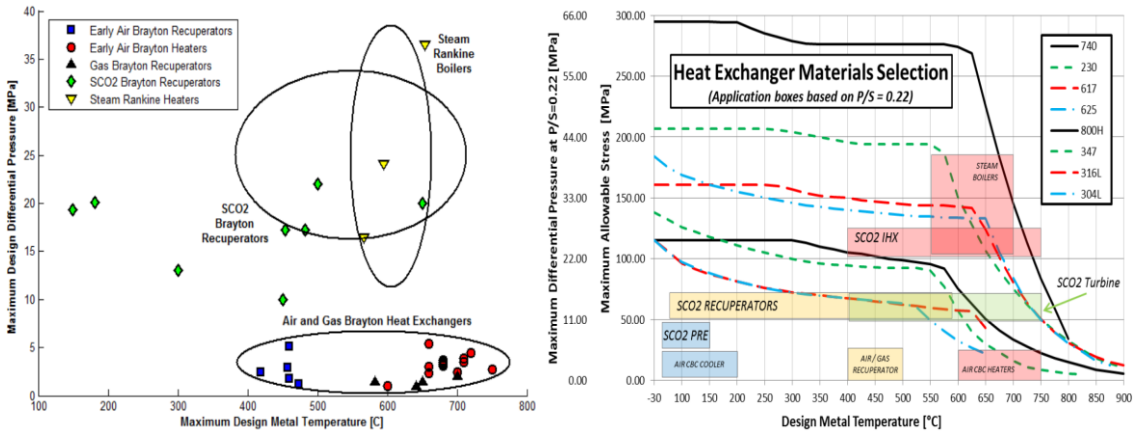

Figure 2-7 sCO_2 cycle heat exchanger left) Range of pressure and temperature, right) Material strength [75]

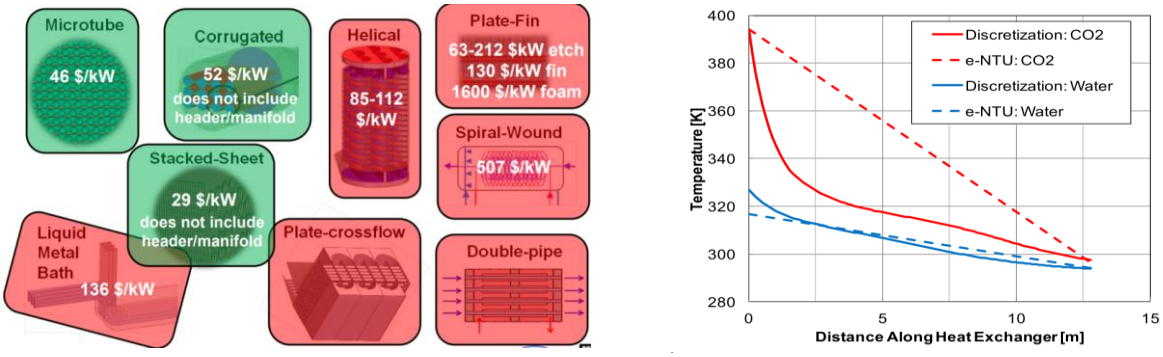

Figure 2-8 Left) Selection of Compact Heat exchanger, right) Temperature profile along the length of the heat exchanger with and without discretisation [75–77]

The double pipe configuration increased the pressure drop without increasing the heat transfer, whereas the plate cross-flow requires more number of tube count compared to microtube [75]. The shell and tube configuration is higher than

compact printed circuit heat exchanger (1000-2000 m^2/m^3 [78]) and plate-fin heat exchanger (PFHE) at a higher scale [76]. PCHE costs about \$90/kW_{th} [78], or \$50/kg [79,80], therefore, different technologies to reduce the cost is under research. As the plant size increases, the cost per kW of the heat exchanger decreases due to economy of scale.

Since sCO_2 properties vary dramatically, the temperature- heat curve (T-Q diagram) of the recuperator varies drastically when reducing the inlet temperature away from the designed operating temperature. The pinch occurring location can change from LTR to HTR when the inlet temperature is lowered too much, leaving LTR redundant [81]. Although the cycle is designed to operate above the critical point, CO_2 can condense in the precooler during cold day conditions [76]. Since the traditional log-mean temperature difference method (LMTD) assumes a constant isobaric specific heat (c_p), this method cannot be applied to supercritical fluids where the variation of c_p is higher [78,82]. The pinch can occur within the heat exchanger, therefore, discretisation is crucial when sizing the heat exchanger as shown in Figure 2-8 (right) [77]

Lei Chai and Savvas Tassou [83] compared the effect of different cross-section geometry on the thermohydraulic performance using CFD simulation, observing that semi-circular flow passage shape reduces the pressure drop by about 4.5% compared to the circular duct for the same hydraulic diameter whilst circular and elliptical shapes have a higher heat transfer coefficient [84]. The rectangular channel with a width to height ratio of 2 achieves the most balanced stress characteristic and higher thermal-hydraulic performance [85]. The heat transfer pressure drop correlations for different geometry configurations are discussed in [86–90]. For an air-cooled precooler, the pressure drop in the airside has to be reduced to allow shorter channel lengths and larger flow areas on the airside, whilst maintaining long flow paths on the sCO_2 side with high Reynolds numbers (E.g. Harsco® cooler) [91]. The plant capital cost of the optimised air-cooled sCO_2 recompression cycle is 4833 \$/kW_e for 105 MW_e Advanced Fast Reactor (AFR)-100 Sodium-Cooled Fast Reactor Small Modular Reactor. This corresponds to

only about 1-5% increase in the plant capital cost compared to the reference water-cooled sCO_2 recompression cycle (i.e. 4780 $/$kW_e$) [13,92].

2.4.2 Turbomachinery

The liquid to vapour density ratio of sCO_2 is roughly a factor of 3:1, because of this small density ratio, a radial compressor may be able to "pump" liquid CO_2, supercritical vapour and two-phase mixtures [93]. However, the range of the compressor can be limited owing to the larger variation of the volumetric flow rate. The real gas effect on the compressor design is discussed by Baltadjiev [2] and the centrifugal compressor design procedure is discussed by Brenes [94]. sCO_2 behaves fairly as an ideal gas at conditions expected at the turbine inlet, reducing the design challenges. However, the power density of the turbine is about 10 times higher than the equivalent steam Rankine cycle, which increases the force acting on the blade per unit volume [27]. The design procedure for a radial compressor using the commercial software AxSTREAM® is discussed by Samad et al. [95]. The sealing and high speed bearing are also challenging, particularly for a smaller plant size, which is discussed elsewhere [96–99]. The component technology selection options as a function of the plant size are shown in Figure 2-9.

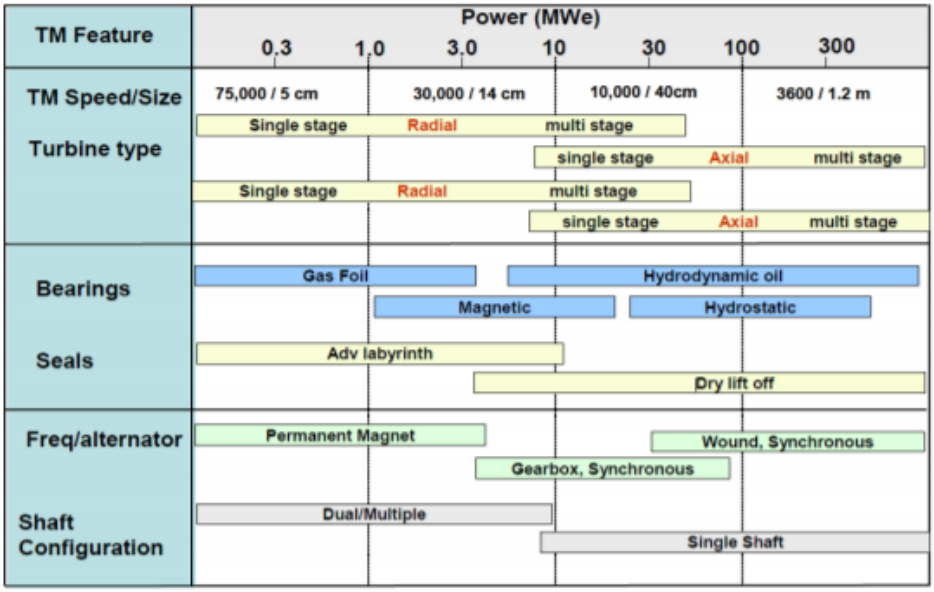

Figure 2-9 Technology Scaling Options [100]

2.5 Critical Review of the Modelling Assumptions

The process modelling assumptions including the compressor isentropic efficiency, turbine isentropic efficiency, recuperator effectiveness, compressor inlet temperature (CIT) and turbine inlet temperature (TIT) have to be realistic in order to guarantee the reliability of the generated results. Since the thermal physical properties close to the critical point varies dramatically, the CIT and the compressor inlet pressure can increase the difficulty of the compressor design process and stable off-design operation. A CIT of 32 °C is often regarded as a standard value unless the ambient temperature is higher than this value. The TIT is limited by the material viability and the current state of the art materials developed for advanced ultra-supercritical (AUSC) steam plants can handle up to 760 °C, therefore, this thesis limits the TIT up to 760 °C.

Based on the mean-line 1D models, a compressor isentropic efficiency of 83-90% is achievable [49,101] depending on whether the compressor type is radial or (multi-stage) axial. On the other hand, a turbine efficiency of 90.6-93% [97,102] can be realisable. Therefore, the selected turbomachinery efficiency lies within this range reported in the literature. The recuperator effectiveness can be as high as 98% [103], however, this is an economical attribute.

2.6 References

[1] Zhao Q, Mecheri M, Neveux T, Privat R, Jaubert JN. Selection of a Proper Equation of State for the Modeling of a Supercritical CO_2 Brayton Cycle: Consequences on the Process Design. Ind Eng Chem Res 2017;56:6841–53. doi:10.1021/acs.iecr.7b00917.

[2] Baltadjiev ND. An Investigation of Real Gas Effects in Supercritical CO_2 Compressors. Massachusetts Institute of Technology, 2012. doi:10.1115/1.4029616.

[3] Lemmon EW, Huber ML, McLinden MO. NIST Standard Reference Database 23. Natl Inst Stand Technol 2013;V 9.1.

[4] Anderson MR. Super Critical CO_2 Compressor Design 2020.

https://www.conceptsnrec.com/blog/super-critical-co2-compressor-design (accessed 10 September 2020).

[5] Conboy T, Wright S. Experimental Investigation of the CO_2 Condensing Cycle. Supercrit. CO2 Power Cycle Symp. 2011, 2011, p. 1–14.

[6] Wright S a, Radel RF, Vernon ME, Rochau GE, Pickard PS. Operation and Analysis of a Supercritical CO2 Brayton Cycle. SANDIA Rep SAND2010-0171 2010:101. doi:SAND2010-0171.

[7] Steven WA, Tom C, Edward P, Tom L, Gary R, J S-AA. Summary of the Sandia Supercritical CO_2 Development Program. Int. SCO2 Power Cycle Symp., Boulder, Colorado: 2011.

[8] Bennett J, Wilkes J, Allison T, Pelton R, Wygant K. Cycle modeling and optimization of an integrally geared sCO2 compander. ASME Turbo Expo, 2017, p. 1–8. doi:10.1115/GT2017-63707.

[9] Rodgers C. Centrifugal compressor inlet guide vanes for increased surge margin. J Turbomach 1991;113:696–702. doi:10.1115/1.2929136.

[10] Anderson MR. Atypical fluid behavior on the liquid side of the saturation line of CO_2 with implications for compressor design. 6th Int Symp - Supercrit CO2 Power Cycles 2018.

[11] Hacks AJ, Schuster S, Brillert D. Stabilizing effects of supercritical CO_2 fluid properties on compressor operation. Int J Turbomachinery, Propuls Power 2019;4. doi:10.3390/ijtpp4030020.

[12] Kiran E, Debenedetti PG, Peters CJ. Supercritical Fluids Fundamentals and Applications. 2000. doi:10.1007/978-94-011-3929-8_17.

[13] Ranjan D. Fundamental Study Of Key Issues Related To Advanced sCO_2 Brayton Cycle : Prototypic HX Development And Cavitation. n.d.

[14] Saravi SS, Tassou SA. An investigation into sCO_2 compressor performance prediction in the supercritical region for power systems. Energy Procedia, vol. 161, Elsevier B.V.; 2018, p. 403–11.

doi:10.1016/j.egypro.2019.02.098.

[15] Brenes BM. Design of supercritical carbon dioxide centrifugal compressors Design of supercritical carbon dioxide centrifugal compressors 2014.

[16] Angelino G. Real Gas Effects in Carbon Dioxide Cycles. ASME- Pap 69-Gt-102 1969:1–12. doi:10.1115/69-GT-102.

[17] Angelino G. Carbon dioxide condensation cycles for power production. J Eng Gas Turbines Power 1968;90:287–95. doi:10.1115/1.3609190.

[18] Angelino G. Perspectives for the liquid phase compression gas turbine. J Eng Gas Turbines Power 1967;89:229–36. doi:10.1115/1.3616657.

[19] Feher EG. The Supercritical Thermodynamic Power Cycle. Energy Convers 1968;8:85–90. doi:10.1016/0013-7480(68)90105-8.

[20] Dostal V, Driscoll MJ, Hejzlar P. A Supercritical Carbon Dioxide Cycle for Next Generation Nuclear Reactors. 2004. doi:MIT-ANP-TR-100.

[21] Ahn Y, Bae SJ, Kim M, Cho SK, Baik S, Lee JI, et al. Review of supercritical CO_2 power cycle technology and current status of research and development. Nucl Eng Technol 2015;47:647–61. doi:10.1016/j.net.2015.06.009.

[22] Zhu Q. High-efficiency power generation – review of alternative systems. 2015.

[23] Allam R, Martin S, Forrest B, Fetvedt J, Lu X, Freed D, et al. Demonstration of the Allam Cycle: An Update on the Development Status of a High Efficiency Supercritical Carbon Dioxide Power Process Employing Full Carbon Capture. Energy Procedia, vol. 114, The Author(s); 2017, p. 5948–66. doi:10.1016/j.egypro.2017.03.1731.

[24] Allam RJ, Palmer MR, Brown GW, Fetvedt J, Freed D, Nomoto H, et al. High efficiency and low cost of electricity generation from fossil fuels while eliminating atmospheric emissions, including carbon dioxide. Energy Procedia 2013;37:1135–49. doi:10.1016/j.egypro.2013.05.211.

[25] Wang K, He YL, Zhu HH. Integration between supercritical CO_2 Brayton cycles and molten salt solar power towers: A review and a comprehensive comparison of different cycle layouts. Appl Energy 2017;195:819–36. doi:10.1016/j.apenergy.2017.03.099.

[26] Kulhánek M, Dostál V. Thermodynamic Analysis and Comparison of Supercritical Carbon Dioxide Cycles. Proc SCCO2 Power Cycle Symp 2011:1–7.

[27] Weiland NT, Dennis RA, Ames R, Lawson S, Strakey P. Fossil energy. Elsevier Ltd; 2017. doi:10.1016/B978-0-08-100804-1.00012-8.

[28] Lecompte S, Ntavou E, Tchanche B, Kosmadakis G, Pillai A, Manolakos D, et al. Review of experimental research on supercritical and transcritical thermodynamic cycles designed for heat recovery application. Appl Sci 2019;9:1–26. doi:10.3390/app9122571.

[29] Cho J, Shin H, Cho J, Kang YS, Ra HS, Roh C, et al. Preliminary experimental study of a supercritical CO2 power cycle test loop with a high-speed turbo-generator using R134a under similarity conditions. Front Energy 2017;11:452–60. doi:10.1007/s11708-017-0504-4.

[30] Black & Veatch. Molten Salt Concept Definition & Capital Cost Estimate, Prepared for SunShot U.S. Department of Energy. 2016. doi:10.2172/1335150.

[31] Crespi F, Gavagnin G, Sánchez D, Martínez GS. Supercritical carbon dioxide cycles for power generation: A review. Appl Energy 2017;195:152–83. doi:10.1016/j.apenergy.2017.02.048.

[32] Crespi F, Sánchez D, Sánchez T, Martínez GS. Capital Cost Assessment of Concentrated Solar Power Plants Based on Supercritical Carbon Dioxide Power Cycles. J Eng Gas Turbines Power 2019;141:1–9. doi:10.1115/1.4042304.

[33] Poerner M, Rimpel A. Waste heat recovery. Elsevier Ltd; 2017. doi:10.1016/B978-0-08-100804-1.00010-4.

[34] Kimzey G. Development of a Brayton Bottoming Cycle using Supercritical Carbon Dioxide as the Working Fluid. 2012.

[35] Cho SK, Kim M, Baik S, Ahn Y. Investigation of the Bottoming Cycle for High Efficiency Combined Cycle Gas Turbine System With Supercritical Carbon Dioxide. Proc. ASME Turbo Expo 2015 Turbine Tech. Conf. Expo., 2015, p. 1–12.

[36] Held TJ. Supercritical CO_2 Cycles for Gas Turbine Combined Cycle Power Plants. Power Gen Int., 2015.

[37] Wright S, Scammell W. Economics. Fundam Appl Supercrit Carbon Dioxide Based Power Cycles 2017:127–45. doi:10.1016/B978-0-08-100804-1.00006-2.

[38] Khadse A, Blanchette L, Kapat J, Vasu S, Ahmed K. Optimization of supercritical CO_2 Brayton cycle for simple cycle gas turbines exhaust heat recovery using genetic algorithm. ASME Turbo Expo 2017:1–8. doi:10.1115/GT2017-63696.

[39] Bejan A, Moran MJ. Thermal Design and Optimization. 1996. doi:10.1016/S0140-7007(97)87632-3.

[40] Lazzaretto A, Tsatsaronis G. SPECO: A systematic and general methodology for calculating efficiencies and costs in thermal systems. Energy 2006;31:1257–89. doi:10.1016/j.energy.2005.03.011.

[41] Bejan A. Thermodynamic Optimization of Complex Energy Systems. 1999. doi:10.1007/978-94-011-4685-2.

[42] Wang X, Dai Y. Exergoeconomic analysis of utilizing the transcritical CO_2 cycle and the ORC for a recompression supercritical CO_2 cycle waste heat recovery: A comparative study. Appl Energy 2016;170:193–207. doi:10.1016/j.apenergy.2016.02.112.

[43] Wang X, Yang Y, Zheng Y, Dai Y. Exergy and exergoeconomic analyses of a supercritical CO2cycle for a cogeneration application. Energy

2017;119:971–82. doi:10.1016/j.energy.2016.11.044.

[44] Luo D, Huang D. Thermodynamic and exergoeconomic investigation of various SCO 2 Brayton cycles for next generation nuclear reactors. Energy Convers Manag 2020;209:112649. doi:10.1016/j.enconman.2020.112649.

[45] Miller JD, Buckmaster DJ, Hart K, Held TJ, Thimsen D, Maxson A, et al. Comparison of supercritical CO_2 power cycles to steam Rankine cycles in coal-fired applications. ASME Turbo Expo 2017 Turbomach. Tech. Conf. Expo., 2017, p. 1–12. doi:10.1115/GT2017-64933.

[46] Zhao Q. Conception and optimization of supercritical CO_2 Brayton cycles for coal-fired power plant application, PhD Thesis. Université de Lorraine, Lorraine, France, 2018.

[47] Zhao Q, Mecheri M, Neveux T, Privat R, Jaubert J-N. Design of SC-CO_2 Brayton cycles using MINLP optimization within a commercial simulator. 6th Int. Supercrit. CO2 Power Cycles Symp., Pittsburgh, Pennsylvania: 2018, p. 1–13.

[48] Mecheri M, Le Moullec Y. Supercritical CO_2 Brayton cycles for coal-fired power plants. Energy 2016;103:758–71. doi:10.1016/j.energy.2016.02.111.

[49] Le Moullec Y. Conceptual study of a high efficiency coal-fired power plant with CO_2 capture using a supercritical CO_2 Brayton cycle. Energy 2013;49:32–46. doi:10.1016/j.energy.2012.10.022.

[50] Neises T, Turchi C. Supercritical CO2 Power Cycles: Design Considerations for Concentrating Solar Power. 4th Int Symp - Supercrit CO2 Power Cycles 2013;53:1689–99. doi:10.1017/CBO9781107415324.004.

[51] Neises T, Turchi C. A comparison of supercritical carbon dioxide power cycle configurations with an emphasis on CSP applications. Energy Procedia 2013;49:1187–96. doi:10.1016/j.egypro.2014.03.128.

[52] Clementoni EM, Cox TL, King MA. Steady-State Power Operation Of A Supercritical Carbon Dioxide Brayton Cycle With Thermal-Hydraulic Control. ASME Turbo Expo 2016 Turbomach. Tech. Conf. Expo., Seoul, South Korea: 2016, p. 1–10. doi:10.1115/GT2016-56038.

[53] Clementoni EM, Cox TL, King MA. Off-Nominal Component Performance in a Supercritical Carbon Dioxide Brayton Cycle. J Eng Gas Turbines Power 2015;138:011703. doi:10.1115/1.4031182.

[54] Clementoni EM, Cox TL, King MA, Rahner KD. Transient power operation of a supercritical carbon dioxide Brayton cycle. ASME Turbo Expo, Charlotte, NC, USA: 2017. doi:10.1115/GT2017-63056.

[55] Clementoni EM, Cox TL. Effect of compressor inlet pressure on cycle performance for a supercritical carbon dioxide brayton cycle. 6th Int. Supercrit. CO2 Power Cycles Symp., vol. 9, Pittsburgh, Pennsylvania: 2018, p. 2–10.

[56] John J. Dyreby. Modeling the Supercritical Carbon Dioxide Brayton Cycle with Recompression. 2014.

[57] Tse LA, Neises T. Analysis and optimization for off-design performance of the recompression sCO2 cycles for high temperature CSP applications. 5th Int Symp CO2 Power Cycles 2016:1–13.

[58] Bennett J, Wilkes J, Allison T, Pelton R, Wygant K. Cycle modeling and optimization of an integrally geared sCO_2 compander. ASME Turbo Expo, Charlotte, NC, USA: 2017, p. 1–8. doi:10.1115/GT2017-63707.

[59] Clementoni EM, Cox TL. Effect of compressor inlet pressure on cycle performance for a supercritical carbon dioxide brayton cycle. Proc. ASME Turbo Expo, vol. 9, Oslo, Norway: 2018, p. 1–8. doi:10.1115/GT2018-75182.

[60] Anselmi E, Johnston M, Bunce I. An Overview of the Rolls-Royce sCO_2 Test Rig Project at Cranfield. 6th Int. Symp. - Supercrit. CO2 Power Cycles, Pittsburgh, Pennsylvania: 2018.

[61] Duniam S, Veeraragavan A. Off-design performance of the supercritical carbon dioxide recompression Brayton cycle with NDDCT cooling for concentrating solar power. Energy 2019;187:115992. doi:10.1016/j.energy.2019.115992.

[62] Wright SA, Davidson CS, Husa C. Off-design performance modeling results for a supercritical CO_2 waste heat recovery power system. 6th Int Symp - Supercrit CO2 Power Cycles 2018:1–10.

[63] Wang X, Li X, Li Q, Liu L, Liu C. Performance of a solar thermal power plant with direct air-cooled supercritical carbon dioxide Brayton cycle under off-design conditions. Appl Energy 2020;261:114359. doi:10.1016/j.apenergy.2019.114359.

[64] Lambruschini F, Zitney SE, Liese E, Traverso A. Dynamic Model Of A 10 MW Supercritical CO_2 Recompression Brayton Cycle. Proc. ASME Turbo Expo 2016, 2016, p. 1–9.

[65] Yan XL. Dynamic Analysis and Control System Design for an Advanced Nuclear Gas Turbine Power Plant. Massachusetts Institute of Technology, 1990.

[66] J.H.Horlock. Advanced Gas Turbine Cycles. 1st ed. Pergamon; 2003.

[67] Frutschi HU. Closed-Cycle Gas Turbines: Operating Experience and Future Potential. ASME Press; 2005. doi:10.1115/1.802264.

[68] Alfani D, Astolfi M, Binotti M, Campanari S, Casella F, Silva P. Multi objective optimization of flexible supercritical CO_2 coal-fired power plants. Proc ASME Turbo Expo 2019;3:1–11. doi:10.1115/GT2019-91789.

[69] Singh R, Rowlands AS, Miller SA. Effects of relative volume-ratios on dynamic performance of a direct-heated supercritical carbon-dioxide closed Brayton cycle in a solar-thermal power plant. Energy 2013;55:1025–32. doi:10.1016/j.energy.2013.03.049.

[70] Fleming D, Nm SNL, Kruizenga A, Ca SNL. Identified Corrosion and

Erosion Mechanisms in SCO2 Brayton Cycles 2014.

[71] Zhang DJ, Zeng M, Wang QW. Creep Analysis Of Cross Wavy Primary Surface Recuperator for Microturbine System. Proc ASME Turbo Expo 2008;1:905–10. doi:10.1115/GT2008-51506.

[72] Maziasz PJ, Pint BA, Shingledecker JP, Evans ND, Yamamoto Y, More KL, et al. Advanced alloys for compact, high-efficiency, high-temperature heat-exchangers. Int J Hydrogen Energy 2007;32:3622–30. doi:10.1016/j.ijhydene.2006.08.018.

[73] Shah RK, Sekulic DP. Fundamentals of Heat Exchanger Design. Fundam Heat Exch Des 2003:863–905. doi:10.1002/9780470172605.ch13.

[74] HESSELGREAVES JE, LAW R, Reay DA. Compact Heat Exchangers Selection, Design and Operation. 2017.

[75] Chordia L, Green E, Li D, Portnoff M, Musgrove G, Cich S, et al. Development of Modular , Low-Cost , High-Temperature Recuperators for the sCO2 Power Cycles. 2016.

[76] Carlson M, Conboy T, Fleming D, Pasch J. Scaling Considerations for SCO2 Cycle Heat Exchangers. Proc. ASME Turbo Expo, Dusseldorf, Ger., 2014. doi:10.1115/GT2014-27233.

[77] Musgrove G, Rimpel AM, Wilkes JC. Fundamentals of Supercritical CO2. Supercrit. CO2 Power Cycle Symp. 2016, 2016.

[78] Dunn M, Cook M, Walsh T. High Temperature Heat Exchanger Design and Fabrication for Systems with Large Pressure Differentials: Final Scientific Technical Report 2013.

[79] Kim IH, No HC. Physical model development and optimal design of PCHE for intermediate heat exchangers in HTGRs. Nucl Eng Des 2012;243:243–50. doi:10.1016/j.nucengdes.2011.11.020.

[80] Gezelius K. Design of compact intermediate heat exchangers for gas cooled fast reactors. Massachusetts Institute of Technology, 2004.

[81] Pittaway C, Musgrove GO. Tutorial : Heat Exchangers for Supercritical CO2 Power Cycle Applications, 2013.

[82] Nellis G, Klein S. Heat Transfer. 2009. doi:10.1017/CBO9780511841606.

[83] Chai L, Tassou SA. Effect of cross-section geometry on the thermohydraulic characteristics of supercritical CO2 in minichannels. Energy Procedia 2019;161:446–53. doi:10.1016/j.egypro.2019.02.077.

[84] Marchionni M, Chai L, Bianchi G, Tassou SA. Numerical modelling and transient analysis of a printed circuit heat exchanger used as recuperator for supercritical CO2 heat to power conversion systems. Appl Therm Eng 2019;161:114190. doi:10.1016/j.applthermaleng.2019.114190.

[85] Hou Y, Tang G. Thermal-Hydraulic-Structural Analysis and Design Optimization for Micron-Sized Printed Circuit Heat Exchanger. J Therm Sci 2018;28:252–61. doi:10.1007/s11630-018-1062-8.

[86] Chu W, Li X hui, Ma T, Chen Y tung, Wang Q wang. Experimental investigation on SCO_2-water heat transfer characteristics in a printed circuit heat exchanger with straight channels. Int J Heat Mass Transf 2017;113:184–94. doi:10.1016/j.ijheatmasstransfer.2017.05.059.

[87] Chai L, Tassou SA. A review of printed circuit heat exchangers for helium and supercritical CO2 Brayton cycles. Therm Sci Eng Prog 2020;18:100543. doi:10.1016/j.tsep.2020.100543.

[88] Musgrove GO, Pierres R Le, Nash J. Heat Exchangers for Supercritical CO2 Power Cycle Applications. 4th Int Symp Supercrit CO2 Power Cycles 2014:1–61.

[89] Kim IH, Zhang X, Christensen R, Sun X. Design study and cost assessment of straight, zigzag, S-shape, and OSF PCHEs for a FLiNaK–SCO2Secondary Heat Exchanger in FHRs. Ann Nucl Energy 2016;94:129–37. doi:10.1016/j.anucene.2016.02.031.

[90] Li Q, Flamant G, Yuan X, Neveu P, Luo L. Compact heat exchangers: A

review and future applications for a new generation of high temperature solar receivers. Renew Sustain Energy Rev 2011;15:4855–75. doi:10.1016/j.rser.2011.07.066.

[91] Moisseytsev A, Lv Q, Sienicki JJ. Heat exchanger options for dry air cooling. ASME Turbo Expo 2017:1–11. doi:10.1115/GT2017-63187.

[92] Pidaparti SR, Moisseytsev A, Hruska PJ, Sienicki JJ, Ranjan D. Technical and Economic Feasibility of Dry Air Cooling for the Supercritical Co2 Brayton Cycle Using Existing Technology. 5th Int Symp - Supercrit CO2 Power Cycles 2016:1–23.

[93] Wright SA, Conboy TM, Radel RF, Rochau GE. Modeling and experimental results for condensing supercritical CO2 power cycles. SANDIA Rep SAND2010-8840 2011:1–47. doi:10.2172/1030354.

[94] Brenes BM. Design of supercritical carbon dioxide centrifugal compressors Design of supercritical carbon dioxide centrifugal compressors. Universidad de Sevilla, 2014.

[95] El Samad T, Teixeira JA, Oakey J. Investigation of a radial turbine design for a utility-scale supercritical CO_2 power cycle. Appl Sci 2020;10:1–26. doi:10.3390/APP10124168.

[96] A.Bidkar R. Conceptual Designs of 50MW and 450 MW supercritical CO_2 Turbomachinery Trains for Power Generation from Coal.Part2: Compressors. 5th Int. Symp. - Supercrit. CO2 Power Cycles, San Antonio, Texas, USA: 2016, p. 1–18.

[97] Bidkar RA, Mann A, Singh R, Sevincer E, Cich S, Day M, et al. Conceptual Designs of 50MWe and 450MWe Supercritical CO2 Turbomachinery Trains for Power Generation from Coal. Part 1: Cycle and Turbine. 5th Int Symp - Supercrit CO2 Power Cycles 2016:17.

[98] Bidkar R, Hofer D, Mann A, Wang J, Brun K, Kulhanek C, et al. sCO2 Turbomachinery and Low-Leakage sCO2 End Seals n.d.

[99] Li J, Gurgenci H, Guan Z. Bearing and Seal Selection for a High-Temperature Supercritical CO2 Turbine. Proc. Glob. Power Propuls. Soc., Beijing: 2019. doi:10.33737/gpps19-bj-040.

[100] Fleming DD, Conboy TM, Pasch JJ, Rochau GA, Fuller RL, Holschuh T V, et al. Scaling Considerations for a Multi- Megawatt Class Supercritical CO_2 Brayton Cycle and Commercialization. vol. SAND2013-9. 2013.

[101] Noall JS, Pasch JJ. Achievable Efficiency and Stability of Supercritical CO_2 Compression Systems Main Compressor Design Discussion. 4th Int Symp - Supercrit CO2 Power Cycles Sept 2014 2014:1–10.

[102] White CW, Weiland NT, Shelton WW, Shultz TR. sCO_2 cycle as an efficiency improvement opportunity for air-fired coal combustion. 6th Int Symp - Supercrit CO2 Power Cycles 2018:1–30.

[103] Li X, Pierres R Le, Dewson SJ. Heat Exchangers for the Next Generation of Nuclear Reactors The Next Generation of Nuclear Reactors 2006:201–9.

Chapter 3

3 Thermal performance and economic analysis of supercritical carbon dioxide cycles in combined cycle power plant

Dhinesh Thanganadar, Faisal Asfand , Kumar Patchigolla

School of Water, Energy and Environment (SWEE), Cranfield University, Cranfield, MK43 0AL, UK

Published in Applied Energy, 2019

DOI: 10.1016/j.apenergy.2019.113836

Statement of contributions of joint authorship

Dhinesh Thanganadar proposed the novelty, implemented the methods, generated all results, and prepared the manuscript draft. Faisal Asfand and Kumar Patchigolla provided supervision, proof-read and critically commented on the manuscript before submission.

ABSTRACT

A closed-loop, indirect, supercritical Carbon Dioxide (sCO_2) power cycle is attractive for fossil-fuel, solar thermal and nuclear applications owing to its ability to achieve higher efficiency, and compactness. Commercial Gas Turbines (GT's) are optimised to yield maximum performance with a conventional steam Rankine cycle. In order to explore the full potential of a sCO_2 cycle the whole plant performance needs to be considered. This study analyses the maximum performance and cost of electricity for five sCO_2 cascaded cycles. The plant performance is improved when the GT pressure ratio is considered as a design variable to a GT to optimise the whole plant performance. Results also indicate

that each sCO_2 Brayton cycle considered, attained maximum plant efficiency at a different GT pressure ratio. The optimum GT pressure ratio to realise the maximum cost reduction in sCO_2 cycle was higher than the equivalent steam Rankine cycle. Performance maps were developed for four high efficient cascaded sCO_2 cycles to estimate the specific power and net efficiency as a function of GT turbine inlet temperature and pressure ratio. The result of multi-objective optimisation in the thermal and cost (c$/kWh) domains and the Pareto fronts of the different sCO_2 cycles are presented and compared. A novel sCO_2 cycle configuration is proposed that provides ideal-temperature glide at the bottoming cycle heat exchangers and the efficiency of this cycle, integrated with a commercial SGT5-4000F machine in lieu of a triple-pressure steam Rankine cycle, is higher by 1.4 percentage point.

Keywords

Supercritical CO_2 cycle, Gas Turbine, Combined Cycle, Multi-Objective Optimisation, Optimum Pressure Ratio, sCO_2

3.1 Introduction

The UK is committed to reducing greenhouse gas emissions by at least 80% of 1990 levels by 2050 [1]. Meeting such a rigorous carbon emission reduction goal requires significant technological breakthroughs in the power generation industries. Although post-combustion carbon capture technologies are technically feasible, it is not economically attractive to implement in coal-fired power plants owing to a penalty in the net efficiency of about 7.7 to 11.9% points [2]. Hence new thermodynamic cycles that enhance CO_2 capture will become more practical if they can produce power at higher efficiency compared to conventional power technologies. sCO_2 cycles are therefore gaining more attention. The Supercritical Carbon Dioxide (sCO_2) Brayton cycle has many advantages over the conventional steam Rankine cycle or Brayton cycle owing to its simple layout, higher efficiency, and compact equipment size. The sCO_2 Brayton cycle is considered suitable for different heat sources such as nuclear, solar thermal, and fossil-fuel. A commercial packaged unit is currently available for low-grade waste heat recovery (WHR) applications from Echogen [3]. Although several research

studies have been done in the context of integrating an sCO_2 Brayton cycle with nuclear and solar applications [4,5] limited attention has been given to cycle optimisation. The National Renewable Energy Laboratory (NREL) is setting up a small scale plant of 10 MW_e capacity after the successful demonstration of a pilot plant having 520 kW_{th} of heater power [6]. Electric Power and Research Institute (EPRI), Institute of Advanced Engineering (IAE) [7], Électricité de France (EDF) and Echogen are leading research on developing an advanced indirect sCO_2 Brayton cycle integrated with a coal-fired power plant [8] whilst NET power is currently testing an oxy-combustion direct-fired sCO_2 Brayton cycle [9].

Crespi et al. [10] presented a review of forty-two sCO_2 cycles for power generation application and categorised them. Zhao et al. [11] proposed a novel cycle configuration that utilises heat from syngas and an oxygen compressor with multi-stream recuperators in a direct-fired sCO_2 cycle using syngas from coal gasification, yielding 43.7% net efficiency on an LHV basis. Heo et al. [12] performed a thermodynamic study on iso-thermal compression (i.e., near isothermal compression by adding multiple interstage cooler) for WHR which identified performance improvement potential. This study showed that ~50% of the compression work can be reduced in the sCO_2 cycle by using iso-thermal compression when the inlet pressure is fixed at 74 bar. Wang et al. [13] demonstrated the performance of transcritical CO_2 (tCO_2) cycle and Organic Rankine Cycle (ORC) for different fluids such as R123, R245fa, toluene, isobutane, isopentane and cyclohexane to recover the low-grade heat from a recompression supercritical CO_2 cycle before the precooler using exergo-economic analysis. They concluded that the performance of tCO_2 cycles is better for lower sCO_2 cycle pressure ratios and the ORC cost is slightly lower than tCO_2 cycles. Baik et al. [14] on the other hand, compared tCO_2 cycles with a transcritical R125 (t-R125) cycle for low-grade WHR (100 °C) application concluding that t-R125 cycle produces about 14% more power than a tCO_2 cycle.

The sCO_2 cycle pressure ratio is lower relative to a steam Rankine cycle and also the isobaric specific heat capacity (C_p) of sCO_2 is 2 to 4 times lower than that of steam on a mass basis over the temperature range of interest. Hence the sCO_2 mass flow is 8 to 12 times higher than the steam mass flow at the same thermal

input [15]. Moreover, the C_p is highly variable due to the occurrence of a pseudo-critical condition and therefore the capacitance (the product of mass flow and isobaric specific heat) of the sCO_2 stream changes significantly as a function of pressure and temperature, which limits the maximum possible heat extraction from the flue gas side with a single heat exchanger (or a single sCO_2 mass flow) because of the pinch point. The C_p of sCO_2 shown in Figure 3-1 clearly shows that, with a single mass flow, the high-pressure sCO_2 stream can extract the heat from a GT exhaust flue gas heat between ~600 °C and ~300 °C with high exergetic efficiency. The increase in sCO_2 isobaric specific heat at a lower temperature (<300 °C) requires a reduction in sCO_2 flow rate to match the stream capacitances to obtain further heat extraction whilst avoiding a pinch point. Therefore, the heat extraction has to be split in order to maximise the energy transfer with a higher second law efficiency, making cascade cycles attractive options.

Khadse et al. [16] performed an optimisation study for a Simple Recuperative Brayton Cycle (SRBC) and Recuperated Recompression Cycles (RRC) to recover the waste heat from a GT exhaust concluding that using an sCO_2 cycle as the bottoming cycle in lieu of a conventional steam Rankine cycle reduces cost by ~28%. Khadse et al. [17] also performed an optimisation and highlighted that the sCO_2 turbine inlet temperature tends to reach the lower boundary in the search space when maximising the net power produced from WHR as the main heat exchanger pinch point is the limiting parameter. Marchionni et al. [18] compared the thermal and economic performance of eight sCO_2 cycles for WHR applications for TIT 250-600 °C and concluded that the SRBC was economically attractive for small-scale WHR applications. Kimzey [19] compared the standard higher efficiency sCO_2 cycles such as SRBC, RCBC finding that, although these cycles can yield higher efficiency for constant heat flux heat sources, it is not attractive for sensible heat sources but cascade cycles performed better. Cho et al. [20] studied recompression with partial heating cycle, precompression cycle with partial heating cycle and three cascade cycles proposed in Kimzey [19] as a bottoming cycle solution for SGT5-4000F GT exhaust conditions. This study concluded that cascade cycle 2 and cascade cycle 3 performance were superior

to the other cycles studied and the plant efficiency increased by 0.7%pts with cascade cycle 3 over the steam cycle. Integration of the bottoming cycle is highly sensitive to the quality of flue gas from the GT exhaust [16] which indicates that different sCO_2 cycles can be attractive for a different exhaust gas temperatures. Wright et al. [21] performed an economic study of SRBC, cascade cycle, dual recuperative cycle and preheating cycle finding that although the efficiency of the cascaded and preheating cycle was higher the unit capacity cost ($/kW$_e$) was also higher than the other cycles.

Despite having a high-temperature difference across the primary heat exchanger, the partial cooling cycle [22] limits the potential to achieve high efficiency because the single flue gas heat exchanger in the partial cooling cycle and the initial results show that the modified layouts with an anabranch from the compressor for partial heating didn't offer comparable performance to the cascade cycles. In a nutshell, it can also be concluded that the SRBC and RCBC cycles can't extract maximum heat from the flue gas with higher exergic efficiency as they use one primary heat exchanger with a single sCO_2 mass flow, therefore, this study focused on high-efficient cascade cycles as a bottoming cycle solution. Held et al. [22] proposed a dual-rail cycle (designated as cascade cycle#4 in this paper), which is an extension of the cycle described as cascade 3 in this paper, which offers an ideal temperature glide between the two streams of the exhaust heat exchanger because of the additional degrees of freedom. It should be noted that this perfect capacitance match in a Heat Recovery Steam Generator (HRSG) is limited, even after having three pressure stages in a conventional steam Rankine cycle, owing to the evaporator (latent heat transfer process). That study considered six different capacity GT's, from small to heavy-duty machines and confirmed that the trend in cost-saving potential with increasing GT capacity remains valid for that sCO_2 cycle. Huck et al. [23] performed an exergic study of the sCO_2 cycle for higher temperature exhaust gas (~700 °C) for next-generation bottoming cycle for CCPP (>63% net efficiency) and concluding that exergy destruction is higher, and accordingly, performance is lower for a sCO_2 cycle than a triple-pressure HRSG.

The thermal performance of a Gas Turbine (GT) is highly influenced by the air compressor pressure ratio and GT Turbine Inlet Temperature (TIT). For a given GT TIT the pressure ratio that maximises GT net efficiency is higher than the pressure ratio that maximises GT specific power. Specific power is an important parameter for a GT as a higher value allows a smaller size of GT to produce the same output power. Davidson and Keeley [24] highlighted that the optimum GT pressure ratio selection has to minimise the major heat losses (in a conventional steam-based CCPP occur at the HRSG and the steam condenser) which generally translates to maximising the output power fraction of the topping cycle (analogues to GT specific power). Maximising the GT specific power is contrary to maximising the GT efficiency as maximising GT specific power tends to increase the net power generation of the higher cycle (topping cycle) which eventually increases the fuel flow to the combustor. In order to increase the fuel flow to the combustor for a given GT firing temperature, the combustor inlet air temperature should be lower and this implies a lower pressure ratio. Maximising the efficiency, on the other hand, tends to increase the pressure ratio in order to minimise the fuel flow to the combustor up to the level of economic compression. Cerri [25] highlighted that the optimum pressure ratio of a GT in CCPP is intermediate between those for which the efficiency and GT specific power are maximum. Horlock [26] also compared the optimal pressure ratio for dry and humid cycles. Najjar and Ismail [27] analysed the impact of operating parameters in the optimal pressure ratio and the study concludes that the pressure ratio corresponds to maximum GT specific power is more sensitive than those for which efficiency is maximum. The CC specific power reaches a maximum at a lower pressure ratio than that corresponding to the maximum GT specific power, due to the utilisation of exhaust heat by the bottoming cycle. Previous studies on conventional CCPP also showed that increasing GT firing temperature also increases the optimal pressure ratio of a GT [24]. Moreover, the optimal GT pressure ratio can vary as the isentropic efficiencies of the air compressor and GT change [27].

Previous studies have analysed the performance of different sCO_2 Brayton cycles for only a single, commercially available, GT exhaust condition. However, this

methodology doesn't guarantee to yield maximum performance of sCO_2 Brayton cycles as commercially available GT's are optimised to yield maximum performance when coupled with a bottoming steam Rankine cycle [15]. Also, that does not identify whether underperformance of one sCO_2 cycle at a single GT exhaust condition can be generalised to different GT exhaust conditions. In order to access the complete design space of a sCO_2 Brayton cycle for bottoming cycle applications, the whole plant model has to be either optimised to maximise both plant efficiency and net power or minimise the total cost in combination with the GT. This paper introduces a general concept for integrating sCO_2 cycles with Combined Cycle Power Plant (CCPP) and also demonstrates the maximum potential of sCO_2 cycles without being limited to any commercially available GT. Four different cycles, named the cascade cycle#2, the cascade cycle#3 [20], and cycle 4 were presented by Held et al. [22] and a novel cascade cycle (designated as cascade cycle#5 in this paper) are analysed as a bottoming cycle solution and multi-objective optimisation is performed to compare the Pareto front for different cycles on an equivalent basis in view of whole plant thermal performance and cost. The optimal pressure ratio requirement of GT air compressor to yield maximum efficiency of an integrated sCO_2-combined cycle power plant is compared with the pressure ratio which will provide maximum GT specific power. Since commercial GT pressure ratio is fixed, set of performance maps for all the four sCO_2 cycles were developed, which helps to estimate the performance of sCO_2 cycles for a given GT pressure ratio and TIT.

3.2 Supercritical CO_2 Cycle Configurations

The isobaric specific heat of sCO_2 varies widely with the temperature, as shown in Figure 3-1 for three different pressure levels, due to the occurrence of a pseudo-critical state. It can be clearly seen that the C_p at low-temperature is roughly twice the C_p at higher-temperature. The typical GT exhaust gas temperature of a heavy-duty GT is about 500-620 °C (this range is broader for aero-derivative engines) and this exhaust gas temperature has to be cooled down to ~70-150 °C. The minimum exhaust stack temperature is dictated by the conversion of sulphur from the fuel into SO_3 that reacts with moisture and forms sulphuric acid, which condenses and corrodes the tube material if the local tube

$$\eta_{cycle,net} = \frac{W_{GT,net} + W_{ST,net}}{m_{fuel} * LHV} \quad (3\text{-}1)$$

$$\eta_{bottom,net} = \frac{W_{ST,net}}{Q_{in} - Q_{stack}} \quad (3\text{-}2)$$

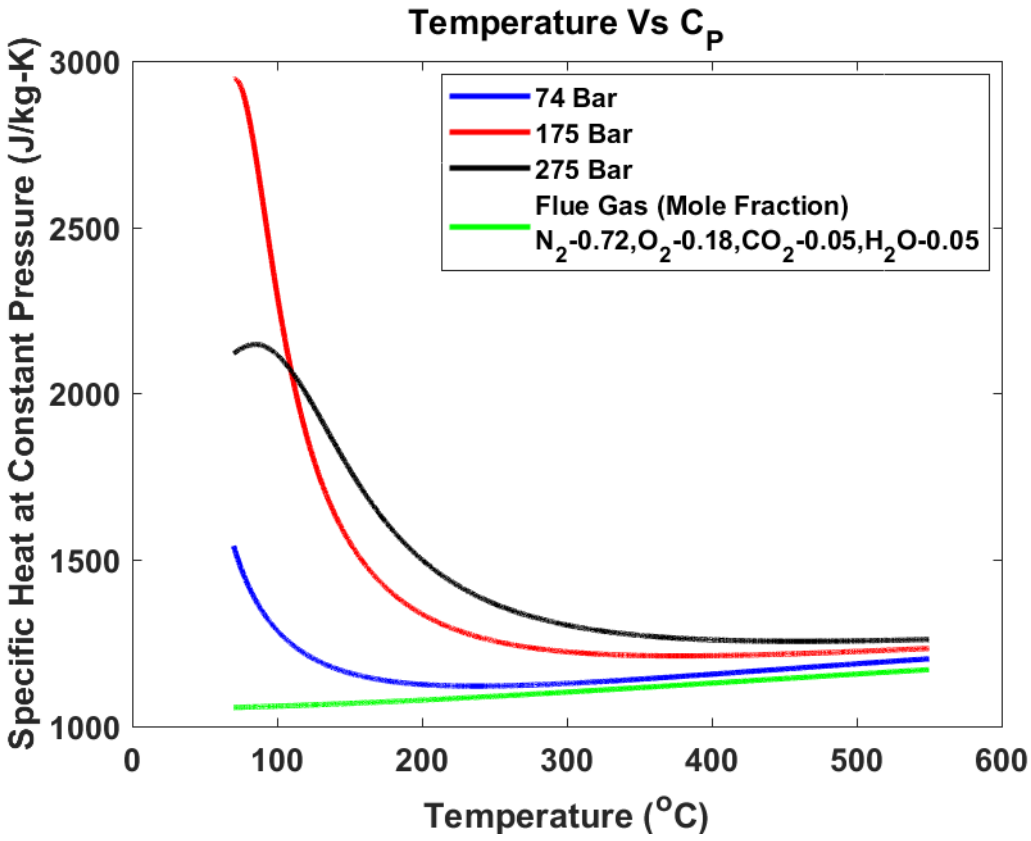

Figure 3-1 Isobaric specific heat variation as a function of Temperature for three different pressures of sCO_2 and a typical flue gas

metal temperature is lower than the dew point temperature. The dew point temperature is a function of sulphur concentration in the fuel [28]. Since the UK and many other countries are moving towards utilising natural gas as the fuel in the near future, or fuel with low sulphur content, the exhaust stack temperature can go below 100 °C. To utilise the maximum heat energy from flue gas within this window of ~600 to 100 °C with a heat exchanger that operates with a single mass flow will trade-off its outlet sCO_2 temperature. Maximising the cycle net efficiency will also ensure maximum net power output of the cycle whilst simulating both topping and bottoming cycle (Eq.(3-1) as opposed to modelling only the bottoming cycle where the net energy transfer has to be maximised. In

the latter case, maximising the efficiency will lower the waste heat recovery from the flue gas (minimising the denominator in Eq.(3-2) [19].

3.2.1 Cascade Cycle 1

The integrated cascade Brayton cycle configuration with the commercial GT SGT5-4000F is shown in Figure 3-2 and the Temperature-Entropy (TS) diagram is shown in Figure 3-3.

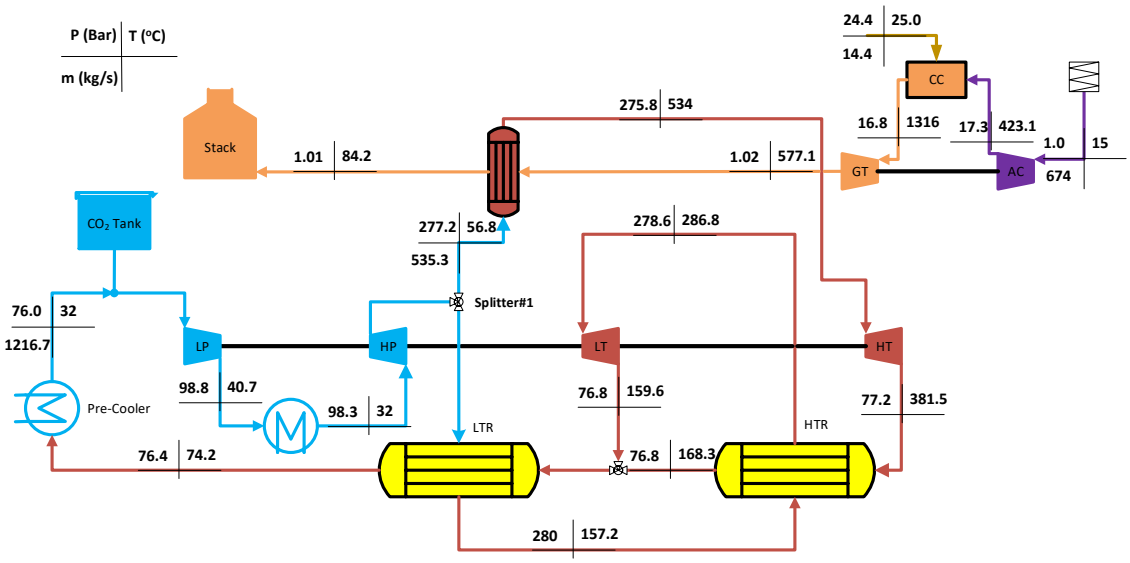

Figure 3-2 Cascade Cycle 1 Configuration (Cycle 1)

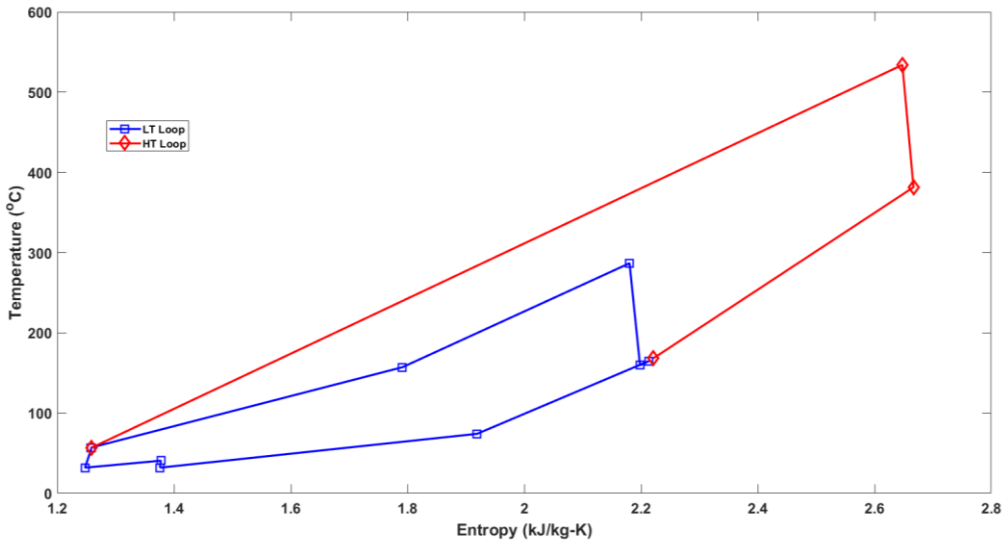

Figure 3-3 Cascade Cycle 1: TS Diagram

The layout is simulated in Thermoflex and optimised to maximise the overall cycle net efficiency by changing the sCO_2 mass flow, high and low-pressure levels of the sCO_2 cycle, splitter #1 fraction, and sCO_2 compressor intercooler upstream pressure. Although Cho et al. [20] simulated this bottoming cycle, both topping and bottoming cycles were optimised in this work. The splitter finds the optimal position to maximise the heat extraction from both flue gas heater and recuperators. This configuration has only one flue gas heat exchanger and the UA of the heat exchanger is relatively low owing to higher LMTD hence the cost of the heat exchanger might potentially be lower than other cycles. Therefore, this cycle becomes attractive where the efficiency becomes less significant such as lower capacity WHR applications due to its simple layout compared to other cascade cycles. The Temperature-Heat Transfer (T-Q) diagram is shown in Figure 3-4 which shows that the heat transfer is limited by the pinch at the inlet of the LT Recuperator (LTR) and as a consequence, heat transfer is a trade-off with sCO_2 turbine inlet temperatures.

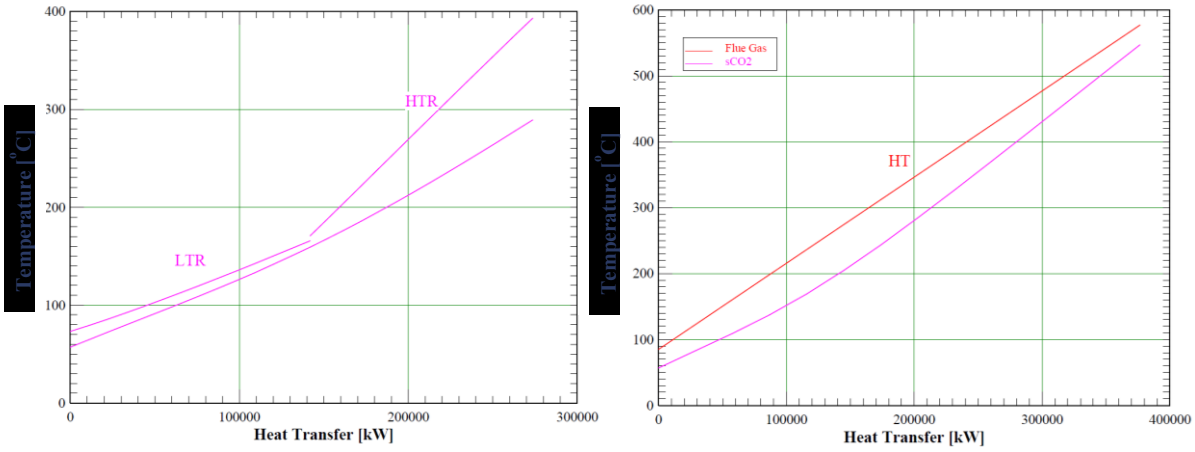

Figure 3-4 T-Q Diagram of Cascade Cycle 1: Left- Recuperators, Right- Flue gas Heat exchanger

3.2.2 Cascade Cycle 2

The layout is optimised to maximise the cycle net efficiency by optimising the same parameters considered for Cycle 1. Whilst performing the optimisation to maximise the overall cycle net efficiency, the splitter fraction is optimised so that maximum heat can be transferred from the exhaust flue gas heater and the

recuperators with higher exergetic efficiency. This fraction will be the critical control parameter to ensure maximum cycle efficiency and therefore it has to be re-optimised for every design or change in operating parameter, e.g., ambient temperature.

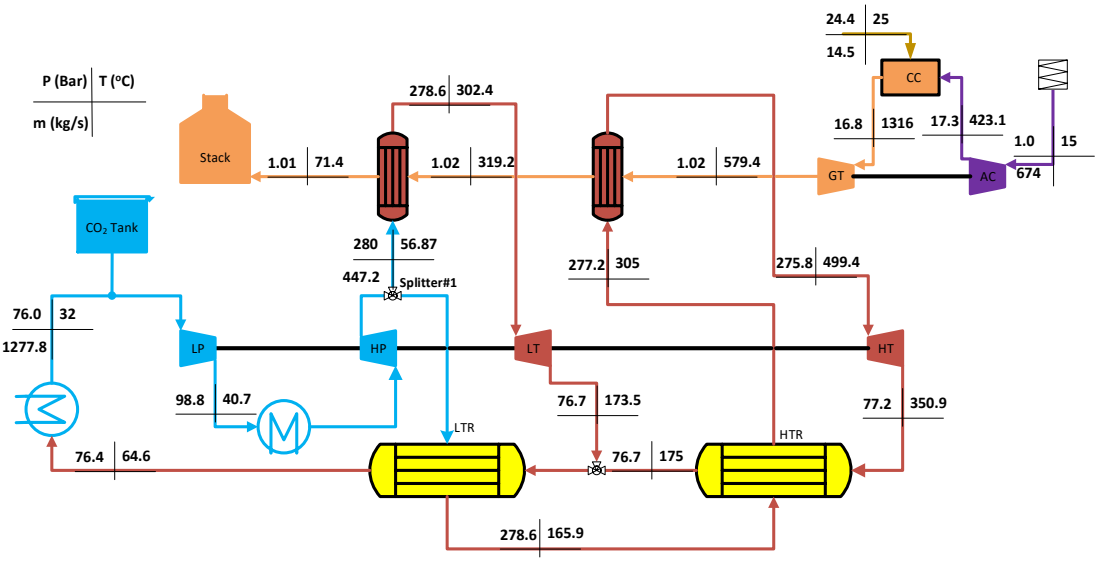

Figure 3-5 Cascade Cycle 2 Configuration (Cycle 2)

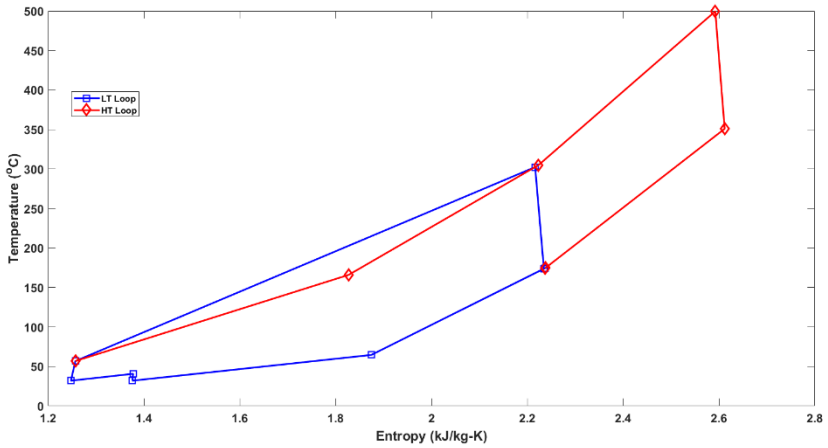

Figure 3-6 Cascade Cycle 2: TS Diagram

This cycle does not have the full flexibility of matching the capacitance of hot and cold streams in the LTR and HT Recuperator (HTR), and exhaust heat exchangers owing to the highly varying specific heat of sCO_2 as a function of pressure and temperature. Hence the heat exchanger minimum pinch point will decide the optimal size of the heat exchanger and that in turn will control the plant cost. A trade-off has to be made between higher efficiency and cost, as a smaller

pinch increases the cost exponentially. This study considers a minimum pinch point of 3 °C. The optimum design maximises the energy transfer in the recuperator and exhaust heat exchanger by matching the capacitance of both LTR and LT flue gas with the trade-off in exergetic efficiency of HTR and HT flue gas heater as shown in Figure 3-7.The integrated cascade Brayton Cycle 2 configuration with the commercial SGT5-4000F machine is shown in Figure 3-5 and the TS diagram is shown in Figure 3-6.

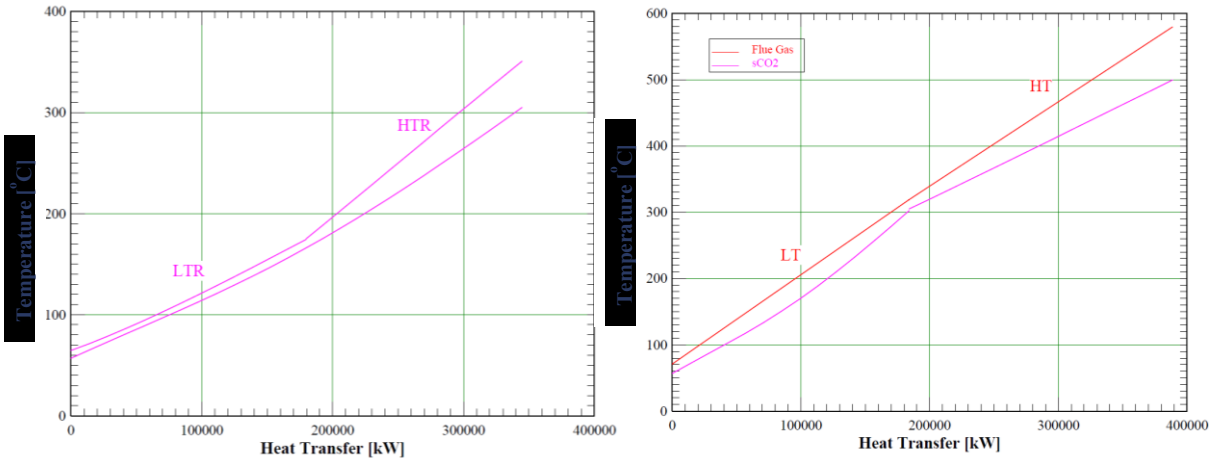

Figure 3-7 T-Q Diagram of Cascade Cycle 2: Left- Recuperators, Right- Flue gas Heat exchanger

3.2.3 Cascade Cycle 3

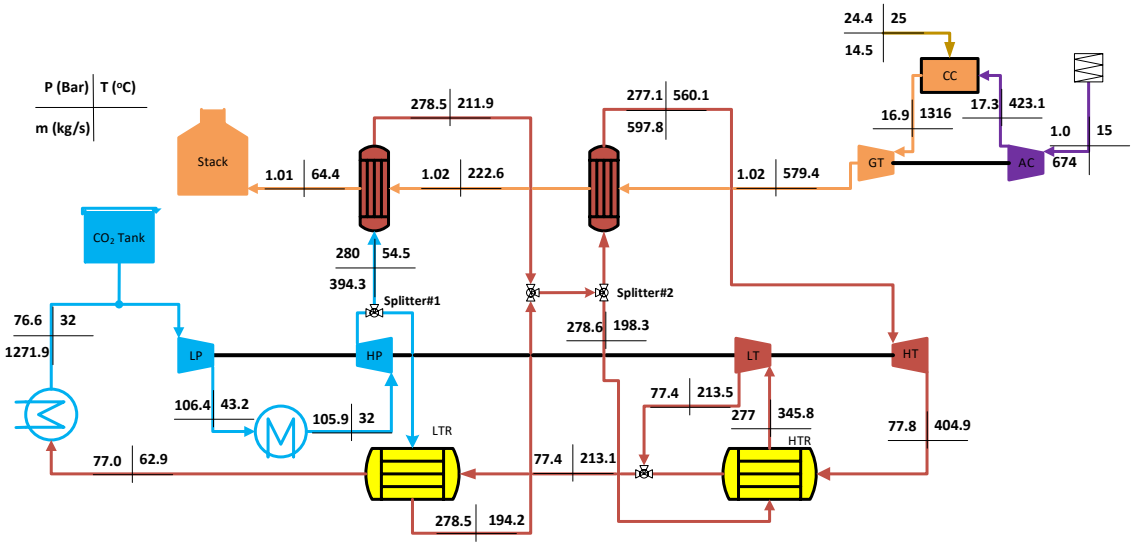

Figure 3-8 Cascade Cycle 3 Configuration (Cycle 3)

Cycle 3 is an adaptation of Cycle 2 in order to improve the overall efficiency of the cycle by changing the configuration as shown in Figure 3-8. The TS diagram of Cycle 3 is shown in Figure 3-9. Splitter 2 adds another degree of freedom to control the flow requirement between the HTR and HT flue gas heat exchanger. This configuration ensures maximum energy transfer in the exhaust gas heat exchangers and recuperator. The optimal cycle results in lower exergetic efficiency in the HTR as shown in Figure 3-10.

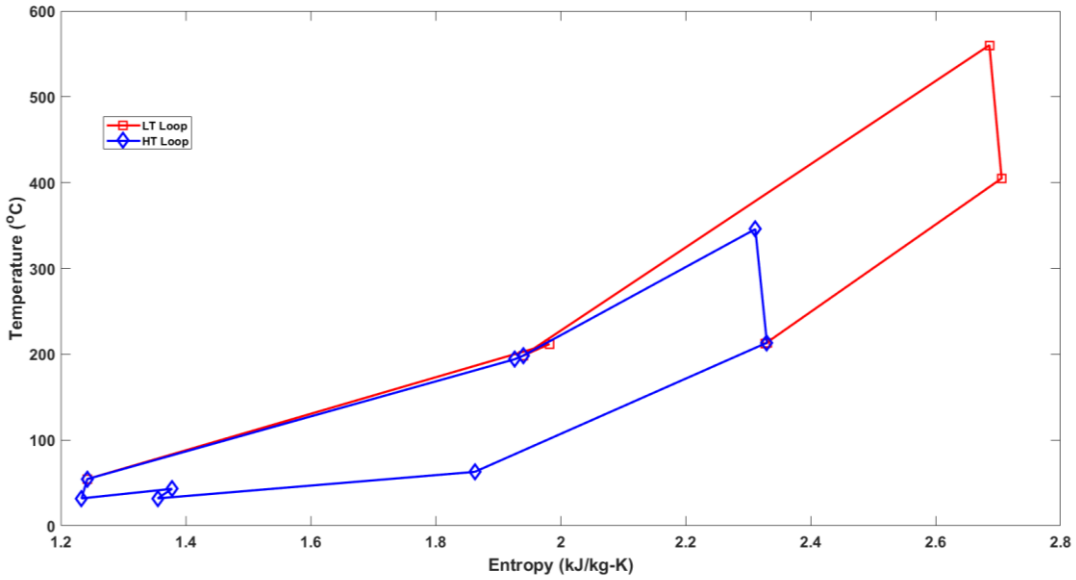

Figure 3-9 Cascade Cycle 3: TS Diagram

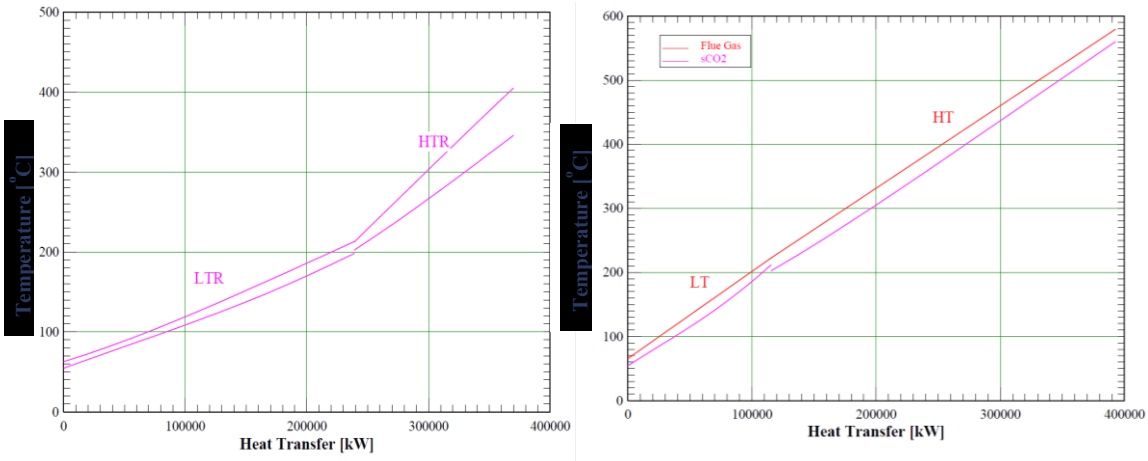

Figure 3-10 T-Q Diagram of Cascade Cycle 3: Left- Recuperators, Right- Flue gas Heat exchanger

3.2.4 Cascade Cycle 4

In order to improve the efficiency further, Echogen proposed a cycle named “Dual-rail” cycle (in this paper this cycle is designated as Cycle 4) which is the modified version of Cycle 3 [22]. This new cycle mixes an anabranch from the outlet of the HTR cold stream that mixes with the outlet of the MT flue gas heat exchanger and supplies a higher mass flow to the HT flue gas heat exchanger as shown in Figure 3-11. The TS diagram of Cycle 4 is shown in Figure 3-12. It can be seen from Figure 3-1 that the mass flow of sCO_2 to the exhaust gas heat exchanger as has to be increased to accommodate the change in specific heat from low temperature to a high temperature so that the slope of the dropping temperature profile can be matched. The cycle pressure ratio fixes the outlet temperature of the HT sCO_2 turbine and this fix the cold stream outlet temperature of the HTR outlet temperature by the decided minimum approach temperature. This becomes the inlet to the LT sCO_2 turbine.

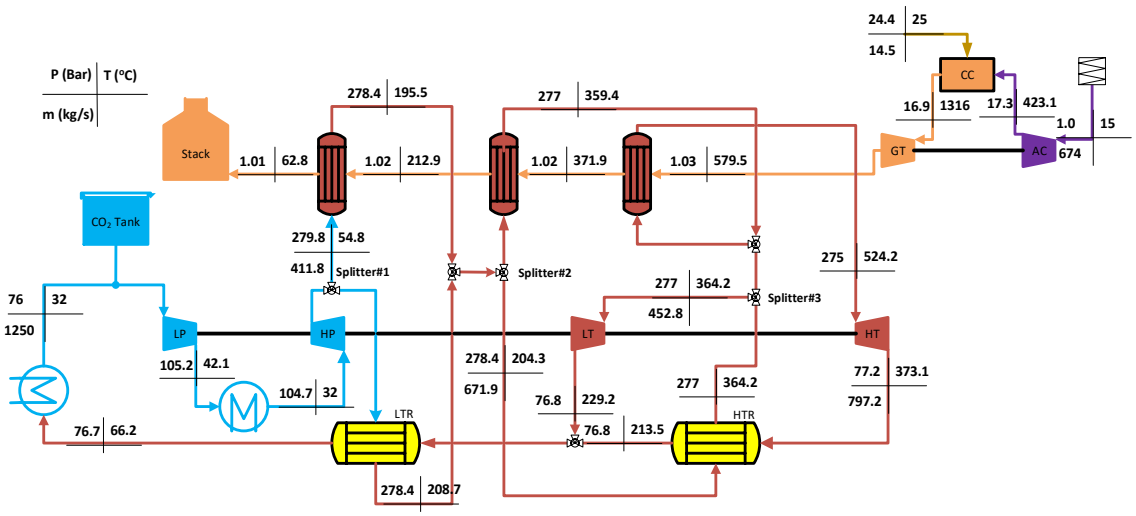

Figure 3-11 Cascade Cycle 4 Configuration (Cycle 4)

The decision as to the optimum value of sCO_2 mass flow to the HT exhaust gas heater is the trade-off between maximising the exergetic efficiency and maximising the heat transfer as the pinch occurs at the cold end of the HT flue gas heater (owing to higher isobaric heat capacity at lower temperature), and this leads to ~50 °C lower approach temperature for the SGT5-4000F machine exhaust conditions as shown in Figure 3-13. It is worth noting that the conventional steam Rankine cycle cannot have this perfect temperature

matching, i.e., 'ideal temperature gliding' owing to the occurrence of a phase-change which might shift the pinch point to the outlet of the evaporator.

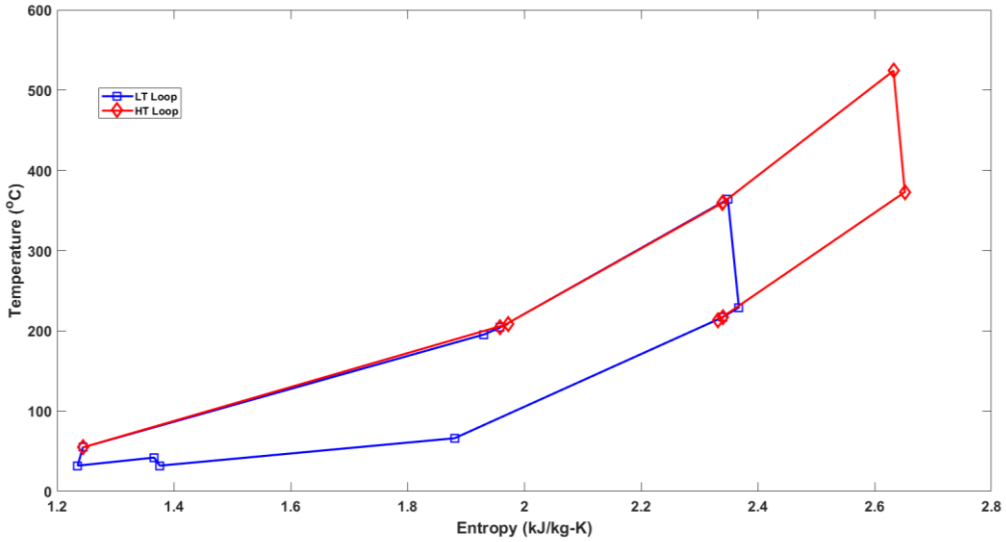

Figure 3-12 Cascade Cycle 4: TS Diagram

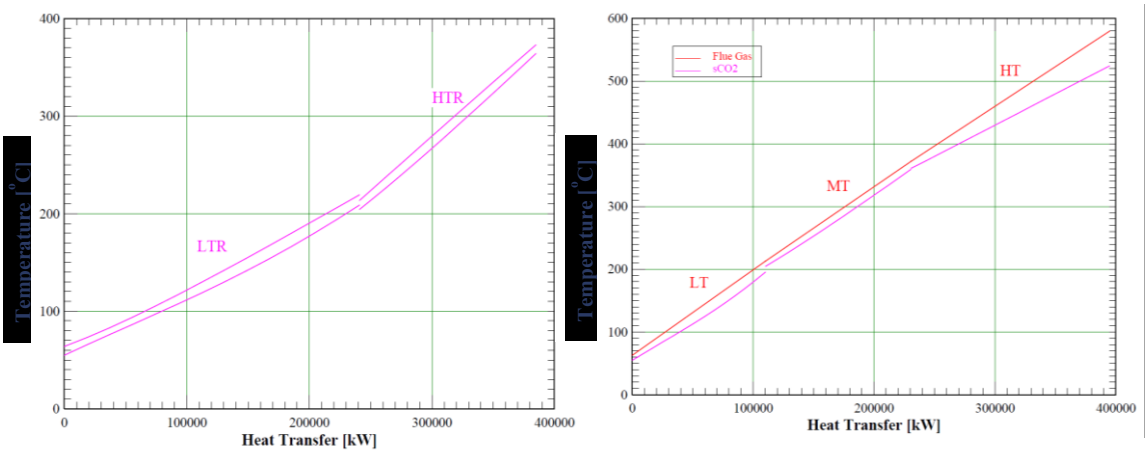

Figure 3-13 T-Q Diagram of Cascade Cycle 4: Left- Recuperators, Right- Flue gas Heat exchanger

3.2.5 Cascade Cycle 5

The difference in temperature at the HT flue gas heater can be further minimised with the layout proposed in Figure 3-14 and the corresponding TS diagram is shown in Figure 3-15. This cycle adds another degree of freedom to the cycle by integrating an exhaust gas heat exchanger, splitter, recuperator and a turbine.

This modification has the full flexibility to control the mass flow to maximise energy transfer with higher exergic efficiency which matches the slope of hot and cold fluid temperature change in both recuperators and exhaust heat exchangers as shown in Figure 3-16, and therefore improves the net efficiency further.

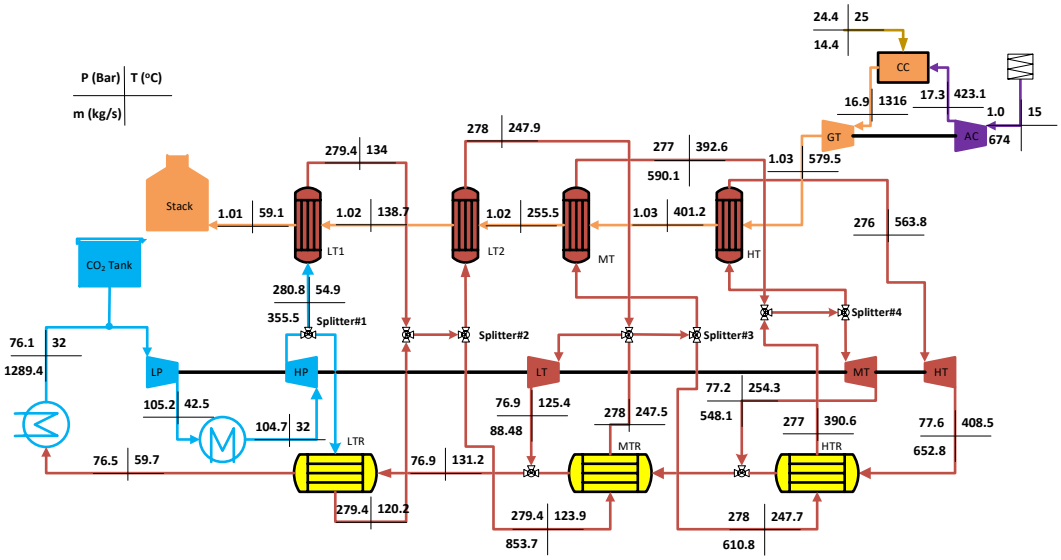

Figure 3-14 Cascade Cycle 5 Configuration (Cycle 5)

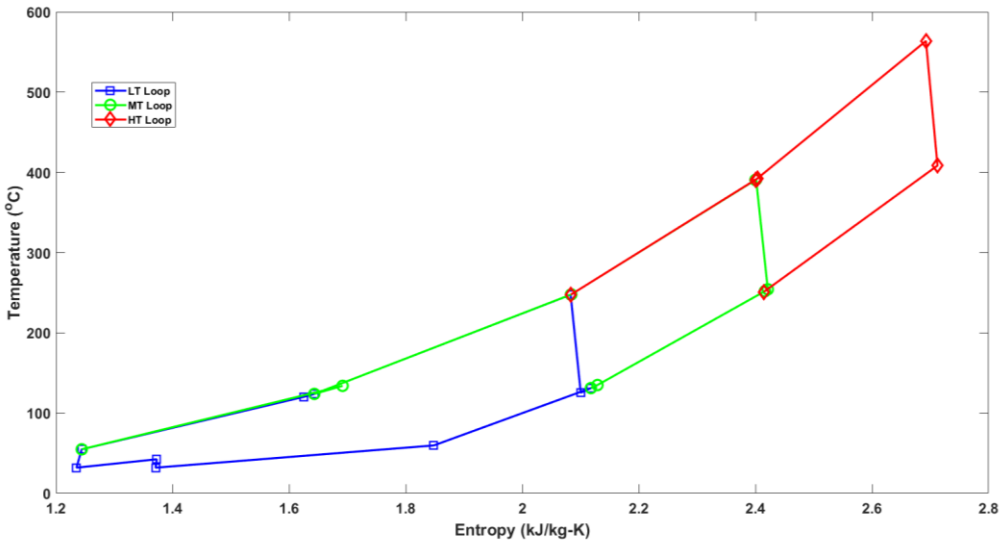

Figure 3-15 Cascade Cycle 5: TS Diagram

Although this cycle offers the maximum net efficiency, the improvement in performance is not significant for its increased complexity, therefore, the Cost of Electricity (COE) can be higher. From Figure 3-16, it is clear that the hot stream

follows well with the cold stream that will make the UA higher than other cycles owing to a lower LMTD. This may further increase the COE. However, this cycle can be attractive when the GT exhaust gas temperature is higher in order to better match the larger variation of sCO_2 Cp with lesser exergy destruction in the exhaust gas heat exchangers.

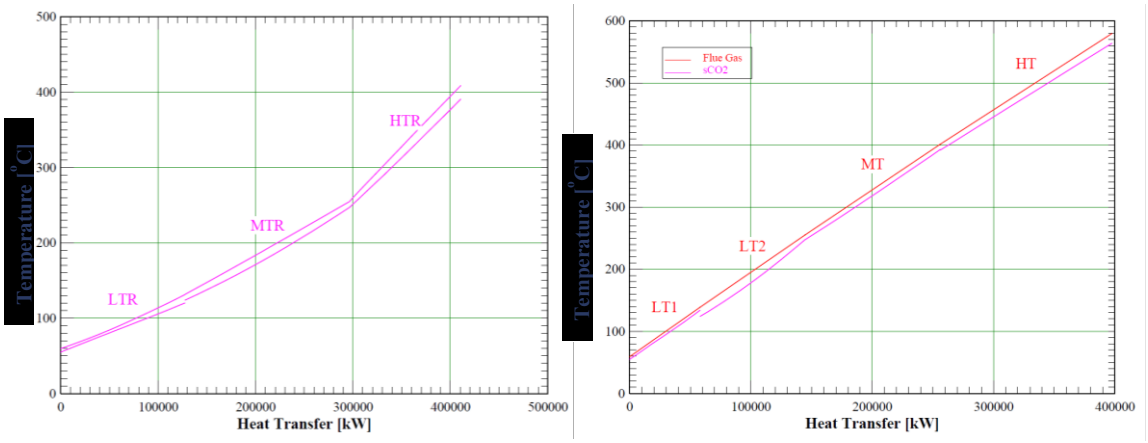

Figure 3-16 T-Q Diagram of Cascade Cycle 5 Left- Recuperators, Right- Flue gas Heat exchanger

3.3 Methodology

The thermodynamic cycles were simulated for an SGT5-4000F turbine to benchmark with results by Cho et al. [20]. In order to investigate the maximum cycle net efficiency and minimum cost whilst integrating sCO_2 cycles with a different scale of GT's, both the GT and the sCO_2 cycle has been modelled. The main design variables for different sizes of GT in the topping cycle were the pressure ratio and the GT inlet temperature, compressor inlet air mass flow, pressure drop, cooling flow fraction and the turbomachinery isentropic efficiency. In this study, only the compressor pressure ratio and GT TIT are considered as variables whilst the air mass flow, the turbomachinery isentropic efficiency and the pressure drop at air intake/ combustors were kept constant in the optimisation study. The GT and Combined Cycle (CC) specific power (kJ/kg) are calculated using Eq.(3-3). Note the air mass flowrate is considered for specific power calculation and net efficiency is reported in this paper unless otherwise specified.

$$SP_{GT} = \frac{W_{GT,net}}{\dot{m}_{air}};\ SP_{CC} = \frac{W_{GT,net} + W_{sCO_2\ Turbine,net}}{\dot{m}_{air}} \quad (3\text{-}3)$$

3.3.1 Model Assumptions and Input Conditions

A thermodynamic process model was developed in Thermoflex, a commercial heat and mass balance software, which uses the REFPROP fluid property database developed by the National Institute of Standards and Technology (NIST) [29], which is the most accurate equation of state available to predict sCO_2 thermodynamic properties [30]. REFPROP uses the Span-Wagner Equation of State (EoS) to calculate the properties of the pure components [31]. The cycles are modelled at ISO ambient condition and no lower limit in stack temperature is imposed. The piping pressure loss and heat loss to the ambient are neglected in this study. Table 3-1 shows the thermodynamic model assumptions considered for this study. Methane was used as a fuel and the air mass flow ate to gas turbine via air compressor for SGT5-4000F machine was obtained from Thermoflex (i.e., 674 kg/s). A 2 MWe was considered as the power requirement for the cooling system, which was obtained from initial Thermoflex simulations. The TIT of SGT5-4000F was obtained from Thermoflex database.

Table 3-1 Thermodynamic Model Assumptions

Description	Unit	Value
Polytropic efficiency of air compressor [a]	%	89.65
Polytropic efficiency of GT [a]	%	88.1
Combustor pressure loss	%	3
sCO_2 turbine isentropic efficiency [b]	%	92 [20]
sCO_2 compressor isentropic efficiency [b]	%	88 [20]
Minimum pinch	°C	3
Pressure loss in Heat exchangers	%	0.5% of the inlet pressure [20]
Recuperator Effectiveness [32]	%	95 [20]
Generator Efficiency	%	98 [20]
Parasitic load [c]	MW_e	2

[a] – 99.8% mechanical efficiency is considered

[b] – No mechanical losses are considered

Thermoflex solves the steady-state heat and mass balance for all the components.

The component steady-state mass balance of a component is calculated by Eq.3-4,

$$\sum \dot{m}_{in} = \sum \dot{m}_{out} \tag{3-4}$$

The steady-state energy balance of a component is calculated by Eq.3-5,

$$\sum \dot{m}_{in} * h_{in} - \sum \dot{m}_{out} * h_{out} + Q - W = 0 \tag{3-5}$$

Where $\dot{m}$ is the mass flow rate, Q is the heat flows, W is the shaft work and h is the enthalpy.

The air compressor of GT is modelled in Thermoflex using polytropic efficiency as an input and the outlet temperature is calculated using Eq.3-6,

$$T_o = T_i * \left(\left(\frac{P_o}{P_i} \right)^{\frac{R}{\bar{c}_p * \eta_p}} \right) \tag{3-6}$$

The GT outlet temperature can be calculated using Eq.3-7,

$$T_o = T_i * \left(\left(\frac{P_o}{P_i} \right)^{\frac{R * \eta_p}{\bar{c}_p}} \right) \tag{3-7}$$

where, the P_o, P_i are the pressure at the outlet and the inlet respectively, R is the gas constant, $\eta_p$is the polytropic efficiency, $\bar{c}_p$is the average specific heat and T_o, T_i are the absolute temperature at the outlet and the inlet respectively.

The sCO_2 turbine was modelled based on isentropic efficiency using Eq.3-8,

$$h_{o,turb} = h(P_o, s_i) * \eta_{i,turb} \tag{3-8}$$

The sCO_2 compressor was modelled based on isentropic efficiency using Eq.3-9,

$$h_{o,comp} = \frac{h(P_o, s_i)}{\eta_{i,comp}} \tag{3-9}$$

where h is the enthalpy and s is the entropy.

The heat exchangers were modelled based on effectiveness method using Eq.3-10 and the heat exchanger is discretized into sub-heat exchangers (more details on the heat exchanger discretization can be found in Chapter 9) in order to capture the variation of the fluid properties along the path,

$$\epsilon = \frac{Q}{Q_{max}} \tag{3-10}$$

The maximum possible heat transfer is calculated as the product of flow rate and enthalpy change of the stream with lesser heat capacity if it were to be heated (or cooled) through the temperature range corresponding to the two incoming temperatures [33]. Thermoflex, on the other hand, reduces this maximum possible heat transfer if achieving that would result in a negative temperature difference anywhere in the path; essentially setting the maximum heat transfer to be the heat transfer that occurred with a pinch temperature difference of zero somewhere within the heat exchanger. Since sCO_2 properties are highly variable, the pinch point can occur within the heat-exchanger thus the heat exchanger sizing (heat transfer and the conductance) can be very different between the two methods for the same value of effectiveness. This effect can be very pronounced if the operating parameters are close to a critical point. The recuperator effectiveness values stated in this paper used the Thermoflex approach as the modelling has been done in Thermoflex.

Table 3-2 Variable Ranges of Parameters Considered in Optimisation

Range	Pressure ratio [a]	Max. Pressure (bar)	Min. Pressure (bar)	Intermediate Pressure [b] (bar)	SF#1*	SF#2*	SF#3*	sCO_2 Mass Flow (kg/s)
min	10	200	74	100	0.1	0.1	0.1	1000
max	35	300	90	175	0.9	0.9	0.9	1400

* SF- Split Fraction

[a] – Air compressor pressure ratio

[b] – Upstream pressure of the intercooler in sCO_2 cycle

Table 3-2 shows the variable ranges considered in the optimisation. However, in a few exceptional cases, the ranges have been increased, particularly the mass flow lower bound, to capture the complete Pareto front.

3.3.2 Optimisation Algorithm

Multi-objective optimisation is optimising (i.e., maximising or minimising) more than one objective function simultaneously subject to equality and non-equality constraints. An individual X(a) is said to be a dominant solution if X(a) is better than other solutions in all objective functions or X(a) is strictly better than other solutions in at least one objective subjected to the constraints [34]. A non-dominated Sorting Genetic Algorithm (NSGA II) was linked with the Thermoflex model via excel VBA [35] to perform the optimisation study and the flowchart of the code is shown in Figure 3-17 [36].Thanks to Prof. Gade Pandu Rangaiah for supplying the NSGA II Excel macro [34], which was modified to interface with Thermoflex to perform the optimisation.

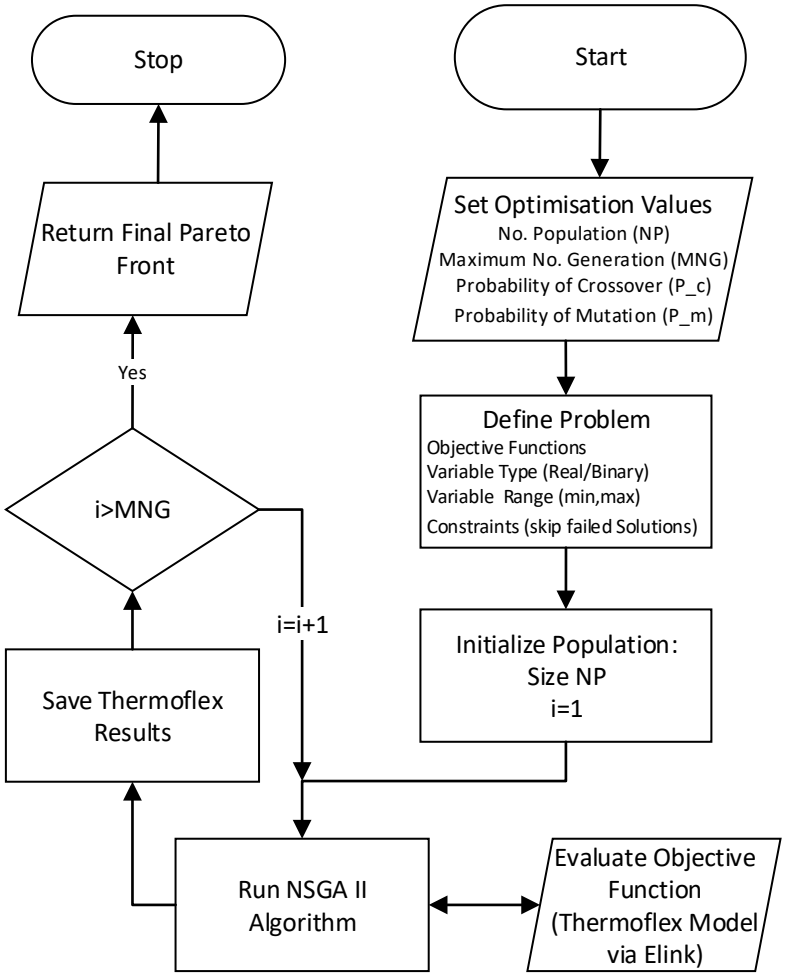

Figure 3-17 NSGA II Algorithm Flowchart Used in this Study

Simulation in Thermoflex tends to be slow when simulating sCO_2 cycles due to the inherent delay in calculating the thermodynamic state properties from the

computationally heavy REFPROP. Despite the simulation speed and lack of compatibility to parallelize the simulation in thermoflex, the number of generation and populations were selected to be 10 times the number of variables to be optimised to ensure a globally optimal solution. The crossover and mutation probability were selected based on a few test runs. Two different objective functions were considered: 1) maximise net efficiency and specific power, 2) maximise net efficiency and minimise cost per unit electricity generation. The uncertainty of the sCO_2 component cost functions is higher, therefore, the maximum efficiency and the minimum cost designs have to be explored by the optimisation algorithm. Thus, a multi-objective optimisation is considered as opposed to single-objective cost-based optimisation.

From the Pareto front, the optimal solution is chosen to compare different cycles using a linear programming technique for multidimensional analysis of preference (LINMAP) decision-making [37,38]. This method chooses a solution which has a minimum Euclidean distance from the ideal solution for a set of given weights to all the objective functions assumed in the study. F_{ij} is the objective function matrix where i is the index of each point in the Pareto front and j is the index of each objective function. Then the non-dimensionalised objective function (F_{ij}^{n}) can be calculated by Eq.3-11,

$$F_{ij}^{n} = w_j * \frac{F_{ij}}{\sqrt{\sum_{i=1}^{n} F_{ij}^{2}}} \tag{3-11}$$

where w_j is the weight of j^{th} objective function and $\sum_{j=1}^{m} W_j = 1$

The Euclidean distance (d_{i+}) from the ideal solution can be calculated by Eq.3-12,

$$d_{i+} = \sqrt{\sum_{j=1}^{m} (F_{ij} - F_j^{ideal})} \tag{3-12}$$

where F_j^{ideal} is the ideal solution of the j^{th} objective function and the ideal solution refers to the point at which each objective function is optimised in the Pareto front regardless of the other objective function. The recommended solution is having

the smallest Euclidean distance d_{i+}. This study considers net efficiency and specific power/cost as objective functions.

3.3.3 Economic Model

Various cost curves have been proposed to calculate the CAPEX of sCO_2 turbomachinery and heat exchangers. Ho et al. [39] used the cost of the heat exchanger as shown in Eq.3-13 which was the fitted equation for various heat exchanger types utilising the data from ESDU [40] with a multiplication factor to account for different material. The parameters C,\$/W-K and m will change for different heat exchanger fluid combination and the type.

$$Cost\ (\$) = C * (UA)^m \tag{3-13}$$

Table 3-3 Component Cost Functions

Components	Cost Function ($)
Gas turbine (Turbo-expander)* [43]	$\frac{C_1 * A_1 * m_{gas}(\frac{kg}{s}) * \ln(PR) * (1 + e^{(0.036*(T_{out}(K)-54.4*C_2))})}{0.92 - \eta_T}$
Air compressor* [43]	$\frac{C_1 * A_2 * m_{air}(\frac{kg}{s}) * PR * \ln(PR)}{0.9 - \eta_c}$
Combustor* [43]	$\frac{C_1 * A_3 * m_{air}\left(\frac{kg}{s}\right) * (1 + e^{(0.018*(T_{out}(K)-26.4*C_2))})}{0.995 - \frac{P_{out}}{P_{in}}}$
Precooler (water)	$A_4 * UA\ (W_{th}/K)$
Intercooler (Water)	$A_4 * UA\ (W_{th}/K)$
HT Recuperator	$A_5 * UA\ (W_{th}/K)$
LT Recuperator	$A_5 * UA\ (W_{th}/K)$
Turbomachinery+Generator+Mtotor+Gear+ Piping+Skid+I&C+Aux.BOP Cost	$A_6 * Power\ (kW_e)$
Flue gas-sCO_2 Heat exchanger	$A_7 * UA\ (W_{th}/K)$

*- inflation correction is added (71%) [44]
$C_1 = 1.051$ [43]
$C_2 = 1.207$ [43]

Marchionni et al. [41] and Wang and Dai [13] on the other hand proposed a function of heat exchanger area with an average value of overall heat transfer coefficient for different combinations of fluid to calculate the heat transfer area. Because the sCO_2 cycle is a highly recuperative cycle, compact heat exchangers such as Printed Circuit Heat Exchangers (PCHE) can be considered for recuperators and precooler. Zada et al. [42] proposed that the cost of PCHE is

changing almost linearly as a function of conductance, the product of the overall heat transfer coefficient (U) and the heat transfer area (A), and proposed different unit rates for HTR and LTR due to the different operating temperatures which requires to have different materials.

The flue gas heat exchanger is most likely to be the same as a conventional HRSG arrangement as the limiting factor is the exhaust gas heat transfer coefficient by convection which represents 85-95% of the overall thermal resistance, hence the size should be of similar magnitude [22]. Wright et al. [21] proposed First of a Kind (FOAK) cost functions as a function of UA and this is a conservative estimate. Since the purpose of this study is not to compare the cost reduction potential against a steam Rankine cycle but rather to compare different sCO_2 cycle maximum performance and optimal GT requirements, the FOAK cost functions were considered.

To calculate the cost of sCO_2 turbomachinery, this study also considers FOAK cost functions proposed by Wright et al. [21] as this also includes the conservative estimate of generator cost and other Balance of Plant (BOP). Table 3-3 shows the list of cost functions used to calculate the CAPEX of every component in the cycle and Table 3-4 shows the constants used in Table 3-3.

Table 3-4 Value of Constants for the Cost Functions listed in Table 3-3

Constants in Table 3-3	Unit	Value
A_1 [43]	\$-s/kg	266.3
A_2 [43]	\$-s/kg	39.5
A_3 [43]	\$-s/kg	25.6
A_4 [21]	\$-K/W_{th}	1.7
A_5 [21]	\$-K/W_{th}	2.5
A_6 [21]	\$/kW_e	1000
A_7 [21]	\$-K/W_{th}	5

The Capital Recovery Factor (CRF) is calculated by Eq.3-14,

$$CRF = i * \frac{(1+i)^n}{(1+i)^n - 1} \tag{3-14}$$

The Cost Rate (CR, \$/s) is calculated by Eq.3-15,

$$CR = \frac{CRF * MF * \sum Z_i}{OH * 3600} \quad (3\text{-}15)$$

where Z_i is the CAPital EXpenditure (CAPEX) of i^{th} component, and MF, OH are given in Table 3-5.

Table 3-5 Economic Model Assumptions

Description	Unit	Value
Life Time (n)	Years	20 [13]
Interest Rate (i)	%	12 [13]
Annual Operating Hours (OH)	Hrs	8000 [13]
Maintenance Factor (MF)	-	0.06 [13]
Fuel Cost (FC)	$/GJ	4 [45]
Fuel LHV (LHV)	kJ/kg	50,047 (Thermoflex)

The total cost rate is the summation of CR and Fuel Rate (FR, $/s) whilst the latter is calculated by Eq.3-16,

$$FR = \frac{LHV * m_{dot} * FC}{10^6} \quad (3\text{-}16)$$

where m_{dot} is the fuel flow, kg/s.

The cost of unit electricity generation (c$/kWh) is calculated by Eq.3-17,

$$Cost = \frac{(CR + FR) * 3600 * 10^5}{Net\ Power} \quad (3\text{-}17)$$

The economic model assumptions are shown in Table 3-5.

3.4 Comparison with Literature

The thermodynamic model Pareto front is validated against the results published by Cho et al. [20] for SGT5-4000F machine as his work optimised the bottoming cycle parameters to maximise the net energy generation with errors shown in *Table 3-6.* Cho et al. modelled the sCO_2 cycles using the in-house code named KAIST_CCD which was developed in MATLAB. Although Cho et al. modelled the heat exchanger based on the discretized ε-NTU method in this study the heat exchangers were sized by explicitly specifying the outlet fluid temperature owing to a different definition of effectiveness in Thermoflex. Moreover, the sCO_2 mass flow is optimised to maximise the net power generation with relaxed heat

exchanger outlet temperature boundary condition. Since the error percentage is small, the thermoflex model is considered acceptable.

Table 3-6 Comparison of model results (GT TIT = 1316 °C and Pressure Ratio = 17.2)

Cycle Layout	sCO_2 mass flow (kg/s)			Net Efficiency (%)			Bottoming Cycle Net Power (MW)		
	Literature [20]	Model	Error (%)	Literature [20]	Model	Error (%)	Literature [20]	Model	Error (%)
Cycle 1 w/o intercooling	1240	1260	1.6%	56.1	56.1	0.0%	118.5	118.5	0.0%
Cycle 1 with intercooling	1200	1195	-0.4%	56.3	56.3	0.0%	120.0	120.1	0.0%
Cycle 2 w/o inter cooling	1290	1316.7	2.1%	58.1	57.9	-0.2%	132.6	131.6	-0.7%
Cycle 2 with intercooling	1290	1286.7	-0.3%	58.5	58.5	0.1%	135.4	135.9	0.4%
Cycle 3 with intercooling	1300	1288.9	-0.9%	59.1	59.1	0.1%	139.9	140.2	0.2%

3.5 Results and Discussion

3.5.1 Cascade Cycle 1

This cycle with intercooler achieves maximum net efficiency of 56.6% for a GT TIT of 1316 °C at the pressure ratio of 25.0. The maximum specific power of SGT5-4000F machine, operating in a simple cycle, occurs at the air compressor pressure ratio of 15.1, 16.9 and 19.7 for a GT TIT of 1216 °C, 1316 °C and 1416 °C respectively. The corresponding GT specific powers are 367.1, 424.4 and 484.9 kJ/kg respectively. Figure 3-18 highlights the design which is selected based on a LINMAP algorithm giving equal weight to maximising net efficiency and minimising the cost (referred henceforth as the cost Pareto front) and maximising both GT specific power and CC efficiency (referred henceforth as the thermal Pareto front). The maximum efficiency of Cycle 1 is significantly lower than the equivalent Cycle 2 performance (i.e., 3%). This cycle has not, therefore, been analysed at different GT TIT's although this cycle can be considered in small scale WHR applications owing to its compact footprint.

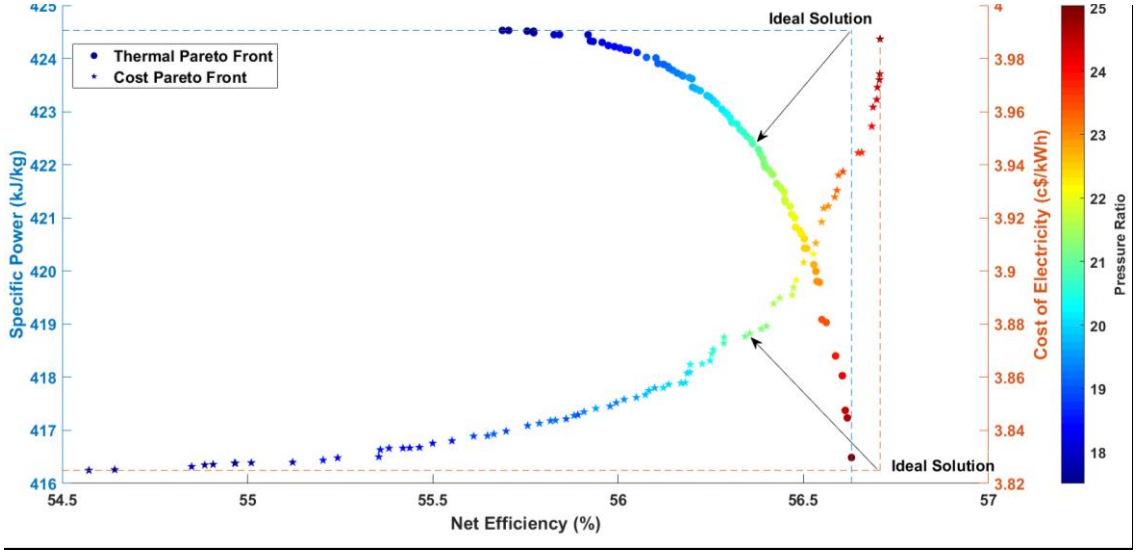

Figure 3-18 Cycle 1 Cost Pareto Front at GT TIT-1316 °C

3.5.2 Cascade Cycle 2

For a combined cycle power plant, the CC specific power has to be maximised. For a steam-based CCPP, CC specific power is maximum at lower pressure ratios than the pressure ratio of maximum GT specific power. This is because the exhaust gas heat can be utilised by the HRSG. But it is not clear whether maximising the GT specific power and CC specific power are conflicting objectives or not at a higher pressure ratio range. Figure 3-19 shows the variation of the Cycle 2 pressure ratio for three Pareto fronts 1) maximising GT specific power and CC efficiency 2) maximising CC specific power and CC efficiency 3) minimising COE and maximising CC efficiency.

Examining Figure 3-19, it is evident that maximising the CC specific power and GT specific power are converging to the same solution in the thermal Pareto front until the maximum GT specific power is reached. Beyond which the CC specific power continues to increase at lower GT pressure ratios whilst GT specific power reduces (not an optimal solution, therefore, discarded in the Pareto front). Minimising the COE, on the other hand, yields a different design in the cost Pareto front although the pressure ratio that corresponds to the minimum COE design is roughly equivalent to the pressure ratio at which maximum GT specific power occurs (Figure 3-19). It's worth highlighting that the cost Pareto front and the thermal Pareto front are converging to the same plant design at higher CC

efficiency and this confirms that the optimisation models are finding their globally optimal solutions.

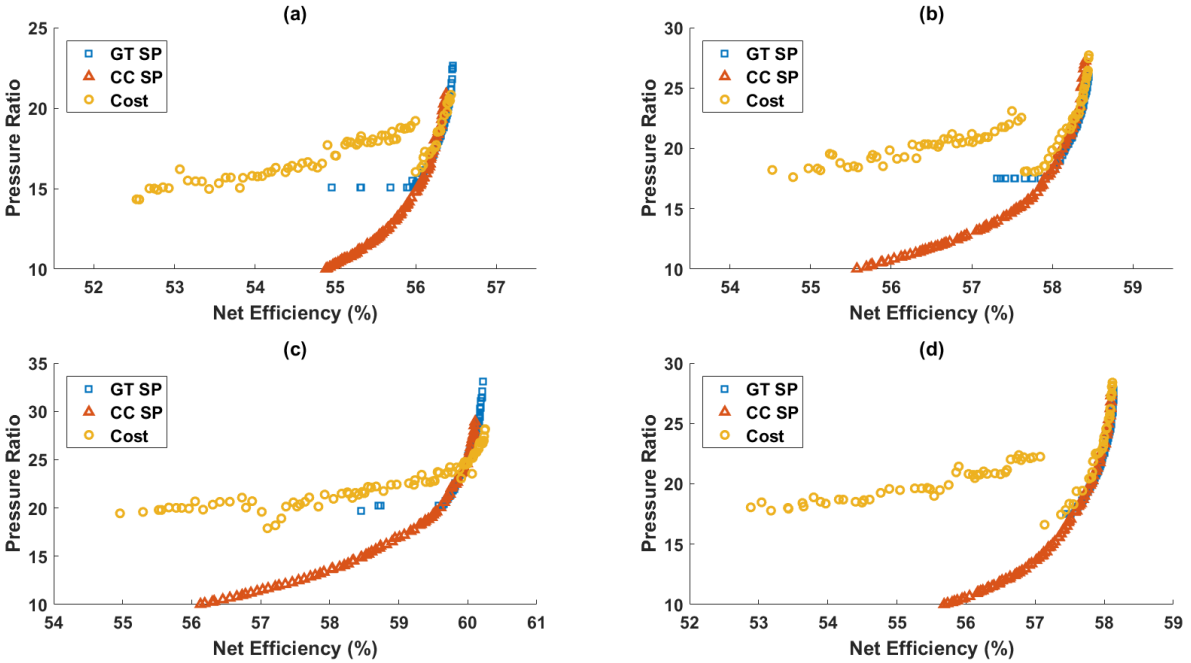

Figure 3-19 Pressure ratio of Cycle 2 for three Pareto fronts: (a) GT TIT-1216 °C, (b) GT TIT-1316 °C, (c) GT TIT-1416 °C, (d) GT TIT-1316 °C w/o intercooler

Figure 3-20 shows the thermal Pareto front and the corresponding air compressor pressure ratio for all the three GT inlet temperatures modelled. The maximum efficiency and GT specific power of cascade Cycle 2 with intercooler for the base case for a GT TIT of 1316 °C (equivalent to SGT5-4000F) are 58.5% and 414 kJ/kg respectively. Although the efficiency is equal to the reported Cycle 2 efficiency by Cho et al. [20] for SGT5-4000F machine, the GT pressure ratio is different (i.e. 26 in this study as opposed to 17.2 for SGT5-4000F machine). The reason is that Cho et al. [20] considered the conventional effectiveness method for sizing the heat exchanger whilst the definition of heat exchanger effectiveness is different in Thermoflex as explained in section 3.3.1. In the Thermoflex method, the maximum heat transfer can be equal or lower than the conventional effectiveness method for a given effectiveness as the maximum heat transfer is reduced when the second-law is violated along the path of the heat exchanger. Additionally, this study considered a 2 MW_e parasitic load to account for the

circulating water pumping power which was not considered in the work by Cho et al. [20]. Hence the calculated efficiency in this work is always lower than the reported value in Cho et al. [20] for the same GT pressure ratio.

The GT pressure ratio was increased to achieve a maximum combined cycle efficiency whilst the GT specific power reduces as shown in Figure 3-20. Interestingly, the GT pressure ratio was increasing as the GT TIT increases, which indicates that the maximum combined cycle efficiency and minimum cost can be obtained within a narrow range of GT pressure ratios. Maximum efficiencies of 56.5, 58.5, and 60.2 were obtained for a GT TIT of 1216 °C, 1316 °C, and 1416 °C respectively. The corresponding GT pressure ratios are 22.6, 26.0, and 33.1. On the other hand, maximum GT specific power of 366, 423, 483 kJ/kg are obtained at the pressure ratio of 15.1, 17.5, 19.7 for a GT TIT of 1216 °C, 1316 °C, and 1416 °C respectively. From a thermal performance standpoint, the optimal pressure ratio can be defined as the pressure ratio which will give maximum CC efficiency [46].

The pressure ratio corresponds to maximum CC efficiency is not close to the pressure ratio that yields maximum GT specific power as shown in Table 3-7. Since the efficiency is changing very little at higher pressure ratios (Figure 3-20) a small reduction in efficiency can change the pressure ratio and specific power by a significant amount. Table 3-7 shows the efficiency, specific power and pressure ratio of three cases 1) maximum CC efficiency 2) maximum GT specific power 3) 85% weight to CC efficiency and 15% weight to GT specific power. The weights of 85:15 for Case3 is chosen to have a 0.1% point reduction in CC efficiency to all the different GT TIT cases. The specific power range between maximum specific power and maximum efficiency has reduced by 62% and the pressure ratio at maximum efficiency case was reduced by ~15% for a GT TIT 1216 °C. The reduction in pressure ratio of 85:15 case from the pressure ratio of maximum GT specific power case is 4.3, 5.4 and 7.3 for a GT TIT of 1216 °C, 1316 °C, and 1416 °C respectively. It is clear that at lower GT TIT the pressure ratio of maximum GT specific power case and 85:15 ratio case is proximate and it diverges as the GT TIT increases. This implies that Cycle 2 can better integrate

with lower GT TIT's for which the optimal pressure ratio can be chosen with a smaller trade-off in specific power and CC efficiency. It is worth highlighting that since the pressure ratio at maximum CC efficiency (i.e., optimal pressure ratio) is 26.0 for a GT TIT of 1316 °C which is higher than the equivalent SGT5-4000 machine pressure ratio (i.e., 17.2), then integration of an sCO_2 cycle with a commercially operating GTs cannot achieve the maximum performance as a fully flexible CCPP design with a sCO_2 bottoming cycle. This is because the pressure ratio of conventional CCPP for maximum efficiency is close to maximum GT specific power [46], therefore, the commercial GT's pressure ratio is proximate to maximum GT specific power. Although the pressure difference between Case2 and Case3 are relatively smaller at GT TIT of 1216 °C, the difference diverges as the GT TIT increases. This questions the ability to integrate Cycle 2 with higher TIT GTs. Therefore, the sCO_2 cycle configuration plays a critical role in integrating a sCO_2 bottoming cycle with a commercially available GT. The energy share from the bottoming cycle (ratio between the net power from sCO_2 cycle and CC net power) reduces as the GT TIT increases at maximum efficiency point (see Table 3-7- Case 1). This is because, although the GT pressure ratio increases with the GT TIT, the consequential increase in TET is lower, which reduces the bottoming cycle energy share. This indicates that the energy losses from the bottoming cycle at higher GT TITs are relatively higher than the losses from the topping cycle, therefore, the topping cycle energy share increases with the GT TIT in order to maximise whole plant efficiency. This is also true for a steam-based bottoming cycle [24]. Moreover, it is worth highlighting that the bottoming cycle energy share is higher for the case with intercooler than without intercooler because the intercooler reduces the sCO_2 temperature to the low-temperature exhaust heat exchanger, aiding heat recovery, thereby making the bottoming cycle more efficient. The bottoming cycle energy share for a triple-pressure steam Rankine cycle with the commercial SGT5-4000F is around ~32.1%, which is higher than this sCO_2 cycle.

The maximum efficiency from the cost Pareto front is 58.5% and this is attained at a GT pressure ratio of 29.1 for a GT TIT of 1316 °C. The maximum efficiency

obtained from cost Pareto front is the same as the thermal Pareto front, nevertheless, the pressure ratio is different.

Table 3-7 Cycle 2: Three cases from thermal Pareto front for a GT TIT of 1216 °C, 1316 °C and 1416 °C

GT TIT (°C)	Efficiency (%)			Specific Power (kJ/kg)			Pressure Ratio			% Share Bot.cycle [d]		
	Case1[a]	Case2[b]	Case3[c]	Case1[a]	Case2[b]	Case3[c]	Case1[a]	Case2	Case3	Case1	Case2	Case3
1216	56.5	55.0	56.4	356.8	366.2	362.6	22.6	15.1	19.3	28.1	31.6	29.9
1316	58.5	57.3	58.4	413.8	423.4	418.9	26.0	17.5	22.9	27.7	31.4	29.0
1416	60.2	58.5	60.1	467.8	483.9	478.0	33.1	19.7	27.0	26.3	30.4	28.3
1316[e]	58.1	57.4	58.0	410.4	423.4	418.0	27.8	17.5	23.5	26.7	31.5	28.5

[a] – maximum efficiency case

[b] – maximum GT specific power case

[c] – 85:15 weight between efficiency and specific power respectively in LINMAP

[d] – Power output share from the bottoming cycle

[e] – without intercooler case

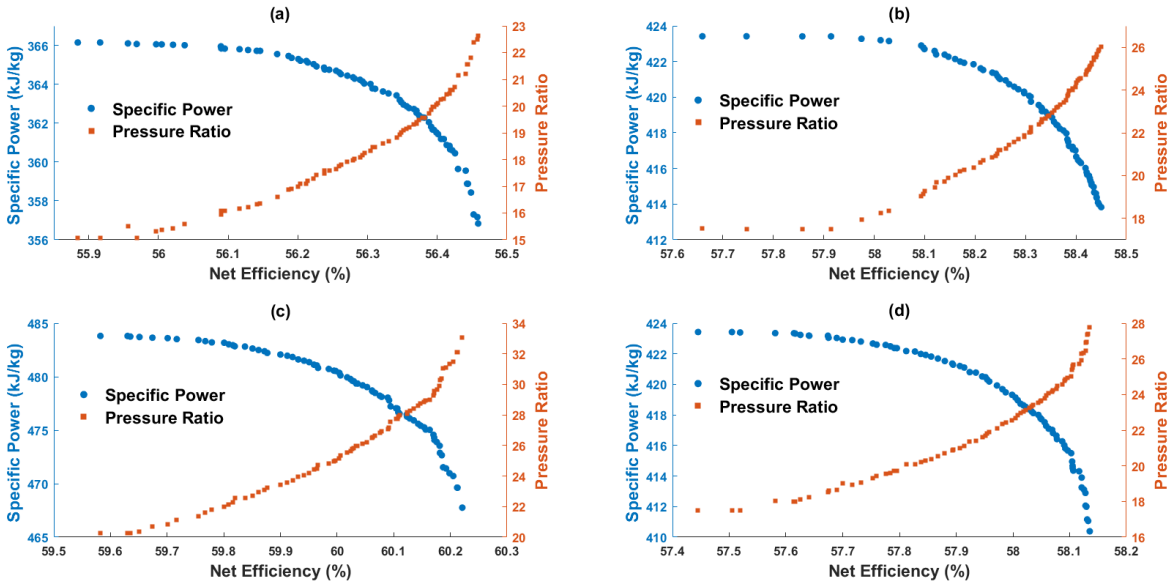

Figure 3-20 Cycle 2 Thermal Pareto fronts: (a) GT TIT-1216 °C, (b) GT TIT-1316 °C, (c) GT TIT-1416 °C, (d) GT TIT-1316 °C w/o intercooler

This is because the efficiency change plateaus at a higher pressure ratio. Despite a few scatter points of pressure ratio in the cost Pareto front, in general, the pressure ratio was found to increase with the increase in the net-efficiency as shown in Figure 3-21. There is a discontinuity in the change in pressure ratio for

GT TIT 1316 °C and 1416 °C which was caused by the step change of the split ratio to the low-temperature recuperator (not plotted here). Table 3-8 shows three cases of the cost Pareto front 1) maximum CC efficiency 2) minimum COE 3) 95% weight to CC efficiency and 5% weight to COE.

Table 3-8 Cycle 2: Three cases from cost Pareto front for a GT TIT of 1216 °C, 1316 °C and 1416 °C

GT TIT (°C)	Efficiency (%)			COE (c$/kWh)			Pressure Ratio			% Share Bot.cycle [d]		
	Case1[a]	Case2[b]	Case3[c]	Case1[a]	Case2[b]	Case3[c]	Case1[a]	Case2[b]	Case3[c]	Case1[a]	Case2[b]	Case3[c]
1216	56.4	52.6	56.3	4.4	4.0	4.3	22.4	14.7	19.2	29.0	29.2	29.7
1316	58.5	54.3	58.4	4.3	3.8	4.2	29.1	17.3	24.5	27.1	27.3	28.5
1416	60.3	55.0	60.2	4.1	3.7	4.0	33.2	20.2	29.6	26.3	25.6	27.4
1316[e]	58.1	52.9	58.0	4.3	3.8	4.1	28.4	18.1	23.2	26.4	25.2	28.5

[a] – maximum efficiency case

[b] – minimum cost case

[c] – 95: 5 weight between efficiency and cost respectively in LINMAP

[d] – Power output share from the bottoming cycle

[e] – without intercooler case

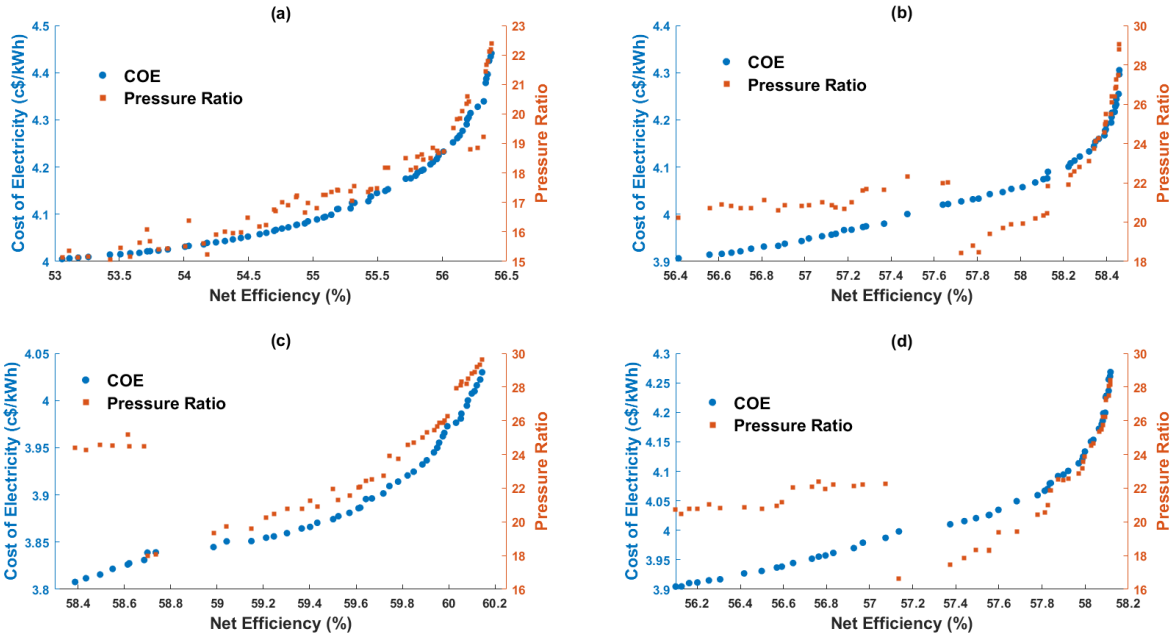

Figure 3-21 Cycle 2 Cost Pareto fronts: (a) GT TIT-1216 °C, (b) GT TIT-1316 °C, (c) GT TIT-1416 °C, (d) GT TIT-1316 °C w/o intercooler

The weight of 95:5 is considered in the cost domain in order to maintain the efficiency difference by 0.1% point from the maximum efficiency. The pressure ratio difference between Case2 and Case3 are increasing as the GT TIT increases from 1216 °C to 1416 °C. This infers that the trade-off range of pressure ratios is higher for higher GT TIT and this emphasises that Cycle 2 cannot integrate well for higher GT TIT cases to realise the maximum economic benefit. The minimum cost pressure ratio is apparently close to the pressure ratio that yields maximum GT specific power (Table 3-8- case2). The energy share from the bottoming cycle is reduces as the GT TIT increases. The bottoming cycle energy share reduces for both minimum cost case and maximum efficiency case (Table 3-8- case1 and 2) and that is roughly close to each other.

The intercooler in Cycle 2 increases the maximum net efficiency by ~0.4% point with the increased COE of ~1%. The intercooler increases the plant net efficiency due to 1) the reduction of compressive power (isothermal compression) and 2) lower compressor outlet temperature that aids more heat transfer from the flue gas. Cycle 2 with intercooler produces 0.8% higher specific power at the maximum efficiency condition as compared to Cycle 2 without an intercooler. The pressure ratio of the thermal Pareto front at maximum efficiency for Cycle 2 without intercooler is higher than Cycle 2 with intercooler by 1.8. The exclusion of the intercooler does not significantly change the optimal pressure ratio. The improvement in efficiency will reduce if the exhaust stack minimum temperature limitation is imposed.

The net efficiency, thermal Pareto front pressure ratio, specific power and the cost of electricity are varying almost linearly as a function of turbine inlet temperature within the range studied i.e., 1216-1416 °C. Even though there is an influence of higher-order terms, it is hard to capture with only three data points, however, a linear trend provides a reasonable fit to these data.

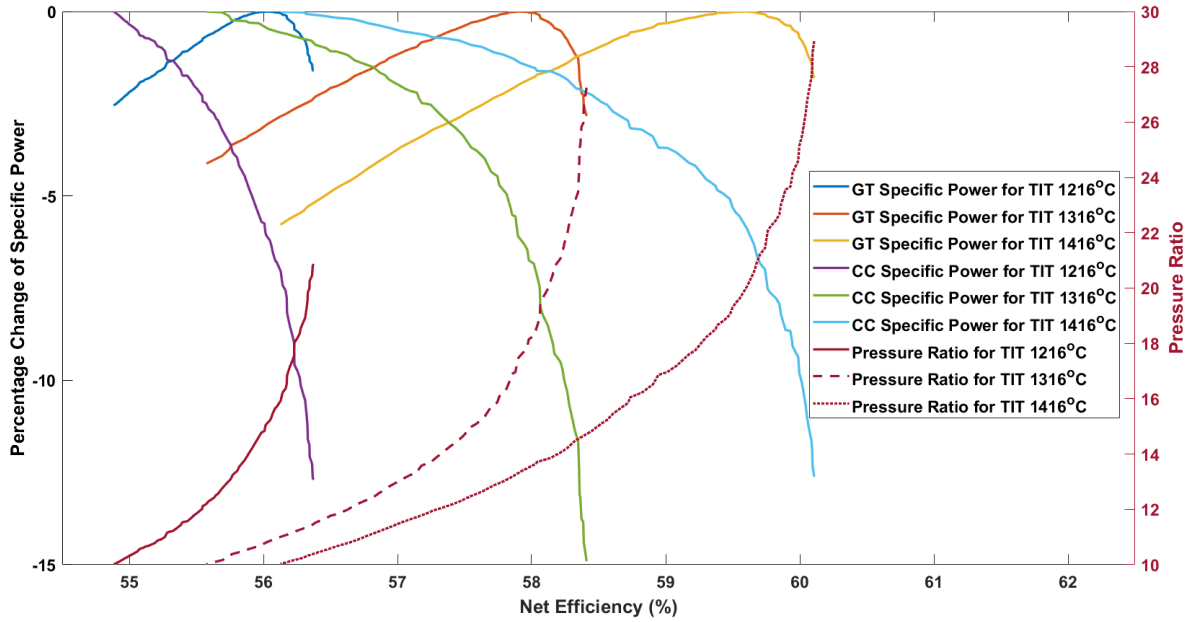

Figure 3-22 Relationship between Pressure ratio, efficiency and Specific power for Cycle 2 for a GT TIT of 1216 °C, 1316 °C and 1416 °C

Figure 3-22 shows the CC specific power, GT specific power, CC efficiency, and GT pressure ratio for a GT TIT of 1216 °C, 1316 °C and 1416 °C. This curve can be used approximately to estimate the expected CC efficiency and specific power for different GT TIT and pressure ratios. The CC specific powers in Figure 3-22 are normalised with 577.2, 660.7 and 746.9 kJ/kg for a GT TIT of 1216 °C, 1316 °C and 1416 °C respectively and the GT specific powers are normalised to 366.2, 423.4 and 483.9 kJ/kg respectively. These curves are strictly valid for the assumed topping cycle and bottoming cycle component performance. Any deviation of the component performance can introduce some degree of uncertainty and these effects can be approximated by correcting the impact of the particular design parameter change on the efficiency (or specific power) by assuming all the variables are independently affecting the efficiency. The sensitivity of changes in CC efficiency and GT specific power for the changes in the air compressor and GT polytropic efficiency is tabulated in the sensitivity analysis section (Table 3-16 and Table 3-17). It has to be noted that the estimation can only approximate the expected performance as it is neglecting the secondary effects due to the variable interdependency.

3.5.3 Cascade Cycle 3

Figure 3-23 shows the thermal Pareto fronts for all the GT inlet temperatures studied.

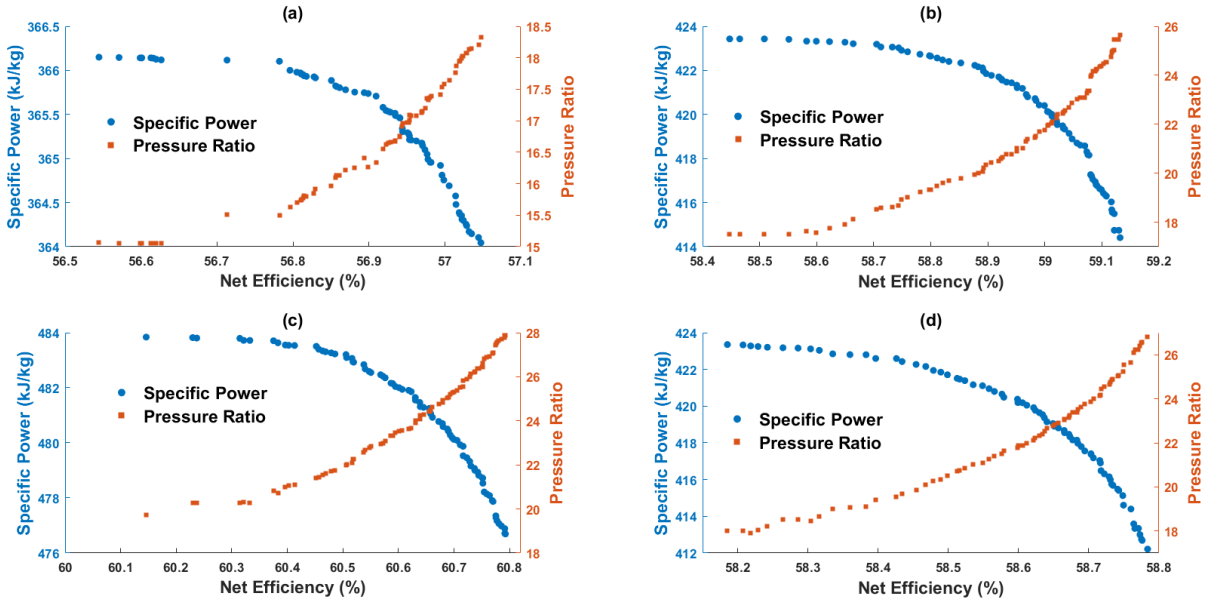

Figure 3-23 Cycle 3 Thermal Pareto fronts: (a) GT TIT-1216 °C, (b) GT TIT-1316 °C, (c) GT TIT-1416 °C, (d) GT TIT-1316 °C w/o intercooler

The maximum efficiency and specific power of cascade Cycle 3 with intercooler for the base case for a GT TIT of 1316 °C (equivalent to SGT5-4000F) are 59.1% and 415 kJ/kg, which is attained at the GT pressure ratio of 25.6. Examining Table 3-9, it can be seen that Cycle 3 is able to achieve higher efficiency at a relatively lower pressure ratio compared to Cycle 2. Similar to Cycle 2, the pressure ratio at maximum efficiency is proximate to the pressure ratio for maximum GT specific power. The pressure ratio difference between Case2 and Case3 is roughly equal (i.e., ~6) for a GT TIT of 1316 °C and 1416 °C. Moreover, these pressure ratio differences for all the GT TIT's are lower than Cycle 2. This infers that Cycle 3 can be a good candidate compared to Cycle 2 for all the GT TIT's studied. The specific power at maximum efficiency case is higher than Cycle 2 for all the GT TIT cases. The specific power at maximum efficiency case has increased by 2.2 kJ/kg when adding an intercooler with Cycle 3 for a GT TIT of 1316 °C. Examining Table 3-9, the Case2 and Case3 pressure ratios with and without intercooler are

roughly the same, but it is higher by 1.2 for Case1. The energy share from the bottoming cycle is higher than Cycle 2 for all the GT TITs and the share is the same for GT TIT 1316 °C and 1416 °C at maximum efficiency point. This indicates that the TET increases at higher GT TIT in order to keep the bottoming cycle energy share the same.

Table 3-9 Cycle 3: Three cases from thermal Pareto front for a GT TIT of 1216 °C, 1316 °C and 1416 °C

GT TIT (°C)	Efficiency (%)			Specific Power (kJ/kg)			Pressure Ratio			% Share Bot.cycle [d]		
	Case1[a]	Case2[b]	Case3[c]	Case1[a]	Case2[b]	Case3[c]	Case1	Case2	Case3	Case1	Case2	Case3
1216	57.0	55.5	57.0	364.0	366.2	364.6	18.3	15.1	17.8	31.0	31.8	31.4
1316	59.1	57.0	59.1	414.4	423.4	418.6	25.6	17.5	23.1	28.4	30.7	29.5
1416	60.8	60.1	60.7	476.7	483.8	479.9	27.9	19.7	25.6	28.4	32.0	29.3
1316[e]	58.8	57.4	58.7	412.2	423.4	418.1	26.8	17.5	23.4	27.8	31.5	29.2

[a] – maximum efficiency case

[b] – maximum GT specific power case

[c] – 85:15 weight between efficiency and specific power respectively in LINMAP

[d] – Power output share from the bottoming cycle

[e] – without intercooler case

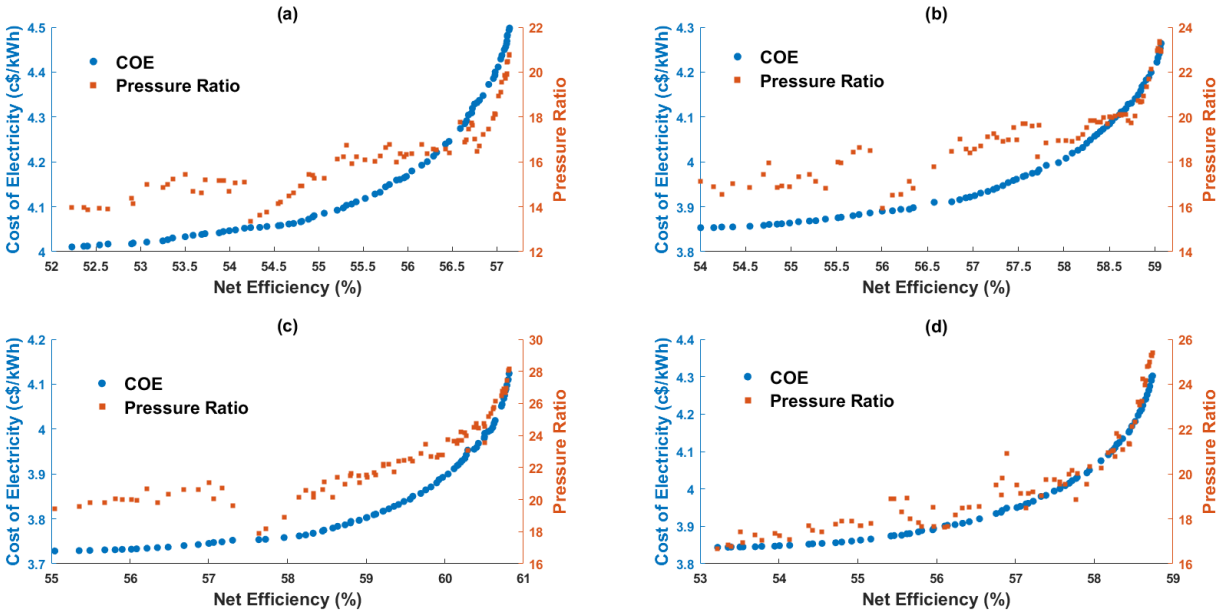

Figure 3-24 Cycle 3 Cost Pareto fronts: (a) GT TIT-1216 °C, (b) GT TIT-1316 °C, (c) GT TIT-1416 °C, (d) GT TIT-1316 °C w/o intercooler

The cost Pareto fronts of Cycle 3 are shown in Figure 3-24. The pressure ratio is not smooth as it is in the thermal Pareto front. In general, it increases as the efficiency increases for all GT TITs. Examining Table 3-10, the difference in pressure ratio between Case2 and Case3 are 4.7, 5.9 and 7.1 for a GT TIT of 1216 °C, 1316 °C and 1416 °C respectively. These are lower than Cycle 2 for a GT TIT of 1316 °C and 1416 °C and it is the same for a GT TIT of 1216 °C. Therefore, Cycle 3 can better integrate with GTs than Cycle 2 for higher GT TITs. The pressure ratio difference between Case2 and Case3 are a bit higher for Cycle 3 without intercooler than Cycle 3 with intercooler. In general, the pressure ratios that has the minimum cost is roughly the same as the pressure ratio of maximum GT specific power. The COE is not significantly different than Cycle 2 for Case1 and Case2.

The intercooler in Cycle 3 increases the efficiency in Case1 by ~0.4% point with the same COE without an intercooler. The pressure ratio of Cycle 3 without intercooler is higher than Cycle 3 with intercooler by 1.3. Since the efficiency improvement will be sacrificed when the stack minimum temperature limitation is imposed, the COE can go higher for Cycle 3 with an intercooler.

The efficiency and the GT specific power of a CCPP when integrating Cycle 3 for different GT TITs can be interpreted from Figure 3-25. Linear interpolation across different GT TITs can be used for the temperature range studied. The CC specific powers in Figure 3-25 are normalised with 585.1, 672.0 and 763.7 kJ/kg for a GT TIT of 1216 °C, 1316 °C and 1416 °C respectively and the GT specific powers are normalised to 366.2, 423.4 and 483.8 kJ/kg respectively. For an SGT5-4000F machine (Pressure ratio -17.2, GT TIT-1316 °C), integrating Cycle 3 as the bottoming cycle can offer the maximum efficiency of 58.6% whilst the maximum efficiency of 59.1% can be achieved at the pressure ratio of 23.1 (Table 3-9-Case3).

Maximising the GT specific power of Cycle 3 also increases CC specific power whilst maximising the CC efficiency. It is worth highlighting that this behaviour is the same as Cycle 2 and a similar trend is observed for Cycle 4, therefore, those plots not repeated for these other cycles.

Table 3-10 Cycle 3: Three cases from cost Pareto front for a GT TIT of 1216 °C, 1316 °C and 1416 °C

GT TIT (°C)	Efficiency (%)			COE (c$/kWh)			Pressure Ratio			% Share Bot.cycle [d]		
	Case1[a]	Case2[b]	Case3[c]	Case	Case	Case	Case1[a]	Case2[b]	Case3[c]	Case1[a]	Case2[b]	Case3[c]
1216	57.1	51.9	57.0	4.5	4.0	4.4	20.8	14.2	18.9	30.1	28.8	31.1
1316	59.1	53.9	59.0	4.3	3.9	4.2	22.9	17.0	22.9	30.1	27.6	30.0
1416	60.8	55.0	60.7	4.1	3.7	4.1	28.2	19.4	26.5	28.8	26.4	29.4
1316[e]	58.7	53.2	58.7	4.3	3.8	4.2	25.4	16.7	24.2	28.4	26.9	28.8

[a] – maximum efficiency case

[b] – minimum cost case

[c] – 95: 5 weight between efficiency and cost respectively in LINMAP

[d] – Power output share from the bottoming cycle

[e] – without intercooler case

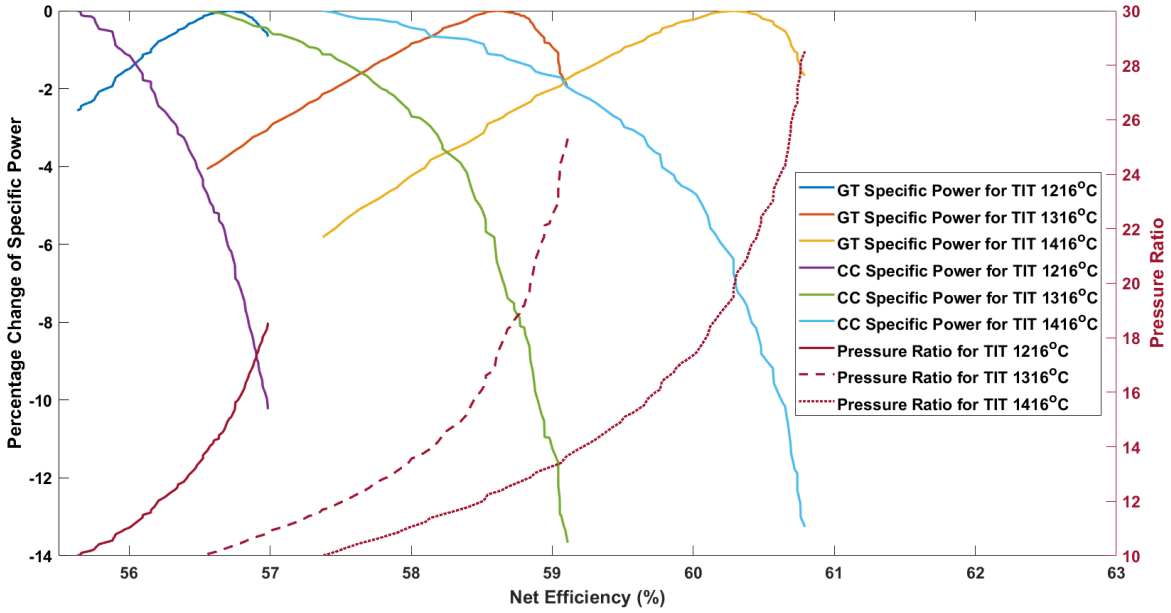

Figure 3-25 Relationship between Pressure ratio, efficiency and Specific power for Cycle 3 for a GT TIT of 1216 °C, 1316 °C and 1416 °C

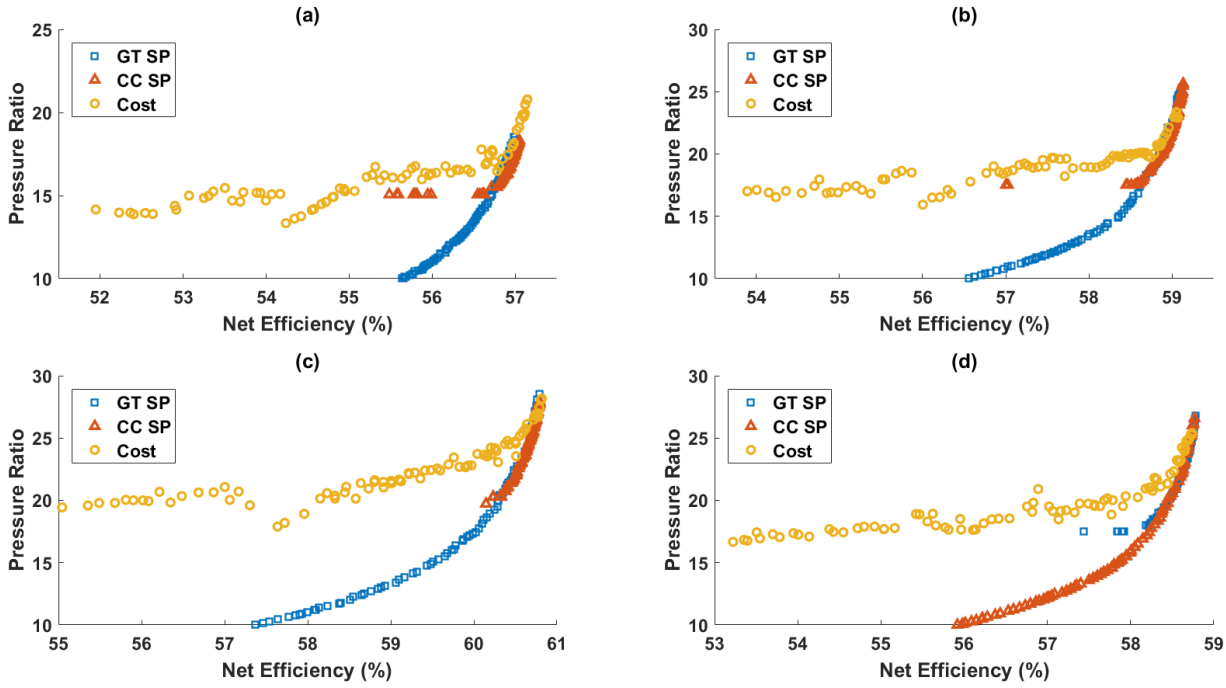

Figure 3-26 Pressure ratio of Cycle 3 for three Pareto fronts: (a) GT TIT-1216 °C, (b) GT TIT-1316 °C, (c) GT TIT-1416 °C, (d) GT TIT-1316 °C w/o intercooler

3.5.4 Cascade Cycle 4

The maximum net efficiency of Cycle 4 thermal Pareto front is 59.5% while it is 58% for a maximum GT specific power case at GT TIT of 1316 °C as shown in Table 3-11 and in Figure 3-27. The corresponding pressure ratio for maximum efficiency design is 24.6 whilst it is 17.5 for maximum GT specific power condition. The maximum specific power has reduced by ~1.1 kJ/kg for all the GT TITs compared with Cycle 3 and Cycle 4. This is because of the increased GT exhaust back pressure owing to the additional heat exchangers added in the flue gas path which leads to a 0.5% pressure loss. Whilst the specific power at maximum efficiency case is also lower than Cycle 3 for GT TIT 1216 °C and 1416 °C, it is a bit higher for 1316 °C with intercooler (i.e., 0.8 kJ/kg). Adding an intercooler can increase the maximum efficiency by 0.4% point with an increase of about 4.8 kJ/kg.

Examining Table 3-11, Cycle 4 is able to achieve higher efficiency at a relatively lower pressure ratio compared to Cycle 2 and roughly at equal pressure ratios

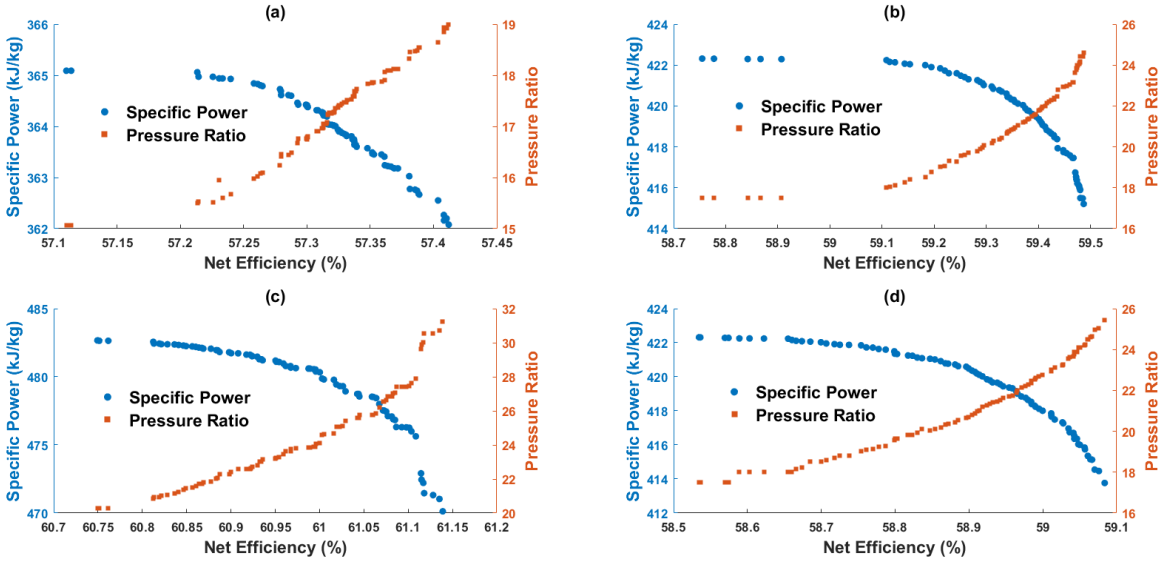

Figure 3-27 Cycle 4 Thermal Pareto fronts: (a) GT TIT-1216 °C, (b) GT TIT-1316 °C, (c) GT TIT-1416 °C, (d) GT TIT-1316 °C w/o intercooler

Table 3-11 Cycle 4: Three cases from thermal Pareto front for a GT TIT of 1216 °C, 1316 °C and 1416 °C

GT TIT (°C)	Efficiency (%)			Specific Power (kJ/kg)			Pressure Ratio			% Share Bot.cycle [d]		
	Case1[a]	Case2[b]	Case3[c]	Case1[a]	Case2[b]	Case3[c]	Case1[a]	Case2[b]	Case3	Case1	Case2	Case3
121	57.4	57.1	57.4	362.1	365.1	363.0	19.0	15.1	18.3	31.5	34.3	32.0
131	59.5	58.0	59.4	415.2	422.3	418.6	24.6	17.5	22.3	29.8	32.3	30.8
141	61.1	60.8	61.1	470.1	482.6	478.4	31.3	20.3	25.8	28.1	32.8	30.1
131	59.1	58.6	59.0	410.4	422.3	417.9	25.4	18.0	22.9	28.9	32.6	30.0

[a] – maximum efficiency case
[b] – maximum GT specific power case
[c] – 85:15 weight between efficiency and specific power respectively in LINMAP
[d] – Power output share from the bottoming cycle
[e] – without intercooler case

compared to Cycle 3 (Case3). The pressure ratio difference between Case2 and Case3 is lower than the corresponding difference in Cycle 3 for a GT TIT of 1316 °C and 1416 °C. This infers that Cycle 4 can be a good candidate for higher temperatures (i.e., > GT TIT of 1316 °C). The bottoming cycle energy share is higher for a GT TIT of 1216 °C and reduces as the TIT increases. For GT TIT of 1316 °C, the energy share is 29.8% which is still lower than the steam cycle integrated with SGT5-4000F (i.e., 32.1%).

Examining Case3 in Table 3-11, the pressure ratio, efficiency and the GT specific power are almost changing linearly as a function of GT TIT. A simulation for a GT TIT of 1366 °C has been carried out to estimate the uncertainty of linear interpolation. The linear curve fit for Case 3 predicts a CC efficiency of 60.2% for a GT TIT of 1366 °C and linear interpolation of the pressure ratio yields 24.0. The CC efficiency from the simulation for Case 3 is 60.2% that corresponds to the pressure ratio of 25.2. This confirms that linear interpolation can reasonably predict the efficiency and the optimal pressure ratio within the GT firing temperature range studied. A linear extrapolation of the optimal pressure ratio and the CC efficiency for a GT TIT of 1516 °C are 29.7 and 63% respectively. The simulation results for a GT TIT of 1516 °C yields 62.6% efficiency that corresponds to the pressure ratio of 29.1. The uncertainty of linear extrapolation for the efficiency is higher than the simulation result and it overpredicts the efficiency (i.e., the efficiency slope reduces as the GT TIT increases). The uncertainty of extrapolating the optimal efficiency, on the other hand, is not significant for this case.

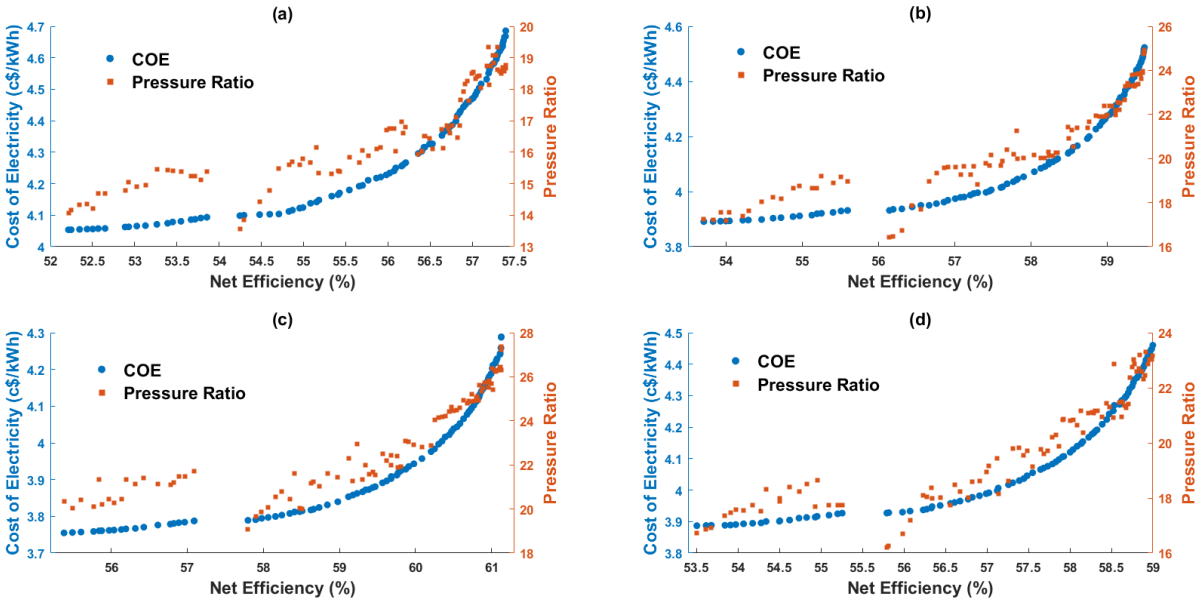

Figure 3-28 Cycle 4 Cost Pareto fronts: (a) GT TIT-1216 °C, (b) GT TIT-1316 °C, (c) GT TIT-1416 °C, (d) GT TIT-1316 °C w/o intercooler

The commercially available H-class machine GT TIT is approximately equal to 1516 °C, therefore, integrating Cycle 4 with the H-class size machine can reach around 63% net efficiency when optimising the pressure ratio. However, this has to be corrected for the changes in the compressor and GT polytropic efficiency compared to the values considered in this study. In order to estimate the uncertainty of extrapolation, Cycle 4 has been simulated for the GT TIT of 1516 °C and the maximum CC efficiency is 62.7% which is obtained at the pressure ratio of 31.3. Since the component efficiencies of a GT are dictated by techno-economic optimisation, the efficiency of 63% can be realisable if those component efficiencies are economically attractive. Since the pressure ratio is higher than the equivalent steam bottoming cycle, the Turbine Exhaust Temperature (TET) will be lower (~600 °C as opposed to ~650 °C), therefore, the bottoming cycle can accept better material. Nevertheless, it has to be also noted that the sCO_2 pressure (~300 bar) is higher than the equivalent steam pressure in a steam-based Rankine cycle (~175 bar) which might increase the cost.

The cost Pareto fronts are plotted in Figure 3-28 for three different GT TIT's together with the pressure ratio. The pressure ratio trend is not smooth along the cost Pareto front. Examining the COE of Cycle 4 in Table 3-12 and comparing with Table 3-10 shows that the COE of Cycle 4 is higher compared to Cycle 3. This is because the efficiency improvement is not high enough to offset the increase in CAPEX which largely resulted in the reduced LMTD in the sCO_2 cycle heat exchangers. Interestingly, the pressure ratio at which maximum efficiency occurs is lower than Cycle 2 and this implies that Cycle 4 can better integrate with a GT with higher TET owing to its increased flexibility.

Although the pressure ratio at maximum efficiency of Cycle 4 is a bit lower than Cycle 3, for a GT TIT of 1416 °C, it is roughly the same for GT TIT of 1216 °C and 1316 °C. Moreover, the pressure ratio difference between Case2 and Case3 are lower compared to Cycle 2 and Cycle 3 for all the GT TIT's which indicates that the efficiency (OPerational EXpenses- OPEX) vs CAPEX trade-off space is lower for Cycle 4.

Figure 3-29 shows the trend of GT specific power, CC specific power, CC efficiency and pressure ratio for three GT TITs. The CC specific powers in Figure 3-29 are normalised with 590.5, 680.5 and 763.6 kJ/kg for a GT TIT of 1216 °C, 1316 °C and 1416 °C respectively and the GT specific powers are normalised to 365.1, 422.3 and 482.7 kJ/kg respectively.

Table 3-12 Cycle 4: Three cases from cost Pareto front for a GT TIT of 1216 °C, 1316 °C and 1416 °C

GT TIT (°C)	Efficiency (%)			COE (c$/kWh)			Pressure Ratio			% Share Bot.cycle [d]		
	Case1[a]	Case2[b]	Case3[c]	Case1[a]	Case2[b]	Case3	Case1[a]	Case2[b]	Case3[c]	Case1[a]	Case2[b]	Case3[c]
121	57.4	53.1	57.3	4.7	4.1	4.6	18.8	14.9	19.1	31.9	29.7	31.5
131	59.5	54.9	59.3	4.5	3.9	4.4	24.9	18.6	23.3	29.8	27.7	30.3
141	61.1	56.3	61.0	4.3	3.8	4.2	27.4	21.1	25.7	29.6	27.0	30.2
131	59.0	54.5	58.9	4.5	3.9	4.4	23.2	18.0	22.6	29.9	27.6	30.0

[a] – maximum efficiency case

[b] – minimum cost case

[c] – 95: 5 weight between efficiency and cost respectively in LINMAP

[d] – Power output share from the bottoming cycle

[e] – without intercooler case

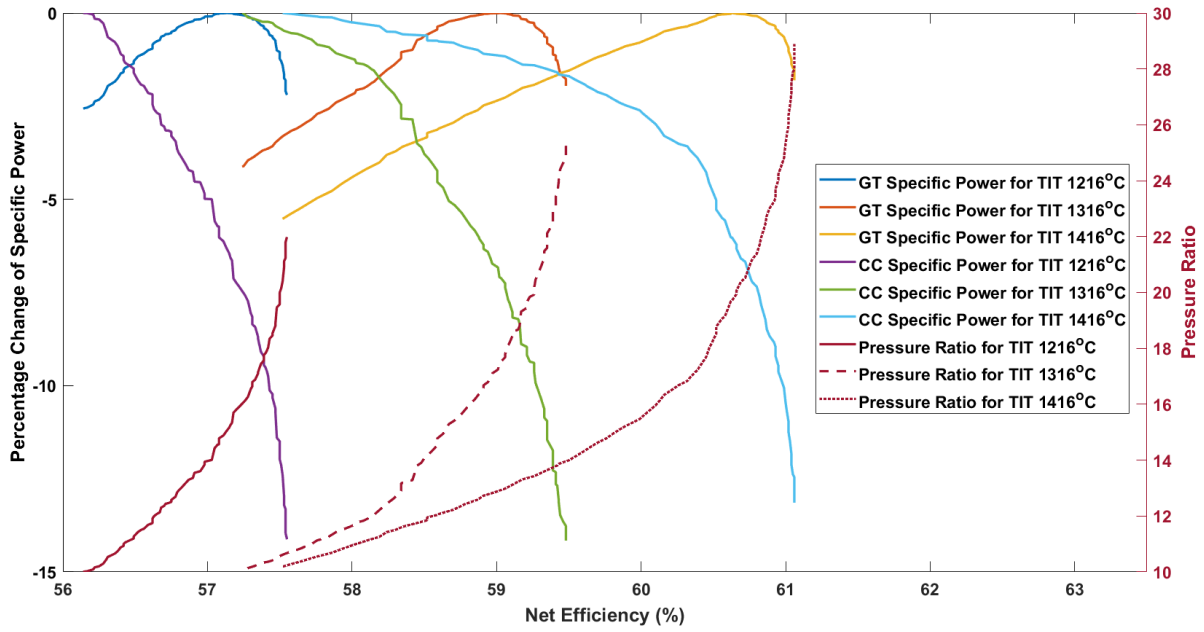

Figure 3-29 Relationship between pressure ratio, efficiency and specific power for Cycle 4 for a GT TIT of 1216 °C, 1316 °C and 1416 °C

This can be used to approximately estimate the expected thermal performance of integrating Cycle 4 with a commercial GT of defined pressure ratio and GT TIT. For an SGT5-4000F machine (Pressure ratio -17.2, GT TIT-1316 °C), integrating Cycle 4 as the bottoming cycle can offer the maximum efficiency of 59.0% whilst the maximum efficiency of 59.5% can be achieved at the pressure ratio of 24.6 (Table 3-11, case-1). This efficiency penalty might be higher for higher GT TITs owing to the diverging difference in pressure ratio between Case2 and Case3 as shown in Table 3-11.

3.5.5 Cascade Cycle 5

Figure 3-30 illustrates the thermal Pareto front of Cycle 5 for three different GT TIT's. Examining Table 3-13, the maximum efficiency of Cycle 5 for a GT TIT of 1316 °C is 59.7% that was obtained at the pressure ratio of 20.0. This maximum efficiency for a GT TIT of 1316 °C is higher than Cycle 4 by 0.25% point and was obtained at an 18.5% lower pressure ratio than Cycle 4. Similarly, for a GT TIT of 1416 °C, the maximum efficiency of Cycle 5 is higher than Cycle 4 by 0.4% point which was obtained at a lower pressure ratio than Cycle 4 by ~21%.

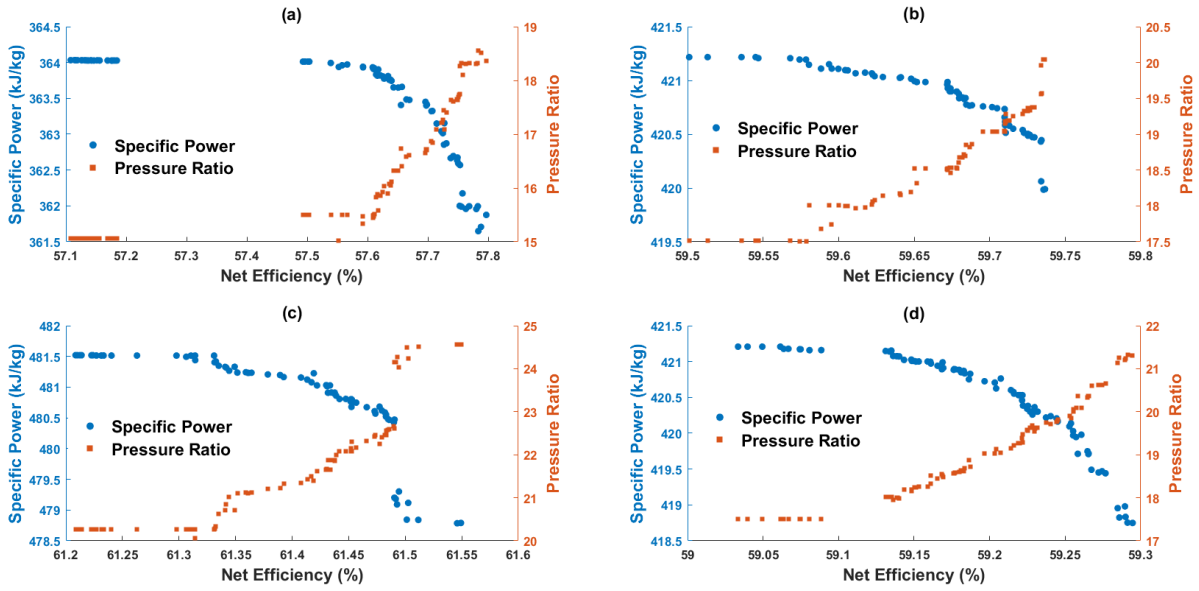

Figure 3-30 Cycle 5 thermal Pareto fronts: (a) GT TIT-1216 °C, (b) GT TIT-1316 °C, (c) GT TIT-1416 °C, (d) GT TIT-1316 °C w/o intercooler

On the other hand, for Case3 the pressure drop is lower by 12.4% and 4.9% for a GT TI of 1316 °C and 1416 °C respectively. The difference in pressure ratio between Case2 and Case3 are 3.3, 2.1 and 4.8 for a GT TIT of 1216 °C, 1316 °C and 1416 °C respectively which is lower than cycler 4 for all the cases. This implies that despite the additional complexities involved with Cycle 5, this cycle might be a better candidate to integrate with higher GT TITs with lower pressure ratios.

Table 3-13 Cycle 5: Three cases from thermal Pareto front for a GT TIT of 1216 °C, 1316 °C and 1416 °C

GT TIT (°C)	Efficiency (%)			Specific Power (kJ/kg)			Pressure Ratio			% Share Bot.cycle [d]		
	Case1[a]	Case2[b]	Case3[c]	Case1[a]	Case2[b]	Case3[c]	Case1	Case2	Case3	Case1	Case2	Case3
1216	57.8	56.5	57.8	361.6	364.0	362.0	18.4	15.1	18.3	33.6	34.4	34.6
1316	59.7	57.7	59.7	420.0	421.2	420.4	20.0	17.5	19.6	32.7	32.8	33.3
1416	61.5	60.1	61.5	478.8	481.5	478.8	24.6	19.7	24.6	31.4	32.5	32.3
1316[e]	59.3	58.7	59.3	418.7	421.2	420.0	21.3	17.5	20.1	31.4	33.3	32.2

[a] – maximum efficiency case
[b] – maximum GT specific power case
[c] – 85:15 weight between efficiency and specific power respectively in LINMAP
[d] – Power output share from the bottoming cycle
[e] – without intercooler case

Although Cycle 5 can achieve ideal temperature gliding in both recuperators and flue gas heat exchangers, the maximum thermal efficiency occurs at the pressure ratio of 20.0 for a GT TIT of 1316 °C which is 16.5% higher than the equivalent steam-based SGT5-4000F pressure ratio. This indicates that in order to realise the maximum performance and cost reduction potential of a sCO_2 cycle integrated with GT's, the whole plant has to be optimised. It is worth noting that the bottoming cycle energy share for a GT TIT of 1316 °C is higher than the equivalent steam Rankine cycle with SGT5-400F by 0.6% point (Table 3-13, Case-1). This indicates that this sCO_2 cycle can be attractive than steam cycles for higher GT TITs.

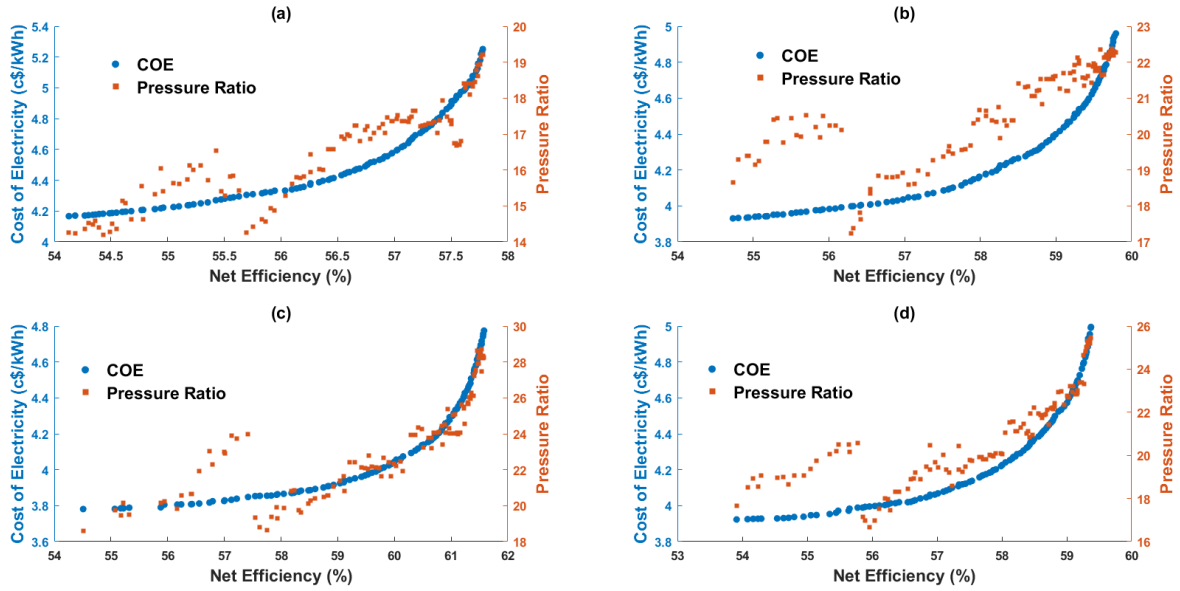

Figure 3-31 Cycle 5 cost Pareto fronts: (a) GT TIT-1216 °C, (b) GT TIT-1316 °C, (c) GT TIT-1416 °C, (d) GT TIT-1316 °C w/o intercooler

Table 3-14 Cycle 5: Three cases from cost Pareto front for a GT TIT of 1216 °C, 1316 °C and 1416 °C

GT TIT (°C)	Efficiency (%)			COE (c$/kWh)			Pressure Ratio			% Share Bot.cycle [d]		
	Case1[a]	Case2	Case3[c]	Cas	Case2	Case3[c]	Case1	Case2	Case3[c]	Case1	Case2[b]	Case
1216	57.8	54.1	57.5	5.3	4.2	4.9	19.2	14.3	17.4	24.4	24.2	24.6
1316	59.8	54.7	59.5	5.0	3.9	4.7	22.3	18.7	21.7	31.4	27.6	31.3
1416	61.6	54.5	61.3	4.8	3.8	4.4	28.3	18.6	25.7	30.0	26.7	29.9
1316[e]	59.4	53.9	59.1	5.0	3.9	4.7	25.4	17.7	22.8	29.4	27.3	29.6

[a] – maximum efficiency case
[b] – minimum cost case
[c] – 95: 5 weight between efficiency and cost respectively in LINMAP
[d] – Power output share from the bottoming cycle
[e] – without intercooler case

Figure 3-31 illustrates the cost Pareto front of Cycle 5 and Table 3-14 shows the three cases from the cost Pareto front. As expected, the COE of Cycle 5 is higher by ~10% compared to Cycle 4 for a GT TIT of 1316 °C. The pressure ratio at the lowest COE is roughly the same as the pressure ratio which causes maximum GT specific power.

Figure 3-32 can be used to estimate the maximum CC efficiency by integrating Cycle 5 with a particular GT and this curve is strictly valid for the considered

modelling assumptions in this paper (Table 3-1). It is worth noting that the maximum CC occurs near to the maximum GT specific power condition.

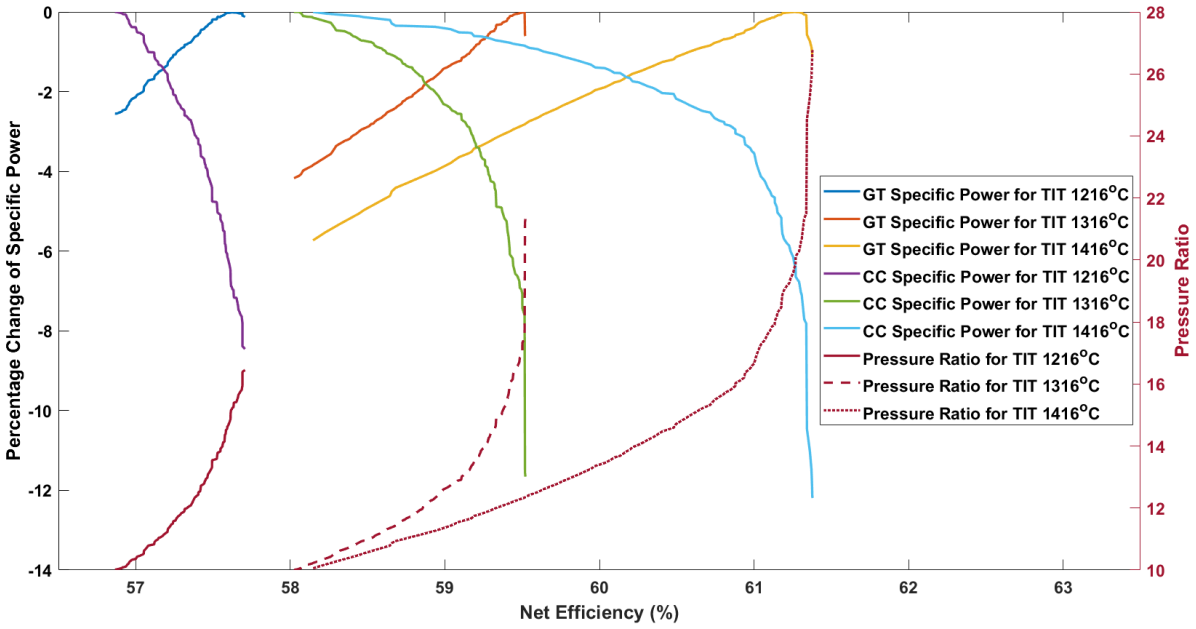

Figure 3-32 Relationship between pressure ratio, efficiency and specific power for Cycle 5 for a GT TIT of 1216 °C, 1316 °C and 1416 °C

3.6 Comparison between Cascade Cycles

The efficiency improvements from Cycle 2 to Cycle 5 is mainly caused by the trade-off between efficient exhaust heat recovery/recuperation and the bottoming cycle energy share. Since the exergy efficiency of the exhaust heat recovery and recuperation increases as the cycle complexity increases, the bottoming cycle energy share increases. In general, Cycle 3 achieves a higher efficiency at a lower pressure ratio compared with Cycle 2 while Cycle 4 surpasses Cycle 3 efficiency. The specific power of Cycle 4 and Cycle 5 are lower than Cycle 2 and Cycle 3 because of the increased back pressure by the additional heat exchangers in the flue gas path (Figure 3-33). The optimal GT pressure ratio reduces from Cycle 2 to Cycle 5 for a given GT TIT, which indicates that the corresponding turbine exhaust temperature increases hence also the bottoming cycle energy share, to maximise the CC net efficiency, provided the cycle is flexible enough to maintain the stack temperature. Despite increasing the optimal

GT pressure ratio for higher GT TITs, the bottoming cycle energy share of a sCO_2 cycle reduces as the GT TIT increases, similar to a steam bottoming cycle, as summarised in Table 3-9, Table 3-11, and Table 3-13.

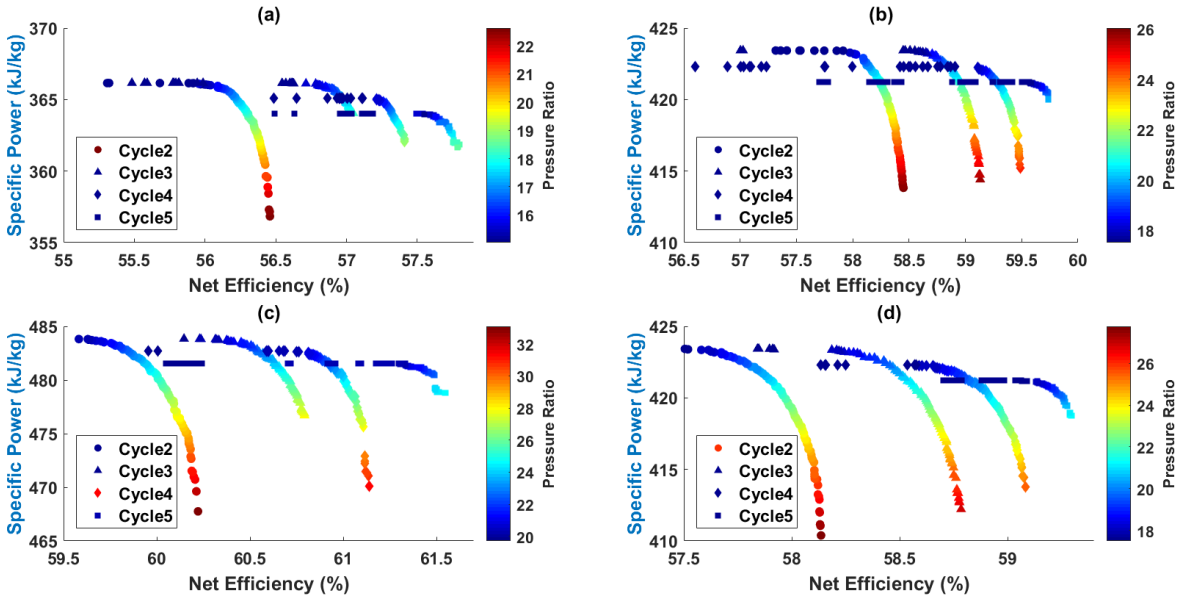

Figure 3-33 Comparison of thermal Pareto fronts of Cycle 2, Cycle 3, Cycle 4 and Cycle 5: (a) GT TIT-1216 °C, (b) GT TIT-1316 °C, (c) GT TIT-1416 °C, and (d) GT TIT-1316 °C w/o intercooler

Examining Figure 3-34, the COE of Cycle 2 at a maximum efficiency design is lower compared to Cycle 4 whilst it is higher than Cycle 3 by 1%. In general, Cycle 2 is not economically viable for higher GT TIT's (i.e., 1416 °C) as compared to Cycle 3. Even for lower GT TIT's, the COE of Cycle 3 is lower than Cycle 2 at higher cycle efficiencies. In addition, the higher efficiency of Cycle 3 was attained at relatively lower pressure ratios than Cycle 2, therefore, Cycle 3 can be integrated well for lower pressure ratio GTs. Cycle 2 may fit well with higher pressure ratio GTs (lower turbine exhaust temperature) for a small-scale plant owing to the simple cycle of Cycle 2.

The COE of Cycle 4 and Cycle 5 are higher than Cycle 3 for all the GT TITs. Although Cycle 4, and 5 can reach higher efficiencies than Cycle 3, the COE at the maximum efficiency point is higher than Cycle 3 which indicates that the

increase in efficiency (reduction in OPEX) does not offset the increased CAPEX, therefore, these Cycles might not be economically attractive. This is evident from

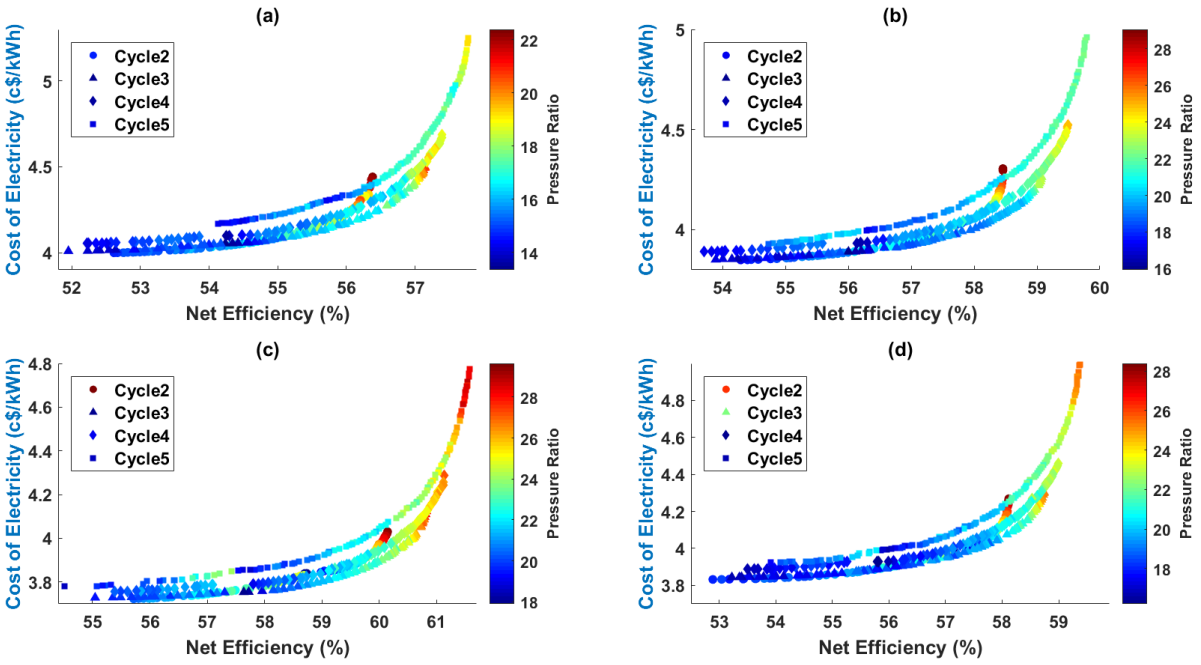

Figure 3-34 Comparison of cost Pareto fronts of Cycle 2, Cycle 3, Cycle 4 and Cycle 5: (a) GT TIT-1216 °C, (b) GT TIT-1316 °C, (c) GT TIT-1416 °C, and (d) GT TIT-1316 °C w/o intercooler

Figure 3-34 where the COE of Cycle 3 is minimum for all the GT TITs studied at maximum efficiency point. It has to be noted that Cycle 4 and Cycle 5 can become an attractive option when the fuel cost is higher. However, in view of selecting an sCO_2 cycle for a commercially available GT for which the TIT and pressure ratio are fixed, Cycle 4 and Cycle 5 may be a good candidate for lower pressure ratio and higher temperature machines (higher turbine exhaust temperature) as the maximum efficiency of Cycle 4 and Cycle 5 is reached at a lower pressure ratio compared to Cycle 3. Nevertheless, an economic study has to be made as the COE of Cycle 4 and Cycle 5 is exponentially increasing near the maximum efficiency point (Figure 3-34).

For a few commercial GTs, the GT firing temperature and the compressor pressure ratio may be not known from the open literature. For this case, the net

power produced from a sCO_2 cycle as bottoming cycle solution can be roughly predicted as a function of GT exhaust gas temperature.

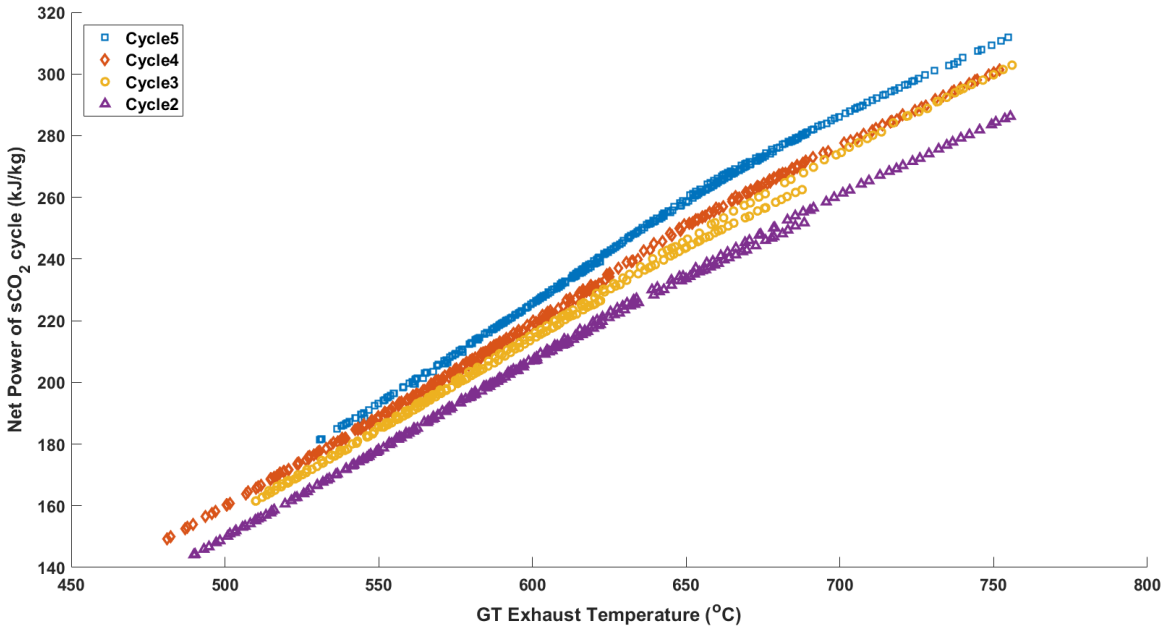

Figure 3-35 Variation of net power of sCO_2 bottoming cycle for different GT outlet temperature

Figure 3-35 shows that the bottoming cycle specific power varies almost linearly for the change in GT TET and Cycle 5 produces noticeably higher specific power than Cycle 3 and Cycle 4 for a higher GT TETs. Net power produced from the bottoming cycle per unit mass flow of exhaust gas can be approximately estimated using Eq.3-18,

$$Net\ Power_{sCO_2 cycle} = A * TET^2 + B * TET + C \qquad (3\text{-}18)$$

where TET is the GT exhaust temperature in °C and the constants A, B and C are listed in Table 3-15 for different cycles with intercooler case. Also, the statistical coefficient of determination (R^2) value and the valid TET range of this equation are tabulated. It is worth noting that the influence of the second order terms is minimal.

Table 3-15 Constant values for estimating the sCO_2 bottoming cycle net power

Cycle	A	B	C	R^2	TET Min (°C)	TET Max (°C)
Cycle 2	-0.000259	0.866439	-219.59280	0.9995	490	755
Cycle 3	-0.000104	0.716074	-177.28884	0.9990	510	755
Cycle 4	-0.000211	0.843716	-210.68713	0.9988	480	755
Cycle 5	-0.000611	1.390283	-387.67091	0.9989	530	730

3.7 Sensitivity Analysis

Since this study focused on modelling the heavy duty SGT5-4000F machine, the applicability and the uncertainties of extending these results to different capacity GT's are discussed here.

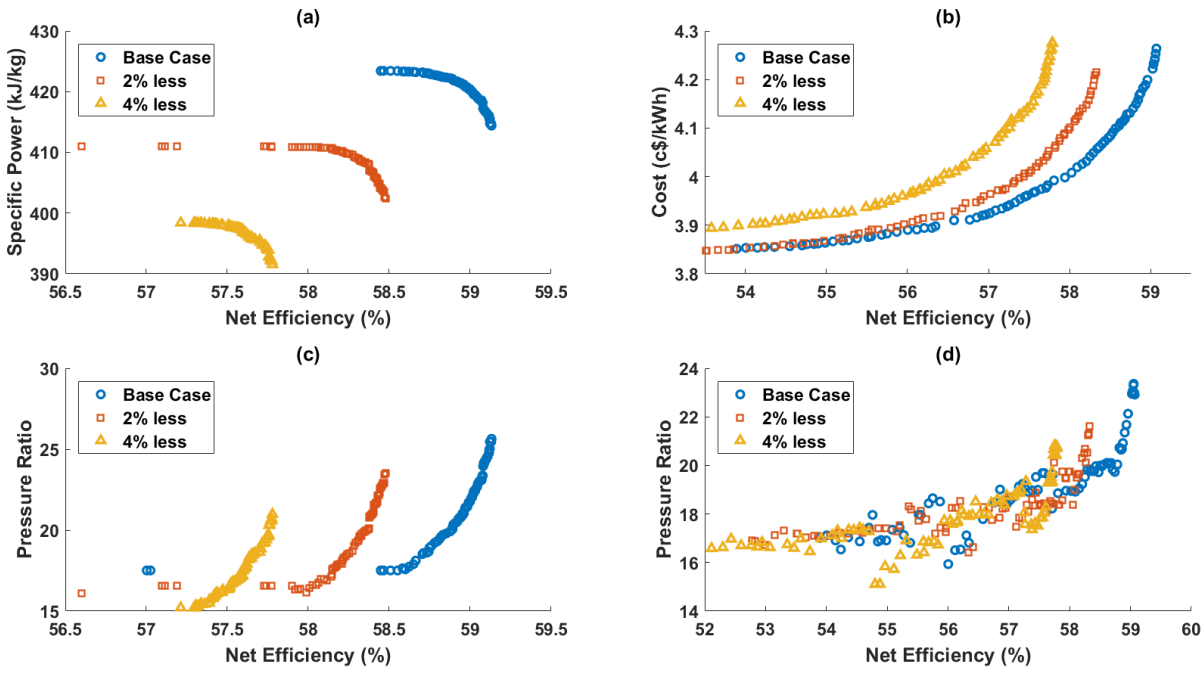

Figure 3-36 Sensitivity study with compressor polytropic efficiency a) Thermal Pareto front b) Cost Pareto front c) Pressure ratio of thermal Pareto front d) Pressure ratio of cost Pareto front

The air compressor polytropic efficiency and GT polytropic efficiency were kept constant during the optimisation process and therefore the uncertainty of the

optimal pressure ratio for a GT TIT of 1316 °C is analysed by performing a sensitivity study for Cycle 3 with intercooler.

Table 3-16 Impact of change in compressor polytropic efficiency

Case	Pareto Front	Efficiency (%)			Specific Power/ COE (kJ/kg-s/c$/kWh)			Pressure Ratio		
		Case1	Case2	Case3	Case1	Case2	Case3	Case1	Case2	Case3
Base	Thermal	59.1	57.0	59.1	414.4	423.4	418.6	25.6	17.5	23.1
-2%[a]		-1.1%	2.4%	-1.2%	-2.9%	-2.9%	-2.5%	-8.2%	-8.2%	-12.9%
-4%[b]		-2.3%	0.4%	-2.3%	-5.5%	-5.9%	-5.7%	-18.2%	-13.2%	-16.8%
Base	Cost	59.1	53.9	59.0	4.3	3.9	4.2	22.9	17.0	22.9
-2%[a]		-1.3%	-2.1%	-1.3%	-1.1%	-0.2%	-1.5%	-5.6%	-0.6%	-10.7%
-4%[b]		-2.2%	-3.3%	-2.3%	0.3%	0.9%	-0.5%	-9.1%	-2.5%	-16.0%

[a] – 2% lesser polytropic efficiency for air compressor
[b] – 4% lesser polytropic efficiency for air compressor

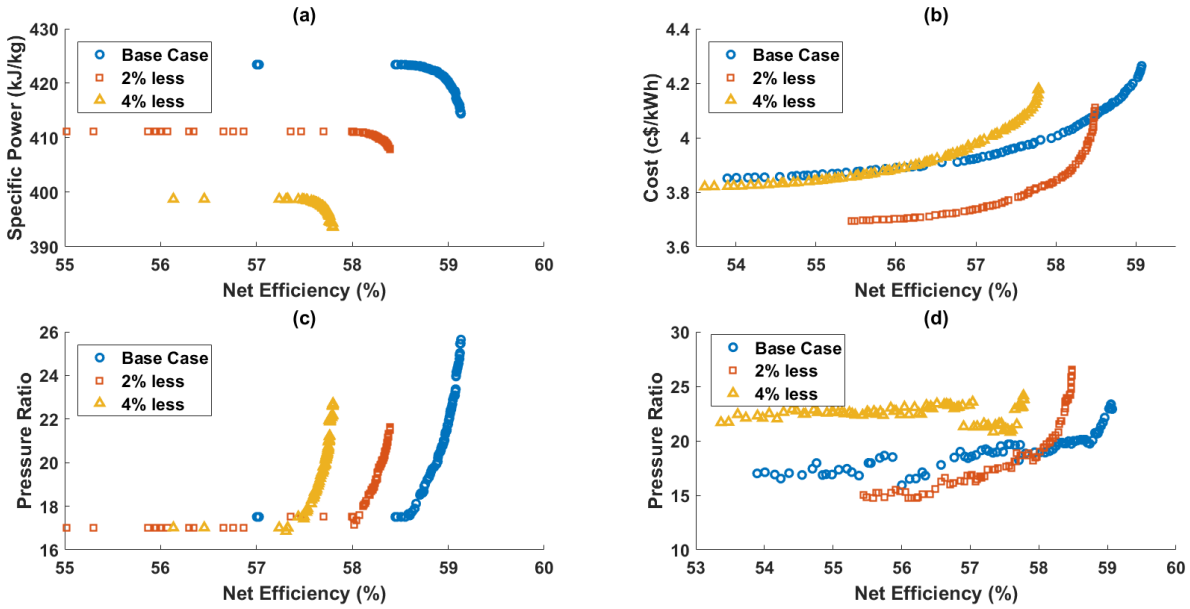

Figure 3-37 Sensitivity study on gas turbine polytropic efficiency a) Thermal Pareto front b) Cost Pareto front c) Pressure ratio of thermal Pareto front d) Pressure ratio of cost Pareto front

Moreover, the optimal pressure ratio is expected to change when the component cost functions change by changing the energy share of the bottoming cycle. Also, the fuel cost can change the pressure ratio which provides the minimum cost owing to the changes in the weight between CAPEX and OPEX in the calculation of COE. Agazzani and Massardo [43] indicated that the uncertainty of the cost function for GT components are ±15%. Therefore, a sensitivity study is performed for the change in air compressor, combustor and GT cost variation by ±20% to see the impact on the optimal pressure ratio of Cycle 3 with intercooler configuration. Since this study considered FOAK cost functions for sCO_2 cycle components the component cost can drop for N^{th} of a Kind (NOAK) plant. Therefore, a sensitivity study has also been undertaken for the variation in sCO_2 cycle components cost by -20% and -50%, however, it has to be noted that the uncertainty of sCO_2 cycle components is high.

From Figure 3-36, it is evident that the variation in air compressor polytropic efficiency changes the thermal and cost Pareto fronts. The maximum specific power, maximum efficiency (Figure 3-36 (a)) and the corresponding pressure ratio (Figure 3-36 (c)) are reducing almost linearly as the compressor polytropic efficiency reduces. Table 3-16 shows three cases 1) maximum efficiency design 2) maximum (or minimum) specific power (or cost) and 3) 85% (or 95%) weight for efficiency and 15% (or 5%) weight to specific power (or COE). Table 3-16 indicates that the pressure ratio corresponding to maximum efficiency is lowered by ~18% for a 4% reduction in compressor polytropic efficiency. Although, the pressure ratio in the cost Pareto front is more scattered, the pressure ratio at which the COE is minimum is roughly the same for all the cases (Figure 3-36 (d), Table 3-16- Case2).

Figure 3-37 depicts the thermal and cost Pareto fronts for three different GT polytropic efficiencies. Although the maximum efficiency and maximum GT specific power are reducing almost linearly as the GT polytropic efficiency reduces (Figure 3-37 (a), Table 3-17), the corresponding pressure ratio is highly non-linear.

Table 3-17 Impact of change in gas turbine polytropic efficiency

Case	Pareto Front	Efficiency			Specific Power/ COE			Pressure Ratio		
		Case1	Case2	Case3	Case1	Case2	Case3	Case1	Case2	Case3
Base	Thermal	59.1	57.0	59.1	414.4	423.4	418.6	25.6	17.5	23.1
-2%[a]		-1.2%	-3.5%	-1.2%	-1.6%	-2.9%	-2.4%	-15.6%	-2.9%	-9.3%
-4%[b]		-2.3%	-1.5%	-2.2%	-5.0%	-5.8%	-5.3%	-11.4%	-2.9%	-10.8%
Base	Cost	59.1	53.9	59.0	4.3	3.9	4.2	22.9	17.0	22.9
-2%[a]		-1.0%	2.9%	-1.1%	-3.6%	-4.1%	-6.2%	15.9%	-11.6%	0.0%
-4%[b]		-2.2%	-1.0%	-2.2%	-2.0%	-0.8%	-2.6%	5.4%	27.5%	1.2%

[a] – 2% lesser polytropic efficiency for a gas turbine
[b] – 4% lesser polytropic efficiency for a gas turbine

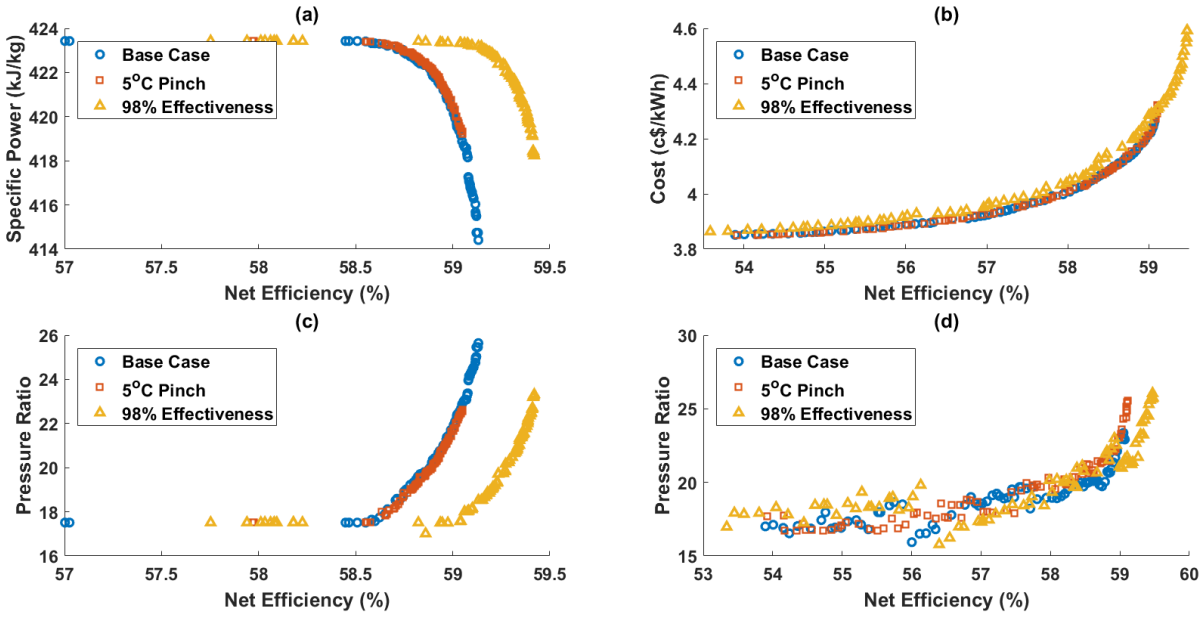

Figure 3-38 Sensitivity study sCO_2 component performance change a) Thermal Pareto front b) Cost Pareto front c) Pressure ratio of the thermal Pareto front d) Pressure ratio of the cost Pareto front

The COE at the maximum efficiency design is lower than the base case for a reduction of GT polytropic efficiency by 4% (Figure 3-37 (a)) whilst this is higher than the -2% case. The pressure ratio in the cost Pareto front is more scattered and also the pressure ratio at which the COE is minimum is not the same for all

three cases (Figure 3-37 (d), Table 3-17- Case2). In general, the pressure ratio for maximum thermal efficiency is significantly changed (non-linearly) when the GT polytropic efficiency is changing.

Figure 3-38 compares the thermal and cost Pareto fronts of the base case with two different sCO_2 cycle performance parameter; A) 98% effectiveness (Thermoflex method) for the sCO_2 cycle recuperators B) 5 °C minimum pinch constraint for the heat exchangers. Examining Figure 3-38, Case B doesn't notably influence the performance of the cycle compared to the base case. For Case A, on the other hand, the maximum efficiency increased by ~0.7% in the cost Pareto front. It is worth noting from Figure 3-38 (b) that the cost Pareto front for Case B is shifted up by a lightly from the base case in the cost coordinates along with an exponential increase in cost near the maximum efficiency design (7.7% increment). In general, the Case A and Case B have little impact on the pressure ratio at which maximum efficiency/specific power or minimum cost is obtained (Table 3-18).

Table 3-18 Impact of change in sCO_2 component performance

Case	Pareto Front	Efficiency			Specific Power/ COE			Pressure Ratio		
		Case1	Case2	Case3	Case1	Case2	Case3	Case1	Case2	Case3
Base	Thermal	59.1	57.0	59.1	414.4	423.4	418.6	25.6	17.5	23.1
Case A[a]		0.5%	1.3%	0.5%	0.9%	0.0%	0.4%	-9.1%	0.0%	-5.7%
Case B[b]		-0.1%	1.7%	-0.1%	1.2%	0.0%	0.4%	-11.8%	0.0%	-5.5%
Base	Cost	59.1	53.9	59.0	4.3	3.9	4.2	22.9	17.0	22.9
Case A[a]		0.7%	-1.0%	0.4%	7.7%	0.3%	3.3%	12.4%	-0.2%	-5.4%
Case B[b]		0.1%	0.0%	0.0%	1.4%	0.0%	0.0%	11.6%	4.0%	1.4%

[a] – 98% Recuperator effectiveness
[b] – 5 °C pinch

Figure 3-39 and Table 3-19 illustrates the impact of the cost Pareto fronts for the changes in component costs by a fixed factor. Four cases were simulated A) the total GT components cost was reduced by 80% B) the total GT components cost

was reduced by 120% C) the total sCO_2 components cost was reduced by 80% D) the total sCO_2 components cost was reduced by 50%.

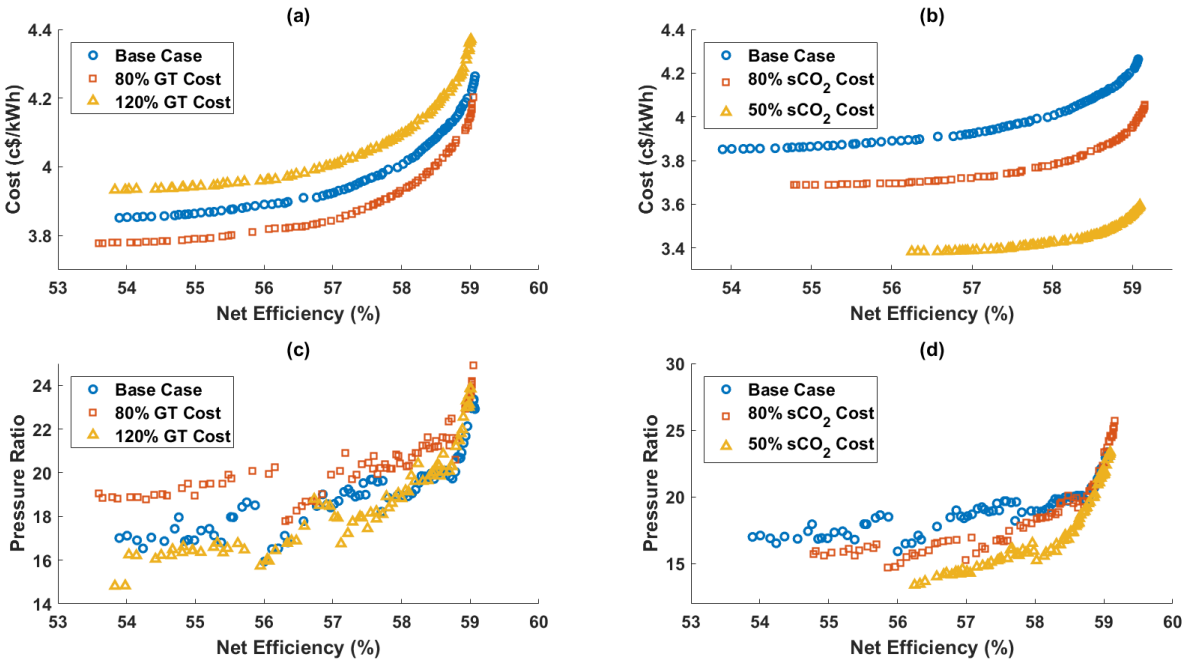

Figure 3-39 Sensitivity study: Impact of component cost a) Change of GT cost b) Change of sCO_2 cost c) Pressure ratio of change of GT cost d) Pressure ratio of change of sCO_2 cost

Table 3-19 Impact in Cycle performance for changes in component cost

Case	Efficiency			COE			Pressure Ratio		
	Case1	Case2	Case3	Case1	Case2	Case3	Case1	Case2	Case3
Base	59.1	53.9	59.0	4.3	3.9	4.2	22.9	17.0	22.9
Case A[a]	0.0%	-0.6%	-0.1%	-1.4%	-1.9%	-2.4%	8.7%	12.0%	0.5%
Case B[b]	-0.1%	-0.1%	-0.2%	2.5%	2.1%	1.3%	4.1%	-	-4.2%
Case C[c]	0.1%	1.6%	0.1%	-	5.3%	-5.4%	12.1%	-7.6%	5.4%
Case D[d]	0.0%	4.4%	0.0%	-	-6.6%	-	1.9%	-	-0.5%

[a] – 80% of GT components cost
[b]– 120% of GT components cost
[c] – 80% of sCO2 components cost
[d] – 50% of sCO2 components cost

The maximum efficiency didn't change for all the four scenarios which reinforce the robustness toward converging to the globally optimum solution. Examining Figure 3-39 (c, d), it is clear that increasing the GT component cost reduces the pressure ratio and vice versa and reducing the sCO_2 cycle component cost reduces the pressure ratio. The CC efficiency corresponding to a minimum cost is highly dependent on the component cost functions (CAPEX) and fuel cost (OPEX). Reducing the sCO_2 cycle component cost increases the efficiency corresponding to the minimum cost design in the cost Pareto front and it is evident in Figure 3-39 (d). The pressure ratio for changes in component cost functions does not significantly change the pressure ratio at which maximum efficiency can be obtained.

3.8 Conclusions

This study considered five sCO_2 cascade cycles in lieu of a conventional steam Rankine cycle in a CCPP with an industrial SGT5-4000F class heavy-duty GT and analysed using multi-objective optimisation with regard to thermal and economic performance. To the authors knowledge, for the first time this optimisation included the GT pressure ratio as a design variable in a combined cycle power plant, finding that this has significant impact on the cycle performance. Simulations were performed for several GT TITs to explore the change in performance for different sCO_2 cycle configurations. The maximum CC efficiency with a sCO_2 bottoming cycle occurs at a higher GT pressure ratio compared to equivalent conventional steam Rankine cycle. Therefore, a sCO_2 cycle integrated with a commercial GT does not offer its maximum efficiency and maximum cost reduction unless the GT pressure ratio is proximate to the optimal value reported in this work. For example, integrating Cycle 4 with an SGT5-4000F machine without optimising the GT pressure ratio penalises the maximum efficiency by 0.5% point.

At maximum CC efficiency the optimal GT pressure ratio increases with GT firing temperature increases, which indicates that the energy share from the bottoming cycle is reduced. The pressure ratio that corresponds to maximum CC efficiency of a complex sCO_2 cycle configuration (i.e., Cycle 5, Cycle 4 and Cycle 3) is lower than simple configurations (i.e., Cycle 2, Cycle 1). Furthermore, the difference in pressure ratio between maximum CC efficiency and maximum GT specific power is highest for Cycle 2 and reduces as the degrees of freedom of the sCO_2 bottoming cycle increase (i.e., Cycle 3, Cycle 4 and Cycle 5). Therefore, complex cycles are good for industrial heavy-duty machines that typically have a lower pressure ratio, to maximise the combined cycle efficiency. This paper gives performance maps for four sCO_2 Cycles, which helps in estimating the CC efficiency and specific power for any given GT pressure ratio and TIT, though extrapolation of these maps requires attention. Also, empirical correlation between net power from each sCO_2 Cycle and the hot flue gas temperature was proposed, which can also be used for WHR applications.

It was also observed that for all the GT TITs and for the sCO_2 configurations studied the GT pressure ratio corresponding to the lower COE design is proximate to the GT pressure ratio of the maximum GT specific power case. The efficiencies at the lowest COE are lower than a steam-based cycle, nevertheless, that is highly sensitive to the component cost functions (CAPEX) and fuel cost/efficiency (OPEX), therefore, NOAK cost functions may yield higher efficiencies at lower COE design.

The novel sCO_2 cycle proposed yields a 1.4% point higher net efficiency than a conventional three pressure steam Rankine cycle integrated with the SGT5-4000F machine; this cycle offers an ideal temperature glide in the heat exchangers. This is equivalent to a reduction of annual CO_2 emission from 1,143,639 ton/year (SGT5-4000F machine) to 1,116,865 ton/year i.e., a reduction of 26,774 ton/year (2.3%). The COE of this Cycle is higher than Cycle 4, nonetheless, the pressure ratio that corresponds to maximum efficiency occurs at a lower pressure ratio than Cycle 4. Therefore, this cycle can be attractive for high-temperature sensible heat sources owing to its large degree of flexibility that

helps in accommodating the large variation in C_p to a lower stack temperature. In Cycle 5, the recuperators and exhaust heat exchangers were arranged in parallel and connected via splitter/mixers in order to control the mass flow split, additional recuperators and exhaust heat exchangers can be connected, though the improvement in performance might be negligible in comparison to the added cost.

3.9 References

[1] Guidance 2050 Pathways. GovUk 2013. https://www.gov.uk/guidance/2050-pathways-analysis (accessed 12 December 2018).

[2] Herzog HJ, Rubin ES, Rochelle GT. Comment on 'Reassessing the Efficiency Penalty from Carbon Capture in Coal-Fired Power Plants'. Environ Sci Technol 2016;50:6112–6113. doi:10.1021/acs.est.6b00169.

[3] Persichilli M, Kacludis A, Zdankiewicz E, Held T. Supercritical CO_2 Power Cycle Developments and Commercialization: Why sCO_2 can Displace Steam Steam. Power-Gen India Cent. Asia, 2012, p. 1–15.

[4] Dostal V, Driscoll MJ, Hejzlar P. A Supercritical Carbon Dioxide Cycle for Next Generation Nuclear Reactors. 2004. doi:MIT-ANP-TR-100.

[5] Turchi CS, Ma Z, Neises T, Michael W. Thermodynamic Study of Advanced Supercritical Carbon Dioxide Power Cycles for High Performance Concentrating Solar Power Systems. Proc. ASME 2012 6th Int. Conf. Energy Sustain., 2012. doi:10.1115/ES2012-91179.

[6] Steven WA, Tom C, Edward P, Tom L, Gary R, J S-AA. Summary of the Sandia Supercritical CO_2 Development Program. Int. SCO2 Power Cycle Symp., Boulder, Colorado: 2011.

[7] Park SH, Kim JY, Yoon MK, Rhim DR, Yeom CS. Thermodynamic and economic investigation of coal-fired power plant combined with various supercritical CO_2 Brayton power cycle. Appl Therm Eng 2018;130:611–23. doi:10.1016/j.applthermaleng.2017.10.145.

[8] Thimsen D, Weitzel P. Challenges in Designing Fuel-Fired sCO_2 Heaters for Closed sCO_2 Brayton Cycle Power Plants. 5th Int. Symp. - Supercrit. CO2 Power Cycles, 2016.

[9] Allam R, Martin S, Forrest B, Fetvedt J, Lu X, Freed D, et al. Demonstration of the Allam Cycle: An Update on the Development Status of a High Efficiency Supercritical Carbon Dioxide Power Process Employing Full Carbon Capture. Energy Procedia, vol. 114, The Author(s); 2017, p. 5948–66. doi:10.1016/j.egypro.2017.03.1731.

[10] Crespi F, Gavagnin G, Sánchez D, Martínez GS. Supercritical carbon dioxide cycles for power generation: A review. Appl Energy 2017;195:152–83. doi:10.1016/j.apenergy.2017.02.048.

[11] Zhao Y, Zhao L, Wang B, Zhang S, Chi J, Xiao Y. Thermodynamic analysis of a novel dual expansion coal-fueled direct-fired supercritical carbon dioxide power cycle. Appl Energy 2018;217:480–95. doi:10.1016/j.apenergy.2018.02.088.

[12] Heo JY, Kim MS, Baik S, Bae SJ, Lee JI. Thermodynamic study of supercritical CO_2 Brayton cycle using an isothermal compressor. Appl Energy 2017;206:1118–30. doi:10.1016/j.apenergy.2017.08.081.

[13] Wang X, Dai Y. Exergoeconomic analysis of utilizing the transcritical CO_2 cycle and the ORC for a recompression supercritical CO_2 cycle waste heat recovery: A comparative study. Appl Energy 2016;170:193–207. doi:10.1016/j.apenergy.2016.02.112.

[14] Baik YJ, Kim M, Chang KC, Kim SJ. Power-based performance comparison between carbon dioxide and R125 transcritical cycles for a low-grade heat source. Appl Energy 2011;88:892–8. doi:10.1016/j.apenergy.2010.08.029.

[15] Weiland NT, Dennis RA, Ames R, Lawson S, Strakey P. Fundamentals and applications of supercritical carbon dioxide (sCO_2) based power cycles-Fossil energy. Elsevier Ltd; 2017. doi:10.1016/B978-0-08-100804-1.00012-8.

[16] Khadse A, Blanchette L, Kapat J, Vasu S, Ahmed K. Optimization of supercritical CO_2 Brayton cycle for simple cycle gas turbines exhaust heat recovery using genetic algorithm. ASME Turbo Expo 2017:1–8. doi:10.1115/GT2017-63696.

[17] Khadse A, Blanchette L, Kapat J, Vasu S, Ahmed K. Optimization of Supercritical CO_2 Brayton Cycle for Simple Cycle Gas Turbines Exhaust Heat Recovery Using Genetic Algorithm. Energy Resour Technol 2018;140:1–8. doi:10.1115/1.4039446.

[18] Marchionni M, Bianchi G, Tassou SA. Techno-economic assessment of Joule-Brayton cycle architectures for heat to power conversion from high-grade heat sources using CO_2 in the supercritical state. Energy 2018;148:1140–52. doi:10.1016/j.energy.2018.02.005.

[19] Kimzey G. Development of a Brayton Bottoming Cycle using Supercritical Carbon Dioxide as the Working Fluid. 2012.

[20] Cho SK, Kim M, Baik S, Ahn Y. Investigation of the Bottoming Cycle for High Efficiency Combined Cycle Gas Turbine System With Supercritical Carbon Dioxide. Proc. ASME Turbo Expo 2015 Turbine Tech. Conf. Expo., 2015, p. 1–12.

[21] Wright SA, Davidson CS, Scammell WO. Thermo-Economic Analysis of Four sCO_2 Waste Heat Recovery Power Systems. 5th Int Symp - Supercrit CO2 Power Cycles 2016:1–16.

[22] Held TJ. Supercritical CO_2 Cycles for Gas Turbine Combined Cycle Power Plants. Power Gen Int., 2015.

[23] Huck P, Freund S, Lehar M, Peter M. Performance comparison of supercritical CO_2 versus steam bottoming cycles for gas turbine combined cycle applications. 5th Int Symp - SCO2 Power Cycles 2016;1:1–14. doi:10.1017/CBO9781107415324.004.

[24] B.J.Davidson, K.R.Keeley. The Thermodynamics of Practical Combined Cycles. Proc IMechE Conf Comb Cycle Gas Turbines 1991:28–50.

[25] Cerri G. Parametric Analysis of Combined Gas-Steam Cycles. J Eng Gas Turbines Power 1987;109.

[26] J.H.Horlock. Advanced Gas Turbine Cycles. 1st ed. Pergamon; 2003.

[27] Najjar YSH, Ismail MS. Optimum pressure ratios for different gas turbine cycles. High Temp Technol 1990;8:283–9. doi:10.1080/02619180.1990.11753494.

[28] The Babcock & Wilcox Company. Steam Its generation and use. vol. 53. 2019. doi:10.1017/CBO9781107415324.004.

[29] Thermoflow. Tflow16 Update Letter 2006. https://www.thermoflow.com/UpdateLetters/TF16_UPDATE_LETTER.html (accessed 20 June 2018).

[30] Zhao Q, Mecheri M, Neveux T, Privat R, Jaubert JN. Selection of a Proper Equation of State for the Modeling of a Supercritical CO_2 Brayton Cycle: Consequences on the Process Design. Ind Eng Chem Res 2017;56:6841–53. doi:10.1021/acs.iecr.7b00917.

[31] Lemmon EW, Bell IH, Huber ML, McLinden MO. NIST Standard Reference Database 23: Reference Fluid Thermodynamic and Transport Properties-REFPROP, Version 10.0. 2010. doi:10.18434/T4JS3C.

[32] Heatric. Compact Heat Exchange. Meggitt Smart Eng Extrem Environ 2018:1–5.

[33] Nellis G, Klein S. Heat Transfer. 2009. doi:10.1017/CBO9780511841606.

[34] Avval HB, Ahmadi P, Ghaffarizadeh AR, Saidi MH. Thermo-economic-environmental multiobjective optimization of a gas turbine power plant with preheater using evolutionary algorithm. Int J Energy Res 2010. doi:10.1002/er.1696.

[35] Sharma S, Rangaiah GP, Cheah KS. Multi-objective optimization using MS Excel with an application to design of a falling-film evaporator system. Food Bioprod Process 2011;90:123–34. doi:10.1016/j.fbp.2011.02.005.

[36] Rangaiah GP. Multi-Objective Optimization Techniques and Applications in Chemical Engineering. vol. 1. 2009. doi:10.1007/0-387-28356-0_10.

[37] Ahmadi MH, Hosseinzade H, Sayyaadi H, Mohammadi AH, Kimiaghalam F. Application of the multi-objective optimization method for designing a powered Stirling heat engine: Design with maximized power, thermal efficiency and minimized pressure loss. Renew Energy 2013;60:313–22. doi:10.1016/j.renene.2013.05.005.

[38] Wang Z, Rangaiah GP. Application and Analysis of Methods for Selecting an Optimal Solution from the Pareto-Optimal Front obtained by Multiobjective Optimization. Ind Eng Chem Res 2016;56:560–74. doi:10.1021/acs.iecr.6b03453.

[39] Ho CK, Carlson M, Garg P, Kumar P. Technoeconomic Analysis of Alternative Solarized sCO_2 Brayton Cycle Configurations. J Sol Energy Eng 2016;138:051008. doi:10.1115/1.4033573.

[40] ESDU 92013: Selection and costing of heat exchangers. 1994.

[41] Marchionni M, Bianchi G, Tsamos KM, Tassou SA. Techno-economic comparison of different cycle architectures for high temperature waste heat to power conversion systems using CO_2 in supercritical phase. Energy Procedia, vol. 123, Elsevier B.V.; 2017, p. 305–12. doi:10.1016/j.egypro.2017.07.253.

[42] Zada KR, Kim R, Wildberger A, Schalansky CP. Analysis of supercritical CO_2 Brayton cycle recuperative heat exchanger size and capital cost with variation of layout design. 6th Int. Symp. - Supercrit. CO2 Power Cycles, 2018.

[43] Agazzani A, Massardo AF. A Tool for Thermoeconomic Analysis and Optimization of Gas, Steam, and Combined Plants. Eng Gas Turbines Power 1997;1. doi:10.1115/1.2817069.

[44] McMahon T. Inflation Rate Calculator 2018. https://inflationdata.com/Inflation/Inflation_Calculators/Inflation_Rate_Calc

ulator.asp (accessed 12 December 2018).

[45] Valero A, Lozano MA, Serra L, Tsatsaronis G, Pisa J, Frangopoulos C, et al. CGAM Problem: Definition and Conventional Solution. Energy 1994;19:279–86. doi:10.1016/0360-5442(94)90112-0.

[46] Horlock JH. The optimum pressure ratio for a combined cycle gas turbine plant. Proc Inst Mech Eng Part A J Power Energy 1995;209:259–64. doi:10.1243/PIME_PROC_1995_209_004_01.

Chapter 4

4 Multi-Objective Optimisation and Exergoeconomic Analysis of sCO_2 Brayton Cycles for Combined Cycle Power Plant

Dhinesh Thanganadar, Faisal Asfand , Kumar Patchigolla

School of Water, Energy and Environment (SWEE), Cranfield University, Cranfield, MK43 0AL, UK

Abstract is submitted to 1st FERIA Conference, the European Conference on Fuel and Energy Research and Its Applications

---

Statement of contributions of joint authorship

Dhinesh Thanganadar proposed the novelty, implemented the methods, generated all results, and prepared the manuscript draft. Faisal Asfand and Kumar Patchigolla provided supervision, proof-read and critically commented on the manuscript before submission.

ABSTRACT

Supercritical carbon dioxide (sCO_2) power cycles can achieve higher efficiencies at a higher turbine inlet temperature (>550 ^oC) with a compact plant footprint. sCO_2 cycles are a potential candidate for bottoming cycle application, nevertheless, current researches were focussed on integrating the sCO_2 cycle with a commercial Gas Turbine (GT). Commercial topping cycle GTs are optimised for steam Rankine bottoming cycles and this does not yield the maximum performance when integrated with sCO_2 cycles. In this study, a multi-objective optimisation is performed to analyse the whole plant performance by optimising both topping and bottoming cycles. Detailed exergy and exergo-economic analyses were also performed to identify the areas of improvement.

The results show that efficiency can be improved by about 1% point when integrating a sCO_2 cycle in lieu of a steam cycle. In addition, the topping cycle pressure ratio reaches a higher value than the equivalent steam cycle to maximise the plant efficiency and this value changes with the GT firing temperature. The exergy destruction of the heat recovery steam generator and recuperators are reduced by about 3.6% and 4.8% respectively for SGT5-4000F machine, when optimising the topping and bottoming cycles to maximise the plant efficiency and these reductions are 2.2% and 3.7% for 7HA.02 machine.

Keywords

sCO_2, sensible heat, Multi-Objective optimisation, Exergy, Exergo-economic

4.1 Introduction

Supercritical carbon dioxide (sCO_2) cycles are highly studied for power generation application such as nuclear, fossil-fired, waste heat recovery and concentrated solar power owing to its ability to achieve higher efficiency with compact footprint. Numerous cycles have been proposed and Crespi et al. (2017) reviewed forty-two of them [1]. Although many of the cycles are ideally studied for constant flux heat sources, the optimal cycle for a sensible heat source needs to be explored as the isobaric specific heat of sCO_2 largely varies close to the (pseudo) critical point. This activates the pinch within the heat-exchanging network, thus limiting the exergy efficiency. Huck et al. (2016) [2] analysed the potential of using sCO_2 cycle as a bottoming cycle for a next-generation combined cycle power plant (CCPP). They concluded that the potential of sCO_2 cycles is limited as the exergy losses from the compressor outweighs the reduction of the exergy destruction in the Heat Recovery Steam Generator (HRSG). But, they optimised only the bottoming cycle by considering the exhaust condition of state-of-the-art commercial GT's and this doesn't explore the full cycle potential as the commercial GTs are optimised for steam based Rankine cycles [3]. Therefore, in-order to explore the maximum potential of sCO_2 cycles, the whole plant has to be optimised together with the GT. This paper compared the performance of two commercial GTs integrated with a sCO_2 bottoming cycle

and compares their performance differences with the steam Rankine cycle. Furthermore, the GTs were optimised to yield maximum plant performance for sCO_2 cycle and this is compared with the base case where the topping cycle was not optimised. The optimisation was performed using a multi-objective optimisation technique to maximise the plant net efficiency and minimise the cost of electricity. sCO_2 cascade cycle is considered in this study owing to the flexibility of controlling the mass flow to the HRSG and its superior performance for sensible heat sources. A detailed exergy and exergo-economic analysis were also performed to identify areas for improvements.

4.2 Methodology

4.2.1 Thermodynamic Modelling

Thanganadar et al. (2019) [3] compared the performance of five cascade cycles and Cascade Cycle 3 was chosen for this study owing to its relatively higher performance with minimum number of components. The cycle configuration integrated with SGT5-4000F machine (firing temperature is ~1316 °C, obtained from Thermoflex database), a commercial GT, is shown in Figure 4-1. GE 7HA.02 GT is selected as the second GT for this study due to its higher firing temperature (~1515 °C, obtained from Thermoflex database) and this represents the current state-of-the-art industrial GT technology. All the sCO_2 turbomachinery's are connected in the same shaft for steady-state process design, however, the off-design performance, control strategy and plant turndown need to be considered (out of scope) to validate this hypothesis.

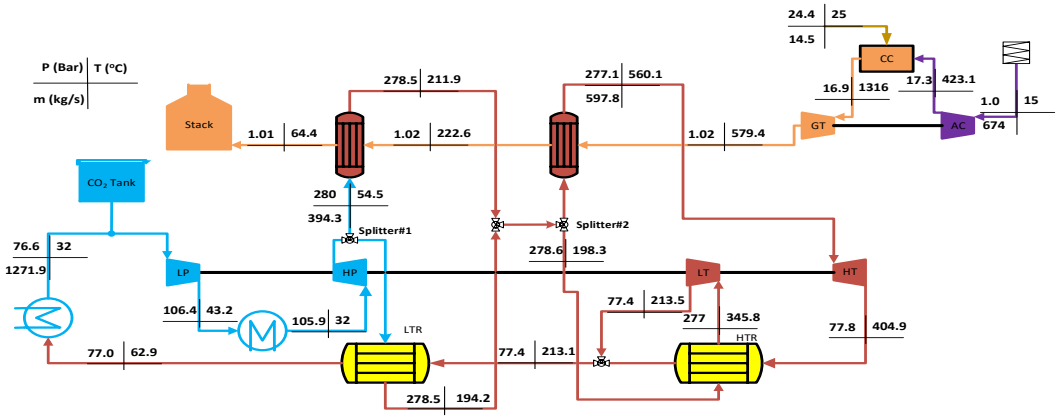

Figure 4-1 Cycle Configuration of Cascade Cycle 3 [3]

Since the sCO_2 cycle performance was compared against the conventional bottoming cycle i.e., triple-pressure steam Rankine cycle, the steam plant models with the triple-pressure HRSG with 16 heat exchangers were developed in Thermoflex, a commercial software. This was done to estimate the HRSG conductance. The overall heat transfer coefficient of a HRSG is mainly limited by the thermal resistance from the flue gas side, therefore, regardless of the changes in heat transfer coefficient of water/ sCO_2, the heat transfer area of the HRSG for both the cases has to be similar. The steam cycle performance can be increased by changing the number of pressure levels in the HRSG (increasing the heat transfer area) whereas the heat recovery of the sCO_2 cycle can be increased by closely matching the Temperature - Enthalpy (TQ) profile and this increases the conductance (UA) exponentially. Therefore, in order to make a clear comparison from thermodynamic standpoint, the HRSG conductance has to be the same for both the cases. Methane was used as a fuel.

Table 4-1 Thermodynamic model assumptions

Description	Unit	SGT5-4000F	7HA.02
Air mass flow (Thermoflex)	kg/s	674	688
Calculated HRSG Conductance (UA)	MW/K	15.7	13.1
Air compressor pressure ratio	-	17.6	23.3
sCO_2 turbine isentropic efficiency	%	95 [2]	
sCO_2 compressor isentropic efficiency	%	95 [2]	
Minimum pinch	°C	4	
Effectiveness	%	95	
Generator Efficiency	%	99	
Parasitic load	MW_e	2	

A thermodynamic model for all the plant components were developed in MATLAB®. The heat exchanger is a one-dimensional model (discretised to 15 segments), as the pinch point could occur within the heat exchanger owing to the large variation of isobaric specific heat. The GT and air compressors were modelled using polytropic efficiencies as the pressure ratios were optimised during GT optimisation. The combustor model is a five species model with JANEF thermochemical table [4] used for combustion properties calculation. REFPROP is used for thermo-physical properties calculation of CO_2, water, air and flue gas. NSGA II algorithm is integrated in the process simulation code with the cycle net efficiency maximised whilst the unit cost of electricity was minimised. This

algorithm optimised eight continuous variables: GT pressure ratio, sCO_2 main compressor inlet pressure, intercooler pressure, sCO_2 compressor outlet pressure, split fraction #1, split fraction #2, sCO_2 mass flow, conductance share between the two exhaust gas heat exchangers within the bound constraints. Table 4-1 shows the thermodynamic model assumptions used for process modelling. The heat exchanger pressure drops were simulated as per Huck et al. (2016) [2].

4.2.2 Exergo-Economic Analysis

Flow and chemical exergies were calculated for each stream and the exergy destruction in all the plant components were calculated by performing an exergy balance [5]. SEPCO method [6] was applied to calculate the exergy cost for each stream. The cost balance for each component was performed together with the auxiliary equations in order to calculate the stream specific cost [5]. The sCO_2 cycle compact heat exchanger CAPEX was calculated based on Carlson et al. (2017) [7] which fits the ESDU database with the limited vendor data. Also, the sCO_2 turbomachinery cost was calculated based on Carlson et al. (2017) [7]. The air compressor, combustor and GT cost was calculated based on Thanganadar et al. [3]. Table 4-2 shows the plant operational and economic assumptions for calculating the Cost of Electricity (COE).

Table 4-2 Economic Model Assumptions

Description	Unit	Value
Life Time	Years	20 [8]
Interest Rate	%	12 [8]
Annual Operating Hours	Hrs	8000 [8]
Maintenance Factor	-	0.06 [8]
Fuel Cost	$/GJ	4 [9]

4.3 Results and Discussion

4.3.1 Multi-Objective Optimisation

The sCO_2 bottoming cycle was optimised for two commercial GT's, with and without optimising the topping cycle and the corresponding Pareto fronts are plotted in Figure 4-2. It is clear that optimising only the bottoming cycle for a fixed

the efficiency is further reduced with an increase in COE which is omitted (non-dominant solution) in the Pareto front by NSGA-II algorithm.

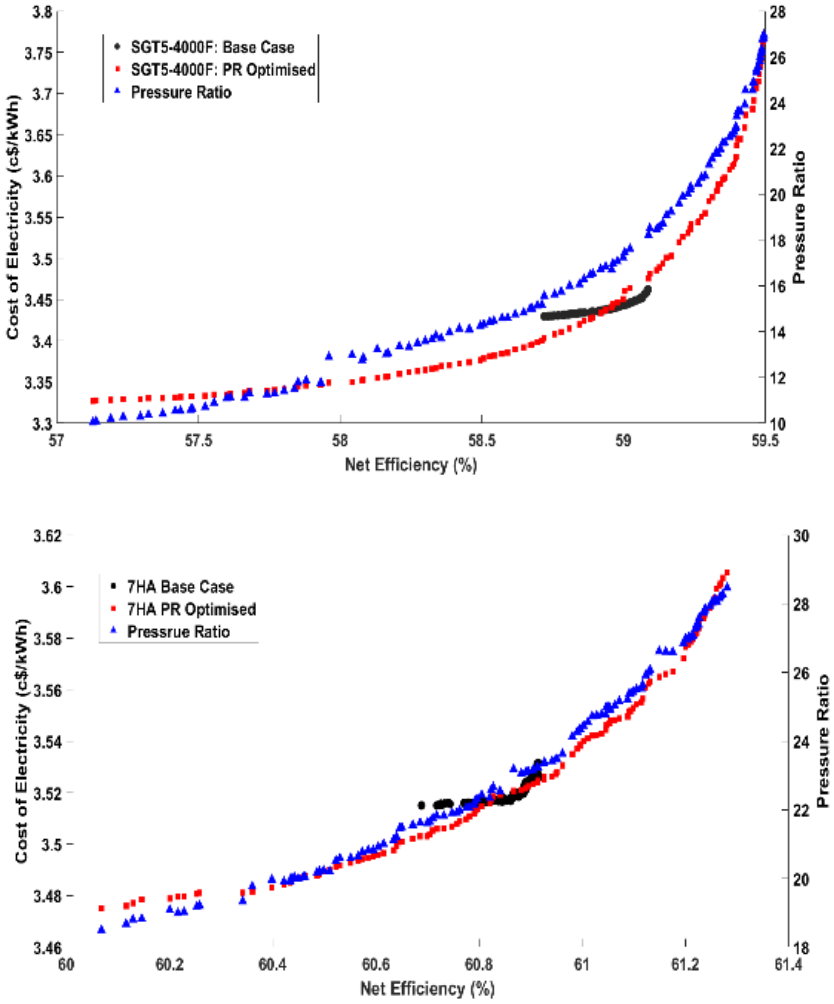

Figure 4-2 Efficiency and cost Pareto fronts, Top: SGT5F-4000F, Bottom: 7HA.02

GT exhaust condition explores part of the Pareto front whilst optimising the topping cycle together with the bottoming cycle explores the complete Pareto front of the plant. The efficiency of the sCO_2 bottoming cycle is higher than the steam cycle when the topping cycle is not optimised by 0.7% point and 0.5% point for SGT5-4000F and 7HA.02 machines respectively. The plant efficiency can be further increased by 0.4% point for SGT5-4000F machine when optimising the topping cycle whereas it is 0.5% point improvement for 7HA.02 machine. Figure 4-2 also depicts that the GT pressure ratio tends to increase in order to increase the plant efficiency. This means that the sCO_2 bottoming cycle can better fit with

a GT that has a higher pressure ratio such as aero-derivative engines or dual-expansion GTs. The GT pressure ratio to yield maximum Combined Cycle (CC) efficiency is higher for 7HA.02 as compared to SGT5-4000F machine owing to its higher firing temperature. Minimum COE is obtained at an optimal efficiency point (for example, 57.1% efficiency for SGT5-4000F PR optimised case), below which

The COE of 7HA.02 is lower than SGT5-4000F machine at the maximum efficiency case by 0.16 c$/kWh whilst it is reversed at the minimum COE case (difference between the top and bottom figure in Figure 4-2). Even though, the efficiency of the plant increases by optimising the GT for sCO_2 cycle, it comes at higher COE for both the machines studied. This is because increasing the GT pressure ratio also increases the cost of the topping cycle whereas the improvement from the bottoming cycle performance does not offset the increased plant cost. The GT pressure ratio at the minimum cost case is lower than the commercial GT optimised for a steam Rankine cycle. This infers that the increase in the sCO_2 bottoming cycle cost for the higher heat transfer (GT exhaust temperature is higher because of the lower pressure ratio) is lower than the reduction in the topping cycle cost. In other words, the topping cycle cost is dominant.

4.3.2 Exergy Analysis

Figure 4-3 shows the exergy balance of the sCO_2 bottoming cycle, with and without optimising the topping cycle pressure ratio, for both the maximum efficiency case and minimum COE case. The fuel exergy input reduces by optimising the topping cycle pressure ratio, which also reduces the plant exergy destruction at the maximum efficiency case. Nevertheless, the fuel energy input increased when minimising the COE despite higher exergy loss from the combustor.

Figure 4-4 shows the normalized exergy destruction of the bottoming cycle components. HRSG and recuperators exergy losses were reduced at the maximum efficiency case by optimising the topping cycle pressure ratio as it aids matching the T-Q profile. In addition, the sCO_2 turbine and precooler exergy

losses are reduced as the sCO_2 mass flow reduces because of the reduced energy share to the bottoming cycle while the opposite happens when minimising the COE owing to increased energy share to the bottoming cycle. Minimising the COE also increases the exergy loss from the HRSG, and recuperator as reduction in the size of these components help to reduce the cost.

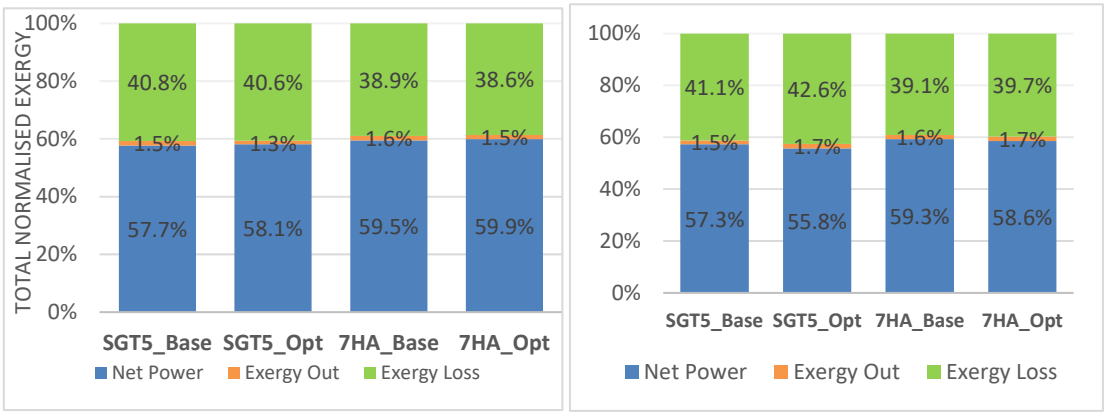

Figure 4-3 Plant normalized exergy: Left- maximum efficiency case, Right- minimum cost case

4.3.3 Exergo-economic Analysis

Table 4-3 shows the sum of the cost rate of energy destruction (C_D) and capital cost rate (Z) which includes the capital cost and O&M cost for k^{th} component. The data show the total cost rate of the maximum efficiency and minimum cost cases with/without optimising the topping cycle for the two GTs studied. The total cost rate of the Low Temperature Recuperator (LTR) is higher than High Temperature Recuperator (HTR) while the High Temperature Heater (HTH) has a higher cost rate than the Low Temperature Heater (LTH) owing to the higher CAPEX.

Although total C_D reduces for maximum efficiency case, as compared to the base case when optimising the topping cycle pressure ratio, the total cost rate increases by 3.1% because of the increased Z for the SGT5-4000F machine. On the other hand, the total cost rate reduces by 0.3% for 7HA.02 machine. The LTR total cost rate reduces by 18.3% when minimising the COE without optimising the topping cycle compared to the maximum efficiency case and the HTR total cost

rate reduces by 22.8%, and the total cost rate of the precooler increased by 3.1% owing to the increased heat rejection.

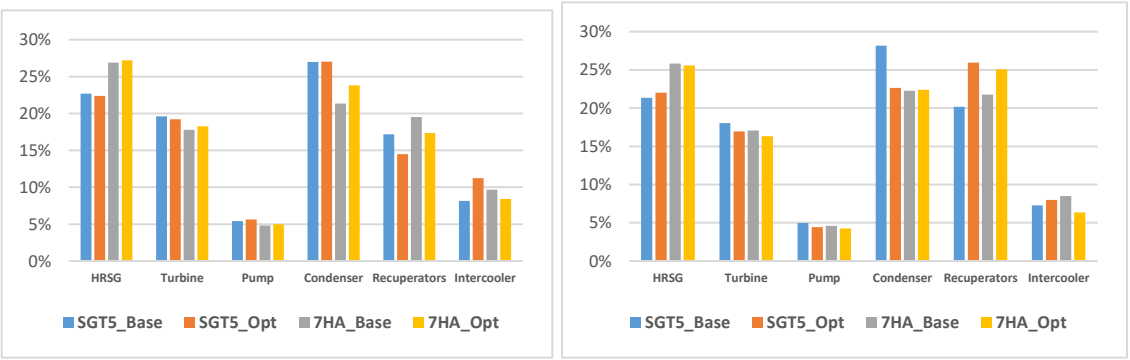

Figure 4-4 Normalized exergy destruction of bottoming cycle, left: maximum efficiency case, right: minimum COE case

When optimising the topping cycle pressure ratio, the combustor size is reduced at the maximum efficiency case, while the GT and air compressor (AC) cost rate is increased, due to the increased pressure ratio. Since the bottoming cycle energy share is reduced from the base case, the total cost rate of all the bottoming cycle components, except the LTH, reduced. In the base case, the exergo-economic factor of LTR and HTR reduced by 15% and 14% respectively, when minimising the COE from the maximum efficiency case for SGT5-4000F machine. For 7HA.02 machine, they reduced by 7% and 16% respectively. This infers that the size reduction of the LTR and HTR aids cost reduction of the bottoming cycle and LTR has more weight owing to the higher total cost rate.

Table 4-3 Total cost rate (C_D+Z) of base case and topping cycle optimised case

Component	SGT5-4000F ($/hr)				7HA.02 ($/hr)			
	Base Eta	**Opt. Eta**	**Base COE**	**Opt. COE**	**Base Eta**	**Opt. Eta**	**Base COE**	**Opt. COE**
Combustor	4,217	4,003	4,217	4,570	8,161	8,038	8,161	8,345
GT#1	1,228	1,815	1,228	791	1,111	1,249	1,111	973
Precooler	934	848	962	1,030	1,037	1,056	1,073	1,191
Air Compressor1	785	1,039	785	550	1,273	1,435	1,273	1,112
LTR	749	663	611	853	927	872	851	976

HTH	735	681	713	748	756	680	747	698
HT Turbine	579	522	551	623	668	641	644	672
Compressor 2	510	393	502	510	492	523	500	543
LTH	475	503	497	533	489	537	493	585
LT Turbine	452	385	451	555	541	507	547	596
HTR	317	283	245	267	345	354	296	293
Intercooler	249	290	232	303	370	314	336	289
GT2	230	277	230	177	306	332	306	278
Air Compressor2	195	232	195	155	749	699	749	880
Compressor 1	142	221	132	204	248	185	224	201

4.4 Conclusions

Multi-objective optimisation of a sCO_2 cascade (bottoming) cycle for two commercial GTs with and without optimising the topping cycle was performed with the goal of maximising the efficiency and minimising the cost of electricity (COE). Since the optimal GT pressure to yield the maximum efficiency is higher than the equivalent triple-pressure steam Rankine cycle, sCO_2 cycle could be optimally integrated with higher pressure ratio GTs such as aero-derivative or dual-firing engines.

The size of the recuperators is critical to minimising the plant cost and LTR has more weight than HTR owing to its higher total cost rate. The minimum COE case inclines to increase the energy share of the bottoming cycle as the total cost rate of the topping cycle has higher weightage compared to the bottoming cycle.

4.5 References

[1] Crespi F, Gavagnin G, Sánchez D, Martínez GS. Supercritical carbon dioxide cycles for power generation: A review. Appl Energy 2017;195:152–83. doi:10.1016/j.apenergy.2017.02.048.

[2] Huck P, Freund S, Lehar M, Peter M. Performance comparison of supercritical CO_2 versus steam bottoming cycles for gas turbine combined

cycle applications. 5th Int Symp - SCO2 Power Cycles 2016;1:1–14. doi:10.1017/CBO9781107415324.004.

[3] Thanganadar D, Asfand F, Patchigolla K. Thermal performance and economic analysis of supercritical Carbon Dioxide cycles in combined cycle power plant. Appl Energy 2019;255. doi:10.1016/j.apenergy.2019.113836.

[4] Stull DR, Prophet H, Branscomb LM. JANAF Thermochemical Tables. 2nd editio. National Bureau of Standards U.S; 1971.

[5] Bejan A, Moran MJ. Thermal Design and Optimization. 1996. doi:10.1016/S0140-7007(97)87632-3.

[6] Lazzaretto A, Tsatsaronis G. SPECO: A systematic and general methodology for calculating efficiencies and costs in thermal systems. Energy 2006;31:1257–89. doi:10.1016/j.energy.2005.03.011.

[7] Carlson MD, Middleton BM, Ho CK. Techno-Economic Comparison of Solar-Driven sCO_2 Brayton Cycles Using Component Cost Models Baselined With Vendor Data. Proc ASME 2017 Power Energy Conf 2017:1–7. doi:10.1115/ES2017-3590.

[8] Wang X, Dai Y. Exergoeconomic analysis of utilizing the transcritical CO_2 cycle and the ORC for a recompression supercritical CO_2 cycle waste heat recovery: A comparative study. Appl Energy 2016;170:193–207. doi:10.1016/j.apenergy.2016.02.112.

[9] Valero A, Lozano MA, Serra L, Tsatsaronis G, Pisa J, Frangopoulos C, et al. CGAM Problem: Definition and Conventional Solution. Energy 1994;19:279–86. doi:10.1016/0360-5442(94)90112-0.

Chapter 5

5 Techno-economic Analysis of Supercritical Carbon Dioxide Cycle Integrated with Coal-Fired Power Plant

Dhinesh Thanganadar[a], Faisal Asfand[a,b], Kumar Patchigolla[a], Peter Turner[a]

[a]*School of Water, Energy and Environment (SWEE), Cranfield University, Cranfield, MK43 0AL, UK*

[b]*The School of Computing and Engineering, University of Huddersfield, Huddersfield, HD1 3DH, UK*

Published in Energy Conversion Management, 2021

DOI: 10.1016/j.enconman.2021.114294

Statement of contributions of joint authorship

Dhinesh Thanganadar proposed the novelty, implemented the methods, generated all results, and prepared the manuscript draft. Faisal Asfand and Peter Turner proof-read and critically commented on the manuscript before submission. Kumar Patchigolla provided supervision, proof-read, and critically commented on the manuscript before submission.

ABSTRACT

Supercritical carbon dioxide (sCO_2) cycles can achieve higher efficiencies than an equivalent steam Rankine cycle at higher turbine inlet temperatures (>550°C) with a compact footprint (tenfold). sCO_2 cycles are low-pressure ratio cycles (~4-7), therefore recuperation is necessary, which reduces the heat-addition temperature range. Integration of sCO_2 cycles with the boiler requires careful management of low-temperature heat to achieve enable higher plant efficiency. This study analyses four novel sCO_2 cycle configurations which captures the low-

temperature heat in an efficient way and their performance is benchmarked against the state-of-the-art steam Rankine cycle. The process parameters (13-16 variables) of all the cycle configurations are optimised using a genetic algorithm for two different turbine inlet temperatures (620°C and 760°C) and their techno-economic performance are compared against the advanced ultra-supercritical steam Rankine cycle. An sCO_2 power cycle can achieve a higher efficiency than a steam Rankine cycle by about 3-4%pts, which is correspond to which corresponds to a plant level efficiency of 2-3%pts, leading to cost of electricity (COE) reduction leading to a reduction of cost of electricity (COE). Although the cycle efficiency has increased when increasing sCO_2 turbine inlet temperature from 620°C to 760°C, the COE does not notably reduce owing to the increased capital cost. A detailed sensitivity study is performed for variations in compressor and turbine isentropic efficiency, pressure drop, recuperator approach temperature and capacity factor. The Monte-Carlo analysis shows that the COE can be reduced up to 6-8% compared to steam Rankine cycle, however, the uncertainty of the sCO_2 cycle cost functions can diminish this to 0-3% at 95% percentile cumulative probability.

Keywords

Supercritical CO_2 cycle, Fossil-fired, Techno-economic, Cost of Electricity, Multi-variable optimisation

5.1 Introduction

A flexible thermal power plant has a significant role in the future energy view to maximise higher penetration of variable renewable energy generation into the grid. National Energy Technology Laboratory (NETL), USA is funding researches to develop flexible fossil-fuel power plants with the integration of thermal energy storage [1]. Supercritical carbon dioxide (sCO_2) cycles are investigated to enhance the plant performance and flexibility owing to their compact footprint [2]. Semi-closed, direct-fired sCO_2 cycles such as Allam cycles can be integrated with a coal-fired plant by adapting a commercial gasification unit. Moreover, additional technological challenges need to be addressed such as high-pressure combustor design and the corrosion and erosion issues caused by the impurities in coal and

particulates [3]. Various indirect cycle configurations have been proposed for different applications and Crespi et al. [4] had reviewed forty-two cycle configurations. Thanganadar et al. [5] has integrated five cascade cycle configurations with the bottoming cycle, and the study showed that the cascade cycles can be integrated with a sensible heat source with a larger temperature difference across the primary heat exchanger (ΔT). Conventionally, the Brayton cycles are thermodynamically compared using efficiency vs specific power curves with the objective of maximising both of them [6]. The typical cost share of the steam boiler is about 30-50% of the whole plant cost whilst the other systems including turbine, feed water heater, steam piping, cooling system covers the remaining [7]. This indicates that increasing the efficiency reduces both the fuel cost and the size of the boiler (reducing the boiler heat duty) for a given electrical power output, thus strongly reducing the cost of electricity (COE). In addition, turbomachines are volumetric devices; therefore, reducing the volumetric flow can reduce their size and cost by increasing the specific power for a given fluid. Therefore, maximising both of them also minimises the COE.

sCO_2 cycles are generally more efficient than an equivalent steam Rankine cycle when the turbine inlet temperature (TIT) is >550 °C [8]. The closed-loop sCO_2 cycle is inefficient without recuperation as the cycle pressure ratio is small (around 4-7) owing to the higher critical pressure of CO_2 73.8 bar. The effectiveness of the recuperation circuit is limited by the occurrence of a pinch point, as the isobaric specific heat of sCO_2 varies dramatically, limiting the maximum heat transfer. A Recompression cycle (RCBC) is highly efficient as it has two recuperators and the cold stream capacitance of the low temperature recuperator (LTR) is controlled by a parallel compression loop, which is analogous to direct mixing recuperation. However, the ΔT is lower (220 °C) for this cycle due to the smaller pressure ratio, leading to lower specific power. Therefore, integration of this cycle with a coal-fired power plant might not be able to cool the flue gas close to the required air preheater (APH) temperature, thereby penalising the boiler efficiency. Alternatively the ΔT of a simple recuperative cycle and partial cooling cycle is about 285 °C for a TIT of 750 °C at 300 bar [9] which makes them attractive, though the efficiency of the former cycle is lower. Miller et

al. [10] proposed a maximum APH temperature of 371 °C which is unlikely to be achieved with the standard proposed cycles, therefore, alternative cycle configurations are investigated. The partial cooling cycle has a higher ΔT with a small penalty in efficiency, therefore this cycle could offer a lower CAPEX configuration [11]. Cascade cycles can accept the heat over a large temperature range; however, the efficiency of these cycles is generally lower [12]. Therefore, these cycles are less attractive for applications where internal recycling of the hot source is possible, increasing the mean Carnot heat addition temperature, such as nuclear and CSP [12]. Sun et al. [13] proposed to integrate a bottoming cycle in the low-temperature flue gas path of a coal fired power plant and investigated five sCO_2 cycles as a bottoming cycle solution, concluding that recompression and partial cooling cycles better matches the temperature profile. Low temperature thermal management is crucial for sCO_2 cycles particularly when integrated with sensible heat sources. For instance, Mohammadi et al. [14] proposed a triple power cycle concept for a combined cycle power plant to better utilise the low-temperature heat from the flue gas. For a coal-fired plant, the flue gas has to be cooled to the maximum air preheater temperature limit in order to maximise the plant efficiency, therefore, the cascade cycles and their variants can be attractive depending on the ΔT requirement. Miller at.al. [10] showed that the theoretical maximum efficiency of cascade cycles is 27% and 32% whilst the maximum efficiency of RCBC is 34% and 34.5% when the TIT is 593 °C and 730 °C respectively. Also, despite having three primary heat exchangers as opposed to one in RCBC without low-grade heat recovery, the cost of the cascade cycle was lower than the base cycle whilst the cost of RCBC was roughly twice for a TIT of 593 °C [10]. On the other hand, the cost index of the cascade cycle increases almost in a similar manner for both cascade cycle and RCBC for a TIT of 730 °C, which implies that the cycle selection can be primarily affected by the TIT.

Qiao Zhao [15] performed a superstructure based optimisation to explore the optimal cycle configuration and concluded that the selection of compressor inlet temperature doesn't influence the optimal layout selection based on cycle efficiency whilst the TIT impacts the efficiency without notable changes in

component size, within the investigated search space. The superstructure was formulated by combining the partial cooling cycle, recompression cycle and cascade cycles and the optimal configuration to maximise efficiency favours two-stage reheating, double recompression and a preheater tapping from the main compressor outlet for low-grade heat recovery [16]. On the other hand, a lower Levelised Cost of Electricity (LCOE) solution is achieved with an intercooled single-reheat SRBC with low-grade heat management. Mercheri et.al. [17] integrated RCBC and their variants with coal-fired plant concluded that sCO_2 cycles can achieve an efficiency of about 47.8% (LHV) and single reheater offers 1.5%pts increase in efficiency whilst double reheat and double recompression increases the efficiency by 0.3 and 0.5%pts respectively. Yann Le Moullec [18] has integrated a sCO_2 cycle with and without post-combustion carbon capture (mono- ethanolamine as solvent) and showed that a net efficiency of 41.3% (LHV basis) is achievable when the CO_2 is compressed to 110 bar. Bai et.al. [19] has proposed to have three recuperators and a branching stream from the cold outlet of the second stage recuperator is supplied for the boiler low-grade thermal management, concluding that a net cycle efficiency of 49.5%LHV basis (assumed boiler efficiency of 97%) can be achievable with 296 bar and 650 °C. Park et.al. [20] analysed four sCO_2 cycles for coal-fired power plant concluding that maximum efficiency of 43.9%HHV is achieved, which is increased to 45.4%HHV by the addition of transcritical CO_2 (tCO_2) bottoming cycle. Michalski et al. [21] integrated three advanced power cycles including sCO_2 recompression cycle with calcium looping coal-fired power plant, concluding that sCO_2 cycle achieved 0.9% higher efficiency than equivalent steam Rankine cycle. Wei et al. [22] performed a techno-economic analysis of sCO_2 cycle integrated coal/biomass fired power plant with oxy-combustion, concluding that efficiency of 30.5% is achievable using coal as a fuel at a cost of 84.2 €/MWh.

Huang and Sonwane [23] has modelled a double recuperation recompression Brayton cycle and concluded that the TIT is the main driver to increase the efficiency than the turbine inlet pressure. However, increasing the cycle pressure ratio also helps increase the cycle specific power and thereby helps in reduction of CAPEX. Therefore, the optimal pressure and temperature selection is a trade-

off between thermodynamic efficiency and economic cost factors. Alfani et.al. [24] performed a multi-objective optimisation of a 100MWe recompression sCO_2 cycle integrated with the coal-fired plant to investigate the trade-off between system performance and plant flexibility concluding that the sCO_2 cycles half the response time with a 2%pts higher efficiency than conventional steam cycles. White et.al. [25] analysed the thermodynamic trend of sCO_2 integrated with the coal-fired power plant that gives insight to the component size (volumetric flow rate for turbomachinery and heat duty for heat exchangers) and efficiency as a function of cycle pressure ratio. A NETL report by White et.al. [26] analysed the techno-economic performance of indirect sCO_2 cycles using an oxy-fired circulating fluidized bed, concluding that increasing TIT from 620 °C to 760 °C increased the plant efficiency by 4.4-4.8%pts. The efficiency enhances due to the inclusion of intercooler and reheater is more pronounced at 620 °C than at 760 °C. The COE reduces with the addition of an intercooler for both 620 °C and 760 °C whilst the addition of a reheater reduces the COE at 620°C but slightly increases the COE at 760°C, mainly due to the increased high-temperature piping cost. White et.al. [27] integrated a sCO_2 cycle with a NETL baseline commercial air-fired pulverised boilers (B12A) and oxygen-fired circulating fluidized bed for a TIT of 620 °C and 760 °C. This study concluded that the efficiency increased by 5%pts compared to the NETL baseline pulverised coal power plant with an Advanced Ultra-supercritical steam Rankine cycle (AUSC), and reduced the water consumption by 22-33% owing to the reduction in sink heat duty and the elimination of boiler blowdown. A downdraft boiler is considered for AUSC to reduce the high energy nickel steam piping length between boiler and turbine, consequently reducing cost [28]. Nathan et.al. [29] integrated a sCO_2 cycle with an Oxy- circulating fluidised bed boiler and highlighted that the sCO_2 piping cost is higher than an equivalent steam cycle as the mass flow rate is higher. Therefore, increasing the cycle specific power is desired in order to reduce the power cycle component cost by reducing the recuperator heat duty and turbomachine volumetric flow rate. In most of the studies, boiler low-grade heat is managed by a branching-off stream from the sCO_2 cycle. However, other options such as increasing the pressure ratio to increase the heat addition ΔT has

seldom been investigated, even though the cycle specific power is increased [25]. In particular, partial cooling cycles are known to offer better efficiencies than a recompression cycle for a higher CIT mainly because the turbine exhaust pressure and main compressor inlet pressures are disconnected by the partial compressor in the former case, whilst they only differ by the pressure drop of the recuperators in the latter case [11,30]. Since the pressure ratio of the partial cooling cycle is higher than a recompression cycle for a given maximum pressure, partial cooling cycle performance can be less sensitive to an absolute boiler pressure drop than RCBC, which is critical for coal-fired boiler [11]. The partial cooling cycle variants are seldom investigated for coal-fired applications although the heat addition ΔT and specific power are higher compared to RCBC [9]. Secondly, in most of the above studies, the boiler isn't modelled and a fixed boiler efficiency is considered in the literature. Boiler efficiency is notably dependent on the flue gas exit temperature. For example, every 22 °C increase in the flue gas outlet temperature from the APH reduces the boiler efficiency by 1% [10,31]. Therefore, a whole plant model, which integrates both the boiler and sCO_2 power cycle, needs to be modelled and optimised to comprehend the realistic performance of sCO_2 cycles.

This paper investigates four thermodynamic cycle configurations, which are the variants of recompression, partial cooling cycle, and cascade cycle for two different TITs (620 °C and 760 °C). The steam conditions of an ultra-supercritical steam Rankine (USC) cycle are about 620 °C whilst AUSC operates around 760 °C [28][32], therefore these two operating temperatures are considered for investigation. Above 620 ^{o}C, a high-strength nickel alloy tubes are required [33] and Babcock & Wilcox has designed an AUSC boiler operating at 760 ^{o}C [28]. A detailed techno-economic analysis is performed for these cycles and the process parameters are optimised using multivariable metaheuristic procedure based on a genetic algorithm (GA) for both the TIT's (2×4 cases). The number of continuous process variables ranges from 13-16 which significantly complicates the optimisation. The cycle performances are compared against the equivalent baseline NETL steam Rankine cases to benchmark the performance improvements. In order to quantify the risk of developing sCO_2 cycles, a Monte

Carlo analysis is performed to assess the cumulative probability distribution of COE due to the uncertainty associated with the cost function of sCO_2 technology. Finally, a sensitivity study is performed for changes in the turbomachinery efficiency, LTR approach temperature, primary heat exchanger pressure drops, and capacity factor.

5.2 sCO_2 Cycle Configurations

Four novel sCO_2 cycle configurations were developed in this study by combining the features of recompression (RCBC), partial cooling (PCC) and cascade cycles. Case1 and 2 were developed by integrating a partial cooling cycle with a cascade cycle and the difference between them is the number of recuperators and economiser, i.e., Case 1 has two recuperator/economiser whereas Case 2 contains three. Case 3 and Case4 integrates a recompression cycle with a cascade cycle and the number of recuperators/economisers are two for the former case and three for the latter case.

5.2.1 Cycles derived from PCC (Case 1 and 2)

Figure 5-1 shows Case 1 configuration which combines partial cooling cycle with a cascade cycle (Cascade Cycle 3 [5]) with a two-stage intercooler and single-stage reheater. The selection of a single reheat and two-stage intercooler is according to White et al. [27]. The main heater (MH) and the reheater (RH) are located in parallel to the flue gas stream so that the flow fraction can be optimised, thereby enable the functionality of adding/removing the reheater into the process. The turbine outlet of HT2 is in the supercritical vapour phase as opposed to the supercritical state in Case 3 and Case 4.

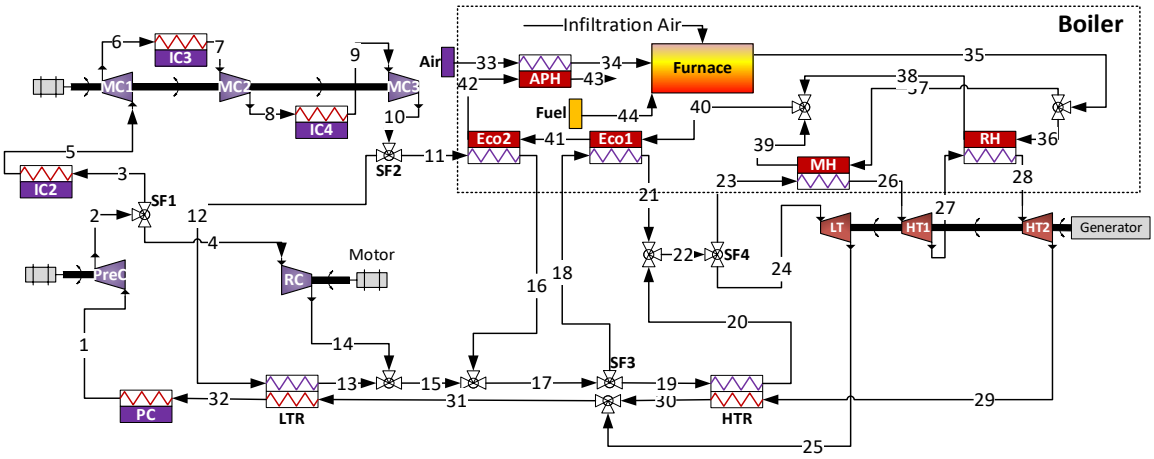

Figure 5-1 Partial cooling and cascade integrated cycle with two recuperators- Process Configuration of Case 1

The expanded sCO_2 from the 2nd stage turbine (HT2) is passed through two-stages of recuperation i.e., HTR and LTR respectively. The hot stream outlet of the LTR is partially cooled in a precooler, then compressed above the critical pressure using a pre-compressor (PreC). A fraction of the outlet stream is compressed using a recompressor and connects downstream of the LTR whereas the remaining flow is cooled at the intercooler and compressed using two-stage intercooler main compressors. A fraction of the flow downstream of the main compressor is passed through the LTR, whilst the remaining passes through the economiser#2 (Eco2). The LTR cold stream outlet is mixed with the recompressor outlet, followed by mixing with the Eco2 outlet stream, and part of the flow is split to the economiser #1 (Eco1), whilst the remaining flow goes through the HTR. The outlet of the HTR and Eco1 are mixed and a fraction of the flow is passed through a low temperature (LT) turbine while the remaining flow passes thought he main heater, then partially expanded in the 1st HT turbine (HT1), followed by the RH and a 2nd stage expansion in HT2. Figure 5-2 shows the typical T-Q diagram of Case 1, where the temperature matching between the cold and hot streams can be compared, inferring the exergy destruction. The temperature discontinuities in the T-Q diagram are due to the temperature drop caused by the stream mixer.

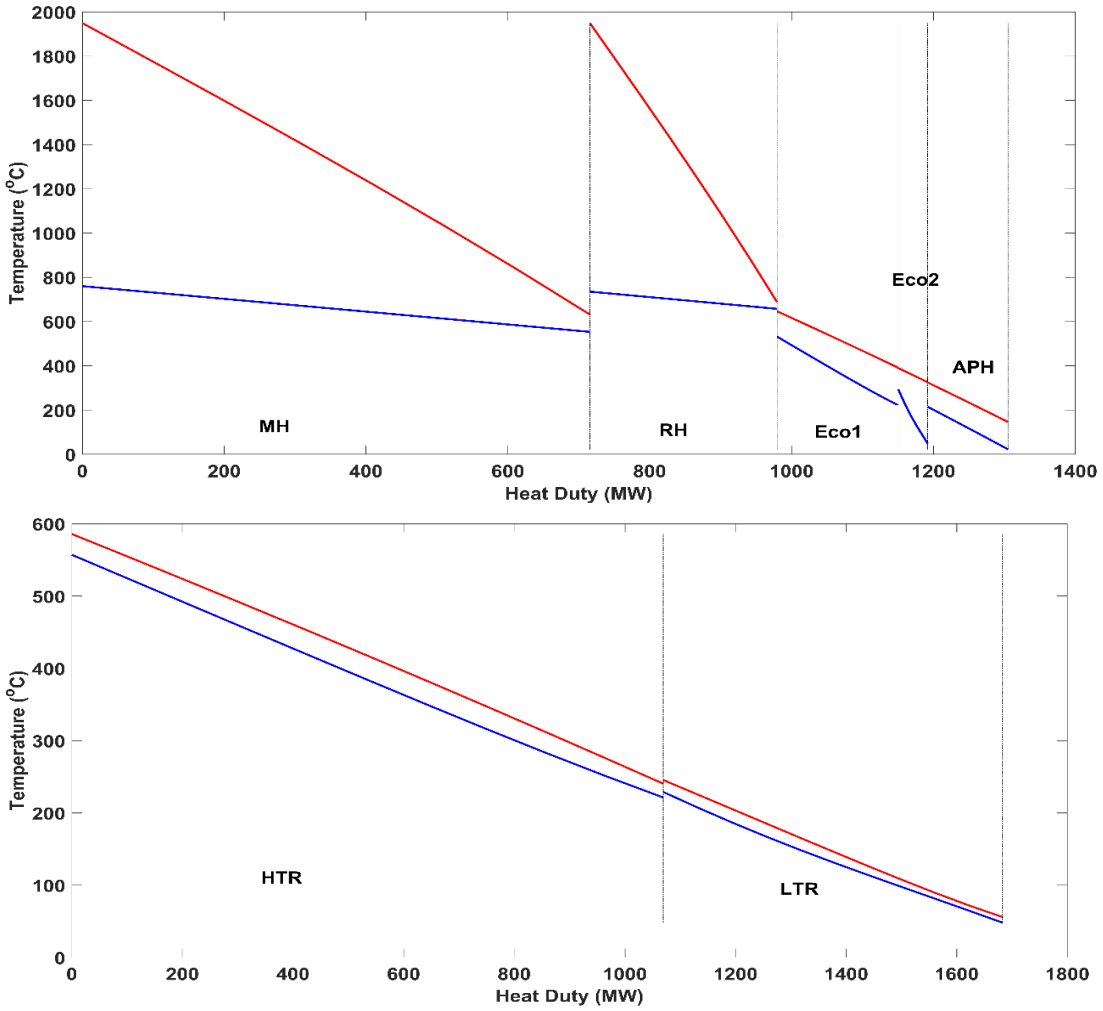

Figure 5-2 Temperature-Enthalpy (T-Q) diagram of Case 1, Top) primary heat exchanger train bottom) recuperator train

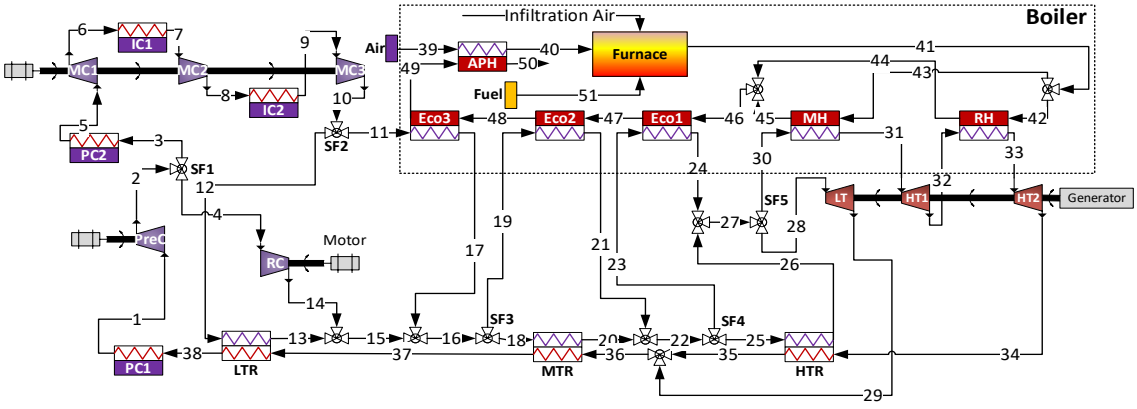

Figure 5-3 Partial cooling and cascade integrated cycle with three recuperators-Process Configuration of Case 2

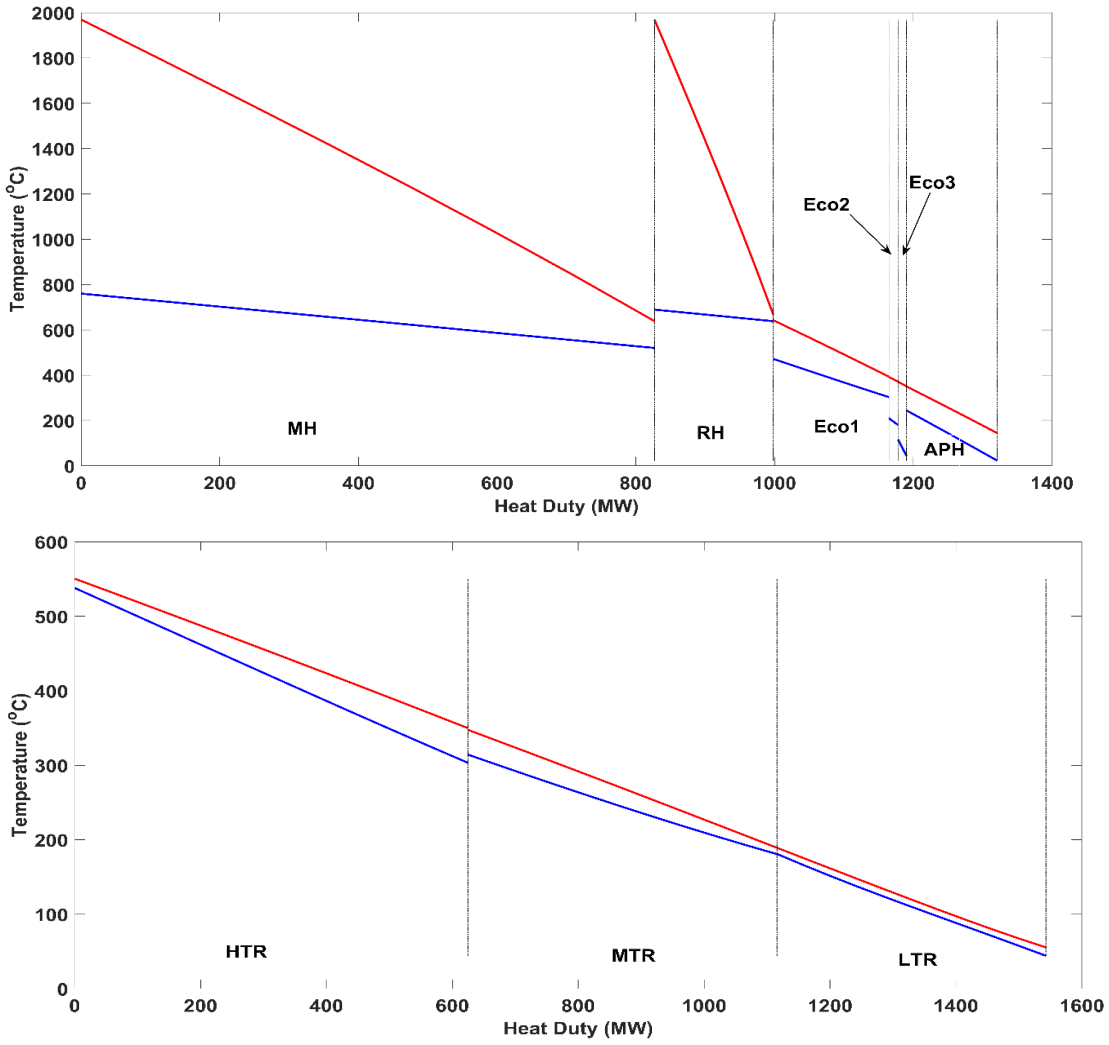

Figure 5-4 Temperature-Enthalpy (T-Q) diagram of Case 2, Top) primary heat exchanger train bottom) recuperator train

Figure 5-3 shows the configuration of Case 2 that has three recuperators and economisers as opposed to two in Case 1. This cycle is developed for two reasons, 1) to provide an additional degree of freedom which facilitates the better matching of the T-Q profile in the recuperator and primary heat exchanger, reducing the exergy destruction 2) to reduce the heat load of the HTR, which uses an expensive material when the maximum temperature goes over 550 °C, so that the cost of recuperators can be lowered. It should be noted that the former tends to reduce the log-mean temperature driving force, resulting in an increase of conductance, thus the surface area for a given heat duty, therefore a trade-off is required. Figure 5-4 shows the typical T-Q diagram of Case 2.

5.2.2 Cycles Derived from RCBC (Case 3 and 4)

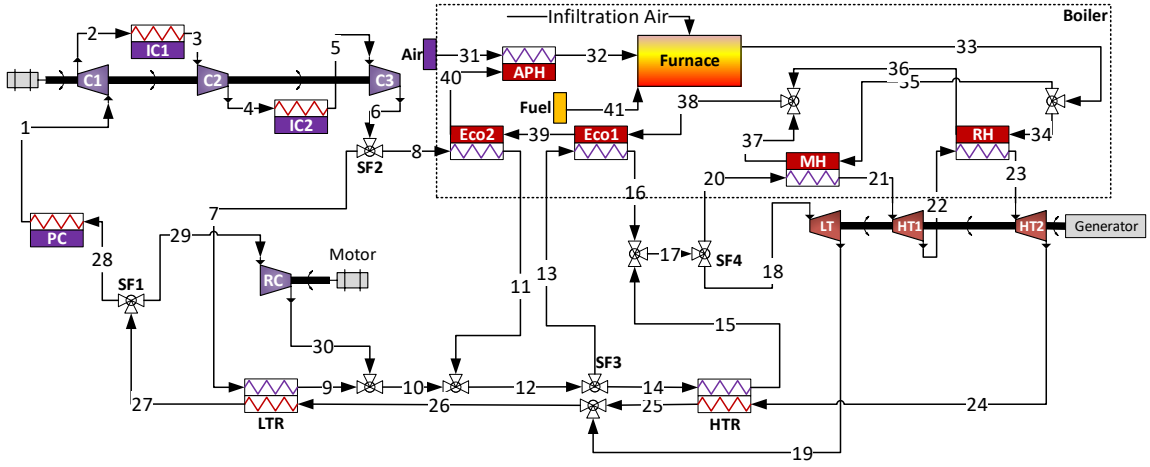

Figure 5-5 Recompression and cascade integrated cycle with two recuperators-Process Configuration of Case 3

The recuperator and boiler side components of cycle 3; similar to Case 1 and the only difference is on the heat rejection and compression side components. The cycle configuration 3 combines the features of RCBC and cascade cycles with the two-stage intercooler compressor and single-stage reheater (Figure 5-5). Removing the low temperature turbine (LT) changes this configuration close to the alternative configuration studied in White et al. [27]. The expanded sCO_2 from the 2nd stage turbine (HT2) is passed through two-stages of recuperation i.e., HTR and LTR respectively, then part of the sCO_2 flow is diverted through a recompressor (RC) which connects to the LTR cold outlet, bypassing the LTR cold stream. The remaining flow is passed through the precooler (PC), then it is compressed in a two-stage intercooler compressor and part of the flow is passed through the LTR, whilst the remaining passes through economiser#2 (Eco2). The LTR cold stream outlet is mixed with the recompressor outlet followed by mixing with the Eco2 outlet stream, and part of the flow is split to the economiser #1 (Eco1), whilst the remaining flow goes through the HTR. The remaining process on the high temperature side is similar to Case 1. The temperature-heat duty (T-

Q) diagram of the low temperature recuperator (LTR), high temperature recuperator (HTR) and boiler heaters are shown in Figure 5-6.

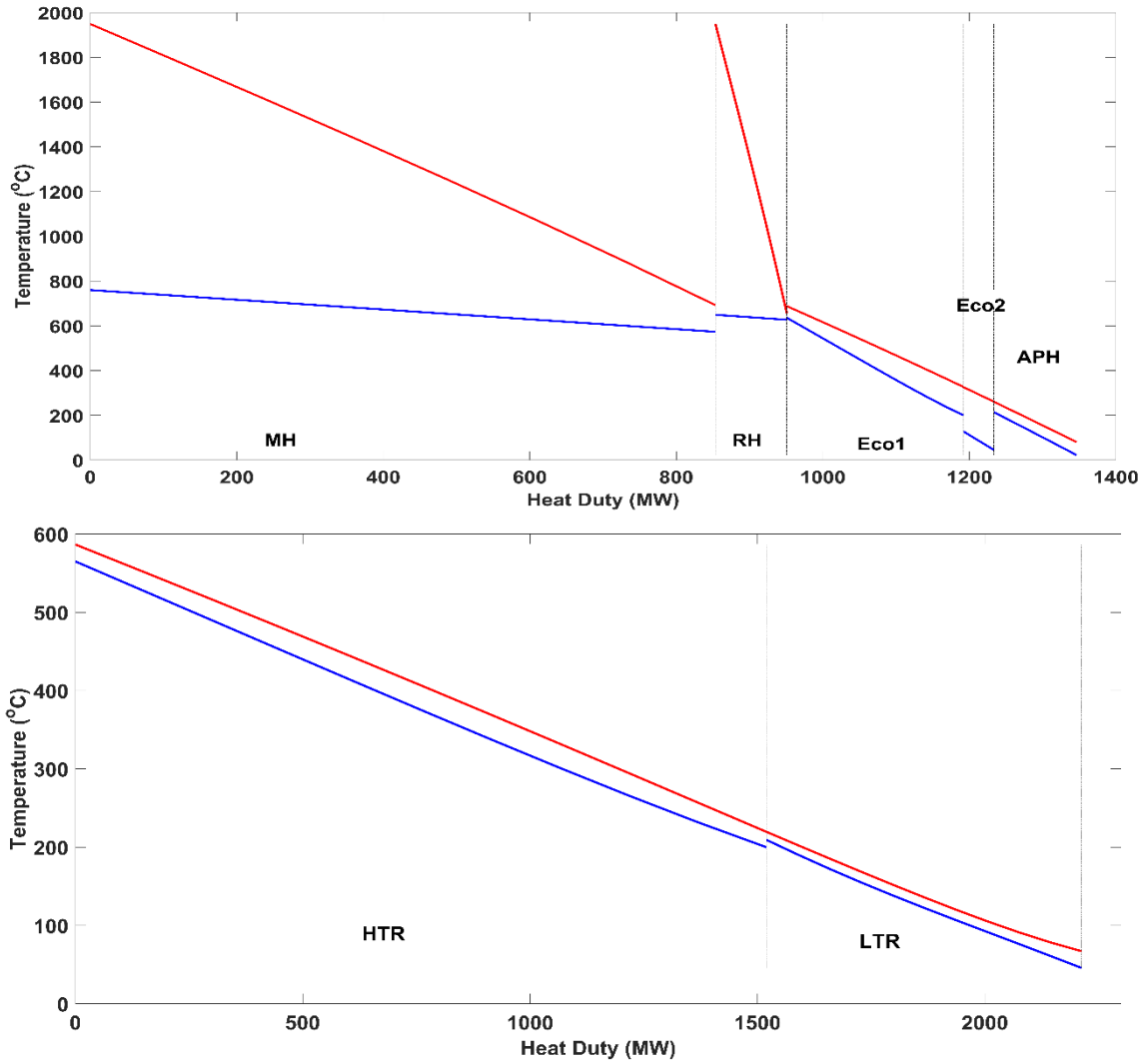

Figure 5-6 Temperature-Enthalpy (T-Q) diagram of Case 3, Top) primary heat exchanger train bottom) recuperator train

Figure 5-7 shows the cycle configuration 4 (Case 4) is derived from cycle 3 by adding an additional medium temperature recuperator (MTR) and economiser #3 (Eco3). For the sake of completeness, the T-Q diagram of cycle 4 is shown in Figure 5-8.

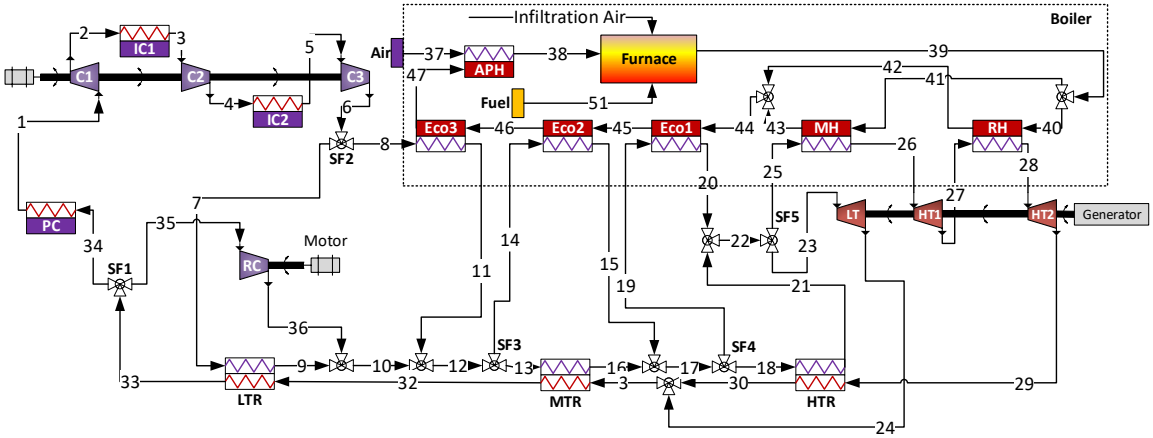

Figure 5-7 Recompression and cascade integrated cycle with three recuperators- Process Configuration of Case **4**

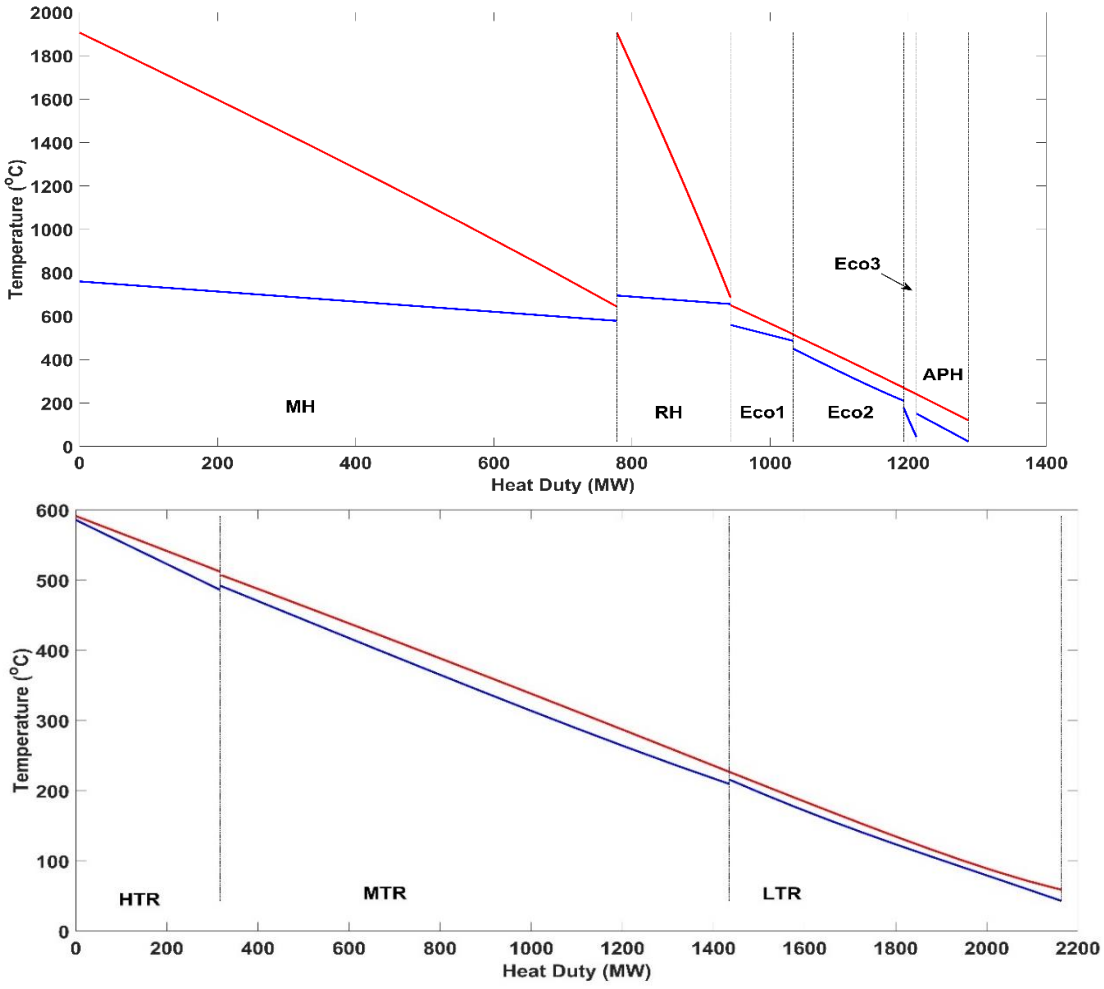

Figure 5-8 Temperature-Enthalpy (T-Q) diagram of Case 4, Top) primary heat exchanger train bottom) recuperator train

5.3 Thermodynamic Modelling

An in-house code has been developed in MATLAB® for all the process components such as compressor/ pump, turbine, heat exchanger (one-dimensional), valve, splitter and mixer. The plant-level code sequentially solves the component models in a flexible way, which allows modelling any plant configuration in a robust manner. For a simulation of the closed-loop cycles or recycle streams, the plant solver guesses the tear stream values and converges the solution within the predefined tolerance using a non-linear iterative solver, which is the Newton-Raphson iterative method and Broyden algorithm for calculation of the Jacobian matrix. The thermal physical properties of sCO_2 are calculated using the REFPROP library [34], which uses an iterative routine minimising Helmholtz free energy. The number and the location of the tear streams changes depending on the process configurations.

Since this work adapts the NETL base case steam boiler (B12A) to a sCO_2 based cycle, the fuel input and the air mass flow are fixed as the same as B12A. The ultimate analysis of the Illinois No.6 coal is shown in Table 5-1. The coal flow is 49.8 kg/s and the primary airflow, secondary airflow and the infiltration airflow are 121.7 kg/s, 396.1 kg/s and 8.7 kg/s respectively [35]. B12A base case uses hydrated lime injection for SO_3 control and is located upstream of the air preheater, allowing the APH flue gas outlet temperature to 143 °C. Since the fuel flow and airflow were maintained the same as B12A the capacity and cost of the sorbent handling system is the same as the base case.

Table 5-1 Coal Specification (Illinois No.6 coal)

Parameter	Unit	Value
High Heating Value (HHV)	kJ/kg	27,113
Low Heating Value (LHV)	kJ/kg	26,151
Ultimate Analysis		
Moisture	weight%	11.12

Carbon	weight%	63.75
Hydrogen	weight%	4.5
Nitrogen	weight%	1.25
Chlorine	weight%	0.29
Sulfur	weight%	2.51
Ash	weight%	9.7
Oxygen	weight%	6.88

Steady-state mass and energy conservations are applied to all the components to calculate their outlet state properties from the inlet conditions. The recuperators are modelled based on effectiveness while the cooler and the primary heater are modelled based on the outlet temperature set points.

The sCO_2 turbomachinery is simulated as a zero-dimensional model based on their isentropic efficiencies (η_{isen}) The outlet enthalpy (h_{out}) of the turbine is calculated using Eq. (5-1) and the compressor is calculated using Eq. (5-2), where h_{2s} is a function of outlet pressure (P_{out}) and inlet entropy (s_{in}).

$$h_{out,turb} = h_{in,turb} - (h_{in,turb} - h_{2s,turb}) \times \eta_{isen,turb} \quad (5\text{-}1)$$

$$h_{out,comp} = h_{in,comp} + \frac{h_{2s,comp} - h_{in,comp}}{\eta_{isen,comp}} \quad (5\text{-}2)$$

The heat exchanger is a one-dimensional code in order to capture the nonlinear property variation of sCO_2 along the length of the heat exchanger (10 zones). The number of zones is selected based on an initial set of simulations that captures the nonlinear property variation across the length of the heat exchanger with the computational speed. The heat exchanger function sizes the heat exchanger based on effectiveness (ϵ) using Eq. (5-3) or specifying the outlet temperature of either the hot or cold stream.

$$\epsilon = \frac{\dot{Q}}{\dot{Q}_{max}} \quad (5\text{-}3)$$

The actual amount of heat transfer (Q) is calculated from the given input of effectiveness and calculated $\dot{Q}_{max}$. The $\dot{Q}_{max}$ is calculated based on Eq. (5-4).

$$\dot{Q}_{max} = \min(C_{cold}, C_{hot}) \times (T_{h,in} - T_{c,in}) \quad (5\text{-}4)$$

The capacitance rate of the cold stream ($C_{cold}\ in \frac{W}{K}$) is calculated based on Eq. (5-5) and a similar equation can also be applied to calculate the hot stream capacitance rate (C_{hot}).

$$C_{cold} = m_{cold} \times \frac{h_{c,in} - h_{c,out,max}}{T_{c,in} - T_{c,out,max}} \quad (5\text{-}5)$$

where the $h_{c,out,max} = f(P_{c,out}, T_{c,out,max})$ and $T_{c,out,max} = T_{h,in}$

The conductance (UA) is calculated for all the heat exchanger zones using the NTU method [36] and the total conductance is the sum of the conductance of all the zones. The heat duty of the heat exchanger is reduced if the minimum pinch temperature constraint is violated within the heat exchanger or any temperature crossover is detected.

5.3.1 Modelling Assumptions

Thermodynamic modelling assumptions are listed in Table 5-2. All the cycle configurations are simulated for two sets of turbine inlet temperatures (TITs), i.e., 620 °C and 760 °C. All the cycle minimum, maximum and intercooler pressures, economiser cold outlet temperatures, sCO_2 mass flow rate and the split fractions are optimised to maximise the objective function i.e., net efficiency. The cycle minimum pressure, intercooler pressure, split fractions, sCO_2 mass flow rate, economiser cold outlet temperatures and reheater cold inlet pressure were optimised to maximise the efficiency.

Table 5-2 Thermodynamic modelling assumptions

Description	Unit	Value
Turbine isentropic efficiency [27]	%	92.7
Main compressor isentropic efficiency [27]	%	85
Recompressor isentropic efficiency [27]	%	85

Pre-compressor isentropic efficiency	%	85
Recuperator Effectiveness	%	95
Recuperator minimum pinch [27]	°C	5.6
High Pressure (Main Compressor Outlet)	bar	350
Precooler/intercooler outlet temperature	°C	32
Turbine Inlet Temperature	°C	620,760 (Varied)
Boiler minimum pinch temperature	°C	30
Economiser minimum pinch temperature	°C	30
Ljungström APH minimum pinch temperature	°C	30
Maximum flue gas temperature to APH [35]	°C	143
Minimum flue gas outlet temperature from APH [10]	°C	371
Pre-cooler approach temperature [37]	°C	15
Intercooler approach temperature [37]	°C	15
Cold side pressure drop of Precooler	%	1
Hot side pressure drop of Precooler	%	0.8
Cold side pressure drop of intercooler	%	1
Hot side pressure drop of intercooler	%	0.1
Cold side pressure drop of Primary Heat Exchanger	%	1
Hot side pressure drop of Primary Heat Exchanger	%	1
Cold side pressure drop of economiser	%	0.3
Hot side pressure drop of economiser	%	0.3
Cold side pressure drop of Recuperator	%	0.3
Hot side pressure drop of Recuperator	%	0.8
Generator efficiency [35]	%	98.5

Table 5-3 shows the auxiliary power breakdown considered and the cooling water pump, cooling tower fan power is scaled as a function of both precooler and intercoolers duty. Since the thermal input to the boiler is maintained as the same as the NETL B12A base case [35], the auxiliary power related to fuel/ash handling and flue gas treatment systems isn't affected whereas the transformer losses are scaled as a function of the generator gross power output.

Table 5-3 Auxiliary Power Breakdown ***[35]***

System	Unit	Value	Scaling
Coal Handling and Conveying	kW_e	430	Thermal Input (B12A)
Pulverizers	kW_e	2,690	
Sorbent Handling & Reagent Preparation	kW_e	850	
Ash Handling	kW_e	620	
Primary Air Fans	kW_e	1,330	
Forced Draft Fans	kW_e	1,700	
Induced Draft Fans	kW_e	6,660	
Selective Catalytic Reduction (SCR)	kW_e	40	
Activated Carbon Injection	kW_e	22	
Dry sorbent Injection	kW_e	86	
Baghouse	kW_e	90	
Wet Flue Gas Desulphurisation (FGD)	kW_e	2,830	
Miscellaneous Balance of Plant	kW_e	2,000	Constant
Steam Turbine Auxiliaries	kW_e	400	
Condensate Pumps	kW_e	800	
Ground Water Pumps	kW_e	460	
Circulating Water Pumps	kW_e	4,520	Condenser Duty
Cooling Tower Fans	kW_e	2,340	
Transformer Losses	kW_e	1,820	Gross Power

5.3.2 Economic Modelling

The COE is calculated by using Eq. (5-6) and Eq. (5-7), where CCF is the capital charge factor using a value of 0.102 [35], and a capacity factor (CF) of 85%.

$$COE = \frac{capital\ charge + \ fixed\ operating\ cost + variable\ operating\ cost}{annual\ net\ energy\ generated} \quad (5\text{-}6)$$

$$COE = \frac{CCF * TASC + \ OC_{fixed} + CF \times OC_{variable}}{CF \times MWh} \quad (5\text{-}7)$$

The total as spent capital (TASC), also known as CAPEX, is calculated using Eq.(5-8) where the TASC multiplier is taken as 1.134 [38].

$$TASC = TASC\ Multiplier \times TOC \quad (5\text{-}8)$$

The total overnight cost (TOC) is calculated using Eq. (5-9). Since the TOC is calculated at the base year, TASC expressed in mixed- year current dollars, spread over the capital expenditure period.

$$TOC = Owners\ Cost + TPC \quad (5\text{-}9)$$

The owner's cost is calculated using the same breakdown provided in the NETL steam cycle baseline report [35] so that the cycles can be compared.

The total plant cost (TPC) is calculated by using Eq. (5-10),

$$TPC = BEC + Contingencies + H.O.Fee \quad (5\text{-}10)$$

The home office (H.O.) fee is assumed as 10% of the bare erected cost (BEC) [35], and a 15% of the BEC is considered as the project contingency [35]. The process contingency is neglected to be in line with the cost estimation of the NETL base case B12A.

The BEC includes the equipment, material and both the direct and indirect labour costs. Since fuel supply to the boiler is fixed as same as base case (B12A) value, the cost of fuel handling, ash handling and another subsystem cost are constant. On the other hand, the size and the cost of the cooling water system, boiler and the turbine building cost change for different configurations. The scaling method is applied to the NETL base cost structure to account the cost variation for the changes in the reference parameter as shown in Eq. (5-11). Table 5-4 shows the scaling parameter, reference parameter, cost reference and the exponent used [39,40].

$$cost_{scaled} = cost_{reference}\left(\frac{scaling\ parameter}{reference\ parameter}\right)^{exponent} \quad (5\text{-}11)$$

Table 5-4 Bare Erected Cost (BEC) functions and scaling method for sCO_2 cycle ***[35,39]***

Item No.	Description	Reference Cost for 620°C (k$) [35]	Scaling Parameter [39]	Scaling exponent [39]	Reference Value	Unit
1	**Coal & Sorbent Handling**	45,397	Fixed		NA	
2	**Coal & Sorbent Prep & Feed**	21,531	Fixed			
3	**Feedwater & Miscellaneous BOP Systems**					
3.1	Feedwater System	36,316	NA		NA	
3.2	Water Makeup & Pre-treating	9,079	Fixed			
3.3	Other Feedwater Subsystems	12,184	NA			
3.4	Service Water Systems	2,104	Fixed			
3.5	Other Boiler Plant Systems	20,387	NA			
3.6	FO Supply Sys & Nat Gas	897	Fixed			
3.7	Waste Treatment Equipment	7,145	Fixed			
3.8	Misc. Equip. (Cranes, Air Comp., Comm	5,532	Fixed			
4	**Boiler & Accessories**	Calculated from Power cycle (Table 5-5)				
5A	**Gas Clean-up & Piping**	167,272	Fixed		NA	
7	**Duct work & Stack**	45,629	Fixed			
8	**sCO_2 Power Cycle**					
8.1, 8.2, 8.3	Power block components: compressors, recuperator, coolers, turbines, Auxiliaries	Calculated from power cycle (Table 5-5)				
8.4	sCO_2 Piping [26]	90,132	mass flow rate	0.7	3,674	kg/s
8.5	TG Foundations [26]	6,156	Gross power	0.71	685,265	kW
9	**Cooling Water System**					
9.1	Cooling tower	16,814	Cooling duty	0.74	609,002	kW
9.2	Circulating water pump	2,732	Cooling duty	0.73	609,002	kW
9.3	Circ. Water System Auxiliaries	803	Cooling duty	0.63	609,002	kW
9.4	Circ. Water Piping	11,906	Cooling duty	0.63	609,002	kW
9.5	Make-up Water System	1,526	Fixed	-	-	NA
9.6	Component Cooling Water Sys.	1,068	Cooling duty	0.63	609,002	kW

9.7	Circ. Water Foundations & Structures	9,187	Cooling duty	0.58	609,002	kW
10	**Ash & Spent Sorbent Handling Systems**	16,778	Fixed	-		NA
11	**Accessory Electric Plant**					
11.1	Generator Equipment	2,664	Gross power	0.57	685,265	kW
11.2	Station Service Equipment	5,184	Auxiliary Power	0.43	29,688	kW
11.3	Switchgear & Motor	5,352	Auxiliary Power	0.43	29,688	kW
11.4	Control Conduit & Cable Tray	13,831	Auxiliary Power	0.43	29,688	kW
11.5	Wire & Cable	17,352	Auxiliary Power	0.43	29,688	kW
11.6	Protective Equipment	1,658	Fixed	NA	NA	NA
11.7	Standby Equipment	1,854	Gross power	0.46	685,265	kW
11.8	Main Power Transformers	12,163	Gross power	0.46	685,265	kW
11.9	Electrical Foundations	1,678	Gross power	0.69	685,265	kW
12	**Instrumentation & Control**	26,316	Auxiliary Power	0.13	29,688	kW
13	**Improvements to Site**	16,394	Bare Erected Cost	0.2	1,030,996	k$
14	**Buildings & Structures**					
14.1	Boiler Building	23,566	Bare Erected Cost	0.09	1,030,996	k$
14.2	Turbine Building	34,597	Bare Erected Cost	0.12	1,030,996	k$
14.3	Administration Building	1,827	Bare Erected Cost	0.1	1,030,996	k$
14.4	Circulation Water Pump house	457	Gross power	0.6	609,002	kW
14.5	Water Treatment Buildings	1,576	Fixed		NA	
14.6	Warehouse	993	Bare Erected Cost	0.1	1,030,996	
14.7	Machine Shop	806	Bare Erected Cost	0.1	1,030,996	
14.8	Other Buildings & Structures	609	Bare Erected Cost	0.1	1,030,996	
14.9	Waste Treating Building & Str.	2,540	Fixed		NA	

The cost functions of the sCO_2 power block components are listed in Table 5-5 , where the temperature correction factor, material and labour cost are also shown [41–43]. The estimation of the high-temperature sCO_2 piping and foundation are scaled from the sCO_2 cycle NETL report [26]. Since the piping material and

turbine foundation cost changes with temperature, the reference cost, reference parameter values changes for the two TITs considered. The fuel price of 2.94 $/MMBTU is considered and the fixed and variable operation and maintenance (O&M) costs breakdowns are estimated using the procedure given in the NETL baseline report [35].

Table 5-5 sCO_2 cycle cost functions ***[42,43]***

Component	Cost Function ($)	Scaling Factor (-)	Installation Cost Percentage (%)	
			Material	Labour
Compressor	$1{,}230{,}000 \times P^{0.3992}$	NA	8	12
Turbine	$182{,}600 \times P^{0.5561} \times f$	$f = \begin{cases} 1, & T < 550 \\ 1 + 1.106e^{-4}(T-550)^2, & T \geq 550 \end{cases}$	8	12
Recuperators	$49.45 \times UA^{0.7544} \times f$	$f = \begin{cases} 1, & T < 550 \\ 1 + 0.02141(T-550), & T \geq 550 \end{cases}$	2	3
Precooler/Inter cooler	$32.88 \times UA^{0.75}$	NA	8	12
Primary Heat Exchanger	$820{,}800 \times Q^{0.7327} \times f$	$f = \begin{cases} 1, & T < 550 \\ 1 + 5.3e^{-6}(T-550)^2, & T \geq 550 \end{cases}$	50	

5.4 Metaheuristic Optimisation

A single-objective optimisation was performed to explore the maximum thermal performance for changes in the boundary conditions. Genetic algorithm (GA) is used which maximises the plant net efficiency ($\eta_{boiler} \times \eta_{cycle}$) by optimising the power cycle process variables including pressure(s), mass flow rate, economiser outlet temperatures, and split fractions. Table 5-6 shows the optimisation parameters and their ranges used for each of the four sCO_2 cycles, obtained from a set of initial runs. The minimum/maximum bounds were adjusted if a variable reached close to their bounds at the optimal solution. The process flow models are integrated with GA in MATLAB® to perform the optimisation study and the structure of the code is shown in Figure 5-9. The number of population and the number of generations are selected between 15-20 times the numbers of variables to ensure global convergence.

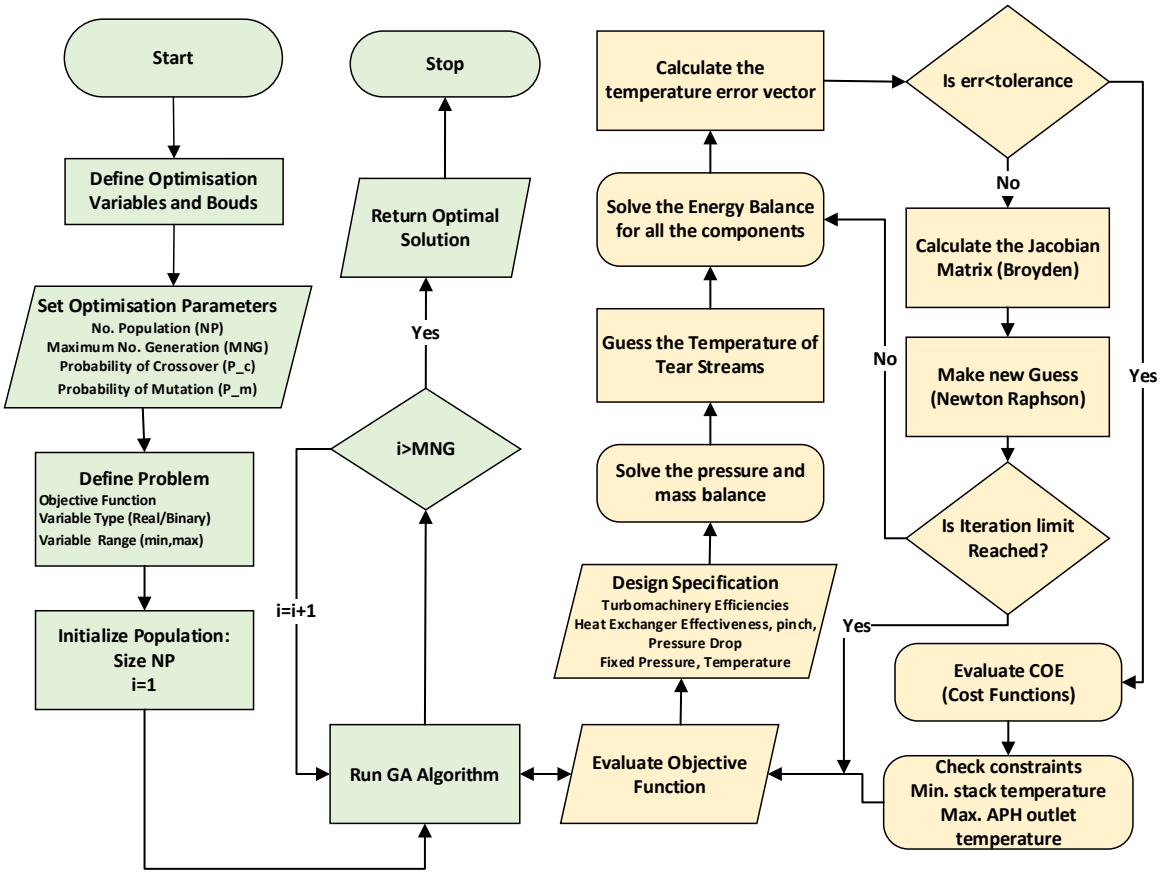

Figure 5-9 GA Algorithm flowchart used in this study

Two constraints are considered in the optimisation 1) the maximum flue gas inlet temperature to APH is 371 °C (commercial availability [10]), 2) the minimum flue gas outlet temperature of APH is 142.8 °C (same as B12A base case [35]). The components are modelled in a flexible way to handle a wide range of inputs. For instance, the optimisation algorithm can set a compressor outlet pressure lower than its inlet pressure in which case the compressor acts as a pressure-reducing valve and the outlet temperature are calculated using the isenthalpic process. Similarly, if the cold outlet temperature of an economiser set by GA is lower than its cold inlet temperature or the hot inlet temperature is lower than the cold inlet temperature plus the minimum pinch, then the economiser will be bypassed and the pressure drop is set to zero. In this way, the thermodynamic process code is flexible to handle a wide range of search space without it failing.

Table 5-6 Variable ranges of parameters considered in optimisation

Parameter	Unit	PCC		RCBC	
		Minimum bound	Maximum bound	Minimum bound	Maximum bound
Pre-compressor Inlet Pressure	bar	50	60	NA	NA
1st stage maincompressor Inlet Pressure	bar	75	100	75	90
2nd stage maincompressor Inlet Pressure	bar	120	175	120	175
3rd stage maincompressor Inlet Pressure	bar	175	250	175	250
HT turbine#1 outlet pressure	bar	120	175	120	175
Economiser#1 cold outlet temperature	°C	300	550	300	650
Economiser#2 cold outlet temperature	°C	100	350	100	450
Economiser#3 cold outlet temperature	°C	100	300	100	350
APH cold outlet temperature	°C	25	370	25	370
Flow split to recompressor	-	0	0.5	0	0.5
Flow split to economiser#1	-	0	0.4	0	0.4
Flow split to economiser#2	-	0	0.6	0	0.6
Flow split to economiser#3	-	0	0.2	0	0.2
Flow split to LT turbine	-	0	0.3	0	0.3
Flue gas flow split to reheater	-	0	0.5	0	0.5
sCO_2 mass flow rate at the inlet of main compressor	kg/s	1600	3000	1600	3000

5.5 Comparison with Literature

Moisseytsev and Sienicki [44] reference cycle condition is used for comparison which shows the design data of 96MW_e sodium-cooled fast reactors. The sCO_2 cycle configuration is a recompression cycle with a TIT of 471.8 °C is modelled in MATLAB. Although the turbine and compressor isentropic efficiencies weren't

reported, they have been back calculated from the outlet temperature values stated. These resulted in efficiencies of 93.3%, 90.7% and 93.5% for the main compressor, recompressor and turbine respectively. Generator efficiency of 98.5% and a mechanical loss of 1% are considered for both the turbine and compressors. The state temperature differences are matching with the literature reported values with the maximum relative percentage error of 0.2% as shown in Table 5-7. The state points number follows Figure 6-1.

Table 5-7 Benchmark of the supercritical recompression CO_2 cycle stream data with Moisseytsev and Sienicki ***[44]***

State	Temperature (°C)			State	Temperature (°C)		
	Literature [44]	**This Study**	**Relative Error (%)**		**Literature** [44]	**This Study**	**Relative Error (%)**
1	32.79	32.79	-0.0	**7**	362.30	362.27	0.0
2	84.40	84.40	-0.0	**8**	190.70	190.88	-0.1
3	171.80	171.84	-0.0	**9**	90.20	90.41	-0.2
4	175.20	175.33	-0.1	**10**	90.20	90.41	-0.2
5	323.30	323.30	0.0	**11**	90.20	90.41	-0.2
6	471.80	471.80	0.0	**12**	183.80	184.04	-0.1

5.6 Results and Discussion

5.6.1 Thermal Performance Comparison

All the four cases are optimised for two different turbine inlet temperatures (TITs), i.e., 620 °C and 760 °C. In order to distinguish both the simulation results, a suffix “a” is added for 620 °C results and “b” is added for 760 °C results. For instance, Case1a refers to the simulation results of Case1 for a TIT of 620 °C whereas Case1b refers a TIT of 760 °C.

The thermodynamic performance of all the four cases for a TIT of 620 °C and 760 °C is shown in Table 5-8. Since the amount of fuel supplied is kept the same as the steam Rankine base case (B12A), maximising the plant net efficiency also maximises the net power output. The maximum sCO_2 power cycle efficiency

($\eta_{cycle} = \frac{Net\ Power}{Heat\ input_{cycle}}$) cycle achieved for a TIT of 620 °C is 49.3% (Case 2a), which is increased to 53% (Case 1b) when the TIT increased to 760 °C. This is equivalent to an increase of about 3.5-3.6%pts higher than the equivalent steam Rankine cycle. The maximum plant net efficiency on HHV basis ($\eta_{boiler} \times \eta_{cycle} = \frac{Net\ Power}{Fuel\ mass\ flow \times High\ Heating\ Value}$) is 43.5% and 46.9% (Cases 1a and 1b), which corresponds to an increase of 3.4%pts over the steam Rankine cycle. This implies increasing the TIT can aid in reducing the COE if the benefits due to the increased efficiency are not compensated by the increased capital cost owing to the use of high-temperature alloy materials. Inclusion of a third recuperator (Case 2 and Case 4) does not notably increase the efficiency, therefore this may not be economically justified over Case 1 and Case 3 respectively. Cycles derived from the partial cooling cycle (Case 1 and 2) offered a similar level of efficiency as the cycles derived from a recompression cycle for both the TITs studied.

Table 5-8 Thermodynamic performance summary table

Parameters	**Unit**	**Steam**	**Partial Cooling Cycle (PCC)**		**Recompression Cycle (RCBC)**	
		B12A	**Case 1a**	**Case 2a**	**Case 3a**	**Case 4a**
TIT=620°C						
Net Power	MW	550.0	586.9	587.3	586.6	587.5
Power cycle efficiency	%	45.7	49.1	49.3	48.8	48.9
Plant Efficiency	%	40.7	43.5	43.5	43.4	43.5
TIT=760°C						
		AUSC	**Case 1b**	**Case 2b**	**Case 3b**	**Case 4b**
Net Power	MW	550.3	633.0	629.8	627.8	632.2
Power cycle efficiency	%	49.5	53.0	52.6	52.4	52.8
Plant Efficiency	%	44.1	46.9	46.6	46.5	46.8

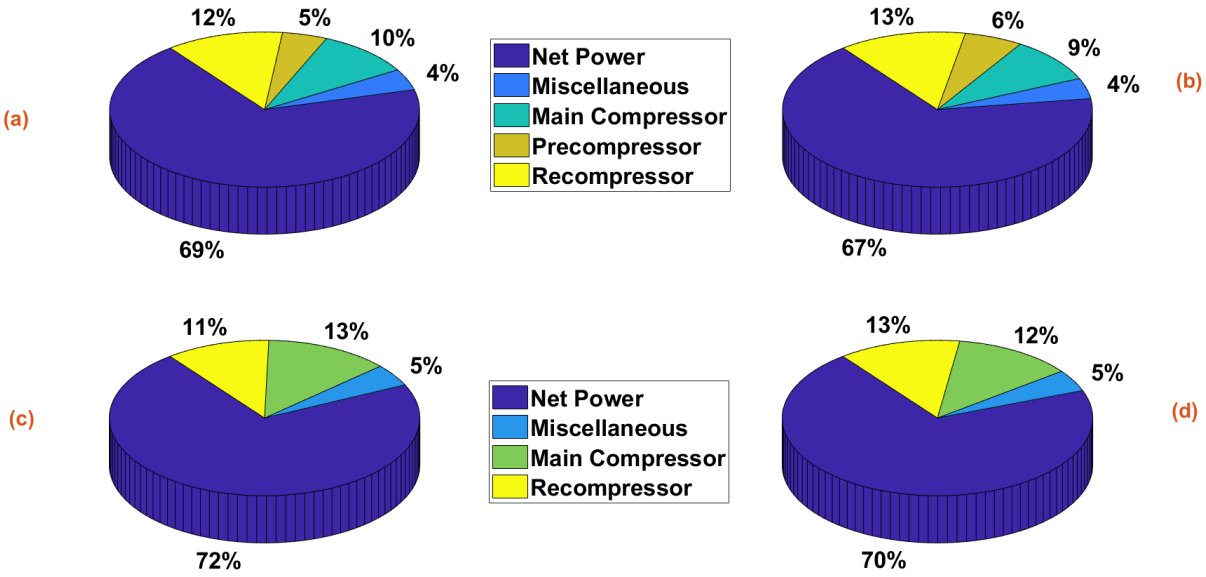

Figure 5-10 Turbine power breakdown for a TIT of 620°C, a) Case 1a, b) Case 2a, c) Case 3a, d) Case 4a

The flue gas exit temperature notably influences boiler efficiency. It should be noted that the maximum plant efficiency reported by White et al. [38] is 49.5%HHV, which is higher than value obtained in this study. The reason is that the flue gas exit temperature is constrained to 142.8 °C in this work in order to be in line with the steam base case (B12A). However, White et al. [38] considered a minimum flue gas temperature of 50 °C by implementing in-bed sulphur capture using circulating fluidised bed combustion, which helped to increase the boiler efficiency from ~89% to 92.9%. This clearly shows that changing the boiler from pulverised coal-fired with flue gas desulphurisation unit to circulating fluidised bed with in-bed sulphur capture aids in enhancing the plant efficiency by about 2.5%pts. Optimisation of the recompression cycle based cases closed the split fraction to the LT turbine when maximising the efficiency, which reduces this cycle similar to the White et al. [38] proposed cycle. This is also valid for the cycles derived from partial cooling cycles when maximising the efficiency.

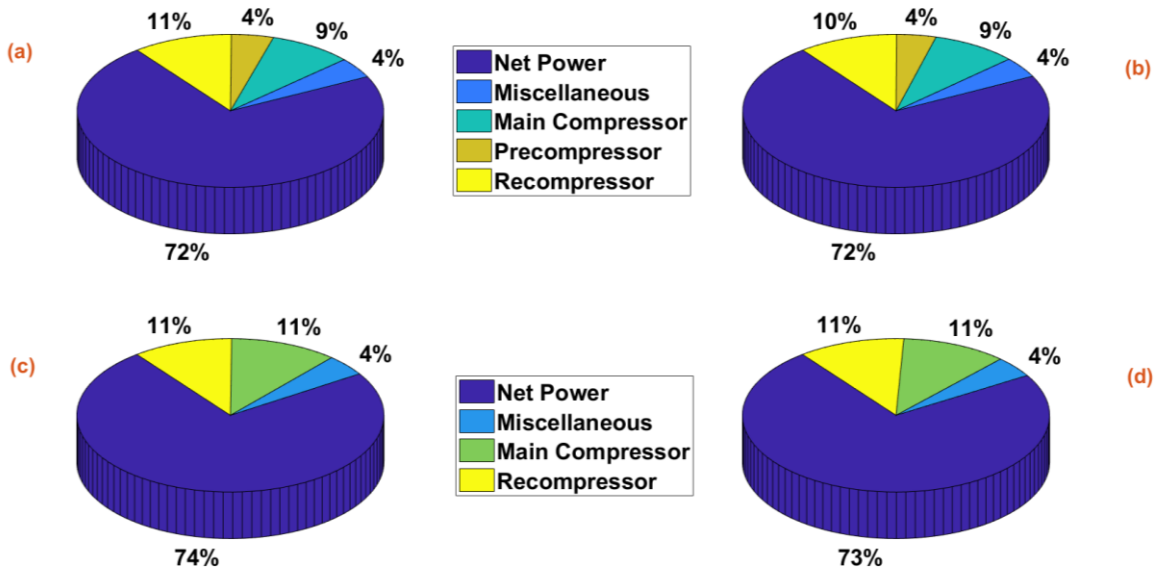

Figure 5-11 Turbine power breakdown for a TIT of 760°C, a) Case 1b, b) Case 2b, c) Case 3b, d) Case 4b

Figure 5-10 shows the breakdown of the turbine shaft power of all the four cases for a TIT of 620 °C and Figure 5-11 shows the breakdown for a TIT of 760 °C. The turbine shaft power generated for the partial cooling based cycles are higher than recompression cycle as the pressure ratio is higher. For the partial cooling based cycles at 620 °C, the compressive power is about ~27-28% of the total turbine shaft power whilst the miscellaneous category accounts for the generator loss and plant auxiliary power (4%). The turbine shaft power for the recompression based cycles are less as the compressive power accounts for about 24-25% for a TIT of 620°C. The compressive power share is reduced to about 23-24% for partial cooling based cycles when the TIT increased to 760 °C (Figure 5-11), whilst it is about 22% for recompression based cycles.

The energy balance of all the eight cases is shown in Table 5-9 and the Sankey diagram [45] of Case1a and Case 1b are shown in Figure 5-12. The major low-grade heat rejection in the cycle is at the condenser (42-42.6%), followed by the boiler sensible heat loss (about 11-11.7%). The share of auxiliary power and generator loss from the thermal input is 2.1% and 0.7% respectively. The boiler loss has increased by 0.7% (Case 2a) from a minimum value of 11% (Case 3a),

which is caused by the higher flue gas exit temperature than the minimum flue gas outlet temperature from APH (i.e., 142.8 °C). When increasing the TIT from 620 °C to 760 °C, the heat rejection at the cooler is reduced (38.7-39.7%) owing to the increased Carnot efficiency at a higher TIT (Table 5-9). Reducing the cooler heat duty also reduces the amount of water/air required to cool the system; for instance, the mass flow rate of the cooling medium for Case 1b is about 15% lower than B12A. In the case of water-cooled plants, the elimination of boiler blowdown further assists in reducing water consumption. Furthermore, the CO_2 emission reduces by 6.4% for Case 1a compared to B12A. The base case (B12A) annual CO_2 emission is 3,169,762 ton/year which is reduced to 2,965,732 ton/year for Case 1a. This is equivalent to a reduction of 204,031 ton/year CO_2 emission.

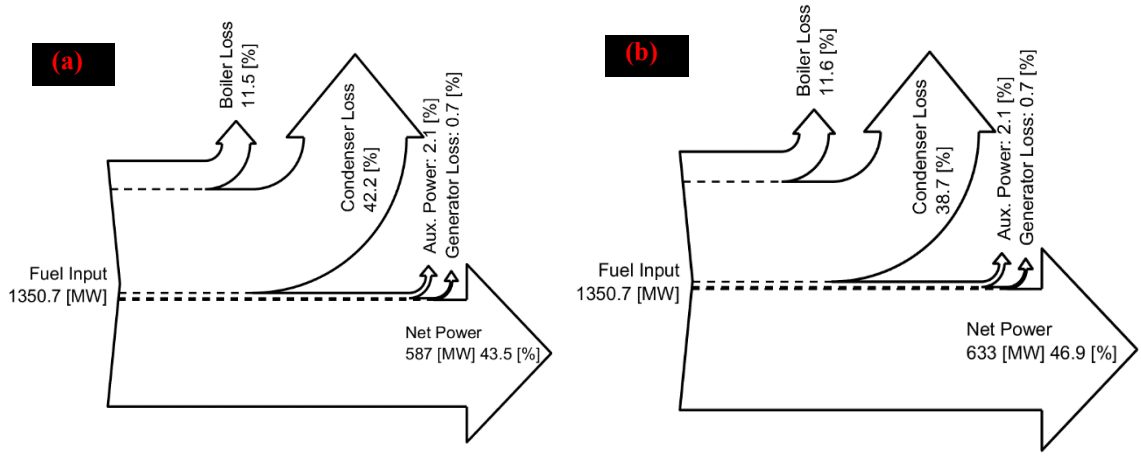

Figure 5-12 Energy balance Sankey diagram, a) Case 1a (TIT of 620°C), b) Case 1b (TIT of 760°C)

Table 5-9 First-law energy balance for both TIT of 620°C and TIT of 760°C

Parameters	Unit	Partial Cooling Cycle (PCC)		Recompression Cycle (RCBC)	
		Case 1a	Case 2a	Case 3a	Case 4a
Fuel input	MW	1350.7 (100%)			
Boiler Loss	%	11.5	11.7	11.0	11.1
Condenser Loss	%	42.2	42.0	42.7	42.6

Auxiliary Power	%	2.1	2.1	2.1	2.1
Generator Loss	%	0.7	0.7	0.7	0.7
Net Power (Net Efficiency)	%	43.5	43.5	43.4	43.5
		Case 1b	**Case 2b**	**Case 3b**	**Case 4b**
Fuel input	MW	1350.7 (100%)			
Boiler Loss	%	11.6	11.4	11.4	11.3
Condenser Loss	%	38.7	39.2	39.4	39.1
Auxiliary Power	%	2.1	2.1	2.1	2.1
Generator Loss	%	0.7	0.7	0.7	0.7
Net Power (Net Efficiency)	%	46.9	46.6	46.5	46.8

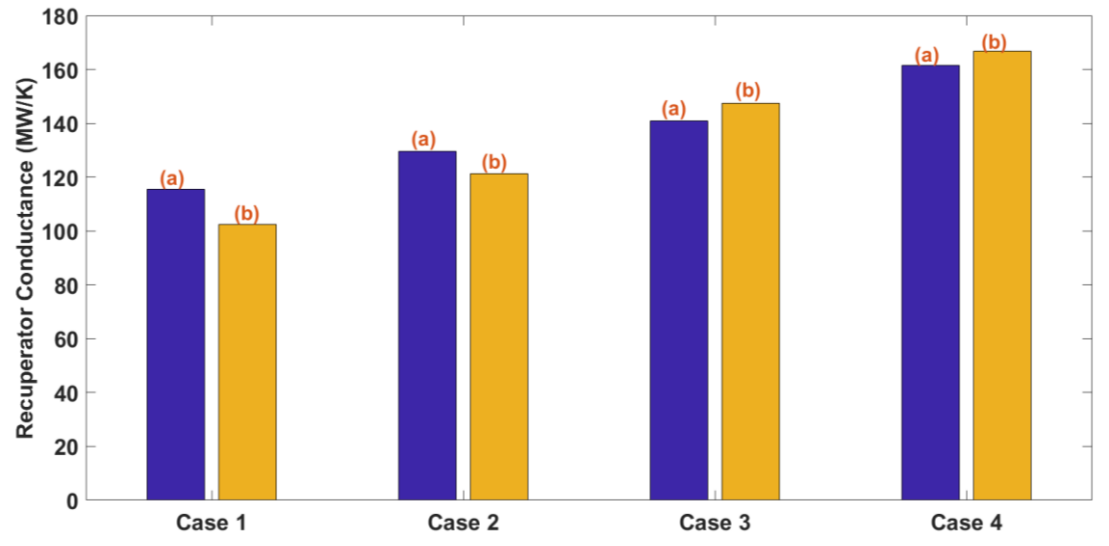

Figure 5-13 Recuperator conductance (UA) of all the cycle configurations studied

The recuperator conductance (UA) of all the cycle configurations studied are shown in Figure 5-13. Increasing the number of recuperators from two to three (Case 2 and Case 4) also increased the conductance due to the reduced

temperature driving force. The conductance of the cycles derived from partial cooling cycles (Case 1 and Case 2) is lower than the recompression based cycles as the heat duty of the former cases is lower than the latter cases by about 25%. This is because the turbine exhaust temperature of partial cooling based cycles are lower than recompression based cycles owing to a higher pressure ratio. Also, the recompression cycle better matches the hot and cold stream temperature profile than a partial cooling cycle, resulting in a reduced temperature driving force. Increasing the TIT from 620 °C to 760 °C reduces the recuperator conductance for partial cooling based cycles whereas they increased for recompression based cycles. Although the plant efficiency of all the four cycles are roughly similar for a TIT of 620 °C, partial cooling cycle shall be preferred owing to its superior off-design performance than recompression cycle at higher ambient temperatures [16].

5.6.2 Economic Performance

Figure 5-14 and Figure 5-15 shows the total plant cost (TPC) breakdown of the boiler and turbine block for a TIT of 620 °C and 760 °C respectively. This will be referred as power cycle equipment capital cost in this paper as it only includes the cost of boiler, turbine, compressor, recuperator and coolers. Table 5-10 includes the piping cost and foundation cost. It is worth highlighting that the boiler and turbine shares about 52-60% of the power cycle equipment's capital cost, depending on the cycle configuration, whilst the remaining cost associated with other sub-system are shown in Table 5-10. The cost share of the boiler and economiser is significantly higher than all the other power cycle equipment's capital cost. For instance, the cost of the boiler (main heater+ reheater + economisers) is about 60-67% of the power cycle equipment's capital cost for both the TITs studied. Despite having higher efficiency, the power cycle equipment capital cost is notably increased by about 20% when increasing the TIT from 620 °C to 760 °C for partial cooling based cycles whereas it increased by about 10-16% for recompression based cycles. This clearly shows that the increased efficiency isn't enough to offset the increased power cycle equipment capital cost.

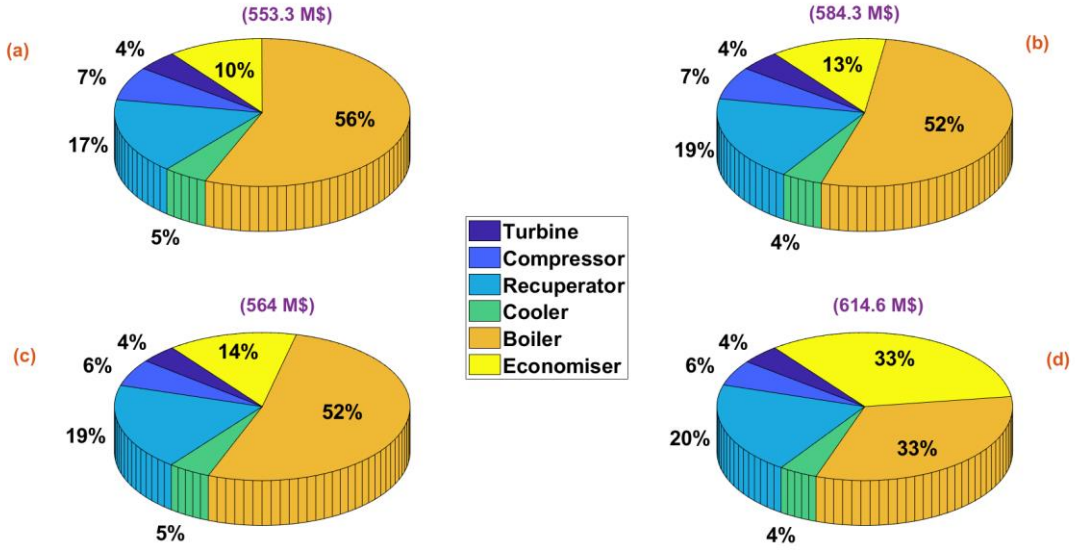

Figure 5-14 Capital cost breakdown of boiler and turbine block for a TIT of 620°C, a) Case 1a, b) Case 2a, c) Case 3a, d) Case 4a

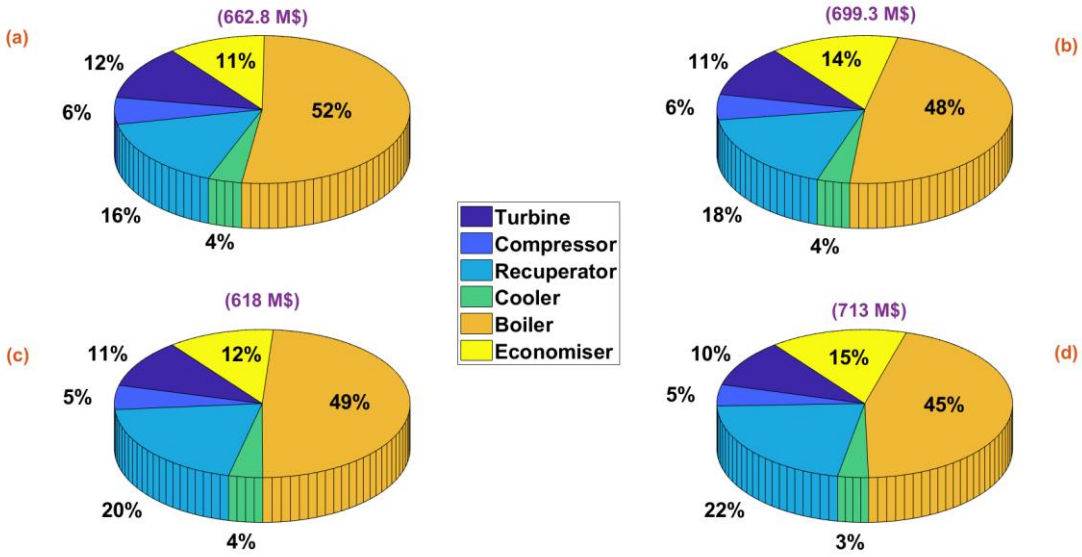

Figure 5-15 Capital cost breakdown of boiler and turbine block for a TIT of 760°C, a) Case 1b, b) Case 2b, c) Case 3b, d) Case 4b

However, the capital cost of balance of the plant (BOP) and fuel cost also reduces at higher efficiencies and that may contribute to reducing the COE. The cost share of the compressor is higher than the turbine when the TIT is 620 °C, but the turbine cost share increased notably at TIT of 760 °C owing to the temperature correction factor to account for the change in the materials. The

recuperator shares a significant portion of the BEC (16-22%), therefore the selection of the appropriate approach temperature and pressure drop can significantly influence the overall cost.

Table 5-10 shows the complete breakdown of the unit TPC for both the TIT (a) and TIT (b) studied. The contribution of power block equipment cost and boiler in the TPC is in the range of 52-60%. The TPC of sCO_2 is higher than equivalent steam Rankine cycle within a range of 1-7% for all the cases for a TIT of 620 °C and 760 °C except for Case 3b where TPC is same as the steam Rankine cycle. The increase capital cost of item 4 and 8 are mainly compensated by the reduced cost of item 3 i.e., feed water and miscellaneous BOP for a TIT of 600 °C. The base case coal input to the AUSC [38] is different than the B12A case as White et al. [38] adjusted the fuel feed in the former case to match the net power output to approximately 550MW, whilst this study kept the fuel input constant. Therefore, comparing the absolute TPC of AUSC with sCO_2 cycles are not possible, but the normalised TPC with net power output can be compared. The contribution of all the items except power cycle equipment cost of sCO_2 cycle cases are lower than equivalent steam Rankine cycle. For a TIT of 760 °C, the increased cost of power cycle equipment is larger than the reduction in cost from other items, resulting in a net increase of TPC. On the other hand, the TPC of Case 1a is lower than B12A by 5.6%.

Table 5-10 Unit total plant cost (TPC) Summary in $/kW

Item No	Parameter (TIT= 620 °C)	Unit	**B12A** [35]	Case 1a	Case 2a	Case 3a	Case 4a
1	Coal & Sorbent Handling	$/kW	82.5	77.3	77.3	77.4	77.3
2	Coal & Sorbent Prep & Feed	$/kW	39.1	36.7	36.7	36.7	36.7
3	Feedwater & Miscellaneous BOP Systems	$/kW	170.3	42.2	42.2	42.2	42.1
4	Boiler & Accessories	$/kW	621.3	628.9	648.5	638.0	688.0
5A	Gas Cleanup & Piping	$/kW	304.1	285.0	284.8	285.2	284.7
7	Duct work & Stack	$/kW	83.0	77.7	77.7	77.8	77.7
8	Steam/sCO_2 Power Cycle	$/kW	303.5	372.1	405.0	388.4	422.5

9	Cooling Water System	$/kW	80.1	71.9	72.3	73.0	72.2
10	Ash & Spent Sorbent Handling Systems	$/kW	30.5	28.6	28.6	28.6	28.6
11	Accessory Electric Plant	$/kW	112.2	107.0	107.5	106.4	106.5
12	Instrumentation & Control	$/kW	47.8	44.6	44.6	44.6	44.5
13	Improvements to Site	$/kW	29.8	28.0	28.1	28.1	28.3
14	Buildings & Structures	$/kW	121.8	113.6	113.8	113.8	114.1
	Total Plant Cost (TPC)	$/kW	2,026.1	1,913.5	1,967.0	1,940.1	2,023.2
Item No	**Parameter (TIT= 760 °C)**	**Unit**	**AUSC** [38]	**Case 1b**	**Case 2b**	**Case 3b**	**Case 4b**
1	Coal & Sorbent Handling	$/kW	78.5	71.7	72.1	72.3	71.8
2	Coal & Sorbent Prep & Feed	$/kW	37.1	34.0	34.2	34.3	34.1
3	Feedwater & Miscellaneous BOP Systems	$/kW	145.9	39.1	39.3	39.4	39.2
4	Boiler & Accessories	$/kW	610.7	656.0	688.8	594.3	676.8
5A	Gas Cleanup & Piping	$/kW	286.6	264.2	265.6	266.5	264.6
7	Duct work & Stack	$/kW	81.8	72.1	72.4	72.7	72.2
8	Steam/sCO_2 Power Cycle	$/kW	326.2	506.8	537.1	525.5	582.6
9	Cooling Water System	$/kW	72.3	63.0	63.9	64.6	63.5
10	Ash & Spent Sorbent Handling Systems	$/kW	29.2	26.5	26.6	26.7	26.5
11	Accessory Electric Plant	$/kW	109.3	99.2	99.6	99.6	99.0
12	Instrumentation & Control	$/kW	47.3	41.2	41.4	41.6	41.3
13	Improvements to Site	$/kW	28.4	26.6	26.9	26.7	26.9
14	Buildings & Structures	$/kW	118.6	106.7	107.5	107.3	107.4
	Total Plant Cost (TPC)	$/kW	1,972.0	2,007.2	2,075.5	1,971.4	2,105.9

Figure 5-16 shows the breakdown of COE for all the eight cases investigated. It can be seen that a maximum cost reduction of 7.6% can be achieved by using Case 2b compared to B12A, which corresponds to a reduction of 3.4% compared to AUSC. Although the TASC of sCO_2 cycles is about the same as steam Rankine

cycles, the capital cost contribution on COE is lower due to higher energy generation owing to its increased efficiency. Likewise, the fixed O&M, variable O&M and fuel cost is less than the equivalent steam Rankine cycle owing to the increased amount of energy generation. It should be noted that despite achieving higher efficiency (Table 5-9), increasing the TIT from 620 °C to 760 °C does not noticeably reduce the COE (Figure 5-16). However, increasing the cycle efficiency also offers other benefits such as reduction in the cooling water requirement in the cooler and the carbon emission, which are outside the scope of this study.

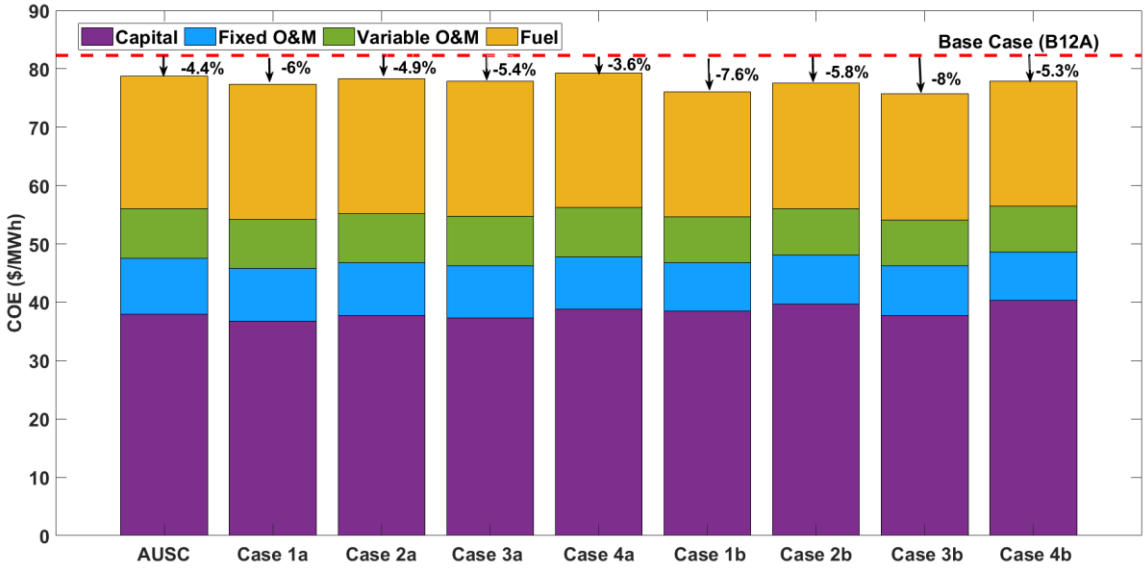

Figure 5-16 Cost of Electricity (COE) comparison with steam Rankine cycle (B12A)

5.6.3 Monte-Carlo Uncertainty Analysis

Since the manufacturing experience of sCO_2 power block components is so limited, the uncertainty of them is larger. Therefore, an uncertainty estimation is essential in order to foresee the range of COE with the cumulative probability to reduce the financial risk. The cost functions uncertainty is listed in Table 5-11, and Monte-Carlo uncertainty analysis is performed for all the eight sCO_2 cases. The total number of samples considered in each cycle COE estimation is 10,000. The uncertainty ranges of all the sCO_2 power cycle cost functions reported by Weiland et al. [42] are used in this study.

Table 5-11 Component cost uncertainty ranges used in Monte-Carlo simulation

Component	Minimum	Maximum
Compressor/Pump	0.6	1.48
Turbine	0.75	1.3
Boiler (MH, RH, Eco)	0.75	1.25
Recuperators	0.69	1.38
Coolers	0.75	1.28

Figure 5-17 shows the cumulative probability distribution of COE for all eight cases. It clearly shows that the Case 3b and Case 1b are the lowest COE alternatives and the lowest COE of 72 $/MWh is achievable whilst it can be as high as 79.9 $/MWh for Case 3b. This implies that the COE can be reduced by up to 12% at zero cumulative probability and the reduction is only about 3% at the maximum cumulative probability compared to B12A. On the other hand, when comparing against AUSC, Case 3b COE reduces by up to 8% at the minimum cumulative probability while it increases by about 2% at the maximum cumulative probability. This implies that the cost reduction potential of a sCO_2 cycle compared with steam Rankine cycles are within the uncertainty range of the cost functions. Therefore, sCO_2 cycles may reduce the COE of equivalent steam Rankine cycles up to 0-8% depending on the uncertainty of the cost functions. It is worth highlighting that the variation of COE is smaller despite having larger uncertainty ranges for sCO_2 cycle components owing to relatively lower cost share on the total cost. The configurations with three recuperators and economisers are not economical compared to two recuperator cycles. This study excluded the carbon taxing, in which case sCO_2 cycles can offer higher economic benefits as the efficiency of the sCO_2 cycle is higher than the equivalent steam Rankine cycle.

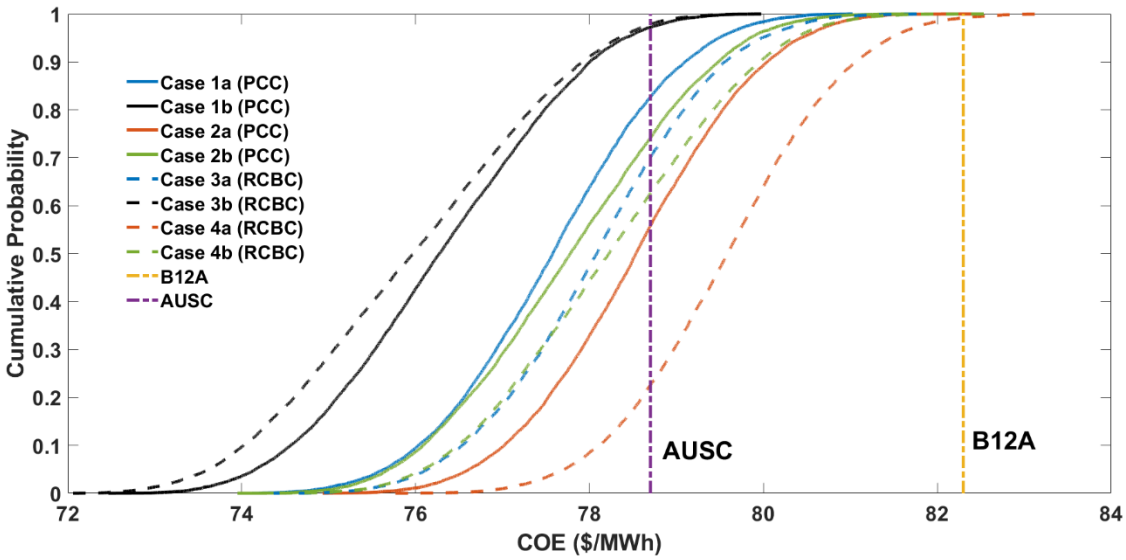

Figure 5-17 Cumulative probability distribution of COE from Monte-Carlo analysis

5.6.4 Sensitivity Analysis

sCO_2 cycle performance is sensitive to the component design assumptions including compressor isentropic efficiency, turbine isentropic efficiency, pressure drop and recuperator approach temperature [11]. Therefore, a sensitivity study has been performed for the partial cooling based cycle (Case 1b) and the results are plotted in Figure 5-18. The cycle efficiency drops by about 1%pts when increasing the low temperature recuperator approach temperature from 3 to 20 °C. There is a clear cost minimal solution existing below the conductance of the recuperator that exponentially increases but the increase in efficiency cannot offset the increased recuperator cost. The optimal LTR approach temperature is around 10 °C. The change in efficiency for changes in LTR approach temperature has two different slopes pivoting at the minimum cost optimal point. It is well noted that the minimum pinch temperature and effectiveness of the MTR and HTR were kept unchanged at 5.6 °C and 95% respectively.

Since the pressure ratio of sCO_2 cycles is small (~4-7), the cycle performance is very sensitive to pressure drop. For instance, the efficiency drops by about 0.5%pts when the boiler main heater cold side pressure drop increased by 2% (equivalent to ~7 bar), which also increased the COE by 0.9$/MWh. The boiler pressure drop of an sCO_2 cycle has to be higher in order to ensure the cooling of

the radiant zone [11]. The efficiency reduction slope per percentage increase of main heater cold stream pressure drop is 0.2%pts, which corresponds to a reduction of COE by around 0.45 $/MWh. However, this absolute value can change depending on the cycle pressure ratio and main heater inlet pressure.

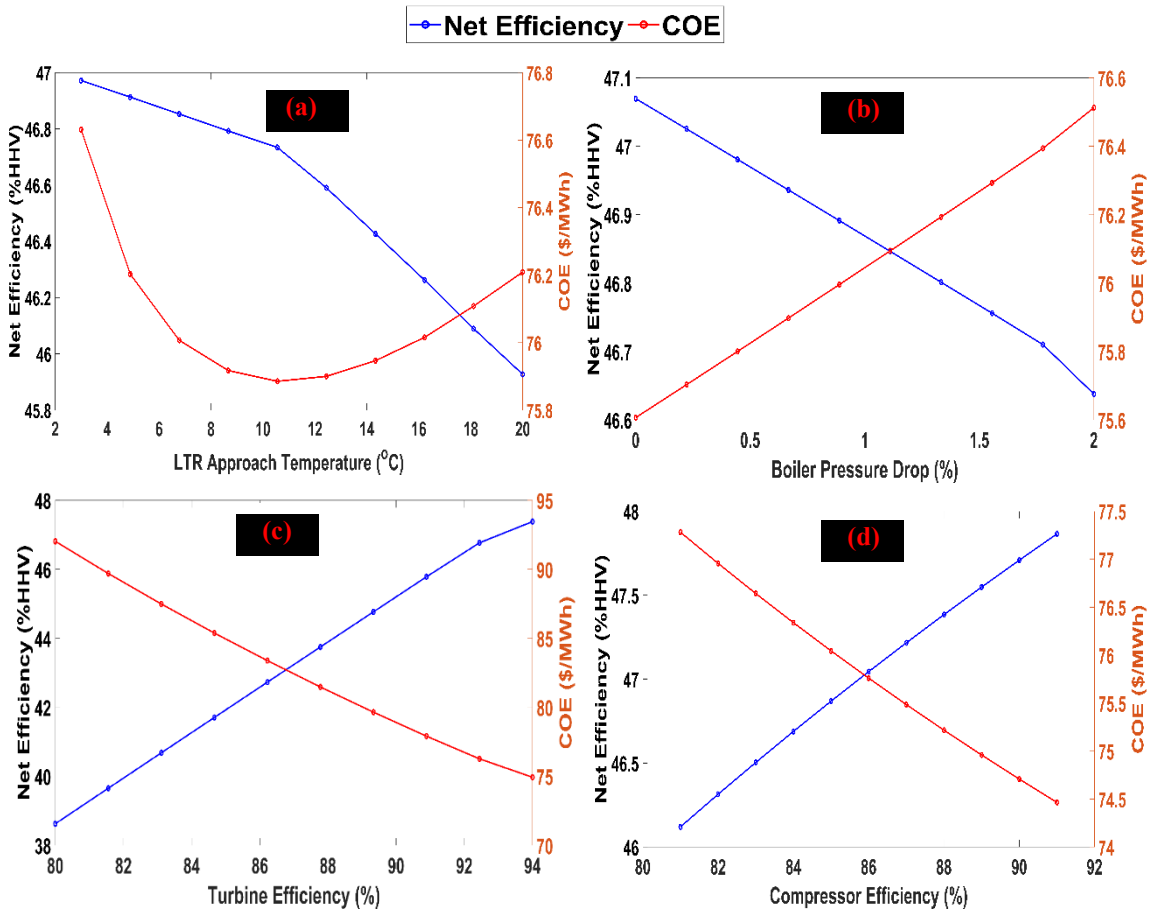

Figure 5-18 Sensitivity study of Case 1b a) LTR approach temperature, b) main heater pressure drop c) Turbine isentropic efficiency d) compressor isentropic efficiency

For the 550MW plant, the turbine has to be a multi-stage axial type [46] whilst the main compressor can be axial or radial [47,48]. The radial compressor can offer a higher operating range, which is essential for sCO_2 cycles as the variation of the fluid density is significant close to the critical point. Noall and Pasch [49] indicated that a compressor efficiency of about 83-85% is realistically achievable for a 50MW plant using a radial compressor. Using mean line models, Yann Le Moullec [18] indicated that using a multi-stage axial compressor can achieve 90% isentropic efficiency. Bidkar et al. [50] estimated a multi-stage turbine efficiency

of about 90.6-91.6% for 450MW plant. A sensitivity study covering this range, of 81-91% for compressor and 80-94% for the turbine, have been evaluated. The results show that the sCO_2 cycle efficiency is more sensitive to turbine efficiency than compressor efficiency changes, as shown in Figure 5-18 ((c), (d)): this also influences the COE. The effect of compressor and turbine efficiency change on the plant efficiency and COE may also be influenced by the compressor inlet pressure and temperature, which are maintained at the same design value used in the sensitivity study.

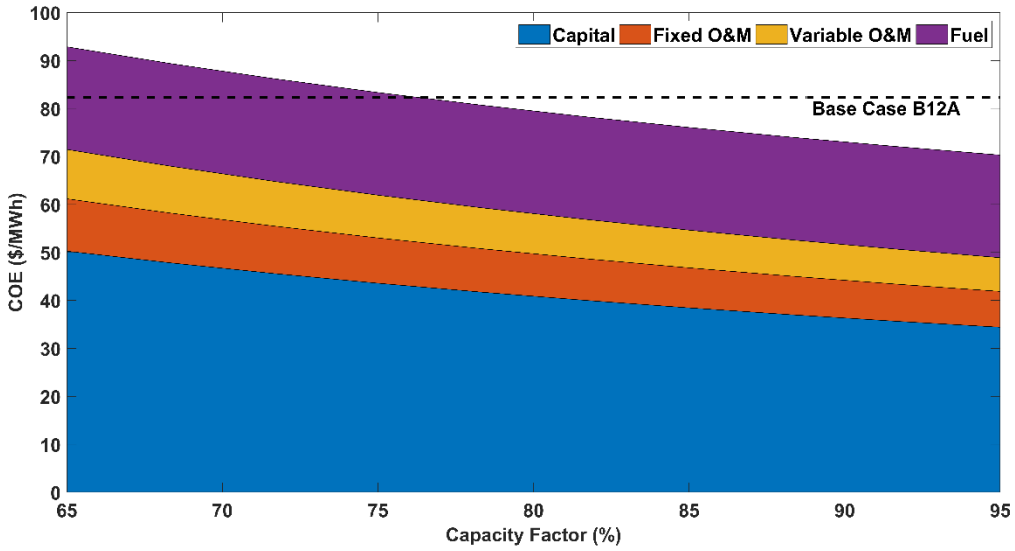

Figure 5-19 Effect of plant capacity factor on COE for Case 1b

Increasing penetration of the high volatile variable renewable energy generation units to the grid demands more flexible power generation plants suitable for cyclic operation. This reduces the plant capacity factor ($\frac{actual\ annual\ energy\ generation}{8760 * net\ power}$) notably as the conventional power generation units are no longer expected to be operated in baseload [51]. Therefore, a sensitivity study is also performed for different capacity factors and the variation of COE for Case 1b is shown in Figure 5-19. It should be noted that the base case B12A steam Rankine cycle assumes a capacity factor of 85%.

5.7 Conclusions

This work investigated the performance of four novel cycle configurations that combines the features of the partial cooling cycle, recompression cycle and cascade cycle. The thermal-economic performance of these four cycles is evaluated for two different turbine inlet temperatures i.e., 620 °C and 760 °C and their performance are compared with an equivalent steam Rankine cycle. The cycle configurations are modelled using in-house developed code in MATLAB® and the cycle process parameters (13-16 variables) are optimised using a genetic algorithm. sCO_2 cycles can achieve higher efficiency in the range of 3-4%pts, which leads to a reduction of about 4-6% in the cost of electricity (COE) compared to a steam Rankine cycle (NETL base case- B12A). Increasing the turbine inlet temperature from 620 °C to 760 °C increases the efficiency further by 3-4%pts. Despite achieving higher efficiencies, the reduction in COE is smaller (1-4%) when compared with advanced ultra-supercritical (AUSC) steam Rankine cycle for a turbine inlet temperature of 760 °C owing to the increased capital cost from high-grade materials for the cost functions considered, making them less attractive. Increasing the number of recuperators and economisers from two to three in both recompression and partial cooling based cycles doesn't offset the COE, therefore, a simple two recuperators and economiser based configurations are recommended. Cycles derived from partial cooling cycles achieved higher efficiency and reduction in COE similar to the cycles derived from recompression cycle, therefore, partial cooling cycles can be considered owing to their higher operational freedom due to the ability in controlling the main compressor inlet pressure independent from the turbine exhaust pressure.

Since the uncertainty of sCO_2 cycle cost functions is higher owing to the lower technology readiness level, a Monte-Carlo analysis is performed to realise the associated financial risk. The Monte-Carlo analysis shows that the COE reduction range compared to steam Rankine cycle can be as high as 8%, however, this falls within the range of the cost function uncertainty i.e., the COE reduction diminishes to 0-3% at a 95-percentile cumulative probability. A sensitivity analysis shows that the turbine efficiency influences the efficiency and COE more than a compressor. For instance, the plant efficiency changes by 0.66%pts per 1%pts

changes in turbine isentropic efficiency whilst it changes by 0.18%pts per 1%pts change in compressor efficiency. The boiler pressure drop affects the efficiency by 0.2%pts for 1%pts change in main heater pressure drop.

5.8 References

[1] National Energy Technology Laboratory. Energy Storage for Fossil Fuel Energy Systems 2020. https://netl.doe.gov/coal/crosscutting/energy-storage (accessed 16 June 2020).

[2] HORIZON 2020. Supercritical CO_2 Cycle for Flexible and Sustainable Support to the Electricity System 2020. https://ec.europa.eu/inea/en/horizon-2020/projects/h2020-energy/carbon-capture-storage-power-plants/sco2-flex (accessed 16 June 2020).

[3] Zhu Q. Power generation from coal using supercritical CO_2 cycle Power generation from coal using supercritical CO_2 cycle 2017.

[4] Crespi F, Gavagnin G, Sánchez D, Martínez GS. Supercritical carbon dioxide cycles for power generation: A review. Appl Energy 2017;195:152–83. doi:10.1016/j.apenergy.2017.02.048.

[5] Thanganadar D, Asfand F, Patchigolla K. Thermal performance and economic analysis of supercritical Carbon Dioxide cycles in combined cycle power plant. Appl Energy 2019;255:113836. doi:10.1016/j.apenergy.2019.113836.

[6] Angelino G. Real Gas Effects in Carbon Dioxide Cycles. ASME- Pap 69-Gt-102 1969:1–12. doi:10.1115/69-GT-102.

[7] Kehlhofer R, Bahmann R, Nielsen H, Warner J. Combined-cycle gas & steam turbine power plants. second edi. PennWell; 1999.

[8] Dostal V, Driscoll MJ, Hejzlar P. A Supercritical Carbon Dioxide Cycle for Next Generation Nuclear Reactors. 2004. doi:MIT-ANP-TR-100.

[9] Crespi F, Sánchez D, Sánchez T, Martínez GS. Capital Cost Assessment of Concentrated Solar Power Plants Based on Supercritical Carbon Dioxide

Power Cycles. J Eng Gas Turbines Power 2019;141:1–9. doi:10.1115/1.4042304.

[10] Miller JD, Buckmaster DJ, Hart K, Held TJ, Thimsen D, Maxson A, et al. Comparison of supercritical CO_2 power cycles to steam Rankine cycles in coal-fired applications. ASME Turbo Expo 2017 Turbomach. Tech. Conf. Expo., 2017, p. 1–12. doi:10.1115/GT2017-64933.

[11] Brun K, Friedman P, Dennis R. Fundamentals and applications of supercritical carbon dioxide (sCO_2) based power cycles. 2017.

[12] Held TJ. Supercritical CO_2 Cycles for Gas Turbine Combined Cycle Power Plants. Power Gen Int., 2015.

[13] Sun E, Hu H, Li H, Liu C, Xu J. How to Construct a Combined S-CO_2 Cycle for Coal Fired Power Plant? Entropy 2018;21:19. doi:10.3390/e21010019.

[14] Mohammadi K, Ellingwood K, Powell K. A novel triple power cycle featuring a gas turbine cycle with supercritical carbon dioxide and organic Rankine cycles: Thermoeconomic analysis and optimization. Energy Convers Manag 2020;220:113123. doi:10.1016/j.enconman.2020.113123.

[15] Zhao Q. Conception and optimization of supercritical CO_2 Brayton cycles for coal-fired power plant application, PhD Thesis. Université de Lorraine, Lorraine, France, 2018.

[16] Zhao Q, Mecheri M, Neveux T, Privat R, Jaubert J-N. Design of SC-CO_2 Brayton cycles using MINLP optimization within a commercial simulator. 6th Int. Supercrit. CO2 Power Cycles Symp., Pittsburgh, Pennsylvania: 2018, p. 1–13.

[17] Mecheri M, Le Moullec Y. Supercritical CO_2 Brayton cycles for coal-fired power plants. Energy 2016;103:758–71. doi:10.1016/j.energy.2016.02.111.

[18] Le Moullec Y. Conceptual study of a high efficiency coal-fired power plant with CO_2 capture using a supercritical CO_2 Brayton cycle. Energy

2013;49:32–46. doi:10.1016/j.energy.2012.10.022.

[19] Bai Z, Zhang G, Li Y, Xu G, Yang Y. A supercritical CO_2 Brayton cycle with a bleeding anabranch used in coal-fired power plants. Energy 2018;142:731–8. doi:10.1016/j.energy.2017.09.121.

[20] Park SH, Kim JY, Yoon MK, Rhim DR, Yeom CS. Thermodynamic and economic investigation of coal-fired power plant combined with various supercritical CO_2 Brayton power cycle. Appl Therm Eng 2018;130:611–23. doi:10.1016/j.applthermaleng.2017.10.145.

[21] Michalski S, Hanak DP, Manovic V. Advanced power cycles for coal-fired power plants based on calcium looping combustion: A techno-economic feasibility assessment. Appl Energy 2020;269:114954. doi:10.1016/j.apenergy.2020.114954.

[22] Wei X, Manovic V, Hanak DP. Techno-economic assessment of coal- or biomass-fired oxy-combustion power plants with supercritical carbon dioxide cycle. Energy Convers Manag 2020;221:113143. doi:10.1016/j.enconman.2020.113143.

[23] Huang M, Sonwane C. Thermodynamics of conventional and non conventional sCO_2 recompression Brayton cycles with direct and indirect heating. 4th Int Symp - Supercrit CO2 Power Cycles 2014:1–9. doi:10.1017/CBO9781107415324.004.

[24] Alfani D, Astolfi M, Binotti M, Campanari S, Casella F, Silva P. Multi objective optimization of flexible supercritical CO_2 coal-fired power plants. Proc ASME Turbo Expo 2019;3:1–11. doi:10.1115/GT2019-91789.

[25] White C, Shelton W, Dennis R. An assessment of supercritical CO_2 power cycles integrated with generic heat sources. J Chem Inf Model 2013;53:1689–99. doi:10.1017/CBO9781107415324.004.

[26] White C, Gray D, Plunkett J, Shelton W, Weiland N, Shultz T. Techno-economic evaluation of utility-scale power plants based on the indirect sCO_2 Brayton cycle. 2017. doi:10.2172/1490272.

[27] White CW, Weiland NT, Shelton WW, Shultz TR. sCO_2 cycle as an efficiency improvement opportunity for air-fired coal combustion. 6th Int Symp - Supercrit CO2 Power Cycles 2018:1–30.

[28] Weitzel PS. Component test facility (comtest) phase 1 engineering for 760C (1400F) advanced ultra- supercritical (A-USC) steam generator development. Am Soc Mech Eng Power Div POWER 2015;2015-Janua:1–131. doi:10.1115/POWER201549411.

[29] Nathan Weiland WS, White C. Design of a Commercial Scale Oxy-Coal Supercritical CO_2 Power Cycle 2015;2015/1733.

[30] Turchi CS, Ma Z, Neises TW, Wagner MJ. Thermodynamic Study of Advanced Supercritical Carbon Dioxide Power Cycles for Concentrating Solar Power Systems. J Sol Energy Eng 2013;135:041007. doi:10.1115/1.4024030.

[31] The Babcock & Wilcox Company. Steam Its generation and use. vol. 53. 2019. doi:10.1017/CBO9781107415324.004.

[32] Purgert R, Phillips J, Tanzosh H, Shingledecker J, James. Materials for Advanced Ultra-supercritical (A-USC) Steam Turbines - A-USC Component Demonstration Pre-FEED Final Technical Report. DE-FE0026294 2016. doi:10.2172/1332274.

[33] Weiland NT, Dennis RA, Ames R, Lawson S, Strakey P. Fundamentals and applications of supercritical carbon dioxide (sCO_2) based power cycles-Fossil energy. Elsevier Ltd; 2017. doi:10.1016/B978-0-08-100804-1.00012-8.

[34] Lemmon EW, Huber ML, McLinden MO. NIST Standard Reference Database 23. Natl Inst Stand Technol 2013;V 9.1.

[35] Fout T, Zoelle A, Keairns D, Turner M, Woods M, Kuehn N, et al. Cost and Performance Baseline for Fossil Energy Plants Volume 1a: Bituminous Coal (PC) and Natural Gas to Electricity Revision 3. Natl Energy Technol Lab 2015;1a:240. doi:DOE/NETL-2010/1397.

[36] Nellis G, Klein S. Heat Transfer. 2009. doi:10.1017/CBO9780511841606.

[37] Schmitt J, Wilkes J, Bennett J, Wygant K, Pelton R. Lowering the levelized cost of electricity of a concentrating solar power tower with a supercritical carbon dioxide power cycle. ASME Turbo Expo, Charlotte, NC, USA: 2017, p. 1–10. doi:10.1115/GT2017-64958.

[38] White CW, Shelton WW, Weiland NT, Shultz TR. sCO_2 Cycle as an Efficiency Improvement Opportunity for Air-fired Coal Combustion. 2018. doi:10.2172/1511695.

[39] National Energy Technology Laboratory. Quality Guidelines for Energy System Studies: Capital Cost Scaling Methodology. 2013. doi:10.2172/1513277.

[40] National Energy Technology Laboratory. Quality Guideline for Energy System Studies: Cost Estimation Methodology for NETL Assessments of Power Plant Performance. 2019.

[41] Carlson MD, Middleton BM, Ho CK. Techno-Economic Comparison of Solar-Driven sCO_2 Brayton Cycles Using Component Cost Models Baselined With Vendor Data. Proc ASME 2017 Power Energy Conf 2017:1–7. doi:10.1115/ES2017-3590.

[42] Weiland NT, Lance BW, Pidaparti SR. SCO_2 power cycle component cost correlations from DOE data spanning multiple scales and applications. Proc. ASME Turbo Expo, vol. 9, 2019, p. 1–17. doi:10.1115/GT2019-90493.

[43] Couper JR, Penney WR, Fair JR, Walas SM. Chemical Process Equipment: Selection and Design. Third Edit. 2012. doi:10.1016/B978-0-12-396959-0.00025-2.

[44] Moisseytsev A, Sienicki JJ. Investigation of alternative layouts for the supercritical carbon dioxide Brayton cycle for a sodium-cooled fast reactor presentsation. Nucl Eng Des 2009;239:1362–71. doi:10.1016/j.nucengdes.2009.03.017.

[45] Spelling J. drawSankey (https://www.mathworks.com/matlabcentral/fileexchange/26573-drawsankey). MATLAB Cent File Exch 2021.

[46] Fleming DD, Conboy TM, Pasch JJ, Rochau GA, Fuller RL, Holschuh T V, et al. Scaling Considerations for a Multi- Megawatt Class Supercritical CO_2 Brayton Cycle and Commercialization. Sandia Rep 2013;SAND2013-9.

[47] A.Bidkar R. Conceptual Designs of 50MW and 450 MW supercritical CO_2 Turbomachinery Trains for Power Generation from Coal.Part2: Compressors. 5th Int. Symp. - Supercrit. CO2 Power Cycles, San Antonio, Texas, USA: 2016, p. 1–18.

[48] Weiland N, Thimsen D. A Practical Look at Assumptions and Constraints for Steady State Modeling of sCO_2 Brayton Power Cycles. 5th Int SCO2 Symp 2016:1–14.

[49] Noall JS, Pasch JJ. Achievable Efficiency and Stability of Supercritical CO_2 Compression Systems Main Compressor Design Discussion. 4th Int Symp - Supercrit CO2 Power Cycles Sept 2014 2014:1–10.

[50] Bidkar RA, Mann A, Singh R, Sevincer E, Cich S, Day M, et al. Conceptual Designs of 50MWe and 450MWe Supercritical CO2 Turbomachinery Trains for Power Generation from Coal. Part 1: Cycle and Turbine. 5th Int Symp - Supercrit CO2 Power Cycles 2016:17.

[51] NREL. Renewable Electricity Futures Study: Executive Summary. vol. 1. 2012. doi:NREL/TP-6A20-52409-1.

Chapter 6

6 Thermo-economic Analysis, Optimisation and Systematic Integration of Supercritical Carbon Dioxide Cycle with Sensible Heat Thermal Energy Storage for CSP Application

Dhinesh Thanganadar[a], Francesco Fornarelli[b,c], Sergio Camporeale[b], Faisal Asfand[a,d], Jonathon Gillard[a], Kumar Patchigolla[a]

[a]*School of Water, Energy and Environment (SWEE), Cranfield University, Cranfield, MK43 0AL, UK*
[b]*Dipartimento di Meccanica, Matematica e Management (DMMM) Politecnico di Bari, Bari, Italy*
[c]*National Group of Mathematical Physics (GNFM), National Institute of High Mathematics (INDAM)*
[d]*The School of Computing and Engineering, University of Huddersfield, Huddersfield, HD1 3DH, UK*

Submitted to Energy Journal and Under Review, 2021

Statement of contributions of joint authorship

Dhinesh Thanganadar proposed the novelty, implemented the methods, generated all results, and prepared the manuscript draft. Francesco Fornarelli, Sergio Camporeale, Faisal Asfand, and Jonathon Gillard proof-read and critically commented on the manuscript before submission. Kumar Patchigolla provided supervision, proof-read and critically commented on the manuscript before submission.

ABSTRACT

Integration of thermal energy storage with concentrated solar power (CSP) plant aids in smoothing of the volatile energy generation from renewable sources. Supercritical carbon dioxide (sCO_2) cycles can reduce the levelised cost of

electricity of a CSP plant through its higher efficiency and compact footprint compared to steam Rankine cycles. This study systematically integrates nine sCO_2 cycles including two novel configurations for CSP applications with a two-tank sensible heat storage system using a multi-objective optimisation technique. The thermal performance requirement of an ideal power cycle to reduce the plant overnight capital cost is determined and performance of the sCO_2 cycles is compared. Since cycle selection is dependant on the compressor inlet temperature (CIT) and maximum turbine inlet temperature (TIT), the performance of each cycle is compared for two different TIT and CIT (i.e. 600, 700°C and 32, 55°C respectively). The effect of these boundary conditions on the cycle selection criteria is discussed. A Monte-Carlo simulation accounting for the uncertainty range of the cost functions is also presented. Results reveal that the addition of an intercooler is advantageous for a CIT of 55 °C, and increasing the TIT from 600 to 700 °C increases the capital cost. One of the novel cycle configurations (C8) proposed can reduce the overnight capital cost by 10.8% in comparison to a recompression Brayton cycle (C3) for a CIT of 55°C and TIT of 700°C. This work describes design guidelines facilitating development/ selection of an optimal cycle for a CSP application integrated with two-tank thermal storage.

Keywords

Supercritical CO_2 cycle, CSP, Overnight Capital Cost, Thermal Energy Storage, Multi-objective optimisation, Central Power Tower

6.1 Introduction

Renewable energy technologies including concentrated solar power (CSP) plants have a significant role to play in keeping the global average temperature increase below 2 °C according to Paris agreement. Integrating thermal energy storage (TES) with a CSP plant not only reduces the levelised cost of electricity (LCOE) [1][2] but also increases the plant dispatchability, capacity factor and reliability. This is because integration of TES enables operating the power block during night hours which increases the annual energy generation for a given solar field and power block capacity. The increased TES capital cost is compensated by the increase annual energy generation until optimal storage size. CSP plants are

capital intensive, but with essentially no fuel cost, consequently, the LCOE principally depends on the capital cost and the regional solar resource [3]. The US Department of Energy (DOE) SunShot program has a goal to reduce the LCOE of CSP plants below 6¢/kWh [4]. National Renewable Energy Laboratory (NREL), USA prepared a roadmap to realise the cost reduction for three CSP technologies including falling particle receiver, molten salt receiver integrated with a sensible heat storage system and molten salt central receiver integrated with Phase Change Material (PCM) heat storage system. The SunShot initiative has set component level performance targets and the power block has to achieve >50% efficiency with dry cooling at 55 °C ambient temperature at a unit cost of <950 $/kW$_e$ [5]. Closed loop supercritical carbon dioxide (sCO_2) Brayton cycles have been considered as a power conversion cycle for all the three technologies owing to their higher efficiency compared to steam Rankine cycles, when the turbine inlet temperature (TIT) is >550 °C, and compact plant footprint [4,6]. Coventry and Pye [7] reviewed the current state-of-the-art of heliostat cost reduction pathways for mirrors, tracking systems and heliostat design in the context of reducing the cost related to manufacturing and assembly, heliostat size and wind load. The storage material cost of the two-tank sensible heat storage system is about half of the total cost of TES system, indicating that the inventory shares a significant cost share, whilst the remaining is accounted to tank/insulation, accessories, foundation, electrical and instrumentation [8].

Numerous cycle configurations have been proposed to meet the requirements for different applications with Crespi et al. [9] reviewing forty-two of them. Turchi et al. [10] analysed advanced sCO_2 cycle configurations in order to realise the SunShot power cycle targets. Crespi et al. [11] compared twelve sCO_2 cycles on the basis of efficiency and specific work diagrams, and outlined the potential areas for cycle development. Conventionally, Brayton cycles are compared using efficiency vs specific work curves with the objective of maximising both of them [12]. Maximising the efficiency aids in reducing the energy input whilst the latter helps in reducing the power cycle component size and thus capital cost. Crespi et al. [13] also investigated the Overnight Capital Cost (OCC), of twelve sCO_2 cycles integrated with CSP and two-tank TES systems, concluding that

transcritical CO_2 (tCO_2), Allam Cycle and partial cooling cycles achieved lower OCC than the highly efficient recompression cycle. This infers that higher efficiency (and therefore lower solar field cost) doesn't guarantee a reduction in the overall plant capital cost, however, the effect of storage tank temperature difference is not analysed. Crespi et al. [14] compared the effect of cycle efficiency and temperature across solar receiver on the cost for the partial cooling cycle and tCO_2 cycle, concluding that tCO_2 achieved lower capital cost. Echogen® has a packaged commercial unit for Waste Heat Recovery (WHR) applications [15]. NREL [16] have tested a pilot sCO_2 facility of 520 $kW_{th,}$ and other research facilities are reviewed by Lecompte et al. [17]. NREL are building a 10 MW_e plant which is designed to operate at a TIT of 716 °C [18]. Clementoni et al. provided steady-state [19], off-design [20] and transient operational results [21] of the 100kW_e experimental facility at Naval Nuclear Laboratory, USA. Thanganadar et al. [22] compared the design, off-design and annual performance of simple recuperative, recompression and the partial cooling cycle, concluding that the partial cooling cycle can achieve lower LCOE when operating the plant in maximum power mode. Thanganadar et al. [23] analysed the off-design performance of the recompression cycle, concluding that the capacity of the thermal energy storage system can be reduced by 25% when the compressor inlet temperature (CIT) is increased from its design of 42 °C to 55 °C.

The power cycle accounts for 10-30% of the overall plant capital cost whilst the solar field represents about 50-60% in a central power tower CSP plant [24]. The solar field cost decreases with increases in power block efficiency since the thermal rating of the solar receiver and the number of heliostats decreases to meet the desired plant net power output [25]. The cost of a sensible heat two-tank storage system increases with the reduction in the temperature difference between the hot and cold tank storage temperature (denoted as ΔT hereafter) and power cycle efficiency as they dictate the amount of storage inventory required for a given number of storage hours [13]. It is clear that maximising the power cycle efficiency reduces the cost of both solar field and TES, although maximising the ΔT primarily reduces the cost of TES, when neglecting the second order effect of reduction in receiver loss owing to the lower receiver mean

temperature. Conversely, maximising the ΔT penalizes the real power cycle efficiency as only a small fraction of the heat is available at the maximum temperature, reducing the Carnot mean heat addition temperature. This implies that maximum ΔT cannot guarantee cost reduction as it negatively impacts the power cycle efficiency, indicating that there should be an optimum ΔT, at which the effect on efficiency is smaller, but the total cost of TES and solar field is minimised, purely dictated by the cost share of TES and solar field. Therefore, an ideal power cycle for minimising the capital cost (CC) of the CSP plant will have maximum efficiency at a ΔT close to the optimal heat addition ΔT dictated by the cost function of the solar field and TES. In addition, the specific power of the power cycle must be higher in order to reduce the capital cost of the power block, which contributes about 10-30% of the total CSP plant CC. The SunShot program target for the power block only enforces the power block efficiency and power block unit cost and does not explicitly target the temperature difference between the two storage tanks despite its significant impact on the cost of the TES system [5].

In order to achieve higher efficiency, many advanced power generation cycles have been investigated including combined cycle [26] and closed-loop Brayton cycles with alternative working fluids such as helium [27], argon [27] and sCO_2. The amount of recuperation in sCO_2 cycles is limited by the occurrence of the pinch point phenomenon caused by the highly nonlinear changes in isobaric specific heat. Maximising the recuperation (minimising the pinch point limitation) is often achieved by splitting the recuperators into two or more and controlling the mass flow of the cold stream (recompression and partial cooling cycle). Dunham et al. [28] investigated six power cycle configurations namely regenerated He-Brayton, regenerated CO_2-Brayton, CO_2 recompression Brayton, Steam Rankine and CO_2-ORC Combined cycle and sCO_2 recompression cycle, concluding that the latter offers higher efficiency above 600 °C. Johnson et al. [29] have developed and patented a novel sCO_2 cycle configuration derived from the cascade cycle configurations that have a higher temperature difference across the primary heat exchanger (denoted as ΔT henceforth, which equates to the temperature difference between hot and cold tank when the piping heat losses

are neglected) in order to realise a lower LCOE. Thanganadar et al. [30] integrated five cascade cycle configurations with a bottoming cycle, and the study has shown that cascade cycles can be integrated with a sensible heat source having a larger ΔT.

Increasing the power cycle heat addition ΔT for a given TIT can be achieved by increasing the cycle pressure ratio, or advanced sCO_2 cycles derived from cascade [31] or condensed cycle (tCO_2) configurations [32]. Since the critical temperature and pressure of CO_2 is 30.98 °C and 7.38 MPa, it is not feasible to directly condense the cycle at 55 °C ambient condition (i.e., at the SunShot target). SCARABEUS [33] is a current European research project exploring sCO_2 blends that increase the critical temperature to enable the condensing cycle. However, the development of novel sCO_2 cycles derived from cascade cycles are seldom studied for CSP applications, except for the patented configuration by Johnson et al. [29]. Crespi et al. [34] showed that higher system pressure contributes more to increasing the thermal and economic performances than higher peak temperature cycle, concluding that a bulkier high pressure resistant system is more favourable than high-temperature alloy materials. However, the development of novel sCO_2 cycle configurations that maximise the cycle pressure ratio for CSP applications and their economic impact on the plant LCOE is seldom studied. The ΔT of the recompression cycle is lower (220 °C), whereas it is as high as 285 °C for the simple recuperative cycle and partial cooling cycle when the turbine inlet temperature and pressure are 750 °C and 300 bar respectively [13]. Clementoni et al. [35,36] investigated the effect of compressor inlet temperature (CIT) on the performance of sCO_2 cycles, which is highly sensitive to ambient temperatures. Asfand et al. [37] integrated an absorption chiller with the simple recuperative Brayton cycle (SRBC) to cool the cooling water so that the efficiency penalty at a higher temperature can be reduced. The compressor inlet pressure has to be close to the (pseudo) critical pressure for different compressor inlet temperatures so that the compressive power is minimised, in turn maximising the efficiency [38]. Since the pseudo critical pressure increases with temperature, the cycle pressure ratio reduces for a given cycle maximum pressure economical limit (around 250-300 bar) when the compressor inlet

temperature increases [13]. Consequently, the differential temperature across the primary heat exchanger reduces at higher ambient temperatures. Therefore, at a higher ambient temperature, the capital cost will increase not only due to the reduction in efficiency (due to increase in solar field cost) but also the TES cost owing to the reduction in ΔT. However, to the best of the author's knowledge, the effect of the ambient temperature and TIT on the plant capital cost and the requirements on power cycle design to reduce the cost has not been investigated.

This paper aids in selecting the best power cycle configuration and design point and also shows the optimal heat addition ΔT that minimises the cost of both solar field and TES. This paper also investigates the thermodynamic performance of nine sCO_2 cycles, of which seven are the commonly studied cycle configurations of simple recuperated Brayton cycle (with and without intercooling), recompression cycle (with and without intercooling), partial cooling cycle (with and without intercooling) and transcritical CO_2 cycle. However, two novel cycle configurations derived by combining the features of recompression and cascade cycles with the objective of maximising the heat addition ΔT, are also investigated. The effect of ambient temperature on the selection of cycle configuration for two different turbine inlet temperatures (600 °C and 700 °C) are investigated using multi-objective optimisation techniques. The cycle configurations are systematically integrated with a central power tower and two-tank sensible heat storage system with the objective of minimising the overall capital cost and they are compared against the optimal heat addition ΔT derived from an ideal power cycle. The trade-off trends between the power cycle thermodynamic parameters such as efficiency, specific power and heat addition ΔT are investigated to minimise the plant capital cost for a 50 MW_e plant. A Monte-Carlo simulation is performed in this study in order to consider the uncertainty of all the cost functions.

6.2 sCO_2 Cycle Configurations

Figure 6-1 shows the cycle integration scheme with the TES and CSP plant using recompression cycle (C3) as an example. All nine cycle configurations studied are shown in Figure 6-2 and the cycle naming convention is shown in Table 6-1.

In the simple recuperative cycle (C1), sCO_2 is compressed at supercritical conditions and passed through a recuperator followed by the primary heat exchanger (PHEX), where the fluid achieves the maximum temperature. The hot sCO_2 is then expanded in a turbine before a proportion of the heat is transferred to the cold stream via a recuperator and the remaining heat is rejected in the precooler. For C2, a two-stage intercooled compressor is considered. The recompression cycle (C3) recuperates more heat than C1 by splitting the recuperator into two and controlling the cold stream mass flow through the low-temperature recuperator, which eventually eliminates the pinch limitation that occurs in C1 and C2. C4 adds an intercooler to the recompression cycle (C3). The partial cooling cycle (C5) partially cools the hot stream return from the low-temperature recuperator to a superheated state, then pre-compresses the CO_2 above the critical point. Part of the flow bypasses the low temperature recuperator (LTR) via the recompressor whist the remaining flow goes through the cooler and main compressor. The high-temperature side processes of C5 are similar to C3 and C4. These five cycles (C1- C5) have commonly been studied independently, without integration with TES and CSP, and so are considered to compare their integration characteristics systematically through multi-objective optimisation.

Cycle C6 replaces the pre-compressor and the main compressor with two-stage intercooled compressors. Because of the added intercooler in the pre-compressor, the minimum pressure of the cycle is allowed to drop to 30 bar for the optimisation. C7 is derived by combining the recompression cycle and cascade cycle [30]. In this configuration, the PHEX is split into two with the low-temperature PHEX adding heat parallel to the HTR while mass flow to the high temperature PHEX is controlled by branching off some flow through a low temperature turbine. C8 adds a two-stage compression to the main compressor loop with an intercooler. C9 is the transcritical CO_2 cycle which condenses at the heat rejection unit. Temperature- Entropy (TS) diagrams of the processes are shown in Figure 6-3. Since reheating increases the average temperature of heat addition to the cycle (close to isothermal process), it is not considered in this study as the aim of this study is to explore the cycle configurations that maximise the heat addition ΔT.

The cooler is air-cooled and the PHEX is heated via hot molten salt from the solar field. The precooler is a direct air-cooled type with a pinch of 15 °C whilst the recuperator and the primary heat exchangers are compact Printed Circuit Heat Exchangers (PCHE).

Table 6-1 Cycle configuration considered in this study

Cycle Code	Name	Acronym
C1	Simple recuperative Brayton cycle	SRBC
C2	Simple recuperative Brayton cycle with intercooling	SRBC+IC
C3	Recompression cycle	RCBC
C4	Recompression cycle with intercooling	RCBC+IC
C5	Partial cooing cycle	PCC
C6	Partial cooing cycle with intercooling	PCC+IC
C7	Recompression-Cascade cycle	RCBC+ Cascade
C8	Recompression-Cascade cycle with intercooling	RCBC+ Cascade+ IC
C9	Transcritical CO_2 cycle	tCO_2

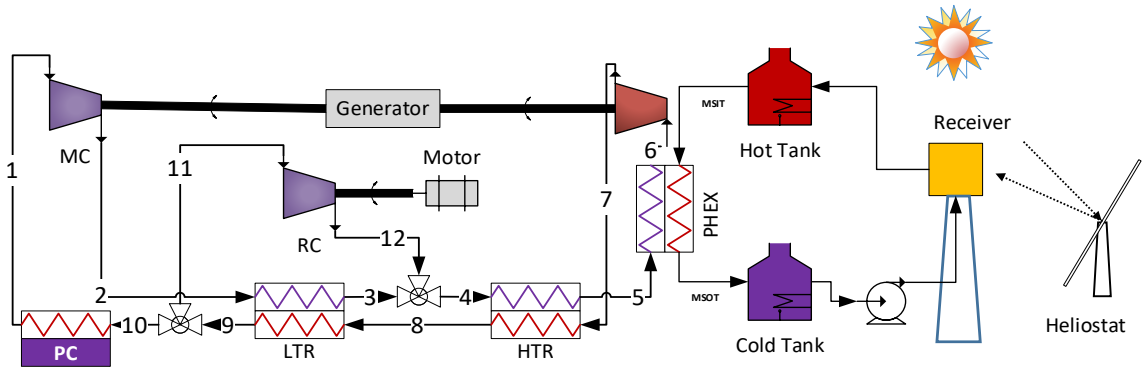

Figure 6-1 Simplified Cycle Integration Scheme with CSP and TES systems (C3 is shown as an example)

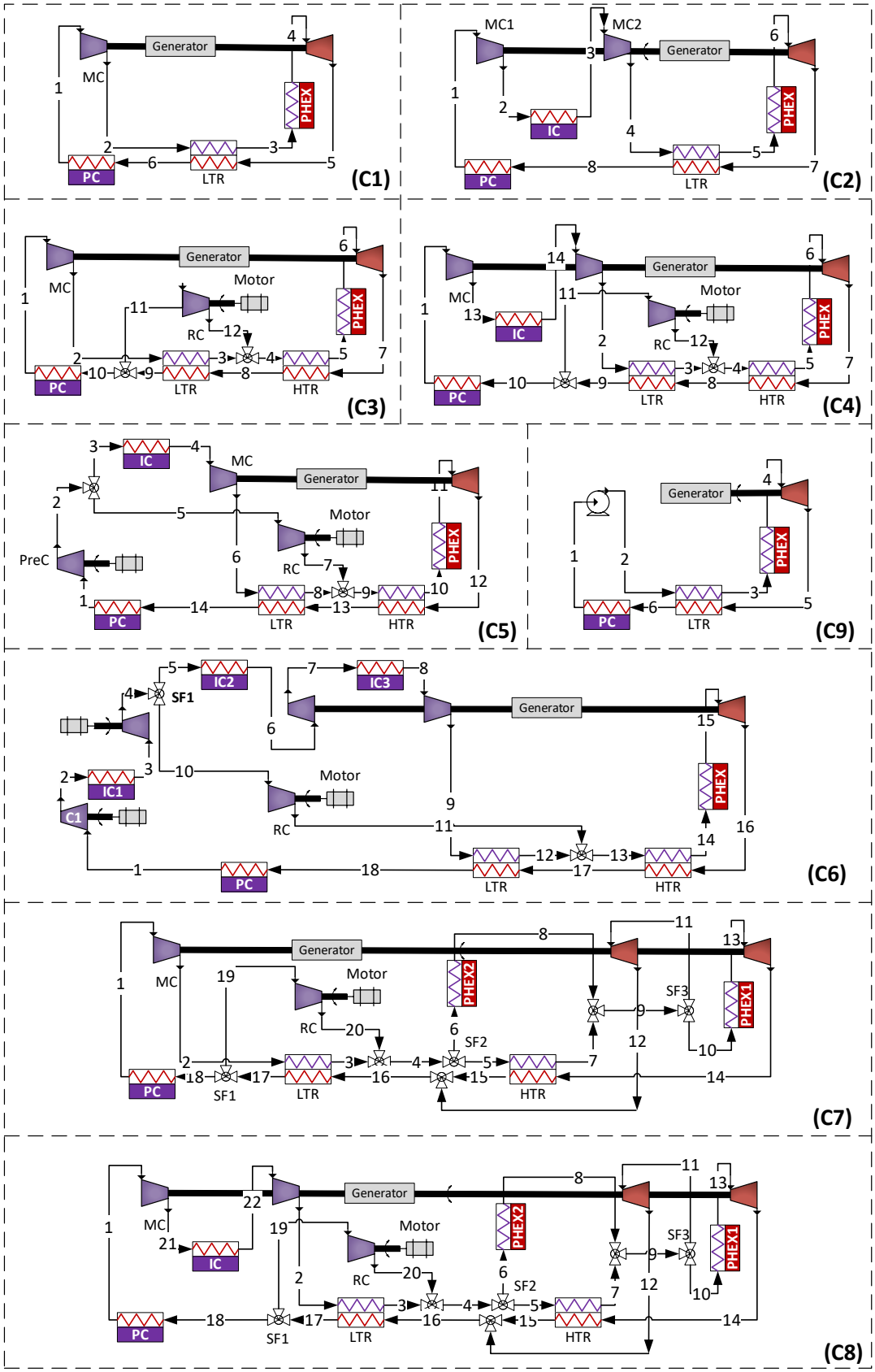

Figure 6-2 sCO_2 cycle configurations

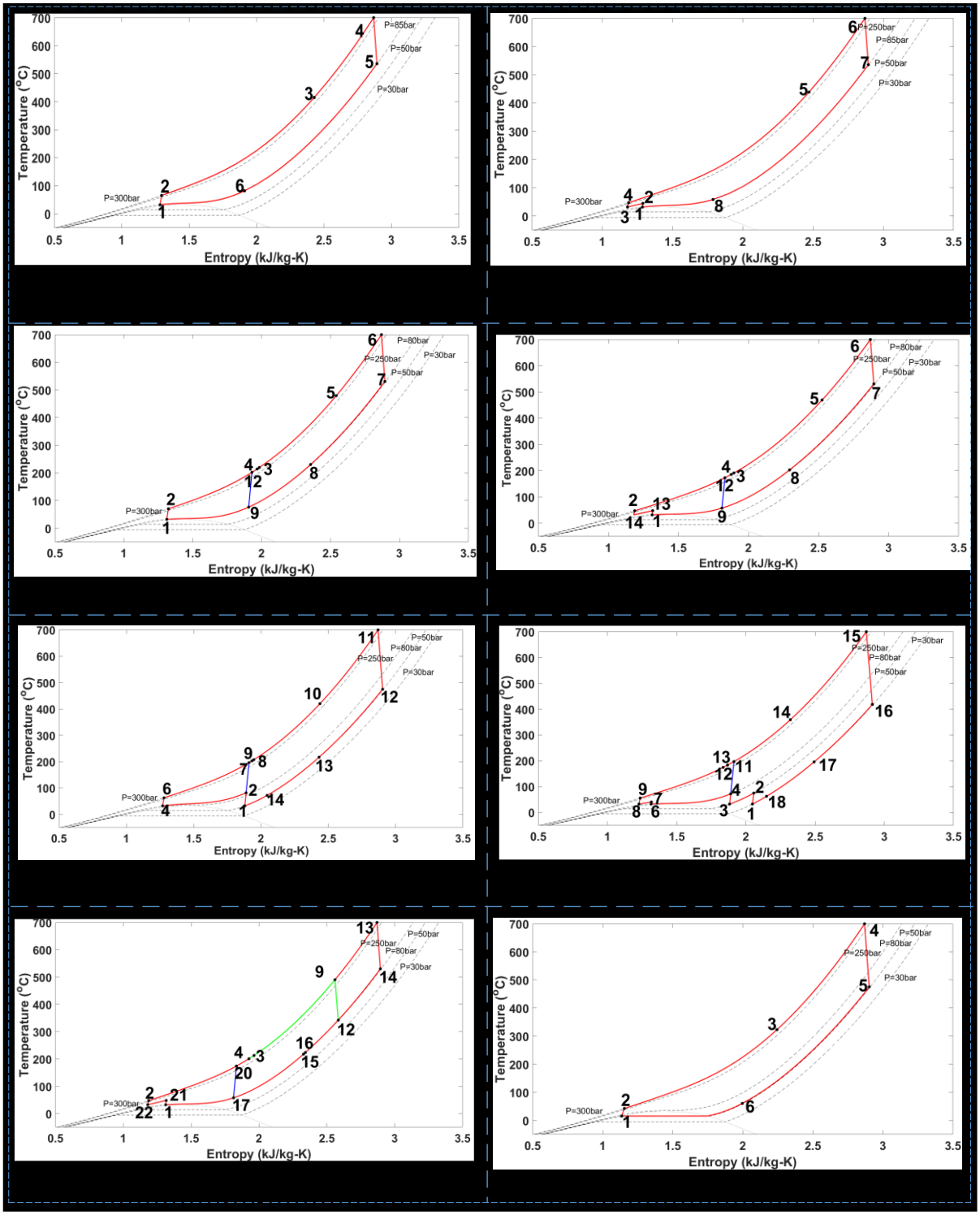

Figure 6-3 Temperature- Entropy (TS) diagrams (Except the intercooler, the TS diagram of C7 and C8 are similar, therefore excluded)

6.3 Thermodynamic Modelling

The thermodynamic models for all the process components including heat exchanger (one-dimensional), compressor/ pump, turbine, valve, splitter and mixer were developed in MATLAB®. The component models are integrated into the plant level in a flexible manner so that any plant configuration can be modelled. The plant solver guesses the tear stream values (initial guesses to the nonlinear iterative solver) and converges the solution using a non-linear iterative solver. The Newton-Raphson iterative method is implemented and Broyden algorithm is used for the calculation of the Jacobian matrix. The thermal physical properties of sCO_2 are calculated using the REFPROP library [39], which uses an iterative routine minimising Helmholtz free energy. The sCO_2 mass flow rate is adjusted to achieve the desired net power output from the plant (i.e., 50 MW_e). The molten salt mass flow rate is adjusted to match the desired pinch value in the PHEX. The cooling air mass flow is calculated using a temperature rise of 11 °C across the precooler, according to the US National Energy Technology Laboratory (NETL) base case [40]. Eutectic molten chloride salt mixture of 32% $MgCl_2$- 68% KCl (mole %) is considered as the Heat Transfer Fluid and the sensible storage medium. The thermal physical properties of the molten salt are calculated based on Xu et al. [41] and listed in Table 6-2. The choice of this mixture is motivated by the following reasons.

For a given maximum molten salt temperature, the heat addition ΔT is also constrained by the freezing point of the molten salt mixture. The freezing point of conventional solar-salt is ~270 °C which limits the heat addition ΔT to about 300 °C. Higher temperature molten salt, such as chloride salts ($MgCl_2$+KCl -32+68 mol%) has a freezing temperature of 450 °C. For 720 °C molten salt inlet temperature, the heat addition ΔT is about 250 °C. However, the freezing temperature of the chloride salts can be extended by adding $ZnCl_2$ (melting temperature is 204 °C) [42]. The melting temperature of tertiary chloride molten salt of $ZnCl_2$+KCl+NaCl (68.6+23.9+7.5 wt%) is 204 °C with a maximum stability limit of 850 °C [43], equivalent to a heat addition ΔT of about 650 °C. On the other hand, the melting temperature of liquid sodium is 98 °C with a maximum thermal stability limit of up to 883 °C which is equivalent to a heat addition ΔT of

about 785 °C [44]. The cold storage tank temperature has to be above the melting temperature value with sufficient safety margin (~50 °C [45]) in order to avoid salt freezing. Although the maximum heat addition ΔT of this molten salt is limited to ~ 250 °C owing to the higher salt freezing temperature, addition of $ZnCl_2$ can reduce the freezing temperature further. Since the aim of this study is to investigate the optimal heat addition ΔT requirement of a sCO_2 cycle when integrating with TES and CSP system, the minimum freezing temperature limitation is not implemented to compare all the cycles on an equal footing. It's worth highlighting that changing the molten salt also changes the thermal capacity of the salt (ρc_p) which impacts the storage cost and may change the absolute OCC, however, the relative comparison between the cycles still holds (Refer to Appendix-A for further details where sensitivity studies are performed).

Table 6-2 Thermal-physical properties of molten salt

Property	Unit	Function (T in °C)
Isobaric Specific Heat (C_p)	kJ/kg-K	$0.9896+1.046\times10^{-4}\times$ (T-430)
Density (ρ)	kg/m^3	$1903.7-0.552\times T$
Dynamic Viscosity (μ)	cP	$14.965-0.0291\times T+1.784\times10^{-5}\times T^2$
Thermal Conductivity (k)	W/m-K	$0.5047-0.0001\times T$
Melting Temperature (T_m)	°C	424.4

The sCO_2 turbomachinery is simulated as a zero-dimensional model based on their polytropic efficiencies (η_{poly}) as the pressure ratio varies for different cycles studied. The isentropic efficiencies (η_{isen}) are calculated by assuming infinitesimal quasi-compression/ expansion stages (100 steps). The outlet enthalpy (h_{out}) of the turbine is calculated using Eq. (6-1) and compressor is calculated using Eq. (6-2), where h_{2s} is a function of outlet pressure (P_{out}) and inlet entropy (s_{in}).

$$h_{out,turb} = h_{in,turb} - (h_{in,turb} - h_{2s,turb}) \times \eta_{isen,turb} \quad (6\text{-}1)$$

$$h_{out,comp} = h_{in,comp} + \frac{h_{2s,comp} - h_{in,comp}}{\eta_{isen,comp}} \quad (6\text{-}2)$$

The heat exchanger is a one-dimensional code in order to capture the nonlinear property variation of sCO_2 along the length of the heat exchanger (15 zones). The heat exchanger functions size the heat exchanger based on effectiveness (ϵ) using Eq. (6-3) or specifying the outlet temperature of either the hot or cold stream.

$$\epsilon = \frac{\dot{Q}}{\dot{Q}_{max}} \quad (6\text{-}3)$$

The actual amount of heat transfer (Q) is calculated from the given input of effectiveness and calculated Q_{max}. The $\dot{Q}_{max}$ is calculated based on Eq. (6-4).

$$\dot{Q}_{max} = \min(C_{cold}, C_{hot}) \times (T_{h,in} - T_{c,in}) \quad (6\text{-}4)$$

The capacitance rate of the cold stream ($C_{cold}\ in \frac{W}{K}$) is calculated based on Eq. (6-5) and a similar equation can also be applied to calculate the hot stream capacitance rate (C_{hot}).

$$C_{cold} = m_{cold} \times \frac{h_{c,in} - h_{c,out,max}}{T_{c,in} - T_{c,out,max}} \quad (6\text{-}5)$$

where the $h_{c,out,max} = f(P_{c,out}, T_{c,out,max})$ and $T_{c,out,max} = T_{h,in}$

The conductance (UA) is calculated for all the heat exchanger zones using the NTU method [46] and the total conductance is the sum of the conductance of all the zones. The heat duty of the heat exchanger is reduced if the minimum pinch temperature constraint is violated within the heat exchanger or any temperature crossover is detected.

The steady-state mass and energy conservations are applied to all components to calculate their outlet state properties from the inlet conditions. The recuperators are modelled based on effectiveness while the cooler and the primary heater are modelled based on the outlet temperature set points.

6.3.1 Modelling Assumptions

The thermodynamic assumptions for cycle modelling are tabulated in Table 6-3. The turbomachinery's mechanical losses were neglected. tCO_2 cycles are simulated using a precooler hot outlet temperature (equal to CIT) of 15 °C, to facilitate condensation, whereas all the other eight cycles are simulated for two different CIT's (32 and 55 °C) and TIT's (600 and 700 °C). All the cycle minimum, maximum and intercooler pressures, and the split fractions are optimised to maximise the objective functions. All the cycle minimum pressure, intercooler pressure and the split fractions were optimised to maximise the objective function.

Table 6-3 Thermodynamic modelling assumptions

Description	Unit	Value
Turbine polytropic Efficiency	%	90
Main Compressor polytropic Efficiency	%	89
Recompressor polytropic Efficiency	%	89
Pre-Compressor polytropic Efficiency	%	89
Recuperator Effectiveness	%	95
Recuperator minimum pinch	°C	5
High Pressure (Main Compressor Outlet)	bar	300
Precooler Outlet Temperature	°C	15,32,55 (Varied)
Turbine Inlet Temperature	°C	600,700 (Varied)
PHEX Pinch Temperature	°C	20
Pre-cooler Pinch Temperature [47]	°C	15
Intercooler Pinch Temperature [47]	°C	15
Cold side pressure drop of Precooler/Intercooler*	%	1
Hot side pressure drop of Precooler/Intercooler*	%	0.5
Cold side pressure drop of Primary Heat Exchanger*	%	0.5
Hot side pressure drop of Primary Heat Exchanger*	%	1
Cold side pressure drop of Recuperator*	%	0.5
Hot side pressure drop of Recuperator*	%	1

*- the pressure drops are applied per heat excahnger

6.3.2 Solar Field

The solar field is designed for a 50 MWe plant using System Advisory Model (SAM V2018.11.11) for the selected location of Daggett, California. The design parameters are listed in Table 6-4. The heliostat field layout, tower height and receiver dimensions are optimised in SAM to evaluate the cost of heliostat field, tower and receiver as a function of power cycle efficiency. The solar multiple is

defined as $\frac{Thermal\ capacity_{solar}}{Thermal\ input_{power\ block}}$. Ten hours of TES is considered, which is considered as the default optimal storage in SAM.

Table 6-4 Solar field model assumptions for costs estimation *[5]*

Performance factors	Unit	Value	Performance factors	Unit	Value
Solar Multiple	-	2.4	TES Storage Hours	Hrs.	10
Heliostat Field Cost *[5]*	$/m^2	140	Design DNI	W/m^2	950
Site Improvement cost	$/m^2	16	Location	-	Daggett,California
Land cost	$/Acre	10,000	Gross to Net Power Conversion Factor	-	0.9

6.4 Multi-Objective Optimisation

A multi-objective optimisation was performed to explore the complete Pareto front for changes in the boundary conditions so that a techno-economical optimal solution can be envisaged. A Non-dominated Sorting Genetic Algorithm (NSGA-II) [48] is used which maximises the net efficiency and heat addition ΔT by optimising the power cycle process variables including pressure(s) and split fractions. Table 6-5 shows the optimisation parameters and their ranges used for each of the eight sCO_2 cycles, obtained from a set of initial runs with the objective of capturing the complete Pareto front. The minimum/maximum bounds were adjusted if a variable reached proximate to the bound in the Pareto front. The minimum pressure of transcritical CO_2 cycle (C9) is not optimised as it is dictated by the precooler outlet temperature to ensure condensation (51 bar is used in this work).

Multi-objective optimisation considers many objective functions simultaneously subject to equality and non-equality constraints. An individual X(a) is said to be a dominant solution if X(a) is better than other solutions in all objective functions or X(a) is strictly better than other solutions in at least one objective subjected to the constraints [49]. A non-dominated sorting genetic algorithm (NSGA II) was coded in MATLAB® [50–52] to perform the optimisation study and the flowchart of the code is shown in Figure 6-4. The number of population and the number of generations are selected between 15-25 times the numbers of variables to ensure global convergence.

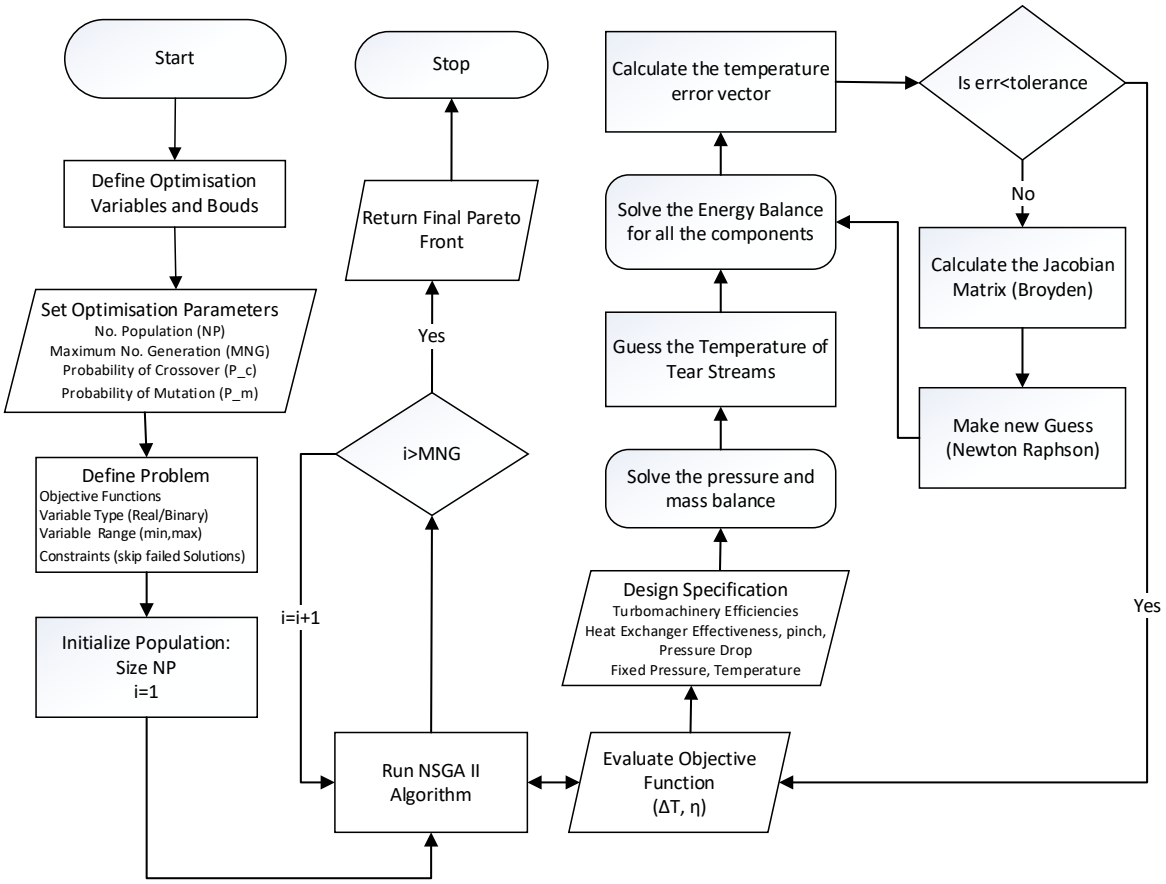

Figure 6-4 NSGA II Algorithm flowchart used in this study

Table 6-5 Variable ranges of parameters considered in optimisation

Parameters	Unit	Bounds	C1	C2	C3	C4	C5	C6	C7	C8
Minimum Pressure	bar	Lower	75	75	75	75	50	30	75	75
		Upper	120	120	90	90	50	50	120	120
Split Fraction to Recompressor (SF1)	-	Lower	-	-	0.15	0.15	0.2	0.2	0.1	0.1
		Upper			0.45	0.45	0.55	0.55	0.5	0.5
Main Compressor intercooler inlet Pressure	bar	Lower		90	-	90	-	120	-	120
		Upper		170		170		170		170
Split Fraction to PHEX2 (SF2)	-	Lower		-		-		-	0	0
		Upper							0.7	0.7

Split Fraction to LT turbine (SF3)	-	Lower			0	0
		Upper			0.7	0.7
Pre-compressor intercooler inlet Pressure	bar	Lower		30	-	-
		Upper		50		
Pre-compressor Outlet Pressure	bar	Lower	75	75		
		Upper	120	120		

6.5 Economic Modelling

6.5.1 Solar Field Cost

The solar field cost depends on the thermal rating of the field, calculated using Eq. (6-6), and for a given solar multiple and power output it is a function of the power cycle efficiency (η_{PB}). The energy incident on the receiver can be calculated using Eq. (6-7) accounting for the receiver efficiency using Eq. (6-8) [53]. The absorptivity (α), emissivity (ϵ), view factor (F_{view}), convection factor (f_{conv}), convective coefficient (h), concentration ratio (C), field efficiency (η_{field}) are obtained from Ho and Iverson [53] for calculation of the scaling factor. The receiver cost is calculated from Eq. (6-9) and the tower cost is calculated using Eq. (6-10). Scaling exponents of 0.7 and 0.0113 are used to calculate the cost of the solar receiver and the tower, respectively. The plant geometry parameters such as number of heliostats, tower height, receiver height and diameter, and heliostat height are calculated using SAM by performing optical simulation. A solar multiple of 2.4 and 10 hrs storage hours of are assumed for this study. The variation of tower, receiver and heliostat cost for a 50 MW_e plant calculated for different power block efficiency are presented in Figure 6-5.

$$Capacity_{thermal} = Solar\ Multiple \times \frac{Net\ Power}{\eta_{PB}} \quad (6\text{-}6)$$

$$Capacity_{incident} = Capacity_{thermal} \times \frac{1}{\eta_{receiver}} \quad (6\text{-}7)$$

$$\eta_{receiver} = \alpha - \frac{\left(\epsilon\sigma F_{view} T_r^4 + f_{conv} h (T_r - T_{amb})\right)}{CI_{DNI}\eta_{field}} \quad (6\text{-}8)$$

$$Cost_{Receiver} = Cost_{reference} \times \left(\frac{Area_{Receiver}}{Area_{reference}}\right)^{scailng\ exponent} \quad (6\text{-}9)$$

$$Cost_{Tower} = Cost_{fixed} \times e^{scailng\ exponent \times \left(\frac{Height_{Tower}+Height_{Receiver}}{2} + \frac{Height_{Heliostat}}{2}\right)} \quad (6\text{-}10)$$

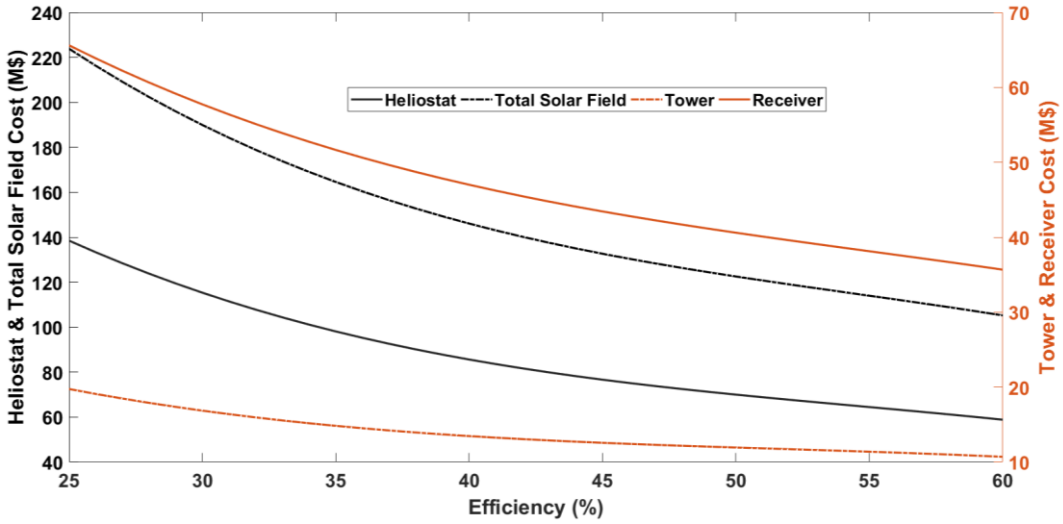

Figure 6-5 Solar field cost breakdown for different power cycle efficiency

This enables calculation of the total cost of solar field (heliostat + tower + receiver) for different power cycle efficiencies. The receiver cost is multiplied by a factor of 1.3 when the receiver operating temperature is elevated from 620 to 720 °C, to consider the change in material and a higher risk of developing high-temperature receiver [13]. The receiver efficiency reduces as the receiver temperature (T_r) changes from 620 to 720 °C due to the increase of the convective and radiation losses. This is incorporated in the calculation of the capacity by Eq. (6-7), which also impacts the heliostat field size.

6.5.2 Thermal Energy Storage Cost

The cost of thermal energy storage is scaled from the reference Abengoa® plant data provided in Mehos et al. [42]. The hot tank cost, cold tank cost, structural cost, insulation cost, electrical accessories, foundation cost, and cost related to site work, are scaled with an exponent of 0.8 [42]. A reference tank volume of 30,000 m^3 is used for scaling with an exponential scaling factor for the molten salt inventory cost of one. Since the reported cost values are for a 550 °C hot tank temperature, a correction factor has been applied to include the change in the cost owing to high-temperature materials (Table 6-6). The storage inventory is calculated based on Eq. (6-11) from which the volume of the tank can be calculated, knowing the molten salt density (ρ). During tank volume calculation, 10% is added as a pump safety height and another 10% added as the drain volume to the tank. A molten salt unit cost of 350$/t is used [42]. It can be seen that the cost of the TES system depends on power cycle efficiency (η_{PB}), and heat addition ΔT according to Eq. (6-11) as they affect the molten salt storage inventory, which affects the inventory cost and tank size. The cost variation of TES with power cycle efficiency at different heat addition ΔT is shown as Figure 6-6.

$$Mass_{TES} = Hrs_{TES} \times \frac{Net\ Power * 3600}{\eta_{PB} * c_p(T_{hot} - T_{cold})} \quad (6\text{-}11)$$

Table 6-6 Cost scaling factor for different tank temperatures

Component	Temperature- 620 °C [54]	Temperature- 720 °C [42]
Hot Tank	1.23	6.6
Cold Tank	1.11	2.3

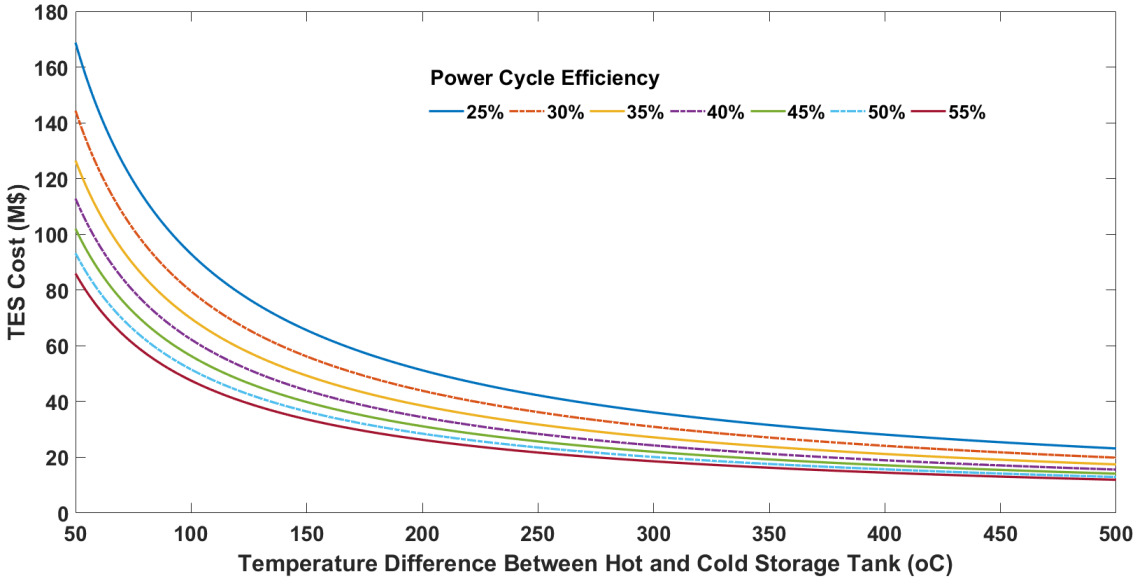

Figure 6-6 Cost of sensible heat storage system for different power cycle efficiency and temperature difference between hot and cold tank

6.5.3 Power Block Cost

The cost functions of the power block components are listed in Table 6-7. Since no standard cost data is currently available for primary heat exchangers (molten salt to sCO_2) for CSP applications, the cost function derived from the ESDU database is adapted [55]. However, the cost scaling factor for temperature is applied from Weiland et al. [56]. The installation cost for a PCHE type primary heat exchanger is expected to be similar to the recuperators owing to its modularity, therefore the same values were assumed. The C^*, which enforces the asymptote changes in the cost at a larger UA, is calculated using Eq. (6-12) [55]. The pump cost is calculated based on Couper et al. [57] and stainless steel, grade 304 or 316 material is considered, consequently the F_m is taken as 2. A 20% factor is applied to the overall CAPEX to account piping cost (10%), and balance of plant (BOP) cost (10%). The contingency and owners' cost are not considered as they do not influence the selection of cycles.

$$C^* = e^{\left(\ln(C_1)+\frac{\ln\left(\frac{C_1}{C_2}\right)\ln\left(\frac{UA}{UA_1}\right)}{\left(\ln\left(\frac{UA_1}{UA_2}\right)\right)}\right)} \tag{6-12}$$

Table 6-7 sCO_2 cycle cost functions *[56,57]*

Component	Cost Function ($)	Scaling Factor (-)	Installation Cost Percentage (%)	
			Material	Labour
Compressor	$1{,}230{,}000 * P^{0.3992}$	NA	8	12
Pump	$F_m * F_T * C_b$	$F_T = e^{9.8849 - 1.6164 \ln(Q\sqrt{H}) + 0.083\left(\ln(Q\sqrt{H})\right)^2}$ $C_b = 3e^{8.833 - 0.6019 \ln(Q\sqrt{H}) + 0.0519\left(\ln(Q\sqrt{H})\right)^2}$ $Q\ in\ gpm, H\ in\ ft\ head$	8	12
Turbine	$182{,}600 * P^{0.5561} * f$	$f = \begin{cases} 1, & T < 550 \\ 1 + 1.106e^{-4}(T - 550)^2, & T \geq 550 \end{cases}$	8	12
Recuperator	$49.45 * UA^{0.7544} * f$	$f = \begin{cases} 1, & T < 550 \\ 1 + 0.02141(T - 550), & T \geq 550 \end{cases}$	2	3
Precooler	$32.88 * UA^{0.75}$	NA	8	12
Primary Heat Exchanger	$3.5 * C^* * UA * f$	$f = \begin{cases} 1, & T < 550 \\ 1 + 5.4e^{-5}(T - 550)^2, & T \geq 550 \end{cases}$	2	3
Gearbox	$177{,}200 * P^{0.2434}$	NA	8	12
Generator	$108{,}900 * P^{0.5463}$	NA	8	12

6.6 Comparison with Literature

Moisseytsev and Sienicki [58] reference cycle condition is used for comparison which shows the design data of 96MW_e sodium-cooled fast reactors. The sCO_2 cycle configuration is a recompression cycle (C3) and a TIT of 471.8 °C is modelled in MATLAB. Although the turbine and compressor isentropic efficiencies were not reported, they have been back calculated from the outlet temperature values stated. These resulted in efficiencies of 93.3%, 90.7% and 93.5% for the main compressor, recompressor and turbine respectively. Generator efficiency of 98.5% and a mechanical loss of 1% are considered for both turbine and compressors. The state temperature differences are matching with the literature reported values with a maximum relative percentage error of 0.2% as shown in Table 6-8.

Table 6-8 Benchmark of the supercritical recompression CO_2 (C3) cycle stream data with Moisseytsev and Sienicki *[58]*

State	Temperature (°C)			State	Temperature (°C)		
	Literature [58]	This Study	Relative Error (%)		Literature [58]	This Study	Relative Error (%)
1	32.79	32.79	-0.0	7	362.30	362.27	0.0
2	84.40	84.40	-0.0	8	190.70	190.88	-0.1
3	171.80	171.84	-0.0	9	90.20	90.41	-0.2
4	175.20	175.33	-0.1	10	90.20	90.41	-0.2
5	323.30	323.30	0.0	11	90.20	90.41	-0.2
6	471.80	471.80	0.0	12	183.80	184.04	-0.1

6.7 Results and Discussion

6.7.1 Optimal heat addition ΔT for an ideal power cycle

The power cycle efficiency can be assumed as a factor of the Carnot efficiency $(1 - \frac{T_{sink}}{T_{source}})$, where the factor is denoted as the Carnot factor [13] or exergy efficiency as this factor measures the relative cycle performance compared with the theoretical maximum Carnot efficiency accounting for the overall cycle irreversibility.

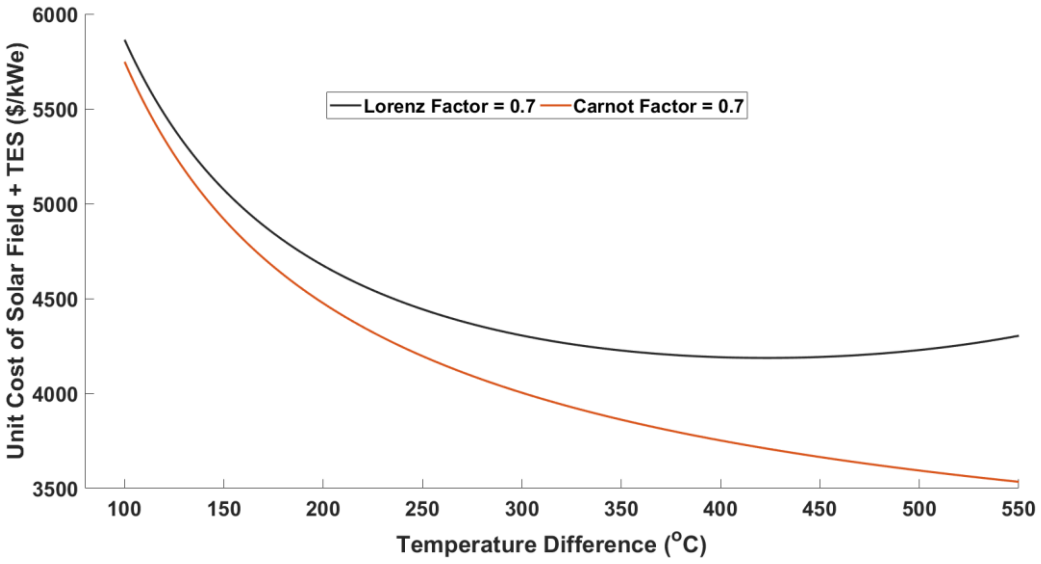

Figure 6-7 Unit cost of solar field and TES with Carnot factor of 0.7 and Lorenz factor of 0.7, SM=2.4, TES=10hrs, plant size =50 MW_e, TIT=700 °C, CIT=32 °C

Since the heat addition process is isothermal in an ideal Carnot process, the Carnot efficiency is independent of the heat addition ΔT, however, achieving the same power cycle efficiency in reality at a higher heat addition ΔT for a given maximum temperature is highly unlikely as only a small proportion of the heat is supplied at the maximum temperature. Therefore, Lorenz efficiency [59] ($1 - \frac{T_{sink}}{T_{source,avg}}$), also referred to as equivalent Carnot efficiency, calculated based on mean-effective temperature [60] is adopted in this work where the heat is added over a temperature range (heat addition ΔT). Power block efficiency is calculated using Eq. (6-13) as some fraction of the Lorenz efficiency, referred to as the Lorenz factor in this work, where the average temperature ($T_{h,avg}$) is the log-mean temperature, calculated using Eq. (6-14) [60].

$$\eta_{PB,i} = f_{LZ} \times \left(1 - \frac{T_c}{T_{h,avg}}\right) \tag{6-13}$$

$$T_{h,avg} = \frac{T_{h,in} - T_{h,out}}{\ln\left(T_{h,in}\right) - \ln\left(T_{h,out}\right)} \tag{6-14}$$

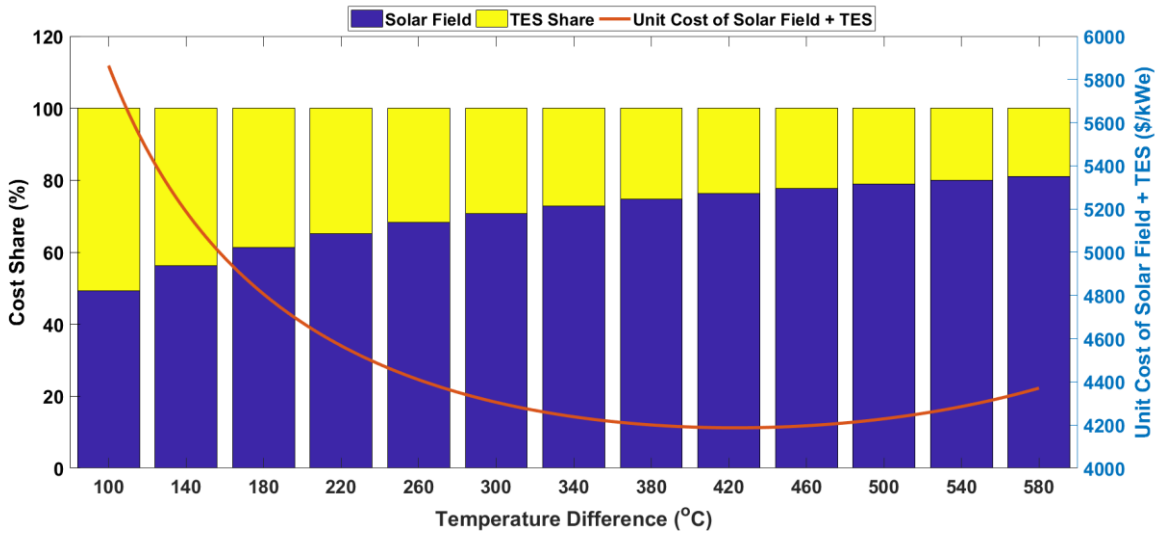

Figure 6-8 Cost Share and total unit cost of solar field + TES, Lorenz factor = 0.7, SM=2.4, TES=10hrs, plant size =50 MW_e, TIT=700 °C, CIT=32 °C

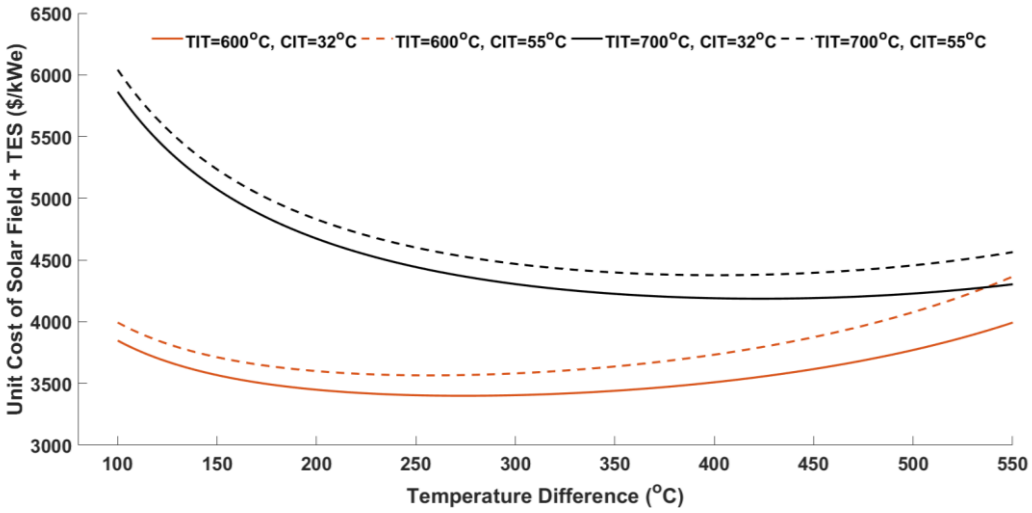

Figure 6-9 Total unit cost of solar field + TES for different CIT and TIT, Lorenz factor=0.7

Table 6-9 Optimal heat addition ΔT for different TIT and CIT

Lorenz Factor	TIT (°C)	CIT (°C)	Optimal heat addition ΔT (min bound-max bound) (°C)
0.7	600	32	274 (212-343)
0.7	600	55	257 (200-322)
0.7	700	32	423 (348-500)
0.7	700	55	401 (330-474)
0.85	600	32	286 (219-359)
0.85	600	55	270 (208-338)
0.9	700	32	436 (356-517)
0.9	700	55	416 (341-492)

*- The values within the parenthesis represent the minimum and the maximum limits where the unit cost of solar field+ TES is lower than 101% of the lowest value

The outlet temperature of the PHEX ($T_{h,out}$) is dictated by the $T_{h,in}$ and heat addition ΔT ($T_{h,in} - T_{h,out}$). The unit cost of the solar field and TES system

assuming Carnot and Lorenz factors of 0.7 are plotted in Figure 6-7 for comparison. It is clear that a fixed Carnot factor always reduces the unit cost with an increase in heat addition ΔT owing to the reduction in the TES cost as the cycle efficiency is independent of heat addition ΔT. On the other hand, assuming a fixed Lorenz factor also affects the cycle efficiency, consequently there is an optimal heat addition ΔT after which the reduction in the cost of TES is outweighed by the increase in cost due to the power cycle efficiency (Figure 6-8).

The optimum heat addition ΔT, at which the unit cost of the solar field and TES reduces, can vary depending on many factors including the cost functions, source temperature, sink temperature, Lorenz factor (efficiency), power plant size, solar multiple and storage hours. Figure 6-9 shows how the unit cost varies with heat addition ΔT for two different Lorenz factors, source and sink temperatures. Since the unit cost of the solar field and TES curve is plateaued over a large temperature difference near the minimum cost point, the range of heat addition ΔT where the cost is lower than 101% of the minimum value is shown in Table 6-9 (denoted as upper and lower bound of optimal heat addition ΔT henceforth). The ideal power cycle has to achieve the maximum efficiency proximate to the optimal heat addition ΔT in order to realise the maximum cost reduction potential for given cost functions. Increasing the Lorenz factor, which also increases the efficiency linearly for a given heat addition ΔT (Eq. (6-13), always reduces the solar field and TES system integration cost. For a power block at either the upper or lower bound optimal heat addition ΔT to reduce the minimum integration cost by 1%, necessitates either >5% power block cost reduction (assuming that the power cycle is 20% of total plant cost) to realise cost reduction at the plant level when the Lorenz factor is unaffected, or requires the Lorenz factor or efficiency to increase by >1.2% to realise cost reduction in the plant level when the power block cost is unaffected. It is clear from Table 6-9 that the heat addition ΔT has to be more than 274 °C for a TIT of 600 °C and about 423 °C for a TIT of 700 °C for a Lorenz factor of 0.7 which increases about 10 °C when the Lorenz factor increases to 0.85. It is also clear that the variation of the optimal heat addition ΔT is predominant for changes in maximum source temperature rather than changes in CIT (i.e., ambient temperature). This is because changes in TIT not only affects

the Lorenz efficiency but also increases the storage system cost more than the increase in solar field cost (receiver cost) owing to the requirement of high-temperature materials for the hot/cold tanks. Consequently, the heat addition ΔT increases further to reduce the TES system cost. Figure 6-9 shows the effect of Lorenz factor, plant size, cost function and TES size on the optimal heat addition ΔT via a sensitivity study.

The LCOE of the plant can be calculated using Eq. 6-15, where OCC and CRF refers to overnight capital cost and capital recovery rate respectively. Primarily, the OCC and capacity factor changes for different cycle and across the Pareto front. For a given capacity factor, the LCOE and OCC varies linearly, therefore the cycles are compared on the basis of OCC. It should be noted that the capacity factor of different design/cycle configuration changes [22,23]. Since the interest is relative comparison than absolute comparison [61,62], a fixed capacity factor shall be assumed

$$LCOE = \frac{OCC \times CRF + fixed\ O\&M}{8760 * capacity\ factor} + variable\ O\&M \quad (6\text{-}15)$$

6.7.2 Performance of sCO_2 cycles

6.7.2.1 Comparison of Cycles for a CIT of 32 °C and TIT of 600 °C

Figure 6-10 shows the optimal Pareto front of the nine CO_2 cycles, where net efficiency and temperature difference across the PHEX (heat addition ΔT) are maximised. Although the CIT of tCO_2 cycle (C9) is 15 °C to ensure condensation in the precooler, they are compared with other supercritical cycles at a CIT of 32 °C. It is worth highlighting that the cycle with maximum efficiency cannot yield a lower OCC when the heat addition ΔT deviates from the optimal heat addition ΔT obtained from the ideal cycle analysis (Table 6-9) unless the increased integration cost of TES and CSP from its minimum value (referred as integration penalty henceforth) is compensated by the increased cycle efficiency or reduction in the power block cost. This optimal heat addition ΔT can be obtained for a given set of cost functions of the solar field and TES (relative cost weightage of solar field and TES dictates the optimal heat addition ΔT), and the effect of changes in the Lorenz factor is negligible (~10 °C). In order to achieve the lowest cost from the

solar field and TES, the heat addition ΔT has to be around 280 °C for a CIT of 32 °C and TIT of 600 °C (Table 6-9). The optimal heat addition ΔT range listed in Table 6-9 is also plotted together with the Pareto front in Figure 6-10 to aid in selecting the optimal cycle configuration and design points in the context of reducing the cycle integration cost penalty.

The heat addition ΔT of RCBC configurations (C3) when maximising the efficiency is roughly 70 °C higher than optimal heat addition ΔT of the ideal cycle, however, it is only about 10 °C higher, when a 1% integration penalty is allowed (Table 6-9). This indicates that this cycle design can only be economically attractive if the unit cost of the power cycle is low enough (about 5% power block cost) or cycle efficiency increases by 1.2% to compensate for the increased cost from integration of TES and solar field.

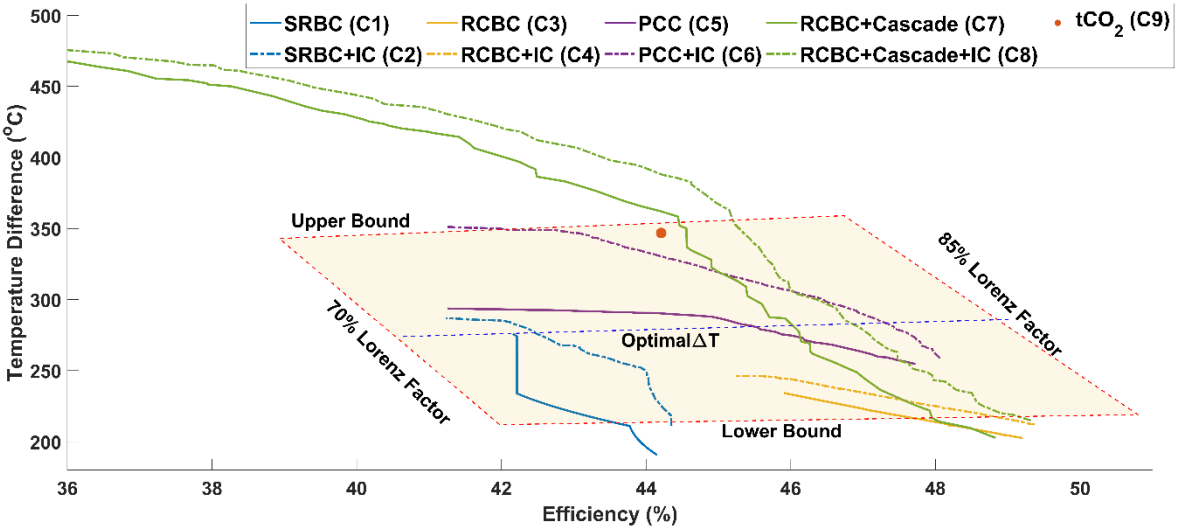

Figure 6-10 Pareto fronts obtained from NSGA-II for CIT= 32 °C and TIT= 600 °C

The heat addition ΔT approaches the optimal heat addition ΔT for C3 with a trade-off in the efficiency and this cycle efficiency penalty may be economically justified if the integration penalty is minimised by increasing the cycle heat addition ΔT. The economical optimal design point selection in the Pareto front is dictated by variation of the power cycle cost and cycle efficiency across the Pareto front. For tCO_2 cycle (C9), the heat addition ΔT is higher than the optimal heat addition ΔT by about 70 °C, which also penalizes the integration cost. All the nine cycle configurations studied fall within the 1% integration penalty range considered,

therefore the trade-off between the power block cost and the cycle efficiency dominates the selection of cycle configuration and optimal design point.

The heat addition ΔT is always higher when adding an intercooler, as expected. RCBC with intercooler configuration (C4) achieved the highest efficiency of 49.4% at a heat addition ΔT of 212.2 °C, whilst the RCBC (C3) achieved an efficiency of 49.2% at 202.6 °C. C8 and C9 are also able to achieve similar maximum efficiencies, i.e., 48.8% and 49.3% respectively, by reducing to the RCBC configuration (i.e., closing the split fraction to PHEX2 and low temperature turbine). However, the heat addition ΔT of C7 and C8 are higher than RCBC at the minimum efficiency points as they have a higher degree of freedom. These cycles also achieved higher heat addition ΔT compared to the partial cooling and tCO_2 cycles for a heat addition ΔT corresponding to the tCO_2 cycle.

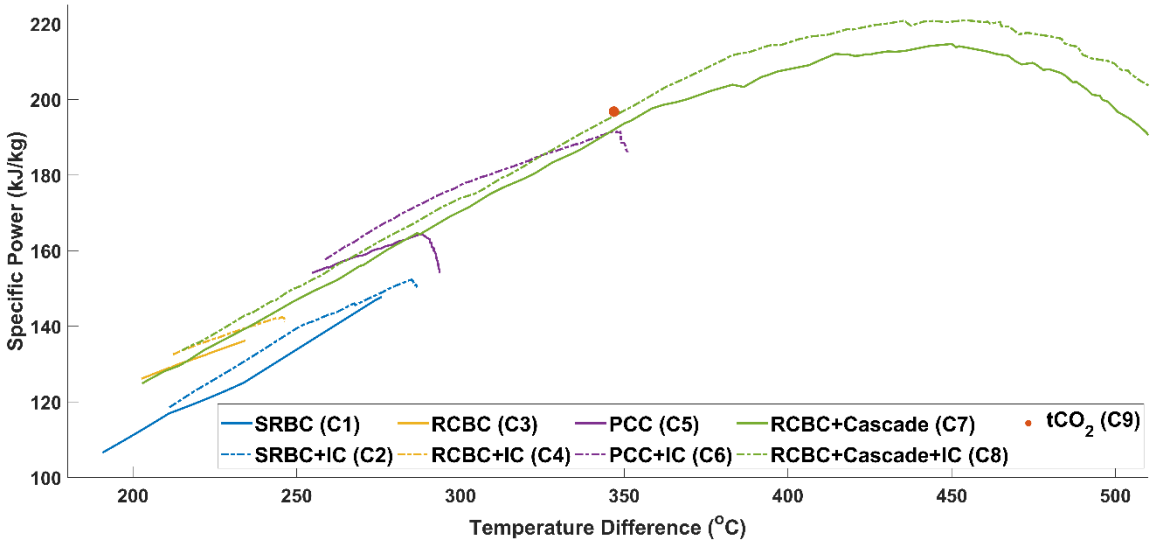

Figure 6-11 Specific Power across the Pareto front (shown in Figure 6-10) for CIT= 32 °C and TIT= 600 °C

The specific work across the Pareto front is plotted in Figure 6-11, which should be interpreted together with Figure 6-10. For example, the maximum efficiency point of a cycle in Figure 6-10 corresponds to the minimum heat addition ΔT point in Figure 6-11. It is clear that the specific work is roughly linear for SRBC (C1, C2) and RCBC (C3, C4) cycles, however, it is reduced when maximising the heat addition ΔT for partial cooling cycles (C5, C6) and RCBC+ cascade cycles (C7,

C8) due to different cycle intercooler pressure selection. For example, in partial cooing cycle (C5), maximising the specific power tends to close the split fraction and the inlet pressure of the main compressor stays close to the (pseudo) critical point to reduce the compressive work.

However, maximising the heat addition ΔT tends to achieve a lower temperature at the main compressor outlet, thus increasing the inlet pressure of the main compressor so that the increased temperature from the pre-compressor is cooled by the intercooler. In RCBC the main compressor inlet pressure stays close to the (pseudo) critical point whereas the split fraction linearly changes across the Pareto front to reduce the recompressor power requirement, achieving maximum specific power at the lowest split fraction. Addition of an intercooler extends the Pareto front towards maximum heat addition ΔT with different slope by maximising the intercooler operating pressure at the minimum split fraction so that the main compressor outlet temperature is lowered. For RCBC (C3, C4) and PCC (C5, C6), the slope is smaller than other cycles, which infers that the efficiency drop is larger to increase the heat addition ΔT.

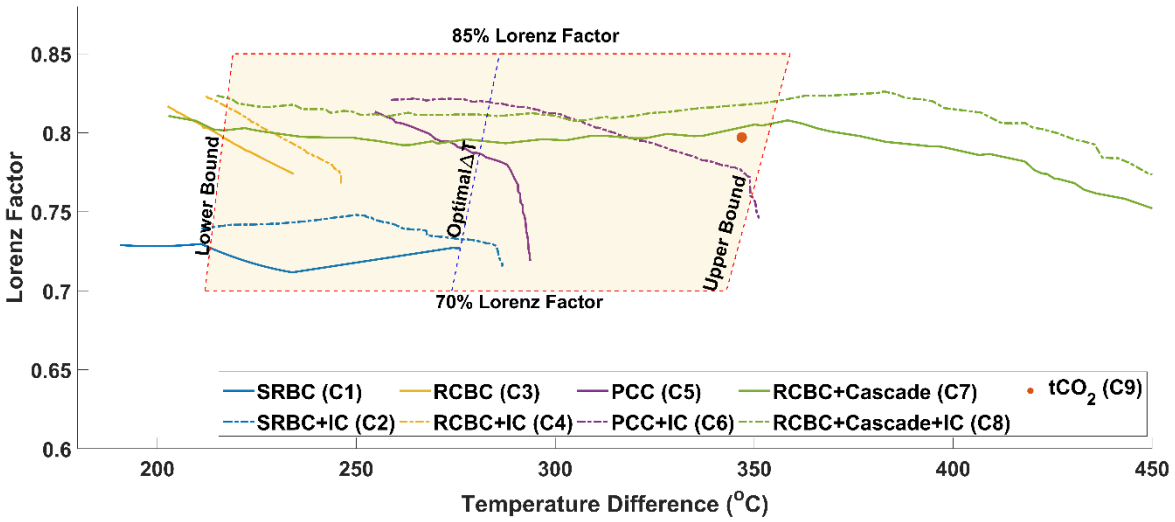

Figure 6-12 Lorenz factor across the Pareto front (shown in Figure 6-10) for CIT= 32 °C and TIT= 600 °C

The specific power plays a significant role in the cost of the power block itself. For a given power output and temperature driving force, the cost of the primary heat exchanger and cooler are dictated by the cycle efficiency, which decides the

amount of heat addition and heat rejection. On the other hand, the cost of the volumetric components including turbomachinery depend on the specific power as it reduces the required mass flow rate to achieve the same net power output. Although the maximum specific power of C7 and C8 are higher than tCO_2 cycle, the specific power of tCO_2 cycle and C8 are almost the same at the heat addition ΔT corresponding to tCO_2 cycle. This implies that the power block cost of tCO_2 cycles can be lower owing to its higher specific power with the least number of components in the cycle compared to C7 and C8.

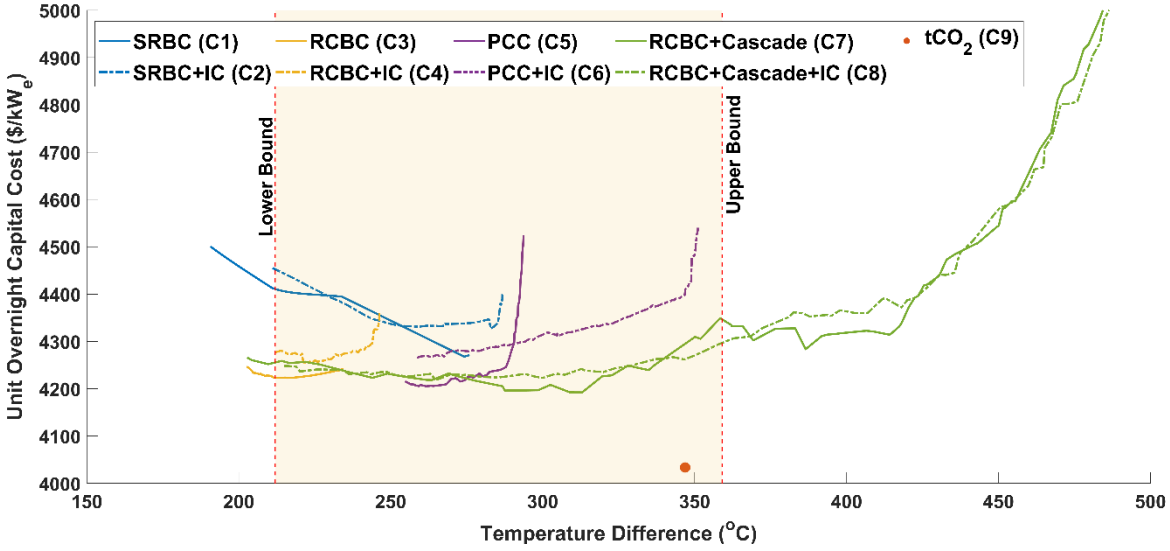

Figure 6-13 Overnight Capital Cost across the Pareto front (shown in Figure 6-10) for CIT= 32 °C and TIT= 600 °C

Figure 6-12 shows the Lorenz factor plotted across the Pareto front is shown in Figure 6-10. The Lorenz factor decreases abruptly after a certain heat addition ΔT for C4, C5, C6, C7 and C8. Maintaining an approximately flat Lorenz factor with an increase in heat addition ΔT indicates that the reduction in cycle efficiency roughly compensates for the reduction of Lorenz efficiency (Eq.(6-13)), thus the Lorenz factor is plateaued. After a certain threshold, the reduction in cycle efficiency is steeper than the changes in heat addition ΔT, which reduces the Lorenz factor steeply, and it is very unlikely to justify the increase in heat addition ΔT in this regime as the efficiency penalty is dominant. The maximum Lorenz factor of RCBC (C3, C4), and PCC (C5, C6) were higher than tCO_2 (C9) cycle at a lower heat addition ΔT. C6 Lorenz factor is lower than tCO_2 at a heat addition

ΔT corresponding to the tCO_2 cycle whilst it is slightly higher for C7 and C8 (Figure 6-12).

Figure 6-13 shows the OCC plotted across the Pareto front shown in Figure 6-10. Recompression cycles (C3, C4) and partial cooling cycles (C5, C6) achieved a lower cost proximate to the maximum efficiency point (minimum heat addition ΔT point in Figure 6-13). On the other hand, simple recuperative cycles (C1, C2) reached minimum OCC proximate to the maximum heat addition ΔT point in the Pareto front despite having lower efficiencies, where the cycle minimum pressure reaches the lower bound. This is because the Lorenz factor is not affected at higher heat addition ΔT points (Figure 6-12) for SRBC whilst RCBC and PCC are significantly penalised with increases in heat addition ΔT. For C7 and C8, the minimum OCC occurs neither at the maximum efficiency point nor at the maximum heat addition ΔT point, but it lies in-between maximum efficiency and maximum heat addition ΔT. By comparing Figure 6-12 and Figure 6-13, it can be interpreted that the increase in heat addition ΔT to reduce the OCC is favourable as long as it doesn't notably affect the Lorenz factor significantly (neglecting the variation of power block cost), although the absolute efficiency changes (Figure 6-10). The OCC of tCO_2 cycle is the lowest in comparison to all the other cycles i.e., 4.5% lower than the minimum OCC of RCBC, however, it should be noted that the additional cooling system cost in tCO_2 cycle required to achieve 15 °C at the precooler outlet is not considered here. The minimum OCC of SRBC is 1.1% higher than RCBC whilst for C8 it reduces by 0.6% compared to RCBC (C3). It is worth highlighting that comparing the cycle configurations at their maximum efficiency point can be misleading, as it will exclude the other potential cycles which have better efficiency at a heat addition ΔT closed to the optimal heat addition ΔT that minimises the integration penalty. Therefore, the cycle selection process has to also consider the heat addition ΔT and Lorenz factor to screen the cycle configurations or design points obtained from thermodynamic analysis.

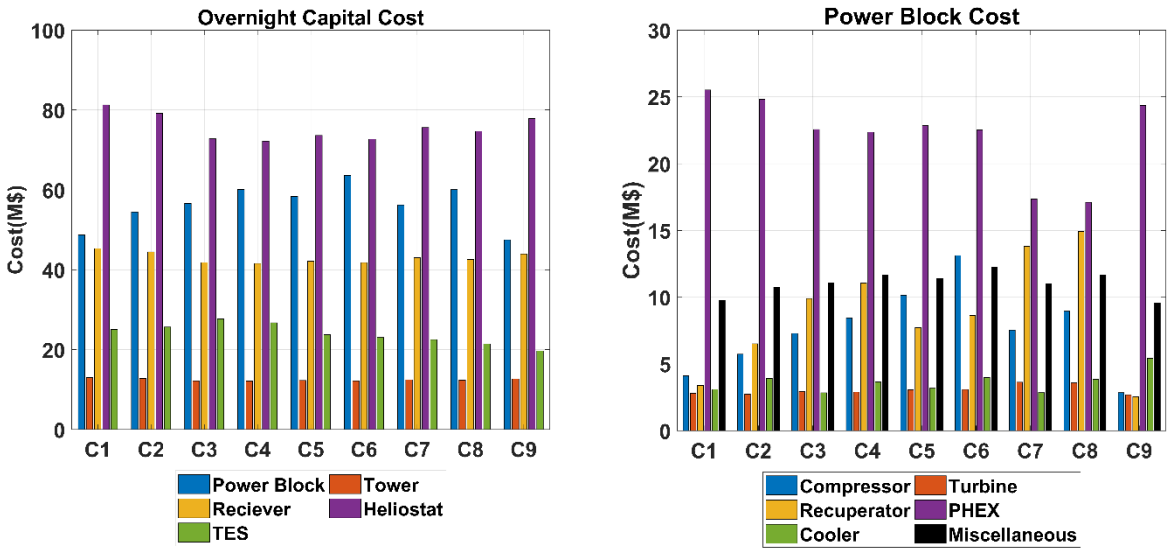

Figure 6-14 Cost breakdown for CIT= 32 °C and TIT= 600 °C at the minimum overnight capital cost point: Left) Total capital cost Right) Power block cost breakdown

The OCC and the power block cost break down at the minimum OCC point for each cycle are plotted in Figure 6-14 and their thermal and economic performances are tabulated in Table 6-10. It should be noted that the PHEX cost dominates the power block cost in all the nine cycles studied. The cost of the PHEX of C7 and C8 are lower than other cycles mainly because the heat addition (PHEX) is split into two heat exchangers and the optimisation identified roughly equal heat duty, which lowers the temperature correction (material grade requirement) of the low temperature PHEX, whilst the entire heat addition occurs in a single heat exchanger in other cycles which consequently use high-grade material. On the other hand, the recuperator cost is higher for C7 and C8 compared to other cycles primarily due to better temperature matching between hot and cold streams, which increases the conductance owing to a reduced temperature driving force. The recuperator cost of C9 is the least because not only the heat duty is lower (higher cycle pressure ratio) but also the temperature driving force is higher. Contrarily, the cooler cost is higher in C9 due to the increased heat rejection duty (cooling to 15 °C) whilst the cooler cost of other cycles without intercooler is dictated by the efficiency (i.e., heat rejection). TES cost share in the OCC is smaller than the contribution of power block and solar field, which indicates a further cost reduction mandates reducing the power block

cost (reducing the number of components and size) and increasing the cycle efficiency without deviating from the optimal heat addition ΔT requirement.

Table 6-10 Performance summary at the minimum overnight capital cost point for CIT= 32 °C and TIT= 600 °C

Parameters	Unit	C1	C2	C3	C4	C5	C6	C7	C8	C9
Net Efficiency	%	42.2	42.8	47.8	48.2	47.1	47.9	45.7	46.4	44.2
Heat addition ΔT	°C	233.9	267.8	216.1	223.3	261.6	265.1	287.5	299.9	346.9
Specific Power	kJ/kg	147.0	143.0	130.7	136.3	156.3	162.3	164.3	173.9	196.8
Lorenz Factor	%	72.7	73.2	79.8	80.8	80.6	82.2	79.3	81.1	79.7
Power Block Cost	$/kW$_e$	974	1,089	1,133	1,202	1,168	1,273	1,125	1,201	950
Overnight Capital Cost	$/kW$_e$	4,268	4,331	4,223	4,255	4,205	4,268	4,196	4,223	4,034

6.7.2.2 Comparison of Cycles for a CIT of 32 °C and TIT of 700 °C

The Pareto fronts for all the nine cycles are plotted in Figure 6-15 for a TIT of 700 °C. Although the general trends are similar to TIT 600 °C (Figure 6-10), the cycle relative positions with respect to the optimal heat addition ΔT to reduce the integration penalty is different, which can make different cycles attractive at this temperature level.

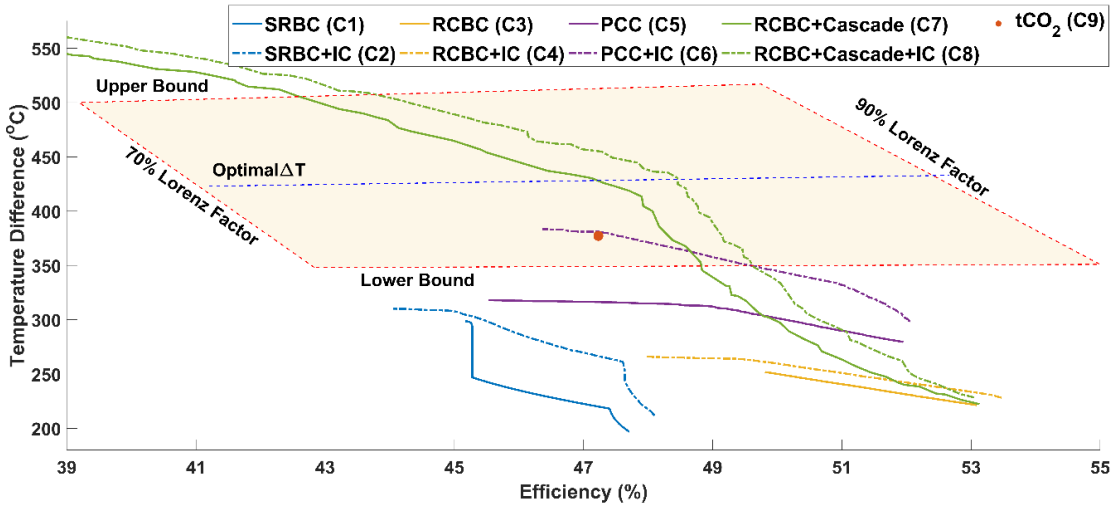

Figure 6-15 Pareto fronts obtained from NSGA-II for CIT= 32 °C and TIT= 700 °C

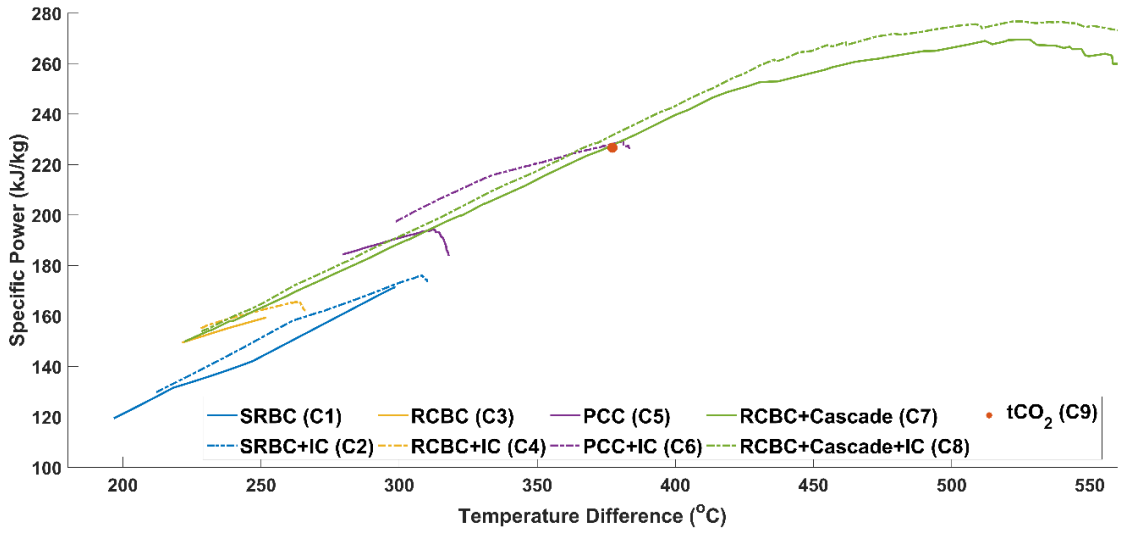

Figure 6-16 Specific Power across the Pareto front (shown in Figure 6-15) for CIT= 32 °C and TIT= 700 °C

For instance, the heat addition ΔT of the intercooled partial cooling cycle (C6) is the same as the tCO_2 cycle at the same efficiency level and both are close to the optimal heat addition ΔT. The heat addition ΔT of C7 and C8 are higher than tCO_2 cycle by 51 and 68 °C respectively at the same efficiency level. This implies that if the reduction in the integration penalty due to this increased heat addition ΔT is higher than the increased power block cost, resulting from the increased number of components, then C7 or C8 can be attractive. The optimal heat addition ΔT from an ideal cycle is around 430 °C and only C6, C7, C8 and C9 are able to achieve such heat addition ΔT values, even with a 1% integration penalty consideration. It should be noted that the power cycle efficiency is reduced to about 50% (C6 and C8) within the optimal heat addition ΔT range (intersection of heat addition ΔT lower bound with the Pareto front in Figure 6-15) although the maximum cycle itself can be up to 53.5% (C4). This implies that the higher efficiency cycles such as C4 need to overcome the integration penalty by the increased Lorenz factor and reduction in the power block cost in order to be economically attractive. Since the unit cost of TES and solar field (Figure 6-9) monotonically increased below a heat addition ΔT of about 250 °C due to increased TES cost, any cycle configurations with lower heat addition ΔT may not achieve a reduction in OCC and therefore, the cycle configurations C3 and C4 can be omitted from further analysis. Although the heat addition ΔT of C1 and C2

can be higher than ~250 °C, this is achieved at a lower efficiency point which indicates that the power cycle cost reduction is overcome by the integration penalty, which makes these cycles uncompetitive as well.

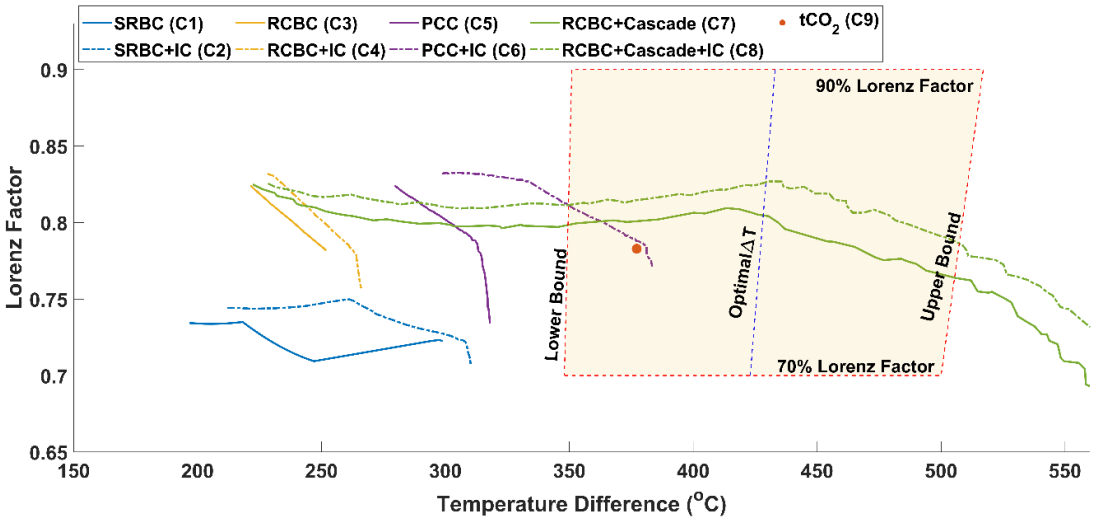

Figure 6-17 Lorenz factor across the Pareto front (shown in Figure 6- 15) for CIT= 32 °C and TIT= 700 °C

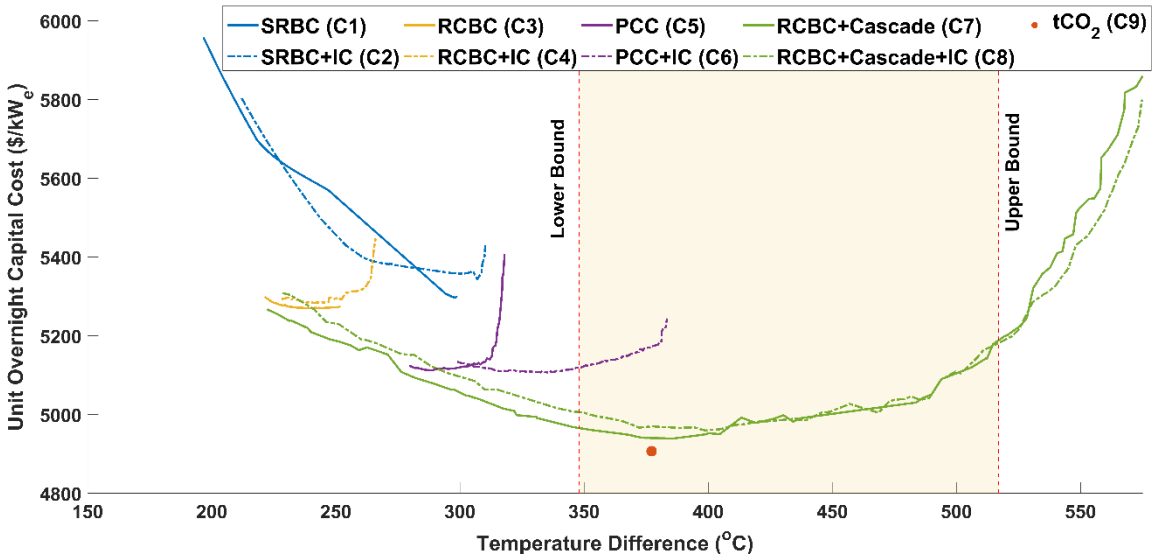

Figure 6-18 Overnight capital cost across the Pareto front (shown in Figure 6- 15) for CIT= 32 °C and TIT= 700 °C

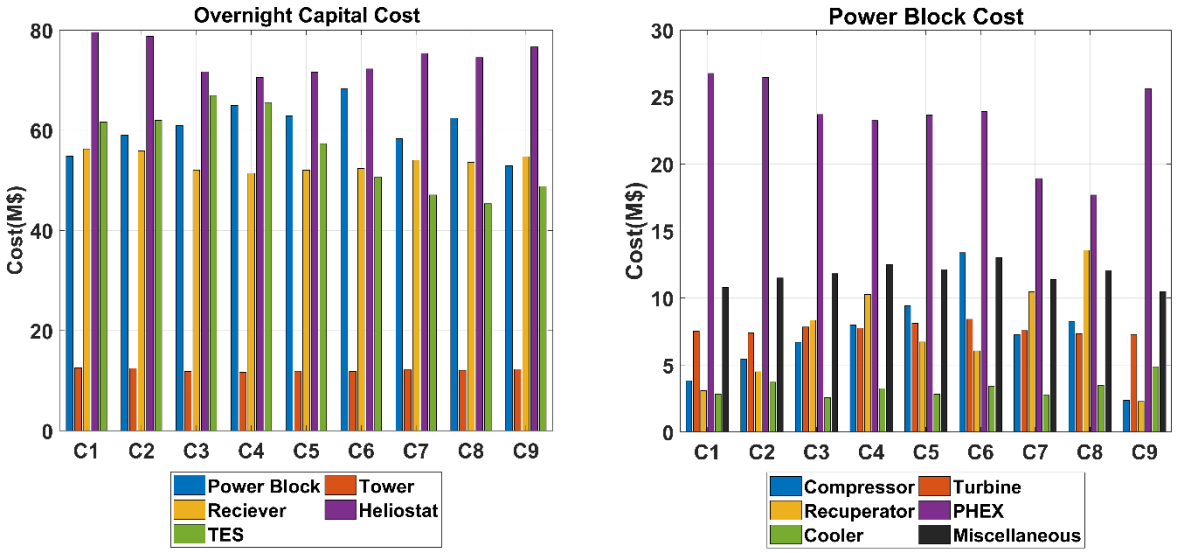

Figure 6-19 Cost breakdown for CIT= 32 °C and TIT= 700 °C at the minimum overnight capital cost point: Left) Total capital cost Right) Power block cost breakdown

Figure 6-16 shows the specific power across the Pareto front (Figure 6-15). Although the heat addition ΔT of C7 and C8 are higher than tCO_2 cycle, the specific power is roughly the same, therefore the power block cost of tCO_2 cycle may be lower owing to the lower number of components at the same heat addition ΔT point. Figure 6-17 shows the Lorenz factor across the Pareto front. C7, C8 and intercooled partial cooling cycle (C6) are higher than tCO_2 cycle, whereas the other cycles have a lower heat addition ΔT compared to the tCO_2 cycle.

The OCC is plotted in Figure 6-18 and the cost of cycles C7 and C8 are almost the same as the cost of the tCO_2 cycle. This is equivalent to an OCC reduction of 6.3% compared to the minimum cost of RCBC (C3). It is evident that the optimal economic cycle selection also depends on the maximum operating temperature as the same C7 and C8 configurations were not economically optimal for 600 °C.

Table 6-11 Performance summary at the minimum overnight capital cost point for CIT= 32 °C and TIT= 700 °C

Parameters	Unit	C1	C2	C3	C4	C5	C6	C7	C8	C9
Net Efficiency	%	45.2	45.7	51.1	52.1	51.2	51.2	48.2	48.8	47.2
Heat addition ΔT	°C	298.1	292.9	240.0	241.6	288.3	326.3	386.1	398.8	377.2

Specific Power	kJ/kg	171.2	170.1	155.7	159.9	187.2	216.8	232.1	242.5	226.7
Lorenz Factor	%	72.3	73.0	79.8	81.4	81.4	83.3	80.2	81.8	78.3
Power Block Cost	$/kW$_e$	1,097	1,180	1,219	1,300	1,257	1,365	1,167	1,248	1,059
Overnight Capital Cost	$/kW$_e$	5,297	5,363	5,270	5,284	5,113	5,108	4,939	4,960	4,907

The primary driver for this is the dramatic increase in the TES system cost in comparison with the cost of the solar field, which shifts the optimal heat addition ΔT higher. Conversely, the intercooled partial cooling cycle (C6) OCC is still 4.1% higher than that of the tCO_2 cycle. From a thermal performance perspective (Lorenz factor and heat addition ΔT), this cycle has equivalent characteristics to the tCO_2 cycle, yet the overall cost is higher due to the increase in power block cost. Although C7 and C8 layout have more components than the partial cooling cycle, their costs are equivalent to the tCO_2 cycle due to 1) increased Lorenz factor and 2) reduced power block cost. As indicated from the thermal analysis, the OCC of C1 to C5 doesn't yield the lowest OCC as their heat addition ΔT deviate significantly from the optimal heat addition ΔT and the higher power block efficiency is not sufficient to offset the integration penalty.

From Figure 6-19, it can be observed that although the increase in the molten salt inlet temperature increases the power block efficiency, which reduces the heat duty of the PHEX for a given net electric power output, the cost of the PHEX is slightly higher than the equivalent 600 °C case owing to the high temperature material correction factor. On the other hand, the cooler cost reduces in all the cycles owing to the reduced amount of heat rejection. For the same turbine shaft power, the turbine cost increases by a factor of 2.73 when the TIT increases from 600 to 700 °C. Likewise, the turbine cost of all the cycles has increased significantly (100-170% compared to 600 °C cases) despite increasing the specific power of the cycle and reducing the absolute turbine shaft power, whilst the cost of the compressor(s) is lower than 600 °C cases. Overall, the power block cost has increased by 11.5 % for C9 but it is only increased by 3.9% for C8 (Table 6-10 and Figure 6-16 shows the specific power across the Pareto front (Figure 6-15). Although the heat addition ΔT of C7 and C8 are higher than tCO2 cycle, the specific power is roughly the same, therefore the power block cost of

tCO2 cycle may be lower owing to the lower number of components at the same heat addition ΔT point. Figure 6-17 shows the Lorenz factor across the Pareto front. C7, C8 and intercooled partial cooling cycle (C6) are higher than tCO2 cycle, whereas the other cycles have a lower heat addition ΔT compared to the tCO2 cycle.

The OCC is plotted in Figure 6-18 and the cost of cycles C7 and C8 are almost the same as the cost of the tCO2 cycle. This is equivalent to an OCC reduction of 6.3% compared to the minimum cost of RCBC (C3). It is evident that the optimal economic cycle selection also depends on the maximum operating temperature as the same C7 and C8 configurations were not economically optimal for 600 °C.

*Table **6-11***). The cost of TES increased by 109.3% and 111.6% for C8 and C9, respectively. The receiver cost increased by about 25.7% with a slight reduction in the tower cost (~2.5%). The heliostat cost of C8 and C9 has not reduced with the increase in temperature from 600 to 700 °C as the increased power cycle efficiency is balanced by the increased receiver loss at a higher temperature. However, a reduction of about 2.3% is realised for C4 owing to the highest power cycle efficiency. This leads to an increase in OCC by 17.5% and 17.7% for C7 and C8, respectively. Despite increasing the cycle efficiency, increase in power cycle TIT does not offer any reduction, neither in the cost of power block nor in the OCC, instead it increased both for all the cycles studied, for example, tCO_2 cycle OCC increased by 21.7%. This suggests that 600 °C operation can be favoured purely from an economical perspective. The future developments in order to reduce the OCC should either 1) develop a novel cycle with higher efficiency proximate to the optimal heat addition ΔT without increasing the power block unit cost, or 2) reduce the cost of high temperature TES system so that the optimal heat addition ΔT requirement is reduced, in which case the integration penalty of the sCO_2 cycles can be lowered. It is worth highlighting that selection of cycle configuration based on efficiency favours C4 but the OCC at the maximum efficiency point is higher than the minimum OCC of C9 by 7.7% and

therefore, the optimal heat addition ΔT should be considered whilst selecting the cycle configuration or design point.

6.7.2.3 Comparison of Cycles for a CIT of 55 °C and TIT of 600 °C

In order to understand the effect of CIT in the cycle selection, the optimisation is repeated for a 55 °C CIT and the Pareto fronts are shown in Figure 6-20. It has to be noted that the tCO_2 cycle is not simulated as condensing CO_2 at a higher temperature demands blending fluid mixtures to increase the critical temperature, which is out of the scope of this study. The maximum cycle efficiency of all the eight cycles is reduced by the increase in CIT within a range of 3-4.3% point. The maximum efficiency of partial cooling cycles (C5, C6) is lower than C4 by 1.6% point and 1.3% point, respectively. The maximum heat addition ΔT also reduces for all the cycles as the increase in CIT also increases the cold stream inlet temperature to the recuperator, thereby increasing the cold inlet temperature of the PHEX. On the other hand, the increase in heat addition ΔT by the addition of intercooler for a CIT =55 °C is higher than the equivalent cases for a CIT of 32 °C.

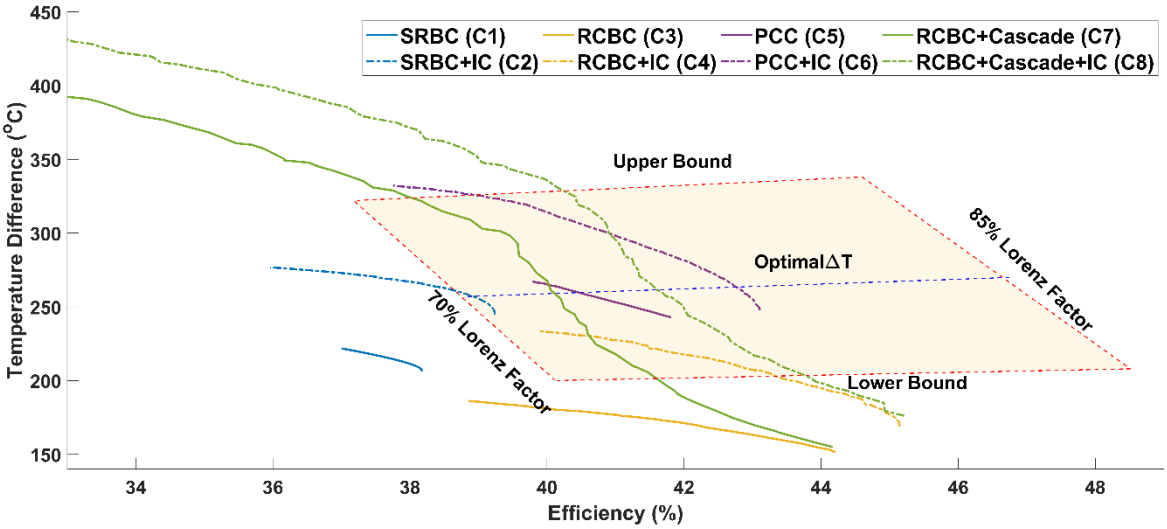

Figure 6-20 Pareto fronts obtained from NSGA-II for CIT= 55 °C and TIT= 600 °C

For example, the heat addition ΔT at the maximum efficiency point of SRBC with intercooler (C2) is higher than SRBC (C1) by 38.4 °C whereas it increased only by 20.4 °C for a CIT of 32 °C. The optimal heat addition ΔT of an ideal cycle is

around 265 °C (Table 6-9) and all of the cycle configurations except C1 and C3 are able to achieve this level of heat addition ΔT.

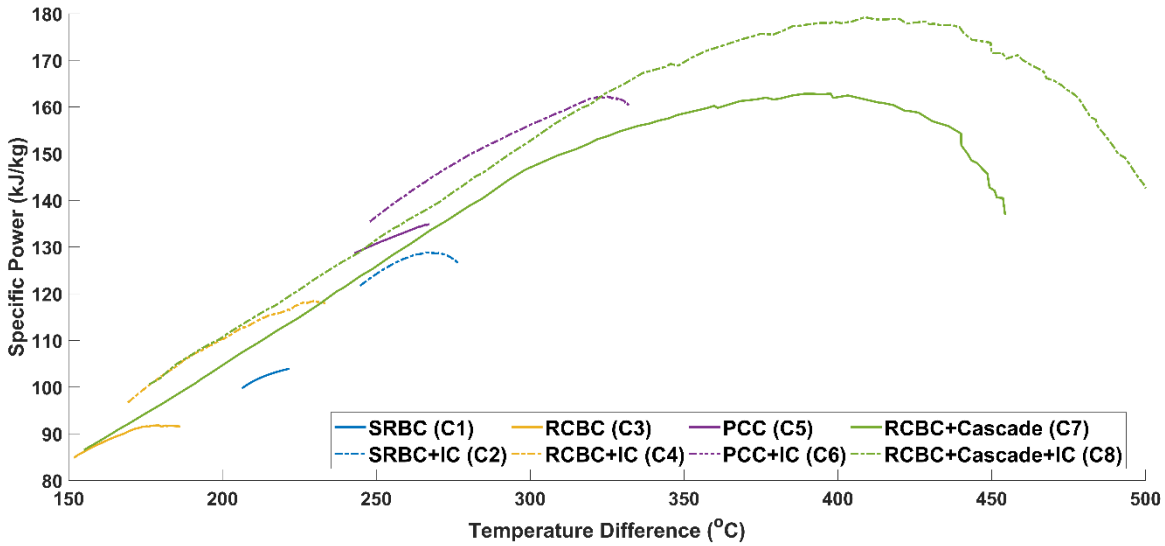

Figure 6-21 Specific Power across the Pareto front (shown in Figure 6- 20) for CIT= 55 °C and TIT= 600 °C

The heat addition ΔT of C2 is proximate to the optimal heat addition ΔT values at the maximum efficiency point, which infers that this cycle configuration can be better if the absolute lower efficiency offsets the increased solar field and TES cost. On the other hand, the heat addition ΔT of C3 is lower than the optimal heat addition ΔT, yet the higher efficiency could potentially offset the integration penalty. Therefore, all the cycle configurations except C1 can be considered for detailed investigation.

The specific work across the Pareto front is shown in Figure 6-21 and the intercooler significantly improves the specific power of the cycle. By the addition of an intercooler, the specific work increased by 24.9 kJ/kg (23.9%) at the maximum heat addition ΔT point for SRBC (C1). However, the absolute maximum specific power for a CIT=55 °C has reduced for all the cycles compared to CIT of 32 °C i.e., minimum reduction of 15.3% for partial cooling cycle with intercooling (C6) and a maximum drop of 32.6% for RCBC (C3). This is because the compressor work is increased when compressing away from the (pseudo) critical

point, reducing the specific power. The maximum specific work of C7 and C8 are 74.5 (81.1%) and 89.8 (97.9%) kJ/kg higher than BRCB (C3), respectively.

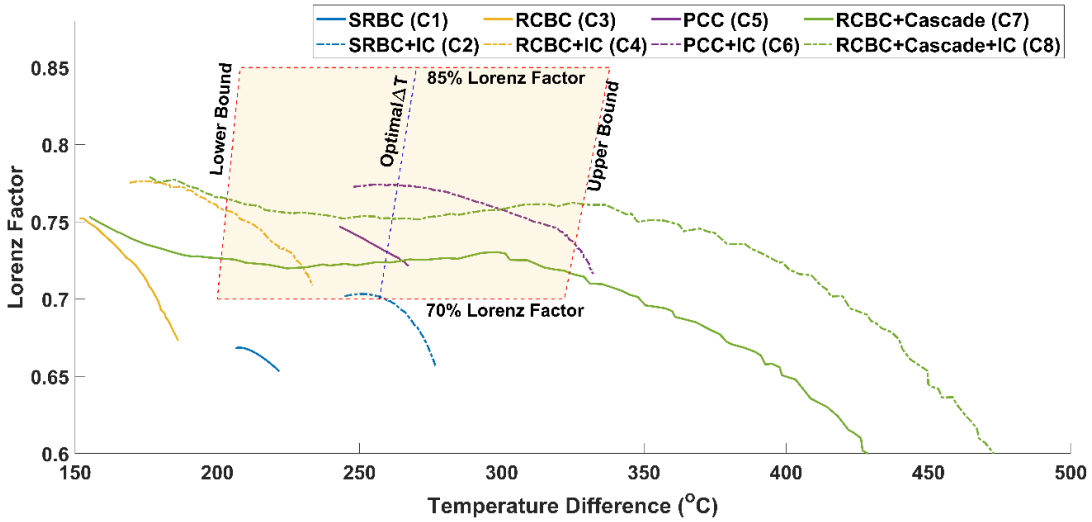

Figure 6-22 Lorenz factor across the Pareto front (shown in Figure 6- 20) for CIT= 55 °C and TIT= 600 °C

The Lorenz factor across the Pareto front is shown in Figure 6-22 and they are lower than the equivalent factors for a CIT of 32 °C owing to the lower cycle efficiency. The maximum Lorenz factor of the cycles without intercooler is reduced by about 5.7% point for C7 and 6.6% point for partial cooling cycle (C5) compared to a CIT of 32 °C. The Lorenz factor of RCBC with intercooling (C4) and partial cooling cycle with intercooling (C6) are higher than RCBC (C3) and partial cooling cycle (C5) by 2.3 and 2.6% point respectively, which accounts for the increase in efficiency due to the inclusion of an intercooler. The Lorenz factor of partial cooling cycle with intercooler (C6) reaches a higher value than C7 and C8 proximate to the optimal heat addition ΔT, which indicates that C6 will reduce the integration penalty and this cycle can be attractive if the power block unit cost is not significantly higher. Further cost reduction requires an increase in the cycle efficiency with the heat addition ΔT close to the optimal heat addition ΔT.

The OCC of all the cycles is shown in Figure 6-23 and it can be clearly seen that the addition of an intercooler with SRBC (C1), RCBC (C3), PCC (C5) and RCBC+ Cascade (C7) reduce the OCC by 3.2, 3.2, 0.3 and 2% respectively (Table 6-12), which is expected from their increased thermal performance. PCC + IC (C6) and

RCBC+ Cascade + IC (C8) show similar minimum OCC (OCC of C6 is 0.7% higher than C8) at around 257 and 261 °C heat addition ΔT respectively, therefore C6 is attractive over C8 owing to its lower complexity.

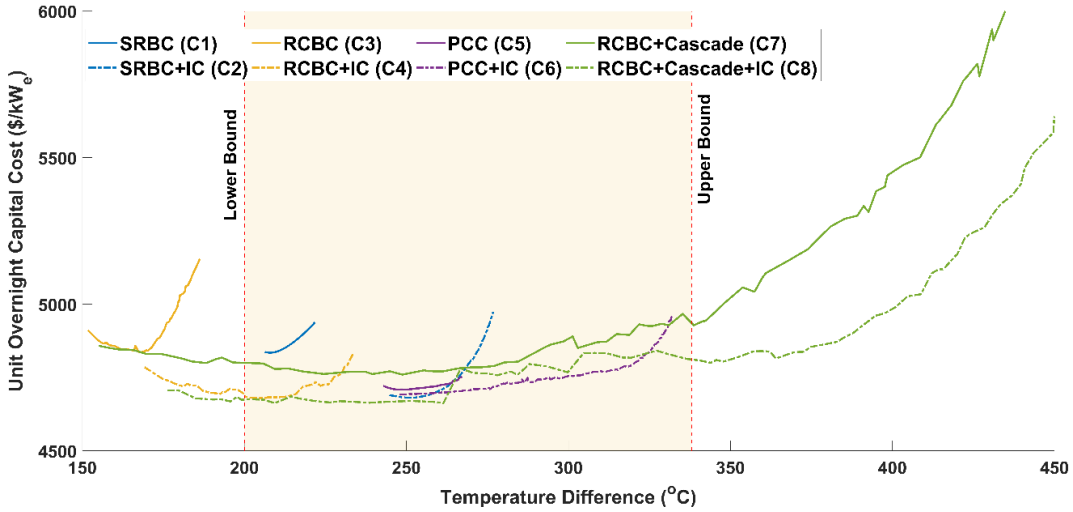

Figure 6-23 Overnight capital cost across the Pareto front (shown in Figure 6- 20) for CIT= 55 °C and TIT= 600 °C

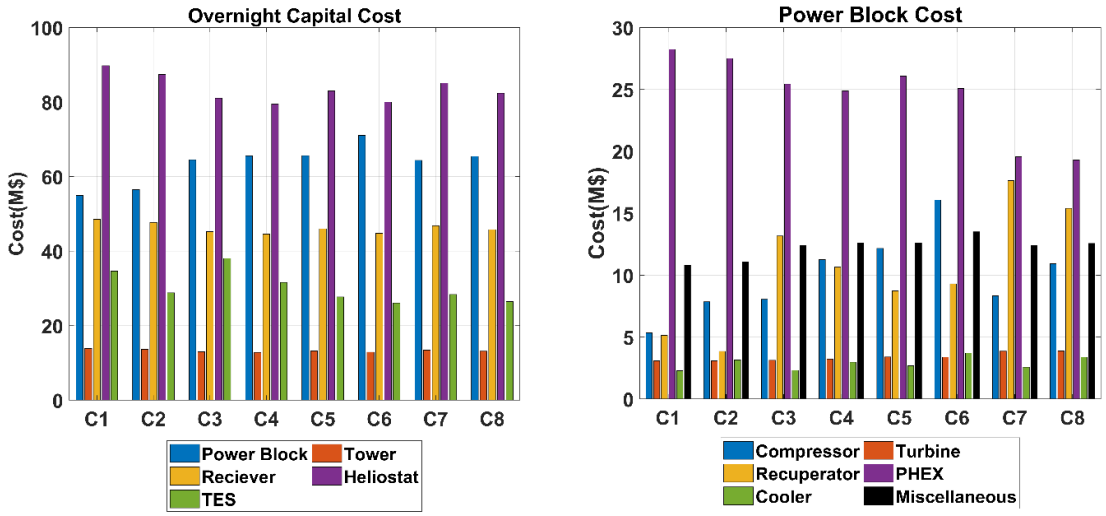

Figure 6-24 Cost breakdown for CIT= 55 °C and TIT= 600 °C at the minimum overnight capital cost point: Left) Total capital cost Right) Power block cost breakdown

It is worth highlighting that C6 was not economically attractive for a CIT of 32 °C, however, the OCC of PCC (C5), RCBC with intercooling (C4) and SRBC with intercooling (C2) also reached similar OCC as PCC +IC (C6) configuration, which indicates that the simple SRBC cycle configuration can be economically attractive

owing to its simpler configuration with a lower number of components. The reduction of efficiency with the increase in CIT from 32 to 55 °C contribute to an increase of OCC by 8.1% and 10.4% for C2 and C8 respectively.

Table 6-12 Performance summary at the minimum overnight capital cost point for CIT= 55 °C and TIT= 600 °C

Parameters	Unit	C1	C2	C3	C4	C5	C6	C7	C8
Net Efficiency	%	38.1	38.9	42.3	43.3	41.3	42.9	40.3	41.6
Heat addition ΔT	°C	209.5	257.9	168.0	204.2	249.2	257.1	248.7	261.4
Specific Power	kJ/kg	100.3	124.6	90.0	111.9	130.5	140.0	125.3	136.2
Lorenz Factor	%	66.8	69.8	72.7	75.7	74.1	77.4	72.2	75.2
Power Block Cost	$/kW$_e$	1,098	1,130	1,290	1,312	1,313	1,421	1,287	1,309
Overnight Capital Cost	$/kW$_e$	4,835	4,681	4,836	4,680	4,709	4,696	4,760	4,663

The cost break down is shown in Figure 6-24 and the performance parameters are summarised in Table 6-12. The heat duty of the PHEX and cooler have increased from their corresponding values for a CIT of 32 °C in the range of 10.6% (C1) and 14% (C5). Despite increasing the cooler heat duty, the cost of the cooler for all the eight cycles has decreased compared with a CIT of 32 °C owing to the increased temperature driving force. The compressor shaft power increases for CIT of 55 °C, which also increased the cost of the compressor for all the cycles in the range of 10.3% (C7) to 29.6% (C1). The cost of the turbine has also increased as the increased compressor shaft power (6-12.4%) is supplied from the turbine. Overall, this increases the power block cost in a range from 8.9% (C8) to 13.8% (C3) compared to a CIT 32 °C. The TES cost also increases from a minimum of 13.2% (C8) to a maximum of 38.3% (C1) due to both drop in efficiency and heat addition ΔT. The cost of the heliostat, receiver and tower also increases due to the reduced efficiency compared to a CIT of 32 °C.

6.7.2.4 Comparison of Cycles for a CIT of 55 °C and TIT of 700 °C

The Pareto fronts that maximise both efficiency and heat addition ΔT are plotted in Figure 6-25 and the corresponding specific power across the Pareto front is shown in Figure 6-26. The maximum efficiency of the cycle has increased from a minimum of 3.5% point (C1) to a maximum of 4.9% point (C5) when the TIT

increased from 600 to 700 °C. The maximum heat addition ΔT and specific power also increase when the TIT increases, however, the absolute changes in magnitude are different for each cycle. The maximum specific power increases between 18.5% to (C2) 28% (C7). The heat addition ΔT of C6, C7 and C8 lie within the 1% integration penalty bounds listed in Table 6-9 and all the other cycle configurations studied fall outside of these bounds, which infers that they suffer from the integration penalty. It is safe to neglect C1 and C2 for detailed analysis as their heat addition ΔT and efficiency are both lower and therefore highly unlikely to overcome the integration penalty solely with power block cost reduction. Similarly, C3 and C4 can be omitted as their heat addition ΔT is lower than 250 °C where the TES system cost increases monotonically (Figure 6-9) therefore, this configuration cannot offset the integration penalty. Although heat addition ΔT of C5 falls outside the 1% integration penalty lower bound, the heat addition ΔT is higher than C7 and C8 at the maximum efficiency point.

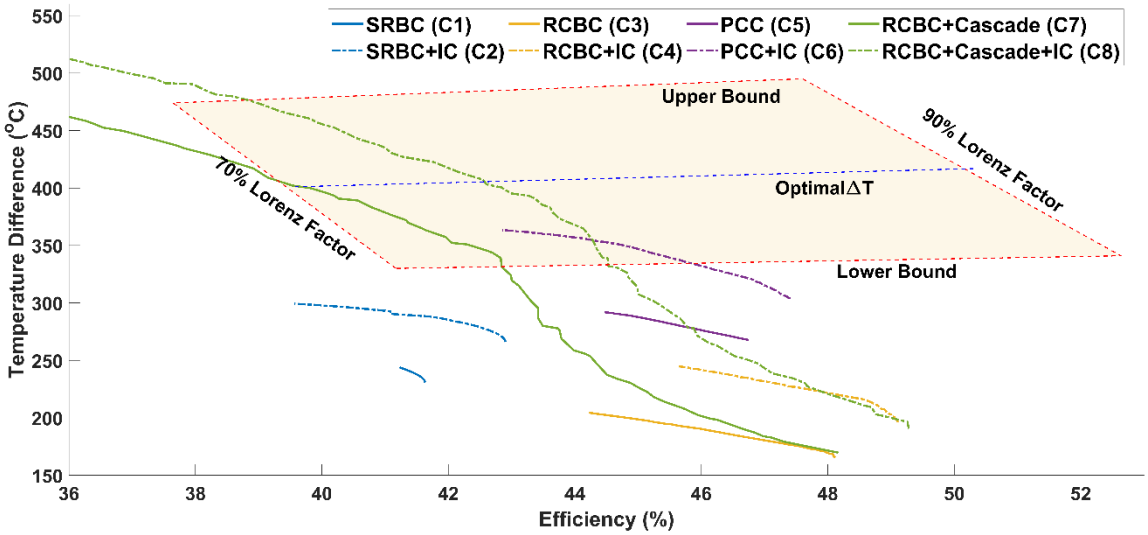

Figure 6-25 Pareto fronts obtained from NSGA-II for CIT= 55 °C and TIT= 700 °C

Furthermore, the power block cost of C5 is expected to be lower than C7 and C8 owing to the lower number of components, therefore, this should still be considered for detailed analysis. PCC+ IC (C6) achieved the highest Lorenz factor at the maximum efficiency point in comparison with all the other cycles owing to their reduced Lorenz efficiency because of higher heat addition ΔT

(Figure 6-27), however, the Lorenz factor of C8 increases when the heat addition ΔT is proximate to the optimal heat addition ΔT.

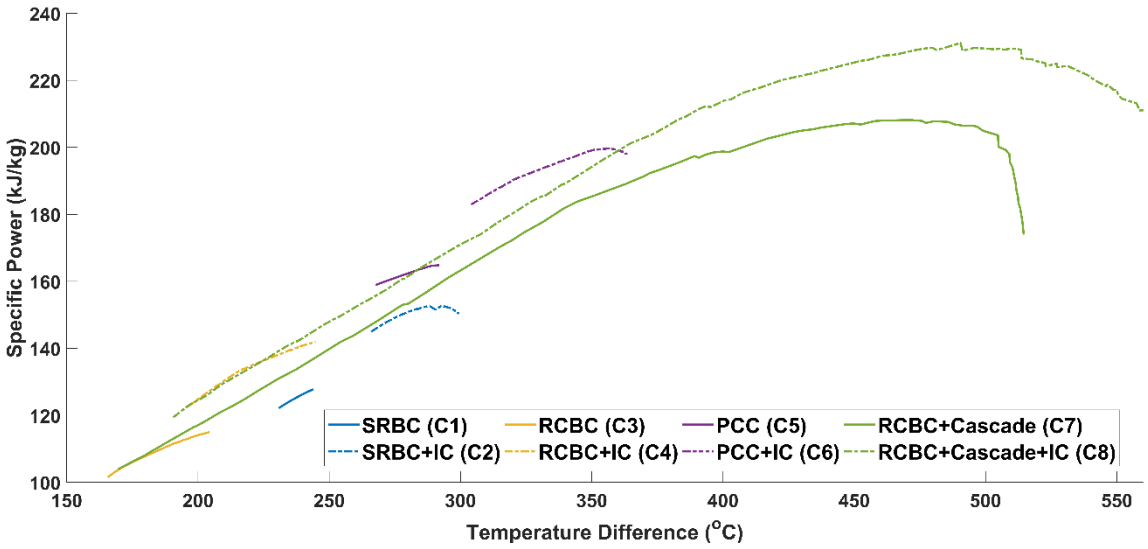

Figure 6-26 Specific Power across the Pareto front (shown in Figure 6- 25) for CIT= 55 °C and TIT= 700 °C

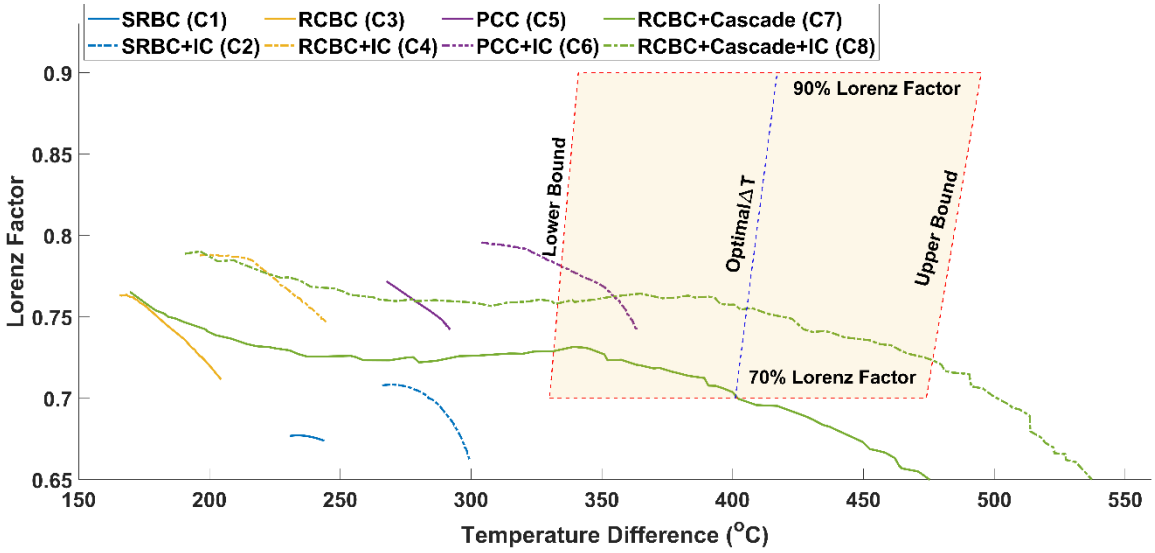

Figure 6-27 Lorenz factor across the Pareto front (shown in Figure 6- 25) for CIT= 55 °C and TIT= 700 °C

The Lorenz factor of C7 and C8 are nearly plateaued over a larger range of heat addition ΔT then start to drop-off steeply.

The optimal heat addition ΔT of an ideal cycle (Table 6-9) is about 410 °C, therefore, C6 and C8 may able to achieve higher cost reduction unless the power cycle cost of the other cycles offsets the cost penalty occurred from the solar field+ TES integration.

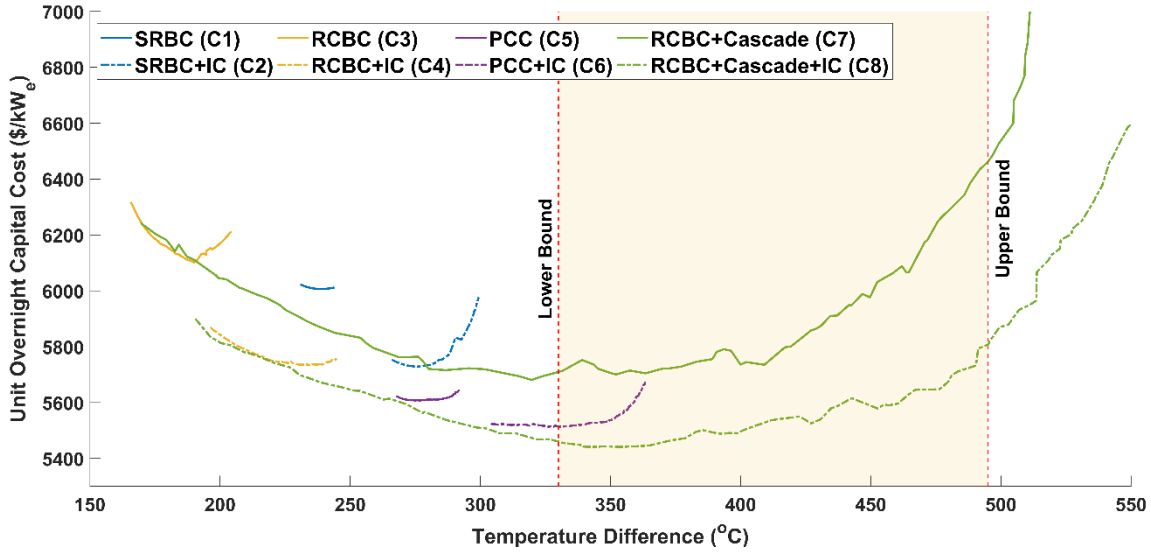

Figure 6-28 Overnight capital cost across the Pareto front (shown in Figure 6- 25) for CIT= 55 °C and TIT= 700 °C

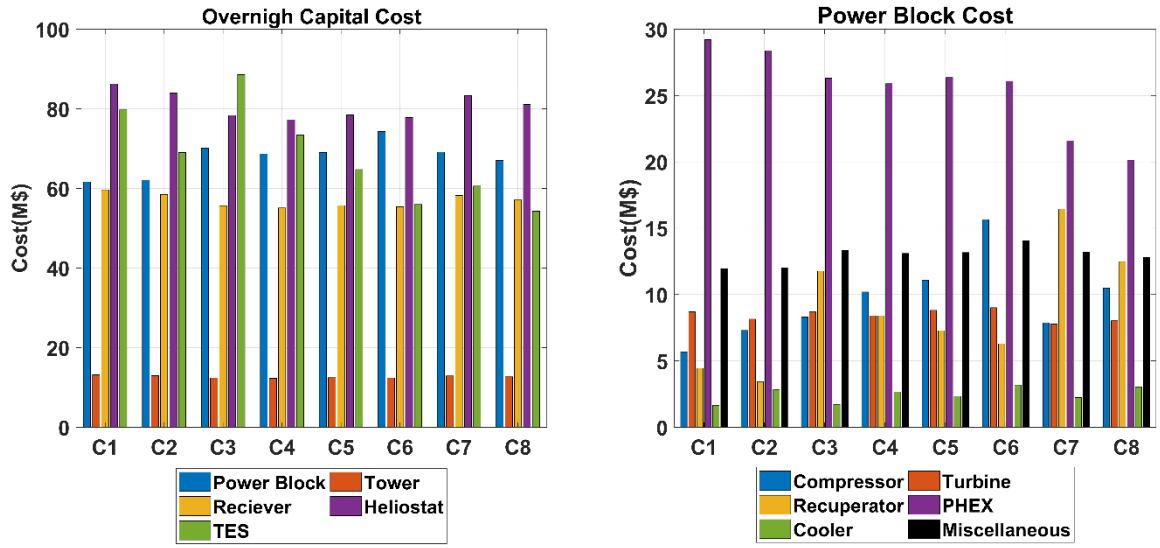

Figure 6-29 Cost breakdown for CIT= 55 °C and TIT= 700 °C at the minimum overnight capital cost point: Left) Total capital cost Right) Power block cost breakdown

The OCC across the Pareto front is shown in Figure 6-28 and C8 achieved the lowest OCC followed by C6 as expected from the thermal performance. The minimum OCC of PCC + IC (C6) is plateaued from its maximum efficiency point (minimum heat addition ΔT point in Figure 6-28) and increases when the Lorenz factor starts to reduce steeply. The minimum OCC of all the cycles has increased within the range of 16.7% (C8) to 26.2% (C2) by increasing the TIT from 600 to 700 °C at 55 °C CIT. Likewise, the OCC increases from a minimum of 6.8% (C2) to a maximum of 15% (C7) due to the increase in CIT from 32 °C to 55 °C.

Table 6-13 Performance summary at the minimum overnight capital cost point for CIT= 55 °C and TIT= 700 °C

Parameters	Unit	C1	C2	C3	C4	C5	C6	C7	C8
Net Efficiency	%	41.5	42.2	46.0	46.8	45.9	47.2	43.0	44.3
Heat addition ΔT	°C	238.7	283.4	189.9	234.4	276.9	309.1	319.7	353.9
Specific Power	kJ/kg	125.8	149.5	111.3	139.3	161.6	192.2	172.3	196.1
Lorenz Factor	%	67.6	69.9	73.7	76.1	76.2	80.1	72.7	76.3
Power Block Cost	$/kW$_e$	1,232	1,242	1,403	1,373	1,380	1,485	1,382	1,339
Overnight Capital Cost	$/kW$_e$	6,006	5,729	6,102	5,735	5,608	5,514	5,681	5,441

The cost breakdown and the performance parameters at the minimum OCC points are shown in Figure 6-29 and Table 6-13 respectively. Increasing the TIT from 600 to 700 °C also increases the cost of high temperature cycle components including PHEX and turbine. The increase in the cost of the turbine is significant, for example, the turbine cost of C8 increases by 106.8% and C6 increases by 166.1%. The cost of PHEX of all the cycles increased compared to the equivalent 600 °C cases within a range of 1.1% (C5) to 10.3% (C7). Although the increase in efficiency reduces the heat duty of the PHEX, the temperature correction factor for high grade material dominates, resulting in a net increase. The cost of the PHEX can be reduced by splitting the PHEX into two (or more) heat exchangers in series, where this results in different grade of materials. Increasing the TIT also increased the OCC for all the cycles studied with a CIT of 55 °C, which may decrease in the future when the cost of the high-grade materials become cheaper

(temperature correction factor lowers) or when the cost of high temperature TES system reduces which lowers the optimal integration heat addition ΔT.

6.7.3 Monte-Carlo Uncertainty Analysis

Since the cost function of the sCO_2 power block components are not N^{th} of a Kind (NOAK), the uncertainty of them is still larger. Therefore, an uncertainty estimation is essential in order to foresee the range of OCC with the cumulative probability to reduce the financial risk. The cost functions uncertainty is listed in Table 6-14, and Monte-Carlo uncertainty analysis is performed at the minimum OCC points of all the cycles. The total number of samples considered in each cycle OCC estimation is 10,000. The uncertainty range of commercially available components is limited to 1.1 (heliostat, tower), whereas the uncertainty upper bound of the receiver and TES are taken as 1.3 owing to the risks associated with the high temperature. The uncertainty ranges of all the cost functions of the sCO_2 cycle components reported by Weiland et al. [56] are used in this study.

Table 6-14 Component cost uncertainty ranges used in Monte-Carlo simulation

Component	Minimum	Maximum
Compressor/Pump	0.6	1.48
Turbine	0.75	1.3
PHEX	0.75	1.25
Recuperator	0.69	1.38
Cooler	0.75	1.28
Gearbox	0.85	1.2
Generator	0.81	1.23
Heliostat Field	1	1.1
Receiver	1	1.3
Tower	1	1.1
TES	0.8	1.3

From Figure 6-30, it can be seen that the tCO_2 cycle (C9) has a lower cost for a CIT of 32 °C when the TIT is 600 °C whereas the cost of C9 is tentatively similar to the cost of C7 and C8 at the higher TIT of 700 °C. For a CIT of 55 °C, intercooled SRBC (C2) is preferred from the cycles studied with the current cost function when the TIT is 600 °C owing to its simple configuration, whereas C8 is attractive followed by C6 at the higher TIT of 700 °C. It is worth highlighting that, splitting the PHEX into high-temperature and low-temperature heat exchangers with different grade materials can reduce the cost of power block, especially for a TIT of 700 °C or higher. Also, intercooled cycles reduce the cost significantly for a CIT of 55 °C compared to cycles without intercooler whilst intercooler slightly increases the cost for a CIT of 32 °C. The OCC of RCBC is the highest compared to all the other cycles studied when the TIT is 700 °C. New cycle configurations targeting a TIT of 700 °C or above that increase efficiency with the cycle heat addition ΔT around the optimal heat addition ΔT can aid in reducing the OCC. High temperature TES system cost reduction can greatly help to further reduce the OCC by minimising the requirement of optimal heat addition ΔT, so that the real benefits of higher efficient cycles can be realisable.

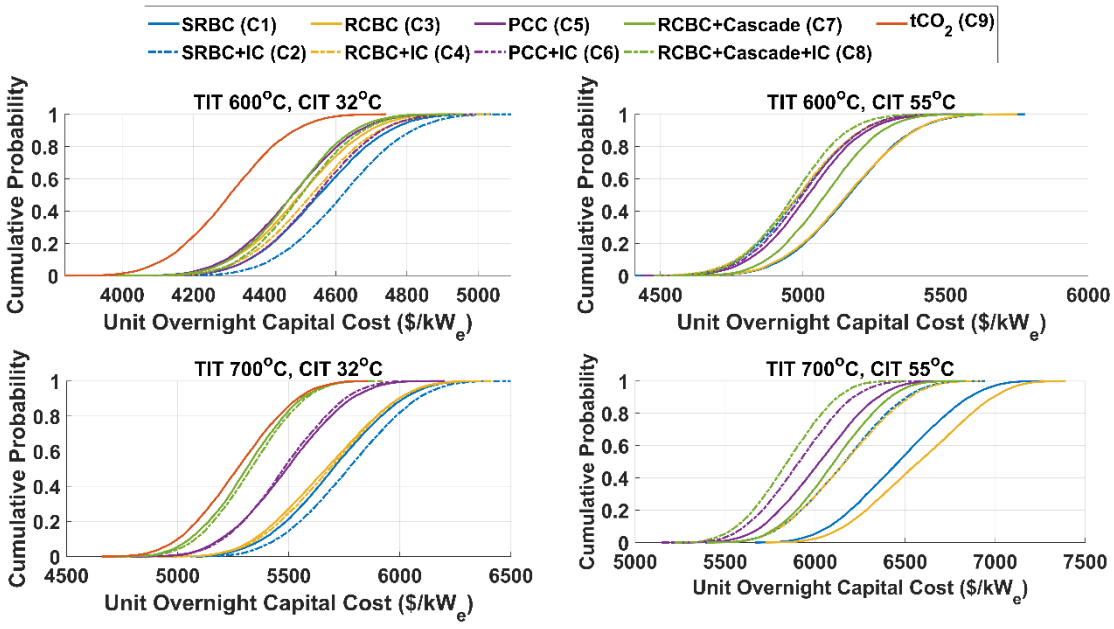

Figure 6-30 Cumulative probability distribution of overnight capital cost per kW

It is worth highlighting that the optimal heat addition ΔT listed in Table 6-10, Table 6-11, Table 6-12 and Table 6-13 are close to the corresponding minimum cumulative probability cases (Figure 6-30). This is because the minimum bound of the solar field is set to 1, which shares a significant amount of the plant OCC. Since the cumulative probability curve slope of all the cycles are approximately the same without any crossover, C9 is highly likely to remain the lowest cost cycle and C1, C2 are likely to remain the highest cost for a CIT and TIT of 32 °C and 600 °C respectively. This also implies that the cycle selection is not (or less) influenced by the variation of the power block component cost owing to their minimal weight on the OCC, or equal relative share between the cycles.

6.8 Conclusions

Selection of an optimal sCO_2 cycle for a CSP application with a two-tank TES system was performed using multi-objective optimisation and nine sCO_2 cycles including two novel cycle configurations were investigated. The optimal molten salt temperature drop (heat addition ΔT) across the primary heat exchanger (PHEX) using an ideal power cycle was defined for different boundary conditions. The optimal heat addition ΔT of an ideal power cycle for a TIT of 600 °C is about 270 °C which increases to about 420 °C when the TIT is increased to 700 °C. Power cycle efficiency alone is not the primary driver from an economic perspective, especially if the maximum cycle efficiency is achieved away from the optimal heat addition ΔT. Screening the cycle configurations based on the power cycle efficiency without considering an optimal heat addition ΔT and Lorenz factor can lead to the selection of uneconomical cycle configurations. Cycle configurations that achieve a higher or lower heat addition ΔT to the optimal heat addition ΔT need to overcome an integration penalty caused by the CSP and TES systems to become economically attractive. This can be achieved by either 1) a significant increase in power cycle efficiency, or 2) a significant reduction in the power block specific cost.

Addition of an intercooler is recommended for a CIT of 55 °C whereas this may not be economically justified for a CIT of 32 °C. Increasing the TIT from 600 to 700 °C also increased both the power block and overnight capital cost (OCC) for

both CITs of 32 °C and 55 °C. In order to realise a cost reduction for a TIT >700 °C either 1) the storage system cost must be reduced, which reduces the optimal heat addition ΔT and minimises the power block integration penalty, or 2) novel cycle configurations must be developed that achieve higher efficiency proximate to the optimal heat addition ΔT without increasing the power block cost. For a higher TIT, splitting the PHEX into two (or more) in series, where difference grade of materials can be adopted, is recommended to reduce the cost.

Among the cycle configurations investigated, the simple recuperative cycle with intercooler (C6) is attractive when the CIT is 55 °C for a TIT of 600 °C whereas the novel recompression cycle + cascade cycle with intercooler (C8) is attractive for a TIT of 700 °C. The partial cooling cycles show promising economic performance for a TIT of 700 °C compared to recompression cycle. The transcritical CO_2 (tCO_2) cycle shows high potential primarily due to its lower power block cost (fewer components and large temperature driving force in the recuperator thus reducing the recuperator cost), however, this study does not consider the additional cost of any cooling systems required to achieve the condenser outlet temperature during the hot ambient condition. A tCO_2 cycle with sCO_2 blending may be economical if it does not significantly deteriorate the cycle performance by the addition of blends.

6.9 References

[1] Musi R, Grange B, Sgouridis S, Guedez R, Armstrong P, Slocum A, et al. Techno-economic analysis of concentrated solar power plants in terms of levelized cost of electricity. AIP Conf Proc 2017;1850. doi:10.1063/1.4984552.

[2] Kuravi S, Goswami Y, Stefanakos EK, Ram M, Jotshi C, Pendyala S, et al. Thermal Energy Storage for Concentrating Solar Power Plants. Technol Innov 2012;14:81–91. doi:10.3727/194982412X13462021397570.

[3] IRENA. Renewable Energy Technologies: Cost Analysis Series - Concentrating Solar Power. vol. 1. 2012. doi:10.1016/B978-0-12-812959-3.00012-5.

[4] Mehos M, Turchi C, Vidal J, Wagner M, Ma Z, Ho C, et al. Concentrating Solar Power Gen3 Demonstration Roadmap. 2017.

[5] Mehos M, Turchi C, Jorgenson J. Advancing Concentrating Solar Power Technology, Performance, and Dispatchability. SunShot 2016:1–66. doi:10.1016/B978-0-08-087872-0.00319-X.

[6] Dostal V, Driscoll MJ, Hejzlar P. A Supercritical Carbon Dioxide Cycle for Next Generation Nuclear Reactors. 2004. doi:MIT-ANP-TR-100.

[7] Coventry J, Pye J. Heliostat cost reduction - Where to now? Energy Procedia 2013;49:60–70. doi:10.1016/j.egypro.2014.03.007.

[8] Kelly B, Kearney D. Thermal Storage Commercial Plant Design Study for a 2-Tank Indirect Molten Salt System Final Report, National Renewable Energy Laboratory (NREL) 2006:1–32.

[9] Crespi F, Gavagnin G, Sánchez D, Martínez GS. Supercritical carbon dioxide cycles for power generation: A review. Appl Energy 2017;195:152–83. doi:10.1016/j.apenergy.2017.02.048.

[10] Turchi CS, Ma Z, Neises T, Michael W. Thermodynamic Study of Advanced Supercritical Carbon Dioxide Power Cycles for High Performance Concentrating Solar Power Systems. Proc. ASME 2012 6th Int. Conf. Energy Sustain., 2012, p. 375–83. doi:10.1115/ES2012-91179.

[11] Crespi F, David S, Mart GS. Analysis of the thermodynamic potential of supercritical carbon dioxide cycles : A systematic approach. ASME Turbo Expo 2017:1–14. doi:10.1115/GT2017-64418.

[12] Angelino G. Real Gas Effects in Carbon Dioxide Cycles. ASME- Pap 69-Gt-102 1969:1–12. doi:10.1115/69-GT-102.

[13] Crespi F, Sánchez D, Sánchez T, Martínez GS. Capital Cost Assessment of Concentrated Solar Power Plants Based on Supercritical Carbon Dioxide Power Cycles. J Eng Gas Turbines Power 2019;141:1–9. doi:10.1115/1.4042304.

[14] Crespi F, Sánchez D, Rodríguez JM, Gavagnin G. A thermo-economic methodology to select sCO_2 power cycles for CSP applications. Renew Energy 2020;147:2905–12. doi:10.1016/j.renene.2018.08.023.

[15] Persichilli M, Kacludis A, Zdankiewicz E, Held T. Supercritical CO_2 Power Cycle Developments and Commercialization: Why sCO_2 can Displace Steam Steam. Power-Gen India Cent. Asia, 2012, p. 1–15.

[16] Steven WA, Tom C, Edward P, Tom L, Gary R, J S-AA. Summary of the Sandia Supercritical CO_2 Development Program. Int. SCO2 Power Cycle Symp., Boulder, Colorado: 2011.

[17] Lecompte S, Ntavou E, Tchanche B, Kosmadakis G, Pillai A, Manolakos D, et al. Review of experimental research on supercritical and transcritical thermodynamic cycles designed for heat recovery application. Appl Sci 2019;9:1–26. doi:10.3390/app9122571.

[18] Black & Veatch. Molten Salt Concept Definition & Capital Cost Estimate, Prepared for SunShot U.S. Department of Energy. 2016. doi:10.2172/1335150.

[19] Clementoni EM, Cox TL, King MA. Steady-State Power Operation Of A Supercritical Carbon Dioxide Brayton Cycle With Thermal-Hydraulic Control. ASME Turbo Expo 2016 Turbomach. Tech. Conf. Expo., Seoul, South Korea: 2016, p. 1–10. doi:10.1115/GT2016-56038.

[20] Clementoni EM, Cox TL, King MA. Off-Nominal Component Performance in a Supercritical Carbon Dioxide Brayton Cycle. J Eng Gas Turbines Power 2015;138:011703. doi:10.1115/1.4031182.

[21] Clementoni EM, Cox TL, King MA, Rahner KD. Transient power operation of a supercritical carbon dioxide Brayton cycle. ASME Turbo Expo, Charlotte, NC, USA: 2017. doi:10.1115/GT2017-63056.

[22] Thanganadar D, Fornarelli F, Camporeale S, Asfand F, Patchigolla K. Analysis of Design, Off-Design and Annual Performance Of Supercritical CO_2 Cycles For CSP Application. Proc. ASME Turbo Expo 2020, 2020.

[23] Thanganadar D, Fornarelli F, Camporeale S, Asfand F, Patchigolla K. Off-design and annual performance analysis of supercritical carbon dioxide cycle with thermal storage for CSP application. Appl Energy 2021;282:116200. doi:10.1016/j.apenergy.2020.116200.

[24] Kolb GJ, Ho CK, Mancini TR, Gary JA. Power tower technology roadmap and cost reduction plan. Conc Sol Power Data Dir an Emerg Sol Technol 2012:223–50.

[25] Ho CK, Carlson M, Garg P, Kumar P. Cost and Performance Tradeoffs of Alternative Solar-Driven S-CO2 Brayton Cycle Configurations. Proc. ASME 2015 Power Energy Convers. Conf., 2015, p. 1–10. doi:http://dx.doi.org/10.1016/j.jhydrol.2013.03.030.

[26] Spelling J, Laumert B, Fransson T. Advanced hybrid solar tower combined-cycle power plants. Energy Procedia 2014;49:1207–17. doi:10.1016/j.egypro.2014.03.130.

[27] Kusterer K, Braun R, Moritz N, Sugimoto T, Tanimura K, Bohn D. Comparative study of solar thermal brayton cycles operated with helium or argon. Proc ASME Turbo Expo 2013;4:1–9. doi:10.1115/GT2013-94990.

[28] Dunham MT, Iverson BD. High-efficiency thermodynamic power cycles for concentrated solar power systems. Renew Sustain Energy Rev 2014;30:758–70. doi:10.1016/j.rser.2013.11.010.

[29] Johnson GA, McDowell MW, O'Connor GM, Sonwane CG, Subbaraman G. Supercritical CO2 cycle development at pratt & whitney rocketdyne. Proc ASME Turbo Expo 2012;5:1015–24. doi:10.1115/GT2012-70105.

[30] Thanganadar D, Asfand F, Patchigolla K. Thermal performance and economic analysis of supercritical Carbon Dioxide cycles in combined cycle power plant. Appl Energy 2019;255:113836. doi:10.1016/j.apenergy.2019.113836.

[31] Kimzey G. Development of a Brayton Bottoming Cycle using Supercritical Carbon Dioxide as the Working Fluid. 2012.

[32] Angelino G. Carbon dioxide condensation cycles for power production. J Eng Gas Turbines Power 1968;90:287–95. doi:10.1115/1.3609190.

[33] 2020 H. Supercritical CARbon dioxide/Alternative fluids Blends for Efficiency Upgrade of Solar power plants 2019. https://cordis.europa.eu/project/id/814985 (accessed 15 May 2020).

[34] Crespi F, Sánchez D, Rodríguez JM, Gavagnin G. Fundamental Thermo-Economic Approach to Selecting sCO2 Power Cycles for CSP Applications. 4th Int. Semin. ORC Power Syst., vol. 129, 2017, p. 963–70. doi:10.1016/j.egypro.2017.09.215.

[35] Clementoni EM, Cox TL. Effect of compressor inlet pressure on cycle performance for a supercritical carbon dioxide brayton cycle. 6th Int. Supercrit. CO2 Power Cycles Symp., vol. 9, Pittsburgh, Pennsylvania: 2018, p. 2–10.

[36] Clementoni EM, Cox TL. Effect of compressor inlet pressure on cycle performance for a supercritical carbon dioxide brayton cycle. Proc. ASME Turbo Expo, vol. 9, Oslo, Norway: 2018, p. 1–8. doi:10.1115/GT2018-75182.

[37] Asfand F, Thanganadar D, Patchigolla K. Thermodynamic performance of a supercritical CO_2 cycle integrated with a recuperative absorption cooling system. ECOS 2019 - Proc. 32nd Int. Conf. Effic. Cost, Optim. Simul. Environ. Impact Energy Syst., vol. 2019- June, WROCLAW, POLAND: 2019, p. 3895–903.

[38] Hacks AJ, Schuster S, Brillert D. Stabilizing effects of supercritical CO_2 fluid properties on compressor operation. Int J Turbomachinery, Propuls Power 2019;4. doi:10.3390/ijtpp4030020.

[39] Lemmon EW, Huber ML, McLinden MO. NIST Standard Reference Database 23. Natl Inst Stand Technol 2013;V 9.1.

[40] Black JB. Cost and Performance Baseline for Fossil Energy Plants Volume 3b: Low Rank Coal to Electricity: Combustion Cases. vol. 3. 2011.

[41] Xu X, Wang X, Li P, Li Y, Hao Q, Xiao B, et al. Experimental Test of Properties of KCl–$MgCl_2$ Eutectic Molten Salt for Heat Transfer and Thermal Storage Fluid in Concentrated Solar Power Systems. J Sol Energy Eng 2018;140:051011. doi:10.1115/1.4040065.

[42] Mehos M, Turchi C, Vidal J, Wagner M, Ma Z, Ho C, et al. Concentrating Solar Power Gen3 Demonstration Roadmap. Nrel/Tp-5500-67464 2017:1–140.

[43] Vignarooban K, Xu X, Wang K, Molina EE, Li P, Gervasio D, et al. Vapor pressure and corrosivity of ternary metal-chloride molten-salt based heat transfer fluids for use in concentrating solar power systems. Appl Energy 2015;159:206–13. doi:10.1016/j.apenergy.2015.08.131.

[44] Heinzel A, Hering W, Konys J, Marocco L, Litfin K, Müller G, et al. Liquid Metals as Efficient High-Temperature Heat-Transport Fluids. Energy Technol 2017;5:1026–36. doi:10.1002/ente.201600721.

[45] Jerden J. Molten Salt Thermophysical Properties Database Development : 2019 Update. 2019. doi:10.2172/1559846.

[46] Nellis G, Klein S. Heat Transfer. 2009. doi:10.1017/CBO9780511841606.

[47] Schmitt J, Wilkes J, Bennett J, Wygant K, Pelton R. Lowering the levelized cost of electricity of a concentrating solar power tower with a supercritical carbon dioxide power cycle. ASME Turbo Expo, Charlotte, NC, USA: 2017, p. 1–10. doi:10.1115/GT2017-64958.

[48] Deb K, Pratap A, Agarwal S, Meyarivan T. A fast and elitist multiobjective genetic algorithm: NSGA-II. IEEE Trans Evol Comput 2002;6:182–97. doi:10.1109/4235.996017.

[49] Avval HB, Ahmadi P, Ghaffarizadeh AR, Saidi MH. Thermo-economic-environmental multiobjective optimization of a gas turbine power plant with preheater using evolutionary algorithm. Int J Energy Res 2010. doi:10.1002/er.1696.

[50] Rangaiah GP. Multi-Objective Optimization Techniques and Applications in Chemical Engineering. vol. 1. 2009. doi:10.1007/0-387-28356-0_10.

[51] Wong JYQ, Sharma S, Rangaiah GP. Design of shell-and-tube heat exchangers for multiple objectives using elitist non-dominated sorting genetic algorithm with termination criteria. Appl Therm Eng 2016;93:888–99. doi:10.1016/j.applthermaleng.2015.10.055.

[52] Sharma S, Rangaiah GP, Cheah KS. Multi-objective optimization using MS Excel with an application to design of a falling-film evaporator system. Food Bioprod Process 2011;90:123–34. doi:10.1016/j.fbp.2011.02.005.

[53] Ho CK, Iverson BD. Review of high-temperature central receiver designs for concentrating solar power. Renew Sustain Energy Rev 2014;29:835–46. doi:10.1016/j.rser.2013.08.099.

[54] Ma Y, Morosuk T, Luo J, Liu M, Liu J. Superstructure design and optimization on supercritical carbon dioxide cycle for application in concentrated solar power plant. Energy Convers Manag 2020;206:112290. doi:10.1016/j.enconman.2019.112290.

[55] Carlson MD, Middleton BM, Ho CK. Techno-Economic Comparison of Solar-Driven sCO_2 Brayton Cycles Using Component Cost Models Baselined With Vendor Data. Proc ASME 2017 Power Energy Conf 2017:1–7. doi:10.1115/ES2017-3590.

[56] Weiland NT, Lance BW, Pidaparti SR. SCO_2 power cycle component cost correlations from DOE data spanning multiple scales and applications. Proc. ASME Turbo Expo, vol. 9, 2019, p. 1–17. doi:10.1115/GT2019-90493.

[57] Couper JR, Penney WR, Fair JR, Walas SM. Chemical Process Equipment: Selection and Design. Third Edit. 2012. doi:10.1016/B978-0-12-396959-0.00025-2.

[58] Moisseytsev A, Sienicki JJ. Investigation of alternative layouts for the supercritical carbon dioxide Brayton cycle for a sodium-cooled fast reactor

presentsation. Nucl Eng Des 2009;239:1362–71. doi:10.1016/j.nucengdes.2009.03.017.

[59] Ennio Macchi MA. Organic Rankine Cycle (ORC) Power Systems: Technologies and Applications. 1st Editio. Woodhead Publishing; 2016.

[60] Can Gülen S, Joseph J. Combined cycle off-design performance estimation: A second-law perspective. J Eng Gas Turbines Power 2012;134:1–11. doi:10.1115/1.4004179.

[61] Neises T, Turchi C. Supercritical carbon dioxide power cycle design and configuration optimization to minimize levelized cost of energy of molten salt power towers operating at 650 °C. Sol Energy 2019;181:27–36. doi:10.1016/j.solener.2019.01.078.

[62] Ma Y, Zhang X, Liu M, Yan J, Liu J. Proposal and assessment of a novel supercritical CO2 Brayton cycle integrated with LiBr absorption chiller for concentrated solar power applications. Energy 2018;148:839–54. doi:10.1016/j.energy.2018.01.155.

Chapter 7

7 Analysis of Design, Off-Design and Annual Performance of Supercritical CO_2 Cycles for CSP Application

Dhinesh Thanganadar[a], Francesco Fornarelli[b,c], Sergio Camporeale[b], Faisal Asfand[a,d], Kumar Patchigolla[a]

[a]*School of Water, Energy and Environment (SWEE), Cranfield University, Cranfield, MK43 0AL, UK*
[b]*Dipartimento di Meccanica, Matematica e Management (DMMM) Politecnico di Bari, Bari, Italy*
[c]*National Group of Mathematical Physics (GNFM), National Institute of High Mathematics (INDAM)*
[d]*The School of Computing and Engineering, University of Huddersfield, Huddersfield, HD1 3DH, UK*

Presented in ASME Turbo Expo 2020 Conference

DOI: 10.1115/GT2020-14790

Statement of contributions of joint authorship

Dhinesh Thanganadar proposed the novelty, implemented the methods, generated all results, and prepared the manuscript draft. Francesco Fornarelli, Sergio Camporeale, and Faisal Asfand proof-read and critically commented on the manuscript before submission. Kumar Patchigolla provided supervision, proof-read and critically commented on the manuscript before submission.

ABSTRACT

Supercritical carbon dioxide (sCO_2) cycles are studied as the next-generation power cycles in order to reduce the cost of Concentrating Solar Power (CSP) plants. The design performance of numerous cycles has been investigated, nevertheless, the off-design and annual performance of these cycles are seldom

studied. This plays a critical role in selecting an optimal cycle for CSP application, as an efficient power cycle influences the solar field size, consequently affecting the Levelised cost of electricity (LCOE). In this study, the design, off-design and annual performance of three sCO_2 cycles; simple recuperative, recompression and partial-cooling cycles are studied. Multi-objective optimisation was performed and the off-design Pareto fronts were compared for the changes in the power cycle boundary conditions. Annual performance simulation was carried out, and the performance of the three cycles was compared when the power cycle is operated in maximum efficiency mode, which facilitates selecting the optimal cycle. The LCOE of the simple recuperated cycle was higher by roughly 1.7¢/kWh than recompression cycle when maximising the power cycle efficiency and the partial cooling cycle is higher by 0.2¢/kWh. However, operating the power cycle in the maximum efficiency mode significantly lowers the plant capacity factor (around 10-20%).

Keywords

sCO_2, CSP, optimisation, design performance, off design performance, annual simulation

7.1 Introduction

Supercritical carbon dioxide (sCO_2) cycles are highly considered for power generation application owing to their attractive thermal-physical properties that offer higher efficiency and compact plant footprint. Therefore, it is considered for Concentrating Solar Power (CSP), nuclear, and fossil-fired applications. Because of the compact machinery, the plant can be more flexible too. National Renewable Energy Laboratory (NREL – USA) considered sCO_2 cycles for Gen3-CSP to reduce the Levelised cost of electricity (LCOE) [1]. Numerous studies have been performed by a number of research groups in the context of designing the sCO_2 cycle, analysis of off-design performance and economic studies [2]. Crespi et al.[3] reviewed forty-two sCO_2 cycles based on the efficiency (reflects the OPerational Expenditure-OPEX), and specific power (reflects the CAPital Expenditure-CAPEX). Thanganadar et al. [4] investigated the performance of five cascade cycles for sensible heat sources. Bufi et al. [5] performed a multi-

objective optimisation of integrating organic Rankine cycle with Thermal Energy Storage (TES). Pantaleo et al. [6] analysed the integration of solar, biomass with TES system. For a CSP application, the cost of the solar field and TES system comprise a significant portion in the overall plant cost, therefore, it is not obvious how to optimise the LCOE by means of the proper CAPEX and OPEX shares. Although numerous authors studied the design performance of different cycles, the off-design performance of these cycles is not compared in detail, except recompression cycle [7,8]. However, this is particularly essential for a CSP application as the plant encounters a significant annual variation in the ambient temperature and heat input (Direct Normal Irradiance-DNI).

Dyreby et al. [9] developed a design and off-design process simulation code for Recompression Cycle (RCBC). Bennett et al. [8] investigated the design and off-design performance of RCBC and its variation (number of reheater and intercooler). Bennett et al. also optimised the cycle control parameters (molten salt flow rate, split fraction and compressor inlet guide vane positions) to maximise the cycle efficiency for different ambient temperatures in order to develop the control strategy. Carstens et al. [10] had developed an transient simulation code for RCBC. Although RCBC is extensively studied, other sCO_2 cycles are seldom studied.

This paper compares the design and off-design performance of three sCO_2 cycles that are suitable for CSP applications, namely simple recuperative Brayton Cycle (SRBC), Recompression Cycle (RCBC) and Partial-Cooling Cycle (PCC). The variation of the cycle net power and net efficiency for different boundary conditions (variation of ambient temperature, a variation of Molten Salt Inlet Temperature- MSIT, and variation of Molten Salt Mass Flow rate -MSFR) were investigated. Multi-objective optimisation was performed to visualize the optimal Pareto fronts for the different off-design condition so that the plant operational strategy can be derived. Finally, annual simulations were also performed when the power cycle operates in either maximum efficiency mode or maximum power mode, and the key performance indexes of these cycles were compared.

7.2 SCO_2 Cycle Modelling

This section outlines the methodology used for design, off-design, and annual simulation.

7.2.1 Design Simulation

Table 7-1 shows the assumptions of the thermodynamic model at the design condition. Steady-state design code for all the cycle components was developed in MATLAB and the architecture is shown in Figure 7-4. The heat exchanger is a one-dimensional code, to capture the nonlinear variation of the sCO_2 isobaric specific heat (discretised to 15 zones), for calculating the conductance (UA). The heat exchanger was sized based on the effectiveness input and the model ensures that the minimum pinch constraint complies. Otherwise, the heat duty is reduced until the minimum pinch condition is satisfied.

The turbine and compressors were modelled based on the isentropic efficiencies. The outlet condition of the turbine and compressors were calculated based on Eq. (7-1) and Eq. (7-2) respectively. All the components were written as separate functions and the main solver guesses the tear stream values and converges by satisfying the steady-state mass (Eq. (7-3)) and energy balance (Eq. (7-4)) equations of the components modelled. The code is flexible to model different cycle configurations without more modifications to the solver. REFPROP was used for calculating the fluid thermal-physical and transport properties.

$$h_{out,turb} = h_{in,turb} - \left(h_{in,turb} - h_{P_{out},S_{in}}\right) \times \eta_{turb} \tag{7-1}$$

$$h_{out,comp} = h_{in,comp} + \frac{\left(h_{P_{out},S_{in}} - h_{in,comp}\right)}{\eta_{comp}} \tag{7-2}$$

Where h is the enthalpy, P is the pressure, S is the entropy, and η is the isentropic efficiency. The subscript in and out represent inlet and outlet respectively

$$\sum \dot{m}_{in} = \sum \dot{m}_{out} \tag{7-3}$$

$$\sum \dot{m}_{in} * h_{in} - \sum \dot{m}_{out} * h_{out} + Q - W = 0 \quad (7\text{-}4)$$

Where $\dot{m}$ is the mass flow rate, h is the enthalpy, Q is the heat, and W is the work.

Cycle minimum pressure, split fraction and intercooler pressures were optimised.

Table 7-1 Thermodynamic Model Assumptions

Parameter	Unit	Value
Maximum pressure	bar	250
Compressor inlet Temperature (CIT)	°C	42
Turbine inlet temperature (TIT)	°C	650
Recuperators pinch Temperature	°C	5
Recuperator effectiveness	%	95
Compressor isentropic efficiency	%	89
Turbine isentropic efficiency	%	90
Heat exchanger pressure drop [9]	%	1
Primary heat exchanger (PHEX) minimum approach	°C	20
Heat exchanger discretisation	-	15
Generator efficiency	%	99
Precooler Pinch Temperature	°C	15

7.2.1.1 Simple Recuperative Brayton Cycle (SRBC)

The cycle configuration is shown in Figure 7-1. By fixing the maximum cycle pressure (P2) to 250 bar, the only degree of freedom of the cycle to maximise the efficiency is the minimum cycle pressure (P1). It has been observed that the minimum cycle pressure tends to reach the lower bound (~74 bar) in order to maximise efficiency and specific power. However, this pressure is close to the critical point and the off-design inventory control requires lowering the pressure (discussed in the results section), therefore, 85 bar was selected for annual

performance simulation. The off-design multi-objective optimisation was performed using 74 bar as the minimum pressure. The turbine and compressor shafts are not connected in the same shaft in order to explore the maximum performance (complete Pareto front) of the cycle.

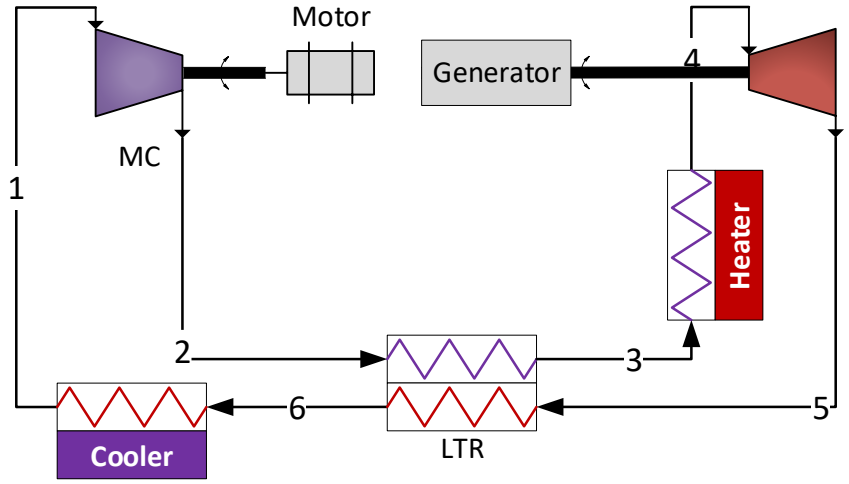

Figure 7-1: Cycle Configuration of SRBC

7.2.1.2 Recompression Cycle (RCBC)

Figure 7-2 shows the configuration of the recompression cycle. The minimum pressure (P1) and split ratio were optimised to maximise the efficiency at the design. A compressor inlet pressure of 93.5 bar and split ratio of 0.288 was selected.

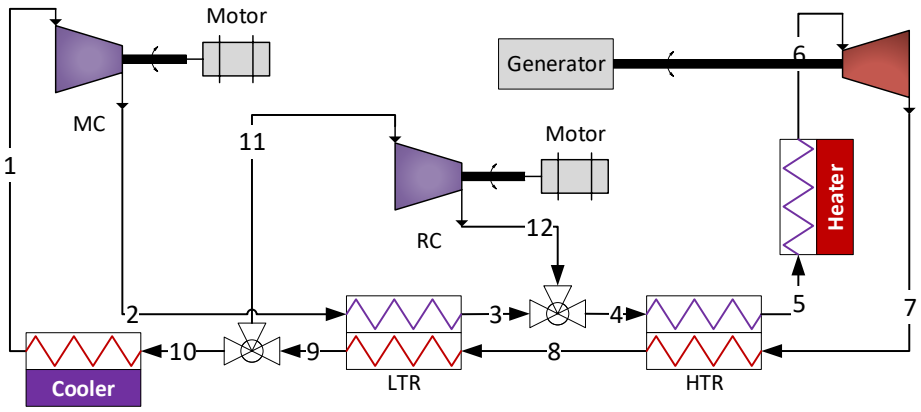

Figure 7-2: Cycle Configuration of RCBC

7.2.1.3 Partial-Cooling Cycle (PCC)

Figure 7-3 shows the configuration of partial-cooling cycle. The minimum pressure (P1), intermediate pressure (P2) and split ratio were optimised to maximise the efficiency, at 55 bar, 99 bar and 0.4 respectively.

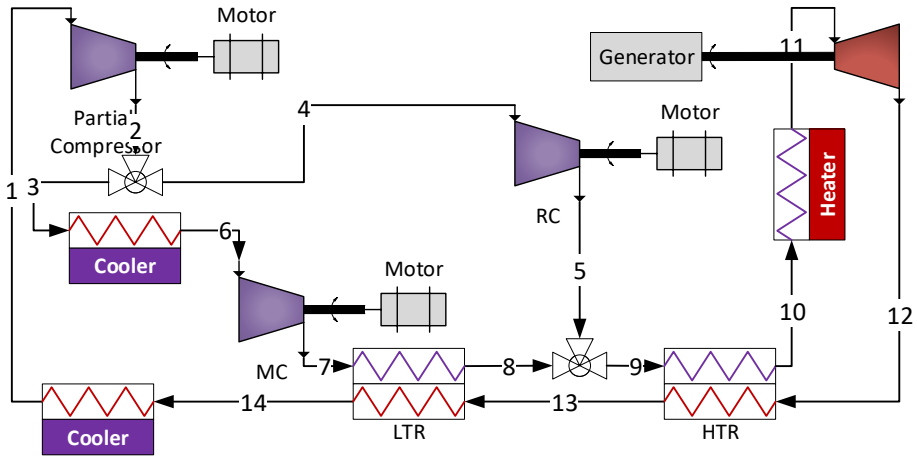

Figure 7-3: Cycle Configuration of Partial-Cooling Cycle

7.2.2 Off-Design Simulation

A flexible cycle code was developed in MATLAB that uses REFPROP for calculating the thermal-physical properties of CO_2. The heat exchanger off-design model scales the pressure drop and conductance using Eq. (7-5 [9] & (7-6 [11], respectively. The turbine and compressor sizing and off-design maps were based on Dyreby et al. [9] who used an empirical model that scales the Sandia test facility turbomachinery performance maps. The compressor shaft speed was adjusted to meet the desired outlet pressure, while the turbine shaft speed was kept the same as the design value. The architecture of the algorithm is shown in Figure 7-4. The heat exchanger model guesses the hot outlet temperature and converges when the calculated conductance matches the desired scaled conductance according to Eq. (7-6. Minimum pinch is also ensured in the off-design condition and the desired conductance is reduced if the thermodynamic second law is violated. The precooler is modelled with the constant pinch temperature difference.

$$DP = DP_{ref} * \left(\frac{\dot{m}}{\dot{m}_{ref}}\right)^{1.75} \quad (7\text{-}5)$$

$$UA = UA_{ref} * \left(\frac{\dot{m}_h * \dot{m}_c}{\dot{m}_{h,ref} * \dot{m}_{c,ref}}\right)^{0.8} * \left(\frac{\dot{m}_{h,ref}^{0.8} + \dot{m}_{c,ref}^{0.8}}{\dot{m}_{h^{0.8}} + \dot{m}_c^{0.8}}\right) \quad (7\text{-}6)$$

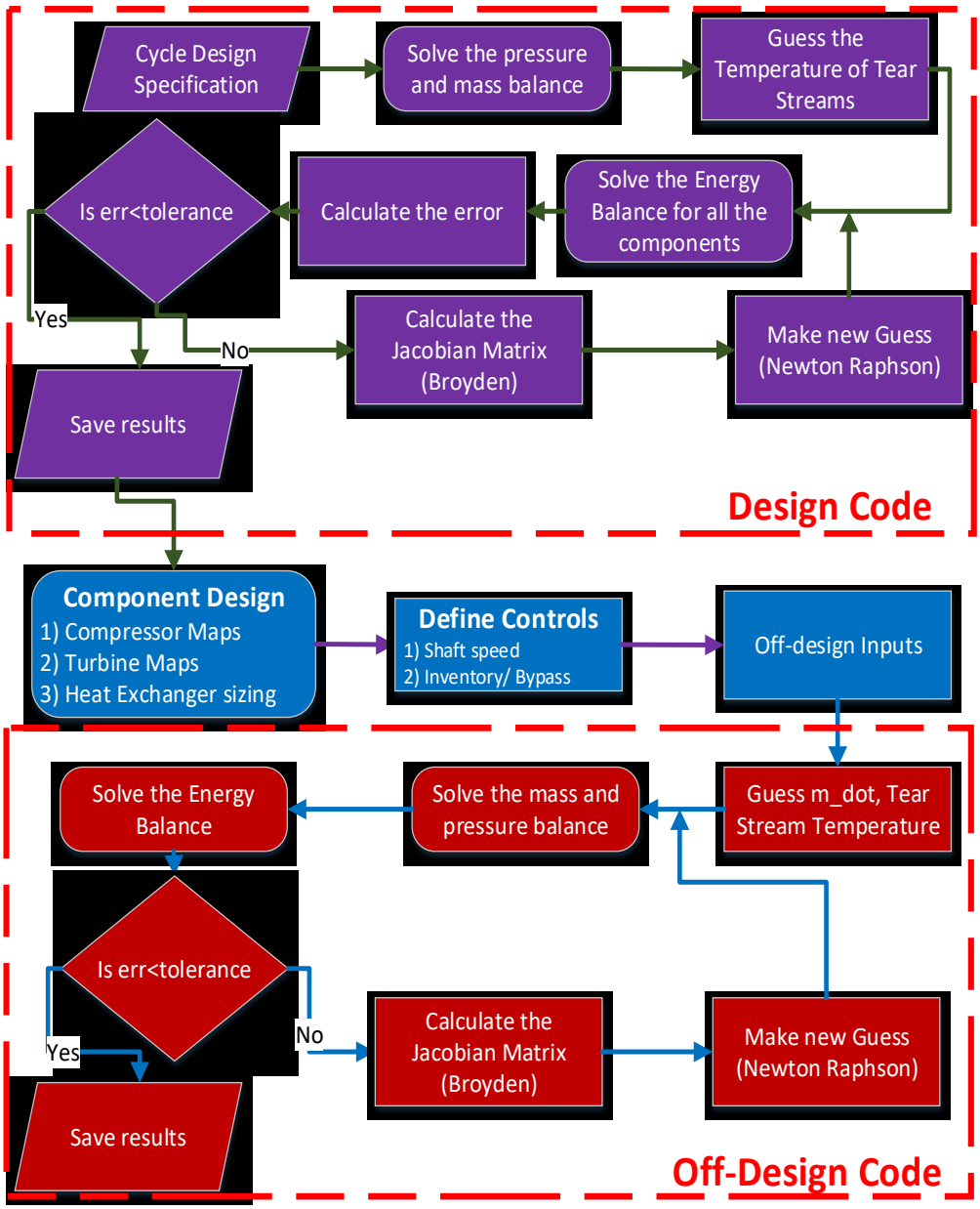

Figure 7-4: Architecture of the Plant Simulation Code

7.2.3 Multi-Objective Optimisation

Table 7-2: Optimisation search space limits

Parameter	Unit	Minimum	Maximum
Minimum Pressure	bar	50	70
Intermediate Pressure*	bar	75	130
Maximum pressure	bar	140	250
Split ratio	-	0.15	0.5

*-This is the minimum pressure range for RCBC and SRBC

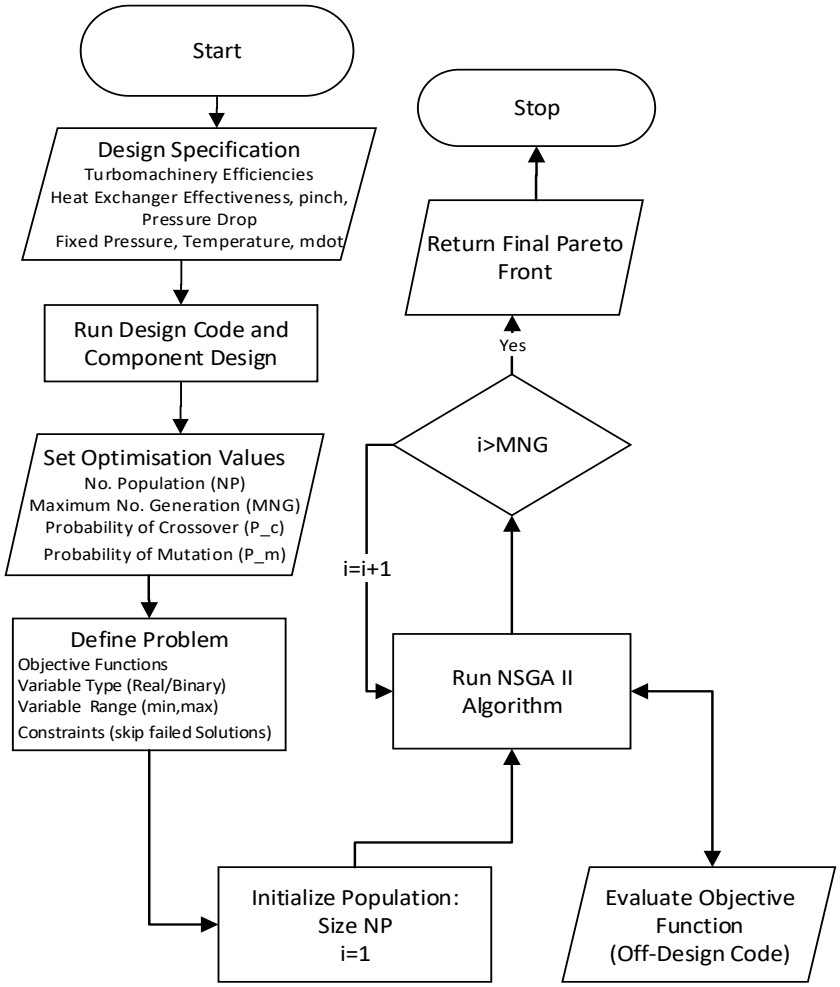

Figure 7-5: Multi-Objective Optimisation Algorithm

A Non-Dominated Sorting Algorithm (NSGA II) is used to perform the multi-objective optimisation with the objective functions are to maximise the power cycle net efficiency and net power. The pseudo-algorithm is shown in Figure 7-5. The optimisation ranges of the variables are shown in Table 7-2. The fact that solar irradiance is free and the solar field is a significant contributor to capital cost leads to the expectation that the solar field utilisation should be maximised by maximising power block net power, regardless of efficiency. Nevertheless, adding the TES to the circuit can provide a degree of flexibility to offset the energy supply to the power block. For example, if maximising the net power penalises the cycle efficiency significantly at a higher ambient temperature, then there is a possibility to run the power block at a maximum efficiency mode by sacrificing the net power of the power cycle and store the remaining thermal energy during hot ambient condition. Then, recover the stored energy during the night (cold ambient condition) at a higher efficiency. Therefore, the cycle efficiency and net power were maximised for the multi-objective optimisation.

7.3 Annual Simulation

A 30MW_e net power solar tower model was developed in the System Advisory Model (SAM V2018.11.11) for Daggett, USA location. sCO_2 cycles are expected to be economically attractive around 30MW_e and above, therefore 30MW_e plant capacity was selected. A solar multiple of three and 14 hours of TES are considered. The heliostat field layout was optimised using the calculated unit power block cost (detailed in Section 2.4). $MgCl_2$-KCl (Mole: 32%-68%) mixture was considered as the Heat Transfer Fluid (HTF) and storage medium. The thermal-physical properties of the Molten Salt (MS) are shown in Table 7-3 [12]. An annual simulation was performed using SAM with the power block of different cycles were modelled using its user-defined power cycle feature. The LCOE is also calculated using SAM.

Table 7-3 Thermo-Physical Properties of Molten Salt

Property	Unit	Function (T in ^oC)
Isobaric Specific Heat	kJ/kg-K	$0.9896+1.046*10^{-4}\times$ (T-430)

Density	Kg/m^3	1903.7-0.552×T
Dynamic Viscosity	cP	14.965-0.0291×T+1.784×10^{-5}×T^2
Thermal Conductivity	W/m-K	0.5047-0.0001×T
Melting Temperature	^{o}C	424.4

7.4 Economic Model

The cost functions and financial model assumptions for LCOE calculation are listed in Table 7-4. The scaling index as shown as Eq. (7-7 was incorporated for estimating the cost of heat exchanger costs as proposed by [13]. SAM default values of 66$/kW-yr. and 3.5$/MWh were considered as fixed cost by generation and variable cost of generation, respectively.

$$C^* = \exp\left(\ln(C_1) + \frac{\ln\left(\frac{C_1}{C_2}\right)\ln\left(\frac{UA}{UA_1}\right)}{\ln\left(\frac{UA_1}{UA}\right)}\right) \quad (7\text{-}7)$$

Table 7-4 Cost functions of sCO_2 cycle components

Component	Unit	Value
sCO_2 Compressor [13]	$	$643.15 * (\mathrm{kW})^{0.9142}$
sCO_2 Turbine [13]	$	$9923.7 * (\mathrm{kW})^{0.5886}$
Recuperator Scaling factor [13]	$-K/kW	1.25
Precooler/Intercooler Scaling factor [13]	$-K/kW	2.3
PHEX Scaling factor [13]	$-K/kW	3.5
TES [14]	$/kWth	15
Heliostat Field Cost [14]	$/m^2	75
Site Improvement cost [14]	$/m^2	10
Land Cost [14]	$/Acre	10,000
Contingency [14]	%	10
EPC and owner cost [14]	%	13

Inflation Rate [2]	%	3
Real discount rate [2]	%	5.5

7.5 Model Verification

The MATLAB model was verified against the open-source Dyreby FORTRAN code for the standard RCBC [9]. The design and off-design models were verified against the process parameters tabulated in Table 7-5 and Table 7-6, respectively. A 30MWe power cycle was modelled in the MATLAB code and the conductance provided as an input to Dyreby FORTRAN code. The efficiency prediction and the process temperatures are compared in Table 7-5 at the design condition.

Since Dyreby FORTRAN code assumes that the main compressor and the turbine shafts are connected, the MATLAB code was amended to share a common shaft for verification. The off-design condition at the compressor inlet temperature of 55^{o}C was simulated in both the MATLAB and FORTRAN code and the power, efficiency, mass flow, maximum pressure and the process temperatures are compared in Table 7-6. The compressor inlet pressure was not optimised for this CIT as the purpose is to validate the model. Since the MATLAB code matches well with the Dyreby FORTRAN code, the model is considered acceptable.

Table 7-5 Design case verification with Dyreby [9]

Parameters	**Unit**	**Design at CIT-42^{o}C**		
		Dyreby RCBC	**This Study**	**Error (%)**
Efficiency	%	49.03	49.02	0.00
Power	kW	30,658	30,658	-0.00
mdot	kg/s	285.71	285.71	-0.00
Pmin	bar	80.0	80.0	Input
Pmax	bar	250.0	250.0	Input
T1	^{o}C	42.00	42.00	-0.00

T2	°C	127.49	127.49	0.00
T3	°C	264.77	264.79	-0.01
T4	°C	264.79	264.80	-0.01
T5	°C	475.83	475.83	0.00
T6	°C	650.00	650.00	0.00
T7	°C	500.33	500.33	-0.00
T8	°C	269.84	269.86	-0.01
T9	°C	140.88	140.89	-0.00
T12	°C	264.82	264.82	- 0.00

Table 7-6 Off-design model verification with Dyreby [9]

Parameters	**Unit**	**Off-Design at CIT- 55°C**		
		Dyreby RCBC	**This Study**	**Error (%)**
Efficiency	%	45.98	45.97	0.01
Power	kW	19,067	19,066	0.01
mdot	kg/s	224.18	224.18	- 0.00
Pmin	bar	80.0	80.0	Input
Pmax	bar	209.9	209.9	0.0
T1	°C	55.00	55.00	Input
T2	°C	137.81	137.81	0.00
T3	°C	278.72	278.73	-0.00
T4	°C	274.39	274.40	- 0.00
T5	°C	501.78	501.77	0.00
T6	°C	650.00	650.00	- 0.00
T7	°C	523.39	523.39	-0.00
T8	°C	281.06	281.08	-0.00
T9	°C	157.48	157.48	-0.00

T12	°C	264.34	264.35	- 0.00

7.6 Design Performance

The design performance indices of all the three cycles studied are tabulated in Table 7-7. Although the efficiency of RCBC is higher than the other two cycles, the MS temperature drop across the PHEX is highest for the PCC. The molten salt mass flow rate of the PCC is lower than the other two cycles owing to its efficiency and temperature drop across the PHEX. Although the temperature drop across the PHEX of SRBC is similar to PCC, the molten salt mass flow required to meet the same net power is higher due to the lower efficiency of the cycle. This suggests that PCC can reduce the size of the solar field piping and TES system compared to the other two cycles investigated in view of their design performance. This also infers that the solar block cost of the PCC is lower compared to the other two cycles studied. In addition, the solar field and TES cost of RCBC could be further exacerbated by the hot molten salt return temperature, which may demand expensive material. Considering the power cycle cost, the RCBC recuperator conductance is the highest and SRBC is the lowest. Therefore, the overnight cost of SRBC is lower and RCBC is higher. The overnight cost trend of the PCC and SRBC are opposite to the cost reduction trend of the solar block and TES whilst the RCBC overnight cost and solar block cost are higher. This suggests selection of the PCC owing to the reduced TES size and solar field piping cost with a slight increase in the overnight cost. However, it is not obvious what weight they share in order to select the economic cycle for CSP. Therefore, selection of a cycle requires annual simulation where the most economic cycle minimises the LCOE, which is location specific owing to the different annual ambient temperature and DNI profile.

Table 7-7 Power block design performance parameters

Parameters	Unit	SRBC	RCBC	PCC
Net Power	MWe	30.1	30.6	30.3
Net Efficiency	%	39.8	47.1	46.3

ΔT across PHEX (sCO_2)	°C	220.4	163.8	232.6
Recuperator UA	MW/K	2.2	8.9	4.8
MS mdot	kg/s	310	345	253
Overnight Cost	$/$kW_e$	1,043	1,360	1,195

7.7 Comparison of Off-Design Pareto Fronts

7.7.1 Effect of Ambient Temperature

From Figure 7-6, the efficiency against net power Pareto front of SRBC is roughly flat which indicates that the impact on cycle efficiency is not significant when maximising the cycle net power, for a given CIT. On the other hand, the efficiency drops significantly as the net power increases in both PCC and RCBC. The net power reduction in RCBC is higher by 14.3% compared to PCC at 55 °C CIT with almost similar maximum efficiency. Since the Pareto front at the maximum efficiency is roughly plateaued with the reduction in the net power, the optimal operating point is the trade-off between these two conflicting objectives for both PCC and RCBC.

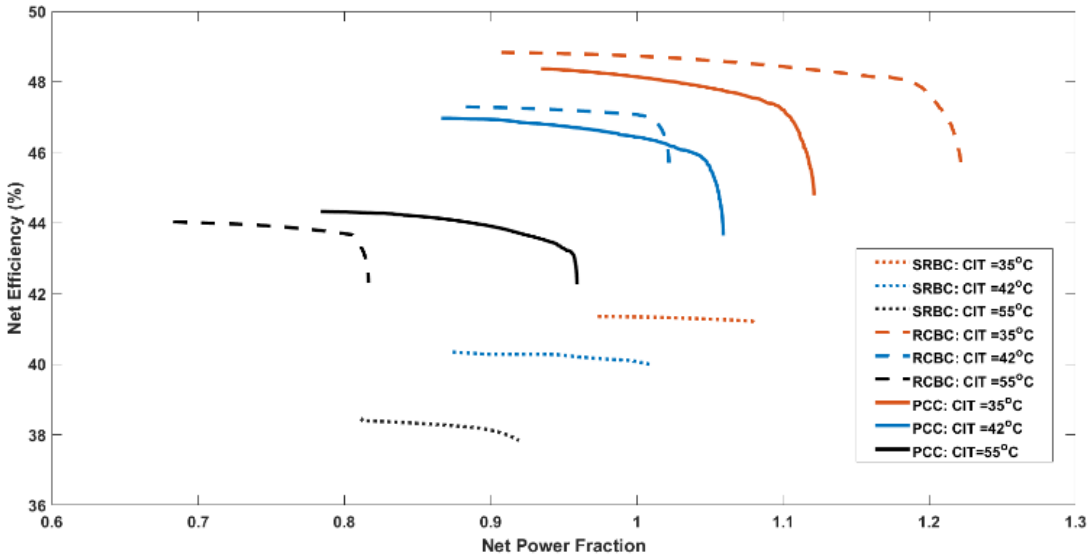

Figure 7-6 Pareto fronts of RCBC, SRBC and partial cooling cycle for three different CIT (35, 42, 55°C)

The Molten Salt Outlet temperature (MSOT) is a critical parameter for a CSP plant as a higher MSOT reduces the energy absorption window in the solar receiver and TES capacity. In general, the design MSOT of RCBC is higher than the other two cycles, which makes the differential temperature (ΔT) across the PHEX minimum owing to higher recuperation. The MSOT of the PCC and SRBC are in a similar range as shown in Figure 7-7. For all the three cycles, it is observed that increasing the CIT shifts the MSOT curve up and this would affect the performance of the solar field. The MSOT of RCBC increases by 4.4% from its design value whilst maximising efficiency at 42 ^{o}C CIT depending on the selection objective of the design (maximum efficiency or maximum specific power). The MSOT further increases by 2.3% from the design value at the maximum efficiency case when the CIT is 55^{o}C. For PCC, the increase in MSOT is 2.1% at the maximum efficiency case when the CIT increases from 42^{o}C to 55^{o}C, which is similar to RCBC. For SRBC, the MSOT increases by 1.2%. However, at the maximum power output case, the MSOT increases by 5.3% for RCBC whilst it is 3.7% for the PCC and 2.9% for SRBC when the CIT increases from 42^{o}C to 55^{o}C with reference to the maximum power point at 42^{o}C. Therefore, the impact of the overall performance of the cycle depends on the power cycle control strategy i.e. whether the power block is operated in maximum power mode or in maximum efficiency mode. If the power cycle of the CSP plant is operated in the maximum net power mode, then not only the net power of RCBC reduces by 14.3% compared to the PCC (Figure 7-6), but also the solar field and TES capacity are affected more for RCBC than PCC. For instance, when the CIT increases from 42 to 55 ^{o}C, the MSOT of PCC is 2% lower than the design MSOT (i.e., storage capacity increases by 3.4%) whilst the MSOT has increased by 3.8% for RCBC, resulting in a reduction of 10.6% in the TES capacity. It should be highlighted that the MSOT of PCC increases by 3.7% for a CIT of 55^{o}C when maximising the net power with reference to the maximum power point at the CIT of 42^{o}C, whereas the MSOT decreases by 2% with reference to the design MSOT.

The MSOT can be seen to increase from its design value while maximising efficiency in each cycle. In Figure 7-7, RCBC displays the largest increases of 4.4% at 42 ^{o}C, and 2.3% at 55^{o}C. For PCC, the increases are similar to but

smaller than RCBC, with an increase of 2.1% at 55°C. SRBC shows the smallest increase of 1.2% for 55°C. The trend is the same for the maximum power output case at 5.3%, 3.7% and 2.9% for RCBC, PCC and SRBC respectively when the CIT increases from 42 to 55°C. Thus, the control strategy adopted whether the power block is operated in maximum power or maximum efficiency mode, as well as the CIT affects the overall performance of the plant as both the solar field and TES capacity are affected by the increased MSOT. This effect is more pronounced for RCBC than for PCC and less for SRBC.

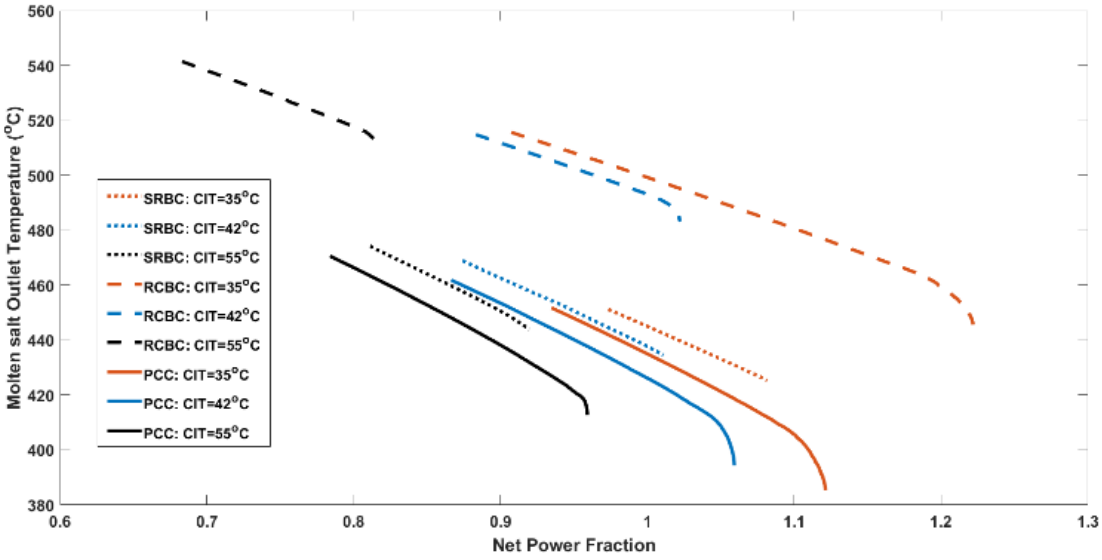

Figure 7-7 Molten Salt Outlet Temperature of the cycles across the Pareto front for three different CIT

The plant control variables across the Pareto front helps in developing the optimal control strategy of the plant. The cycle maximum pressure reduces at a higher ambient temperature to maximise the efficiency for all three cycles. This is opposite to the observation of Bennett et al. [8] for RCBC when maximising the efficiency as they concluded that the maximum pressure always reached its highest bound. The difference is that Bennett et al. also optimised the molten salt flow rate (between 80-120% of the design flow rate) whilst it was fixed in this study. For RCBC and PCC, the main compressor inlet pressure increases for higher CIT in order to maximise the efficiency and this increasing trend was also observed by Bennett et al. [8] for RCBC. The split fraction reaches a higher value

for both RCBC and PCC to maximise the efficiency and it reduces at a higher CIT. This behaviour was observed by Carstens et al. [10] for RCBC.

7.7.2 Effect of Molten Salt Inlet Temperature

The Pareto fronts for three MSIT are plotted in Figure 7-8. The maximum efficiency case in the Pareto front of the PCC is a bit lower than RCBC. However, the maximum power fraction of PCC is higher than RCBC for all the three MSIT's studied. The maximum power fraction of SRBC is slightly lower than the other two cycles for an MSIT of 600°C.

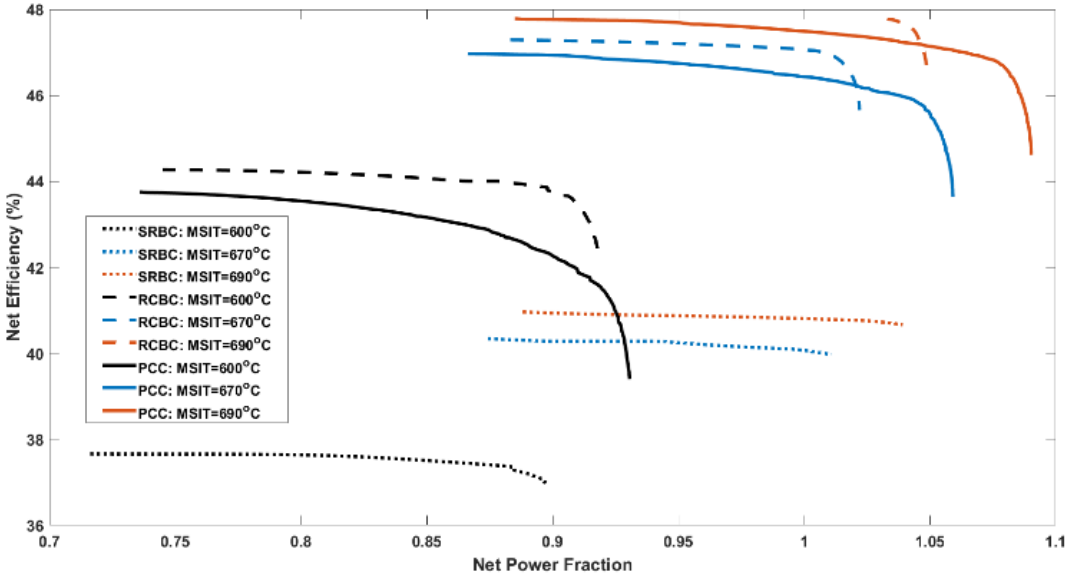

Figure 7-8 Pareto fronts of RCBC, SRBC and partial cooling cycle for three different MSIT

The MSOT reduces by 11.7%, 10.9% and 10.1% for the PCC, RCBC and SRBC respectively at the maximum efficiency case when the MSIT reduces from the design value to 600°C. At the maximum net power case, they reduced by 16.1%, 13.7% and 14% respectively. The reduction in MSOT of the PCC is higher than RCBC at lower MSIT, which helps to attain higher net power for this cycle. However, the molten salt freezing point typically limits the MSOT lower bound. The higher net power from the PCC might not be realisable if the molten salt freezing point limits the MSOT lower bound. This suggests that the cycle selection in view of off-design performance for changes in MSIT depends on the molten

salt freezing limit. Furthermore, lower MSOT is also not desirable as this progressively reduces the temperature of the cold tank, but also improves TES capacity and solar field performance.

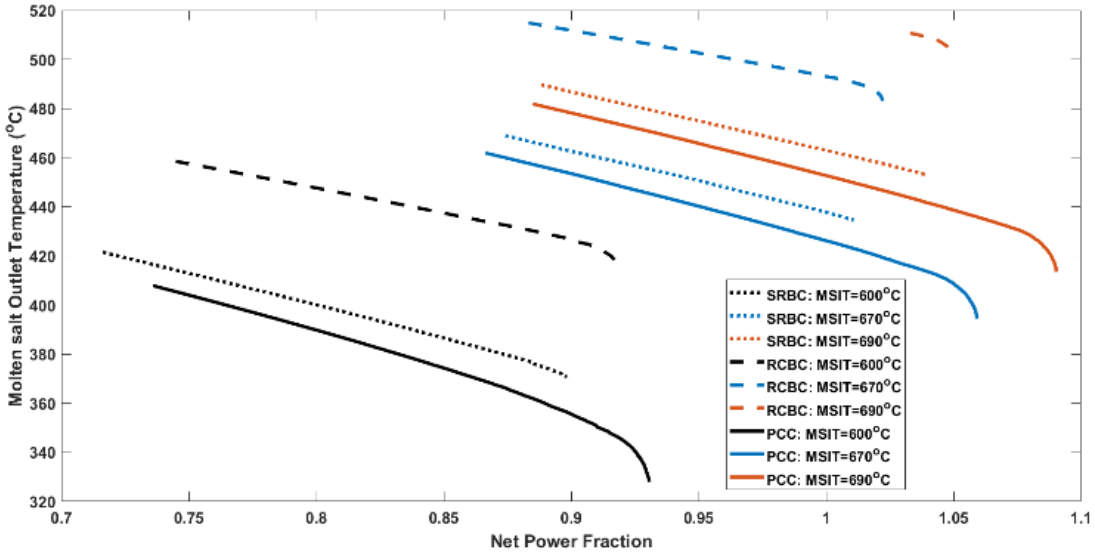

Figure 7-9 Molten Salt Outlet Temperature across the Pareto front

7.7.3 Effect of Molten Salt Mass Flow Rate

The Pareto fronts for three molten salt flow rate (MSFR) are plotted in Figure 7-10. The maximum efficiency case in the Pareto front of the PCC is lower than RCBC for the three MSFR. However, the maximum power fraction of the PCC is higher than RCBC for on or above design MSFR but lower at 50% MSFR. The maximum power fraction of SRBC is slightly lower than the other two cycles at 50% MSFR. The corresponding MSOT across the Pareto fronts are shown in Figure 7-11. The MSOT reduces at the maximum efficiency case by 2.4%, 1.9% and 7.2% for the PCC, RCBC and SRBC, respectively, when the MSFR reduced from the design value to 50% MSFR. At the maximum power case, the MSOT is reduced by 3.2%, 3% for SRBC and RCBC cycles whilst the MSOT increases by 4.1% for the PCC. Consequently, the maximum power for a lower MSFR is higher for RCBC than PCC. This infers that a prolonged lower MSFR at the design CIT can favour RCBC compared to PCC, if the power block has to be operated in maximum power mode.

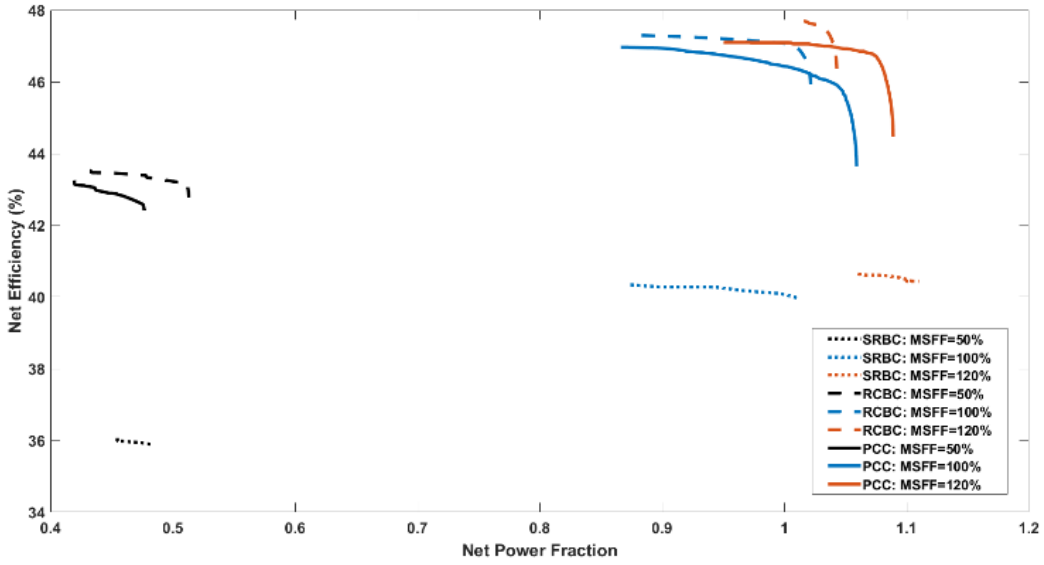

Figure 7-10 Pareto fronts of RCBC, SRBC and partial cooling cycle for three different MS flowrate

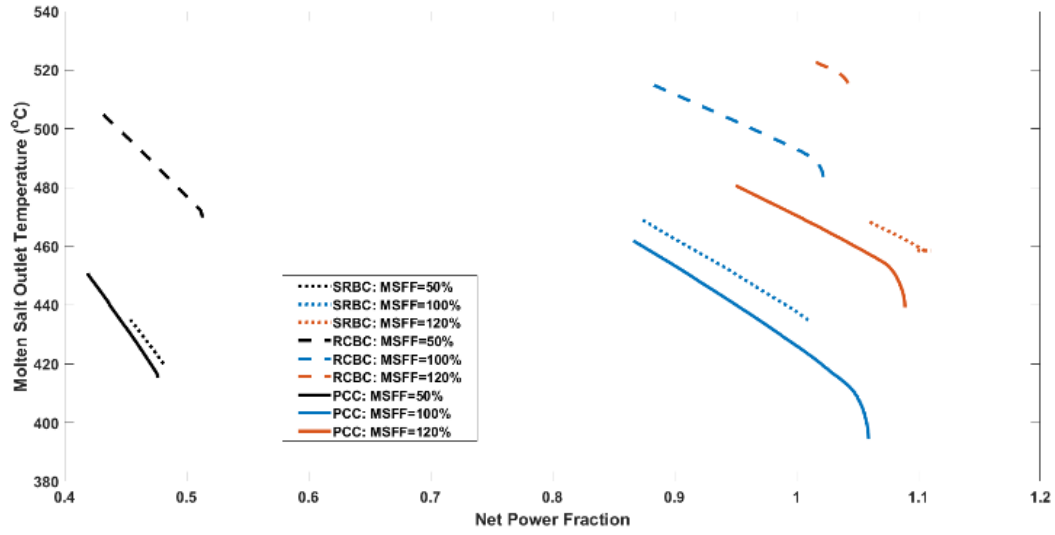

Figure 7-11 Molten Salt Outlet Temperature across the Pareto front

7.8 Annual Simulation

The three sCO_2 cycles are represented as a user-defined lookup table in SAM V2018.11.11. Single objective genetic algorithm was applied to maximise the efficiency for all the data points in the parametric table, which covers the range of boundary conditions that the power cycle is expected to encounter. Sixty-six

data points in the lookup table represent each power cycle and every data point is an optimisation problem for the GA. The annual performance of the three cycles is tabulated in Table 7-8. The capacity factor is lower and the LCOE is higher than similar studies that use SunShot targets [2]. The reason is that the optimisation was performed to maximise the efficiency (not the net power), therefore, the net power was lower for most of the off-design cases. This can be visualized from the Pareto fronts plotted in Figure 7-6, Figure 7-8 and Figure 7-10. The annual energy generation from RCBC is slightly higher than the partial cooling cycle as shown in Table 7-8. SRBC produced lower annual energy yield compared to the other two cycles investigated. Nevertheless, the LCOE of RCBC is slightly lower (~0.2¢/kWh) than the PCC whilst the LCOE of SRBC is higher by ~1.2 ¢/kWh. Despite the higher overnight cost of RCBC, the LCOE is lower for RCBC if the power cycle is operated in the maximum efficiency mode.

Table 7-8 Summary of annual performance when maximising the power cycle efficiency

Description	Unit	SRBC	RCBC	PCC
Field Incident Annual Energy	MWh	1,250,492	1,015,137	974,713
Receiver Incident Annual Energy	MWh	574,158	408,681	375,776
Annual Energy absorbed by the HTF	MWh	512,297	355,804	328,790
Annual Energy charged into TES	MWh	303,775	232,385	232,221
Annual Energy discharged from TES	MWh	295,934	222,226	214,947
Power Cycle Annual Gross Energy	MWh	135,300	168,198	153,204
Annual Energy to Grid	MWh	119,436	141.836	134,745
Capacity Factor	%	45.9	54.5	51.8
Solar to Electric Conversion Efficiency	%	9.55	13.97	13.82
LCOE real	¢/kWh	9.73	8.04	8.25

The capacity factor might be increased with the resulting reduction of the LCOE if the power cycle is operated in maximum net power mode. In order to verify this

hypothesis, the RCBC and PCC were modelled using SAM in-build power cycle. SAM maximises the net power by optimising the cycle variables. SAM also implemented inventory control, which is similar to this study. However, the compressor shaft speeds were fixed to the design value in SAM that produces a conservative estimate of the power block performance. SAM performance estimate is conservative as this study optimises also the compressor shaft speed, therefore, the cycle performance at a fixed compressor speed is a sub-optimal solution in the Pareto front. Both RCBC and the PCC were modelled in SAM and the financial assumptions were updated. The summary of the annual performance is shown in Table 7-9.

Table 7-9 Summary of the annual performance model in SAM

Description	Unit	RCBC	PCC
Field Incident Annual Energy	MWh	1,048,490	1,060,163
Receiver Incident Annual Energy	MWh	494,132	510,733
Annual Energy absorbed by the HTF	MWh	426,393	453,186
Annual Energy charged into TES	MWh	248,859	252,647
Annual Energy discharged from TES	MWh	239,198	245,575
Power Cycle Annual Gross Energy	MWh	198,516	201,016
Annual Energy to Grid	MWh	172,472	182,145
Capacity Factor	%	66.3	70.0
Solar to Electric Conversion Efficiency	%	16.5	17.2
LCOE real	¢/kWh	7.20	6.70

Table 7-9 highlights that the capacity factor can be increased by operating the power block in maximum power mode and consequently the LCOE can be reduced for both RCBC and PCC. The LCOE of the PCC was lower compared to REBC. It can be concluded that the power cycle has to be operated in maximum power mode to realise the higher capacity factor for both PCC and RCBC. The number of power block start-ups is slightly higher for PCC than RCBC. The parametric simulations were performed for different solar multiple at two different thermal storage hours i.e., TES hours 10 and 14. It has been observed that the difference in the capacity factor between the two operating modes (maximum efficiency or maximum power mode) reduces with the reduction of solar multiple. Eventually, they approach approximately to the same value when the solar

multiple is about 2-2.4 for all the three cycles studied. Similar trend was also observed for the LCOE.

7.9 Conclusions

Design, off-design and annual performance of SRBC, RCBC and PCC were compared. RCBC cycle yields higher efficiency whilst the overnight cost of SRBC is the lowest. The differential temperature across the primary heat exchanger for RCBC is lower while it is of a similar magnitude for SRBC and PCC. This affects the size of the solar field as the lower temperature difference increases the molten salt mass flow rate to achieve the same power output, consequently increasing the TES and solar field piping size and cost.

A multi-objective optimisation was performed to explore the off-design Pareto fronts for the changes in three different boundary conditions such as compressor inlet temperature, molten salt inlet temperature and molten salt flow rate. The efficiency and net power Pareto front of SRBC is roughly flat whilst this significantly varies for PCC and RCBC. This concludes that SRBC favours maximum power mode operation.

The molten salt outlet temperature from the primary heat exchanger was also compared for the changes in power cycle boundary conditions as this affects the solar field performance. The reduction in the net power of RCBC is higher by 14.3% compared to PCC for a 13^{o}C increase of CIT from the design value. In addition, the MSOT is also increased from the design by 3.8% for RCBC, resulting in a reduction of thermal storage capacity by 10.6% when the power output is maximised, whereas the MSOT has reduced from its design for PCC by 2%. This infers that the PCC can yield higher net power than RCBC at higher ambient temperatures with the minimum knock-on impact on the solar field.

The annual performance of the three cycles was carried out for Daggett, USA location and the power cycle efficiency were maximised. The capacity factor was lower consequently, the LCOE was higher when the power cycle is operated in maximum efficiency mode as compared to maximum power mode. Indeed, the maximisation of the efficiency reduces the cycle net power so that the LCOE is

heavily penalized. Thus, it suggests that the power cycle has to be operated to maximise the net power to realise a higher capacity factor. However, for PCC and RCBC the optimal operational strategy can be the trade-off between these two modes to minimise the LCOE whilst maximum power mode is preferred to SRBC.

7.10 References

[1] Mehos M, Turchi C, Vidal J, Wagner M, Ma Z, Ho C, et al. Concentrating Solar Power Gen3 Demonstration Roadmap. Nrel/Tp-5500-67464 2017:1–140.

[2] Schmitt J, Wilkes J, Bennett J, Wygant K, Pelton R. Lowering the levelized cost of electricity of a concentrating solar power tower with a supercritical carbon dioxide power cycle. ASME Turbo Expo, Charlotte, NC, USA: 2017, p. 1–10. https://doi.org/10.1115/GT2017-64958.

[3] Crespi F, Gavagnin G, Sánchez D, Martínez GS. Supercritical carbon dioxide cycles for power generation: A review. Appl Energy 2017;195:152–83. https://doi.org/10.1016/j.apenergy.2017.02.048.

[4] Thanganadar D, Asfand F, Patchigolla K. Thermal performance and economic analysis of supercritical Carbon Dioxide cycles in combined cycle power plant. Appl Energy 2019;255. https://doi.org/10.1016/j.apenergy.2019.113836.

[5] Bufi EA, Camporeale S, Fornarelli F, Fortunato B, Pantaleo AM, Sorrentino A, et al. Parametric multi-objective optimization of an Organic Rankine Cycle with thermal energy storage for distributed generation. Energy Procedia 2017;126:429–36. https://doi.org/10.1016/j.egypro.2017.08.239.

[6] Pantaleo AM, Camporeale SM, Sorrentino A, Miliozzi A, Shah N, Markides CN. Solar/biomass hybrid cycles with thermal storage and bottoming ORC: System integration and economic analysis. Energy Procedia 2017;129:724–31. https://doi.org/10.1016/j.egypro.2017.09.105.

[7] John J. Dyreby. Modeling the Supercritical Carbon Dioxide Brayton Cycle with Recompression. 2014.

[8] Bennett J, Wilkes J, Allison T, Pelton R, Wygant K. Cycle modeling and optimization of an integrally geared sCO_2 compander. ASME Turbo Expo, Charlotte, NC, USA: 2017, p. 1–8. https://doi.org/10.1115/GT2017-63707.

[9] Dyreby JJ. Modeling the Supercritical Carbon Dioxide Brayton Cycle with Recompression. 2014.

[10] Carstens NA. Control strategies for supercritical carbon dioxide power conversion systems. Massachusetts Institute of Technology, 2007.

[11] Patnode A. Simulation and performance evaluation of parabolic trough solar power plants. Univ Wisconsin-Madison 2006;Master:5–271.

[12] Xu X, Wang X, Li P, Li Y, Hao Q, Xiao B, et al. Experimental Test of Properties of KCl–$MgCl_2$ Eutectic Molten Salt for Heat Transfer and Thermal Storage Fluid in Concentrated Solar Power Systems. J Sol Energy Eng 2018;140:051011. https://doi.org/10.1115/1.4040065.

[13] Carlson MD, Middleton BM, Ho CK. Techno-Economic Comparison of Solar-Driven sCO2 Brayton Cycles Using Component Cost Models Baselined With Vendor Data. Proc ASME 2017 Power Energy Conf 2017:1–7.

[14] Mehos M, Turchi C, Jorgenson J. Advancing Concentrating Solar Power Technology, Performance, and Dispatchability. SunShot 2016:1–66. https://doi.org/10.1016/B978-0-08-087872-0.00319-X.

Chapter 8

8 Off-design and Annual Performance Analysis of Supercritical Carbon Dioxide Cycle with Thermal Storage for CSP application

Dhinesh Thanganadar[a], Francesco Fornarelli[b,c], Sergio Camporeale[b], Faisal Asfand[a,d], Kumar Patchigolla[a]

[a]*School of Water, Energy and Environment (SWEE), Cranfield University, Cranfield, MK43 0AL, UK*
[b]*Dipartimento di Meccanica, Matematica e Management (DMMM) Politecnico di Bari, Bari, Italy*
[c]*National Group of Mathematical Physics (GNFM), National Institute of High Mathematics (INDAM)*
[d]*The School of Computing and Engineering, University of Huddersfield, Huddersfield, HD1 3DH, UK*

Published in Applied Energy, 2020

DOI: 10.1016/j.apenergy.2020.116200

Statement of contributions of joint authorship

Dhinesh Thanganadar proposed the novelty, implemented the methods, generated all results, and prepared the manuscript draft. Francesco Fornarelli, Sergio Camporeale, and Faisal Asfand proof-read and critically commented on the manuscript before submission. Kumar Patchigolla provided supervision, proof-read and critically commented on the manuscript before submission.

ABSTRACT

Supercritical Carbon Dioxide (sCO_2) cycles can achieve higher efficiency compared to steam-Rankine or Air-Brayton cycles, therefore they are promising for concentrated solar power applications. In the present work a recompression

sCO_2 cycle is connected to a central-tower solar field with two-tank thermal storage delivering molten chloride salt at 670°C. Although sCO_2 cycles show higher design efficiency, the off-design efficiency is highly sensitive to the ambient conditions, impacting the power block net-power and heat input. The temperature of the molten-salt exiting from the power block and returning to the cold storage tank increases by 46°C with respect to the design value when the compressor inlet temperature is raised by 13°C relative to the design condition of 42°C, which implies that the capacity of the thermal storage reduces by 25%. The main focus of this work is to investigate the off-design performance of a sCO_2 recompression cycle under variable ambient temperature, molten-salt inlet temperature and molten-salt flow rate. Multi-objective optimisation is carried-out in off-design conditions using an in-house code to explore the optimal operational strategies and the Pareto fronts were compared. Since the power cycle can either be operated in maximum power mode or maximum efficiency mode, this study compares these two operational strategies based on their annual performance. Results indicate that the capacity factor of the concentrated solar power can be increased by 10.8% when operating in maximum power mode whilst the number of start-ups is reduced by about 50% when operating in maximum efficiency mode.

Keywords:

Supercritical CO_2 cycle, CSP, Annual Performance, Multi-Objective Optimisation, Thermal Energy Storage, Off-design

8.1 Introduction

The Supercritical Carbon Dioxide (sCO_2) Brayton cycle has many advantages over the conventional steam Rankine/ Joule-Brayton cycles owing to its compact footprint and higher efficiency when the turbine inlet temperature is >550 °C [1]. The sCO_2 also has high thermal stability at an elevated temperature, is nonflammable and nontoxic compared to ORC plants. Because of these benefits, sCO_2 cycles are being considered for a range of applications including nuclear, concentrating solar power (CSP), fossil fuel-fired plants, and waste heat recovery [1,2]. Many researchers have extensively studied the performance of sCO_2 cycles

[2–4] and numerous different cycles have been proposed [5]. In particular, Crespi et al. [3] reviewed and categorised forty-two of them while Thanganadar et al. [4] studied five sCO_2 cycle configurations for sensible heat source applications, proposing a set of performance maps to estimate the performance of sCO_2 cycles for the bottoming cycle. Marchionni et al. [5] performed first and second-law analysis for eight Joule-Brayton sCO_2 cycles integrated with a high-grade waste heat sources, concluding that the unit cost ($/kWe) of a cycle follows a parabolic shape, which has an optimum for different exhaust gas temperature, primarily dictated by the cost of the high-temperature heat exchangers. Giovannelli et al. [6] discussed the design processes of radial turbomachinery for a medium-scale sCO_2 power block using one-dimensional and three-dimensional numerical simulation. Demonstration facilities and pilot plants have been built in recent years for testing the performance and reliability of sCO_2 plants. National Renewable Energy Laboratory (NREL), USA tested a 520 kW_{th} pilot plant [7] and is building a scale-up facility of 10 MW_e [8], which is designed to operate at 715.9 °C turbine inlet temperature [8,9]. As far as commercial applications are concerned, Echogen® has commercialised a packaged unit for Waste Heat Recovery (WHR) applications [10].

The critical point of carbon dioxide is 30.98 °C, 73.8 bar while the cycle maximum pressure is typically limited to around 300 bar due to material and economic limitations. This makes the cycle pressure ratio less than 4, which limits the specific work and temperature drop across the turbine, making recuperation necessary in order to increase cycle efficiency. Several recuperated sCO_2 cycles have been proposed in the literature [3]. The basic configuration is the closed-loop simple recuperative Brayton cycle (SRBC), however the degree of recuperation is limited by the occurrence of a pinch point in the recuperator. This can be avoided by the recompression Brayton cycle (RCBC) where the recuperator is split into two heat exchangers and the mass flow rate to the low-temperature recuperator cold-side is lowered to maximise recuperation. Although advanced cycles, such as partial cooling cycles, precompression, cascade cycles are also proposed [3] to increase the cycle specific work, the RCBC is generally preferable due to its higher efficiency and simpler layout, which also makes it

more suitable for CSP applications. Wang et al. [11] investigated the performance of a RCBC integrated with a transcritical CO_2 (tCO_2) bottoming cycle to recover low-grade heat from the RCBC and compared six different fluids in closed-loop cycle. Asfand et al. [12] integrated an absorption chiller with an SRBC cycle to chill the cooling water so that the efficiency penalty at higher ambient temperatures can be reduced. Linares et al. [13] proposed a modification to RCBC that facilitate heat addition at a lower pressure to enable the use of conventional shell and tube heat exchangers in order to reduce the cost of the PHEX for CSP applications. Clementoni et al. provided the steady-state [14], off-design [15] and transient [16] operational results of a 100kW_e experimental facility at the Naval Nuclear Laboratory, USA. Clementoni et al. [17] also reported the operational results of the test facility for different compressor inlet temperature (CIT).

Although the design point performance of RCBC is extensively studied, the off-design performance of an integrated sCO_2 cycle with TES- CSP appears seldom investigated. This is concerning for a CSP plant, because they often encounter off-design operation due to the volatility of the renewable energy source. Dyreby et al. [7] have developed a FORTRAN based design and off-design code that can simulate the recompression cycle. They proposed an empirical turbomachinery scaling method derived from Sandia National Laboratory test loop compressor. The plant solving procedure is specific to recompression cycle which can be cumbersome and error prone when changing the cycle configuration. Tse et al. [8] integrated a primary heat exchanger (PHEX) code with Dyreby's code through an external iterative procedure, concluding that the off-design performance not only effects on the cycle performance, but also can influence the capacity of the TES and the solar receiver performance. Clementoni et al. [18] analysed the effect of compressor inlet pressure on the performance of the sCO_2 cycle and compared with the operational results, concluding that the cycle power output and efficiency are directly affected by the compressor inlet density. Anselmi et al. [19] explained the test facility operations along with the preliminary modelling works of compressor design and control strategy. Duniam et al. [20] analysed the off-design performance of a sCO_2 cycle integrated with a natural draft dry cooling

tower, concluding that the cycle net power reduces by 10% for each 10 °C increase in ambient temperature above the design temperature when cycle inventory and turbine inlet temperature (TIT) are maintained at the design values. Wright et al. [21] investigated four different sCO_2 cycle control strategies for a waste heat recovery application, including; cooling air fan speed control, boost compressor speed control, split fraction control and compressor inlet pressure control. They conclude that the combination of all four controls provide an efficient way to mitigate the effects of heat rejection at a higher ambient temperature. Wang et al. [22] analysed the performance of a direct air-cooled sCO_2 cycle under off-design conditions, observing that the cooling-tower approach temperature varies nonlinearly with the ambient temperature. Son et al. [23] developed a deep neural-network based turbomachinery off-design model for which the training data were generated from a one-dimensional mean-line code for sCO_2 application. Aforementioned studies investigated the performance RCBC for different control techniques, however, there has been no systematic study that explores the optimal operational space (multi-dimensional Pareto front) for different boundary conditions, and investigate the trends of critical control variables including minimum/ maximum pressure, shaft speed and split fraction that aids in developing the optimal control strategy.

Several research groups have performed transient simulations of the standard recompression cycle [10–14], finding that inventory control provides higher efficiency at part load compared to other control techniques such as turbine bypass, turbine inlet temperature and throttling control. Inventory control turndown is limited, however, by the size of the CO_2 storage tank and the pressure pinch between that storage tank pressure and the system pressure. Although a bigger inventory storage tank can push the sCO_2 cycle turndown ratio further, the optimal size is an economical trade-off between the CAPEX and improvement in annual energy generation [15]. Researchers have proposed that turbine bypass control or throttle control is required to extend the plant turndown further [24–26] and to have a faster response during load throw-off as inventory control is slower, which is supported by previous operational experience of closed-loop Brayton cycles.

Bennett et al. [16] observed that the off-design cycle pressure ratio of sCO_2 cycle reduces at higher ambient temperatures. Consequently, the turbine expansion ratio reduces which increases, the turbine exhaust temperature (TET) for a given TIT and since sCO_2 cycles are recuperative Brayton cycles, this higher TET increases the recuperation. Consequently, the cold stream inlet temperature to the primary heat exchanger increases, which causes the molten salt outlet temperature (MSOT) to increase at higher ambient temperatures. This negatively affects solar field performance in two ways: 1) the energy absorption window of the solar receiver reduces when the molten salt mass flow reaches its maximum flow limit, and 2) the cold storage tank temperature gradually increases, reducing the capacity of thermal energy storage (TES) as the differential temperature reduces. Tse et al. [8] quantified this reduction in TES capacity concluding that it can be as high as 20% of the design capacity at hot ambient temperatures. To eliminate the knock-on impact on the TES system an additional MSOT constraint should be considered in CSP-TES-sCO_2 cycle optimisation/operation. However, constraining the power cycle optimisation to respect an MSOT limitation close to its design value may negatively affect power cycle efficiency, although this has not been investigated in the existing literature.

For a CSP plant, the objective is to maximise the annual performance in order to reduce the levelised cost of electricity (LCOE). Reducing the total number of power block start-up/shut-down per annum, however, extends plant life and reduces the start-up/maintenance costs. Generally, the design criterion of the solar field is based on a “solar multiple”, the ratio between the thermal power output of the solar field at the design solar radiation/sun angle, and the design thermal input of the power unit. A solar multiple greater than one is preferred in order to increase the plant capacity factor therefore there is often excess solar energy, which can be stored. The thermal storage capacity of a two-tank TES is typically rated based on the number of hours that the storage system can supply the power block design heat requirement. Implementing TES offers operational flexibility by disconnecting the solar field and power block enabling the thermal energy supply to the power block to be controlled without notably affecting the

heat absorbed in the solar field and as long as the storage system capacity can absorb/supply any imbalance, the power block can be controlled in different ways.

The performance of a sCO_2 cycle drops at a higher ambient temperature when the compressor inlet condition shifts away from the critical point, thus, increasing the compressive power. Maximising the power block off-design net power and net efficiency are not the same for a recuperated closed-loop Brayton cycle as the off-design cycle mass flow rate/the cycle pressure ratio varies depending on the objective [20]. The annual energy yield can be higher by maximising the net power, however, maximising the efficiency could be more attractive as sCO_2 cycle performance is more sensitive to boundary conditions (ambient temperature, and the Molten Salt Inlet Temperature-MSIT). Several global plant operational strategies can therefore be defined to maximise a performance criterion at the current boundary conditions. Case 1) supply the energy required by the power block to maximise power generation and store the remaining energy in TES. Case 2) supply energy to the power block to maximise the power cycle instantaneous efficiency and store the remaining energy in TES. Case 3) give priority to fully charge the TES whilst generating power from the remaining energy. Maximising power block net power utilises the assets to their maximum capacity, however, it also penalises cycle efficiency significantly at higher ambient temperatures. Operating the power block in maximum efficiency mode during hot ambient conditions, while sacrificing some of the available instantaneous net power, allows storage of the remaining thermal energy for production of more power at a later time when cooler ambient conditions enable a higher efficiency, which could be attractive. This approach can be more effective for moderate Direct Normal Irradiance (DNI) days as plant shutdown can be avoided, thereby eliminating the associated start-up energy loss. To the best of the author's knowledge, there are no prior studies investigating how different plant operational strategies influence the annual performance of a sCO_2 cycle.

This paper investigates the off-design performance of a 30 MW_e RCBC power block for different boundary conditions such as variation of the heat transfer fluid (HTF) hot inlet temperature, molten salt mass flow rate, and ambient temperature with and without limiting the MSOT close to the design point, for the first time. A

multi-objective optimisation approach is applied to the in-house cycle design and off-design codes, which maximises both net power and net efficiency by optimising the compressor inlet pressure, outlet pressure, split fraction and the molten salt mass flow rate, in order to explore the optimal operational space (Pareto fronts) in off-design operation. Firstly, the trade-off between the power cycle efficiency penalty when the MSOT is constrained proximate to its design value and the knock-on negative effect on TES capacity at higher ambient temperatures are studied. Secondly, the trends of control variables across the Pareto front, including the minimum pressure, maximum pressure, split fraction and MSOT are discussed which guides developing the plant control strategy and the optimal off-design compressor inlet pressure estimation method is proposed to maximise the cycle efficiency. The compressor operating point variation across the Pareto fronts are visualised by mapping the Pareto fronts on the compressor map for different boundary conditions. Finally, the annual performance of two different power cycle operational strategies 1) operating the power cycle in maximum power mode 2) operating the power cycle in maximum efficiency mode are simulated for the first time. The trade-offs between annual energy yield and the number of start-ups are quantified to appreciate the potential of these operating modes.

8.2 sCO_2 Cycle Configuration

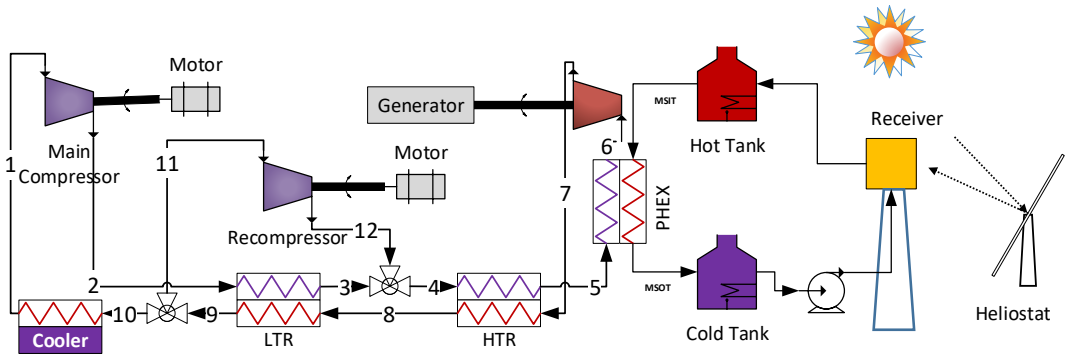

Figure 8-1 Recompression cycle configuration

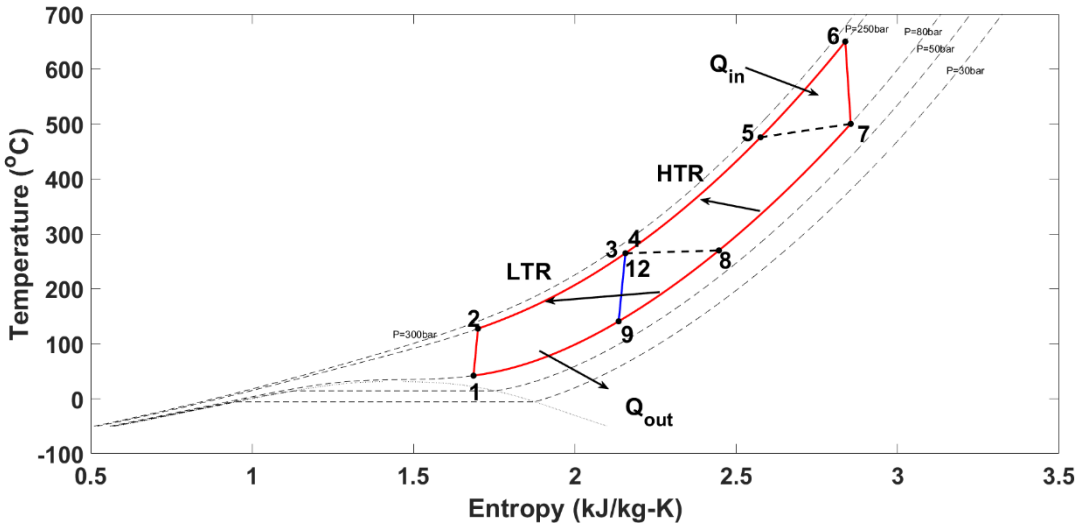

Figure 8-2 Temperature-Entropy (T-S) diagram of recompression Brayton cycle (The dashed grey lines are the isobaric lines of CO_2, the continuous grey line is the CO_2 saturation curve)

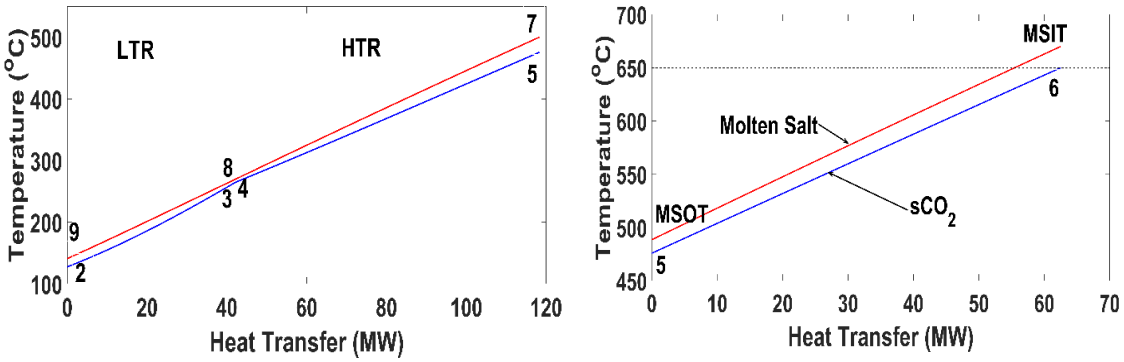

Figure 8-3 Temperature- Heat transfer (T-Q) diagram Left: Recuperator, Right: Primary Heat Exchanger

A schematic of the RCBC is shown in Figure 8-1 and the Temperature- Entropy (TS) diagram of the process is shown in Figure 8-2. For the selected design parameters (Table 6-3), the states 12 and 4 overlay each other in the TS diagram. Processes 2 to 5 are recuperation, 5 to 6 heat addition and 9 to 1 heat rejection process. Figure 8-3 shows the temperature – heat transfer (TQ) curve of the recuperator train and PHEX at the design point (Table 6-3, Table 8-6) where it can be seen that the pinch occurs at the low-temperature recuperator (LTR) cold outlet for the design point selected. Nevertheless, the pinch can change to the

cold stream inlet for a reduced recycle flow rate owing to the nonlinear isobaric specific heat change.

The precooler is air-cooled and the Primary Heat Exchanger (PHEX) is heated via the hot molten salt from the solar field. A central power tower-based solar field with a conventional two-tank sensible heat storage system is considered. Since the MSOT from the solar receiver is 670 °C, conventional nitrate-based molten salts are not stable. The NREL 10MW_e demonstration plant considered $MgCl_2$-KCl (Mole: 32%-68%) in order to achieve these higher operating temperatures [8,9] and the same salt is therefore selected as both HTF and storage medium for this study.

For a closed-loop recuperative cycle, maximising efficiency tends to increase the cold stream inlet temperature to the PHEX so that the average heat addition temperature is increased, which improves the Carnot efficiency of the cycle provided that the recuperator circuit effectiveness is unaffected. On the other hand, increasing the cycle specific power tends to lower the cold stream inlet temperature to the PHEX so that heat addition to the cycle is maximised, with the trade-off to recuperation. The sCO_2 mass flow rate, split fraction and the pressure ratio are all affected by the choice of objective function maximised i.e., efficiency or specific power. For a CSP plant, the product of solar field efficiency and power block efficiency has to be maximised. Integration of TES with optimal storage capacity allows storing of the energy absorbed from the solar field, which allows supplying the required amount of energy to the power block to maximise the objective function.

8.3 Methodology for Thermodynamic Modelling

The thermodynamic models for all the components, including; heat exchanger (one-dimensional), compressor/pump, turbine, valve, splitter, and mixer, were developed in MATLAB®. The thermal physical properties of sCO_2 are calculated using the REFPROP library (V9.1) [27], an iterative routine that minimises Helmholtz free energy. The thermal physical properties of the eutectic molten salt mixture $MgCl_2$-KCl (Mole: 32%-68%) are calculated based on the work of Xu et al. [28] and listed in *Table **8-1***. The melting temperature of the salt is 424.4 °C,

therefore, the cold storage tank temperature has to be above this value by a sufficient safety margin (~50 °C [29]) to avoid salt freezing.

Table 8-1 Thermal-physical properties of molten salt

Property	Unit	Function (T in °C)
Isobaric Specific Heat (C_p)	kJ/kg-K	$0.9896+1.046\times10^{-4}\times$ (T-430)
Density (ρ)	kg/m^3	$1903.7-0.552\times T$
Dynamic Viscosity (μ)	cP	$14.965-0.0291\times T+1.784\times10^{-5}\times T^2$
Thermal Conductivity (k)	W/m-K	$0.5047-0.0001\times T$
Melting Temperature (T_m)	°C	424.4

The sCO_2 turbomachinery (turbine and compressor) are simulated as a zero-dimensional model based on their isentropic efficiencies (η_{isen}). The outlet enthalpies (h_{out}) of the turbine and compressor are calculated using Eq. (8-1 and Eq. (8-2 respectively, where h_{2s} is a function of outlet pressure (P_{out}) and inlet entropy (s_{in}).

$$h_{out,turb} = h_{in,turb} - (h_{in,turb} - h_{2s,turb}) \times \eta_{isen,turb} \quad (8\text{-}1)$$

$$h_{out,comp} = h_{in,comp} + \frac{h_{2s,comp} - h_{in,comp}}{\eta_{isen,comp}} \quad (8\text{-}2)$$

The heat exchanger code is modelled as one-dimensional component in order to capture the nonlinear property variation of sCO_2 along the length of the heat exchanger. The heat exchanger functions size the heat exchanger based on effectiveness (ϵ) using Eq. (8-3 or specifying the outlet temperature of either hot or cold stream.

$$\epsilon = \frac{\dot{Q}}{\dot{Q}_{max}} \quad (8\text{-}3)$$

The actual amount of heat transfer (Q) is calculated from the given input of effectiveness and the $\dot{Q}_{max}$ calculated based on Eq. (8-4.

$$\dot{Q}_{max} = \min\left(C_{cold}, C_{hot}\right) \times \left(T_{h,in} - T_{c,in}\right) \quad (8\text{-}4)$$

Due to the variation of the isobaric specific heat, the capacitance rate of the cold stream ($C_{cold}\ in\frac{W}{K}$) is calculated based on Eq. (8-5 and a similar equation has been applied to calculate the hot stream capacitance rate (C_{hot}).

$$C_{cold} = m_{cold} \times \frac{h_{c,in} - h_{c,out,max}}{T_{c,in} - T_{c,out,max}} \quad (8\text{-}5)$$

where the $h_{c,out,max} = f(P_{c,out}, T_{c,out,max})$ and $T_{c,out,max} = T_{h,in}$

The conductance (UA) is calculated to all the heat exchanger zones using the NTU method [30] with the total conductance the sum of the conductance of all the zones. The heat duty of the heat exchanger is reduced if the minimum pinch temperature constraint is violated within the heat exchanger or any temperature crossover is detected.

The steady-state mass (Eq. (8-6) and energy (Eq. (8-7) conservations are applied to all the components to calculate their outlet state properties from the inlet conditions, where W is the mechanical power, Q the heat power, $\dot{m}$ the mass flow rate and h the enthalpy, while the subscripts in, out refer to the inlet and outlet respectively.

$$\sum \dot{m}_{in} = \sum \dot{m}_{out} \quad (8\text{-}6)$$

$$\sum(\dot{m}_{in} \times h_{in}) - \sum(\dot{m}_{out} \times h_{out}) + \sum Q - W = 0 \quad (8\text{-}7)$$

The recuperators are modelled based on effectiveness while the cooler and the primary heater are modelled based on the outlet temperature set point. The precooler is a direct air-cooled type with a pinch of 15 °C whilst the recuperator and the PHEX are compact Printed Circuit Heat Exchangers (PCHE). The cooling airflow to the precooler is adjusted to achieve the desired compressor inlet temperature.

The component models are integrated at the plant level in a flexible manner so that any plant configuration can be assessed. The plant solver estimates the tear

stream values, calculate the error vector against the initial guess values and converges the solution using a non-linear iterative solver. The multi-variable Newton-Raphson iterative method is implemented and the Broyden algorithm is used for calculation of the Jacobian matrix.

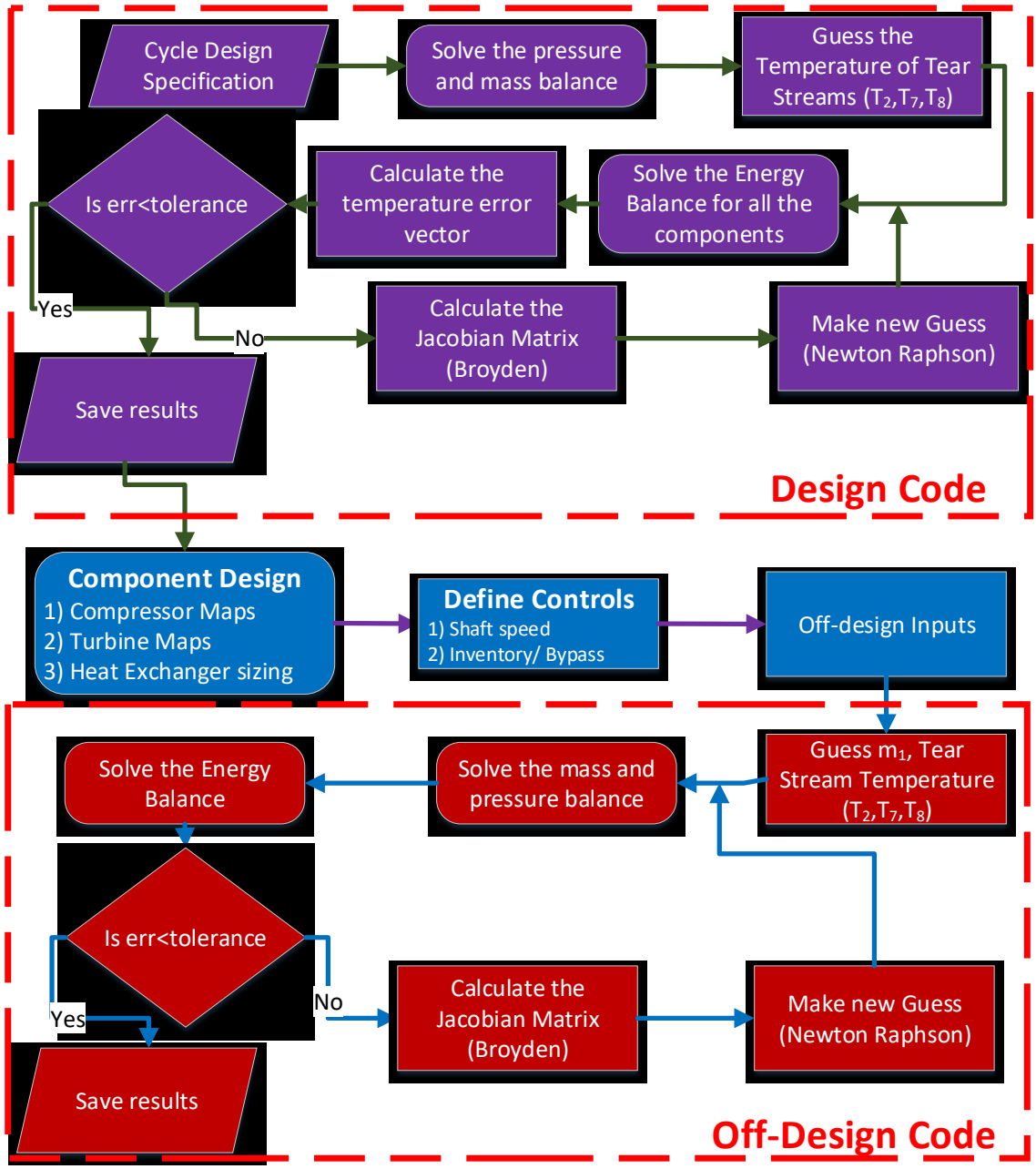

Figure 8-4 Architecture of the plant simulation code

In order to evaluate the plant off-design performance, compressor and turbine maps are needed. A centrifugal compressor is considered based on the Balje non-dimensionalised chart [31] for the size of the plant. The specific speed is

calculated based on average density and isentropic enthalpy rise. The design non-dimensional specific speeds are 0.52 and 0.49 for the main compressor and recompressor, respectively. The performance maps were generated based on the empirical scaling approach that uses the modified flow and modified head coefficient of Sandia National Laboratory (SNL) test loop maps proposed by Dyreby et al. [32]. The modified flow coefficient is maintained the same as the SNL compressor i.e. 0.02971 and the load coefficient is calculated based on the method proposed by Dyreby et al. [32]. The shaft tip speed/rotational speed and the impeller exit diameter are calculated from the calculated flow and load coefficients. In order to calculate the surge compressor constraints, the minimum flow coefficient method is implemented. Liese et al. [33] proposed a ratio of surge point flow coefficient to the design flow coefficient of 0.7216, which gives a surge flow coefficient of 0.02144. Dyreby et al. [32], however, reported the SNL compressor surge flow coefficient is about 0.02 and since the optimisation Pareto front has to explore the complete operational regime, which can be reduced if the surge flow coefficient is increased, a minimum surge flow coefficient of 0.02 is selected for this work. The flow coefficients are calculated based on the compressor inlet conditions similar to Dyreby et al. [32]. A radial turbine is selected for this study considering the size of the plant as mentioned by Fleming et al. [34]. The turbine off-design models are according to Dyreby et al. [32], which scales the SNL test facility machine.

The heat exchanger off-design pressure drop (DP) was scaled as per the procedure described by Dyreby et al. [35] (Eq. (8-8), and the heat exchanger conductance (UA) scaled using Panode [36] (Eq. (8-9). $\dot{m}$ refers to the mass flow rate, the subscripts c, h refer to the cold and hot streams respectively while the subscript ref indicates the design/reference point value. Eq. (8-9 is derived from the Dittus-Boelter heat transfer correlation with an assumption of neglecting the thermal physical property variations from design to off-design conditions along the length of the heat exchanger. Tang et al. [37] used the Dittus-Boelter correlation for straight channel PCHE and validated the simulation results with experimental data published in Clementoni et al. [38]. Jiang et al. [39] proposed 0.809 as the Reynolds number scaling exponent in the Nusselt number

calculation for low angle channels, however, this exponent is reduced to 0.721 for high angle channels. This work assumes a straight channel PCHE configuration; therefore the Reynolds number scaling exponent from the Dittus-Boelter correlation is used as used by Dyreby et al. [35] and Tse at al. [8].

$$DP = DP_{ref} \times \left(\frac{\dot{m}}{\dot{m}_{ref}}\right)^{1.75} \tag{8-8}$$

$$UA = UA_{ref} \times \left(\frac{\dot{m}_h \times \dot{m}_c}{\dot{m}_{h,ref} \times \dot{m}_{c,ref}}\right)^{0.8} \times \left(\frac{\dot{m}_{h,ref}^{0.8} + \dot{m}_{c,ref}^{0.8}}{\dot{m}_h^{0.8} + \dot{m}_c^{0.8}}\right) \tag{8-9}$$

The heat exchanger off-design code guesses the hot stream outlet temperature, matches the calculated conductance (UA) with the scaled UA, and iterates until the temperature converges. The heat duty of the heat exchanger is reduced if the minimum pinch temperature constraint is violated within the heat exchanger or any temperature crossover is detected. Figure 8-4 shows the architecture of the plant level code that performs the process design, followed by the component sizing and the simulation of the off-design performance based on the type of controls defined.

The turbine shaft is connected to the generator and hence the speed was not controlled whilst the speed of the main compressor and recompressor were changed in order to meet the respective outlet pressure set points. Annual simulation is performed using System Advisory Model (SAM V2018.11.11) with the power block simulated as a user-defined power cycle (parametric table) for Daggett, California location.

8.3.1 Modelling Assumptions

The thermodynamic assumptions for cycle modelling are tabulated in Table 6-3. The heat exchanger pressure drop and the turbomachinery's mechanical loss were neglected. The heat exchanger was discretised to 15 zones for both design and off-design conductance calculations based on initial runs, which provides a trade-off between computational speed and accuracy, in order to capture the non-linear variation of isobaric specific heat.

Daggett, California location is selected as an example to perform annual simulation and therefore the histogram of the temperature distribution is analysed in order to select the design ambient temperature. For lower ambient temperatures, the precooler coolant mass flow is reduced to maintain the main compressor inlet temperature above 32 °C so that condensation at the compressor inlet is avoided.

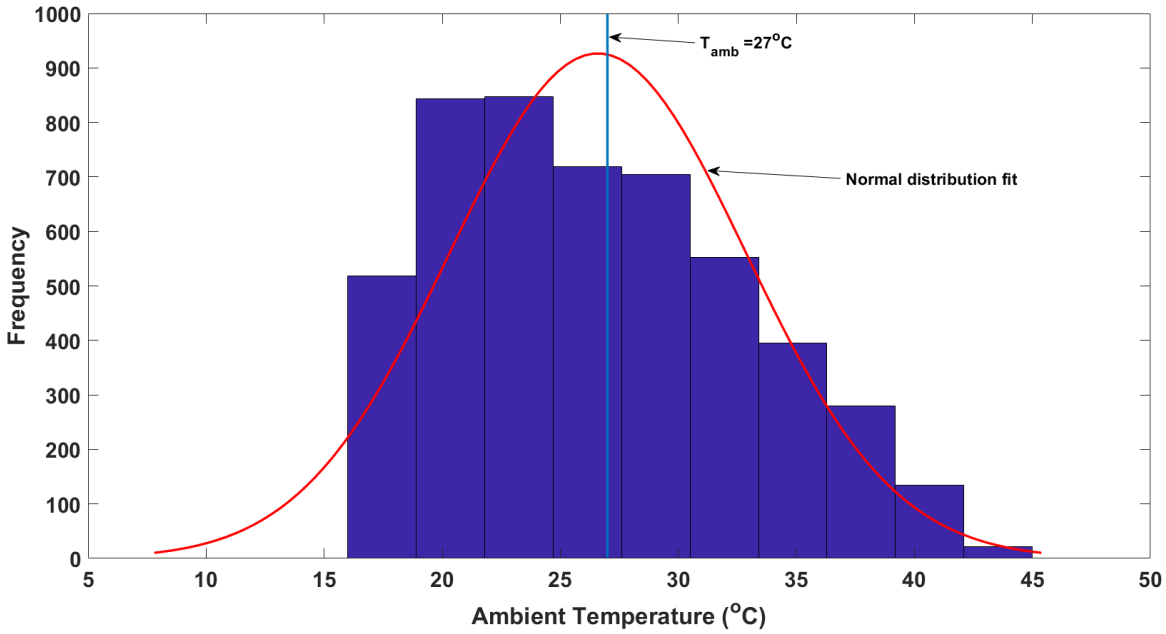

Figure 8-5 Histogram of ambient temperature for Daggett, California (temperature higher than 17 °C)

In order to select the design ambient temperature, therefore, ambient temperatures below 17 °C are not considered due to the 15 °C precooler approach. The histogram of the reduced dataset with a normal distribution fit to aid in selecting the optimal temperature is plotted in Figure 8-5 from this analysis a design ambient temperature of 27 °C is selected. This CIT is approximately 2.5 °C higher than the optimal temperature for the Daggett, California location proposed in [43] through extrapolation of design and off-design results for estimating the annual performance. However, it should be noted that the proposed optimal value could be sensitive to the assumptions in that study and a higher CIT is conservative.

Table 8-2 Thermodynamic modelling assumptions

Description	Unit	Value
Turbine Isentropic Efficiency	%	93
Main Compressor Isentropic Efficiency	%	89
Recompressor Isentropic Efficiency	%	89
Recuperator Effectiveness [40,41]	%	98
Recuperator minimum pinch	°C	5
High Pressure (Main Compressor Outlet)	bar	250
Minimum Pressure	bar	80
Split Fraction	-	0.3
Compressor Inlet Temperature	°C	42
Turbine Inlet Temperature	°C	650
PHEX Approach Temperature	°C	20
Pre-cooler Approach Temperature [42]	°C	15
Design Ambient Temperature (Daggett, California)	°C	27

8.3.2 Optimising the Off-design Condition

In this study, both single and multi-objective optimisations are performed. Firstly optimised power block performance data is modelled as a look-up table for annual simulation. Then, since the focus of this study is to compare the annual performance difference when operating the power block in either maximum efficiency or maximum power mode, two further sets of single-objective optimisations are performed to maximise the objective functions (net power/ efficiency) for each data point of the look-up table. The algorithm optimises the primary process variables such as the main compressor inlet pressure (P_1), main compressor outlet pressure (P_2) and split fraction (m_{11}/m_9), subject to the main compressor and recompressor surge constraints. The objective function is not continuous in the optimisation search space owing to the discontinuous constraints, so the faster nonlinear line-search method (Sequential Quadratic Programming, SQP) often fails to find the global optimal solution and as a result, a heuristic method has been incorporated for optimisation. Considering the computational effort of heuristic algorithms, an initial attempt was made to use a hybrid algorithm, which runs the heuristic algorithm for a fixed number of generations and initialises the SQP to find the global optimum faster. Nonetheless, the number of generations of the heuristic algorithm decides the ability to reach the global optimum and therefore the heuristic genetic algorithm (GA) was chosen for this study.

A multi-objective optimisation was performed to explore the complete Pareto front for changes in the boundary conditions so that the trend of the control variables can be envisaged. A Non-dominated Sorting Genetic Algorithm (NSGA-II) [44] is used which maximises the net efficiency and net power by optimising the power cycle control variables. Table 8-3 shows the range of the optimisation parameters used for both single and multi-objective optimisation.

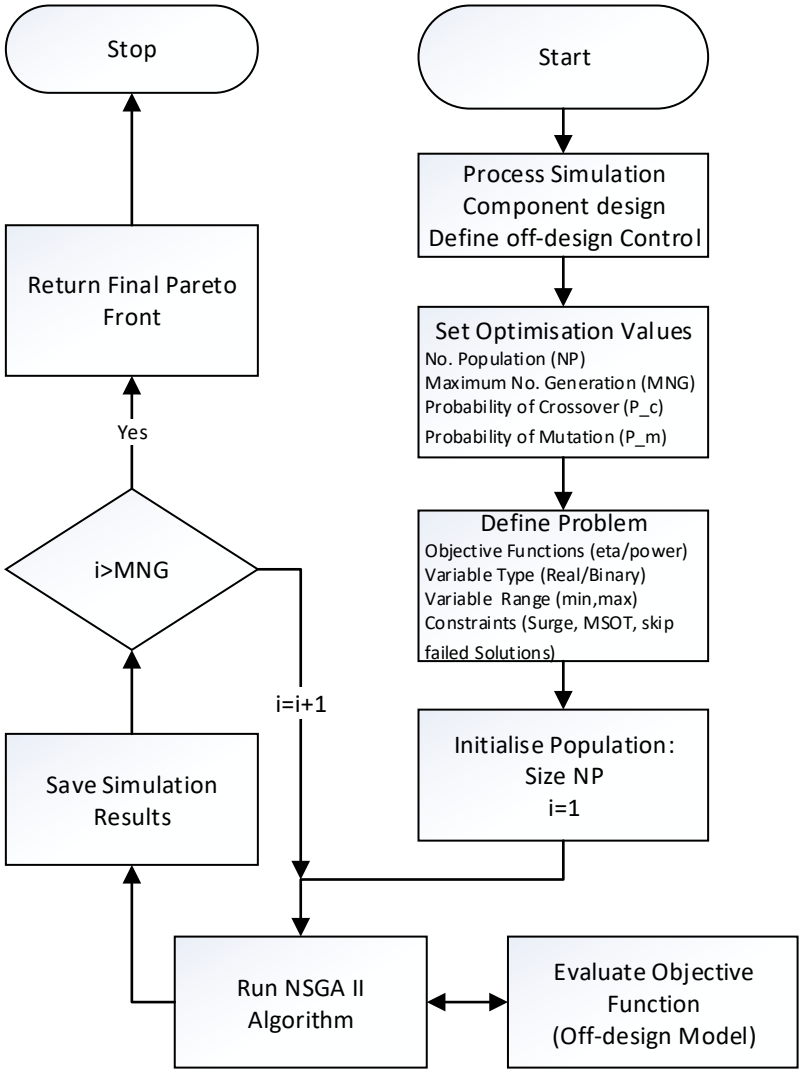

Figure 8-6 NSGA II Algorithm flowchart used in this study

Multi-objective optimisation optimises many objective functions simultaneously subject to equality and non-equality constraints. An individual X(a) is said to be a dominant solution if X(a) is better than other solutions in all objective functions or X(a) is strictly better than other solutions in at least one objective subjected to the constraints [45]. A non-dominated Sorting Genetic Algorithm (NSGA II) was

coded in MATLAB® [46–48] to perform the optimisation study and the flowchart of the code is shown in Figure 8-6. The number of population and the number of generations are selected between 15-30 times the number of variables depending on the number of constraints. A higher number of population and generations are used when the problem is more constrained in order to guarantee convergence to the global optimum solution.

Table 8-3 Variable ranges of parameters considered in optimisation

Variable	Unit	Min bound	Max bound
Minimum Pressure	bar	74	100
Maximum Pressure	bar	150	250
Split Ratio	-	0.15	0.45
Molten Salt Mass flow*	% of design flow rate	90	110%

*mass flow rate was fixed to the desired value in section 8.5.2.2 and 8.5.3

The NSGA-II algorithm optimises the cycle minimum/maximum pressure, split ratio and molten salt mass flow rate with the objective of maximising the cycle net efficiency and net power. The main and recompressor shaft speeds are controlled to achieve the desired outlet pressure set points. The turbine shaft speed is maintained at its design speed as it is connected to the synchronous generator through a gearbox. Implementation of a Variable Frequency Drive (VFD) for the turbine can be costlier as its shaft power is greater than the compressor shaft power. In off-design, once the cycle minimum and maximum pressures are set then the sCO_2 mass flow rate is dictated by the compressor-turbine matching using the performance map of respective components. The compressor surge constraints are checked, however, no surge margin is implemented in order to explore the complete Pareto front so that the Pareto front can be trimmed to any given surge margin. Selection of surge margin also requires consideration of the transient load ramping behaviour of the plant to ensure safe operation. By optimising these four process variables (Table 8-3), the cycle is able to simulate inventory control, TIT control and split fraction control by optimally choosing the variables. Nonetheless, this work does not model either throttling control, which requires an additional valve to throttle the turbine inlet pressure, or the turbine bypass control. In order to understand the power block characteristics for different

ambient temperatures, the CIT has to be fixed although it is actually dictated by the off-design conductance of the precooler for any given cold and hot streams state boundary condition. The mass flow rate of the cold stream is therefore controlled in order to achieve the desired CIT, ensuring the precooler pinch constraints are not violated.

8.3.3 Solar Field

The annual simulation is performed using the System Advisory Model (SAM V2018.11.11), which designs a heliostat field layout optimised for the selected location of Dagget, California. A solar multiple of 2.8 and 14 hours of TES are used in this study [42]. SAM calculates the hourly optical efficiency and evaluates the energy absorbed by the HTF considering both the receiver and piping losses. SAM supplies the heat to the power block to meet the dispatch requirement storing any remaining heat in the TES. Dispatch optimisation is not turned-on and the dispatch method, time of delivery factors and weekly schedule pattern are all retained at the default values for this study, although they could influence the total number of start-ups. The user-defined power block parametric table defines the power output based on the heat supplied to the power block for the changes in the boundary conditions such as ambient temperature, MSIT and molten salt mass flow rate (MSFR). This parametric table is different for each operational strategy so that the only supplies the heat demanded of the power block for the given boundary conditions in order to produce the power output required by the dispatch mode at each time step.

Table 8-4 Solar field model assumptions for costs estimation [49]

Performance factors	Unit	Value	Finance factors	Unit	Value
Thermal Energy Storage	$/kW$_{th}$	15	Inflation rate	%	3
Heliostat Field Cost	$/m^2	75	Real discount rate	%	5.5
Site Improvement cost	$/m^2	10	Contingency	%	10
Land cost	$/Acre	10,000	Analysis Period	Years	35

Since the purpose of the annual simulation is to compare the two different operational strategies, the cost of the sCO_2 power block is fixed for both cases (design point is fixed). The value of 925 $/kW$_e$ is assumed in our study as

suggested by Schmitt et al. [42]. Scaling exponents of 0.7 and 0.0113 are used to calculate the cost of the solar receiver and the tower, respectively. The fixed cost by capacity of 66 $/kW-yr and the variable generation cost of 3.5 $/MWh are considered. All of the financial assumptions are tabulated in Table 6-4 [49].

8.4 Model Verification with Literature

The design code is validated against the data reported in Kulhánek and Dostál [50] by setting up an optimisation that uses sequential quadratic program algorithm in MATLAB. The optimisation algorithm maximises the efficiency by varying the split fraction and cycle pressure ratio. All the heat exchangers are discretised to 15 zones. Performance comparison is performed for two different turbine inlet temperatures (i.e. 600 and 650 °C) for a maximum cycle pressure of 250 bar, CIT of 32 °C, compressor efficiency of 89%, recuperator effectiveness of 95% with a minimum pinch of 5 °C. Kulhánek reported a turbine efficiency of 93%, however, Turchi et al. [51] repeated the same boundary conditions for verification purposes and commented that a turbine efficiency of 90% closely reproduces Kulhánek results, therefore 90% turbine efficiency is used in this work. The results match with the reported values in Turchi et al. [51], however, a maximum relative error of 0.7% was observed against Kulhánek results for a TIT of 650 °C (Table 8-5).

Table 8-5 Cycle efficiency comparison with Kulhánek [50] and Turchi [51]

Turbine Inlet Temperature **(°C)**	**Efficiency (%) (Turchi)**	**Efficiency (%) (Kulhánek)**	**This Study**	
			Efficiency (%)	Split Fraction
600	48.31	48.3	48.32	0.337
650	50.24	49.9	50.25	0.333

In order to verify the off-design code, a 30 MW_e power cycle was modelled in the MATLAB® in-house code and the recuperator conductance was provided as an input to the Dyreby FORTRAN code for verification. The main compressor shaft speed was fixed during off-design simulation as the Dyreby code assumes that

the turbine and main compressor shafts are connected. The efficiency and process temperature results obtained from the two simulation codes are compared for both design CIT of 42 °C and off-design CIT of 55 °C and a maximum the relative percentage error of 0.1% is observed. Since this verification was performed against the Dyreby code, all the component modelling assumptions are known, therefore, the source of discrepancy is due to the numerical tolerance of the nonlinear equation solver.

8.5 Results and Discussion

8.5.1 Design Performance

The split fraction and the compressor inlet pressure cannot be optimised to maximise the efficiency as they reduce the cycle specific power and increase the size of the recuperator, therefore a cycle minimum pressure of 80 bar and split fraction of 0.3 are selected for this study. The corresponding design performance of the recompression cycle is tabulated in Table 8-6 where the differential temperature across the PHEX is about 175 ˚C, the specific work is ~153 kJ/kg and the recuperator conductance are 8.8 MW/K whilst PHEX conductance is 3.8 MW/K.

Table 8-6 Design performance of recompression cycle

Description	Unit	Value
Net Power	MW	30.66
Net Efficiency	%	49.02
ΔT across PHEX (sCO_2 side)	°C	174.2
Recuperator UA (LTR+HTR)	MW/K	8.8 (3.5+5.3)
Primary Heat Exchanger UA	MW/K	3.8

8.5.2 Multi-Objective Optimisation for Off-Design Performance

8.5.2.1 Effect of Ambient Temperature Variation

Figure 8-7 shows the Pareto fronts for different CITs, where it can be seen that both the net efficiency and the net power of the power block significantly decreases at higher CIT's. The net power fraction is the off-design net power output normalised with the design net power and this can exceed one depending

on the boundary conditions (Table 8-3). No constraints on the maximum net power fractions were imposed to explore the complete Pareto front, however, the turbine peak power can limit this, in which case the Pareto front can be shortened. The dotted lines in Figure 8-7 show the Pareto fronts, which have an additional upper MSOT constraint of 2% from its design value (~ 5.4% reduction of the thermal storage capacity).

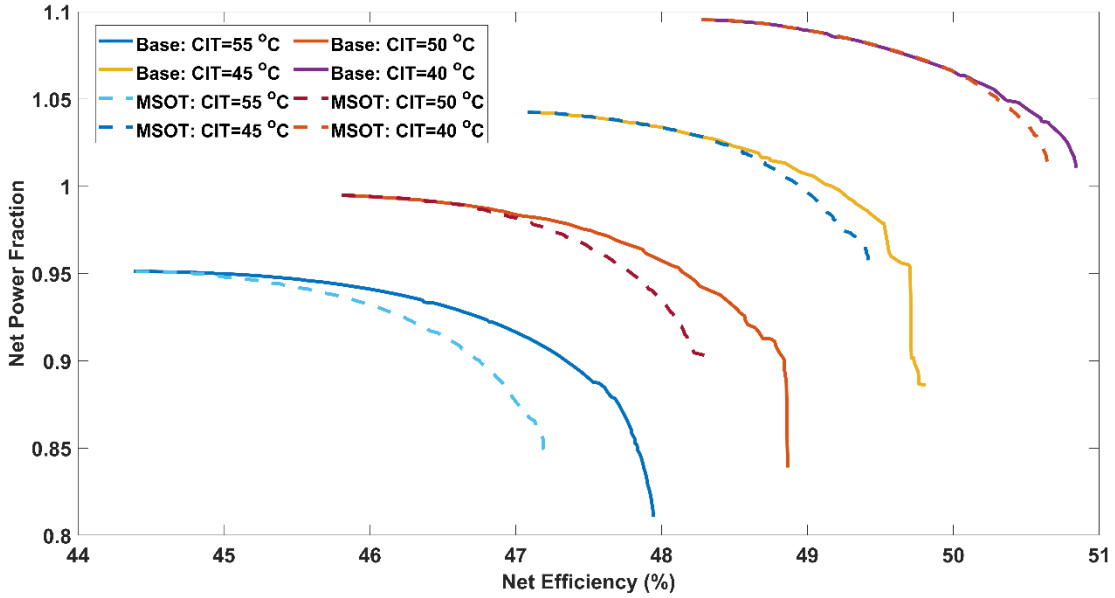

Figure 8-7 Pareto fronts of recompression cycle for different CIT (continuous lines represent the Pareto fronts without limiting the MSOT, dashed lines show the MSOT limiting cases)

It can also be seen from Figure 8-7 that by limiting the MSOT close to its design value, the maximum net power of the Pareto fronts are unaffected, whilst the maximum efficiency cases are negatively affected with the amount of change increasing with the CIT. The CIT of 40 °C is less influenced by the MSOT constraint (design CIT=42 °C), however, the impact is more pronounced as the CIT increases. In Figure 8-8, it is possible to see the MSOT behaviour across the Pareto front for different CITs. The MSOT constrained Pareto fronts are sub-optimal Pareto of the base case and therefore they limit the maximum value of the main compressor inlet pressure (shown in Figure 8-9 (a)) and so also the pressure ratio. The efficiency reduces by 0.8% points at 55 °C CIT by constraining

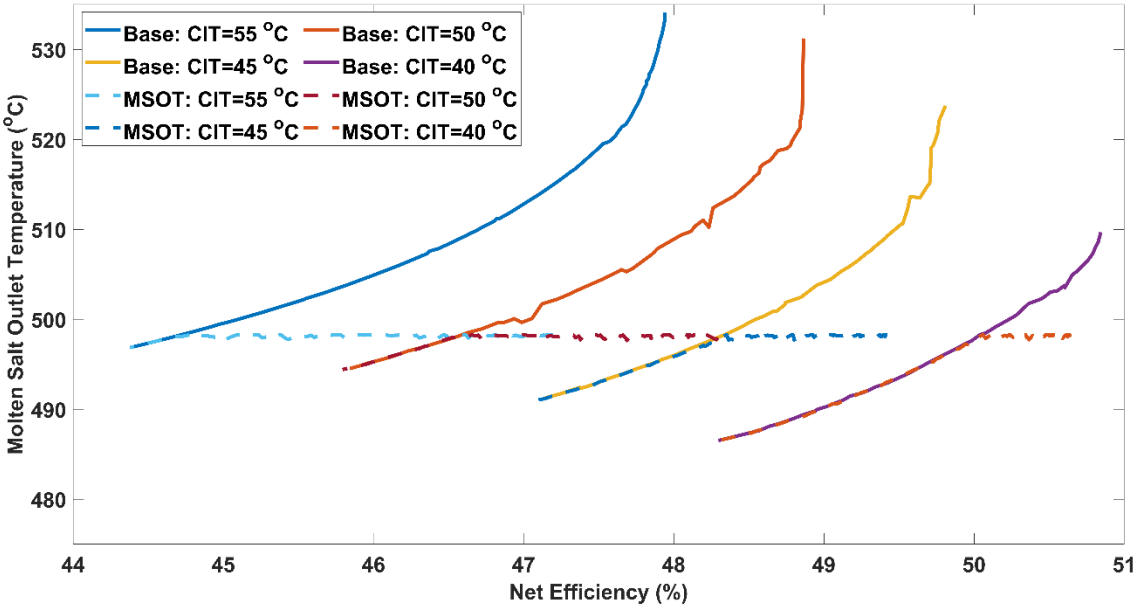

Figure 8-8 MSOT with respect to the net efficiency across the Pareto front (shown in Figure 8-7) for different CIT (Continuous lines represent the Pareto fronts without limiting the MSOT, dashed lines show the MSOT limiting cases)

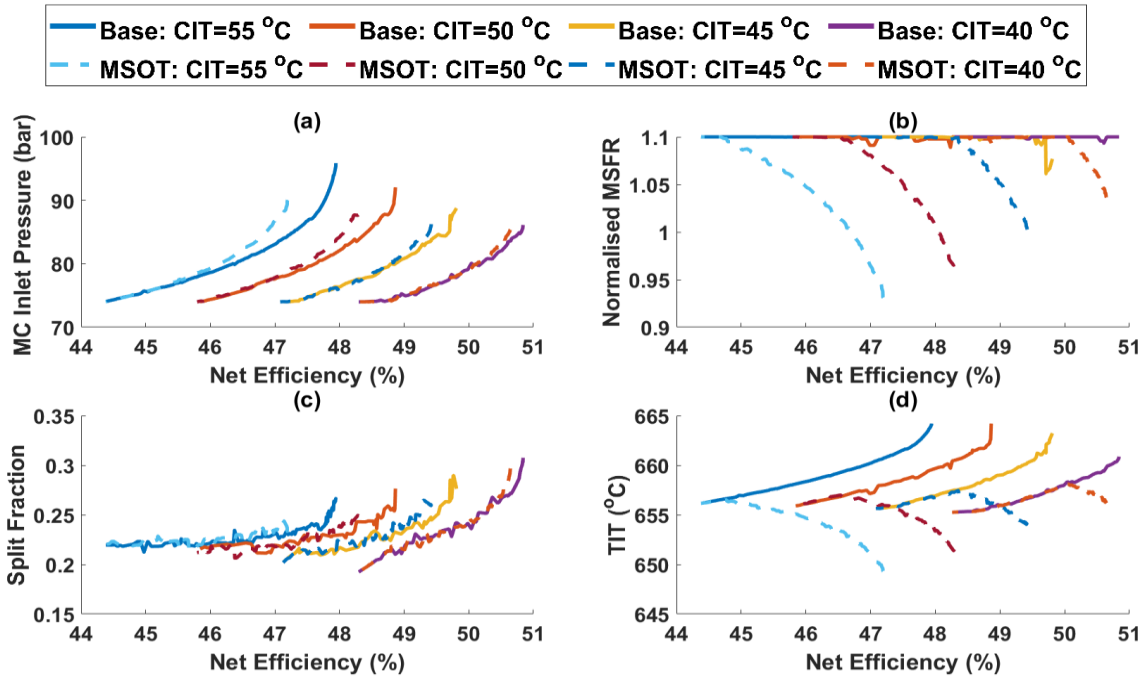

Figure 8-9 Process variables with respect to the net efficiency across the Pareto front (shown in Figure 8-7) for different CIT: a) Main Compressor Inlet Pressure, b) Molten Salt Inlet Flow Rate, c) Split Fraction, d) Turbine Inlet Temperature

the MSOT. For CIT=40°C, however, the majority of the MSOT curve (Figure 8-8) is below the imposed limit of 102% of the design value and thus both control strategies, with or without MSOT limiting, are less affected as can be seen by the curves for CIT=40 °C in Figure 8-7.

From Figure 8-9 (a), it is worth noting that the main compressor (MC) inlet pressure reached the minimum bound when maximising the net power while the MC inlet pressure increases as the compressor inlet temperature increases in order to achieve the maximum cycle efficiency. Maximising the net power output from the power cycle for different compressor inlet temperatures always tends to increase the pressure ratio as the minimum pressure reaches the lower bound and maximum pressure reaches the upper bound as shown in Figure 8-9 (a).

The split ratio of the mass flow rate towards the recompressor is minimum when maximising the net power whilst it increases when maximising the efficiency (Figure 8-9 (c)). It is also worth noting that the difference in the split fraction between the maximum efficiency and maximum net power cases reduce as the CIT increases (Figure 8-9 (c)). The split fraction reduces when maximising the efficiency at a higher CIT because the compressor inlet shifts away from the critical point, therefore, the real gas effect is minimal.

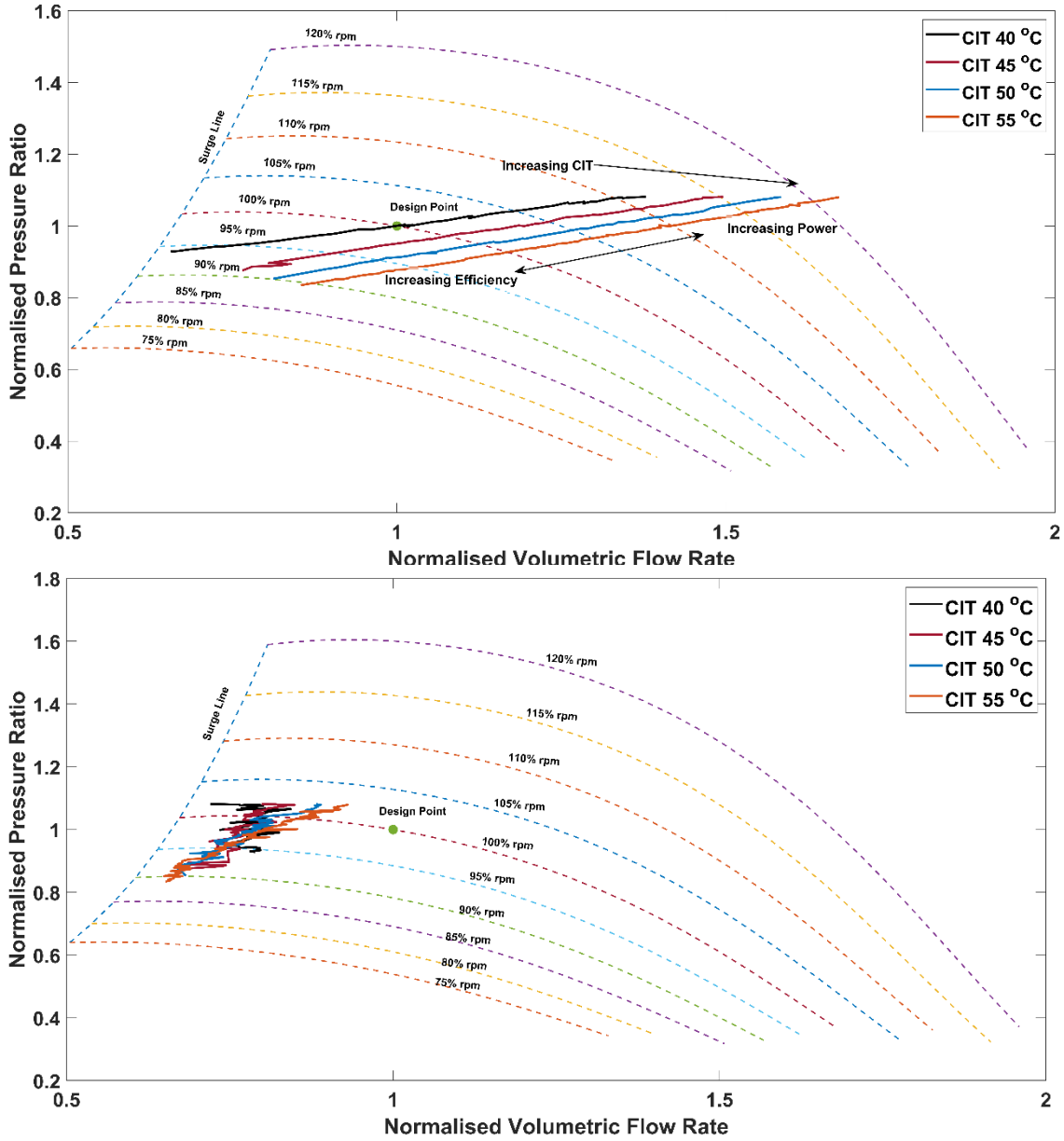

Figure 8-10 Compressor operating point across the Pareto front (shown in Figure 8-7) for different CIT; Top) Main Compressor, Bottom) Recompressor (dashed lines represent the compressor map while the operating points across the Pareto front are plotted as continuous lines)

Consequently, the difference between the cold and hot stream isobaric specific heat also reduces and RCBC approaches towards SRBC configuration (single recuperator). This had been already observed by Carstens et al. [52] i.e. split fraction reduces at a higher CIT, nonetheless, the split fraction corresponding to the maximum net power case is not notably affected for different CITs from which

it can be concluded that split fraction control is less significant when maximising the net power. Increasing the CIT also increases the compressor outlet temperature (compressor inlet conditions move away from the critical point) which also increases the LTR hot stream outlet temperature. This also reduces the capacitance difference between hot and cold streams of LTR, consequently, the split fraction reduces with increase in CIT for maximum efficiency cases.

The molten salt mass flow rate reached 110% (maximum bound) across the complete Pareto front. Although the TIT tends to increase with efficiency for the base case, it does not when the MSOT is constrained (Figure 8-9 (d)). The maximum TIT occurs neither in the maximum net power case nor in the maximum efficiency case. The molten salt flow rate also reduces to increase the maximum efficiency as the CIT increases.

Increases in CIT also increase the compressor inlet volumetric flow rate (for the same mass flow and fixed flow area) and changes the local Mach number (speed of sound changes), consequently the operating point shifts. To minimise the shift of compressor off-design point in the performance map at a higher CIT, the inlet pressure has to increase to compensate for the drop in density. However, this does not return the compressor operating point back to the design as the local Mach number also shifts with the increase in CIT owing to the change in the speed of sound. Nevertheless, it has been observed that the compressor inlet volumetric flow is higher than the design point volumetric flow at higher CIT when the cycle is optimised for maximum efficiency. This observation is in line with Bennett et al. [53] and the trend is expected to depend on the shape of the compressor map.

Maximising the efficiency of a closed-loop Brayton cycle for a given TIT and CIT tends to lower the pressure ratio in a way that minimises the impact on the turbomachinery efficiencies, while the overall recuperation effectiveness is unaffected. It has also been observed that the compressor outlet pressure always tends to reach the maximum bound for both the cases (maximising the net power/maximising the net efficiency), therefore the main compressor inlet pressure variation can also be interpreted as the inverse of the compressor

pressure ratio. The compressor inlet pressure can be increased (thus reducing the pressure ratio) to compensate for the reduction in density owing to the increase in CIT, and by doing so the inlet volumetric flow can be maintained close to the design value. Thus, the compressor efficiency is only affected by the changes in the non- dimensional speed and local Mach number. From the optimisation results, it has been observed that the mass flow rate reduces and also the split fraction reduces at a higher CIT as shown in Figure 8-9 (c). Reduction in the cycle pressure ratio when maximising the efficiency also increases the turbine exhaust temperature for a given TIT, which also increases the cold stream inlet temperature to the PHEX owing to higher recuperation of the HTR, increasing MSOT.

It is clear, therefore, that the cycle pressure ratio drops at a higher CIT when maximising the cycle efficiency and the magnitude varies based on the turbomachinery performance map. Consequently, the turbine exhaust temperature typically tends to increase for the constant turbine inlet temperature, though the latter is not strictly true as shown in Figure 8-9 (d).

This increase in TET also increases the cold stream inlet temperature to the PHEX, therefore the MSOT increases. The MSOT increases by 46 °C at 55 °C CIT and this implies that the TES storage capacity reduces by 25.1% if the operation is continued until the cold tank temperature equalises with MSOT and the duration depends on the instantaneous cold tank inventory.

The compressor operating points across the Pareto fronts for different CIT are plotted on the compressor map as Figure 8-10 to visualise the operational characteristics. The main compressor volumetric flow changes significantly across the Pareto front whilst the recompressor volumetric flow changes are minimal. This is because the density variation at the main compressor inlet changes significantly near the critical point. At higher CIT's, the main compressor volumetric flow increases with the falling pressure ratio when maximising the efficiency. When maximising the power, the volumetric flow to the main compressor increases with the maximum cycle pressure ratio. It has to be noted that a compressor over-speed limitation is not included as a constraint in this

optimisation in order to explore the complete Pareto front, however, in reality the maximum net power is capped by the over-speed limit. If the main compressor shaft is connected to the turbine, which runs at a constant speed, the reduction in maximum power at higher CIT is higher than the indicated values here. On the other hand, the compressor surge margin affects the maximum efficiency of the cycle, particularly at CIT's lower than the design value. The increase in the volumetric flow is not significant in the recompressor when the CIT is higher than 40 °C, therefore, the main compressor operational speed and surge limits are crucial in order to realise the maximum power and maximum efficiency, respectively. Since the cycle minimum pressure and the split fraction at the design do not maximise the power cycle efficiency, the recompressor operates away from the design point. This is mainly driven by the lower split fraction across the Pareto front than the design value of 0.3.

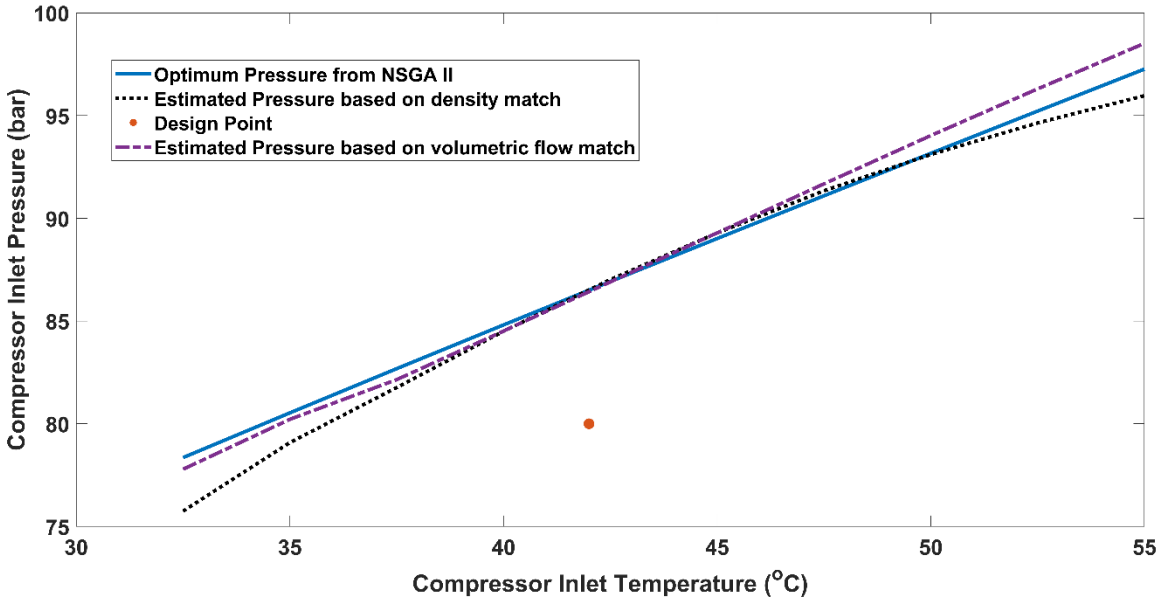

Figure 8-11 Comparison of estimated compressor inlet pressure against the optimised pressure when maximising the efficiency

The design split fraction is only achieved in the Pareto front when maximising the efficiency for a CIT of 40 °C (Figure 8-9 (c)). The corresponding cycle minimum pressure (Figure 8-9 (a)) is slightly higher than the design value (i.e. 80 bar) by ~5 bar with a significant reduction in the recompressor inlet temperature (~30 °C), owing to the recuperation maximising. This increases the recompressor inlet

density and consequently moves the operating point away from the design. Sizing the recompressor for maximum cycle design efficiency eliminates this difference when operating the plant in maximum efficiency mode. However, the selection of optimal split fraction and cycle minimum pressure at the design plays a critical role in the recompressor off-design operation when the plant needs to run in a combination of maximum power and efficiency modes. Although the recompressor speed control helps to bring the operating point close to the design point at a higher ambient temperature when the efficiency is maximised, it doesn't benefit for a lower ambient temperature. Other approaches such as 2×50% recompressor, inlet guide vane and compressor hot-recirculation can aid in handling a large variation in the volumetric flow rate at lower ambient temperatures, however, the latter option can penalties the efficiency of the system.

The compressor inlet pressure required to match the compressor inlet density at the design is calculated for every CIT (Figure 8-11). Matching the compressor inlet density to the design density doesn't guarantee the same volumetric flow at the compressor inlet as the optimal mass flow rate and split fractions are different for every CIT and therefore, the compressor inlet pressure required to match the design volumetric flow is also plotted in Figure 8-11. Nevertheless, it is worth highlighting that the change in the mass flow and split fraction are not known prior to perform a complete optimisation. The estimated pressure based on a constant volumetric flow rate at the compressor inlet is higher when the CIT is high. This implies that the optimised volumetric flow rate from NSGA-II was higher than the design value. On the other hand, the optimised volumetric flow rate at the main compressor inlet was slightly lower than the design value at a lower CIT.

However, the estimated pressure, based on the assumption of constant density predicts lower pressure (higher volumetric flow rate) at very high CIT, although it is relatively similar to the optimal value until the CIT is 50 °C. Nonetheless, this approach deviates significantly from the optimal value at a lower CIT. This deviation occurs owing to the changes in fluid properties which affects the Mach number and the magnitude can vary based on the shape of the compressor map.

It is worth highlighting that the compressor inlet pressure chosen for this study was not an optimal value that maximises the efficiency at the design CIT since the design pressure selection is always a trade-off between maximising net power and efficiency.

8.5.2.1.1 Modified RCBC to Improve Off-Design Performance

It was anticipated that the addition of a bypass valve to the cold stream of the HTR, as shown in Figure 8-12 (red lines), would improve the efficiency for the higher CIT cases by sacrificing some recuperation to maintain MSOT close to the design value. However, the optimisation algorithm determined that zero flow to this bypass valve provided optimal values of net power or efficiency as shown in Figure 8-13.

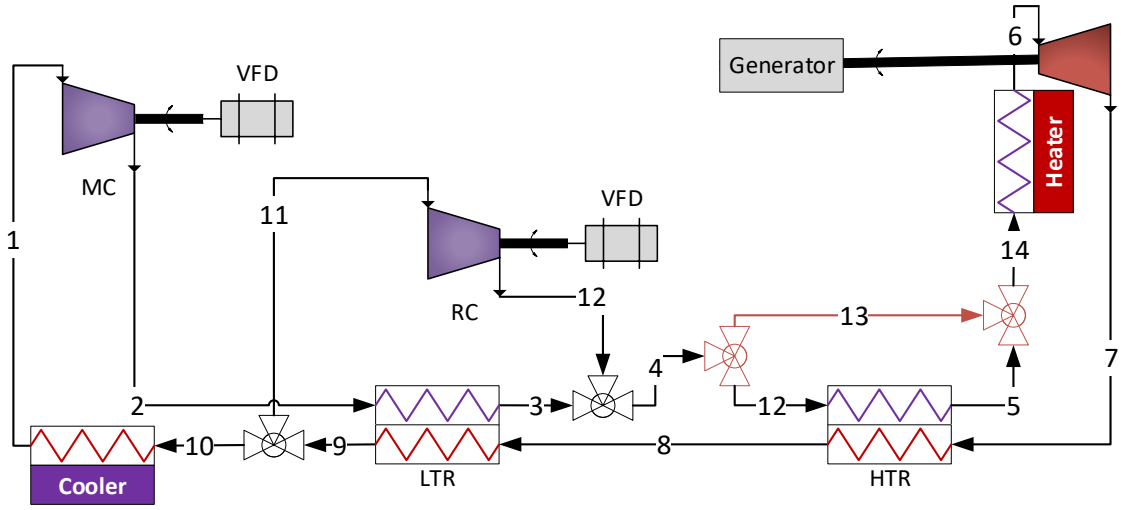

Figure 8-12 Modified recompression cycle configuration (modifications are in red)

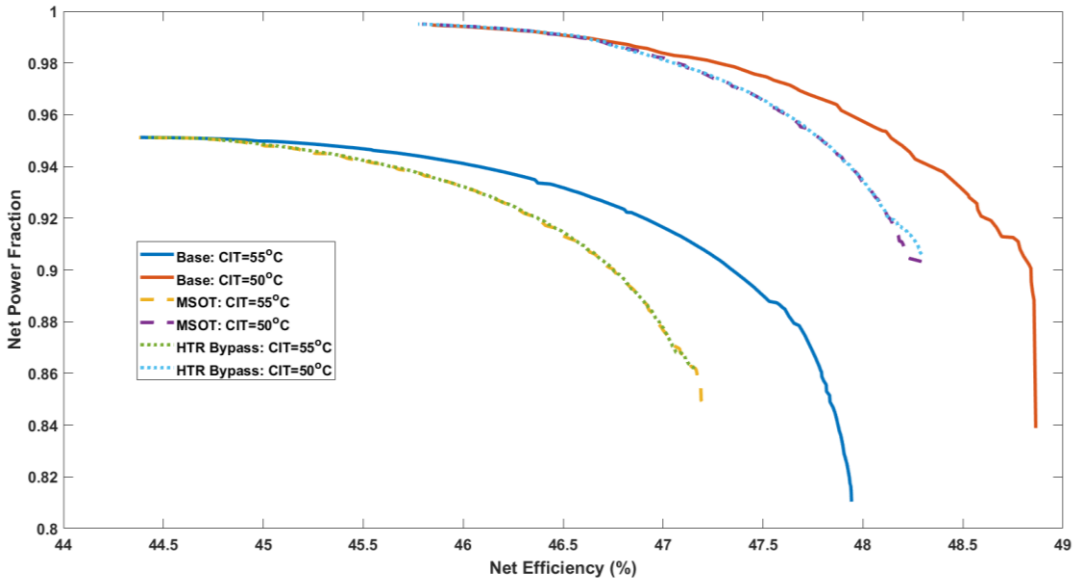

Figure 8-13 Comparison of Pareto fronts of modified recompression cycle against standard recompression cycle

8.5.2.2 Effect of Molten Salt Flow Rate Variation

Since the MSIT and CIT are unaffected from the design value, the speed of sound is unaffected, the compressor and turbine operating point can be kept close to the design value for an ideal gas closed-loop Brayton cycle by lowering the system inventory and keeping the cycle pressure ratio constant. For an ideal gas, this infers that the system pressure drops in proportion to the mass flow reduction in order to keep the density constant [26,54]. Since changes in the system pressure do not affect the specific heat for monotonic ideal gases, the efficiency and the specific power of the cycle can be maintained close to the design value for a large plant turndown ratio (neglecting the variation of the heat exchanger pressure drop and heat transfer coefficient due to changes in the Reynolds number) [26]. For supercritical fluids, the pressure significantly affects the heat capacity, heat transfer coefficient etc. and the relationship between pressure and density is non-linear. Furthermore, the speed of sound is also a function of the compressibility factor which is also sensitive to pressure [55].

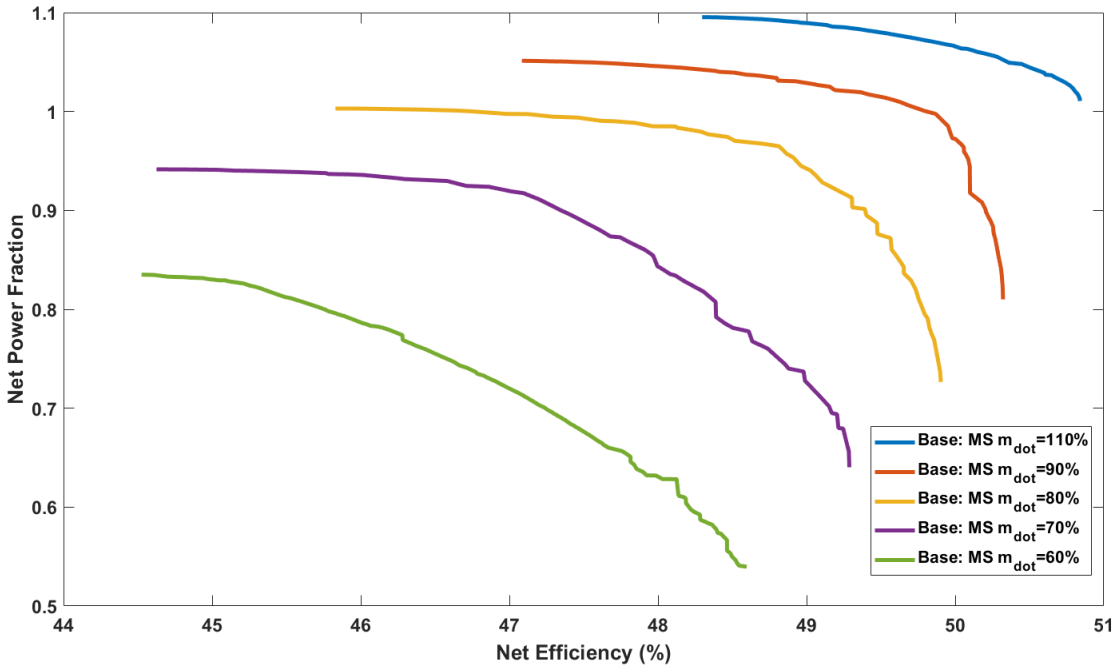

Figure 8-14 Pareto fronts of recompression cycle for different MSFR (The percentages are referred to the design MSFR)

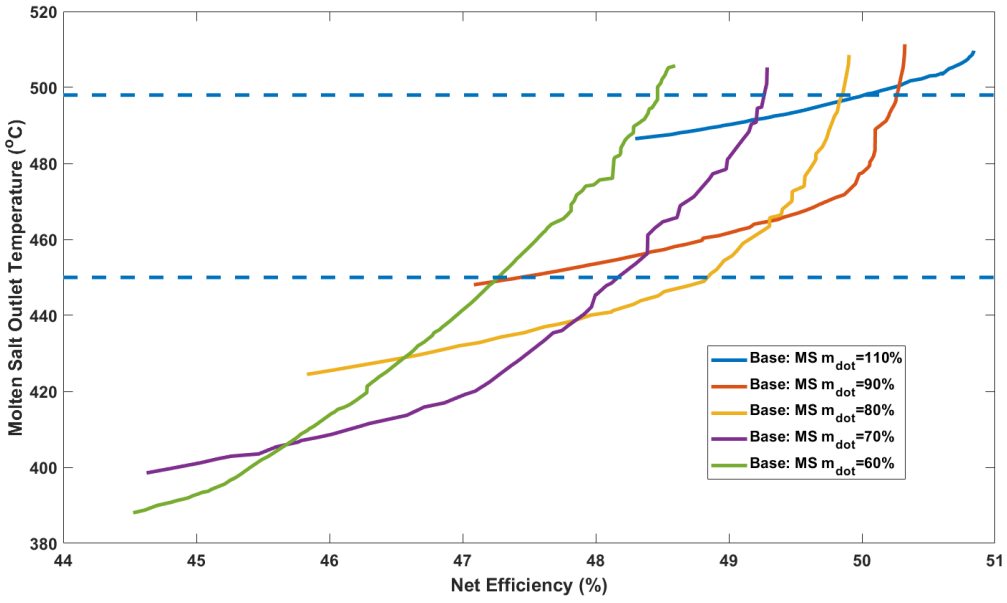

Figure 8-15 MSOT across the Pareto front (shown in Figure 8-14) for different MSFR (The dashed blue lines represent the 102% design MSOT and freezing limit of molten salt)

The off-design Pareto fronts for the variation of the fractional MSFR is shown in Figure 8-14 at the CIT of 40 °C. It can be observed that the net power can be about 83.5% of the design value when the molten salt mass flow rate is 60% of

the rated flow by operating the power block in the maximum power mode. On the other hand, this reduces the efficiency to 44.5%, which can be increased to 48.6% with a sacrifice in the net power to about 54% of the design value. This indicates that the degree of freedom for operating the sCO_2 power block is larger and the efficiency and net power can be changed significantly depends on the operating point dictated by the control strategy.

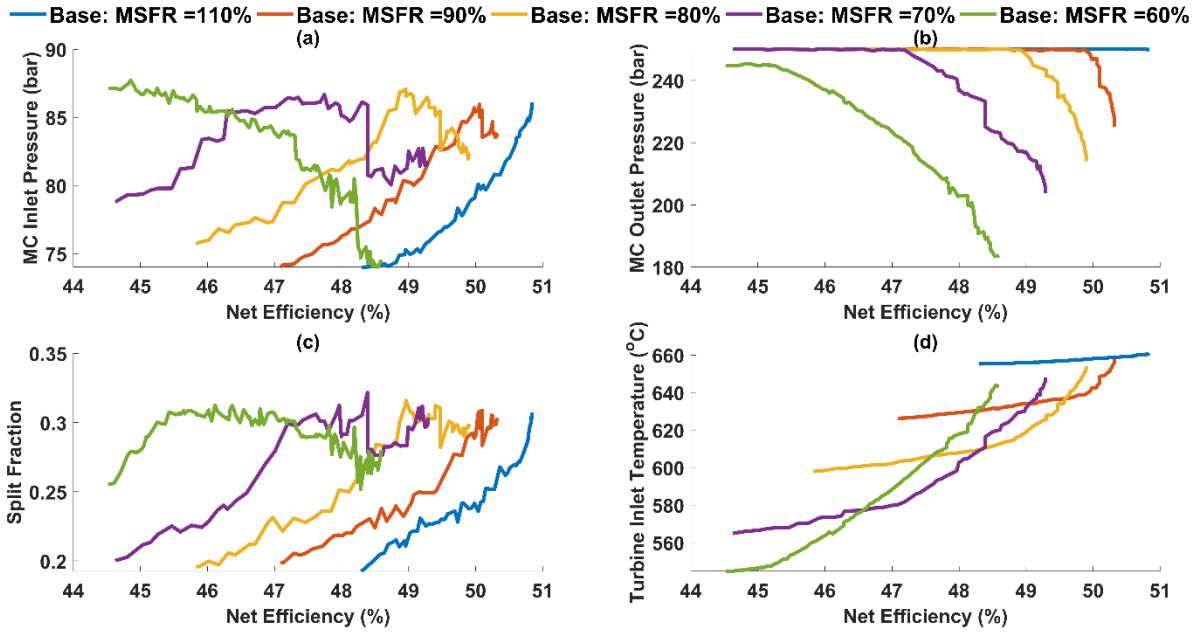

Figure 8-16 Process variables trends across the Pareto front (shown in Figure 8-14) for different MSFR: a) Main compressor Inlet Pressure, b) Main compressor Outlet Pressure, c) Split Fraction, d) Turbine Inlet Temperature

Figure 8-15 shows the MSOT across the Pareto front and it is clear that the reduction in the molten salt mass flow rate also reduces the upper value of MSOT, therefore, the deviation of the MSFR does not negatively affect the solar field/TES capacity. Nevertheless, it is worth noting that the minimum MSOT reduces with the reduction in MSFR, which can be a concern depending on the freezing point of the selected molten salt. Since the melting temperature of the selected molten salt in this study is 424 °C, a minimum MSOT temperature limit of 430 °C is considered in this work, nonetheless, this was not enforced as a minimum constraint in the optimisation in order to explore the complete Pareto front. It has to be noted however that the maximum power can not be realised when the

MSFR is lower than 70% of the design value if the minimum MSOT constraint limits the operation (Figure 8-15). Hence, selecting a molten salt with lower freezing temperature could eliminate this problem. According to Figure 8-16 (a), the compressor inlet pressure is not strictly smooth, however, it is increasing from the maximum net power case to the maximum efficiency case until 70% molten salt mass flow.

At 60% mass flow, a higher value of minimum pressure occurs at the maximum power case. The compressor outlet pressure reduces for the maximum efficiency case whilst it is higher for the maximum net power case (Figure 8-16 (b)). The difference between the compressor outlet pressure for the maximum net power Case and the maximum efficiency case increases as the MSFR reduces. Only at 60% MSFR, the cycle maximum pressure is lower than the upper bound value. The split fraction reaches its lower value for the maximum net power case and it reaches a maximum value for the maximum efficiency case (Figure 8-16 (c)). The maximum and minimum split ratio values are not significantly changed up to 70% of the MSFR and the range reduces at 60% molten salt mass flow. This indicates that the split fraction control is not significant for a reduction in MSFR upto ~70%. TIT reaches a maximum value at the maximum efficiency cases and the absolute magnitude reduces as the molten salt mass flow rate reduces, which implies that the TIT need to be controlled when the MSFR is reduced in order to maximise the cycle efficiency. It is worth noting from Figure 8-16 (d) that the TIT doesn't reach the maximum value (~650 °C) at a lower mass flow rate and this infers that the gain in the Carnot efficiency is not significant as compared to the efficiency loss from the turbomachinery. Furthermore, the cycle pressure ratio at the maximum efficiency case shows a declining trend because of the reduced compressor outlet pressure, whilst it is constant for monoatomic gas cycles. This infers that the changes in the cycle pressure impact the specific heat capacity

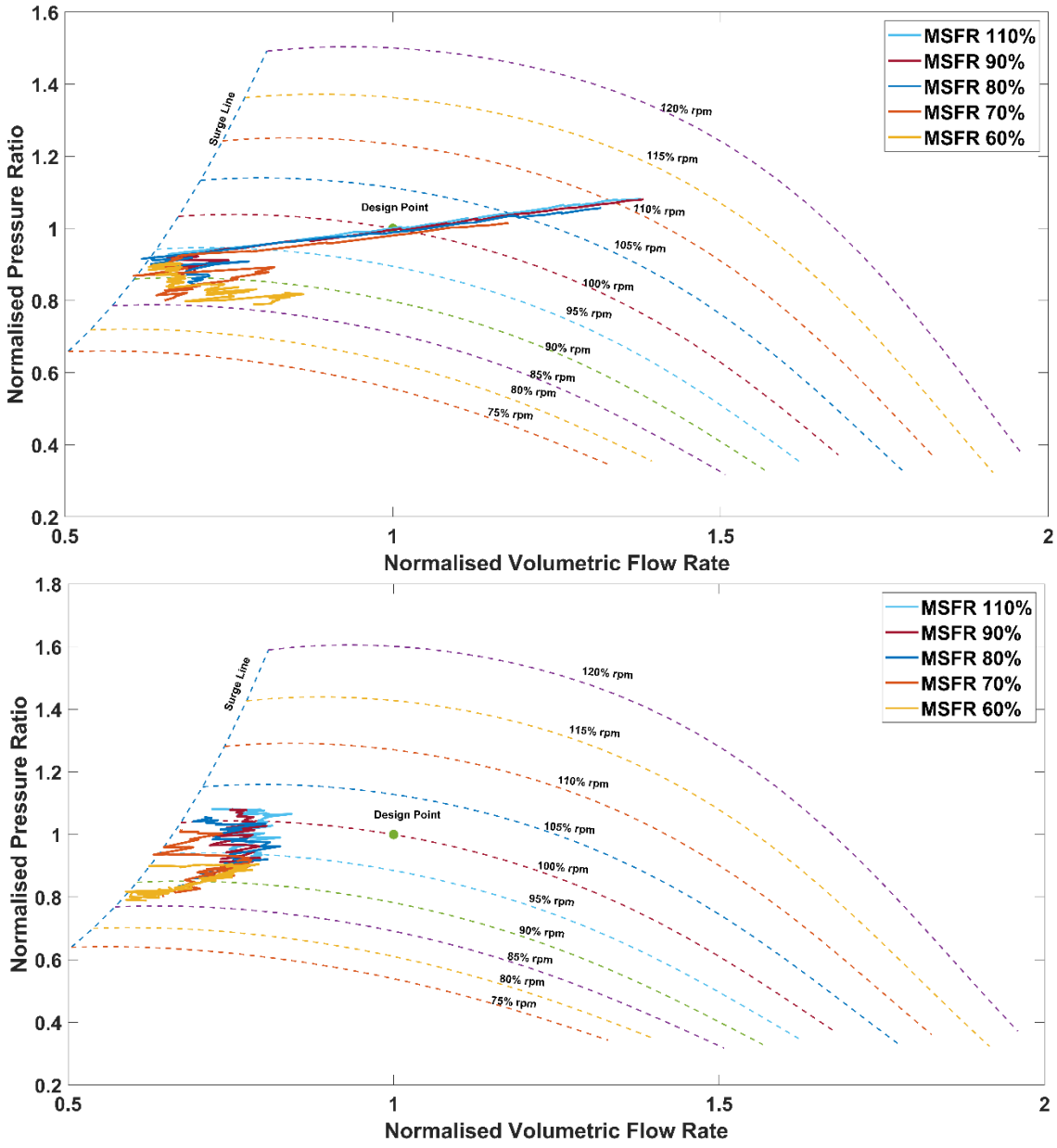

Figure 8-17 Compressor operating point across the Pareto front (shown in Figure 8-14) for different MSFR; a) Main Compressor b) Recompressor

and speed of sound significantly, which changes the cycle optimal pressure ratio. At 60% molten salt mass flow, the MSOT at the maximum net power case approaches close to the sCO_2 inlet temperature to the PHEX. Further reduction of MSFR is expected to cause conflict as the recuperation has to be sacrificed in order to reach the minimum MSOT, which can limit the minimum MSOT.

However, a CSP power plant is very unlikely to encounter such off-design scenarios, therefore, it is assumed to be less severe.

Figure 8-17 shows the main compressor and recompressor operating points across the Pareto front overlay on the corresponding compressor maps. The main compressor operating points are similar for different MSFR when maximising net power whilst they slightly different one other when maximising efficiency (Figure 8-17 (Top)). After a certain point, the main compressor pressure ratio reduces steeply with small changes in the volumetric flow to increase efficiency. This fall in pressure ratio can also be seen in Figure 8-16 (b) where the compressor outlet pressure drops. On the other hand, the recompressor operates with the lesser change in their volumetric flow rate whilst the pressure ratio changes to match with the main compressor outlet pressure (Figure 8-17 (Bottom)). The recompressor operates away from the design point owing to similar reasons discussed in section 8.5.2.1.

8.5.2.3 Effect of Molten Salt Inlet Temperature Variation

For changes to TIT in a given ideal gas closed-loop recuperated Brayton cycle, for a fixed CIT the PR has to reduce but without impacting the turbomachinery efficiencies significantly [56]. Since the sCO_2 behaves like an ideal gas at a higher temperature, the cycle behaviour is expected to be similar to ideal gas closed cycle. This implies that the turbine inlet pressure has to be lowered in order to compensate for the increase in density at a lower TIT so that the turbine inlet volumetric flow rate remains close to the design value.

Figure 8-18 shows four Pareto fronts for different MSITs and a CIT of 40 °C. The net power output can reach about 9% point higher power than the design value when the MSIT is 670 °C, nevertheless, this might not be realisable if the turbine is not oversized. When MSIT is 610 °C, the net power fraction at the maximum power case is close to 1 and the efficiency is 45.04%.

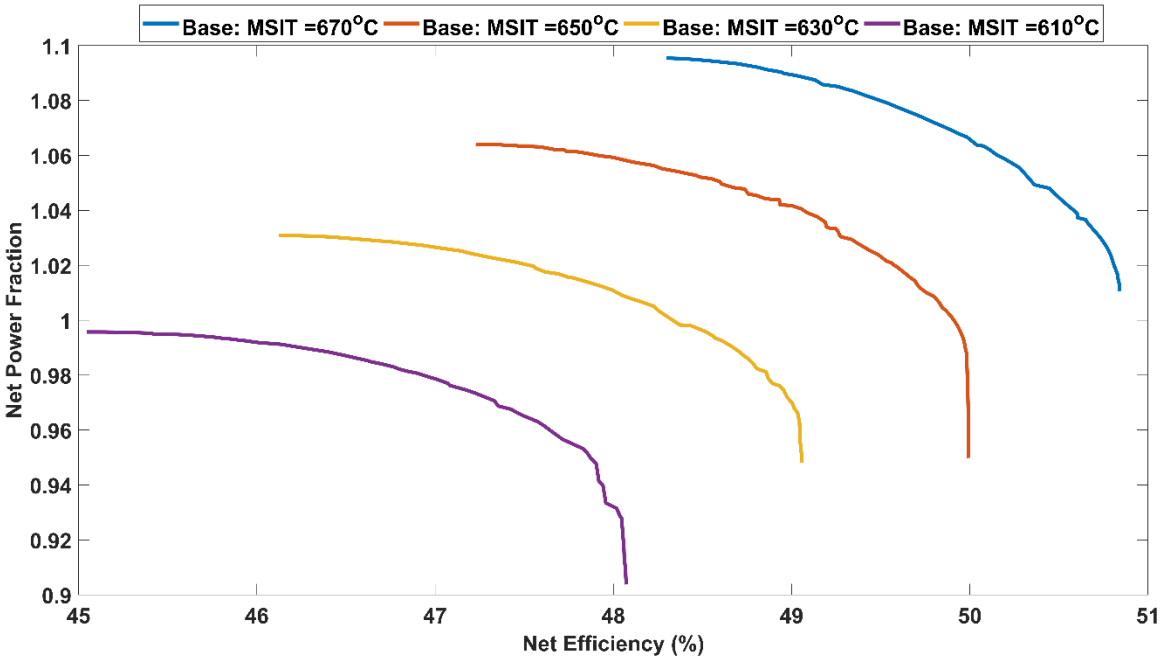

Figure 8-18 Pareto fronts of recompression cycle for different MSIT

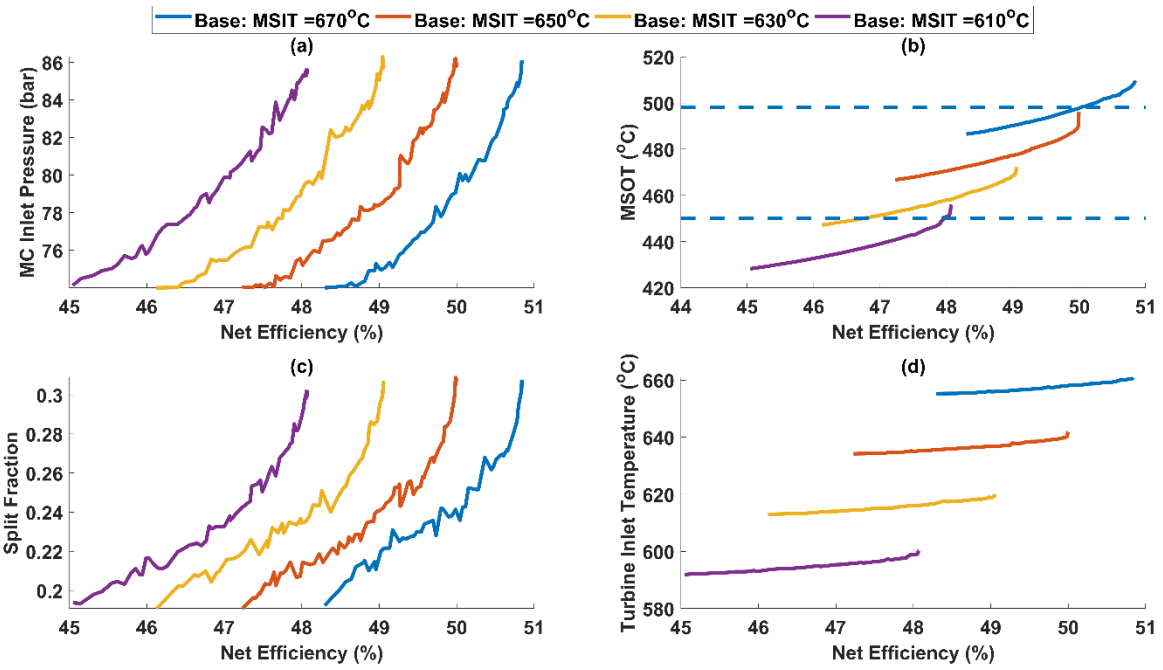

Figure 8-19 Process variables trends across the Pareto front (shown in Figure 8-18) for different MSIT: a) Main Compressor Inlet Pressure, b) Molten Salt Outlet Temperature, c) Split Fraction, d) Turbine Inlet Temperature

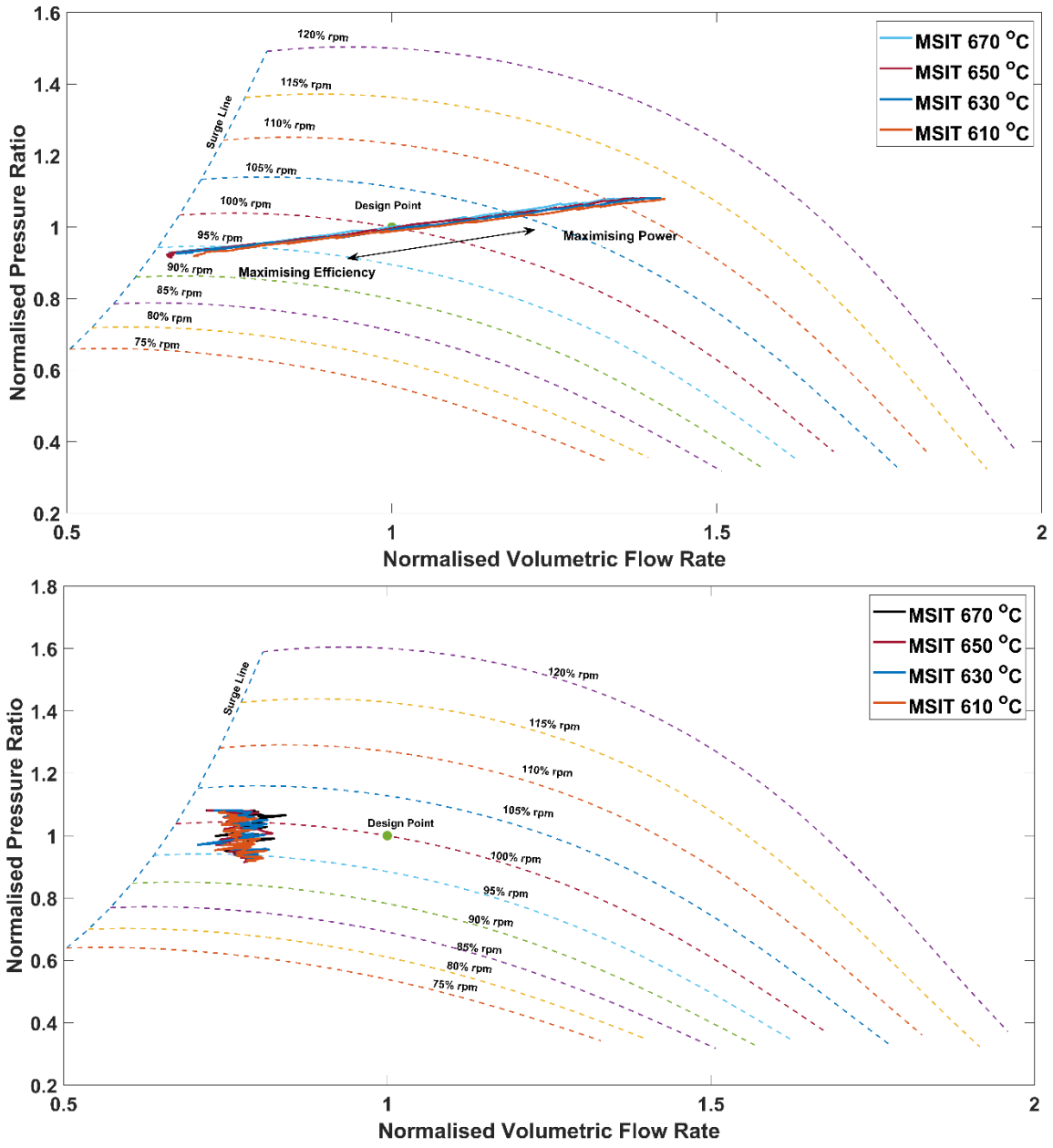

Figure 8-20 Compressor operating point across the Pareto front (shown in Figure 8-18) for different MSIT; Top) Main Compressor Bottom) Recompressor

The efficiency can be increased to 48.1% with a reduction of the net power fraction to around 90.4%, however, this power is achieved by reducing the MSOT to ~428 °C, as shown in Figure 8-19 (b), which is below the MSOT minimum freezing limit of 430 °C. From Figure 8-19 (a), the minimum pressure trend is roughly similar with a horizontal offset for all the MSITs studied, regardless of whether efficiency or net power is maximised, which infers that the main

compressor inlet pressure is not influenced by changes in MSIT. On the other hand the compressor outlet pressure starts to drop with the MSIT, similar to ideal gas cycles. The cycle maximum pressure is 245.4 bar at a MSIT of 610 °C whilst maximising efficiency. Maximising the net power tends to maximise the cycle pressure ratio by reaching the minimum bound on the compressor inlet pressure (Figure 8-19 (a)). The splitter ratio also shows a similar trend for all the MSIT studied with an offset (Figure 8-19 (c)), indicating that no control of split fraction is required. The TIT for the maximum efficiency cases reached a maximum value (Figure 8-19 (d)), showing that the power block operation is extended by lowering the MSOT when MSIT reduces and the efficiency drop is dominated by the reduction of the Carnot efficiency. Since the MSOT upper limit is not reached when the MSIT increases, MSOT constrained simulations were not performed, however, it has to be noted that the MSOT minimum limit was reached.

The main compressor and recompressor operating points are plotted on top of the corresponding compressor maps as shown in Figure 8-20, which indicates that changes in the MSIT do not influence either the main compressor or recompressor. However, the main compressor operates at a lower pressure ratio with a lower volumetric flow when maximising cycle efficiency compared to the maximum power case. On the other hand, the recompressor pressure ratio increases when maximising net power without a noticeable change in the volumetric flow, owing to the changes in the split fraction.

8.5.3 Annual Performance

In order to perform annual simulation, SAM requires the power cycle as a user-defined power cycle. A parametric table was therefore generated from SAM and each data point in the table set-up as a single-objective optimisation problem using a GA that maximises net efficiency while the MSOT freezing limit was imposed as a constraint. Since SAM maximises the net power of the recompression cycle, the maximum net power case was directly modelled in SAM.

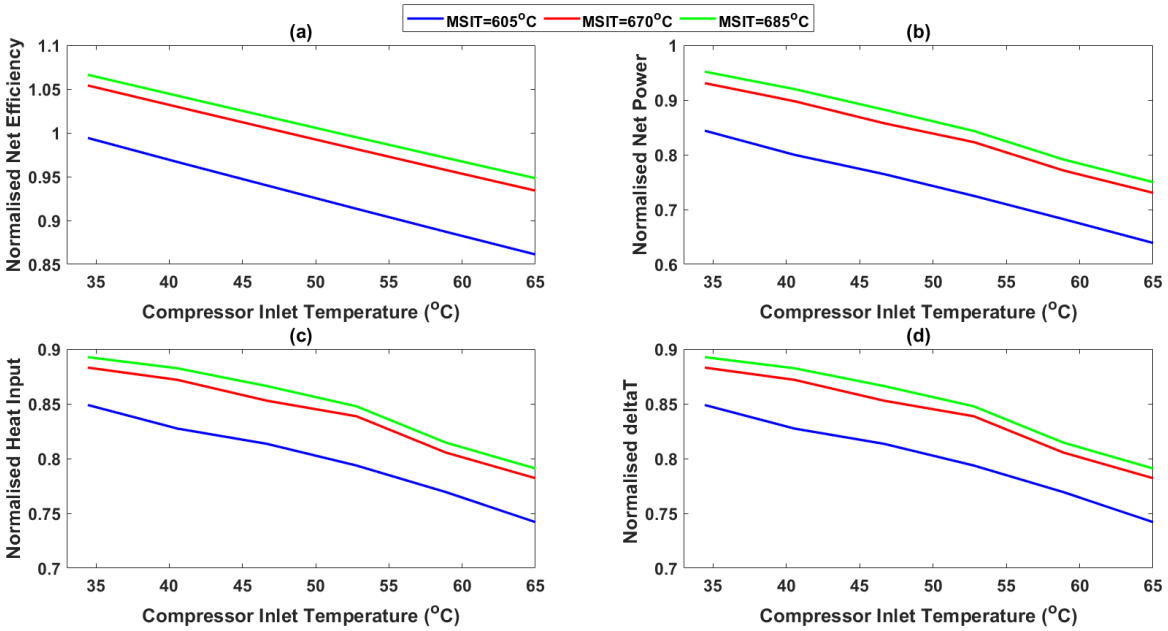

Figure 8-21 Normalised performance when maximising efficiency for different Molten Salt Inlet Temperature (MSIT): a) normalised net efficiency b) normalised net power c) normalised heat input d) normalised differential temperature across the primary heat exchanger

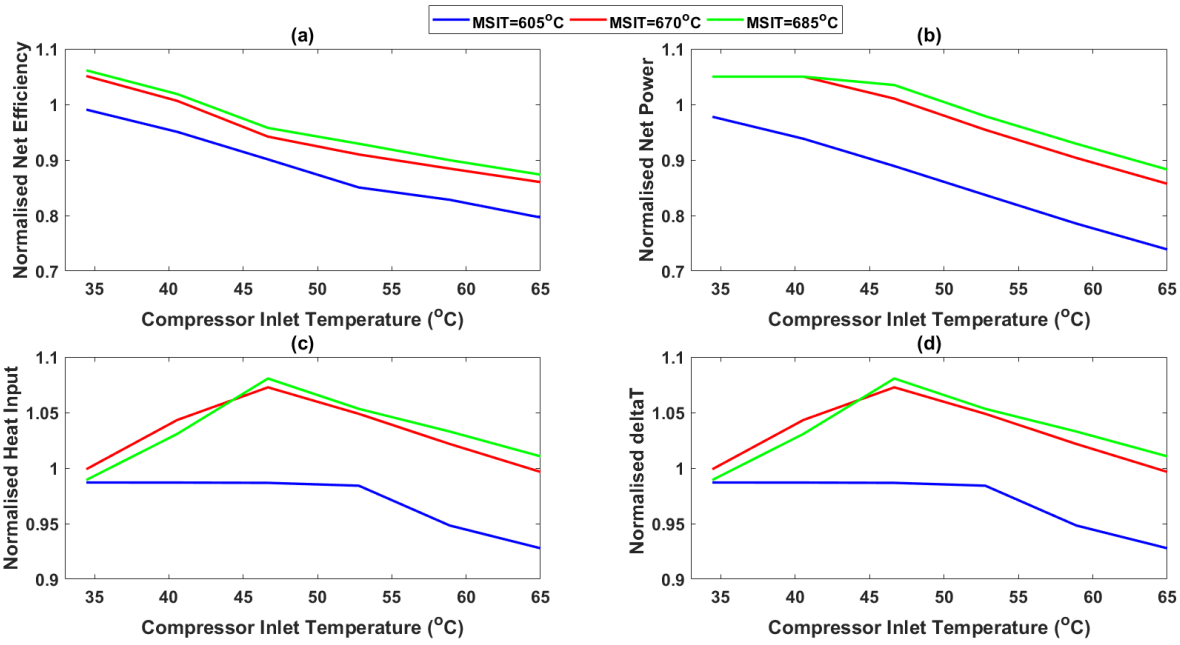

Figure 8-22 Normalised performance when maximising net power for different Molten Salt Inlet Temperature (MSIT): a) normalised efficiency b) normalised net power c) normalised heat input d) normalised differential temperature across the primary heat exchanger

It is worth highlighting, however, that the compressor and turbine shaft speed are fixed to their design values in SAM whilst they were optimised in this study hence the results obtained from SAM would be a sub-optimal solution and it is therefore it is a conservative estimate for maximum power case.

The single objective optimisation results for different CITs are shown in Figure 8-21 and Figure 8-22 with Figure 8-21 showing the normalised efficiency (referenced to the design condition), net power, heat input and differential temperature across the PHEX when maximising the net efficiency whilst Figure 8-22 shows these parameters when maximising the net power.

A linear increase in the efficiency above the design value is observed when the CIT is lower than 42 °C, which is similar to the observations of Schmitt et al., and Bennett et al. [42,53]. The maximum power optimisation reached 105% of the design value, which is set as the maximum bound for the power. Consequently, the heat input and the ΔT across the heat exchanger reaches its maximum around the design CIT. Similar cases were simulated for changes in the molten salt mass flow rate and MSIT and two sets of look-up tables were generated for the maximum efficiency and net power cases for implementation in SAM to perform the annual simulation.

Table 8-7 Annual performance of recompression cycle

Description	Unit	Maximum net power	Maximum efficiency
Field Incident Annual Energy	MWh	923,902	921,521
Receiver Incident Annual Energy	MWh	454,183	371,589
Annual Energy absorbed by the HTF	MWh	399,118	316,241
Annual Energy charged into TES	MWh	225,473	202,742
Annual Energy discharged from TES	MWh	215,609	192,531
Power Cycle Annual Gross Energy	MWh	190,294	160,098
Annual Energy to Grid	MWh	163,867	135,744
Capacity Factor	%	63.0	52.2
Solar to Electric Conversion Efficiency	%	17.7	14.7
$LCOE_{real}$	¢/kWh	6.2	7.4
Number of Start-up	-	283	147

Table 8-7 shows a comparison of annual performance for the maximum the net power and maximum net efficiency cases. The plant capacity factor when maximising the efficiency is 10.8% lower than when maximising net power and consequently, the LCOE is 1.2 ¢/kWh higher when the power cycle is operated

for maximum efficiency. The annual solar to electric efficiency also drops from 17.7% to 14.7% when operating the power cycle in maximising efficiency mode since the solar field efficiency is roughly 9% point lower when maximising the power cycle efficiency. On the other hand, the number of start-ups is roughly 50% lower in comparison to maximising net power, however, the LCOE calculation in SAM assumes a fixed operational cost and therefore the significance of the number of start-ups is not fully captured here. Moreover, many commercial CSP plants are already operating at part load on moderate DNI days in order to avoid plant shutdown. Nonetheless, a detailed cost model is required to realise the benefits and the trade-off with sophisticated controls, which outside the scope of this study. The optimal operational strategy might be a combination of maximising net power and net efficiency depending on the DNI profile and sun angle.

Figure 8-23 shows the capacity factor and LCOE for different solar multiples and TES capacities. It can be observed that maximising the efficiency and net power achieves a similar capacity factor and LCOE when the solar multiple is around 2 but they diverge as solar multiple increases.

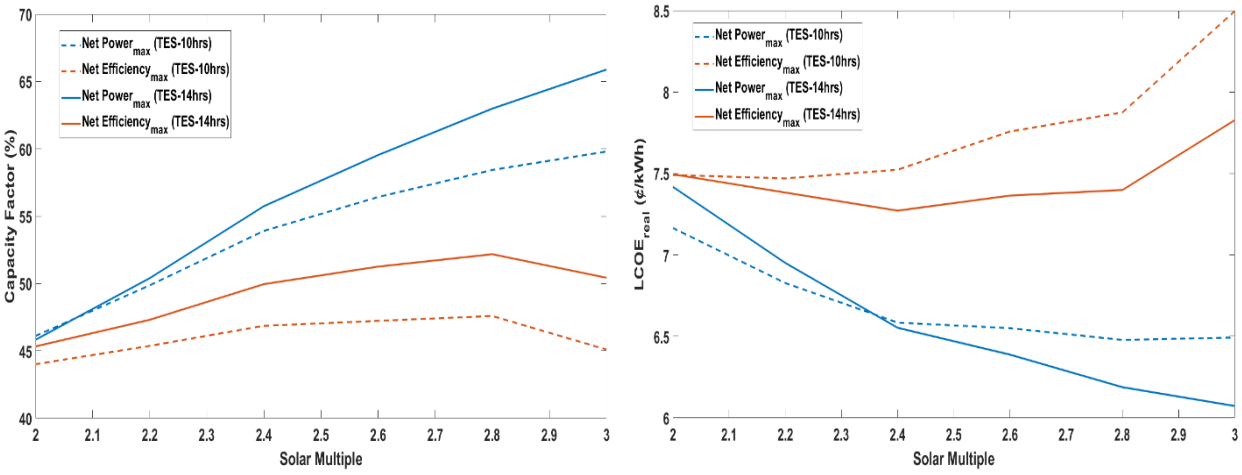

Figure 8-23 Sensitivity study for solar multiple, Left) capacity factor, Right) LCOE

8.6 Conclusions

The off-design performance of the recompression Brayton cycle was investigated for changes in the power cycle boundary conditions including ambient temperature, molten salt mass flow rate and molten salt inlet temperature. Multi-

objective optimisations were performed to maximise the net power and efficiency for different off-design boundary conditions and the operational Pareto fronts with primary process variables were studied. The compressor inlet pressure for maximising the efficiency was estimated based on the assumption that the volumetric flow rate is the same as the design value at higher ambient temperatures with reasonable accuracy.

At higher ambient temperatures, the molten salt outlet temperature from the power cycle is not affected when maximising the net power. When maximising the power cycle efficiency, however, molten salt outlet temperature increased by 46 °C implying that the TES capacity reduces by 25.1% as the temperature difference between hot and cold tanks reduces. On the other hand, constraining the power block operation to maintain the molten salt outlet temperature close to the design value penalises the efficiency by 0.8% point when the compressor inlet temperature is 55 °C (design compressor inlet temperature =42 °C).

The main compressor over-speed limit can be a concern when maximising the net power at higher ambient temperatures whilst the main compressor surge margin can restrict the maximum net efficiency of the cycle at lower ambient temperatures. The recompressor design volumetric flow (i.e. split fraction and inlet pressure) selection influences the recompressor operation significantly, therefore, the primary mode of operation (i.e. maximising the power or efficiency) should be considered when sizing the recompressor. The split fraction does not require any control for changes in the molten salt inlet temperature and up to ~70% reduction in molten salt flow rate, regardless of the mode of operation. On the other hand, the split fraction has to be reduced for an increase in compressor inlet temperature when maximising the efficiency.

The power cycle can be successfully operated in either maximum efficiency mode or maximum power mode showing a high degree of plant operational flexibility but an annual simulation identifies performance differences in these strategies. It was observed that the power cycle capacity factor increased by ~10.8% with a subsequent reduction in the LCOE by 1.2¢/kWh when operating in maximum power mode. On the other hand, the number of plant start-ups is reduced

significantly (by approximately 50%) when operating in maximum efficiency mode, which helps to increase plant life and reduce operational costs. The optimal operational strategy therefore could be a combination of maximising efficiency and net power according to prevailing ambient conditions.

8.7 References

[1] Dostal V, Driscoll MJ, Hejzlar P. A Supercritical Carbon Dioxide Cycle for Next Generation Nuclear Reactors. 2004. https://doi.org/MIT-ANP-TR-100.

[2] Turchi CS, Ma Z, Neises T, Michael W. Thermodynamic Study of Advanced Supercritical Carbon Dioxide Power Cycles for High Performance Concentrating Solar Power Systems. Proc. ASME 2012 6th Int. Conf. Energy Sustain., 2012. https://doi.org/10.1115/ES2012-91179.

[3] Crespi F, Gavagnin G, Sánchez D, Martínez GS. Supercritical carbon dioxide cycles for power generation: A review. Appl Energy 2017;195:152–83. https://doi.org/10.1016/j.apenergy.2017.02.048.

[4] Thanganadar D, Asfand F, Patchigolla K. Thermal performance and economic analysis of supercritical Carbon Dioxide cycles in combined cycle power plant. Appl Energy 2019;255:113836. https://doi.org/10.1016/j.apenergy.2019.113836.

[5] Marchionni M, Bianchi G, Tassou SA. Techno-economic assessment of Joule-Brayton cycle architectures for heat to power conversion from high-grade heat sources using CO_2 in the supercritical state. Energy 2018;148:1140–52. https://doi.org/10.1016/j.energy.2018.02.005.

[6] Giovannelli A, Archilei EM, Di Lorenzo G, Salvini C, Bashir MA, Messina G. Design of power-blocks for medium-scale supercritical carbon dioxide plants. Int J Energy Res 2020:1–24. https://doi.org/10.1002/er.5539.

[7] Steven WA, Tom C, Edward P, Tom L, Gary R, J S-AA. Summary of the Sandia Supercritical CO_2 Development Program. Int. SCO2 Power Cycle Symp., Boulder, Colorado: 2011.

[8] Lecompte S, Ntavou E, Tchanche B, Kosmadakis G, Pillai A, Manolakos D, et al. Review of experimental research on supercritical and transcritical thermodynamic cycles designed for heat recovery application. Appl Sci 2019;9:1–26. https://doi.org/10.3390/app9122571.

[9] Black & Veatch. Molten Salt Concept Definition & Capital Cost Estimate, Prepared for SunShot U.S. Department of Energy. 2016. https://doi.org/10.2172/1335150.

[10] Persichilli M, Kacludis A, Zdankiewicz E, Held T. Supercritical CO_2 Power Cycle Developments and Commercialization: Why sCO_2 can Displace Steam Steam. Power-Gen India Cent. Asia, 2012, p. 1–15.

[11] Wang X, Dai Y. Exergoeconomic analysis of utilizing the transcritical CO_2 cycle and the ORC for a recompression supercritical CO_2 cycle waste heat recovery: A comparative study. Appl Energy 2016;170:193–207. https://doi.org/10.1016/j.apenergy.2016.02.112.

[12] Asfand F, Thanganadar D, Patchigolla K. Thermodynamic performance of a supercritical CO_2 cycle integrated with a recuperative absorption cooling system. ECOS 2019 - Proc. 32nd Int. Conf. Effic. Cost, Optim. Simul. Environ. Impact Energy Syst., vol. 2019- June, WROCLAW, POLAND: 2019, p. 3895–903.

[13] Linares JI, Montes MJ, Cantizano A, Sánchez C. A novel supercritical CO_2 recompression Brayton power cycle for power tower concentrating solar plants. Appl Energy 2020;263:114644. https://doi.org/10.1016/j.apenergy.2020.114644.

[14] Clementoni EM, Cox TL, King MA. Steady-State Power Operation Of A Supercritical Carbon Dioxide Brayton Cycle With Thermal-Hydraulic Control. ASME Turbo Expo 2016 Turbomach. Tech. Conf. Expo., Seoul, South Korea: 2016, p. 1–10. https://doi.org/10.1115/GT2016-56038.

[15] Clementoni EM, Cox TL, King MA. Off-Nominal Component Performance in a Supercritical Carbon Dioxide Brayton Cycle. J Eng Gas Turbines

Power 2015;138:011703. https://doi.org/10.1115/1.4031182.

[16] Clementoni EM, Cox TL, King MA, Rahner KD. Transient power operation of a supercritical carbon dioxide Brayton cycle. ASME Turbo Expo, Charlotte, NC, USA: 2017. https://doi.org/10.1115/GT2017-63056.

[17] Clementoni EM, Cox TL. Effect of compressor inlet pressure on cycle performance for a supercritical carbon dioxide brayton cycle. 6th Int. Supercrit. CO2 Power Cycles Symp., vol. 9, Pittsburgh, Pennsylvania: 2018, p. 2–10.

[18] Clementoni EM, Cox TL. Effect of compressor inlet pressure on cycle performance for a supercritical carbon dioxide brayton cycle. Proc. ASME Turbo Expo, vol. 9, Oslo, Norway: 2018, p. 1–8. https://doi.org/10.1115/GT2018-75182.

[19] Anselmi E, Johnston M, Bunce I. An Overview of the Rolls-Royce sCO_2 Test Rig Project at Cranfield. 6th Int. Symp. - Supercrit. CO2 Power Cycles, Pittsburgh, Pennsylvania: 2018.

[20] Duniam S, Veeraragavan A. Off-design performance of the supercritical carbon dioxide recompression Brayton cycle with NDDCT cooling for concentrating solar power. Energy 2019;187:115992. https://doi.org/10.1016/j.energy.2019.115992.

[21] Wright SA, Davidson CS, Husa C. Off-design performance modeling results for a supercritical CO_2 waste heat recovery power system. 6th Int Symp - Supercrit CO2 Power Cycles 2018:1–10.

[22] Wang X, Li X, Li Q, Liu L, Liu C. Performance of a solar thermal power plant with direct air-cooled supercritical carbon dioxide Brayton cycle under off-design conditions. Appl Energy 2020;261:114359. https://doi.org/10.1016/j.apenergy.2019.114359.

[23] Son S, Jeong Y, Cho SK, Lee JI. Development of supercritical CO_2 turbomachinery off-design model using 1D mean-line method and Deep Neural Network. Appl Energy 2020;263:114645.

https://doi.org/10.1016/j.apenergy.2020.114645.

[24] Yan XL. Dynamic Analysis and Control System Design for an Advanced Nuclear Gas Turbine Power Plant. Massachusetts Institute of Technology, 1990.

[25] J.H.Horlock. Advanced Gas Turbine Cycles. 1st ed. Pergamon; 2003.

[26] Frutschi HU. Closed-Cycle Gas Turbines: Operating Experience and Future Potential. ASME Press; 2005. https://doi.org/10.1115/1.802264.

[27] Lemmon EW, Huber ML, McLinden MO. NIST Standard Reference Database 23. Natl Inst Stand Technol 2013;V 9.1.

[28] Xu X, Wang X, Li P, Li Y, Hao Q, Xiao B, et al. Experimental Test of Properties of KCl–$MgCl_2$ Eutectic Molten Salt for Heat Transfer and Thermal Storage Fluid in Concentrated Solar Power Systems. J Sol Energy Eng 2018;140:051011. https://doi.org/10.1115/1.4040065.

[29] Jerden J. Molten Salt Thermophysical Properties Database Development : 2019 Update. 2019. https://doi.org/10.2172/1559846.

[30] Nellis G, Klein S. Heat Transfer. 2009. https://doi.org/10.1017/CBO9780511841606.

[31] BALJE O. Turbomachines: A Guide to Design, Selection and Therapy. John Wiley & Sons; 1981. https://doi.org/10.1115/1.3241788.

[32] Dyreby JJ, Klein SA, Nellis GF, Reindl DT. Modeling off-design and part-load performance of supercritical carbon dioxide power cycles. Proc. ASME Turbo Expo, vol. 8, San Antonio, Texas, USA: 2013, p. 1–7. https://doi.org/10.1115/GT2013-95824.

[33] Liese E, Zitney SE. The Impeller Exit Flow Coefficient As a Performance Map Variable for Predicting Centrifugal Compressor Off-Design Operation Applied to a Supercritical CO_2 Working Fluid. Proc. ASME Turbo Expo 2017 Turbomach. Tech. Conf. Expo. Supercrit. CO2 Power Cycles; Wind Energy, 2017, p. V009T38A003. https://doi.org/10.1115/GT2017-63090.

[34] Fleming DD, Conboy TM, Pasch JJ, Rochau GA, Fuller RL, Holschuh T V, et al. Scaling Considerations for a Multi- Megawatt Class Supercritical CO_2 Brayton Cycle and Commercialization. vol. SAND2013-9. 2013.

[35] Dyreby JJ. Modeling the Supercritical Carbon Dioxide Brayton Cycle with Recompression 2010:155. https://doi.org/10.1088/1751-8113/44/8/085201.

[36] Patnode A. Simulation and performance evaluation of parabolic trough solar power plants. Univ Wisconsin-Madison 2006;Master:5–271.

[37] Tang C-J, Hofer D, Mcclung A, Megan Huang. Transient modeling of 10 MW supercritical CO_2 Brayton power cycles using Numerical Propulsion System Simulation (NPSS). ASME Turbo Expo 2019, 2019, p. 1–10.

[38] Clementoni EM, Cox TL, King MA. Response of a compact recuperator to thermal transients in a supercritical carbon dioxide Brayton cycle. ASME Turbo Expo 2017:1–11. https://doi.org/10.1115/GT2017-63058.

[39] Jiang Y, Liese E, Zitney SE, Bhattacharyya D. Design and dynamic modeling of printed circuit heat exchangers for supercritical carbon dioxide Brayton power cycles. Appl Energy 2018;231:1019–32. https://doi.org/10.1016/j.apenergy.2018.09.193.

[40] Halimi B, Suh KY. Computational analysis of supercritical CO_2 Brayton cycle power conversion system for fusion reactor. Energy Convers Manag 2012;63:38–43. https://doi.org/10.1016/j.enconman.2012.01.028.

[41] Neises T, Turchi C. A comparison of supercritical carbon dioxide power cycle configurations with an emphasis on CSP applications. Energy Procedia 2013;49:1187–96. https://doi.org/10.1016/j.egypro.2014.03.128.

[42] Schmitt J, Wilkes J, Bennett J, Wygant K, Pelton R. Lowering the levelized cost of electricity of a concentrating solar power tower with a supercritical carbon dioxide power cycle. ASME Turbo Expo, Charlotte, NC, USA: 2017, p. 1–10. https://doi.org/10.1115/GT2017-64958.

[43] De la Calle A, Bayon A, Soo Too YC. Impact of ambient temperature on supercritical CO_2 recompression Brayton cycle in arid locations: Finding the optimal design conditions. Energy 2018;153:1016–27. https://doi.org/10.1016/j.energy.2018.04.019.

[44] Deb K, Pratap A, Agarwal S, Meyarivan T. A fast and elitist multiobjective genetic algorithm: NSGA-II. IEEE Trans Evol Comput 2002;6:182–97. https://doi.org/10.1109/4235.996017.

[45] Avval HB, Ahmadi P, Ghaffarizadeh AR, Saidi MH. Thermo-economic-environmental multiobjective optimization of a gas turbine power plant with preheater using evolutionary algorithm. Int J Energy Res 2010. https://doi.org/10.1002/er.1696.

[46] Rangaiah GP. Multi-Objective Optimization Techniques and Applications in Chemical Engineering. vol. 1. 2009. https://doi.org/10.1007/0-387-28356-0_10.

[47] Wong JYQ, Sharma S, Rangaiah GP. Design of shell-and-tube heat exchangers for multiple objectives using elitist non-dominated sorting genetic algorithm with termination criteria. Appl Therm Eng 2016;93:888–99. https://doi.org/10.1016/j.applthermaleng.2015.10.055.

[48] Sharma S, Rangaiah GP, Cheah KS. Multi-objective optimization using MS Excel with an application to design of a falling-film evaporator system. Food Bioprod Process 2011;90:123–34. https://doi.org/10.1016/j.fbp.2011.02.005.

[49] Mehos M, Turchi C, Jorgenson J. Advancing Concentrating Solar Power Technology, Performance, and Dispatchability. Sandia Rep 2016;NREL/TP-55:1–66. https://doi.org/10.1016/B978-0-08-087872-0.00319-X.

[50] Kulhánek M, Dostál V. Thermodynamic Analysis and Comparison of Supercritical Carbon Dioxide Cycles. Proc SCCO2 Power Cycle Symp 2011:1–7.

[51] Turchi CS, Ma Z, Neises T, Michael W. Thermodynamic Study of Advanced Supercritical Carbon Dioxide Power Cycles for High Performance Concentrating Solar Power Systems. Proc. ASME 2012 6th Int. Conf. Energy Sustain., n.d., p. 375–83. https://doi.org/10.1115/ES2012-91179.

[52] Carstens NA. Control strategies for supercritical carbon dioxide power conversion systems. Massachusetts Institute of Technology, 2007.

[53] Bennett J, Wilkes J, Allison T, Pelton R, Wygant K. Cycle modeling and optimization of an integrally geared sCO_2 compander. ASME Turbo Expo, Charlotte, NC, USA: 2017, p. 1–8. https://doi.org/10.1115/GT2017-63707.

[54] Invernizzi CM. Closed power cycles: Thermodynamic fundamentals and applications. Lect Notes Energy 2013;11. https://doi.org/10.1007/978-1-4471-5140-1.

[55] Baltadjiev ND. An Investigation of Real Gas Effects in Supercritical CO_2 Compressors. Massachusetts Institute of Technology, 2012. https://doi.org/10.1115/1.4029616.

[56] Gad-Briggs A, Pilidis P, Nikolaidis T. Analyses of the Control System Strategies and Methodology for Part Power Control of the Simple and Intercooled Recuperated Brayton Helium Gas Turbine Cycles for Generation IV Nuclear Power Plants. J Nucl Eng Radiat Sci 2017;3. https://doi.org/10.1115/1.4036737.

Chapter 9

9 Recuperator Transient Simulation for Supercritical Carbon Dioxide Cycle in CSP Applications

Dhinesh Thanganadar[a], Francesco Fornarelli[b,c], Sergio Camporeale[b], Faisal Asfand[a,d], Kumar Patchigolla[a]

[a]*School of Water, Energy and Environment (SWEE), Cranfield University, Cranfield, MK43 0AL, UK*

[b]*Dipartimento di Meccanica, Matematica e Management (DMMM) Politecnico di Bari, Bari, Italy*

[c]*National Group of Mathematical Physics (GNFM), National Institute of High Mathematics (INDAM)*

[d]*The School of Computing and Engineering, University of Huddersfield, Huddersfield, HD1 3DH, UK*

Presented in ASME Turbo Expo 2020 Conference

DOI: 10.1115/GT2020-14785

Statement of contributions of joint authorship

Dhinesh Thanganadar proposed the novelty, implemented the methods, generated all results, and prepared the manuscript draft. Francesco Fornarelli, Sergio Camporeale, and Faisal Asfand proof-read and critically commented on the manuscript before submission. Kumar Patchigolla provided supervision, proof-read and critically commented on the manuscript before submission.

ABSTRACT

Supercritical carbon dioxide (sCO_2) cycles are considered to provide a faster response to load change owing to their compact footprint. sCO_2 cycles are generally highly recuperative, therefore the response time is mainly dictated by

the heat exchanger characteristics. This study model the transient behaviour of a recuperator in 10 MW_e simple recuperative Brayton cycle. The response for the variation of inlet temperature and mass flow boundary conditions were investigated using two approaches based on temperature and enthalpy. The performance of these two approaches are compared and the numerical schemes were discussed along with the challenges encountered. The simulation results were validated against the experimental data available in the literature with a fair agreement. The characteristic time of the heat exchanger for a step change of the boundary conditions is reported that supports the recuperator design process. Compact recuperator responded in less than 20 seconds for the changes in the temperature boundary condition whilst it can take up to 1.5 minutes for mass flow change. In order to reduce the computational effort, a logarithmic indexed lookup table approach is presented, reducing the simulation time by a factor of 20.

Keywords

Transient simulation, compact heat exchanger, sCO_2, supercritical carbon dioxide, numerical simulation

9.1 Introduction

Supercritical Carbon Dioxide (sCO_2) cycles are gaining attention in the power generation industry, including Concentrating Solar Power (CSP), nuclear, fossil-fired and Waste Heat Recovery (WHR) applications, owing to their higher cycle efficiency at higher temperatures (>550 °C) and compact footprint. Smaller components facilitate to have a highly flexible plant. Flexible plants are affected by a larger thermal stress in the heat exchanger and turbine owing to the abrupt variation of the inlet boundary conditions. Numerous cycle configurations have been proposed; Crespi et al. [1] reviewed forty-two of them for sensible and CSP applications and Thanganadar et al. [2] studied cascade cycles for sensible heat sources. The degree of thermal stress depends on the type of control techniques implemented and the turbine bypass control can induce higher thermal stress. Therefore, it is essential to understand the transient characteristics of the plant which requires transient heat exchanger modelling that leads to a system-level model. Although a detailed three- dimensional heat exchanger model can

produce accurate results, they are not suitable to integrate with plant transient solver which demands a computationally faster heat exchanger code. The heat managing within the cycle has been extensively analysed by engineers looking at its optimisation [3]. In CSP plants and WHR applications, the heat storage devices have been extensively studied in order to optimise and control their behaviour in the whole system [4,5]. Heat exchanger optimisation recurs in several experimental and numerical investigations [6].

Transient simulation of PCHE was simulated using commercial software such as Aspen [7], GT Suite[8], LMS AMESim [9]. Chen et al. [10] simulated the temperature based energy equation as an ordinary differential equation (treating the space discretisation explicitly). Nathan et al. [11] solved the enthalpy based energy equation and the linear interpolation is used to calculate the flux at the centre flux and the implicit scheme is used in time. Kao et al. [12] modelled the time-dependent enthalpy based energy equations using Momentum Integral method and a semi-implicit scheme. Tank et al. [13] solved the enthalpy based energy equation in Numerical Propulsion System Simulation and the numerical schemes were not reported. However, none of these codes was validated (except [7] and [13]) with sCO_2 PCHE experimental data owing to the lack of publicly available data.

Moreover, the thermal-physical properties of supercritical fluids vary significantly close to the pseudo-critical point, which complicates the numerical solution method for solving coupled one-dimensional transient partial differential equations of the heat exchanger. The numerical scheme requires fine discretization in space and time to reasonably capture the nonlinear effects, therefore the computational effort is higher. Jiang et al. [7] used 100 nodes in the commercial Aspen Dynamics simulation software and the simulation deviates around 5 °C for the cold stream in comparison with experimental results.

Since the thermal-physical properties vary significantly, the selection of the Equation of State (EOS) is crucial and Span-Wagner EOS implemented in REFPROP is considered as the most accurate EOS for sCO_2 [14]. The

computational time is further exacerbated by the iterative procedure of Span-Wagner EoS, which minimises the Helmholtz free energy.

Conventionally, the one- dimensional heat exchanger code solves temperature based energy equations using Crank-Nicholson scheme owing to their second-order accuracy [15,16]. However, they are unstable when modelling sCO_2 fluid owing to the high nonlinear change of the fluid properties including specific heat. Although the specific heat capacity of sCO_2 change significantly close to the pseudo-critical point, the nonlinear enthalpy change is less severe [11]. This favour solving the energy equation in terms of enthalpy which requires significant adaptation of the conventional codes.

This paper compares the numerical and computational performance of solving the temperature based PDE's [17] and enthalpy based PDEs. The model is validated against the experimental data found in Clementoni et al. [18]. Secondly, a logarithmic indexed look-up table is developed in order to reduce the computational effort of thermal-physical properties calculation. The computational performance and accuracy of using logarithmic indexed look-up table as opposed to directly calling REFPROP is compared. Finally, the step response of a 10 MW_e simple recuperative sCO_2 cycle recuperator is presented.

9.2 Heat Exchanger Design and Off-Design Simulation

Printed Circuit Heat Exchanger (PCHE) is considered for recuperators. Design and off-design performance codes are developed in MATLAB. The design procedure uses the iterative procedure illustrated in Kim et al. [19] and its output is the heat transfer area and heat exchanger geometry. The off-design procedure uses a similar approach by guessing the hot outlet temperature and converging when the sum of calculated heat exchanger length matches the design length. This iterative procedure is shown in Figure 9-1.

9.3 Heat Exchanger Transient Simulation

The following assumptions are made to simplify the transient equations,

1. Fluid axial diffusion and the wall axial diffusion along the flow direction terms are neglected. However, the wall conduction resistance normal to the flow direction is included.
2. Heat loss to the ambient is neglected.
3. The momentum equation is decoupled from the mass and energy balance equation and the steady-state pressure drop is applied.

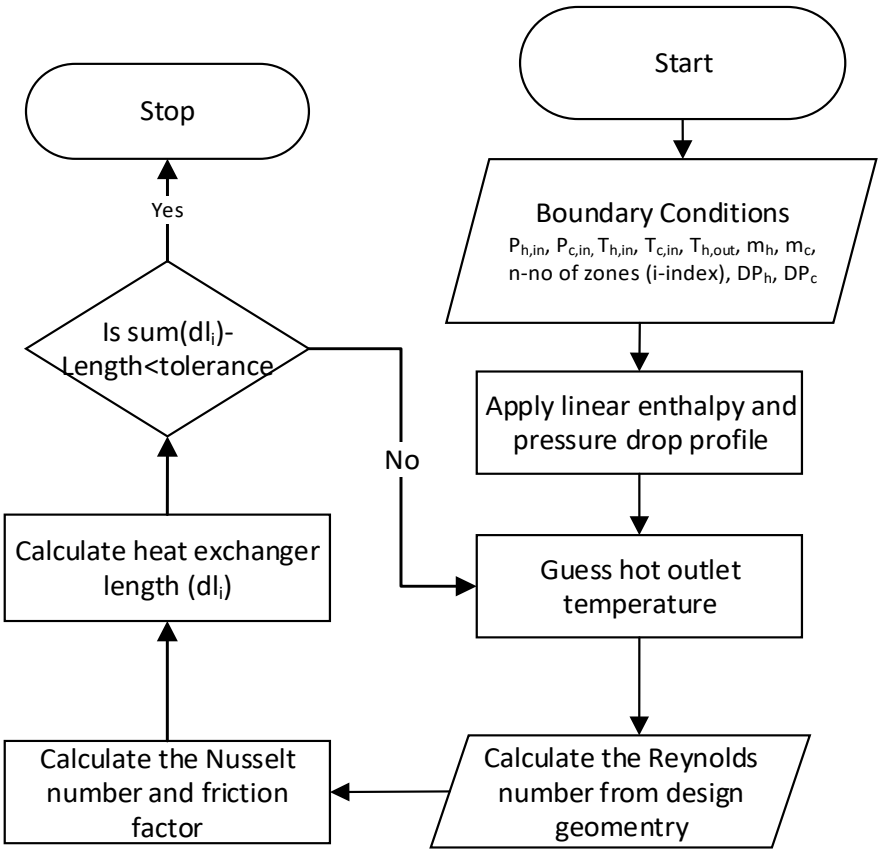

Figure 9-1 Heat Exchanger off-design procedure

9.3.1 Numerical Scheme of Temperature Approach

London et al. [17] proposed non-dimensionalised temperature based energy equations. It should be noted that this equation is valid for ideal gas as it neglects the real gas pressure dependency on the energy equation. These equations can be solved for the three unknown temperatures (hot, cold and wall) in next time step implicitly, with under-relaxation iterative scheme to update the coefficient matrix in the new time-step. Once the temperature fields are solved, then the specific heat, density can be updated using the Equation of State (EoS).

Since the non- dimensionalised equations proposed by London et al. assumed lumped heat exchanger parameters (NTU, heat transfer coefficient etc.), the dimensional equations are considered in order to capture the thermal-physical properties variation of the supercritical fluids (Eq. (9-1 to (9-3),

$$\frac{u-v}{R_h * L} = -\frac{\bar{C}_h}{L} * \frac{\partial u}{\partial t} + \dot{C}_h * \frac{\partial u}{\partial x} \tag{9-1}$$

$$\frac{v-w}{R_c * L} = -\frac{\bar{C}_c}{L} * \frac{\partial w}{\partial t} + \dot{C}_c * \frac{\partial w}{\partial x} \tag{9-2}$$

$$\frac{u-v}{R_h} - \frac{v-w}{R_c} = -\bar{C}_w * \frac{\partial v}{\partial t} \tag{9-3}$$

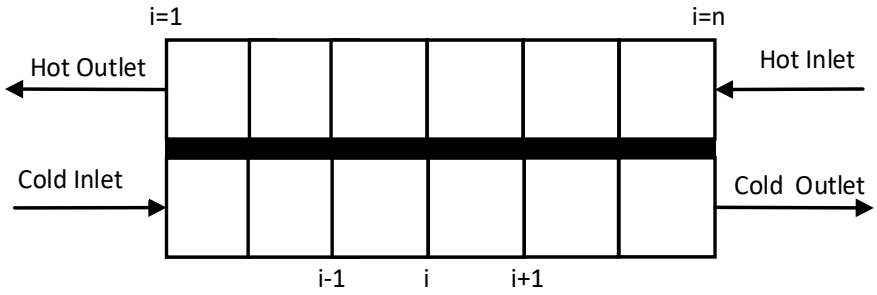

Figure 9-2 Stencil diagram for temperature-based scheme

These coupled energy equations are discretised using the finite difference method (FDM) and the Crank-Nicolson scheme in space and time [15]. This scheme was modified to the backward difference in space and fully implicit scheme in time owing to the stability reason and this is discussed in Section 9.4.2. The PDE's are re-arranged in the following form (Eq. (9-4) to (9-6)),

$$\frac{\partial u}{\partial t} = a_1 * \frac{\partial u}{\partial x} + a_2 * u + a_3 * v \tag{9-4}$$

$$\frac{\partial w}{\partial t} = b_1 * \frac{\partial w}{\partial x} + b_2 * w + b_3 * v \tag{9-5}$$

$$\frac{\partial v}{\partial t} = c_1 * u + c_2 * w + c_3 * v \tag{9-6}$$

Applying backward-difference scheme in space and fully implicit in time for the inner nodes (i=2 to n-1), the equation becomes, (Eq. (9-7 to (9-9),

$$\frac{u_i^{t1} - u_i^{t0}}{\Delta t} = \left[\left(a_1 \frac{u_i^{t1} - u_{i-1}^{t1}}{\Delta x} + a_2 u_i^{t1} + a_3 v_i^{t1}\right)\right] \tag{9-7}$$

$$\frac{w_i^{t1} - w_i^{t0}}{\Delta t} = \left[\left(b_1 \frac{w_i^{t1} - w_{i-1}^{t1}}{\Delta x} + b_2 w_i^{t1} + b_3 v_i^{t1}\right)\right] \tag{9-8}$$

$$\frac{v_i^{t1} - v_i^{t0}}{\Delta t} = [(c_1 u_i^{t1} + c_2 w_i^{t1} + c_3 v_i^{t1})] \tag{9-9}$$

The wall energy equation is re-arranged in terms of the wall temperature at the next time step (v_i^{t1}) and this is a function of cold and hot stream temperatures. This equation is then back substituted into the cold stream and hot stream energy equations in order to eliminate the wall temperature term. This process reduces the three number of coupled PDEs into two coupled energy equations (cold and hot stream temperatures). The two discretised energy equations can be written in the form shown in Eq. (9-10 & (9-11,

$$A_{h,i}^{t1} u_{i-1}^{t1} + B_{h,i}^{t1} u_i^{t1} + C_{h,i}^{t1} u_{i+1}^{t1} + D_{h,i}^{t1} w_{i-1}^{t1} + E_{h,i}^{t1} w_i^{t1} + F_{h,i}^{t1} w_{i+1}^{t1} = H_{h,i}^{t0} \tag{9-10}$$

$$A_{c,i}^{t1} u_{i-1}^{t1} + B_{c,i}^{t1} u_i^{t1} + C_{c,i}^{t1} u_{i+1}^{t1} + D_{c,i}^{t1} w_{i-1}^{t1} + E_{c,i}^{t1} w_i^{t1} + F_{c,i}^{t1} w_{i+1}^{t1} = H_{c,i}^{t0} \tag{9-11}$$

The set of algebraic equations are solved together with the boundary conditions using two-block tri-diagonal solver as shown in Eq. (9-12,

$$\begin{bmatrix} Y_1 & Z_1 & & & & & \\ X_2 & Y_2 & Z_2 & & & & \\ & & & \cdot & \cdot & \cdot & \\ & & & & \cdot & \cdot & \\ & & & & X_{n-1} & Y_{n-1} & Z_{n-1} \\ & & & & & X_n & Y_n \end{bmatrix} \text{x} \begin{bmatrix} U_1 \\ U_2 \\ \cdot \\ \cdot \\ U_{n-1} \\ U_n \end{bmatrix} = \begin{bmatrix} f_1 \\ f_2 \\ \cdot \\ \cdot \\ f_{n-1} \\ f_n \end{bmatrix} \quad (9\text{-}12)$$

Where elements of the coefficient matrix are 2x2 matrices as shown in Eq. (9-13, and the unknown and the RHS are 1x2 matrix as shown in Eq. (9-14,

$$X_i = \begin{bmatrix} A_{h,i} & D_{h,i} \\ A_{c,i} & D_{c,i} \end{bmatrix};\ Y_i = \begin{bmatrix} B_{h,i} & E_{h,i} \\ B_{c,i} & E_{c,i} \end{bmatrix};\ Z_i = \begin{bmatrix} C_{h,i} & F_{h,i} \\ C_{c,i} & F_{c,i} \end{bmatrix} \quad (9\text{-}13)$$

$$U_i = \begin{bmatrix} u_i \\ w_i \end{bmatrix};\ f_i = \begin{bmatrix} H_{h,i} \\ H_{c,i} \end{bmatrix} \quad (9\text{-}14)$$

9.3.2 Numerical Scheme of Enthalpy Approach

The energy balance of the hot stream, cold stream and wall are shown in Eq. (9-15 to (9-17, respectively (fluid axial diffusion and wall axial conduction terms were neglected),

$$\rho_h\, S\, \frac{\partial U_h}{\partial t} = m\, \frac{\partial H_h}{\partial x} - HTC_h P(u - v) \quad (9\text{-}15)$$

$$\rho_c\, S\, \frac{\partial U_c}{\partial t} = -m\, \frac{\partial H_c}{\partial x} + HTC_c P\, (v - w) \quad (9\text{-}16)$$

$$HTC_h\, P(u - v) - HTC_c\, P(v - w) = \rho_w c_{p,w} \frac{V_w}{L} \frac{\partial v}{\partial t} \quad (9\text{-}17)$$

These coupled energy equations are solved for enthalpy and the internal energy term in Eq. (9-15 & (9-16 were replaced with its thermodynamic equivalent as shown in Eq. (9-18,

$$U = H - pV \quad (9\text{-}18)$$

The wall energy equation is discretised using a fully implicit FDM method then the equation is rearranged for the wall temperature at the new time step as shown in Eq. 9-19,

$$v_P^{t1} = \frac{v_P^{to} + z_P HTC_{h,P} u_P^{t1} + z_P HTC_{c,P} w_P^{t1}}{1 + z_P HTC_{h,P} + z_P HTC_{c,P}} \tag{9-19}$$

Where z_P can be calculated using Eq. 9-20,

$$z_P = \frac{L * P * \Delta t}{\rho_w * C_{p,w} * V_w} \tag{9-20}$$

The hot and cold steam energy equations can be integrated over the control volume using Finite Volume Method (FVM) as shown in Eq. 9-21,

$$\frac{1}{V}\int_V \rho_c S \frac{\partial H_c}{\partial t}\, dx = \frac{1}{V}\int_V \left(m_c \frac{\partial H_c}{\partial x} + HTC * P(v - w) \right) dx \tag{9-21}$$

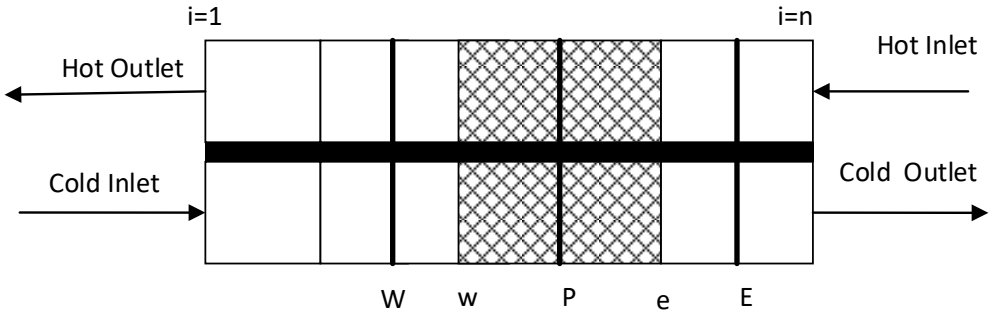

Figure 9-3 Stencil diagram for enthalpy based scheme

Applying the fully implicit scheme to Eq. 9-21 can be discretised as Eq. 9-22

$$\bar{\rho}_{c,P} S(h_P^{t1} - h_P^{t0})\Delta x = \Delta t((m_w h_w - m_e h_e)^{t1} - \Delta x \overline{HTC}_{c,p} P(\bar{v} - \bar{w})^{t1}) \tag{9-22}$$

For numerical stability reasons, the convective flux at the boundary is assumed to be the cell average values, also known as the upwind scheme [20] and this reduces Eq. 9-22 to Eq. 9-23,

$$\bar{\rho}_{c,P} S(h_P^{t1} - h_P^{t0})\Delta x = \Delta t((m_w h_W - m_e h_P)^{t1} - \Delta x \overline{HTC}_{c,p} P(\bar{v} - \bar{w})^{t1}) \tag{9-23}$$

Eq. 9-23 is written in a general form as per Eq. 9-24 to solve the enthalpy for the next time step,

$$a_e h_P + a_w h_w = a_0 \tag{9-24}$$

Similarly, this procedure can be applied to the hot stream energy balance equation with the reversed node numbers. These equations were solved using Tri-Diagonal Matrix Algorithm (TDMA). Since the coefficient matrix uses the thermo-physical properties at $t1$ an under-relaxation iterative scheme is applied until convergence is achieved.

Gnielinski Nusselt number correlation was used to calculate the forced convection heat transfer coefficient [21]. The heat transfer coefficient of the cold stream adds half of the wall conductive resistance incurred from the wall thickness. The same also applies to the hot stream HTC calculation.

9.3.3 Numerical Scheme of Enthalpy Approach

REFPROP is computationally heavy, particularly when the operating point is close to the critical point as it uses an iterative procedure which minimises Helmholtz free energy. Linearly indexed look-up tables can be generated to replace the thermal-physical property calculation of the fluid. The look-up table size can be bigger in order to achieve higher accuracy ($<10^{-4}$) owing to the nonlinear variation of the properties. This eventually can slow-down the property calculations as the interpolation of a bigger table is also slower.

Therefore, a set of logarithmic indexed tables were developed for all the properties as a function of different combinations of temperature, pressure, enthalpy, entropy. The density of the points has to be more close to the critical point and the constant α controls the density distribution. The table parameter value can be defined according to Eq. 9-25 for the supercritical region and Eq. 9-26 for the subcritical region which is a function of index number i. The reverse sign for subcritical region helps to have a higher density close to the critical region [22].

$$P = e^{\frac{i-\beta}{\alpha}} + \gamma \tag{9-25}$$

$$P = -e^{\frac{i-\beta}{\alpha}} + \gamma \tag{9-26}$$

Nathan et al. [22] proposed an iterative procedure to find the values of β, γ for a given α. However, once the α is fixed, the two unknowns can be solved by applying these equations to the table minimum and maximum limits and they can be solved algebraically without needing any iteration. Eq. 9-27 to 9-29 can be used to find the unknowns for subcritical region and Eq. 9-27, 9-30, 9-31 can be used to calculate the unknowns for supercritical region.

$$z = \frac{N_p - 1}{\alpha} \tag{9-27}$$

$$\gamma = \frac{(-P_{min} + P_{max} * e^z)}{1 - e^z} \tag{9-28}$$

$$\beta = 1 - \alpha * \ln(-P_{max} - \gamma) \tag{9-29}$$

$$\gamma = \frac{(P_{max} - P_{min} * e^z)}{1 - e^z} \tag{9-30}$$

$$\beta = 1 - \alpha * \ln(P_{min} - \gamma) \tag{9-31}$$

The computational speed and the accuracy of the logarithmic indexed table in comparison with the linear indexed table is discussed in Nathan et al. [22]. Since the indexes are logarithmic, the interpolation scheme should search the non-uniformly indexed table. A bi-linear interpolation scheme was used. The number of data points in the look-up table was adjusted to get the desired accuracy ($<10^{-4}$).

9.4 Results and Discussion

9.4.1 Design of sCO_2 Recuperator

A 10 MW_e simple recuperative Brayton cycle is simulated with the sCO_2 turbine inlet temperature of 700 °C and recuperator effectiveness of 95% is assumed. The recuperator is discretised into 15 segments to capture the nonlinear variation of the fluid properties. The process boundary condition of the recuperator in the design state is shown in Table 9-1.

Table 9-1 Recuperator boundary conditions

Parameters	Unit	Cold Inlet	Hot Inlet
Temperature	°C	114.7	562.3
Pressure	bar	250	86.7
Mass flow	kg/s	90	90
Heat Duty	kW_{th}	44,791	

A straight channel Printed Circuit Heat Exchanger (PCHE) in a single plate 1x1 configuration for the cold and hot stream considered in SS316 (ρ_m=7990 kg/m^3) is selected for the recuperator. Gnielinski Nusselt number correlation together with the Zigrang-Sylvester friction factor correlation was used [21] for calculating the heat transfer area and pressure drop, respectively. The heat exchanger is designed to minimise the metal mass (which is proportional to the cost of the heat exchanger) subjected to the pressure drop, maximum length, height and width constraints using Genetic Algorithm (GA). Table 9-2 shows the selected design geometry of the recuperator. The wall thickness is selected based on the operating pressure, design stress and corrosion allowance of the selected material [23] and a 20% margin was applied [19]. The additional fluid volume from the nozzle and headers are not considered in this simulation.

Table 9-2 Design specification of the recuperator

Parameters	Unit	Value
Channel Diameter	mm	2

Wall Thickness	mm	1.3
Number of plates	-	1975
Number of Channel	-	161
Heat Transfer Area	m^2	995
Void Fraction	-	0.63
Length	m	1.22
Height	m	2.57
Width	m	0.53
Mass	kg	4,878
Cold side pressure drop (DP_c)	bar	0.26
Hot side pressure drop (DP_h)	bar	0.87

9.4.2 Numerical Scheme

Applying Crank-Nicholson scheme in space and time oscillates significantly and produces non-physical values close to the critical point although it worked away from the critical region. Applying the numerically stable backward differentiation scheme in space reduces the numerical instability close to the critical point with the expense of reducing the accuracy from second-order to first-order. However, it was also observed that this scheme oscillates around the true solution. Implementing the fully implicit backward differentiation scheme with the under-relaxation iterative procedure to update the coefficient-matrix in the next time-step produced stable results and therefore this scheme is considered for solving temperature-based energy equations.

Similar oscillations were also observed when calculating the cell-centre values using distance-weighted interpolation of the face values whilst discretising enthalpy-based energy equations. Therefore, the upwind scheme is applied for the convective flux term (i.e., enthalpy), that assumes a uniform enthalpy within the cell, and fully implicit in time. An under-relaxation iterative method to update the coefficient-matrix is applied.

9.4.3 Grid Sensitivity Study

A grid sensitivity study is performed for enthalpy-based energy equations and the outlet temperatures of cold and hot streams are plotted in Figure 9-4. The Courant-Friedrichs-Levy (CFL) condition of 1 was imposed in order to calculate the time step for different space discretisation. The CFL condition was calculated based on the fluid velocity without accounting the speed of sound as the pressure field was imposed from the steady-state solution. A grid size of 400 was selected for investigating the step response of the heat exchanger as it provides a better trade-off between the accuracy and computational time. The computational effort of using 400 nodes is approximately 10 times higher than using 100 nodes as the time step is also reduced due to the finer grid.

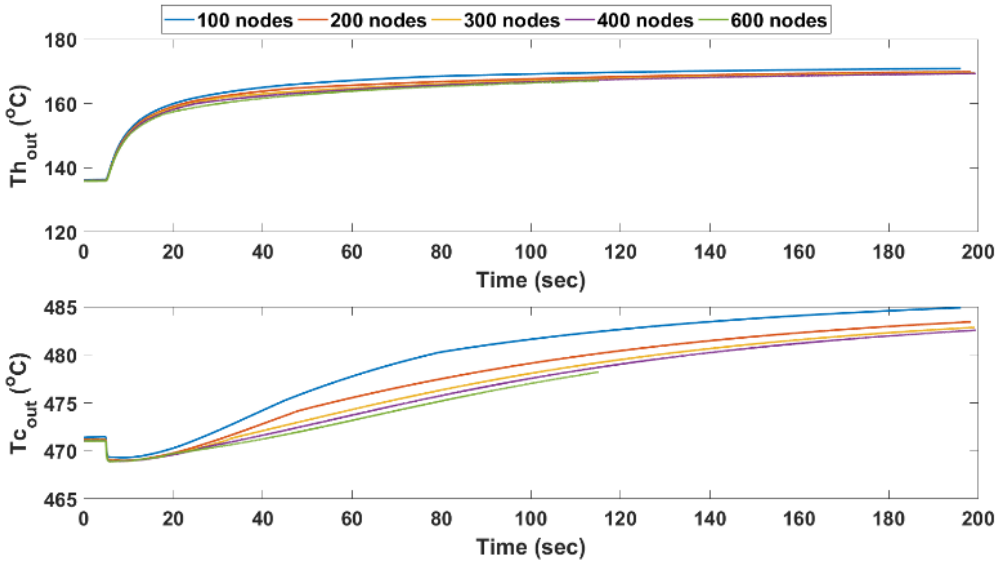

Figure 9-4 Grid sensitivity study for a 30 °C step response of cold inlet temperature: Hot outlet temperature (top) and Cold outlet temperature (bottom)

9.4.4 Transient Response of Recuperator

9.4.4.1 Response to Step Change

The heat exchanger boundary conditions are subjected to step response and the characteristic time was measured. The first-order characteristic time (τ) is defined as the time required to meet $1 - 1/e$ (~63.2%) of its final value [7]. Enthalpy based scheme is used to test the transient response of the recuperator. A step change of 30 °C for cold and hot inlet temperature were studied and the response

on the cold, hot outlet temperature and mass flow are shown in Figure 9-5. Figure 9-6 shows the heat exchanger outlet temperature and mass flow for a step-change in the inlet mass flow rate. The purpose of investigating the step change is to quantity the characteristic time of the heat exchanger.

The step response to the changes in the boundary conditions is investigated and the characteristic time for different boundary conditions are tabulated in Table 9-3. The heat exchanger has responded quickly for changes in temperature boundary condition in comparison to change in the mass flow boundary condition, as observed by Jiang et al. [7]. The heat exchanger responded within ~20 secs for the step changes in the inlet temperature due to lower thermal capacitance and higher heat transfer coefficient of PCHE in comparison to conventional shell

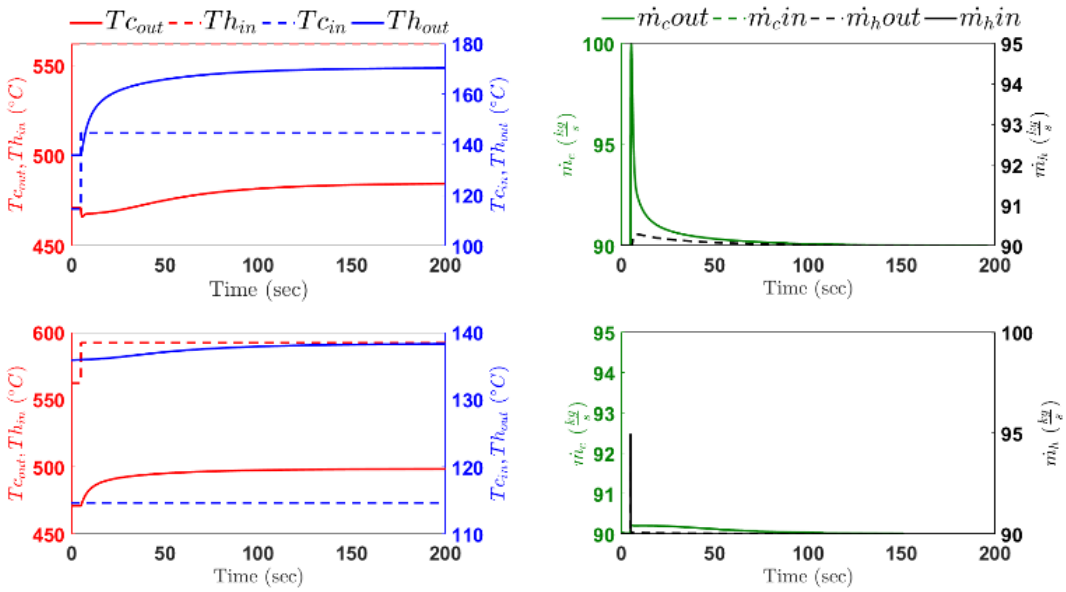

Figure 9-5 Response of the recuperator for step change in the cold inlet temperature (top) and hot inlet temperature (bottom)

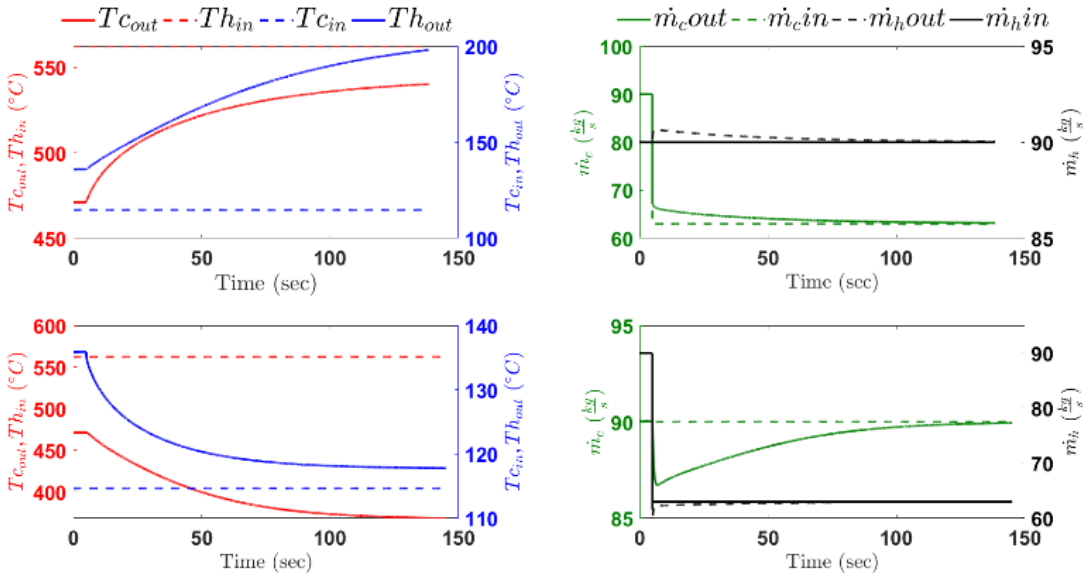

Figure 9-6 Response of the recuperator for step change in the cold inlet mass flow rate (top) and hot inlet mass flow rate (bottom)

and tube configuration [7]. In addition, it is observed that the cold outlet temperature shows a small transient dip (~2 °C) for a step increase in cold inlet temperature, which is not observed in Jiang et al. [7]. This is related to the density reduction in the heat exchanger according to the increased temperature. The heat transfer from the wall is slower than the inventory removal rate which is the function of the increased velocity, consequently, the cold outlet temperature reduced. Later, the cold outlet temperature is recovered by the heat transfer from the wall.

Table 9-3 Characteristic time (τ) of sCO_2 recuperator

τ (sec)	$T_{c,in}$	$T_{h,in}$	$\dot{m}_{c,in}$	$\dot{m}_{h,in}$
$T_{c,out}$	-	17.5	42.7	48.3
$T_{h,out}$	13.6	-	98.2	23.4

9.4.4.2 Response to Linear Ramp

The heat exchanger boundary conditions were subjected to ramp boundary condition (30 secs ramp) and the responses are shown in Figure 9-7 and Figure

9-8. The cold outlet temperature was not dropped for changes in the cold inlet temperature when the ramp is simulated.

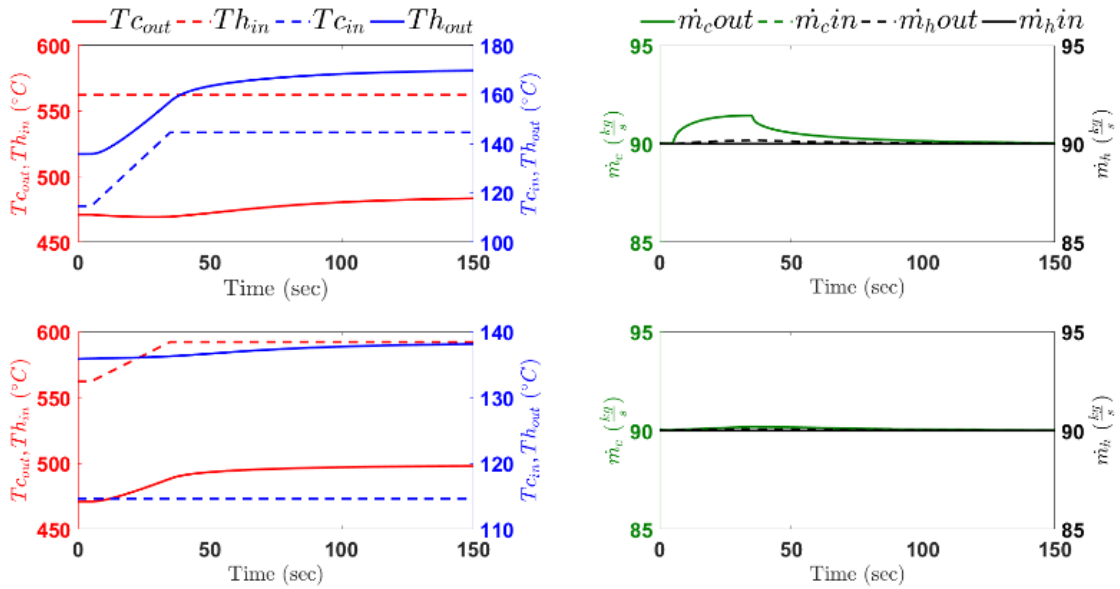

Figure 9-7 Response of the recuperator for a faster ramp in the cold inlet temperature (top) and hot inlet temperature (bottom)

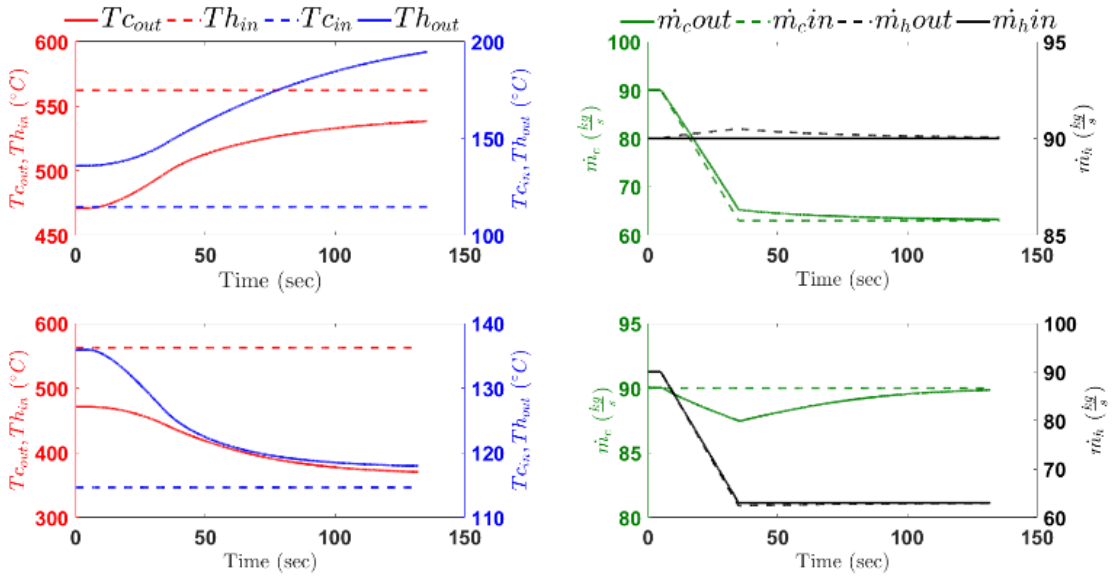

Figure 9-8 Response of recuperator for a faster ramp in the cold inlet mass flow rate (top) and hot inlet mass flow rate

9.4.5 Temperature Based Scheme

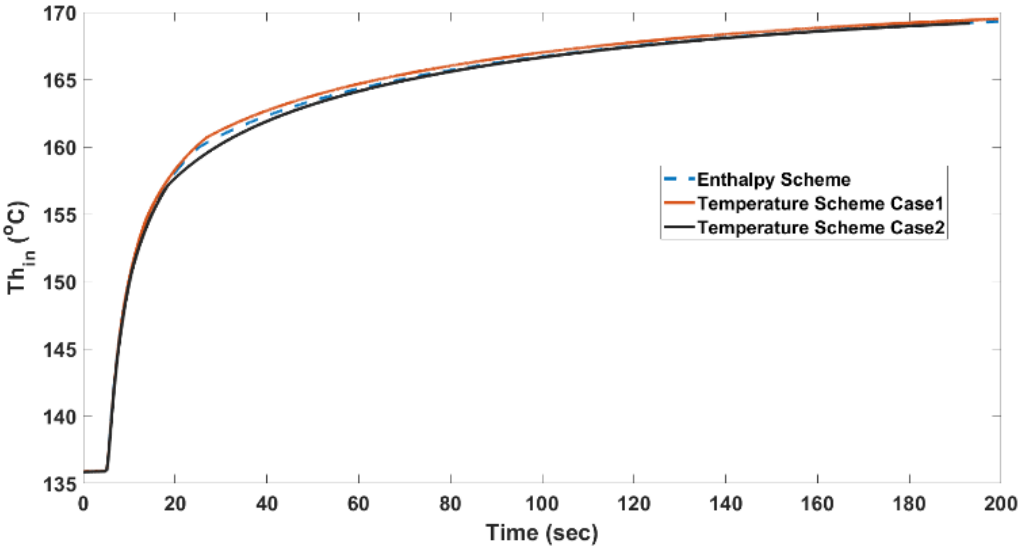

Figure 9-9 Comparison of temperature based scheme with enthalpy based scheme for a 30 °C step response in the cold inlet

Temperature based scheme is tested against the enthalpy based scheme and for two different grid sizes: 1) 400 nodes (Case 1), 2) 600 nodes (Case 2). The CFL=1 condition is enforced for all the simulations to have consistency and the results are plotted in Figure 9-9. Increasing the grid size matches the steady-state solution of the enthalpy scheme that used 400 nodes. From the results, it is clear that the performance of temperature based scheme with backward differencing scheme approximately matches the performance of enthalpy based scheme for this heat exchanger boundary conditions. However, the temperature based scheme requires higher nodes in order to get a similar performance of enthalpy scheme, in view of matching steady-state solution. Furthermore, this observation cannot be generalised as the significance of the pressure term on the energy equation is higher close to the critical point, therefore, this method can be applied for higher temperatures where ideal gas assumption is valid.

9.4.6 Validation with Experimental Data

The enthalpy based scheme is validated against the experimental data provided in Clementoni et al. [18] for down power from 30 kWe to 5 kWe scenario. It has to be noted that the pressure in the cold stream drops from 129.7 bar to 118.5

bar whilst the hot stream pressure drop by 0.5 bar during the power down scenario. Jiang et al. [7] validated the heat exchanger transient code developed in Aspen Plus Dynamics, a commercial software, against the up power data provided in Clementoni and the study reported that the cold stream temperature was off by roughly 5 °C from the experimental data. A wall thickness of 0.63 mm was reported in Jiang et al. [7] and the same is assumed in this study.

Tang et al. [13] validated the recuperator numerical code developed in NPSS against the down power data reported in Clementoni et al. [18]. However, the pressure trend as the function of time was not specified in Clementoni work, particularly for the cold stream as the steady-state pressure change is around 11.2 bar. During the power down scenario, the mass flow rate reduces and the cold inlet temperature reduces as shown in Figure 9-10. They both aid in increasing the cold stream outlet temperature. However, the experimental results reported in Clementoni et al. shows a sudden dip in cold outlet temperature at 50s. Tang et al. [13] showed that the sudden drop in cold outlet temperature at time 50s was due to the change in cold stream pressure (adiabatic expansion) and this can be computationally turned-off by controlling the pressure change and fluid inventory within the heat exchanger. Therefore, the change in the inlet pressure boundary condition is not applied (as the trend was not reported in Clementoni) for the purpose of validating the code.

From Figure 9-10, the simulation results agree with the measured cold outlet temperature without producing the temperature dip as explained in Tang et al. [13]. The maximum temperature difference between the model and experiment is about 2 °C which is lower than the error reported in Jiang et al. [7] i.e. 5 °C and roughly the same as Tang et al. [13] i.e. 2 °C.

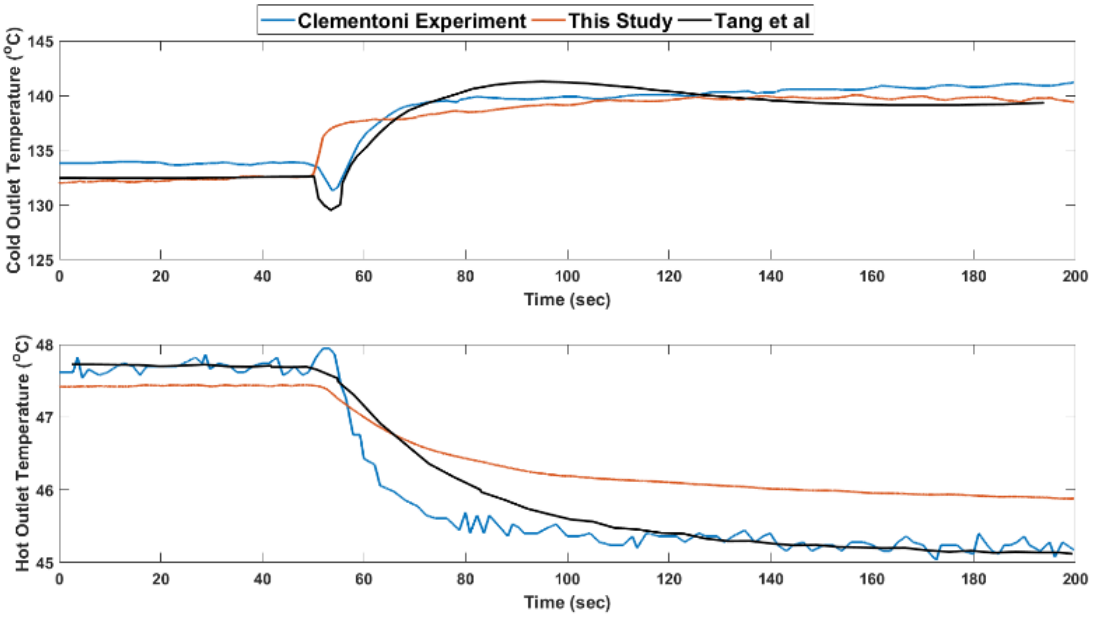

Figure 9-10 Transient response of cold outlet (top) and hot outlet (bottom) temperature

9.4.7 Logarithmic Property Tables Instead of REFPROP

The thermal-physical properties calculation routine (REFPROP) is replaced with the logarithmic indexed look-up table and the cold stream inlet temperature step response simulation was repeated. It is performed to compare the computational performance of using logarithmic indexed table against using REFPROP. The MATLAB code that uses REFPROP was parallelised (used 16 cores) whilst the look-up table approach is using one core. The maximum absolute difference of hot and cold stream outlet temperatures using the look-up table with reference to the REFPROP is lesser than 10^{-4} °C.

The look-up table approach was roughly 20% faster despite using a single core compared to parellised REFPROP code. Therefore, it is projected to have ~20 times speed by using the look-up table approach. The time saving using the look-up table is enhanced close to the critical point, where REFPROP requires more iterations to perform the properties calculations.

9.5 Conclusions

The numerical schemes for enthalpy and temperature based approaches are discussed and the numerical challenges are highlighted. The Crank-Nicolson

central differencing scheme shows numerical instability and the backward differencing or upwind schemes are observed to be stable even though the accuracy reduces from second to first order. The performance of temperature based scheme and enthalpy based schemes are compared and the temperature based schemes require more nodes to produce similar results as the enthalpy based code. Enthalpy scheme is recommended in order to avoid any ambiguity whereas temperature scheme can be applied where ideal gas assumption is valid. The numerical procedure of these two schemes is presented and validated with the literature data. Step response and the characteristic time of the recuperator for 10 MW_e sCO_2 cycle is presented. Compact heat exchangers response faster than conventional heat exchangers for changes in the inlet boundary conditions owing to less metal mass. The recuperator response quicker (<20 seconds) for the variation in the inlet temperatures compared to changes in the mass flow rate which takes roughly 0.5 to 1.5 minutes. A procedure to set-up the logarithmic indexed lookup table to calculate the thermal-physical properties without needing any iteration to find the constants are presented and the lookup table approach shows a promising reduction of the computation time.

9.6 References

[1] Crespi F, Gavagnin G, Sánchez D, Martínez GS. Supercritical carbon dioxide cycles for power generation: A review. Appl Energy 2017;195:152–83. https://doi.org/10.1016/j.apenergy.2017.02.048.

[2] Thanganadar D, Asfand F, Patchigolla K. Thermal performance and economic analysis of supercritical Carbon Dioxide cycles in combined cycle power plant. Appl Energy 2019;255. https://doi.org/10.1016/j.apenergy.2019.113836.

[3] Bennett J, Wilkes J, Allison T, Pelton R, Wygant K. Cycle modeling and optimization of an integrally geared sCO_2 compander. ASME Turbo Expo, Charlotte, NC, USA: 2017, p. 1–8. https://doi.org/10.1115/GT2017-63707.

[4] Ji C, Qin Z, Dubey S, Choo FH, Duan F. Three-dimensional transient numerical study on latent heat thermal storage for waste heat recovery from

a low temperature gas flow. Appl Energy 2017;205:1–12. https://doi.org/10.1016/j.apenergy.2017.07.101.

[5] Fornarelli F, Camporeale SM, Fortunato B. Convective Effects in a Latent Heat Thermal Energy Storage. Heat Transf Eng 2019;0:1–22. https://doi.org/10.1080/01457632.2019.1685240.

[6] Fornarelli F, Lippolis A, Oresta P. Buoyancy Effect on the Flow Pattern and the Thermal Performance of an Array of Circular Cylinders. J Heat Transfer 2016;139:1–10. https://doi.org/10.1115/1.4034794.

[7] Jiang Y, Liese E, Zitney SE, Bhattacharyya D. Design and dynamic modeling of printed circuit heat exchangers for supercritical carbon dioxide Brayton power cycles. Appl Energy 2018;231:1019–32. https://doi.org/10.1016/j.apenergy.2018.09.193.

[8] Marchionni M, Chai L, Bianchi G, Tassou SA. Numerical modelling and performance maps of a printed circuit heat exchanger for use as recuperator in supercritical CO 2 power cycles. Energy Procedia 2019;161:472–9. https://doi.org/10.1016/j.egypro.2019.02.068.

[9] Deshmukh A, Kapat J, Khadse A. Transient thermodynamic modeling of air cooler in supercritical CO2 Brayton cycle for solar molten salt application. Proc ASME Turbo Expo 2019;9:1–12. https://doi.org/10.1115/GT2019-91409.

[10] Chen M, Sun X, Christensen RN, Shi S, Skavdahl I, Utgikar V, et al. Experimental and numerical study of a printed circuit heat exchanger. Ann Nucl Energy 2016;97:221–31. https://doi.org/10.1016/j.anucene.2016.07.010.

[11] Carstens N. Control strategies for supercritical carbon dioxide power conversion systems. Massachusetts Institute of Technology, 2007.

[12] Kao S-P, Gibbs J, Hejzlar P. Dynamic Simulation and Control of a Supercritical CO 2 Power Conversion System for Small Light Water Reactor Applications. Design 2009.

[13] Tang C-J, Hofer D, Mcclung A, Megan Huang. Transient modeling of 10 MW supercritical CO_2 Brayton power cycles using Numerical Propulsion System Simulation (NPSS). ASME Turbo Expo 2019, 2019, p. 1–10.

[14] Zhao Q, Mecheri M, Neveux T, Privat R, Jaubert JN. Selection of a Proper Equation of State for the Modeling of a Supercritical CO_2 Brayton Cycle: Consequences on the Process Design. Ind Eng Chem Res 2017;56:6841–53. https://doi.org/10.1021/acs.iecr.7b00917.

[15] Camporeale SM, Fortunato B, Dumas A. Dynamic modelling of recuperative gas turbines. Proc Inst Mech Eng Part A J Power Energy 2000;214:213–25. https://doi.org/10.1243/0957650001538317.

[16] Camporeale SM, Fortunato B, Dumas A. Dynamic modeling and control of regenerative gas turbines. Proc ASME Turbo Expo 1998;5. https://doi.org/10.1115/98-GT-172.

[17] London AL, Biancardi FR, Mitchell JW. The Transient Response of Gas-Turbine-Plant Heat Exchangers—Regenerators, Intercoolers, Precoolers, and Ducting. J Eng Power 1959;81:433. https://doi.org/10.1115/1.4008112.

[18] Clementoni EM, Cox TL, King MA. Response of a compact recuperator to thermal transients in a supercritical carbon dioxide Brayton cycle. ASME Turbo Expo 2017:1–11. https://doi.org/10.1115/GT2017-63058.

[19] Kim IH, Zhang X, Christensen R, Sun X. Design study and cost assessment of straight, zigzag, S-shape, and OSF PCHEs for a FLiNaK–SCO2Secondary Heat Exchanger in FHRs. Ann Nucl Energy 2016;94:129–37. https://doi.org/10.1016/j.anucene.2016.02.031.

[20] Patankar S V. Numerical heat transfer and fluid flow 1980. https://doi.org/10.13182/nse81-a20112.

[21] Gao C, Zhang B. Development of A Transient Analysis Code for S-CO 2 Power Conversion System. 6th Int Symp - Supercrit CO2 Power Cycles 2018.

[22] Carstens NA. Control strategies for supercritical carbon dioxide power conversion systems. Massachusetts Institute of Technology, 2007.

[23] Nestell, J, Sham TL. ASME Code Considerations for the Compact Heat Exchanger. 2015.

Chapter 10

10 Overall Discussion

sCO_2 cycles are being investigated for various heat sources including waste heat recovery, fossil-fuel, CSP, nuclear, biomass owing to their potential in achieving higher efficiency with a compact footprint (by tenfold), thus reducing the cost. The potential of sCO_2 cycles for three heat sources namely natural gas, coal-fired power plant and CSP applications are investigated in this thesis through a techno-economic study with detailed exploration of off-design performance. The recompression cycle studied mostly for different applications owing to their higher efficiency; however, this project demonstrates that the cycle design has to be adapted depending on the type of heat source. For instance, cascade cycles show attractive performance for bottoming cycle applications (Chapter 3), whereas the novel cycle configurations proposed for the coal-fired plant (Chapter 5) combine the features of cascade, partial cooling and recompression cycles. On the other hand, the novel cycle configurations proposed for CSP plants (Chapter 6) reduce the capital cost, particularly when integrated with a sensible heat storage system.

An initial design study (Chapter 3) was performed using Thermoflex®, a commercial process simulation platform. Accurate thermal physical properties calculation for sCO_2 using REFPROP® is computationally heavy owing to the high nonlinear variation in the vicinity around the critical point. Cycle optimisation requires exploring tens of thousands of configurations to identify the optimal layout and parameters. For example, optimisation of 10 variables using genetic algorithm (GA) would require 10 × (1+20) × 20= 4200 simulations where the number of generations and population are 20 times the number of variables. If the process simulation code takes 60 seconds to run one simulation, then this is equivalent to 72 hours of simulation using a single core machine. The simulation time of the process model depends on many factors such as the number of components, number of tear streams, initial guess and the computational speed

of properties calculation. As the number of recycling streams increases in the process model (i.e. increasing the tear stream, say “n”), the simulation time increases nonlinearly as the size of the Jacobian matrix (n × n) in the nonlinear Newton Raphson solver.

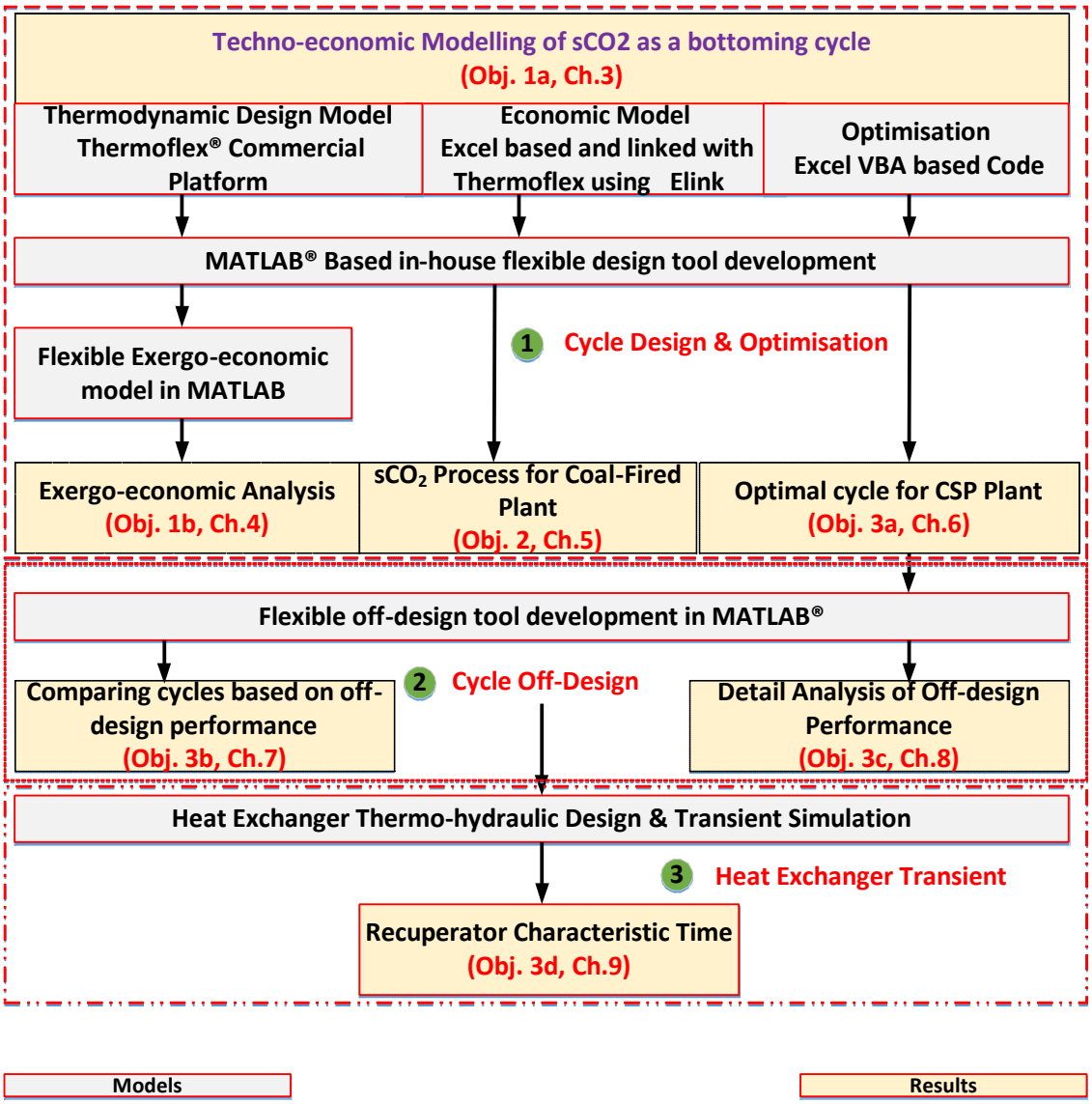

Figure 10-1 Flow of logic connecting all chapters in the thesis

It was observed that Thermoflex model produced in Cycle 5 (Chapter 3), takes about ~2-3 minutes per simulation, which made the optimisation task as computationally heavy. Therefore, it was essential to develop a flexible in-house code that can model any desired cycle configurations in order to explore the

design space for various heat sources. The code shall also be able to utilise multiple-cores (i.e. parallelisation) to decrease the simulation time required.

The degree of flexibility in defining the user-defined compressor maps for off-design performance evaluation can be cumbersome in Thermoflex®. Therefore, the off-design model was also developed and integrated with the in-house design code to identify the optimal control strategy, utilising a higher number of computer cores opted in this project. Figure 10-1 shows the logical connection between all the chapters' in-terms of model development and different heat sources. The design models were developed in MATLAB®, which are used to perform the techno-economic study for all the three heat sources by integrating the respective economic models. Component design and off-design models were implemented to the MATLAB® named as sCO_2 toolbox, and the off-design performance of different cycle configurations was compared. Finally, the one-dimensional heat exchanger thermal-hydraulic design and transient model was added to the MATLAB®.

10.1 Cycle Design Performance

10.1.1 Combined cycle power plant

Chapter 3 compares the performance of five different cascade cycle configurations for bottoming cycle applications, including one novel cycle configuration using Thermoflex® commercial software. Cascade cycles are preferred as the flue gas to be cooled down to the minimum stack temperature (~70 °C), which discards cycles with higher internal heat circulation, i.e. higher recuperation owing to their lower heat addition temperature range (ΔT). Integration of lower ΔT cycle would demand additional third power cycle to utilise the low-temperature heat [1].

Thermodynamic process models were developed and included in the sCO_2 toolbox, and validated/verified using the literature data. The exergo-economic model developed in the sCO_2 toolbox that was used to analyse the exergo-economic performance of sCO_2 cycle for bottoming cycle applications integrated with two commercial gas turbines for the first time (Chapter 4).

10.1.2 Coal-fired power plant

Unlike the bottoming cycle, the coal-fired power plants have a minimum heat recirculation via air preheater (APH) and the amount of this heat is limited by the maximum allowable flue gas temperature limit to APH. Therefore, cycle configurations which combine the features of the partial cooling cycle and recompression cycle have been integrated with the cascade cycle and the optimisation algorithm decides the flow fractions to each of them with the objective of maximising the efficiency (Chapter 5). The sCO_2 cycle component codes developed for simulating bottoming cycle (Section 1.1.1) was modified to model the coal-fired plants and the missing components such as boiler and APH were added. The power cycle code developed under this toolbox was flexible to integrate any configurations or heat sources.

10.1.3 CSP Plant integrated with Sensible heat storage

CSP plants is regarded as constant flux heat source like nuclear plants, therefore, power cycles with higher amount of recuperation (internal heat recirculation) is advantageous for increasing the efficiency. However, increasing the internal heat recirculation also reduces the specific power of the power cycle which would lead to a higher capital cost. Therefore, these highly recuperative cycles is attractive particularly when the cost reduction due to the increased efficiency is higher than the increased power block cost. The cost of the solar field and thermal energy storage (TES) shares a bigger contribution in the overall capital cost of the CSP plant whilst the cost of the power cycle is about ~10-20%, which makes high recuperative cycles more attractive. However, integration of sensible heat storage demands to have a fixed temperature difference between hot and cold storage tank in order to minimise the capital cost of the solar field and TES for a given set of cost functions, receiver outlet temperature, ambient temperatures and Carnot factor (more details given in Chapter 6). Therefore, the highest internal heat recirculation cycle configurations such as double recompression wouldn’t yield a lower plant capital cost. It was not clear which cycle configurations can achieve the lowest capital cost, therefore nine sCO_2 cycle configurations including two novel configurations were investigated (Chapter 6).

The sCO_2 cycle component codes developed in Section 10.1.1 was utilised to model all the nine cycle configurations. The sizing and cost estimation methodology of the solar field and storage was added as part of this task.

Comparing all the three types of heat source, it is clear that one cycle configuration cannot offer superior performance for all the heat sources. Each heat source has its own set of unique requirements, therefore, the cycle configurations must be adapted to yield maximum performance.

10.2 Off-design performance

CSP plants encounter a large variation in boundary conditions such as solar irradiation and ambient temperature. Capital cost contributes primarily to the overall levelised cost of electricity (LCOE) for a CSP plant. However, for a given site location where the annual solar irradiation, ambient temperature and dispatch profile are fixed, different power cycles would yield different capacity factors, affecting the LCOE dissimilarly. This is mainly because sCO_2 Brayton cycles are more sensitive to the boundary conditions (ambient temperature and heat input), and one cycle configuration is more sensitive than others. In order to understand this effect, the off-design performance Pareto fronts of three sCO_2 cycle configurations were compared in Chapter 7. The compressor and turbine performance maps are critical for this study and typically a 1D meanline with empirical loss models, 2D streamline and 3D CFD simulations are required in order to develop the turbomachinery performance maps. Since the purpose of this study is to compare the relative performance difference between different cycles, the performance map scaling methodology proposed by Dyreby et al. [2] was implemented, which empirically scales the turbomachinery maps of Sandia sCO_2 test facility. The conductance scaling method is applied to evaluate the off-design performance of heat exchanger.

In order to realise the optimal control strategy, a detailed off-design performance study was carried-out for recompression cycle as an example (Chapter 8), and this optimisation methodology has been applied to analyse the off-design performance for any cycle configuration. The objective is to quantify the sensitivity

of the cycle performance for variation in boundary conditions in order to develop the optimal control scheme. Therefore, off-design component models were developed in sCO_2 toolbox and integrated with the optimisation algorithm.

10.3 Compact heat exchanger

One of the requirements of the next-generation power plants is operational flexibility and higher plant ramp rate. The ramp rate of sCO_2 cycles is mainly controlled by the response time of the heat exchanger as the volume of the turbomachinery is often negligible. Since the heat duty of the recuperators is higher in the sCO_2 cycles, compact heat exchangers is an attractive option that would facilitate faster ramp rate owing to the reduced thermal mass. In order to quantify the characteristic time of the heat exchanger, a one-dimensional transient heat exchanger model was developed and numerically solved in MATLAB®. The recuperator of a $10MW_e$ simple recuperative cycle is chosen for this study. The temperature based equations can introduce significant error around the critical point as the pressure dependency to the energy equation is higher. Therefore, enthalpy based equations are considered to eliminate any ambiguity. The response time is less than 20 seconds for step changes in temperature whereas it takes up to 1.5 minutes for a step change in mass flow rate, and they are significantly lower than shell-tube heat exchanger [3]. The detail numerical procedure is explained in Chapter 9.

10.4 Uncertainty of the Economic Model

The uncertainty of the cost functions is often larger and this is particularly crucial for low technology readiness level (TRL) technologies, like sCO_2 cycle. Since only a handful of small-scale pilot plant exists, no reliable cost functions for all the components are available. There are some improved cost functions [4] which have been published during the course of this PhD, and they were implemented into the in-house code as they became available. This resulted in the usage of different cost functions for different heat sources to estimate the sCO_2 cycle component cost. To mitigate, a Monte-Carlo uncertainty simulation is performed

and the LCOE for different confidence interval is reported to minimise the financial risk.

10.5 References

[1] Mohammadi K, Ellingwood K, Powell K. A novel triple power cycle featuring a gas turbine cycle with supercritical carbon dioxide and organic Rankine cycles: Thermoeconomic analysis and optimization. Energy Convers Manag 2020;220:113123. doi:10.1016/j.enconman.2020.113123.

[2] Dyreby JJ. Modeling the Supercritical Carbon Dioxide Brayton Cycle with Recompression. 2014.

[3] Jiang Y, Liese E, Zitney SE, Bhattacharyya D. Design and dynamic modeling of printed circuit heat exchangers for supercritical carbon dioxide Brayton power cycles. Appl Energy 2018;231:1019–32. doi:10.1016/j.apenergy.2018.09.193.

[4] Weiland NT, Lance BW, Pidaparti SR. SCO_2 power cycle component cost correlations from DOE data spanning multiple scales and applications. Proc. ASME Turbo Expo, vol. 9, 2019, p. 1–17. doi:10.1115/GT2019-90493.

Chapter 11

11 Conclusions and Recommendations

This PhD thesis analyses the techno-economic performance of integrating sCO_2 cycles with three different heat sources including natural gas, coal-fired and concentrated solar power (CSP) with sensible heat thermal storage. Different novel cycle configurations have been proposed for each of these applications and this study clearly emphasises that the sCO_2 cycle configuration changes depending on the type of heat source. In a nutshell, the cycle has to combine the features of recompression or partial cooling cycle with cascade cycle configurations (with or without low temperature turbine), in order to control the amount of internal heat recirculation (i.e. recuperation) depending on the heat source. The developed flexible in-house in MATLAB® can be used for evaluation of design and off-design performance of any cycle configurations integrated with a heat source. The code also comprises of a heat exchanger thermal-hydraulic design module and a one dimensional (1D) transient heat exchanger module.

11.1 Summary of the Novelty

This study identified novel cycle configurations for all the three heat sources namely natural gas, coal-fired and concentrated solar power plant integrated with sensible heat thermal storage, and the improvements in techno-economic performances are discussed here.

11.1.1 Combined cycle power plant

Research Question (Obj. 1a): *What is the potential techno-economic performance?*

1.4%pts for bottoming cycle applications when using cascade cycle compared to triple-pressure steam Rankine cycle for SGT5-4000F machine. The optimal pressure ratio of the topping cycle is higher when integrating the sCO_2 cycle compared to an equivalent stream Rankine cycle. For instance, the optimal

topping cycle pressure ratio of SGT5-4000F when integrated with the triple-pressure steam Rankine cycle is 17.6 whilst it's increased to about 20-26 depending on the sCO_2 cycle configuration. Furthermore, the optimal pressure ratio increases with increasing the gas turbine firing temperatures. Therefore, a set of performance maps for different cascade cycles have been produced, which aids in estimating the expected performance when integrating a sCO_2 cycle with a gas turbine for different pressure ratios and firing temperature.

Research Question (Obj. 1b): *Which component cost in the cycle is critical from exergo-economic perspective?*

The exergy destruction in the sCO_2 primary heater and recuperator are reduced when optimising the topping cycle pressure ratio. For SGT5 4000F machine, the exergy destruction in the sCO_2 primary heater is 22.7% which is reduced by 3.6%pts when optimising the gas turbine pressure ratio. The exergo-economic analysis on sCO_2 bottoming cycle identified that the recuperator cost is critical in reducing the plant cost when integrating cascade cycle as a bottoming cycle solution. The low-temperature recuperator has more weight than the high-temperature recuperator owing to its higher total cost rate for the gas turbines investigated (i.e. total cost rate of HTR of SGT5 4000F machine is 57.7% lower than LTR).

11.1.2 Coal-fired power plant

Research Question (Obj. 2): *What is the improvement in the thermal and economic performance of sCO_2 cycle for coal plants compared with National Energy Technology Laboratory (NETL) baseline steam Rankine cycles?*

The plant efficiency has increased by 3-4%pts for coal-fired plants compared to NETL- B12A steam Rankine cycle. This increased efficiency leads to a reduction in cost of electricity (COE) by about 6-8% albeit within the uncertainty bounds of the component cost functions. A further increase of 3-4%pts is achieved by increasing the TIT from 620 °C to 760 °C. Despite an increase in efficiency at a higher TIT (from 620 °C to 760 °C) the COE reduction potential is reduced for the cost functions considered.

11.1.3 CSP plant integrated with sensible heat storage

Research Question (Obj. 3a): *What is the optimal sCO_2 cycle configuration and what is the potential improvements in techno-economic performance?*

sCO_2 cycle for concentrated solar plant efficiency is about 49.3% for a TIT of 600 °C and CIT of 32 °C whereas the efficiency of the steam Rankine cycle is 45.5% for the same TIT. sCO_2 cycle efficiency increased to 53.5% when the TIT is 700 °C whereas it is about 46.4%, which is equivalent to 7.1%pts increase. The optimal configuration increases the power cycle efficiency by 3.8-7%pts compared to steam Rankine cycles.

The proposed novel cycle configuration reduces the capital cost of a CSP plant by 10.8% compared to the recompression cycle. The capital cost of CSP plants are about 4200-5000 $/kWe (TIT of 600 °C and CIT of 32 °C) which was approximately 12-26% lower than steam Rankine cycles (i.e. 5700 $/kWe). This makes sCO_2 cycles more attractive for CSP applications, where higher efficiency reduces the plant cost significantly by reducing the solar field and thermal energy storage cost. However, the capital cost increases at higher TITs owing to the increased material cost.

Research Question (Obj. 3b): *How different sCO_2 cycle configurations compare based on off-design performance?*

At higher ambient temperatures, the sCO_2 cycle efficiency, power output and the thermal energy storage capacity reduces. The reduction of the storage capacity was due to increase in the molten salt outlet temperature from the power block. For instance, the storage capacity of the recompression cycle reduces by 25% for a 13 °C increase in the CIT (design CIT=42 °C) when maximising the sCO_2 cycle efficiency. On the other hand, the partial cooling cycle achieved relatively higher power output at higher ambient temperatures compared to equivalent recompression cycle when maximising the power output (i.e., 14.3% increased power for a 13 °C increase in CIT from its design value). Furthermore, the recompression cycle storage capacity is reduced by 10.6% due to the 3.8% increase of molten salt outlet temperature from the power block. Contrariwise, the

molten salt outlet temperature for partial cooling cycle when maximising the power output is lowered by 2% than its design value. Therefore, the partial cooling cycle achieves a higher capacity factor than recompression cycle when the hours of hot ambient temperatures are higher for any given location, reducing the levelised cost of electricity (LCOE).

Research Question (Obj. 3c): *What are the operational challenges of sCO_2 cycle and their influence on sensible heat storage system?*

The inventory control showed higher efficiency at part load for both recompression and partial cooling cycle. The compressor inlet pressure tends to increase during higher CIT operation in order to minimise the change in density with reference to the design value. The split fraction also reduces at a higher CIT for recompression cycle whilst it doesn't need to be controlled for changes in heat input to the power cycle up to ~70% of the design value.

In a CSP plant with thermal energy storage, the power cycle can either be operated in maximum power mode or maximum efficiency mode by controlling the amount of heat supplied to the power cycle, whilst storing the remaining heat from the solar field. Annual simulation concluded that operating the power cycle in the maximum power mode increases the capacity factor by about 10-20% whereas maximum efficiency mode operation reduces the number of start-ups by up to 50%. This implies that the optimal operating strategy could therefore could be a combination of maximising efficiency and net power according to prevailing ambient conditions.

Research Question (Obj. 3d): *Can the recuperator transient response be improved using compact heat exchangers?*

Heat exchanger thermo-hydraulic design and transient models informed that compact heat exchanger aids in achieving faster plant ramp rates owing to their low first-order characteristic time. The compact heat exchanger responded with in 20 seconds for a step-change in the inlet temperatures whereas it took up to 1.5 minutes for a step-change in the mass flow rate.

11.2 Recommendations for Future Work

It is always the case when wrapping up a long research work that one would wish to perform a considerable number of research activities which could advance the technology boundary further and enrich the reliability of the results. This section summarises the future areas that deserve research attention based on the author genuine standpoint.

Alternative Application:

1) Development of simple sCO_2 cycle configuration for low-temperature industrial waste heat recovery applications (<350 °C), as the scope in this scope is abundant. The sCO_2 cycles should be economically viable in comparison to their competitive organic Rankine cycle or Kalina cycle.

Coal and Combined cycle Power Plant:

1) Direct firing cycles integrated with carbon capture technologies shall be studied in detail such as Allam cycle.

Concentrated Solar Power Plant:

1) Although CSP plants benefit from larger internal heat recirculation or achieving higher efficiency, the sensible heat storage component counteracts and forces to have a higher temperature difference between hot and cold storage tank. Therefore, phase change material-based storage is expected to reduce the capital cost as the both the PCM and power cycle favours smaller heat addition temperature difference (Refer Chapter 6 for more details). Cascaded phase change material system will benefit to minimise the exergy loss over the temperature raise.
2) Open literature suggests that sCO_2 cycles can be cost-effective above 30MWe (unlike steam plant). Due to the compact footprint, the power cycle components can be placed on the central tower at different elevations, reducing the high-temperature piping length.
3) Transcritical CO_2 cycles showed competitive economic performance for CSP application. Therefore, the performance of condensed CO_2 Rankine has to be investigated and the addition of different blends to increase the critical

temperature can aid in installing the plant at hot ambient conditions. The binary vapour-liquid equilibrium curves of potential blends mixed with CO_2 has to be generated through experiments.

Process Modelling:

1) Compressor, turbine meanline codes shall be integrated with the process modelling tool so that a robust optimisation can be performed. The turbomachinery efficiencies are sensitive to the process parameters and plant size, which can be captured by the implementation of meanline code (loss models). This produces a more reliable solution compared to the solutions obtained by assuming constant isentropic efficiency.
2) Since the cycle development and optimisation is computationally expensive owing to the thermal physical fluid property library (REFPROP), the usage of deep neural network or machine learning can aid in increasing the computational performance, such as machine learning-based surrogate model.
3) Integrate the transient heat exchanger code with the plant level code so that transient characteristics including load ramp rate, start-up, shut-down and emergency load throw-off can be simulated of any plant configurations. This informs the expected thermal stress on the material which is essential for designing the plant components. In addition, reliable plant controls can be developed and the simulator platform can be used for operator training.

Appendix A Optimal ΔT- Sensitivity Study (Chapter 6)

A.1 Effect of Lorenz Factor

The Lorenz factor can change the optimal heat addition ΔT and Figure_Apx A-1 shows these changes in the optimal heat addition ΔT for different Lorenz factor and CIT for two different TIT's. A changes in Lorenz factor from 0.6 to 0.9 together with a change in CIT from 32 to 55 °C can change the optimal heat addition ΔT by about ±20 °C. The real plant efficiencies are most likely to fall within this range of Lorenz factor, consequently the optimal heat addition ΔT will be less affected by these factors. If the real power cycle heat addition ΔT matches with the optimal heat addition ΔT, then optimal integration of the power cycle with solar field and TES can be achieved.

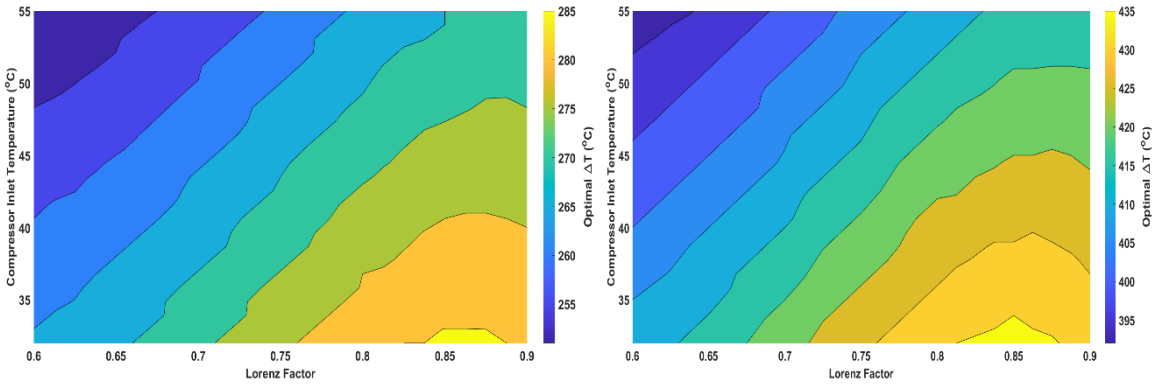

Figure_Apx A-1 Optimal Temperature Difference: Left) TIT -600 °C, Right) TIT 700 °C

A.2 Effect of Lorenz Factor

The component cost functions scale exponentially with the plant size and therefore it is expected that the optimal heat addition ΔT can vary depending on the plant size. Figure_Apx A-2 shows the unit cost of three different plant sizes (10, 50, 100 MW_e) and a 100 MW_e plant with SunShot component cost function. A solar multiple of 2.7 and TES storage hours of 14 is considered for the SunShot estimates [3]. The heliostat and site improvement cost of 75 and10 $/m^2 are considered for the SunShot plant [3] whilst the currently achieved costs i.e. 140 and 16 $/m^2, respectively are considered for the other three plant sizes. From

Figure_Apx A-2, it is clear that there is a significant reduction in the unit cost when the plant size increases from 10 to 50 MW_e whilst a smaller reduction is achieved when this increases to 100 MW_e.

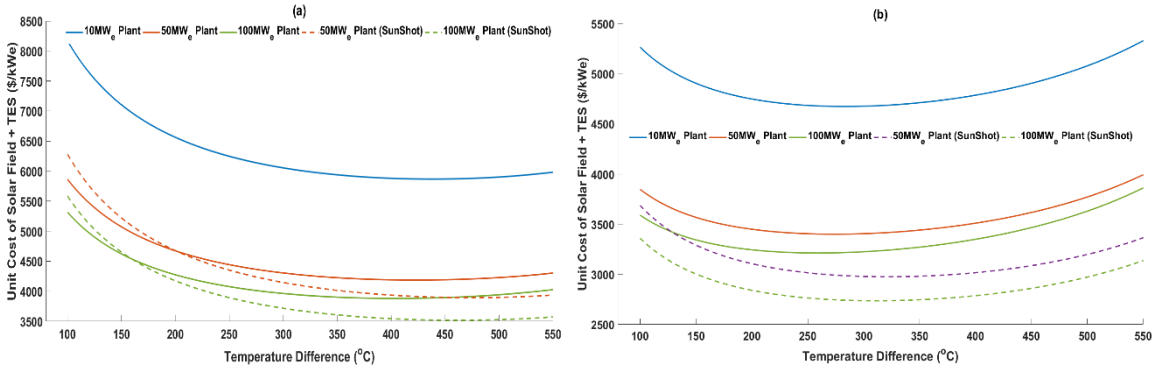

Figure_Apx A-2 Unit cost of solar field and TES for different plant (Lorenz factor =0.7) a) 700 °C TIT, b) 600 °C TIT

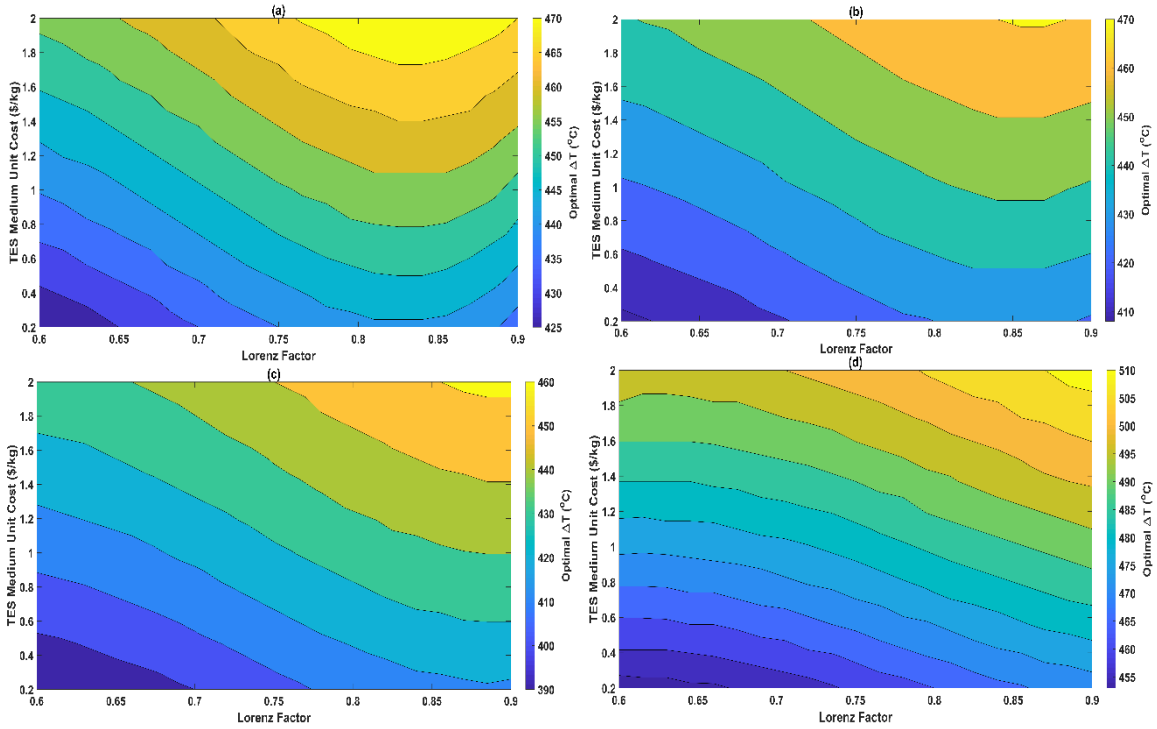

Figure_Apx A-3 Optimal Temperature Difference at 700 °C a) 10 MW_e plant output, b) 50 MW_e plant output, c) 100 MW_e plant output, (SM=2.4, TES Hours =10) d) 100 MW_e plant output with SunShot Targets (SM=2.7, TES Hours =14)

Figure_Apx A-3 and Figure_Apx A-4 show the optimal heat addition ΔT for the three different plant sizes and the SunShot plant when the Lorenz factor and

storage material cost varies. When the storage medium unit price changes from 0.3 to 2 $/kg together with the changes in the Lorenz factor from 0.6 to 0.9, the optimum heat addition ΔT changes by about ±20, ±30, ±35°C for 10, 50 and 100 MW_e plant, respectively. For the SunShot cost functions, the optimal heat addition ΔT shifts about ±25 °C from the current 100 MW_e plant. This is because the SunShot targets implemented reduced the solar field cost without reducing the TES system cost, therefore higher heat addition ΔT is preferred to reduce the TES cost further. The degree of change in optimal heat addition ΔT increases with increasing Lorenz factor as increasing the cycle efficiency reduces the solar field cost, consequently the relative cost share of TES increases.

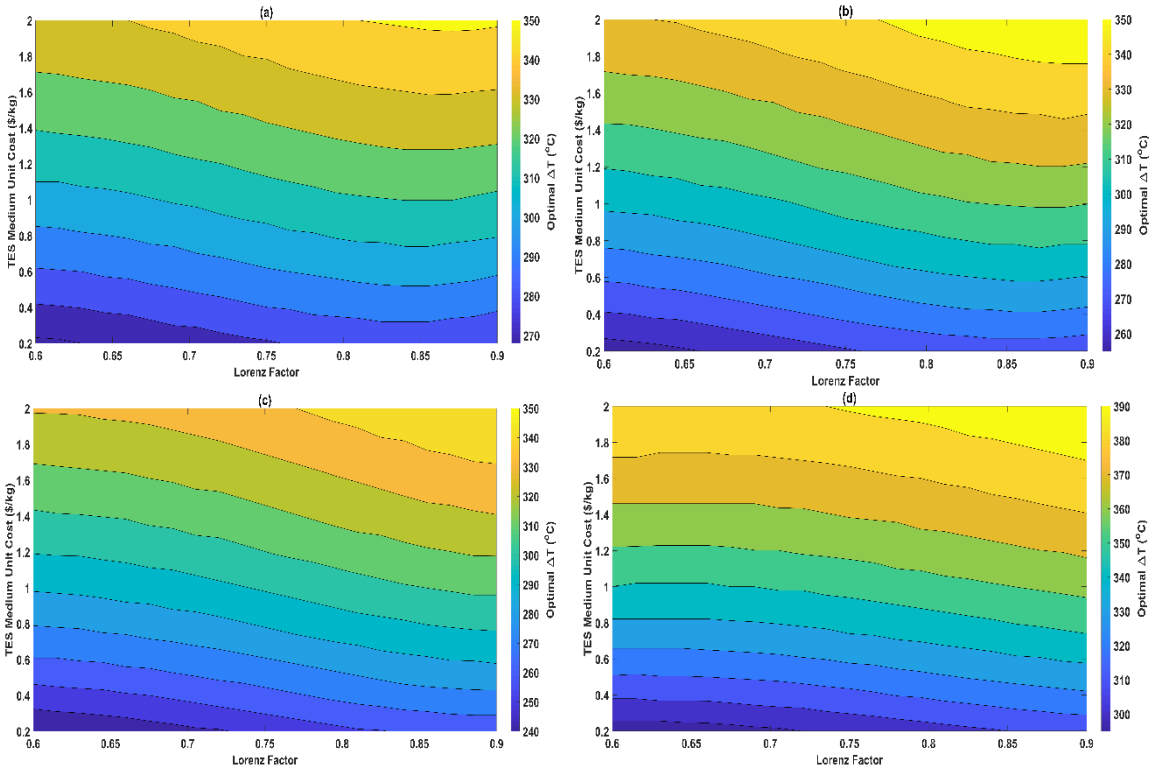

Figure_Apx A-4 Optimal Temperature Difference at 600 °C a) 10 MW_e plant output, b) 50 MW_e plant output, c) 100 MW_e plant output, (SM=2.4, TES Hours =10) d) 100 MW_e plant output with SunShot Targets (SM=2.7, TES Hours =14)

A.3 Effect of Lorenz Factor

Figure_Apx A-5 shows the changes in optimal heat addition ΔT for different TES storage hours and Lorenz factor for two different TITs. Increasing the TES

storage hours also increases the optimal heat addition ΔT significantly for both the TITs. This is because the solar multiple is kept constant during this simulation at 2.4. Ideally, changing the TES storage hours also requires a change to the solar multiple in order to increase the capacity factor of the plant. Therefore, in reality, the change in the optimal heat addition ΔT is expected to be lower as increasing the solar multiple also increases the cost share of the solar field relative to the TES. The optimal heat addition ΔT is lower for 600 °C TIT than 700 °C TIT as increasing the TIT also increases the cost share of the TES system relative to the solar field cost owing to the usage of high-temperature materials.

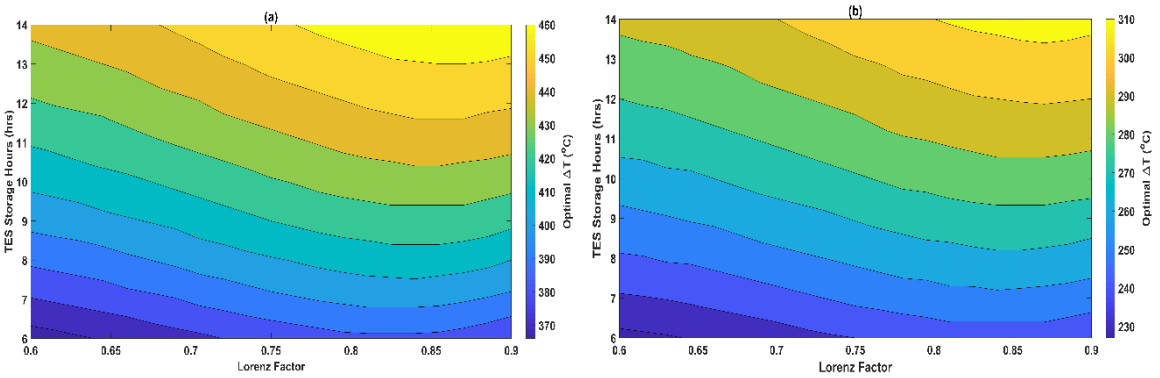

Figure_Apx A-5 Optimum Temperature Difference for a) Varying TES hours at 700 °C b) Varying TES hours at 600 °C, SM-2.4